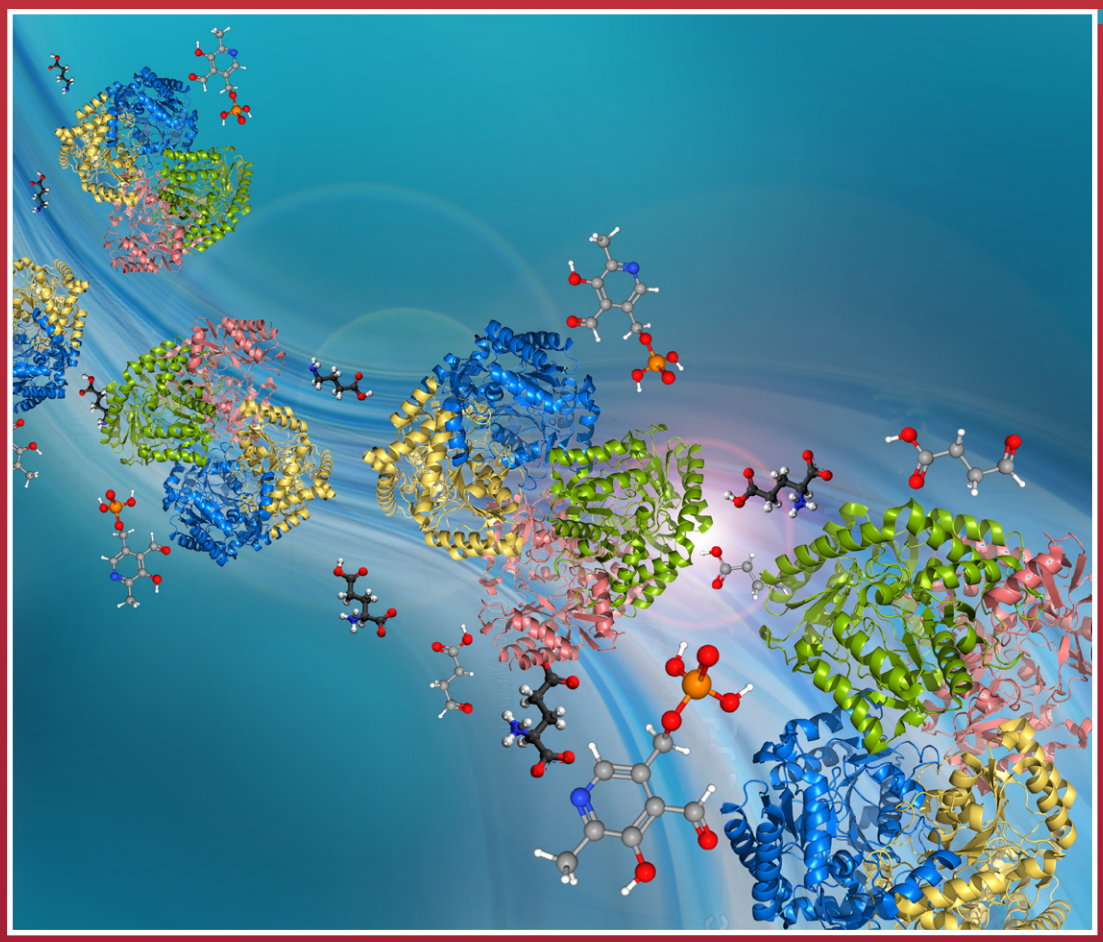
ISSN 1580-3155 Pages 1–246 ■ Year 2021, Vol. 68, No. 1

Slovensko kemijsko društvo
Slovenian Chemical Society

Acta Chimica Slovenica

1

68/2021



http://acta.chem-soc.si

EDITOR-IN-CHIEF

KSENIJA KOGEJ
University of Ljubjana, Facuty of Chemstry and Chemical Technology, Večna pot 113, SI-1000 Ljubljana, Slovenija
E-mail: ACSi@fkkt.uni-lj.si, Telephone: (+386)-1-479-8538

ASSOCIATE EDITORS

Alen Albreht, *National Institute of Chemistry, Slovenia*
Aleš Berlec, *Jožef Stefan Institute, Slovenia*
Janez Cerkovnik, *University of Ljubljana, Slovenia*
Mirela Dragomir, *Jožef Stefan Institute, Slovenia*
Ksenija Kogej, *University of Ljubljana, Slovenia*
Krištof Kranjc, *University of Ljubljana, Slovenia*
Matjaž Kristl, *University of Maribor, Slovenia*
Franc Perdih, *University of Ljubljana, Slovenia*
Aleš Podgornik, *University of Ljubljana, Slovenia*
Helena Prosen, *University of Ljubljana, Slovenia*
Irena Vovk, *National Institute of Chemistry, Slovenia*

ADMINISTRATIVE ASSISTANT

Marjana Gantar Albreht, *National Institute of Chemistry, Slovenia*

EDITORIAL BOARD

Wolfgang Buchberger, *Johannes Kepler University, Austria*
Alojz Demšar, *University of Ljubljana, Slovenia*
Stanislav Gobec, *University of Ljubljana, Slovenia*
Marko Goličnik, *University of Ljubljana, Slovenia*
Günter Grampp, *Graz University of Technology, Austria*
Wojciech Grochala, *University of Warsaw, Poland*
Danijel Kikelj, *University of Ljubljana*
Janez Košmrlj, *University of Ljubljana, Slovenia*
Blaž Likozar, *National Institute of Chemistry, Slovenia*
Mahesh K. Lakshman, *The City College and The City University of New York, USA*
Janez Mavri, *National Institute of Chemistry, Slovenia*
Friedrich Srienc, *University of Minnesota, USA*
Walter Steiner, *Graz University of Technology, Austria*
Jurij Svete, *University of Ljubljana, Slovenia*
Ivan Švancara, *University of Pardubice, Czech Republic*
Jiri Pinkas, *Masaryk University Brno, Czech Republic*
Gašper Tavčar, *Jožef Stefan Institute, Slovenia*
Christine Wandrey, *EPFL Lausanne, Switzerland*
Ennio Zangrando, *University of Trieste, Italy*

ADVISORY EDITORIAL BOARD

Chairman
Branko Stanovnik, Slovenia

Members
Udo A. Th. Brinkman, The Netherlands
Attilio Cesaro, Italy
Vida Hudnik, Slovenia
Venčeslav Kaučič, Slovenia
Željko Knez, Slovenia
Radovan Komel, Slovenia
Stane Pejovnik, Slovenia
Anton Perdih, Slovenia
Slavko Pečar, Slovenia
Andrej Petrič, Slovenia
Boris Pihlar, Slovenia
Milan Randić, Des Moines, USA
Jože Škerjanc, Slovenia
Miha Tišler, Slovenia
Đurđa Vasić-Rački, Croatia
Marjan Veber, Slovenia
Gorazd Vesnaver, Slovenia
Jure Zupan, Slovenia
Boris Žemva, Slovenia
Majda Žigon, Slovenia

Acta Chimica Slovenica is indexed in: *Academic Search Complete, Central & Eastern European Academic Source, Chemical Abstracts Plus, Chemical Engineering Collection (India), Chemistry Citation Index Expanded, Current Contents (Physical, Chemical and Earth Sciences), Digitalna knjižnica Slovenije (dLib.si), DOAJ, ISI Alerting Services, PubMed, Science Citation Index Expanded, SciFinder (CAS), Scopus and Web of Science.* Impact factor for 2019 is IF = 1.263.

Articles in this journal are published under the Creative Commons Attribution 4.0 International License

Izdaja – Published by:
SLOVENSKO KEMIJSKO DRUŠTVO – SLOVENIAN CHEMICAL SOCIETY
Naslov redakcije in uprave – Address of the Editorial Board and Administration
Hajdrihova 19, SI-1000 Ljubljana, Slovenija
Tel.: (+386)-1-476-0252; Fax: (+386)-1-476-0300; E-mail: chem.soc@ki.si

Slovensko kemijsko društvo
Slovenian Chemical Society

Izdajanje sofinancirajo – Financially supported by:
National Institute of Chemistry, Ljubljana, Slovenia
Jožef Stefan Institute, Ljubljana, Slovenia
Faculty of Chemistry and Chemical Technology, University of Ljubljana, Slovenia
Faculty of Chemistry and Chemical Engineering, University of Maribor, Slovenia

Acta Chimica Slovenica izhaja štirikrat letno v elektronski obliki na spletni strani http://*acta.chem-soc.si*. V primeru posvečenih številk izhaja revija tudi v tiskani obliki v omejenem številu izvodov.

Acta Chimica Slovenica appears quarterly in electronic form on the web site *http://acta.chem-soc.si*. In case of dedicated issues, a limited number of printed copies are issued as well.

Transakcijski račun: 02053-0013322846 Bank Account No.: SI56020530013322846-Nova Ljubljanska banka d. d., Trg republike 2, SI-1520 Ljubljana, Slovenia, SWIFT Code: LJBA SI 2X

Oblikovanje ovitka – Design cover: KULT, oblikovalski studio, Simon KAJTNA, s. p. Grafična priprava za tisk: OSITO, Laura Jankovič, s.p.

Graphical Contents



Acta Chimica Slovenica

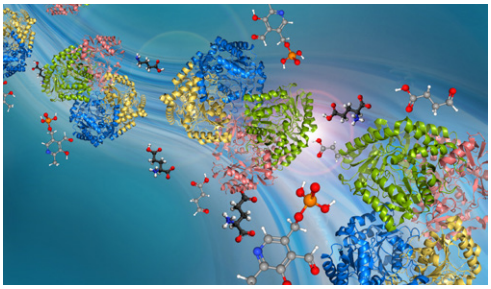
Year 2021, Vol. 68, No. 1

FEATURE ARTICLE

1–16 Feature Article

Let the Biocatalyst Flow

Polona Žnidaršič-Plazl

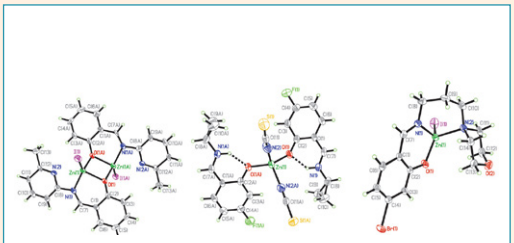


SCIENTIFIC PAPER

17–24 Inorganic chemistry

Zinc(II) Complexes Derived from Schiff Bases: Syntheses, Structures, and Biological Activity

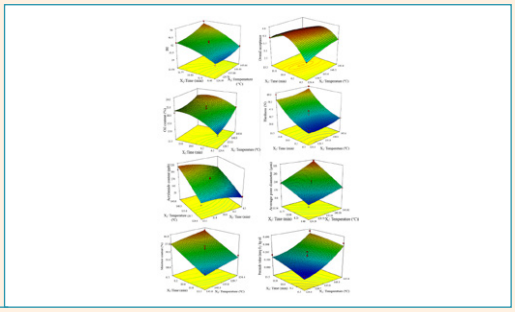
Ling-Wei Xue, Xu Fu, Gan-Qing Zhao and Qing-Bin Li



25–36 Chemical, biochemical and environmental engineering

Effect of Vacuum Frying Conditions on Quality of French Fries and Frying Oil

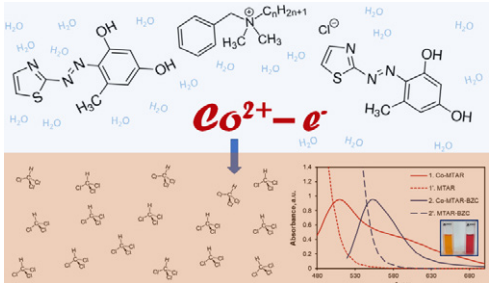
Esra Devseren, Dilara Okut, Mehmet Koç, Özgül Özdestan Ocak, Haluk Karataş and Figen Kaymak-Ertekin



37–43 Inorganic chemistry

Extraction-Chromogenic System for Cobalt Based on 5-Methyl-4-(2-thiazolylazo)Resorcinol and Benzalkonium Chloride

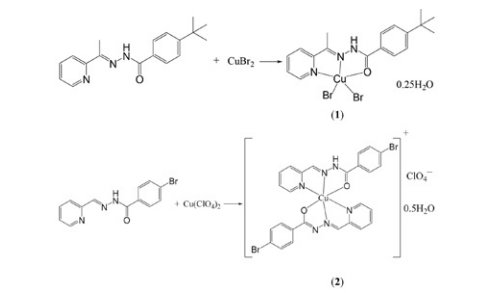
Danail G. Georgiev Hristov, Petya Vassileva Racheva, Galya Konstantinova Toncheva and Kiril Blazhev Gavazov



44–50 Inorganic chemistry

Synthesis, Crystal Structures, Characterization and Catalytic Property of Copper(II) Complexes Derived from Hydrazone Ligands

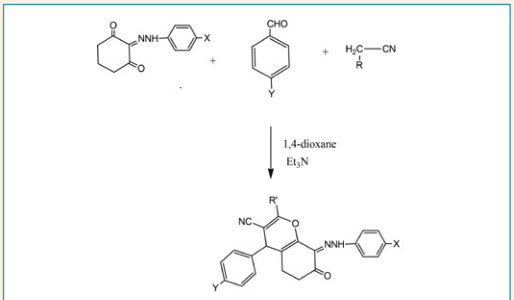
Yao Tan and Yan Lei



51–64 Organic chemistry

Multi-component Reactions of Cyclohexan-1,3-diketones to Produce Fused Pyran Derivatives with Antiproliferative Activities and Tyrosine Kinases and Pim-1 Kinase Inhibitions

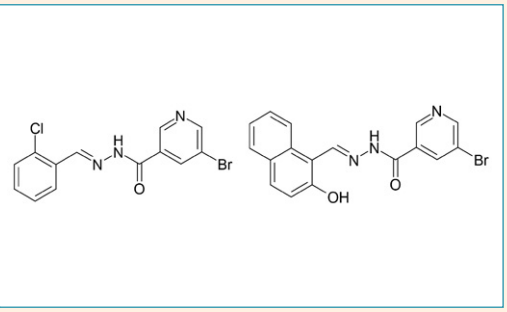
Rafat Milad Mohareb, Rehab Ali Ibrahim and Ensaf Sultan Alwan



65–71 Organic chemistry

6-Bromo-2'-(2-chlorobenzylidene)nicotinohydrazide and 6-Bromo-2'-(3-bromo-5-chloro-2-hydroxybenzylidene)nicotinohydrazide Methanol Solvate: Synthesis, Characterization, Crystal ...

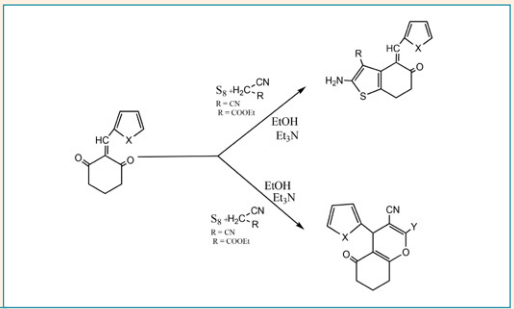
Hai-Yun Zhu



72–87 Organic chemistry

New Approaches for the Synthesis of Heterocyclic Compounds Derived from Cyclohexan-1,3-dione with Anti-proliferative Activities

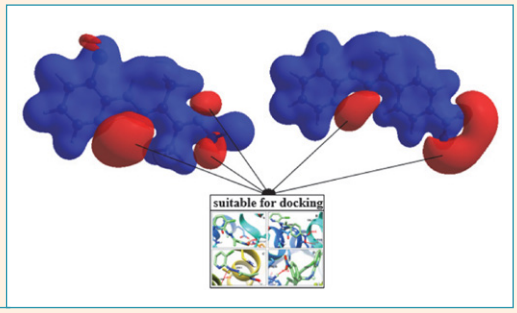
Rafat Milad Mohareb, Yara Raafat Milad and Ayat Ali Masoud



88–101 Biochemistry and molecular biology

Synthesis, Crystallographic Structure, Hirshfeld Surface Analysis, Drug-likeness Properties and Molecular Docking Studies of New Oxime-pyridine Compounds

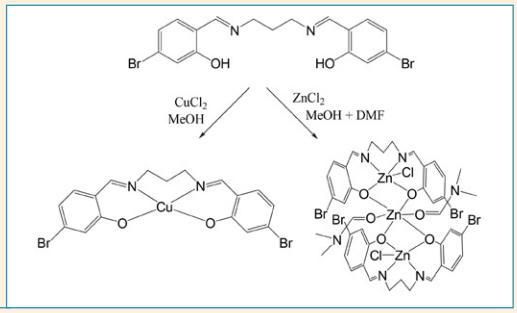
Tufan Topal



102–108 Inorganic chemistry

Copper(II) and Zinc(II) Complexes Derived from *N,N'*-Bis(4-bromosalicylidene)propane-1,3-diamine: Syntheses, Crystal Structures and Antimicrobial Activity

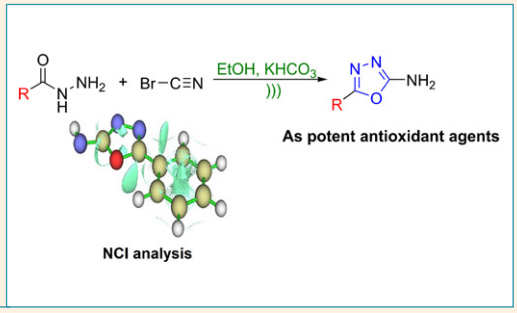
Yu-Mei Hao



109–117 Organic chemistry

Ultrasound-Assisted Synthesis, Antioxidant Activity and Computational Study of 1,3,4-Oxadiazol-2-amines

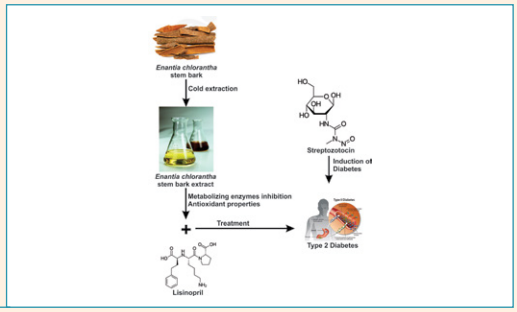
Hamid Beyzaei, Soheila Sargazi, Ghodsieh Bagherzade, Ashraf Moradi, and Elahe Yarmohammadi



118–127 Biochemistry and molecular biology

Antidiabetic Potential of Stem Bark Extract of *Enantia chlorantha* and Lack of Modulation of Its Therapeutic Efficacy in Diabetic Rats Co-Administered ...

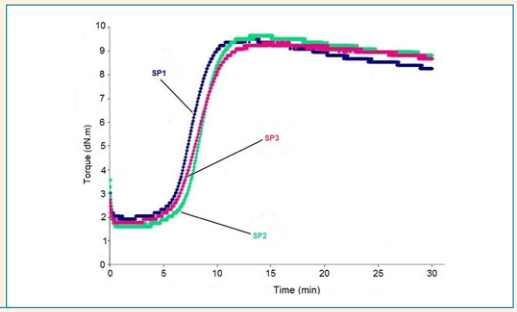
Latifat Bolanle Ibrahim, Patience Funmilayo Idowu, Opemipo Adekanye Moses, Mutiu Adewunmi Alabi and Emmanuel Oladipo Ajani



128–136 Applied chemistry

Application of Silica Supported Calix[4]arene Derivative as Anti-reversion Agent in Tire Tread Formulation

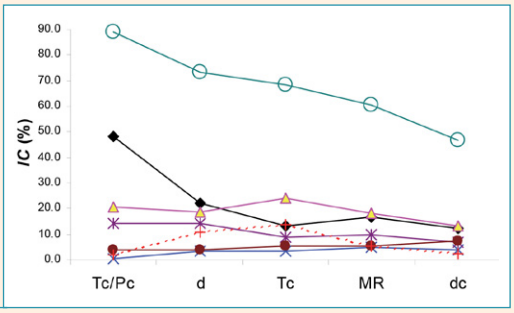
Hediye Mohamadi, Fereshteh Motiee, Saeed Taghvaei-Ganjali and Mandana Saber-Tehrani



137–143 General chemistry

Physicochemical Properties of Octane Isomers in View of the Structural Numbers

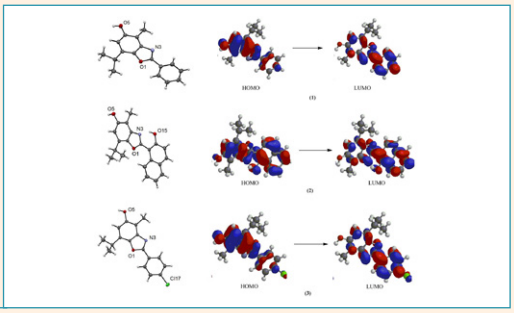
Anton Perdih



144–150 Organic chemistry

Structure of Biologically Active Benzoxazoles: Crystallography and DFT Studies

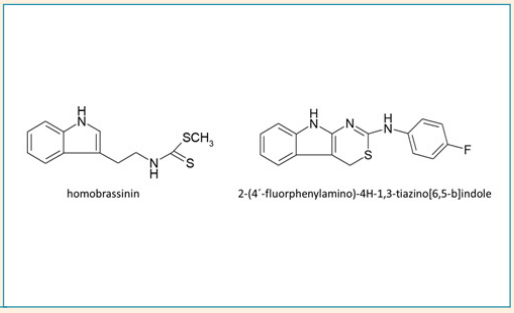
Una Glamočlija, Selma Špirtović-Halilović, Mirsada Salihović, Iztok Turel, Jakob Kljun, Elma Veljović, Selma Zukić and Davorka Završnik



151–158 Biomedical applications

Apoptotic Effect of Homobrassinin and Thiazino[6,5-b] indol is Associated with Downregulation of Heat Shock Proteins in Human Ovarian Adenocarcinoma Cells

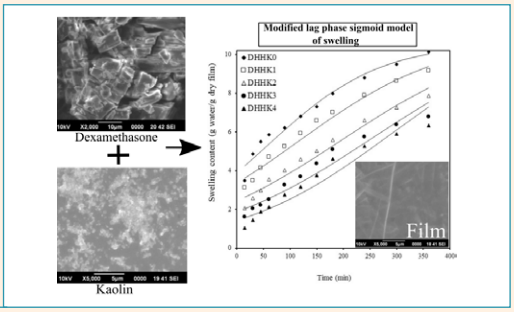
Zuzana Solárová, Martin Kello and Peter Solár



159–169 Physical chemistry

Characterization of Hydration Behaviour and Modeling of Film Formulation

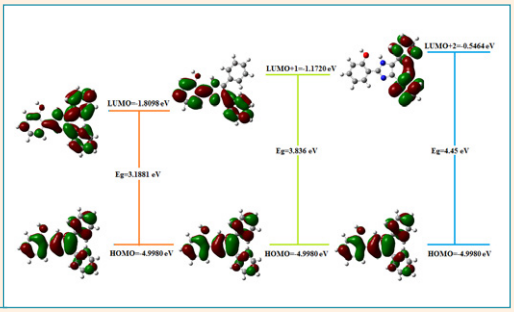
Arunima Pramanik, Rudra Narayan Sahoo, Souvik Nandi, Ashirbad Nanda and Subrata Mallick



170–177 Materials science

4-(4,5-Diphenyl-1H-imidazole-2-yl)phenol: Synthesis and Estimation of Nonlinear Optical Properties using Z-Scan Technique and Quantum Mechanical Calculations

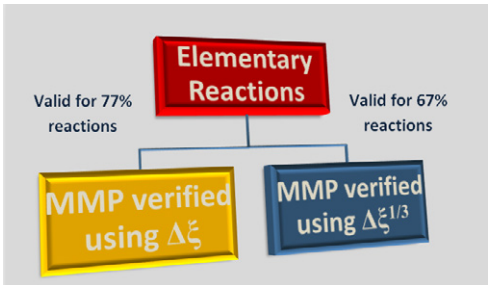
Fatemeh Mostaghni



178–184 Inorganic chemistry

On the Validity of Minimum Magnetizability Principle in Chemical Reactions

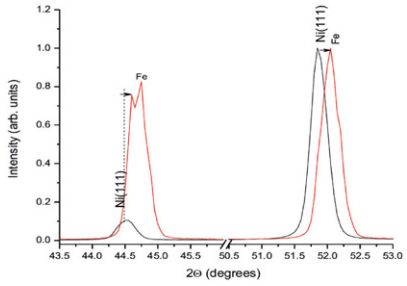
Hiteshi Tandon, Tanmoy Chakraborty and Vandana Suhag



185–192 Physical chemistry

Electrodeposition and Growth of Iron from an Ethylene Glycol Solution

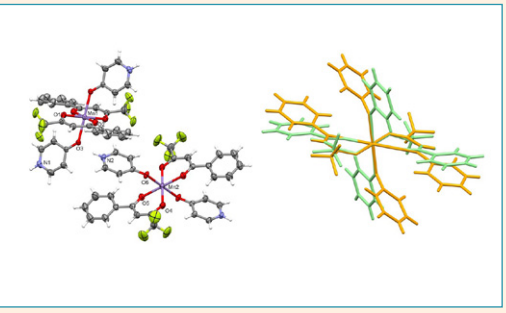
Vusala Asim Majidzade, Akif Shikhan Aliyev, Mahmoud Elrouby, Dunya Mahammad Babanly and Dilgam Babir Tagiyev



193–204 Inorganic chemistry

Manganese(II) β-Diketonate Complexes with Pyridin-4-one, 3-Hydroxypyridin-2-one and 1-Fluoropyridine Ligands: Molecular Structures and Hydrogen-bonded Networks

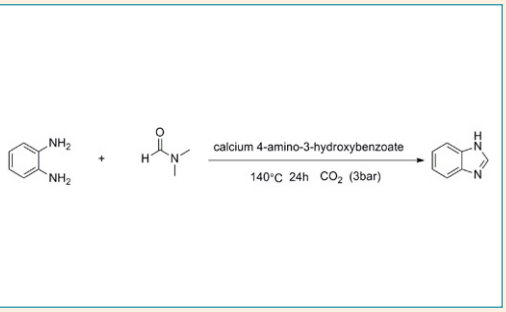
Anže Čavić and Franc Perdih



205–211 Organic chemistry

CO_2 Improved Synthesis of Benzimidazole with the Catalysis of a New Calcium 4-Amino-3-hydroxybenzoate

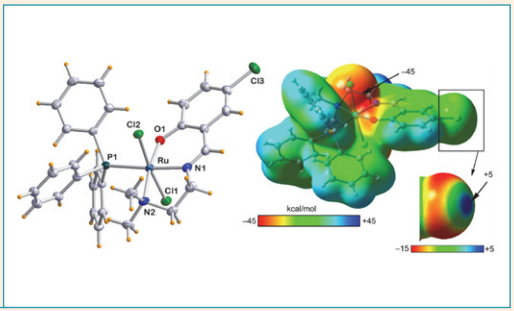
Ruo-Xuan Gao, Yuan-Yuan Gao, Ning Zhu and Li-Min Han



212–221 Inorganic chemistry

Catecholase-Like Activity and Theoretical Study in Solid State of a New Ru(III)-Schiff Base Complex

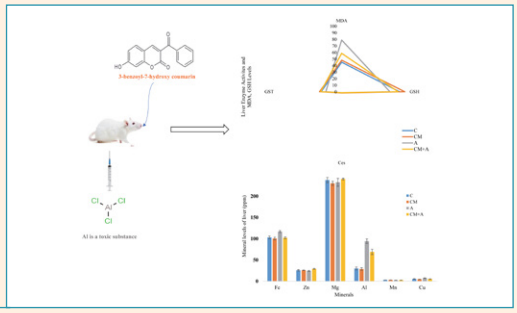
Niladri Biswas, Sandeepta Saha, Ennio Zangrando, Antonio Frontera and Chirantan Roy Choudhury



222–228 Biochemistry and molecular biology

Protective Effects of 3-benzoyl-7-hydroxy Coumarin on Liver of Adult Rat Exposed to Aluminium Chloride

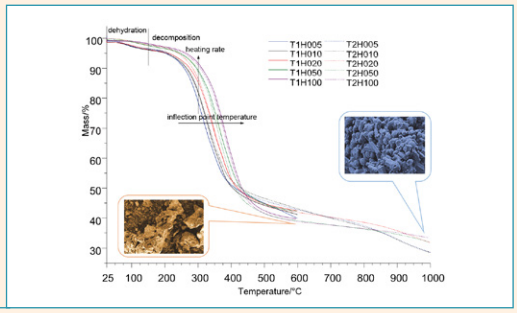
Ahmet Özkaya and Kenan Türkan



229–238 General chemistry

Physico-Chemical Properties of the Pyrolytic Residue Obtained by Different Treatment Conditions of Meat and Bone Meal

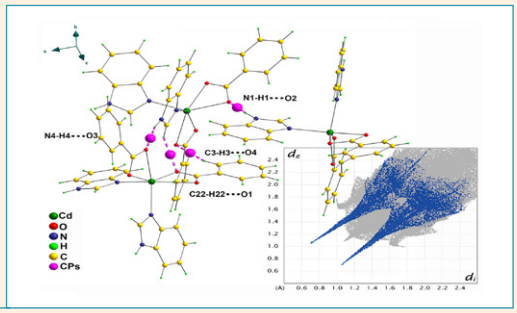
Marija Zupančič and Nataša Čelan Korošin



239–246 Inorganic chemistry

Hydrogen Bonds in Bis(1*H*-benzimidazole-κN³) cadmium(II) Dibenzoate: Hirshfeld Surface Analysis and AIM Perspective

Jia-Jun Wang, Li-Nan Dun, Bao-Sheng Zhang, Zhong-Hui Wang, He Wang, Chuan-Bi Li and Wei Liang



Feature article

Let the Biocatalyst Flow

Polona Žnidaršič-Plazl[1,2,*]

[1] *University of Ljubljana, Faculty of Chemistry and Chemical Technology, SI-1000 Ljubljana, Slovenia*

[2] *University of Ljubljana, Chair of Microprocess Engineering and Technology -COMPETE, SI-1000 Ljubljana, Slovenia*

** Corresponding author: E-mail: polona.znidarsic@fkkt.uni-lj.si*

Received: 11-04-2020

Abstract

Industrial biocatalysis has been identified as one of the key enabling technologies that, together with the transition to continuous processing, offers prospects for the development of cost-efficient manufacturing with high-quality products and low waste generation. This feature article highlights the role of miniaturized flow reactors with free enzymes and cells in the success of this endeavor with recent examples of their use in single or multiphase reactions. Microfluidics-based droplets enable ultrahigh-throughput screening and rapid biocatalytic process development. The use of unique microreactor configurations ensures highly efficient contacting of multiphase systems, resulting in process intensification and avoiding problems encountered in conventional batch processing. Further integration of downstream units offers the possibility of biocatalyst recycling, contributing to the cost-efficiency of the process. The use of environmentally friendly solvents supports effective reaction engineering, and thus paves the way for these highly selective catalysts to drive sustainable production.

Keywords: Microreactor, enzyme, flow biocatalysis, continuous process, process intensification, process integration

1. Introduction

The introduction of so-called "flow chemistry" in synthetic organic chemistry laboratories and also in industrial chemical production at the beginning of the 21st century brought a new paradigm in chemical processing. The availability of miniaturized flow reactors enabled the synthesis of complex molecules under controlled reaction conditions that yielded products of better quality and with fewer undesirable side reactions, as well as the ability to perform chemical reactions that are not possible in traditional batch operations.[1] Over the past two decades, microflow technology has matured from early devices and concepts to today's wide range of commercial devices and a variety of applications that also enable very efficient process analytics and control.[2] Microflow systems are now important tools in chemical processes, from single-step to end-to-end processing, from (photo)catalytic to separation processes, from (nano)materials synthesis to pharmaceutical and fine chemicals production, and in environmental applications. Recent guidelines in the production of fine chemicals and the pharmaceutical industry to replace batch by continuous processes have further spurred interest in the implementation of "flow chemistry".[3–5] Moreover, the quest to reduce the environmental factor, *i.e.* the E-factor (mass of waste per mass of product), which reaches the highest values in the fine chemicals and pharma industries, requires profound changes in production systems.[6]

Biocatalytic processes, along with continuous processing, have been identified as one of the crucial key areas of green engineering research for sustainable production in these sectors. They also play an important role in biomass valorization and circular economy.[7,8] Biocatalysts were already known decades ago as environmentally friendly catalysts operating under mild conditions and with very high regio-, stereo-, and reaction selectivity, making them ideal catalysts for green chemistry.[9] Nevertheless, it has been a major challenge to use these sensitive biomolecules and cells in harsh industrial environments, as they often need to convert non-natural substrates at concentrations several orders of magnitude higher than under natural conditions, and also require non-aqueous media for their solubilization. In addition, the frequently observed substrate or product inhibition, poor operational stability, and short shelf-life of biocatalysts prevented a wider application of biocatalytic processes in industrial production. However, in the last two decades, the understanding of protein and cell structure and function has improved tremendously. Genetic manipulations, metabolic

flux analysis, and the application of new techniques and materials for biocatalyst immobilization have led to unprecedented opportunities to develop more efficient and robust biocatalysts. Moreover, the use of novel solvents such as ionic liquids and deep eutectic solvents has led to efficient medium engineering that allows for more environmentally friendly production and high substrate availability.[10–12]

However, to achieve successful biocatalyst application, enzyme/cell, substrate, and medium engineering need to be complemented by reaction, reactor, and process engineering based on a thorough understanding of the reaction system and the specifics of the biological catalyst.[10–11,13] In this regard, new concepts of reactor and unit operation design that incorporate continuous operation and miniaturization also provide new opportunities for efficient use of novel biocatalysts.[14]

The traditional use of large stirred tank reactors operated in a batch mode, or in some cases packed bed or fluidized bed reactors with biocatalysts retained in the particles appears to be *sine qua non* of industrial biotransformations.[15] The implementation of microflow reactors in biocatalytic process development and operation has been much slower than for their chemical process counterparts.[14,16] Even the term "flow biocatalysis" was introduced in the scientific literature only a few years ago. The first review paper devoted to biotransformations in microstructured reactors written by Bolivar, Wiesbauer, and Nidetzky in 2011, reported a relatively small number of published studies in this field, mostly using dissolved enzymes, and the challenges of biocatalyst reversible immobilization.[17] In the last decade, flow biocatalysis with a special focus on micro- and mesoscale devices has gained increasing attention in the academic and slowly in the industrial community, as evidenced by several comprehensive review articles,[14,16,18–25] special issues of scientific journals, book chapters,[26–29] special sections at scientific conferences with industry participation (Biotrans, Flow Chemistry Europe, Implementation of Microreactor Technology in Biotechnology -IMTB, *etc*.), and specialized webinars such as the "Flow Biocatalysis" organized by European Society of Applied Biocatalysis in October 2020.

Although biocatalyst immobilization is gaining momentum by the application of novel materials and techniques,[23,24,26–30] the majority of industrial biotransformations are carried out in aqueous environments with dissolved enzymes or free cells, which is also reflected in a modest market share of immobilized enzymes in the overall enzyme market.[30,31] This is usually associated with additional immobilization costs and an often perceived decrease in biocatalyst activity related to either additional mass transfer limitations or biocatalyst deactivation.

Due to the typically low solubility of organic substrates in water, the natural and most common environment for biocatalysis, substrates are either engineered by varying the substrate structure, by adding an immiscible liquid phase (typically organic solvent), or in the case of a single-liquid phase, by applying organic co-solvents. To lower the E-factor, the reduced use of organic solvents has been considered in the last two decades, as well as the application of neoteric solvents, such as ionic liquids (IL) and deep eutectic solvents (DES).[6,10] Besides, non-conventional media typically used in environmentally friendly separation processes, such as supercritical CO_2 ($scCO_2$) and aqueous two-phase systems (ATPSs), are also gaining attention in biocatalytic processes and offer new opportunities for green biochemical production.

This feature article addresses the advantages of continuous microflow-based processes for the efficient utilization of non-immobilized biocatalysts, and for rapid biocatalytic process development. Recent achievements in microreaction technology involving dissolved enzymes or suspended cells in the presence of one or more fluids are discussed with an emphasis on the implementation of green solvents for more sustainable production. Process integration enabling the recycling of biocatalysts, as well as opportunities for analytics integration and capacity expansion will also be considered.

2. Microreactors With Biocatalysts in a Single Liquid Phase

The use of continuous operation in microfluidic devices offers several advantages over batch processing, especially when tuning of process variables can prevent biocatalyst deactivation. Most commonly used are simple tubes with diameters ranging from submillimeter to a few mm, typically used in analytical devices such as high-performance liquid chromatography (HPLC), or more sophisticated meander chips (Figure 1a), which are microfabricated from glass or various polymer materials. The intense mixing in stirred tank reactors required to transport substrates and products to and from the active site can lead to interfacial effects that can damage the biocatalyst,[32] while a high flow rate required for the same purpose in conventional plug flow reactors can lead to insufficient residence time for completion of the reaction.[33] This can be circumvented by the use of microflow systems, where μm-scale diffusion paths allow for very efficient mass and heat transport, the latter also allowing for very precise temperature control, which is very important for processes involving thermo-sensitive biocatalysts. Diffusion efficiency can be visualized by the dye distribution at the Y-shaped outlet of the microchannel of 12.5 mm length, 205 μm width, and 100 μm height, where the dyed and pure water were pumped separately into the Y-shaped inlets. As shown in Figure 1b,[34] laminar flow of aqueous methylene blue solution and water in the channel for 0.3 s (flow rate of 50 μL/min) resulted in moderate diffusion of the dye into the water (and *vice versa*), while 3 s residence time (flow rate of 5 μL/min) allowed diffusion throughout the entire channel.

The definition of process parameters such as fluid flow rate, enzyme and substrate inlet concentration, reactor geometry, *etc*. could be established based on mathematical modeling comprising transport phenomena and reaction kinetics.[35]

The advantages of moving from batch to continuous production using, among other devices, a microreactor with dissolved enzyme have been demonstrated for the production of the antidiabetic drug sitagliptin.[33] This chemo-enzymatic production, developed a decade ago by Merck and Codexis, is one of the flagship industrial uses of engineered enzymes, in which a highly efficient and solvent-tolerant amine transaminase was developed based on substrate walking, modeling, and mutation approach followed by directed evolution.[36] Replacing the environmentally problematic rhodium-catalyzed asymmetric enamine hydrogenation with a biocatalytic step resulted in a product with 99.5 % enantiomeric excess, a 10 to 13% increase in overall yield, a 53% increase in productivity, a 19% reduction in overall waste, elimination of all heavy metals, and a reduction in overall manufacturing costs. In addition, the enzymatic reaction could be carried out in multipurpose vessels, eliminating the need for dedicated high-pressure hydrogenation equipment. [33] The study on the multistep synthesis of sitagliptin monophosphate from chloropyrazine encompassed the design of a continuous end-to-end manufacturing process comprising microreactors and microseparators, and optimization of the biocatalytic step with dissolved transaminase based on a steady-state plug-flow model, taking into account enzyme recycling. Based on the evaluated optimized productivity and a comprehensive techno-economic analysis of this process, a net present value of $150 million over 20 years was calculated. Besides, an assessment of the environmental impact of the process demonstrated its sustainability with an E-factor of 53, which outperforms conventional pharma batch processes with a typical E-factor of 200.[33]

Another obstacle that is very often perceived in biocatalysis is the alteration of enzyme microenvironment by the reaction, which can lead to its deactivation. The product may inhibit enzymes or be toxic to cells, while the pH change affects not only the activity and stability of enzymes, but also ionization and stability of substrates, products, and other components in the reaction mixture. Besides, high substrate concentrations can inhibit the biocatalyst, which can be prevented by using a continuous stirred tank reactor with low steady-state substrate concentration. To address this problem in tubular reactors, Szita's group developed a "side-entry reactor" (Figure 1c) in which the principle of a fed-batch substrate feed strategy was efficiently introduced into a microflow reactor. When tested for the transketolase-catalyzed reaction of lithium hydroxypyruvate and glycolaldehyde to L-erythrulose, a 4.5-fold increase in outlet product concentration and a 5-fold increase in throughput were achieved compared to a single-input reactor.[37] Un upgraded version with the integrated optical pH sensors enabled not only monitoring of pH but also adjustment of this parameter *via* the side entries. As a result, the pH drop in the penicillin G acylase-catalyzed synthesis of 6-aminopenicillanic acid was significantly attenuated and the product yield was increased by up to 29% compared to the process without pH adjustment. This contribution represents a further step towards fully instrumented and controlled microfluidic reactors for biocatalytic process development.[38]

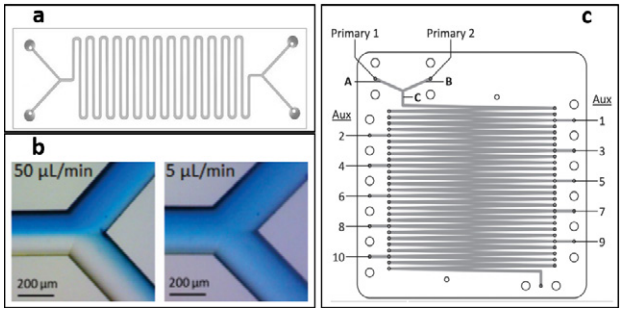


Figure 1: a) A Y-Y-shaped meander chip with 2 inlets and outlets; b) the outlet of the Y-Y channel presented in a) into which stained and pure water were pumped separately; the residence time in the channel was 0.3 and 3 s at the indicated flow rates of 50 µL/min and 5 µL/min, respectively; reproduced with permission from Miložič *et al.*, *Chem. Biochem. Eng. Q.,* 2014 28, 215–223;[34] c) a microfluidic side-entry reactor scheme with the indicated inlets (A, B), and side entries (1–10); all channels in the reactor had a cross section of 1 mm × 0.5 mm, and the length of individual sections of the main channel was 60 mm; reproduced with permission from Lawrence *et al.*, *Biotechnol. J.* 2017, 12, 1600475.[37]

3. Microreactors With Biocatalysts in the Multi-Liquid Phase System

The introduction of another liquid phase into the (typically aqueous) phase containing the biocatalyst opens, among others, the possibility of preventing its inactivation by compartmentalizing the inhibitor (substrate, product) from the biocatalyst, as well as shifting the reaction equilibrium toward product synthesis by *in situ* product removal.[19] Another important result of controlled flow in the microflow systems is the prevention of stable emulsion formation, which often hinders product isolation after multi-liquid phase processing in conventional stirred tank reactors.[39]

Liquid-liquid two-phase flow in microflow devices can be efficiently controlled, resulting in a variety of fluid flow regimes (Figure 2) and efficient transport between compartments. Since diffusion times are proportional to the square of the characteristic length, typical mixing times in microfluidic devices based on diffusion are in the range of milliseconds, which is several orders of magnitude better than in conventional reactors. The flow pattern in microscale channels is a function of operating conditions, such as flow rates, phase ratio and fluid properties. In addition, the flow is influenced by the roughness and

wettability of the channel wall, as well as by the geometry of the inlet channels (Y-, X-, or T-shaped) and the main channel diameter or aspect ratio for cylindrical or rectangular channels, respectively.[19]

Biocatalytic reactions within microflow systems typically involve various alkanes in addition to the aqueous phase. Among non-aqueous media, ionic liquids and recently also deep eutectic solvents (DES), both liquids consisting of ions with melting temperatures below 100 ˚C, are gaining increased attention in biocatalysis because they offer very high solubility of organic substrates. DESs are considered to be the fourth generation of ILs, although they do not consist entirely of ionic species.[40] While the synthesis of ILs requires chemical synthesis, often performed efficiently in microflow reactors,[41] DESs are prepared by simply mixing at least two inexpensive, nontoxic, and readily available components that are capable of self-associating in a specific molar ratio to form a new eutectic phase. The most typical compounds that constitute DESs are choline and urea, although amines, sugars, alcohols, polyols and organic acids are also used.[42] Both solvent classes are nonvolatile, nonflammable, highly viscous, and can be prepared in a plethora of variations, resulting in properties that can be tailored as needed, which also makes them attractive for application in biocatalytic processes.[40,42]

Aqueous two-phase systems (ATPSs) are another green solvents that are gaining importance in biotransformations. They are mostly used in bioseparations to integrate solid phase removal and extraction of the biomolecule of interest based on selective partitioning between phases. Typically, they are formed from two polymers such as polyethylene glycol (PEG) and dextran (Dex) or a polymer and an inorganic salt, e.g. phosphate and sulfate, dissolved in water, although some hydrophilic ILs are also capable of forming IL-ATPSs when mixed with aqueous solutions of inorganic salts.[43] They provide a benign environment for the biocatalyst along with the possibility of reducing substrate and/or product inhibition by compartmentalization in the other of the two phases. The industrial use of ATPSs is still hampered by their drawbacks such as slow diffusive mass transfer, long settling time for phase separation, and batch processing,[44] so processing in microfluidic systems present a promising tool for wider use of this green technology.[45] Recently, we reported the use of the microfluidics for the generation of a temperature-dependent aqueous micellar two-phase system (AMTPS) containing a surfactant in the time frame of a few seconds (Figure 2 d). The ability to change temperature almost instantaneously, and further integration with a microsettler and micro-ultrafiltration unit enabled sustainable and efficient purification of a high value-added value protein from algal biomass extract.[46]

The introduction of an additional liquid phase offers a wealth of flow patterns and attractive features that greatly expand the applications of liquid–liquid two-phase microfluidics. Three-liquid phase systems are widely used for various purposes, such as kinetic studies, microparticle synthesis, sample purification, and pharmaceutical crystallization. In addition to the parallel flow of all three phases (Figure 3 a2) and the generation of double emulsions (Figure 3 b2), which are of interest for the sorting of biocatalyst and other applications, a novel hybrid slug flow-laminar flow system (Figure 3 c2) was reported, where one layer is the laminar aqueous flow and the other layer is the slug flow. This flow was successfully stabilized by installing a partition wall between the two channels.[47]

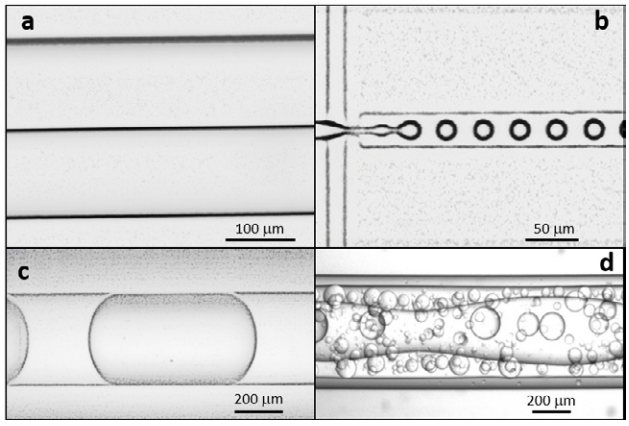


Figure 2: Typical liquid-liquid two-phase flow in microchannels: a) parallel flow of aqueous and organic phase, b) formation of water-in-oil droplets, c) slug or Taylor flow of the hydrophobic ionic liquid in aqueous phase, d) mixed flow of the aqueous micellar two-phase system described by Seručnik *et al.*[46] with core-annular flow and annular flow in the centre of the channel surrounded by droplets.

In the following chapters, the application of multi-liquid systems in biocatalytic processes will be highlighted.

3. 1. Microreactors With a Parallel Flow of Immiscible Liquids With Biocatalysts

Due to their small dimensions and low applied flow rates, laminar flows are typical of microflow systems in which immiscible liquid phases flow in parallel to form a stable and continuous interface through which mass transfer occurs.[47] The use of parallel flows has been achieved in microchannels with 2 Y-Y-shaped (Fig. 1a) or three Ψ- Ψ-shaped inlets and outlets. The main advantage of such processing is the possibility to separate the phases at the output of the microchips with multiple inlets and outlets presented also in Figs. 1a, 1b, so that no further phase separator is required. To achieve this, precise tuning of the flow rates of both phases is required so that the interface can be positioned in the middle of the channel, while exiting channels can be chemically modified to become more or less hydrophobic.

In a comprehensive review on enzymatic reactions utilizing non-aqueous media, several examples of enzymatic reactions with liquid-liquid (Fig. 2a and 3 a1) and liquid-liquid-liquid (Fig. 3 a2) parallel flow were given.[19] A pioneering work by Maruyama *et al.* on the environ-

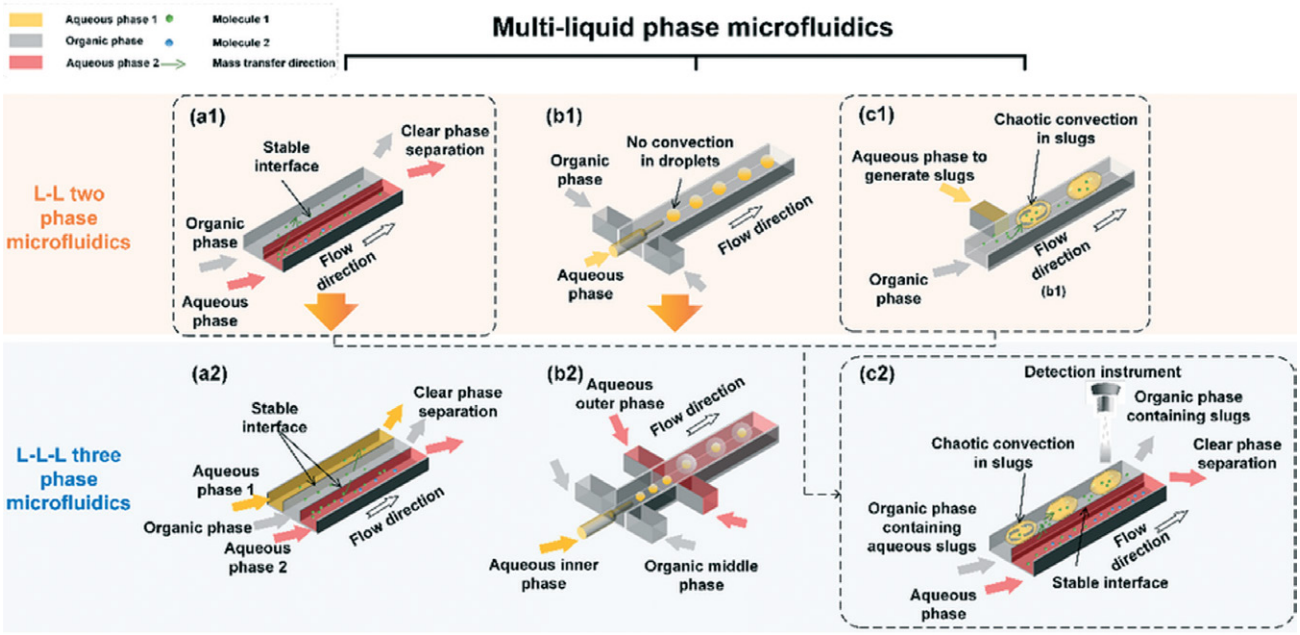


Figure 3: Schematic diagram and characteristics of multi-liquid microfluidics comprising liquid-liquid (L-L) or liquid-liquid-liquid (L-L-L) flow: (a1) L–L: laminar flow shown also in Fig. 1a (a2) L–L–L: three-layer laminar flow, (b1) L–L: droplet flow shown also in Fig.1b, (b2) L–L–L: double emulsions, (c1) L–L: slug flow shown also in Fig. 1c, and (c2) L–L–L: hybrid slug flow-laminar flow. Reproduced with permission from Wang *et al., Lab Chip* 2020, 20, 1891-1897, published by The Royal Society of Chemistry.[47]

mentally relevant laccase-catalyzed dechlorination of *p*-chlorophenol revealed 50-fold better specific productivity than in a laboratory-scale vessel with gentle shaking, achieving nearly 70% dehalogenation of the toxic substrate in 2 s.[48] In later studies, the most frequently used enzyme was *Candida antarctica* lipase B (CaLB), which acts at the interface of the two phases, so that in a parallel flow the reaction surface is well defined. This enabled very accurate modelling and reactor performance prediction for the esterification of isoamyl alcohol and acetic anhydride with substrate and product convection in the flow direction, diffusion in all directions, and reaction at the interface of the Y-Y- shaped microchannel.[49]

Along with aqueous buffers, alkanes are most commonly used as the second liquid phase in parallel flow.[19] The use of an ionic liquid as the second phase was demonstrated in the enantioselective separation of *(S)*-ibuprofen from a racemic mixture based on an enzymatic reaction. A thin film of ionic liquid between two aqueous phases with different lipases in each flow within the Ψ-Ψ-shaped microchannel provided a high interfacial area and processing time of only 30–60 s to achieve efficient enantioselective transport of this drug, which exhibits different pharmaceutical and/or toxicological effects depending on its optical purity.[50]

Urease-catalyzed hydrolysis in an aqueous two-phase system of PEG and Dex using parallel laminar flow in a Y-Y-shaped microfluidic device, schematically shown in Figure 4, showed a 500-fold increase in the apparent reaction rate compared to conventional ATPS in a beaker under gentle stirring. The very short residence time in the channel was increased by 4 consecutive reaction cycles, resulting in a 4-fold increase in conversion.[44]

A theoretical study of the enzymatic production of cephalexin, an important β-lactam antibiotic, using an ATPS based on PEG and phosphate in a microscale device comprising a thin dialysis membrane that provides flow stabilization and prevents transport of the enzyme and enzyme–substrate complex from the salt phase to the PEG phase. In the synthesis catalyzed by penicillin acylase, the effect of counter-current and co-current arrangements on cephalexin yield in microreactors with parallel flow of ATPS was discussed, as well as the possibility of transport enhancement by a direct-current (DC) electric field applied perpendicular to the interface. Based on the mathematical model comprising also mass transport across the membrane induced by an imposed electric field, the counter-current arrangement within the microreactor-separator was found to be suitable for cephalexin synthesis under most of the conditions studied.[51.]

3. 2. Microfluidics-Based Droplets With Biocatalysts

Droplet-based microfluidic systems, which use passive microfluidic structures to rapidly generate and manipulate subnanoliter-volume droplets in microchannel environments, have changed the paradigm of biochemical experimentation.[52] Compartmentalization of liquids into droplets within an immiscible carrier liquid, usually stabilized with a surfactant molecule, has been successfully ap-

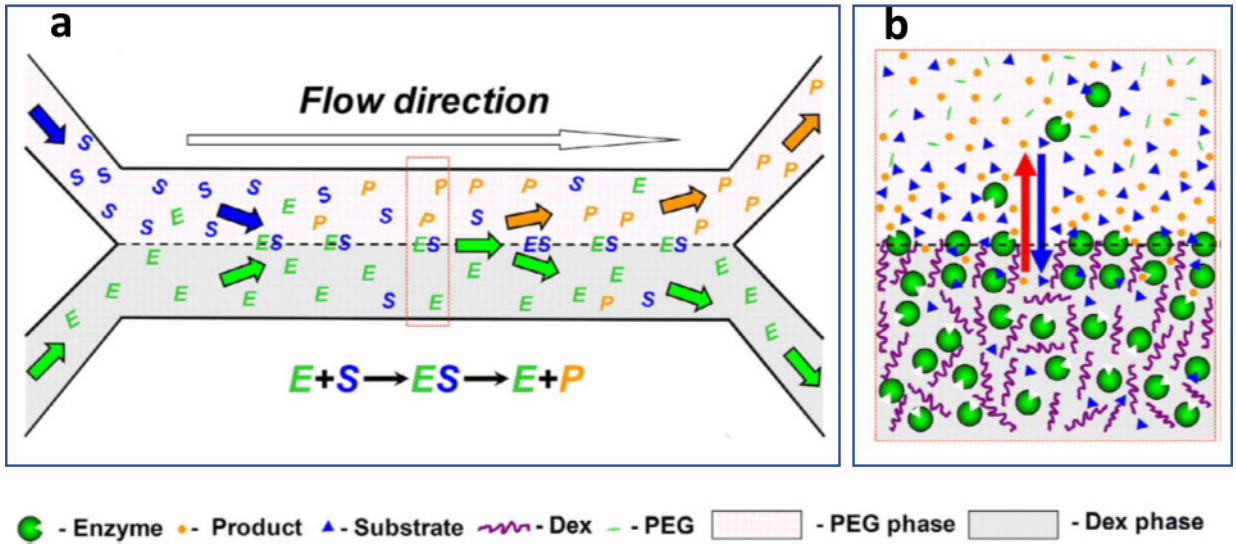


Figure 4. Schematic illustration of the ATPS enzymatic reaction and product separation in microchannel a) and at interface b) with a simple double Y-branched microfluidic device. Reproduced with permission from Meng *et al., Chem. Eng. J.* 2018, 335, 392–400.[44]

plied in numerous fields including single-cell and biomolecule analysis, diagnostics, drug delivery, protein crystallization, and chemical reactions.[22,52,53] Discussed herein are their applications in biocatalytic process development phases, as well as for process intensification.

3. 2. 1. Droplets in Biocatalyst Screening and Characterization

Selecting the most promising among the plethora of mutants generated by genetic manipulation or random mutagenesis is often the rate-limiting step in modern approaches to industrially relevant biocatalysts. Microfluidics-based ultrahigh-throughput screening of native or engineered enzymes and cells using droplets currently represents the most powerful tool for very rapid biocatalyst discovery and evolution at remarkably low cost.[22,52–55] Furthermore, microfluidic platforms developed for directed evolution of enzymes in droplets, allowing screening of 10^7 mutants per round of evolution, have revolutionized the area of enzyme engineering.[56]

Briefly, aqueous droplets in oil generated, as shown in Figs. 2b and 3 b1, at frequencies up to 2 kHz are capable of encapsulating a single enzyme or cell together with the substrate, which is often barcoded. After the reaction, which is performed during on- or off-chip incubation, the droplets are typically re-emulsified into water-in-oil-in-water droplets, as shown in Fig. 3 b2, and re-injected into the sorter and dispersed in an oil stream leading to the Y-shaped junction (Fig. 1b). Here, droplets are flowed into one of the channels, while those containing an active biocatalyst are selected by a detector and directed into the other channel. Most commonly, fluorescence-activated droplet sorting (FADS) based on laser activation is used.[52–57] As an example, a reliable and convenient ultrahigh-throughput screening platform based on flow cytometric droplet sorting (FCDS), shown in Figure 5, was demonstrated to efficiently isolate novel esterases from metagenomic libraries by processing 10^8 single cells per day.[58]

Further encapsulation of single cells producing an enzyme of interest in microfluidic-based droplets along with a fluorogenic substrate and optionally lysing agents ensures that product formation occurs in the same compartment as the catalyst-encoding gene. The fluorescent product-containing droplets can then be sorted using FADS enabling ultrahigh-throughput directed evolution.[59–61] As an example, a droplet-microfluidic screening platform was used to improve a previously optimized artificial aldolase by an additional factor of 30, resulting in a rate increase of over 10^9-fold .[59] Evolutionary units in the form of monodisperse double emulsions or gel-shell beads (GSBs) containing a protein mutant and its coding DNA represent further step towards extremely fast biocatalyst engineering.[62] Another ultra-high throughput protein screening platform called Split-and-Mix Library on Beads (SpliMLiB) was presented by Hollfelder's group. Directed evolution workflows were accelerated by DNA libraries constructed on the surface of microbeads suitable for direct functional screening in water-in-oil emulsion droplets with cell-free expression.[63]

To expand the application of this technique beyond non-fluorogenic substrates/products, assays based on absorbance are being investigated.[64] Future detection modes will include fluorescence-based approaches (anisotropy, Förster resonance energy transfer, lifetime) and label-free approaches based on light scattering (including Raman scattering) or droplet morphology.[55] Reports on the application of positive dielectrophoresis-based Raman-activated droplet sorting for culture-free and label-free screening of enzyme function *in vivo*,[65] and droplet sorting by inter-

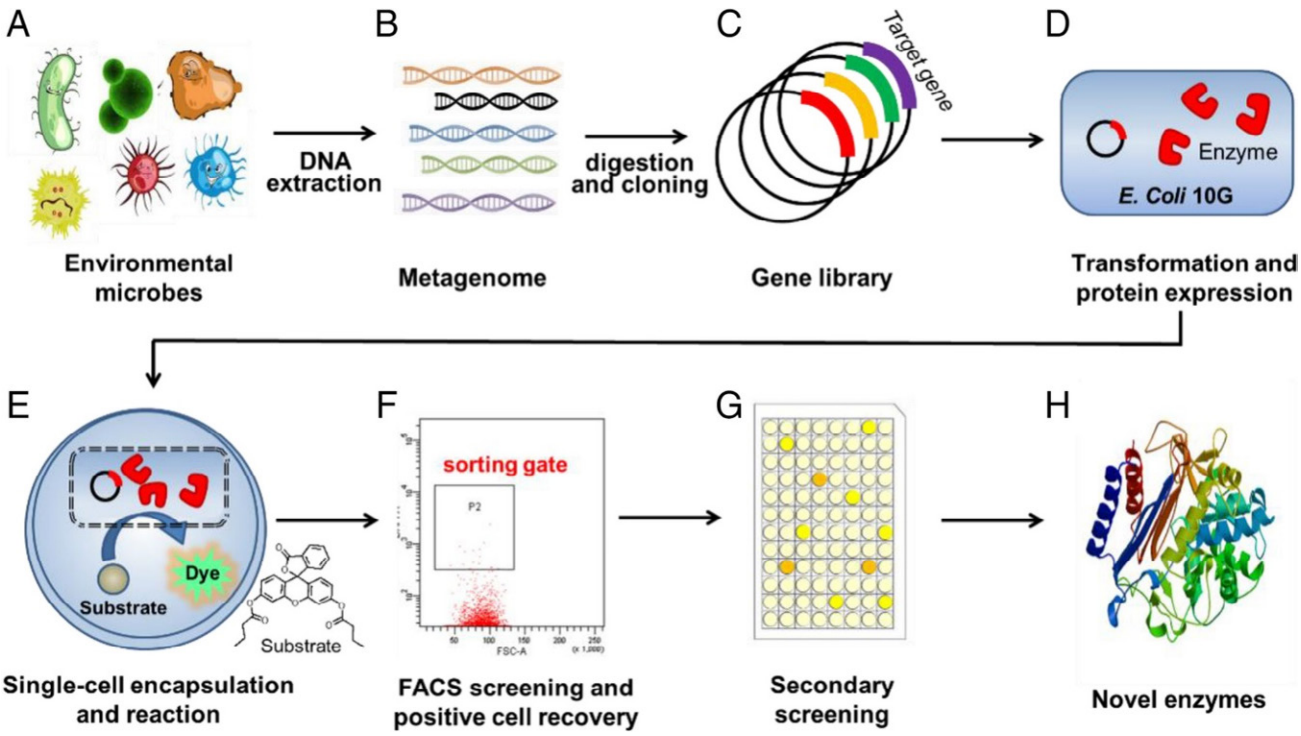


Figure 5 Workflow of the ultrahigh-throughput screening platform based on flow cytometric droplet sorting to mine novel enzymes from metagenomic libraries. A. Collection of environmental microbes. B. Extraction of metagenomic DNA. C. Digestion and cloning of metagenomic DNA into an expression vector. D. Transformation of recombinant plasmids into a host strain for encoded protein expression. E. Encapsulation of single cells into water-in-oil-in-water double emulsion droplets, along with the screening substrate. F. Flow cytometric analysis and sorting of positive droplets. G. Secondary screening based on 96-well plate assays. H. Identification of novel enzymes. Reproduced with permission from Ma *et al., Environ. Microbiol.* 2020, DOI**:** 10.1111/1462-2920.15257.[58]

facial tension[66] confirm these expectations. A sophisticated Raman-activated droplet sorting device uses periodically applied positive dielectrophoresis force to capture fast-moving cells, followed by simultaneous microdroplet encapsulation and sorting. The label-free method of sorting droplets by pH requires no active components and provides a robust platform for enzyme sorting in high-throughput applications.[65] Another promising approach in this regard is the coupling of droplet microfluidics with electrospray ionization – mass spectroscopy (ESI-MS), which provides a label-free high-throughput screening platform. The system also enabled effective *in vitro* transcription-translation within the droplets analyzed directly by MS, demonstrating opportunities to greatly accelerate the screening of enzyme evolution libraries.[67]

Few nL or even pL surfactant-stabilized monodisperse droplets can be regarded as moving reactors that allow an extraordinarily large number of experiments to be performed simultaneously. As they move along channels, the reaction in the droplets can be monitored e.g. *via* laser-induced fluorescence measurements of product concentration that provide a time-dependence of the reaction.[54] Because they consume minute amounts of reagents to provide the necessary information on reaction kinetics and biocatalyst inhibition, they significantly outperform conventional microtiter plates in terms of cost and time.[52,53] In addition, droplet microfluidics offers the potential to generate and analyze enormous amounts of kinetic data through a high degree of integration with detection modalities. Some excellent reviews of droplet applications comprising examples of controlled microfluidic systems used for e.g. automated analysis of enzyme kinetics, screening of protein crystallization conditions and protein solubility can be consulted for further information on this topic.[52,53,57]

However, the requirements for advanced droplet dispensing control and accurate sequential addition of samples or reagents to droplets at a high volumetric flow rate remain a challenging task. To address this, droplet array technologies have begun to offer a pathway to high-throughput screening.[52] After many years of intensive research, and despite the enormous potential for industrial use, few commercial applications have been developed, and significant development in the field is still needed to make them reliable and widely applicable.[68] There is a strong belief that high-throughput, high-sensitivity droplet-based microfluidics will become the gold standard for optimizing computationally engineered enzymes.[61] Exploration of 3-D printing technologies, robotics, and artificial intelligence is paving the way for smart platforms that could change the paradigm and drive the development of industrial biocatalytic processes.[22,52]

3. 2. 2. Droplets in Biocatalytic Processing

Microfluidics-based droplets are characterized by a very high surface-to-volume ratio that allows high mass transfer between the phase containing the biocatalyst and the phase containing substrate and/or product, so their use can lead to process intensification when the reaction is limited by mass transfer. The benefits of using microfluidics-based droplets were demonstrated in the bio-hydration of acrylonitrile to acrylamide using *Rhodococcus ruber* whole cells containing nitrile hydratase, which is one of the important large-scale biotransformations. Conventional processing in stirred tank reactors is hindered by the low aqueous solubility of acrylonitrile, the low concentration of free cells, limitations on external mass transfer resulting in reduced apparent reaction rates, and by the limited ability to increase impeller speed and thus mass transfer due to potential interfacial effects leading to cell damage.[32] To circumvent these problems, acrylonitrile was dispersed into small droplets of 25 to 35 μm using a specially designed membrane dispersion microreactor. This enabled approximately 30% higher product yield in 5-times less time and also proved to extend the life of the free cells.[69,70]

The very high surface-to-volume-ratio of the 190 μm droplets generated in an X-junction microchannel (Fig. 1b) was also advantageous for the *Candida antarctica* lipase B (CaLB)-catalyzed synthesis of isoamyl acetate, allowing the "natural" production of this important aroma. The amphiphilic enzyme positioned together with the substrate in the hydrophilic ionic liquid tends to attach to the surface of the organic phase forming droplets. The high interfacial area as well as the *in-situ* product removal into the organic liquid droplets allowed much higher volumetric productivities than reported in the literature for this esterification. Furthermore, the incorporation of a hydrophobic membrane-based separator allowed separation of the enzyme from the product in the organic phase and several successful recyclations of the biocatalyst.[71]

The same reaction has been studied in flow reactors developed by Corning®, which allow efficient mixing of two-phase systems without the need for high energy or high pressure drop devices. The key component of the system is a fluidic module made of special glass, which consists of a chain of identical cells with variable cross-sections and internal elements. The fluid is forced to split and then recombine in each cell, leading to the renewal of the interface in two-phase systems such as liquid-liquid (Figure 6 a). The ease of their scalability from laboratory to production scale and customization to meet specific requirements provides a cost-effective solution for a broad portfolio of reactions in organic synthesis as well as for extraction.[72,73] Application of the low-flow module to lipase-catalyzed esterification in an aqueous- *n*-heptane two-phase system enabled efficient interfacial mass transfer and *in situ* product removal, resulting in unprecedented volumetric productivities.[74] Further scale-up of the process in a 70-mL modular reactor demonstrated excellent process scalability.[22]

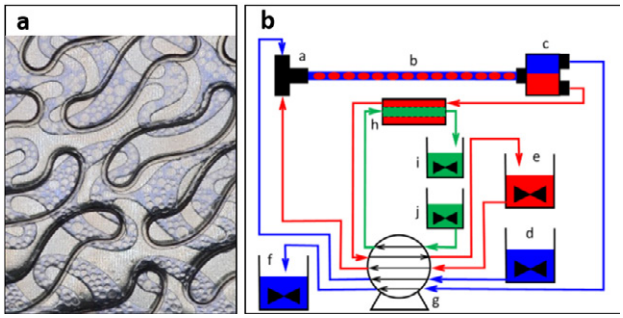


Figure 6: Reactors with two-phase flow: a) a close-up of a liquid-liquid flow regime obtained in a Low Flow Advanced Flow™ Reactor developed by Corning®, and b) a scheme of the microfluidic system with an enzyme recycle: a – a T-shaped element, b – reaction microcapillary, c – settler, d– reservoir of the top phase with dissolved reactants, e – reservoir of the recycle stream, f – product reservoir, g – peristaltic pump, h – dialysis micromodule, i – waste, j – dialysate solution, k – microdialyzer ports. Reproduced with permission from Vobecká *et al., Chem. Eng. J.* 2020, 396, 125236.[75]

The droplets generated by microfluidics were also used for the preparation of semipermeable silica microparticles that allowed compartmentalization of enzymes. The porous shell allowed selective diffusion of substrate and product while protecting the enzymes from degradation by proteinases and maintaining their functionality over multiple reaction cycles. The system was tested for β-glucosidase encapsulation and for the combined compartmentalization of glucose oxidase and horseradish peroxidase, which form a controlled reaction cascade for the glucose detector. The microparticles were trapped in a microfluidic array device in which the enzyme activity could be tested in a single microparticle, which also provided information on reaction kinetic parameters and stability.[76]

3. 3. Segmented-Flow Microreactors With Biocatalysts

Segmented flow with alternating fluid segments (e.g., slug flow in Fig. 1c and Fig 2c) is much easier to achieve than stable parallel flow in a long channel that allows complete conversion, so this type of flow prevails in biocatalytic processing in liquid-liquid systems.[19] It also allows very efficient mass transfer between phases, based on convective motion in each segment that renews the interface, which increases the concentration gradient of the product and facilitates diffusive penetration through the interface.[77] A typical setup consists of the mixing unit (T- or Y-shaped mixer), tubes with lengths that provide the appropriate residence times, and phase separators based on gravity, membranes, *etc.* Compared to batch processes, where the intensive mixing of several phases required for efficient mass transfer regularly leads to emulsification and

thus phase separation problems, this obstacle is reduced in microflow reactors.[39,78]

Applications of slug flow include various reactions and enzymes, from reactions catalyzed by alcohol-dehydrogenase (ADH),[79–82] to hydroxynitrile lyase-catalyzed C-C bond formation,[83] a reduction with pentaerythritol tetranitrate reductase,[84] terpene production catalyzed by aristolochene synthase,[77] penicillin acylase-catalyzed antibiotic synthesis,[75,85,86] and lipase-assisted biodiesel production,[87,88] among others.

An interesting reactor design was reported by Karande *et al.* who combined different sized capillaries from 2.5 mm i.d. to 0.5 mm i.d. to comply with lower substrate concentration along the tubular reactor, where the ADH-catalyzed reaction takes place. This allowed optimization of the conversion of selected aldehyde to corresponding alcohol dissolved in an organic phase and contacted in a slug flow regime with an aqueous phase containing enzyme and cofactor, as well as a cofactor dehydrogenase-based regeneration system.[79] To circumvent the interfacial deactivation of ADH in segmented flow, the addition of surfactant and immobilization of the enzyme in porous beads carried along the tubular reactor within the aqueous segments were tested. Both approaches resulted in very efficient stabilization of the enzyme, with surfactant addition being preferred due to better enzyme activity, less complexity, and ease of implementation in slug flow microreactors.[80]

Significant mechanical energy savings have been reported for lipase-catalyzed soybean oil hydrolysis using a slug flow microreactor. The hydrodynamically well-controlled slug flow generated in a T-shaped microfluidic channel and continued in submillimeter reaction capillaries, ensured uniform residence time of all slugs and enabled the recovery of well-defined products. Further integration with two microfluidic separators resulted in phase separation and the possibility to reuse the dissolved enzyme.[89]

Recently, lipase-catalyzed biodiesel production in a slug-flow microreactor has received considerable attention. Very pure biodiesel with glycerol content below the detection limit was produced in an integrated system with two microchips connected in series. The first Y-shaped microchannel was used for biodiesel production with methanol in one feed and an emulsion of oil, lipase and surfactant in the second. In the Y-shaped microchannels connected in series, simultaneous purification, i.e., glycerol removal, was achieved with DES based on choline chloride and ethylene glycol.[87] In another study by the same group, DES based on choline chloride and glycerol was used for biodiesel production based on lipase-catalyzed transesterification of edible and waste sunflower oil with methanol. The reaction, which was carried out in a Y-Y-shaped microchannel as well as in a mm-scale tube, resulted in a 3-4-fold higher productivity than in the stirred tank reactor operated in batch mode.[88]

Environmentally friendly ATPS prepared from PEG and phosphate buffer was used for an enzyme-catalyzed synthesis of the β-lactam antibiotic cephalexin, which is produced industrially on a multi-tones annual scale. The microfluidic setup shown in Figure 6 b included a slug-flow microreactor that supported efficient mass transfer between penicillin acylase dissolved in the bottom ATPS phase and the substrates in the ATPS's top phase, as well as *in situ* product separation in the latter. Integration of the settler resulted in phase separation and enabled further recycling of the reaction phase containing the dissolved enzyme. The recycling circuit also included a microdyalizer operated in counter-current regime to remove phenylglycine, which tended to clog the system. The system could be operated continuously for 5 h, and the operating time appeared to be limited only by the washout of the enzyme.[75] The same group has also applied various ATPSs in the production of 6-aminopenicillanic acid (6-APA) from penicillin G using dissolved penicillin acylase. Criteria for the selection of ATPS were optimal separation of 6-APA from the enzyme, high buffering capacity to reduce undesirable pH decrease due to dissociation of phenylacetic acid – a byproduct of the reaction, relatively low cost of ATPS components, and the possibility of electrophoretic transport of fine droplets and reaction products to both accelerate phase separation and increase the 6-APA concentration in the product stream. The possibility of electrophoretic transport of the salt-rich droplets in the system was verified in a simple microfluidic device.[85] A continuation of this study led to the development of electric-field-enhanced selective separation of the reaction byproduct in a membrane microcontactor. Application of DC electric field resulted in enhanced mass transfer through a semi-permeable membrane for rapid, continuous, and selective separation of electrically charged low-molecular-weight phenylacetic acid from the original reaction mixture containing free penicillin acylase. Furthermore, the electroosmotic flow through the membrane, which counter-directs the transport of phenylacetic acid, was advantageously used to concentrate the separated product in the acceptor phase.[86]

The importance of minimizing stable emulsion formation, typical of the stirred tank batch processing, was highlighted for the enzymatic reduction of hydrophobic ketone in a biphasic methyl tert-butyl ether (MTBE) - buffer carried out in a segmented flow formed in a Y-shaped mixer and guided in a poly(fluorenylene ethynylene) (PFE) coil of 0.8 mm diameter, and compared with the batch process. While the conversions in both process operations were similar under comparable conditions, emulsification and precipitation were strongly suppressed when the biocatalytic reactions were carried out in flow mode, significantly simplifying and minimizing the effort required for biphasic biocatalytic reaction systems.[90]

The pioneering work of Karande *et al.*[80] inspired the study of segmented flow, in which segments containing a

heterogeneous biocatalyst surrounded by another liquid phase flowed in the microreactor. A segmented hydrogel-organic solvent system was developed based on superabsorbent polymer consisting of partially neutralized cross-linked polyacrylic acid, in whose matrix enzymes and whole cells could be embedded. Such a "fluid heterogeneous phase" was investigated with the ADH-catalyzed reduction of acetophenone and the aldoxime dehydratase-catalyzed dehydration of octanal oxime. Especially for solvent-labile catalytic systems, this approach offers an alternative for the application of immobilized biocatalysts in a continuously running process beyond conventional packed bed and wall-coated reactors.[90]

4. Microreactors With Biocatalysts Containing Gaseous and Liquid Phase

Enzymes can be used as highly selective catalysts for the oxyfunctionalization of unactivated carbons in organic synthesis. Insufficient oxygen supply is often a bottleneck in O_2-dependent reactions, which is why a high influx of the gas phase and intensive mixing are required in conventional stirred tank reactors. In biocatalytic processes, this can lead to enzyme deactivation and gas stripping of substrate and product.[32,91] To circumvent this, a tube-in-tube reactor (TiTR), in which the gaseous substrate enters the reaction chamber along the entire length of the tube, is a promising alternative. A flow-through chemistry apparatus developed a decade ago allows contact between gasses and liquids *via* a semipermeable Teflon AF-2400 membrane of a submillimeter i.d.[92]

The application of such a high-pressure reactor setup providing oxygen supply across the membrane surface from the outside of the reactor system was demonstrated for the synthesis of 3-phenylcatechol using a continuous segmented flow of the aqueous phase with the enzyme and decanol with the substrate as shown in Figure 7. 2-Hydroxybiphenyl- 3-monooxygenase was applied as a biocatalyst for the hydroxylation reaction and also required cofactor regeneration, which was provided by formate dehydrogenase dissolved in an aqueous phase. Very high

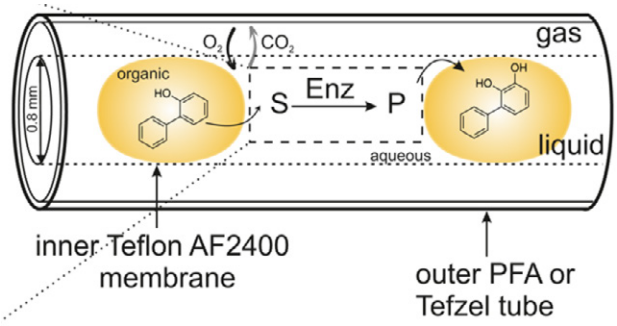


Figure 7. Scheme of a tube-in-tube reactor used for enzymatic hydroxylation using gaseous oxygen as a substrate. Reproduced with permission from Tomaszewski *et al.*, *Org. Process Res. Dev*. 2014, 18, 1516–1526.[91]

volumetric productivities were obtained when the reactor was of sufficient length providing the required residence times, emphasizing the potential of the TiTR as a promising technology for the realization of gas-dependent enzymatic reactions.

The same reactor configuration was also used to study the kinetics of oxygen-dependent reactions catalyzed by glucose oxidase, where the challenges of conventional systems can be avoided by creating a bubble-free aeration system. The TiTR setup was fully automated and computer controlled, allowing characterization of an oxygen-dependent enzyme within 24 hours with minimal manual labor, outperforming the conventional batch setup approach. By pressurizing the system, the dissolved oxygen concentration can reach 25-times the values achievable by air supply under atmospheric conditions. Operation in the low dispersed flow regime allowed the generation of time-series data with an enzymatic catalyst, despite its low diffusivity, and the resulting data were in good agreement with experiments conducted in a batch system.[93]

Direct introduction of the gas phase into enzymatic microreactors, allowing efficient supply of gaseous substrate, has been reported for many biocatalytic processes involving immobilized enzymes that were reviewed elsewhere.[14,16,20-28] A report on the generation of a three-phase slug flow in a microchannel used for dissolved enzyme-catalyzed reaction revealed the benefit of introducing an inert gas phase (nitrogen) into a liquid-liquid slug flow to stabilize the liquid-liquid interface, and improve uniformity and reproducibility of the flow. In this way, uniform reaction-transport properties were created in a heterogeneous reaction system with an unstable interface in a long microchannel, as demonstrated in the lipase-catalyzed hydrolysis of soybean oil.[94]

Among the commercial meso-scale flow reactors enabling efficient direct gas-liquid contact, Corning® Advanced Flow Reactors, such as presented in Figure 6a, are commonly used in chemical industry, but to the author's knowledge, no report of enzymatic reaction with the gas phase in these reactors has been reported. On the other hand, the Coflore™ agitated cell reactor (ACR) and the agitated flow reactor (ATR) have been used for the chiral resolution of DL-alanine using non-immobilized whole *Pichia pastoris* cells with D-amino acid oxidase, where reaction is oxygen limited due to the gas–liquid mass transfer constraints of the conventional vessels. Comparison of a batch process performed in a 250 mL stirred tank reactor at various stirring speeds with a 100 mL Coflore ACR, a dynamically mixed plug flow reactor that uses to promote mixing, revealed a slightly increased reaction rate in the flow reactor. Further comparison of 1 L stirred tank batch reactor with 1 L Coflore ATR tubular reactor using lateral movement showed much greater improvement in volumetric productivity for the flow reactor due to improved gas-liquid mass transfer. In addition, virtually the same results were obtained with AFR when scaling up from 1 to 10 L

without seeing the losses already evident when moving from 1 to 4 L in conventional batch reactor.[95]

5. Process Analytics in Microreactors With Biocatalysts

As described in the chapter on droplet microfluidic platforms used for fast biocatalyst screening, evolution and characterization, highly automated and controlled devices using numerous analytical techniques are under development. Miniaturization and integration of several analytical techniques such as chromatography, electrophoresis, or flow injection analysis in devices referred to as micro Total Analysis Systems (μTAS) were the first applications of microfluidics starting in the 1990s.[96] In contrast, most studies presented in this review use off-line analytical techniques such as HPLC or spectrophotometry. Optical sensors for non-invasive and non-destructive monitoring of e.g. oxygen, pH, carbon dioxide, glucose, and temperature reviewed by Gruber *et al.* (2017) have great potential for on-line and at-line monitoring, both of which have some advantages and disadvantages as listed in Table 1.[97]

An example of in-line analysis of dissolved oxygen and substrate or product concentration in the microchannel outlet stream is shown in Figure 8. Dissolved oxygen concentration was measured using a fiber microsensor within the needle inserted into the stream, while substrate or product concentration was evaluated using the flow-through miniaturized optical detector that measures absorbance at the specific wavelength of interest.

Oxygen can also be monitored on-line by introducing sensory nanoparticles into the fluid and monitoring them using a fluorescence microscope, or by creating measurement points in the channel.[98] As mentioned in Chapter 2, on-line pH measurement has been established based on a similar approach.[97]

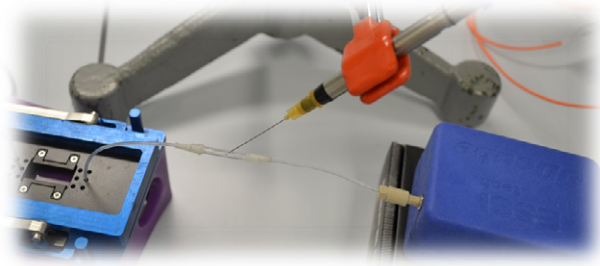


Figure 8. Monitoring of the microchannel outlet stream regarding the dissolved oxygen concentration using fiber microsensor within the needle inserted in the flow, and the substrate or product concentration based on flow-through miniaturized spectrophotometer.

The use of novel manufacturing capabilities offered by 3D printing technology and the integration of novel materials will pave the way for better process monitoring that will also enable process control, which is crucial for the efficient application of biocatalysts.

6. Conclusions and Future Perspectives

If four technological advances evolved in the last decades of the previous century have been recognized as crucial for the acceptance of enzymes as "alternative catalysts" in industry, viz the development of i) techniques for large-scale isolation and purification of enzymes, ii) techniques for large-scale immobilization of biocatalysts, iii) biocatalytic processes in organic solvents, and iv) recombinant DNA technology enabling biocatalyst engineering,[9] the fifth technological advance that can now be added is the development of continuous processing in miniaturized devices designed to efficiently harness these unique cata-

Table 1: Summary of the advantages of on-line and at-line monitoring in microfluidic systems as proposed by Gruber *et al.*, *Lab Chip*, 2017, 17, 2693, published by The Royal Society of Chemistry.[97]

	Advantages	**Disadvantages**
on-line	Real time analysis possible	Possible interaction of sensors with the flow or reactants
	Rapid feedback allows real time process control	Sensors need to be recalibrated and replaced over time
	No manual sampling required	Increase of system complexity (fabrication, design, operation, maintenance)
	Measurement at real temperature	Cross sensitivity with other analytes or interferences can be difficult to quantify
	No sampling required	Limitation to a specific analytical problem and a certain concentration range
	Less risk of contamination	
	Production flow undisrupted by sampling or redirecting	
at-line	Significant number of assays/analytical methods available	Changes in sample before analysis possible
	Can be cost-efficient	Analysis limited to on-site equipment
	Flow cells available	Certain sample volume necessary
	Feedback available quickly	Risk of contamination through sampling

lysts.

The application of microflow systems for biotransformations with free biocatalysts offers several advantages, from reduced shear stress on fragile molecules and cells, to reduced mechanical energy requirements for efficient mixing, to very efficient contacting of multiple phases that allows compartmentalization of biocatalyst and often inhibitory substrates and/or products. Microfluidics-based droplets manipulated in highly automated microfluidic devices provide a revolutionary tool for ultrahigh-throughput biocatalyst evolution and efficient biocatalytic process development. Furthermore, continuous process operation in microflow reactors also allows for easy downstream process integration, enabling enzyme or cell recycling and thus very high total catalyst turnover number, defined as the total moles of product produced per mole of enzyme over the lifetime of the enzyme. The use of environmentally friendly solvents in such production systems can ensure that the goals of green chemistry as well as the bioeconomy are achieved. The requirements for fully controlled microflow systems are driving the intensive development of integrated analytics, with new manufacturing technologies such as 3D printing together with novel materials offering endless possibilities. The use of model-based approaches that allow quantification of mass transfer in various reaction systems and microreactor configurations, as well as apparent reaction rates at different process conditions, will help to exploit the potential of microreactor technology. The use of engineering tools, such as characteristic times analysis and dimensionless numbers evaluation, could be of great value in this endeavor.[22,79,80]

Industrial implementation of flow biocatalysis requires the knowledge transfer between the various disciplines involved in process development. Understanding the fundamental phenomena underlying the structure and function of biocatalysts, biocatalytic reaction mechanisms and kinetics, and the performance of microreactors is therefore a basic requirement and should be implemented in the curricula of chemical, biochemical, and engineering study programs.

Acknowledgements

Financial support from the Slovenian Research Agency (Grants P2-0191, N2-0067 and J4-1775) and from the EC H2020 project COMPETE (Grant 811040) is gratefully acknowledged. The author would like to thank M. Seručnik, L. Ostanek Jurina, B. Perić, T. Pilpah and M. Klemenčič from University of Ljubljana for providing graphical material.

Abbreviations

ACR	Agitated cell reactor
ADH	Alcohol-dehydrogenase
ATR	Agitated flow reactor
6-APA	6-Aminopenicillanic acid
AMTPS	Aqueous micellar two-phase system
ATPS	Aqueous two-phase system
CaLB	Candida antarctica lipase B
DC	Direct current
DES	Deep eutectic solvent
Dex	Dextran
E-factor	Environmental factor
ESI-MS	Electrospray ionization – mass spectroscopy
FADS	Fluorescence-activated droplet sorting
FCDS	Flow cytometric droplet sorting
GSB	Gel-shell beads
HPLC	High-performance liquid chromatography
IL	Ionic liquid
MTBE	Methyl tert-butyl ether
PEG	Polyethylene glycol
PFA	Perfluoroalkoxy
PFE	Poly(fluorenylene ethynylene)
$scCO_2$	Supercritical CO_2
SpliMLiB	Split-and-Mix Library on Beads
TiTR	Tube-in-tube reactor

7. References

1. D. T. McQuade, P. H. Seeberger. Applying flow chemistry: methods, materials, and multistep synthesis. *J. Org. Chem.* **2013**, 78, 6384–6389. **DOI:** 10.1021/jo400583m. **DOI:**10.1021/jo400583m
2. K. F. Jensen. Flow chemistry—Microreaction technology comes of age. *AIChE J.* **2017**, 63, 858–869. **DOI:**10.1002/aic.15642
3. U.S. Department of Health and Human Services, Food and Drug Administration, Center for Drug Evaluation and Research, Center for Biologics Evaluation and Research, Center for Veterinary Medicine: Guidance for Industry: Process Validation: General Principles and Practices. **2011.**
4. U.S. Department of Health and Human Services, Food and Drug Administration, Center for Drug Evaluation and Research: Advancement of Emerging Technology Applications to Modernize the Pharmaceutical Manufacturing Base Guidance for Industry, **2015**.
5. P. Kleinebudde, J. Khinast, J. Rantanen (Eds.) Continuous Manufacturing of Pharmaceuticals; Wiley, Hoboken, NJ. **2017**, ISBN 9781119001324.
6. R. A. Sheldon. The E factor 25 years on: the rise of green chemistry and sustainability. *Green Chem.* **2017**, 19, 18–43. **DOI:**10.1039/C6GC02157C
7. C. Jiménez-González, P. Poechlauer, Q. B. Broxterman, B.-S. Yang, D. am Ende, J. Baird, C. Bertsch, R. E. Hannah, P. Dell'Orco, H. Noorman, S. Yee, R. Reintjens, A. Wells, V. Massonneau, J. Manley. Key Green Engineering Research Areas for Sustainable Manufacturing: A Perspective from Pharmaceutical and Fine Chemicals Manufacturers. *J. Org. Proc.*

Res. Dev. **2011**, *15*, 900–911. **DOI:**10.1021/op100327d
8. R. Wohlgemuth. Biocatalysis – Key enabling tools from biocatalytic one-step and multi-step reactions to biocatalytic total synthesis. *New Biotechnol.* **2021**, *60*, 113–123. **DOI:**10.1016/j.nbt.2020.08.006
9. Đ. Vasić-Rački. History of Industrial Biotransformations – Dreams and Realities. In: A. Liese, K. Seelbach, C. Wandrey (Eds.): Industrial Biotransformations, 2nd Ed., Wiley-VCH Verlag GmbH & Co. KgaA, Weinheim, **2006**, pp. 1–36. **DOI:**10.1002/9783527608188.ch1
10. R. A. Sheldon P. C. Pereira. Biocatalysis engineering: the big picture. *Chem. Soc. Rev.* **2017**, *46*, 2678—2691. **DOI:**10.1039/C6CS00854B
11. R. A. Sheldon, J. M. Woodley. Role of Biocatalysis in Sustainable Chemistry. *Chem. Rev.* **2018**, *118*, 801–838. **DOI:**10.1021/acs.chemrev.7b00203
12. K. Faber, W.-D. Fessner, N. J. Turner. Biocatalysis: Ready to Master Increasing Complexity. *Adv. Synth. Catal.* **2019**, *361*, 2373–2376. **DOI:**10.1002/adsc.201900610
13. U. Kragl. The Role of Reaction Engineering in Bioprocess Development. *Chimia.* **2020**, *74*, 378–381. **DOI:**10.2533/chimia.2020.378
14. R. Wohlgemuth, I. Plazl, P. Žnidaršič-Plazl, K. V. Gernaey, J. M. Woodley. Microscale technology and biocatalytic processes: opportunities and challenges for synthesis. *Trends Biotechnol.* **2015**, *33*, 302–314, **DOI:**10.1016/j.tibtech.2015.02.010
15. A. Liese, K. Seelbach, A. Buchholz, J. Haberland. Processes. In: A. Liese, K. Seelbach, C. Wandrey (Eds.): Industrial Biotransformations, 2nd Ed., Wiley-VCH Verlag GmbH & Co. KgaA, Weinheim, **2006**, pp. 147–514. **DOI:**10.1002/9783527608188.ch6a
16. P. Žnidaršič-Plazl. Biotransformations in microflow systems: Bridging the gap between academia and industry. *J Flow Chem*. **2017**, *7* (3-4), 111–117. **DOI:**10.1556/1846.2017.00021
17. J. M. Bolivar, J. Wiesbauer, B. Nidetzky. Biotransformations in microstructured reactors: more more than flowing with the stream? *Trends Biotechnol.* **2011**, *29*, 333–342. **DOI:**10.1016/j.tibtech.2011.03.005
18. J. M. Bolivar, B. Nidetzky. Multiphase biotransformations in microstructured reactors: opportunities for biocatalytic process intensification and smart flow processing. *Green Process. Synth*. **2013**, *2*, 541–559. **DOI:**10.1515/gps-2013-0091
19. P. Žnidaršič-Plazl. Enzymatic microreactors utilizing non-aqueous media. *Chim. Oggi – Chem. Today* **2014**, *32*, 54–61. https://www.teknoscienze.com/tks_article/enzymatic-microreactors-utilizing-non-aqueous-media/.
20. L. Tamborini, P. Fernandes, F. Paradisi, F. Molinari. Flow Bioreactors as Complementary Tools for Biocatalytic Process Intensification. *Trends Biotechnol.* **2018**, *36*, 73–88. **DOI:**10.1016/j.tibtech.2017.09.005
21. J. Britton, S. Majumdar, G. A. Weiss. Continuous flow biocatalysis. *Chem. Soc. Rev*. **2018**, *47*, 5891–5918. **DOI:**10.1039/C7CS00906B
22. P. Žnidaršič-Plazl. The promises and the challenges of biotransformations in micro-flow. *Biotechnol. J.* **2019**, *14*, 1800580, **DOI:**10.1002/biot.201800580
23. J. M. Bolivar, F. López-Gallego. Characterization and evaluation of immobilized enzymes for applications in flow reactors. *Curr. Opin. Green Sustain. Chem.* **2020**, *25*, 100349. **DOI:**10.1016/j.cogsc.2020.04.010
24. M. Romero-Fernandez, F. Paradisi. Protein immobilization technology for flow biocatalysis. *Curr. Opin. Chem. Biol.* **2020**, *55*, 1–8. **DOI:**10.1016/j.cbpa.2019.11.008
25. P. De Santis, L. Meyer, S. Kara. The Rise of Continuous Flow Biocatalysis – Fundamentals, Very Recent Developments and Future Perspectives. *React. Chem. Eng.* **2020**, *5*(12), 2155–2184. **DOI:**10.1039/D0RE00335B
26. M. S. Thomsen, B. Nidetzky. Continuous-flow Microchannel Reactors with Surface-immobilized Biocatalysts. In: W.-D. Fessner, T, Anthonsen (Eds.): Modern Biocatalysis. Wiley-VCH Verlag GmbH & Co. KgaA, Weinheim, **2009**, pp. 43–54. **DOI:**10.1002/9783527623839.ch3
27. M. Bajić, P. Žnidaršič-Plazl, M. Kingston, V. Hessel. General aspects of immobilized biocatalysts and their applications in flow. In: M. B. Nielsen (Ed.): Science of Synthesis: Knowledge Updates 2018/1. Georg Thieme, Stuttgart; New York. **2018**, pp. 397–443.
28. D. Valikhani, J. M. Bolivar, B. Nidetzky. Enzyme Immobilization in Wall-Coated Flow Microreactors. In: J. Guisan, J. Bolivar, F. López-Gallego, J. Rocha-Martín (Eds.): Immobilization of Enzymes and Cells. Methods in Molecular Biology, Humana, New York, NY, **2020**, vol. 2100. pp. 243–258. **DOI:**10.1007/978-1-0716-0215-7_16
29. G. Stojkovič, P. Žnidaršič-Plazl. Covalent Immobilization of Microbial Cells on Microchannel Surfaces. In: J. Guisan, J. Bolivar, F. López-Gallego, J. Rocha-Martín (Eds.): Immobilization of Enzymes and Cells. Methods in Molecular Biology, Humana, New York, NY, **2020**, vol. 2100. pp. 417–426. **DOI:**10.1007/978-1-0716-0215-7_28
30. R. DiCosimo, J. McAuliffe, A. J. Poulose, G. Bohlmann. Industrial use of immobilized enzymes. *Chem. Soc. Rev*. **2013**, *42*, 6437–6474. **DOI:**10.1039/c3cs35506c
31. J. J. Straathof. Quantitative Analysis of Industrial Biotransformations. In: A. Liese, K. Seelbach, C. Wandrey (Eds.): Industrial Biotransformations, 2nd Ed., Wiley-VCH Verlag GmbH & Co. KgaA, Weinheim, **2006**, pp. 515–520. **DOI:**10.1002/9783527608188.ch7
32. C. R. Thomas, D. Geer. Effects of shear on proteins in solution. *Biotechnol Lett.* **2011**, *33*, 443–456. **DOI:**10.1007/s10529-010-0469-4
33. C.-H. Ho, J. Yi, X. Wang. Biocatalytic Continuous Manufacturing of Diabetes Drug: Plantwide Process Modeling, Optimization, and Environmental and Economic Analysis. *ACS Sustain. Chem. Eng.* **2019**, *7*, 1038−1051. **DOI:**10.1021/acssuschemeng.8b04673
34. N. Miložič, M. Lubej, U. Novak, P. Žnidaršič-Plazl, I. Plazl. Evaluation of Diffusion Coefficient Determination using a microfluidic device. *Chem. Biochem. Eng. Q.* **2014**, *28*, 215–223. **DOI:**10.15255/CABEQ.2014.1938
35. M. Tišma, B. Zelić, Đ. Vasić-Rački, P. Žnidaršič-Plazl, I. Plazl.

Modelling of laccase-catalyzed L-DOPA oxidation in a microreactor. *Chem. Eng. J*. **2009**, *149*, 383–388. **DOI:**10.1016/j.cej.2009.01.025

36. C. K. Savile, J. M Janey, E. C. Mundorff, J. C Moore, S. Tam, W. R. Jarvis, J. C. Colbeck, A. Krebber, F. J. Fleitz, J. Brands, P. N. Devine, G. W. Huisman, G. J. Hughes. Biocatalytic Asymmetric Synthesis of Chiral Amines from Ketones Applied to Sitagliptin Manufacture. *Science* **2010**, *329*, 305–309. **DOI:**10.1126/science.1188934
37. J. Lawrence, B. O'Sullivan, G. J. Lye, R. Wohlgemuth, N. Szita. Microfluidic multi-input reactor for biocatalytic synthesis using transketolase. *J. Mol. Catal. B: Enzym*. **2013**, *95*, 111–117. **DOI:**10.1016/j.molcatb.2013.05.016
38. P. Gruber, M. P. C. Marques, P. Sulzer, R. Wohlgemuth, T. Mayr, F. Baganz, N. Szita. Real-time pH monitoring of industrially relevant enzymatic reactions in a microfluidic side-entry reactor (μSER) shows potential for pH control. *Biotechnol. J.* **2017**, *12*, 1600475. **DOI:**10.1002/biot.201600475
39. P. Žnidaršič-Plazl, I. Plazl. Steroid extraction in a microchannel system: mathematical modelling and experiments. *Lab Chip* **2007**, *7*, 883–889. **DOI:**10.1039/B704432A
40. M. Panić, M. Cvjetko Bubalo, I. Radojčić Redovniković. Designing a biocatalytic process involving deep eutectic solvents. *J. Chem. Technol. Biotechnol.* **2021,** *96*, 14–30. **DOI:**10.1002/jctb.6545
41. M. Cvjetko Bubalo, I. Sabotin, I. Radoš, J. Valentičič, T. Bosiljkov, M. Brnčić, P. Žnidaršič-Plazl. A comparative study of ultrasound-, microwave-, and microreactor-assisted imidazolium-based ionic liquid synthesis. *Green Proc. Synth*. **2013**, *2*, 579–590. **DOI:**10.1515/gps-2013-0086
42. R. A. Sheldon, R. Madeira Lau, M. J. Sorgedrager, F. van Rantwijk, K. R. Seddon. Biocatalysis in ionic liquids. *Green Chem*. **2002**, 4, 147–151. **DOI:**10.1039/b110008b
43. U. Novak, A. Pohar, I. Plazl, P. Žnidaršič-Plazl. Ionic liquid-based aqueous two-phase extraction within a microchannel system. *Sep. Purif. Technol.* **2012**, *97*:172–178. **DOI:**10.1016/j.seppur.2012.01.033
44. S.-X. Meng, L.-H. Xue, C.-Y. Xie, R.-X. Bai, X. Yang, Z.-P. Qiu, T. Guo, Y.-L. Wang, T. Meng. Enhanced enzymatic reaction by aqueous two-phase systems using parallel-laminar flow in a double Y-branched microfluidic device. *Chem. Eng. J.* **2018**, *335*, 392–400. **DOI:**10.1016/j.cej.2017.10.085
45. F. A. Vicente, I. Plazl, S .P. M. Ventura, P. Žnidaršič-Plazl. Separation and purification of biomacromolecules based on microfluidics. *Green Chem.* **2020**, *22*, 4391–4410. **DOI:**10.1039/C9GC04362D
46. M. Seručnik, F. A. Vicente, Ž. Brečko, J. A. P. Coutinho, S. P. M. Ventura, P. Žnidaršič-Plazl. Development of a microfluidic platform for R-phycoerythrin purification using an aqueous micellar two-phase system**.** *ACS Sustain. Chem. Eng.* **2020**, *8* (46), 17097–17105. **DOI:**10.1021/acssuschemeng.0c05042
47. T. Wang, C. Xu. Liquid–liquid–liquid three-phase microsystem: hybrid slug flow–laminar flow. *Lab Chip* **2020**, *20*, 1891–1897. **DOI:**10.1039/D0LC00292E
48. T. Maruyama, J. Uchida, T. Ohkawa, T. Futami, K. Katayama, K. Nishizawa, K. Sotowa, F. Kubota, No. Kamiya, M. Goto. Enzymatic degradation of *p*-chlorophenol in a two-phase flow microchannel system. *Lab Chip* **2003**, *3*, 308–12. **DOI:**10.1039/b309982b
49. P. Žnidaršič-Plazl, I. Plazl. Modelling and experimental studies on lipase-catalyzed isoamyl acetate synthesis in a microreactor. *Process Biochem*. **2009**, *44*, 1115–1121. **DOI:**10.1016/j.procbio.2009.06.003
50. Y. S. Huh, Y. Jun, Y. K. Hong, W. H. Hong, D. H. Kim. Microfluidic separation of (*S*)-ibuprofen using enzymatic reaction. *J. Mol. Catal. B: Enzym*. **2006**, 43, 96–101. **DOI:**10.1016/j.molcatb.2006.06.017
51. K. Marik, L. Ticha, L. Vobecka, M. Pribyl. Theoretical study on enzyme synthesis of cephalexin in a parallel-flow microreactor combined with electrically driven ATPS microextraction. *React. Chem. Eng*. **2020**, *5*, 570–583. **DOI:**10.1039/C9RE00482C
52. Y. Ding, P. D. Howes, A. J. DeMello. Recent Advances in Droplet Microfluidics. *Anal. Chem.* **2020**, *92*, 132–149. **DOI:**10.1021/acs.analchem.9b05047
53. T. S. Kaminski, P. Garstecki. Controlled droplet microfluidic systems for multistep chemical and biological assays. *Chem. Soc. Rev.* **2017**, *46*, 6210–6226. **DOI:**10.1039/C5CS00717H
54. S. L. Sjostrom, Y. Bai, M. Huang, Z. Liu, J. Nielsen, H. N. Joensson, H. Svahn. A. High-throughput screening for industrial enzyme production hosts by droplet microfluidics. *Lab Chip* **2014**, *14*, 806–813. **DOI:**10.1039/c3lc41398e
55. P. Mair, F. Gielen, F. Hollfelder. Exploring sequence space in search of functional enzymes using microfluidic droplets. *Curr. Opin. Chem. Biol.* **2017**, *37*,137–144. **DOI:**10.1016/j.cbpa.2017.02.018
56. B. Kintses, C. Hein, M. F. Mohamed, M. Fischlechner, F. Courtois, C. Laine, F. Hollfelder. Picoliter cell lysate assays in microfluidic droplet compartments for directed enzyme evolution. *Chem. Biol.* **2012**, *19*, 1001–1009. **DOI:**10.1016/j.chembiol.2012.06.009
57. D. Hess, T. Yang, S, Stavrakis. Droplet-based optofluidic systems for measuring enzyme kinetics. *Anal. Bioanal. Chem.* **2020**, *412*, 3265–3283. **DOI:**10.1007/s00216-019-02294-z
58. F. Ma, T. Guo, Y. Zhang, X. Bai, C. Li, Z. Lu, X. Deng, D. Li, K. Kurabayashi, G. Yang. An ultrahigh-throughput screening platform based on flow cytometric droplet sorting for mining novel enzymes from metagenomic libraries. *Environ. Microbiol.* **2020. DOI:**10.1111/1462-2920.15257
59. M. S. Packer, D. R. Liu. Methods for the directed evolution of proteins. *Nat. Rev. Genet*. **2015**, *16*, 379. **DOI:** 10.1038/nrg3927.
60. R. Obexer, A. Godina, X. Garrabou, P. R. E. Mittl, D. Baker, A. D. Griffiths, D. Hilvert. Emergence of a catalytic tetrad during evolution of a highly active artificial aldolase. *Nat. Chem.* **2017**, *9*, 50–56. **DOI:**10.1038/nchem.2596
61. F. W. Y. Chiu, S. Stavrakis. High-throughput droplet-based microfluidics for directed evolution of enzymes. *Electrophoresis* **2019**, *40*, 2860–2872. **DOI:**10.1002/elps.201900222
62. M. Fischlechner, Y. Schaerli, M. F. Mohamed, S. Patil, C. Abell, F. Hollfelder. Evolution of enzyme catalysts caged in

biomimetic gel-shell beads. *Nat. Chem.* **2014**, 6, 791–796. **DOI:**10.1038/nchem.1996

63. L. Lindenburg, T. Huovinen, K. van de Wiel, M. Herger, M. R. Snaith, F. Hollfelder. Split & mix assembly of DNA libraries for ultrahigh throughput on-bead screening of functional proteins. *Nucleic Acids Res.* **2020**, 48, e63,. **DOI:**10.1093/nar/gkaa270
64. F. Gielen, R. Hours, S. Emond, M. Fischlechner, U. Schell, F. Hollfelder. Ultrahigh-throughput–directed enzyme evolution by absorbance-activated droplet sorting (AADS). *Proc. Natl. Acad. Sci. U. S. A*. **2016**, 113, E7383. **DOI:**10.1073/pnas.1606927113
65. X. Wang, Y. Xin, L. Ren, Z. Sun, P. Zhu, Y. Ji, C. Li, J. Xu, B. Ma. Positive dielectrophoresis–based Raman-activated droplet sorting for culture-free and label-free screening of enzyme function in vivo. *Sci. Adv.* **2020**, 6, eabb3521. **DOI:**10.1126/sciadv.abb3521
66. D. G. Horvath, S. Braza, T. Moore, C. W. Pan, L. Zhu, O. S. Pak, P. Abbyad. Sorting by interfacial tension (SIFT): Label-free enzyme sorting using droplet microfluidics. *Anal. Chim. Acta* **2019**, 1089, 108e114. **DOI:**10.1016/j.aca.2019.08.025
67. X. W. Diefenbach, I. Farasat, E. D. Guetschow, C. J. Welch, R. T. Kennedy, S. Sun, J. C. Moore. Enabling Biocatalysis by High-Throughput Protein Engineering Using Droplet Microfluidics Coupled to Mass Spectrometry. *ACS Omega* **2018**, *3*, 1498–1508. **DOI:**10.1021/acsomega.7b01973
68. C. Holtze, S. A. Weisse, M. Vranceanu. Commercial Value and Challenges of Drop-Based Microfluidic Screening Platforms–An Opinion. *Micromachines* **2017**, *8*, 193. **DOI:**10.3390/mi8060193
69. J. H. Li, J. Chen, Y. J. Wang, G. S. Luo, H. M. Yu. Hydration of acrylonitrile to produce acrylamide using biocatalyst in a membrane dispersion microreactor. *Bioresour. Technol.* **2014**, *169*, 416–420. **DOI:**10.1016/j.biortech.2014.07.034
70. J. H. Li, M. Guo, S. Jiao, Y .J. Wang, G.S. Luo, H. M. Yu. A kinetic study of the biological catalytic hydration of acrylonitrile to acrylamide, *Chem. Eng. J.* **2017**, *317*, 699–706. **DOI:**10.1016/j.cej.2017.02.100
71. U. Novak, P. Žnidaršič-Plazl. Integrated lipase-catalyzed isoamyl acetate synthesis in a miniaturized system with enzyme and ionic liquid recycle. *Green Proc Synth*. **2013**, *2*, 561–568. **DOI:**10.1515/gps-2013-0082
72. https://www.corning.com/worldwide/en/innovation/corning-emerging-innovations/advanced-flow-reactors.html
73. F. Zhang, C. Cerato Noyerie, P. Woehl. E. D. Lavric. Intensified liquid/liquid mass transfer in Corning® Advanced-Flow™ reactors. *Chem. Eng. Trans.* **2011**, *24*, 1369–1374. **DOI:** 10.3303/CET1124229.
74. U. Novak, D. Lavric, P. Žnidaršič-Plazl. Continuous lipase B-catalyzed isoamyl acetate synthesis in a two-liquid phase system using Corning® AFR™ module coupled with a membrane separator enabling biocatalyst recycle. *J. Flow Chem.* **2016**, *6*, 33–38. **DOI:**10.1556/1846.2015.00038
75. L. Vobecká, L. Tichá, A. Atanasova, Z. Slouka, P. Hasal, M. Přibyl. Enzyme synthesis of cephalexin in continuous-flow microfluidic device in ATPS environment. *Chem. Eng. J.* **2020**, *396*, 125236. **DOI:**10.1016/j.cej.2020.125236
76. T. A. Hakala, F. Bialas, Z. Toprakcioglu, B. Bräuer, K. N. Baumann, A. Levin, G. J. L. Bernardes, C. F. W. Becker, T. P. J. Knowles. Continuous Flow Reactors from Microfluidic Compartmentalization of Enzymes within Inorganic Microparticles. *ACS Appl. Mater. Interfaces* **2020**, 12, 32951–32960. **DOI:**10.1021/acsami.0c09226
77. X. Tang, R. K. Allemann, T. Wirth. Optimising Terpene Synthesis with Flow Biocatalysis, *Eur. J. Org. Chem.* **2017**, 414–418. **DOI:**10.1002/ejoc.201601388
78. N. Adebar, J. E. Choi, L. Schober, R. Miyake, T. Iura, H. Kawabata, H. Gröger. Overcoming Work-Up Limitations of Biphasic Biocatalytic Reaction Mixtures Through Liquid-Liquid Segmented Flow Processes. *ChemCatChem* **2019**, *11*, 5788–5793. **DOI:**10.1002/cctc.201901107
79. R. Karande, A. Schmid, K. Buehler. Miniaturizing Biocatalysis: Enzyme-Catalyzed Reactions in an Aqueous/Organic Segmented Flow Capillary Microreactor. *Adv. Synth. Catal.* **2011**, *353*, 2511–2521. **DOI:**10.1002/adsc.201100394
80. R. Karande, A. Schmid, K. Buehler. Enzyme Catalysis in an Aqueous/Organic Segment Flow Microreactor: Ways to Stabilize Enzyme Activity. *Langmuir* **2010**, *26*(11), 9152–9159. **DOI:**10.1021/la9048727
81. R. Karande, A. Schmid, K. Buehler. Applications of Multiphasic Microreactors for Biocatalytic Reactions. *Org. Process Res. Dev*. **2016**, *20*, 361–370. **DOI:**10.1021/acs.oprd.5b00352
82. A. Šalić, B. Zelić. ADH catalysed hexanol oxidation with fully integrated NADH regeneration performed in microreactors connected in series. *RSC Adv*. **2014**, *4*, 41714–21. **DOI:**10.1039/C4RA05421K
83. K. Koch, R. J. F. van den Berg, P. J. Nieuwland, R. Wijtmans, H.E. Schoemaker, J.C.M. van Hest, F.P.J.T. Rutjes. Enzymatic enantioselective C–C-bond formation in microreactors. *Biotechnol. Bioeng.* **2008**, *99*, 1028–1033. **DOI:**10.1002/bit.21649
84. S. Mohr, K. Fisher, N. S. Scrutton, N. J. Goddard, P.R. Fielden. Continuous two-phase flow miniaturized bioreactor for monitoring anaerobic biocatalysis by pentaerythritol tetranitrate reductase. *Lab Chip* **2010**, *10*, 1929–1936. **DOI:**10.1039/c003561k
85. L. Vobecká, A. Romanov, Z. Slouka, P. Hasal, M. Přibyl. Optimization of aqueous two-phase systems for the production of 6-aminopenicillanic acid in integrated microfluidic reactors-separators. *New Biotechnol.* **2018**, *47*, 73–79. **DOI:**10.1016/j.nbt.2018.03.005
86. A. Romanov, Z. Slouka, M. Přibyl. Electric-field-enhanced selective separation of products of an enzymatic reaction in a membrane micro-contactor. *Biotechnol. Bioeng.* **2020**, 1–10. **DOI:**10.1002/bit.27597
87. A. Šalić, A. Jurinjak Tušek, A. Sander, B Zelić. Lipase catalysed biodiesel synthesis with integrated glycerol separation in continuously operated microchips connected in series. *New Biotechnol*. **2018**, *47*, 80–88. **DOI:**10.1016/j.nbt.2018.01.007

88. M. Gojun, M. Bačić, A. Ljubić, A. Šalić, B. Zelić. Transesterification in microreactors—overstepping obstacles and shifting towards biodiesel production on a microscale. *Micromachines* **2020**, *11*, 457. **DOI:**10.3390/mi11050457
89. J. Čech, W. Schrott, Z. Slouka, M. Přibyl, M. Brož, G. Kuncová, D. Šnita. Enzyme hydrolysis of soybean oil in a slug flow microsystem. *Biochem Eng J.* **2012**, *67*, 194–202. **DOI:**10.1016/j.bej.2012.06.015
90. N. Adebar, H. Gröger. Heterogeneous Catalysts "on the Move": Flow Chemistry with Fluid Immobilised (Bio)Catalysts. *Eur. J. Org. Chem.* **2020**, 6062–6067. **DOI:**10.1002/ejoc.202000705
91. B. Tomaszewski, A. Schmid, K. Buehler. Biocatalytic Production of Catechols Using a High Pressure Tube-in-Tube Segmented Flow Microreactor. *Org. Process Res. Dev*. **2014**, *18*, 1516–1526. **DOI:**10.1021/op5002116
92. M. O'Brien, I. R. Baxendale, S. V. Ley. Flow Ozonolysis Using a Semipermeable Teflon AF-2400 Membrane To Effect Gas-Liquid Contact. *Org. Lett.* **2010**, *12*,1596. **DOI:**10.1021/ol100322t
93. R. H. Ringborg, A. Toftgaard Pedersen, J. M. Woodley. Automated Determination of Oxygen-Dependent Enzyme Kinetics in a Tube-in-Tube Flow Reactor. *ChemCatChem* **2017**, *9*, 3285–3288. **DOI:**10.1002/cctc.201700811
94. J. Čech, M. Přibyl, D. Šnita. Three-phase slug flow in microchips can provide beneficial reaction conditions for enzyme liquid-liquid reactions. *Biomicrofluidics* **2013**, *7*, 054103. **DOI:**10.1063/1.4821168
95. E. Jones, K. McClean, S. Housden, G. Gasparini, I. Archer. Biocatalytic oxidase: Batch to continuous. *Chem. Eng. Res. Design* **2012**, *90*, 726–731. **DOI:**10.1016/j.cherd.2012.01.018
96. A. Manz, N. Graber, H. M. Widmer. Miniaturized Total Chemical Analysis Systems: a Novel Concept for Chemical Sensing. *Sens. Actuators B* **1990**, *1*, 244–248. **DOI:**10.1016/0925-4005(90)80209-I
97. P. Gruber, M. P. C. Marques, N. Szita, T. Mayr. Integration and application of optical chemical sensors in microbioreactors. *Lab Chip* **2017**, *17*, 2693–2712. **DOI:**10.1039/C7LC00538E
98. B. Ungerböck, A. Pohar, T. Mayr, I. Plazl. Online oxygen measurements inside a microreactor with modeling of transport phenomena. *Microfluid Nanofluid.* **2013**, *14*, 565–574. **DOI:**10.1007/s10404-012-1074-8

Povzetek

Industrijska biokataliza je ena ključnih spodbujevalnih tehnologij, ki skupaj s prehodom na kontinuirno vodenje procesov nudi možnosti za razvoj ekonomsko učinkovitih proizvodenj visoko kvalitetnih produktov in tvorbo majhne količine odpadkov. Izpostavljeni članek osvetljuje vlogo miniaturiziranih pretočnih reaktorjev s prostimi encimi in celicami v teh prizadevanjih na osnovi nedavnih primerov njihove uporabe v eno ali večfaznih reakcijah. Kapljična mikrofluidika omogoča izvedbo ultra visokozmogljivostnih presejalnih testov in hiter razvoj biokatalitskih procesov. Uporaba mikroreaktorjev edinstvenih konfiguracij zagotavlja zelo učinkovito kontaktiranje večfaznih sistemov, kar se odraža v intenzifikaciji procesov in izognitvi problemom, prisotnih pri konvencionalnem šaržnem procesiranju. Nadaljnja integracija z zaključnimi procesi nudi možnosti recikliranja biokatalizatorjev, kar prispeva k ekonomski učinkovitosti procesov. Uporaba okolju prijaznih topil podpira učinkovito reakcijsko inženirstvo in tlakuje pot tem visoko selektivnim katalizatorjem k postavitvi trajnostne proizvodnje.

Except when otherwise noted, articles in this journal are published under the terms and conditions of the Creative Commons Attribution 4.0 International License

Scientific paper

Zinc(II) Complexes Derived from Schiff Bases: Syntheses, Structures, and Biological Activity

Ling-Wei Xue,* Xu Fu, Gan-Qing Zhao and Qing-Bin Li

College of Chemistry and Chemical Engineering, Pingdingshan University, Pingdingshan Henan, 467000 P.R. China

** Corresponding author: E-mail: pdsuchemistry@163.com*

Received: 01-06-2020

Abstract

Three new zinc(II) complexes, $[Zn_2I_2(L^1)_2]$ (**1**), $[Zn(HL^2)_2(NCS)_2]$ (**2**), and $[ZnIL^3]$ (**3**), where L^1 is the anionic form of 2-[(6-methylpyridin-2-ylimino)methyl]phenol (HL^1), HL^2 is the zwitterionic form of 2-(cyclopropyliminomethyl)-5-fluorophenol (HL^2), and L^3 is the anionic form of 5-bromo-2-[(3-morpholin-4-ylpropylimino)methyl] phenol (HL^3), have been prepared and characterized by elemental analyses, IR, UV and NMR spectra, and single crystal X-ray crystallographic determination. Complex **1** is a dinuclear zinc complex, and complexes **2** and **3** are mononuclear zinc complexes. The Zn atoms in the complexes are in tetrahedral coordination. The effect of the complexes on the antimicrobial activity against *Staphylococcus aureus*, *Escherichia coli*, and *Candida albicans* were evaluated.

Keywords: Zinc complex, Schiff base, Crystal structure, Antimicrobial activity

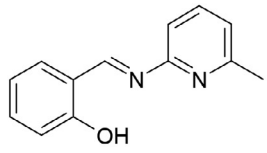
1. Introduction

The rapid increasing interest in the synthesis and structural studies of Schiff bases is due to their bioactivity and coordination properties.[1] Schiff bases are active against fungal, cancer, convulsant, oxidant and diuretic activities.[2] Metal complexes of Schiff bases have attracted considerable attention due to their versatile biological activity, such as antifungal, antibacterial and antitumor.[3] And, in general, the metal complexes have higher biological activities than the free Schiff bases. It has been shown that the Schiff base complexes derived from salicylaldehyde and its derivatives with primary amines, bearing the N_2O, N_2S, NO_2 or NSO donor sets, have potential antimicrobial activities.[4] Zinc is an important biological element, its complexes derived from Schiff bases have received particular attention due to their interesting antimicrobial potential.[5] Recent research indicated that the halide and pseudohalide groups can severely increase the antimicrobial activities.[6] Our research group has reported some metal complexes with effective antimicrobial activities.[7] In pursuit of new and efficient antimicrobial agents, in the present work, three new zinc(II) complexes, $[Zn_2I_2(L^1)_2]$ (**1**), $[Zn(HL^2)_2(NCS)_2]$ (**2**), and $[ZnIL^3]$ (**3**), where L^1 is the anionic form of 2-[(6-methylpyridin-2-ylimino)methyl]phenol (HL^1), HL^2 is the zwitterionic form of 2-(cyclopropyliminomethyl)-5-fluorophenol (HL^2), and L^3 is the anionic form of 5-bromo-2-[(3-morpholin-4-ylpropylimino)methyl]phenol (HL^3) (Scheme 1), are reported. To our knowledge, only two complexes with HL^1,[8] and no complexes with HL^2 and

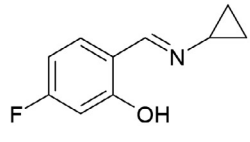
2. Experimental

2. 1. Material and Methods

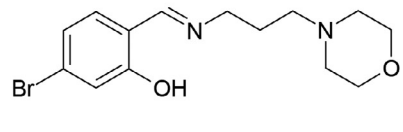
Salicylaldehyde, 4-fluorosalicylaldehyde, 4-bromosalicylaldehyde, 2-amino-6-methylpyridine, cyclopropylamine, and 3-morpholin-4-ylpropylamine were purchased from Fluka. Other reagents and solvents were analytical grade and used without further purification. Ele-



HL^1



HL^2



HL^3 HL^3 have been reported so far.

Scheme 1. The Schiff bases

mental (C, H, and N) analyses were made on a PerkinElmer Model 240B automatic analyser. Zinc analysis was carried out by EDTA titration. Infrared (IR) spectra were recorded on an IR-408 Shimadzu 568 spectrophotometer. UV-Vis spectra were recorded on a Lambda 900 spectrometer. X-ray diffraction was carried out on a Bruker SMART 1000 CCD area diffractometer. ^{1}H and ^{13}C NMR spectra were recorded on a Bruker 300 MHz spectrometer.

2. 2. Synthesis of the Ligands

2. 2. 1. 2-[(6-Methylpyridin-2-ylimino)methyl] phenol (HL^1)

Salicylaldehyde (1.22 g, 0.01 mol) and 2-amino-6-methylpyridine (1.06 g, 0.01 mol) were reacted in methanol (50 mL) for 30 min at 20 °C. The solvent was removed by distillation to give yellow product of HL^1. Analysis Calcd. (%) for $C_{13}H_{12}N_2O$: C 73.56, H 5.70, N 13.20. Found (%): C 73.41, H 5.82, N 13.05. IR data (KBr, cm^{-1}): 1623 (CH=N). UV in acetonitrile (λ, ε): 273 nm, 1.03×10^4 L mol^{-1} cm^{-1}; 350 nm, 2.77×10^3 L mol^{-1} cm^{-1}. ^{1}H NMR (300 MHz, d^6-DMSO): δ 12.11 (s, 1H, O*H*), 8.63 (s, 1H, C*H*=N), 7.68–7.64 (m, 3H, Ar*H* and Py*H*), 7.46 (t, 1H, Ar*H*), 7.10 (t, 1H, Ar*H*), 6.99 (d, 1H, Ar*H*), 6.81 (d, 1H, Py*H*), 2.50 (s, 3H, CH_3). ^{13}C NMR (126 MHz, DMSO) δ 162.32, 161.87, 160.11, 159.23, 138.12, 133.03, 132.72, 121.85, 121.36, 119.77, 115.61, 112.22, 23.70.

2. 2. 2. 2-(Cyclopropyliminomethyl)-5-fluorophenol (HL^2)

4-Fluorosalicylaldehyde (1.40 g, 0.01 mol) and cyclopropylamine (0.57 g, 0.01 mol) were reacted in methanol (50 mL) for 30 min at 20 °C. The solvent was removed by distillation to give yellow product of HL^2. Analysis Calcd. (%) for $C_{10}H_{10}FNO$: C 67.03, H 5.62, N 7.82. Found (%): C 67.16, H 5.54, N 7.96. IR data (KBr, cm^{-1}): 1627 (CH=N). UV in acetonitrile (λ, ε): 233 nm, 1.51×10^4 L mol^{-1} cm^{-1}; 265 nm, 8.38×10^3 L mol^{-1} cm^{-1}; 346 nm, 5.10×10^3 L mol^{-1} cm^{-1}. ^{1}H NMR (300 MHz, d^6-DMSO): δ 12.15 (s, 1H, O*H*), 8.67 (s, 1H, C*H*=N), 7.61 (d, 1H, Ar*H*), 6.87 (d, 1H, Ar*H*), 6.43 (s, 1H, Ar*H*), 1.82 (m, 1H, C*H*), 0.71 (m, 2H, CH_2), 0.43 (m, 2H, CH_2). ^{13}C NMR (126 MHz, DMSO) δ 167.13, 162.77, 161.10, 132.05, 120.54, 109.23, 103.82, 35.11, 6.77.

2. 2. 3. 5-Bromo-2-[(3-morpholin-4-ylpropylimino)methyl]phenol (HL^3)

4-Bromosalicylaldehyde (2.01 g, 0.01 mol) and 3-morpholin-4-ylpropylamine (1.44 g, 0.01 mol) were reacted in methanol (50 mL) for 30 min at 20 °C. The solvent was removed by distillation to give yellow product of HL^3. Analysis Calcd. (%) for $C_{14}H_{19}BrN_2O_2$: C 51.39, H 5.85, N 8.56. Found (%): C 51.31, H 5.77, N 8.71. IR data (KBr, cm^{-1}): 1633 (CH=N). UV in acetonitrile (λ, ε): 228 nm, 1.36×10^4 L mol^{-1} cm^{-1}; 274 nm, 6.73×10^3 L mol^{-1} cm^{-1}; 335 nm, 3.35×10^3 L mol^{-1} cm^{-1}. ^{1}H NMR (300 MHz, d^6-DMSO): δ 11.78 (s, 1H, O*H*), 8.58 (s, 1H, C*H*=N), 7.51 (d, 1H, Ar*H*), 7.47 (s, 1H, Ar*H*), 7.11 (d, 1H, Ar*H*), 3.68 (t, 2H, CH_2), 3.60 (q, 4H, CH_2), 2.43 (t, 2H, CH_2), 2.27 (q, 4H, CH_2), 1.72 (m, 2H, CH_2). ^{13}C NMR (126 MHz, DMSO) δ 162.11, 156.35, 133.20, 125.07, 124.31, 120.89, 114.34, 67.18, 62.83, 59.22, 54.71, 29.67.

2. 3. Synthesis of the Complexes

2. 3. 1. $[Zn_2I_2(L^1)_2]$ (1)

Then, a methanol solution (20 mL) of ZnI_2 (0.319 g, 1.0 mmol) was added to the methanol solution of HL^1 (0.212 g, 1.0 mmol). The mixture was stirred for 1 h at 20 °C to give a colorless solution. Colorless block-shaped single crystals suitable for X-ray diffraction were formed by slow evaporation of the solution in air for several days. The yield was 45% (based on HL^1). Analysis Calcd. (%) for $C_{26}H_{22}I_2N_4O_2Zn_2$: C 38.69, H 2.75, N 6.94, Zn 16.20. Found (%): C 38.82, H 2.63, N 6.85, Zn 16.37. IR data (KBr, cm^{-1}): 1615 (CH=N). UV in acetonitrile (λ, ε): 310 nm, 3.13×10^3 L mol^{-1} cm^{-1}; 410 nm, 2.32×10^3 L mol^{-1} cm^{-1}. ^{1}H NMR (300 MHz, d^6-DMSO): δ 8.71 (s, 1H, C*H*=N), 7.81–7.45 (m, 4H, Ar*H* and Py*H*), 7.10 (t, 1H, Ar*H*), 6.92 (d, 1H, Ar*H*), 6.82 (d, 1H, Py*H*), 2.50 (s, 3H, CH_3). ^{13}C NMR (126 MHz, DMSO) δ 163.41, 162.02, 161.05, 159.33, 138.17, 132.92, 132.65, 121.82, 121.71, 120.14, 115.66, 112.31, 23.70.

2. 3. 2. $[Zn(HL^2)_2(NCS)_2]$ (2)

A methanol solution (20 mL) of $Zn(ClO_4)_2{\cdot}6H_2O$ (0.372 g, 1.0 mmol) and ammonium thiocyanate (0.076 g, 1.0 mmol) was added to the methanol solution of HL^2 (0.179 g, 1.0 mmol). The mixture was stirred for 1 h at 20 °C to give a colorless solution. Colorless block-shaped single crystals suitable for X-ray diffraction were formed by slow evaporation of the solution in air for several days. The yield was 37% (based on HL^2). Analysis Calcd. (%) for $C_{22}H_{20}F_2N_4O_2S_2Zn$: C 48.94, H 3.73, N 10.38, Zn 12.11. Found (%): C 49.13, H 3.82, N 10.28, Zn 12.35. IR data (KBr, cm^{-1}): 2073 (NCS), 1653 (CH=NH). UV in acetonitrile (λ, ε): 270 nm, 3.56×10^3 L mol^{-1} cm^{-1}; 305 nm, 1.91×10^3 L mol^{-1} cm^{-1}; 350 nm, 8.33×10^2 L mol^{-1} cm^{-1}; 397 nm, 2.06×10^2 L mol^{-1} cm^{-1}. ^{1}H NMR (300 MHz, d^6-DMSO): δ 10.82 (s, 1H, N*H*), 8.75 (s, 1H, C*H*=N), 7.61 (d, 1H, Ar*H*), 6.87 (d, 1H, Ar*H*), 6.46 (s, 1H, Ar*H*), 1.83 (m, 1H, C*H*), 0.71 (m, 2H, CH_2), 0.43 (m, 2H, CH_2). ^{13}C NMR (126 MHz, DMSO) δ 167.35, 162.45, 163.27, 135.86, 132.13, 119.71, 109.43, 104.51, 34.78, 6.77.

2. 3. 3. $[ZnIL^3]$ (3)

A methanol solution (20 mL) of ZnI_2 (0.319 g, 1.0 mmol) was added to the methanol solution of HL^3 (0.326 g,

1.0 mmol). The mixture was stirred for 1 h at 20 °C to give a colorless solution. Colorless block-shaped single crystals suitable for X-ray diffraction were formed by slow evaporation of the solution in air for several days. The yield was 54% (based on HL^3). Analysis Calcd. (%) for $C_{14}H_{18}BrIN_2O_2Zn$: C 32.43, H 3.50, N 5.40, Zn 12.61. Found (%): C 32.27, H 3.63, N 5.45, Zn 12.82. IR data (KBr, cm^{-1}): 1637 (CH=N). UV in acetonitrile (λ, ε): 225 nm, 3.78×10^3 L mol^{-1} cm^{-1}; 242 nm, 3.11×10^3 L mol^{-1} cm^{-1}; 278 nm, 1.85×10^3 L mol^{-1} cm^{-1}; 357 nm, 9.28×10^2 L mol^{-1} cm^{-1}. ^{1}H NMR (300 MHz, d^6-DMSO): δ 8.67 (s, 1H, C*H*=N), 7.50 (d, 1H, Ar*H*), 7.45 (s, 1H, Ar*H*), 7.11 (d, 1H, Ar*H*), 3.67 (t, 2H, CH_2), 3.62 (q, 4H, CH_2), 2.37 (t, 2H, CH_2), 2.27 (q, 4H, CH_2), 1.73 (m, 2H, CH_2). ^{13}C NMR (126 MHz, DMSO) δ 164.32, 158.11, 132.87, 125.12, 124.26, 121.81, 114.51, 67.25, 63.02, 59.38, 54.66, 29.71.

2. 4. X-Ray Diffraction

Data were collected from selected crystals mounted on glass fibres. The data were collected with MoK_α radiation (0.71073 Å) at 298(2) K with a Bruker SMART 1000 CCD area diffractometer. The data for the complexes were processed with SAINT[9] and corrected for absorption using SADABS.[10] Multi-scan absorption corrections were applied with ψ-scans.[11] The structures were solved by direct method using SHELXS-97 and refined by full-matrix least-squares techniques on F^2 using anisotropic displacement parameters.[12] The imino H atom in complex **2** was located form a difference Fourier map and refined with N–H distance of 0.90(1) Å. All other hydrogen atoms were placed at the calculated positions. Idealized H atoms were refined with isotropic displacement parameters set to 1.2 (1.5 for methyl groups) times the equivalent isotropic *U* values of the parent carbon atoms. The crystallographic data for the complexes are listed Table 1.

Supplementary material has been deposited with the Cambridge Crystallographic Data Centre (nos. 1448092 (**1**), 1975485 (**2**), 1975486 (**3**)); deposit@ccdc.cam.ac.uk or http://www.ccdc.cam.ac.uk).

2. 5. Antimicrobial Assay

Qualitative determination of antimicrobial activity was done using the disk diffusion method.[13] The antibac-

Table 1. Crystallographic data and experimental details for the complexes

	1	**2**	**3**
Molecular formula	$C_{26}H_{22}I_2N_4O_2Zn_2$	$C_{22}H_{20}F_2N_4O_2S_2Zn$	$C_{14}H_{18}BrIN_2O_2Zn$
Formula weight	807.02	539.91	518.48
Crystal size, mm	0.27×0.26×0.26	0.23×0.22×0.21	0.17×0.15×0.15
Radiation (λ, Å)	MoK_α (0.71073)	MoK_α (0.71073)	MoK_α (0.71073)
Crystal system	Triclinic	Monoclinic	Monoclinic
Space group	*P*-1	*P*2/*c*	$P2_1/c$
Unit cell dimensions:			
a, Å	8.056(2)	10.920(1)	15.065(2)
b, Å	8.659(2)	7.021(1)	9.023(1)
c, Å	11.034(2)	16.122(1)	12.860(1)
α, °	78.264(2)	90	90
β, °	74.640(2)	97.347(1)	105.203(1)
γ, °	69.431(2)	90	90
V, Å^3	689.7(3)	1225.9(3)	1687.0(3)
Z	1	2	4
ρ_{calcd}, g cm^{-3}	1.943	1.463	2.041
F(000)	388	552	1000
T_{min}, T_{max}	0.4109, 0.4222	0.7678, 0.7847	0.4463, 0.4840
Absorption coefficient, mm^{-1}	4.007	1.213	5.659
θ Range for data collection, °	1.93–25.49	1.88–25.50	1.40–25.50
Reflections collected	4159	6294	33117
Independent reflections (R_{int})	2571 (0.0315)	2287 (0.0495)	3135 (0.0809)
Reflections with $I > 2\sigma(I)$	1832	1473	2431
Data/parameters	2571/164	2287/154	3135/190
Restraints	0	1	0
Goodness-of-fit on F^2	1.040	1.024	1.058
Final *R* indices ($I > 2\sigma(I)$)	$R_1 = 0.0457$	$R_1 = 0.0688$	$R_1 = 0.0404$
	$wR_2 = 0.0878$	$wR_2 = 0.1835$	$wR_2 = 0.0936$
R indices (all data)	$R_1 = 0.0736$	$R_1 = 0.1057$	$R_1 = 0.0605$
	$wR_2 = 0.1026$	$wR_2 = 0.2073$	$wR_2 = 0.1081$
$\Delta\rho_{max}$, $\Delta\rho_{min}$, *e* Å^{-3}	1.38, –0.55	1.47, –0.39	0.84, –0.64

terial activity was tested against *B. subtilis*, *E. coli*, *P. fluorescence* and *S. aureus* using MH medium (Mueller–Hinton medium). The MICs (minimum inhibitory concentrations) of the test compounds were determined by a colorimetric method using the dye MTT [3-(4,5-dimethylthiazol-2-yl)-2,5-diphenyltetrazolium bromide]. A stock solution of the synthesized compound (50 μg mL^{-1}) in DMSO was prepared and quantities of the test compounds were incorporated in specified quantity of sterilized liquid MH medium. A specified quantity of the medium containing the compound was poured into micro-titration plates. A suspension of the microorganism was prepared to contain approximately 10^5 cfu mL^{-1} and applied to micro-titration plates with serially diluted compounds in DMSO to be tested and incubated at 37 °C for 24 h. After the MICs were visually determined on each of the micro-titration plates, 50 μL of PBS containing 2 mg of MTT per millilitre was added to each well. Incubation was continued at room temperature for 4–5 h. The content of each well was removed and 100 μL of isopropanol containing hydrochloric acid was added to extract the dye. After 12 h of incubation at room temperature, the optical density (OD) was measured with a micro-plate reader at 550 nm.

3. Results and Discussion

3. 1. Chemistry

The Schiff bases were readily prepared by the reaction of equimolar quantities of aldehyde and amines in methanol, which were used directly for the preparation of the zinc complexes at ambient temperature. The zinc complexes are stable at room temperature in the solid state and soluble in common organic solvents, such as methanol, ethanol, chloroform, and acetonitrile. The results of the elemental analyses are in accord with the composition suggested for the complexes.

3. 2. IR and Electronic Spectra

The IR spectra of the complexes were analyzed and compared with those of their free Schiff bases. The intense absorption bands at 1623, 1627 and 1633 cm^{-1} in the spectra of the Schiff bases HL^1, HL^2 and HL^3, respectively, can be assigned to the C=N stretching. In the complexes, these bands are shifted to 1615, 1653 and 1637 cm^{-1} upon complexation with the zinc atoms, which can be attributed to the coordination of the imine nitrogen to the metal centre.[14] The absorption of this band for complex **2** is located at higher wavelength than complexes **2** and **3**, which is due to the protonation of the imino group. The typical absorption at 2073 cm^{-1} in the spectrum of complex **2** is assigned to the vibration of the NCS ligand.[15]

UV–Vis spectra of the free Schiff bases and the complexes were recorded in HPLC grade acetonitrile solution. The spectra of the Schiff bases exhibit bands at 220–280 nm and 330–360 nm attributed to $\pi\rightarrow\pi^*$ and $n\rightarrow\pi^*$ transitions. In the spectra of the complexes the charge transfer bands at 220–280 nm remain intact, in agreement with the $\pi\rightarrow\pi^*$ transitions of the Schiff base ligands. The remaining bands at 350–410 nm in the spectra of the complexes are assigned to the metal to ligand charge transfer (MLCT) transition.[16]

3. 3. NMR Spectra

The ^1H NMR spectra of the Schiff bases exhibit OH (phenolic) proton resonances at 11.78–12.15 ppm, imine proton resonances at 8.58–8.67 ppm and aromatic proton resonances in the range 6.43–7.68 ppm, respectively. On coordination, the signal due to OH proton disappears, indicating deprotonation of the phenolic OH and subsequent coordination of the phenoxide oxygen to the metal atoms. Involvement of the imine nitrogen in coordination has shifted the resonance signal of the imine proton by 0.7–0.9 ppm. The peaks observed in ^{13}C NMR spectra of the Schiff bases and the complexes are in expected range and values are given in experimental section. The carbonyl C and imine C atoms in the complexes have shifted compared to their ligands, confirming the coordination through carbonyl O and imine N atoms.[17]

3. 4. Crystal Structure Description of the Complexes

Complex **1** is a phenolato-bridged dinuclear zinc(II) compound (Figure 1), with Zn···Zn separation of 3.096(2) Å. The crystal of the complex possesses a crystallographic inversion symmetry, with the inversion center located at the middle of the two zinc atoms. The Zn atom in the complex is coordinated by one pyridine N and two phenolate O atoms from two Schiff base ligands, and one I atom, generating tetrahedral geometry. The Schiff base acts as a bidentate ligand, and forms a six-membered chelate ring with the metal center through the phenolate O and imine N. The bond distances subtended at the metal atoms are

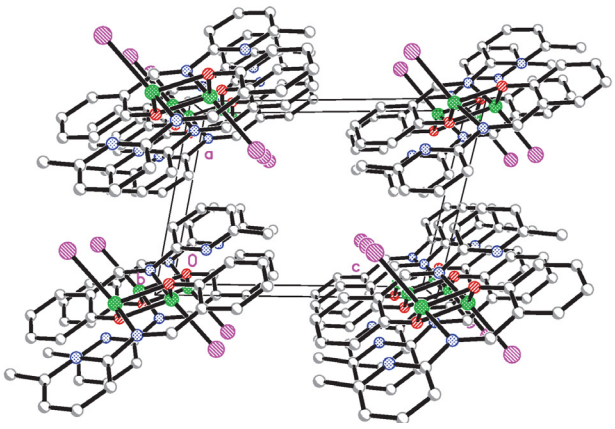


Figure 2. Molecular packing structure of complex **1**.

comparable to those observed in similar zinc(II) complexes with Schiff bases.[18]

In the crystal structure of the complex, molecules are stacked *via* π···π interactions (Table 3) along the *b* axis (Figure 2).

Complex **2** is a thiocyanate-coordinated mononuclear zinc(II) compound (Figure 3). The Zn atom in the complex is coordinated by two phenolate O atoms from two zwitterionic Schiff base ligands, and two thiocyanate N atoms, generating tetrahedral geometry. The Schiff base acts as a monodentate ligand, with the phenol H atom transferred to the imino N group. The bond distances subtended at the metal atoms are comparable to those observed in similar zinc(II) complexes with Schiff bases and thiocyanate ligands.[19]

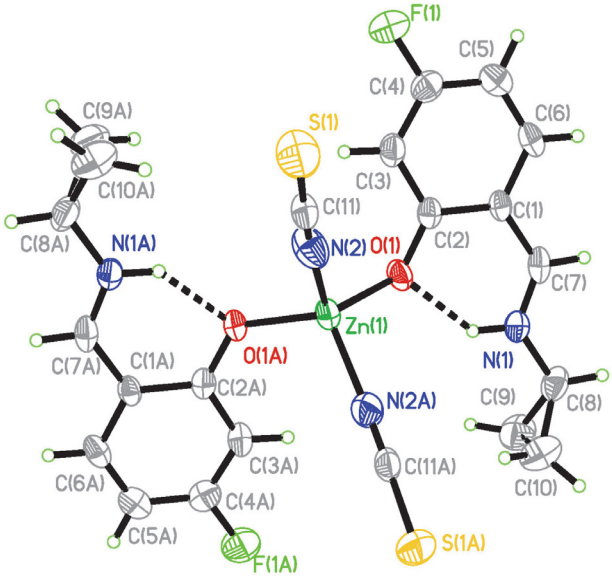


Figure 3. Molecular structure of complex **2**. Atoms labeled with the suffix A are at the symmetry position – *x*, *y*, 1/2 – *z*.

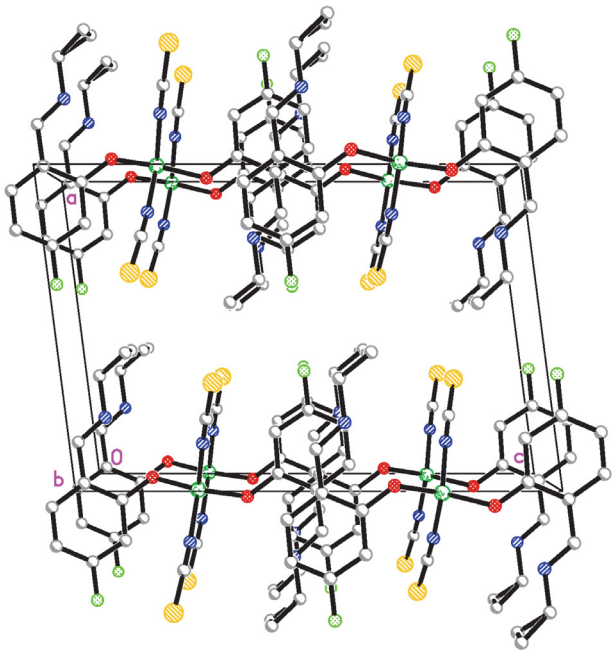


Figure 4. Molecular packing structure of complex **2**.

In the crystal structure of the complex, molecules are stacked *via* π···π interactions (Table 3) including the pyridine ring N(2)-C(8)-C(12)-C(11)-C(10)-C(9) and the chelate ring Zn(1)-N(1)-C(8)-N(2), along the *b* axis (Figure 4).

Complex **3** is an iodide-coordinated mononuclear zinc(II) compound (Figure 5). The Zn atom in the complex is coordinated by one phenolate O, one imino N, and one morpholine N atoms of the Schiff base ligand, and one I atom, generating tetrahedral geometry. The Schiff base acts as a tridentate ligand, with the morpholine ring adopts chair configuration. The bond distances subtended at the metal atoms are comparable to those observed in similar zinc(II) complexes with Schiff bases and thiocyanate ligands.[20]

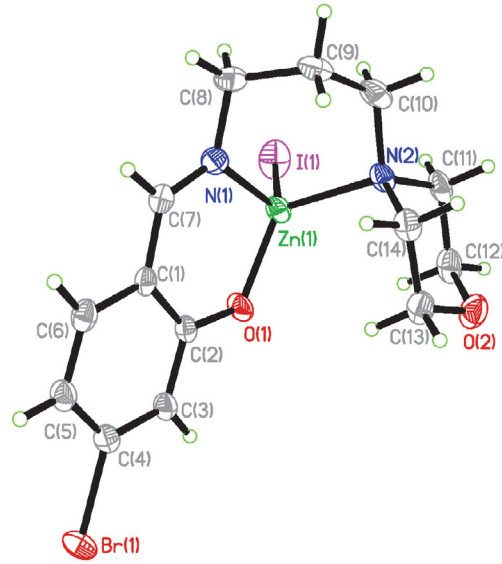


Figure 5. Molecular structure of complex **3**.

In the crystal structure of the complex, molecules are stacked *via* π···π interactions (Table 3) including the phenyl ring C(1)-C(2)-C(3)-C(4)-C(5)-C(6) and the chelate ring Zn(1)-O(1)-C(2)-C(1)-C(7)-N(1), along the *b* axis (Figure 6).

3. 5. Antimicrobial Activity

The results of the antimicrobial activity are summarized in Table 4. A comparative study of minimum inhibitory concentration (**MIC**) values of the Schiff base and the zinc complex indicated that the complex has more effective activity against *Staphylococcus aureus*, *Escherichia coli*, and *Candida albicans* than the free Schiff base. Generally,

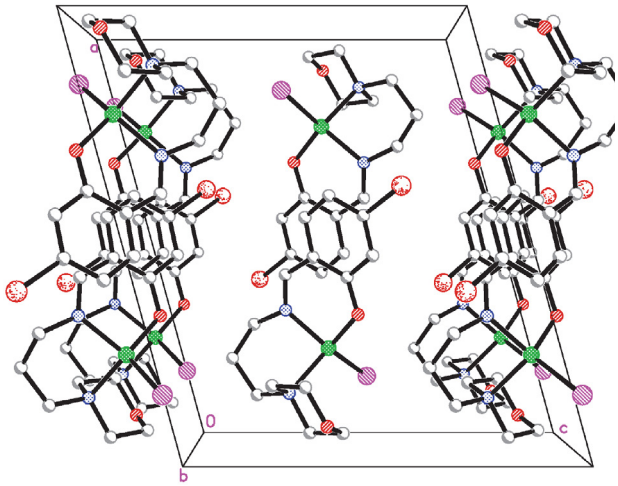


Figure 6. Molecular packing structure of complex **3**.

this is caused by the greater lipophilic nature of the complex than the ligand. Such increased activity of the metal chelates can be explained on the basis of chelating theory.[21] On chelating, the polarity of the metal atoms will be reduced to a greater extent due to the overlap of the ligand orbital and partial sharing of positive charge of the metal atoms with donor atoms. Further, it increases the delocalization of π-electrons over the whole chelate ring and enhances the lipophilicity of the complex. This increased lipophilicity enhances the penetration of the complex into lipid membrane and blocks the metal binding sites on enzymes of micro-organisms.

The complexes have stronger activities against *Staphylococcus aureus*, *Escherichia coli*, and *Candida albicans* than the free Schiff bases. For *Staphylococcus aureus* and *Escherichia coli*, the activities of the complexes are less than the control drug Tetracycline. But for *Candida albi-*

Table 2. Selected bond distances (Å) and angles (°) for the complexes

1			
Zn(1)–O(1)$^{\#1}$	1.990(5)	Zn(1)–O(1)	2.080(4)
Zn(1)–N(1)	2.014(5)	Zn(1)–I(1)	2.541(1)
O(1)–Zn(1)–N(1)$^{\#1}$	122.3(2)	O(1)–Zn(1)–O(1)$^{\#1}$	81.0(2)
O(1)–Zn(1)–N(1)	88.1(2)	O(1)–Zn(1)–I(1)$^{\#1}$	113.3(1)
N(1)–Zn(1)–I(1)	122.9(2)	O(1)–Zn(1)–I(1)	113.1(1)
2			
Zn(1)–O(1)	1.929(4)	Zn(1)–N(2)	1.958(6)
O(1)–Zn(1)–O(1)$^{\#2}$	117.1(2)	O(1)–Zn(1)–N(2)	109.8(2)
O(1)–Zn(1)–N(2)$^{\#2}$	103.8(2)	N(2)–Zn(1)–N(2)$^{\#2}$	112.7(4)
3			
Zn(1)–I(1)	2.5319(8)	Zn(1)–O(1)	1.905(4)
Zn(1)–N(1)	1.989(5)	Zn(1)–N(2)	2.111(4)
O(1)–Zn(1)–N(1)	96.47(18)	O(1)–Zn(1)–N(2)	120.94(19)
N(1)–Zn(1)–N(2)	94.06(19)	O(1)–Zn(1)–I(1)	116.24(13)
N(1)–Zn(1)–I(1)	119.21(14)	N(2)–Zn(1)–I(1)	107.99(12)

Symmetry codes: $^{\#1}$ – *x*, 1 – *y*, 2 – *z*; $^{\#2}$ – *x*, 1 – *y*, 2 – *z*.

Table 3. Parameters between the planes for the complexes

Cg	Distance between ring centroids (Å)	Dihedral angle (°)	Perpendicular distance of Cg(I) on Cg(J) (Å)	Beta angle (°)	Gamma angle (°)	Perpendicular distance of Cg(J) on Cg(I) (Å)
1						
Cg(1)-*Cg*(2)$^{\#1}$	3.879	4.877	3.4456	32.19	27.34	3.2826
Cg(2)-*Cg*(2)$^{\#1}$	3.657	0	3.3852	22.24	22.24	3.3852
Cg(2)-*Cg*(3)$^{\#2}$	3.664	2.391	–3.4737	18.96	18.56	–3.4655
2						
Cg(4)-*Cg*(4)$^{\#3}$	4.152	0	–3.428	34.36	34.36	-3.428
3						
Cg(5)-*Cg*(6)$^{\#4}$	4.143	2.088	–3.295	37.02	37.33	–3.308
Cg(6)-*Cg*(6)$^{\#5}$	4.260	0	3.654	30.91	30.91	3.654

1: *Cg*(1), *Cg*(2) and *Cg*(3) are the centroids of Zn(1)-N(1)-C(8)-N(2), N(2)-C(8)-C(12)-C(11)-C(10)-C(9) and C(1)-C(2)-C(3)-C(4)-C(5)-C(6), respectively. **2**: *Cg*(4) is the centroid of C(1)-C(2)-C(3)-C(4)-C(5)-C(6). **3**: *Cg*(5) and *Cg*(6) are the centroids of Zn(1)-O(1)-C(2)-C(1)-C(7)-N(1) and C(1)-C(2)-C(3)-C(4)-C(5)-C(6), respectively. Symmetry codes: #1: 1-*x*, 1-*y*, -*z*; #2: 2-*x*, 1-*y*, -*z*; #3: -*x*, 1-*y*, -*z*; #4: 1-*x*, 1-*y*, 1-*z*; #5: 1-*x*, 2-*y*, 1-*z*.

cans, the complexes have stronger activities than Tetracycline. Complex **2** has the most activity against *Staphylococcus aureus* with MIC value of 2 μg/mL. The three zinc complexes have higher activities against *Staphylococcus aureus* and lower activities against *Escherichia coli* and *Candida albicans* than the zinc(II) and manganese(II) complexes with the ligand *N*'-(1-(pyridin-2-yl)ethylidene)isonicotinohydrazide.[22] Further work needs to be carried out to investigate the structure-activity relationship.

Table 4. MIC values (μg/mL) for the antimicrobial activities of the tested compounds

Compound	*Staphylococcus aureus*	*Escherichia coli*	*Candida albicans*
HL^1	128	256	> 1024
HL^2	128	128	> 1024
HL^3	64	256	> 1024
1	4	16	128
2	2	32	256
3	4	32	256
Tetracycline	0.25	2.0	> 1024

4. Conclusions

In summary, three new zinc(II) complexes with halide and pseudohalide ligands derived from Schiff bases have been prepared and characterized. The structures of the complexes are confirmed by single crystal X-ray crystallographic determination. The Zn atoms in the complexes are in tetrahedral coordination. The complexes have better activities on the bacteria *Staphylococcus aureus* and *Escherichia coli* than the control drug Tetracycline. Moreover, the complexes have stronger activities against *Candida albicans* than Tetracycline. Interestingly, complex **2** has the most activity against *Staphylococcus aureus* with MIC value of 2 μg/mL.

5. Acknowledgments

This research was supported by the National Sciences Foundation of China (nos. 20676057 and 20877036) and Top-class foundation of Pingdingshan University (no. 2008010).

6. References

1. L. N. Obasi, J. C. Ezeorah, V. Ossai, A. Jude, U. S. Oruma, A. Ibezim, M. Lutter, L. Rhyman, K. Jurkschat, N. Dege, P. Ramasami, *J. Mol. Struct.* **2019**, *1188*, 69–75. **DOI:**10.1016/j.molstruc.2019.03.081
2. (a) S. K. Bharti, G. Nath, R. Tilak, S. K. Singh, *Eur. J. Med. Chem.* **2010**, *45*, 651–660; **DOI:**10.1016/j.ejmech.2009.11.008
(b) M. Ceruso, F. Carta, S. M. Osman, Z. Alothman, S. M. Monti, C. T. Supuran, *Bioorg. Med. Chem.* **2015**, *23*, 4181–4187; **DOI:**10.1016/j.bmc.2015.06.050
(c) W. L. Wang, D. Agustin, R. Poll, *Mol. Catal.* **2017**, *443*, 52–59; **DOI:**10.1016/j.mcat.2017.09.033
(d) M. Hanif, M. Hassan, M. Rafiq, Q. Abbas, A. Ishaq, S. Shahzadi, S.-Y. Seo, M. Saleem, *Pharm. Chem. J.* **2018**, *52*, 424–437; **DOI:**10.1007/s11094-018-1835-0
(e) P. Mishra, P. N. Gupta, K. Ashok, R. Shukla, R. C. Srimal, *Indian J. Physiol. Pharm.* **1995**, *39*, 169–172.
3. (a) K. Venkateswarlu, N. Ganji, S. Daravath, K. Kanneboina, K. Rangan, Shivaraj, *Polyhedron* **2019**, *171*, 86–97; **DOI:**10.1016/j.poly.2019.06.048
(b) R. A. Ammar, A. N. M. A. Alaghaz, M. E. Zayed, L. A. Al-Bedair, *J. Mol. Struct.* **2017**, *1141*, 368–381; **DOI:**10.1016/j.molstruc.2017.03.080
(c) N. R. Palepu, S. L. Nongbri, J. R. Premkumar, A. K. Verma, K. Bhattacharjee, S. R. Joshi, S. Forbes, Y. Mozharivskyj, R. Thounaojam, K. Aguan, M. R. Kollipara, *J. Biol. Inorg. Chem.* **2015**, *20*, 619–638; **DOI:**10.1007/s00775-015-1249-3
(d) M. Aidi, H. Keypour, A. Shooshtari, M. Mahmoudabadi, M. Bayat, Z. Ahmadvand, R. Karamian, M. Asadbegy, S. Tavatli, R. W. Gable, *Polyhedron* **2019**, *167*, 93–102. **DOI:**10.1016/j.poly.2019.02.030
4. (a) C. X. Yuan, L. P. Lu, X. L. Gao, Y. B. Wu, M. L. Guo, Y. Li, X. Q. Fu, M. L. Zhu, *J. Bio. Inorg. Chem.* **2009**, *14*, 841–851; **DOI:**10.1007/s00775-009-0496-6
(b) P. A. Khalf-Alla, S. S. Hassan, M. M. Shoukry, *Inorg. Chim. Acta* **2019**, *492*, 192–197; **DOI:**10.1016/j.ica.2019.04.035
(c) S. Daravath, A. Rambabu, N. Vamsikrishna, N. Ganji, S. Raj, *J. Coord. Chem.* **2019**, *72*, 1973–1993; **DOI:**10.1080/00958972.2019.1634263
(d) M. S. S. Adam, L. H. Abdel-Rahman, A. M. Abu-Dief, N. A. Hashem, *Inorg. Nano-Met. Chem.* **2019**, *50*, 136–150; **DOI:**10.1080/24701556.2019.1672735
(e) M. Sonmez, M. Celebi, I. Berber, *Eur. J. Med. Chem.* **2010**, *45*, 1935–1940; **DOI:**10.1016/j.ejmech.2010.01.035
(f) L. W. Xue, G. Q. Zhao, Y. J. Han, Y. X. Feng, *Russ. J. Coord. Chem.* **2011**, *37*, 262–269; **DOI:**10.1134/S1070328411030110
(g) L. W. Xue, Y. J. Han, G. Q. Zhao, Y. X. Feng, *Russ. J. Coord. Chem.* **2012**, *38*, 24–28. **DOI:**10.1134/S1070328411120104
5. (a) Q.-M. Hasi, Y. Fan, X.-X. Feng, X.-Q. Yao, J.-C. Liu, *Transition Met. Chem.* **2016**, *41*, 685–692; **DOI:**10.1007/s11243-016-0069-9
(b) P. A. Khalf-Alla, S. S. Hassan, M. M. Shoukry, *Inorg. Chim. Acta* **2019**, *492*, 192–197; **DOI:**10.1016/j.ica.2019.04.035
(c) S. Daravath, A. Rambabu, N. Vamsikrishna, N. Ganji, S. Raj, *J. Coord. Chem.* **2019**, *72*, 1973–1993; **DOI:**10.1080/00958972.2019.1634263
(d) M. S. S. Adam, L. H. Abdel-Rahman, A. M. Abu-Dief, N. A. Hashem, *Inorg. Nano-Met. Chem.* **2019**, *50*, 136–150. **DOI:**10.1080/24701556.2019.1672735
6. M. Zhang, D.-M. Xian, H.-H. Li, J.-C. Zhang, Z.-L. You, *Aust. J. Chem.* **2012**, *65*, 343–350. **DOI:**10.1071/CH11424

7. (a) L.-W. Xue, H.-J. Zhang, P.-P. Wang, *Acta Chim. Slov.* **2019**, *66*, 190–195;
(b) G.-X. He, L.-W. Xue, Q.-L. Peng, P.-P. Wang, H.-J. Zhang, *Acta Chim. Slov.* **2019**, *66*, 570–575; **DOI:**10.17344/acsi.2018.4868
(c) L.-W. Xue, Y.-J. Han, X.-Q. Luo, *Acta Chim. Slov.* **2019**, *66*, 622–628. **DOI:**10.17344/acsi.2019.5039
8. (a) A. Castineiras, J. A. Castro, M. L. Duran, J. A. Garcia-Vazquez, A. Macias, J. Romero, A. Sousa, *Polyhedron* **1989**, *8*, 2543–2549; **DOI:**10.1016/S0277-5387(00)81154-7
(b) L. Xu, Y. V. Mironov, X. Qi, S.-J. Kim, *J. Struct. Chem.* **2006**, *47*, 998–1001. **DOI:**10.1007/s10947-006-0418-1
9. Bruker, SMART and SAINT, *Area Detector Control and Integration Software*, Madison (WI, USA): Bruker Analytical X-ray Instruments Inc., 1997.
10. G. M. Sheldrick, SADABS, *Program for Empirical Absorption Correction of Area Detector Data*, Göttingen (Germany): Univ. of Göttingen, 1997.
11. A. C. T. North, D. C. Phillips, F. S. Mathews, *Acta Crystallogr. A* **1968**, *24*, 351–359. **DOI:**10.1107/S0567739468000707
12. G. M. Sheldrick, SHELXL-97, *Program for the Refinement of Crystal Structures*, Göttingen (Germany): Univ. of Göttingen, 1997.
13. (a) A. Barry, *Procedures and Theoretical Considerations for Testing Antimicrobial Agents in Agar Media*, In: Antibiotics in Laboratory Medicine, Lorian, V., Ed., Baltimore: Williams and Wilkins, 1991;
(b) T. Rosu, M. Negoiu, S. Pasculescu, E. Pahontu, D. Poirier, A. Gulea, *Eur. J. Med. Chem.* **2010**, *45*, 774–781. **DOI:**10.1016/j.ejmech.2009.10.034
14. A. Ray, D. Sadhukhan, G. M. Rosair, C. J. Gomez-Garcia, S. Mitra, *Polyhedron* **2009**, *28*, 3542–3550. **DOI:**10.1016/j.poly.2009.07.017
15. S. B asak, S. Sen, S. Banerjee, S. Mitra, G. Rosair, M. T. G. Rodriguez, *Polyhedron* **2007**, *26*, 5104–5112. **DOI:**10.1016/j.poly.2007.07.025
16. M. Enamullah, M. A. Quddus, M. A. Halim, M. K. Islam, V. Vasylyeva, C. Janiak, *Inorg. Chim. Acta* **2015**, 103–111. **DOI:**10.1016/j.ica.2014.11.020
17. D. S. Badiger, R. S. Hunoor, B. R. Patil, R. S. Vadavi, C. V. Mangannavar, I. S. Muchchandi, Y. P. Patil, M. Nethaji, K. B. Gudasi, *Inorg. Chim. Acta* **2012**, 197–203. **DOI:**10.1016/j.ica.2011.11.063
18. (a) F.-W. Wang, Y.-J. Wei, Q.-Y. Zhu, *Chin. J. Struct. Chem.* **2007**, *26*, 1327–1331;
(b) Z.-L. You, X. Han, J. Wang, J.-Y. Chi, *Chin. J. Struct. Chem.* **2006**, *25*, 1043–1046;
(c) T. Chattopadhyay, M. Mukherjee, K. S. Banu, A. Banerjee, E. Suresh, E. Zangrando, D. Das, *J. Coord. Chem.* **2009**, *62*, 967–979; **DOI:**10.1080/00958970802385837
(d) A. Guha, T. Chattopadhyay, N. D. Paul, M. Mukherjee, S. Goswami, T. K. Mondal, E. Zangrando, D. Das, *Inorg. Chem.* **2012**, *51*, 8750–8759; **DOI:**10.1021/ic300400v
(e) J. Qin, Y. Sun, Z. N. Xia, Y. Zhang X. L. Zhao, Z. L. You, H. L. Zhu, *Russ. J. Coord. Chem.* **2016**, *42*, 330–337. **DOI:**10.1134/S1070328416050055
19. (a) N. Wang, L. Chen, L. Yang, Y. Wan, *Synth. React. Inorg. Met.-Org. Nano-Met. Chem.* **2014**, *44*, 315–319; **DOI:**10.1080/15533174.2013.770763
(b) D.-H. Shi, Z.-L. Cao, W.-W. Liu, R.-B. Xu, L.-L. Gao, Q. Zhang, *Synth. React. Inorg. Met.-Org. Nano-Met. Chem.* **2012**, *42*, 864–867. **DOI:**10.1080/15533174.2011.618483
20. (a) J.-N. Li, *Synth. React. Inorg. Met.-Org. Nano-Met. Chem.* **2013**, *43*, 832–837;
(b) S. S. Qian, X. S. Cheng, J. Q. Ren, Z. L. You, H. L. Zhu, *Russ. J. Coord. Chem.* **2013**, *39*, 836–843. **DOI:**10.1134/S1070328413110080
21. J. W. Searl, R. C. Smith, S. Wyard, *J. Proc. Phys. Soc.* **1961**, *78*, 1174–1178. **DOI:**10.1088/0370-1328/78/6/311
22. L.-W. Xue, H.-J. Zhang, P.-P. Wang, *Acta Chim. Slov.* **2019**, *66*, 190–195.

Povzetek

Trije novi cinkovi (II) kompleksi, $[Zn_2I_2(L^1)_2]$ (**1**), $[Zn(HL^2)_2(NCS)_2]$ (**2**) in $[ZnIL^3]$ (**3**), kjer je L^1 anionska oblika 2-[(6-metilpiridin-2-ilimino)metil]fenola (HL^1), HL^2 je zwitterionska oblika 2-(ciklopropiliminometil)-5-fluorofenola (HL^2) in L^3 je anionska oblika 5-bromo-2-[(3-morfolin-4-ilpropilimino)metil]fenol (HL^3), so bili pripravljeni in karakterizirani z elementno analizo, IR, UV in NMR spektroskopijo ter rentgensko difrakcijo na monokristalih. Kompleks 1 je dvojedrni cinkov kompleks, kompleksa 2 in 3 pa sta enojedrna cinkova kompleksa. Atomi Zn v kompleksih so v tetraedrski koordinaciji. Preučevana je bila tudi protimikrobna aktivnost kompleksov proti *Staphylococcus aureus*, *Escherichia coli* in *Candida albicans*.

Except when otherwise noted, articles in this journal are published under the terms and conditions of the Creative Commons Attribution 4.0 International License

Scientific paper

Effect of Vacuum Frying Conditions on Quality of French Fries and Frying Oil

Esra Devseren,[1] Dilara Okut,[1] Mehmet Koç,[2] Özgül Özdestan Ocak,[1] Haluk Karataş[3] and Figen Kaymak-Ertekin[1]*

[1] *Ege University, Faculty of Engineering, Department of Food Engineering, 35100, Bornova, Izmir, Turkey*

[2] *Adnan Menderes University, Faculty of Engineering, Department of Food Engineering, 09010, Aydın, Turkey*

[3] *Arçelik A. Ş., R&D Center, 34940, İstanbul, Turkey*

* *Corresponding author: E-mail: figen.ertekin@ege.edu.tr*
Phone: +90.232.3113006 Fax: +90.232.3427592

Received: 02-06-2020

Abstract

Vacuum frying conditions were investigated with respect to physical, chemical and sensorial properties of French fries and frying oil, besides determining the effect of frying conditions in terms of frying temperature and time. In order to determine the optimum frying conditions of the French fries optimization study was carried out according to Central Composite Rotatable Design. The results were evaluated to determine optimum vacuum frying conditions targeting minimum oil content, 30–45 N in range of hardness, minimum acrylamide content and maximum overall preference. The optimum vacuum frying condition was selected as 124.39 °C of frying temperature and 8.36 min of frying time for French fries. The French fries obtained at optimum conditions for vacuum frying preserved the desired color, textural properties and flavor and it has low oil content and reduced acrylamide formation. In addition, the frying oil quality was preserved with vacuum frying.

Keywords: French fries; vacuum frying; browning index; hardness; acrylamide; microstructure

1. Introduction

Deep fat frying is one of the earliest and most popular way of cooking process where the food is immersed into the hot oil (150–200 °C) at atmospheric pressure. Due to attractive color, texture and flavor of fried foods, deep fat frying is commonly applied both at home and in the food industry.[1] Nowadays, deep fat frying has been remarkably interested by researchers due to rising consumption of fast food and pre-cooked food. Unfortunately, many studies related with deep fat frying reported that excessive oil uptake and high frying temperature had negative effects on health such as coronary heart diseases, cancer, diabetes and hypertension.[2]

As a result of simultaneous heat and mass transfer during deep-fat frying chemical and physical changes in foods have occurred for instance; moisture loss, oil uptake, crust formation, starch gelatinization and color change with the Maillard reaction, oxidation, hydrolysis and polymerization of oil. In addition to these changes, acrylamide was also formed during deep-fat frying process.[3] Although consumer awareness of the relationship between nutrition and health increases, deep fat frying still continues to be one of the main cooking methods.[4] That is why, the researchers have tried to develop alternative frying methods to eliminate the negative effects of deep fat frying and get healthier fried products.

Vacuum frying is one of the new technologies as an alternative to atmospheric pressure frying and it is performed by immersing the food into the oil in a closed system at pressures lower than atmospheric pressure.[5,6] Even though vacuum frying process carried out under the pressure of 6.65 kPa,[7–10] it is increased up to 27.5 kPa in some studies.[6,11–12]

The vacuum frying process is performed at low temperature in low-oxygen frying medium.[9,13] Thus, the vacuum frying is superior to atmospheric frying in terms of the protection of nutritional composition, color and flavor of the fried product, reusability of frying oil and acrylamide formation.[13] Acrylamide, classified as a potential carcinogen by the International Agency for Research on Cancer, is formed in foods rich in both carbohydrates and proteins

during cooking process at high temperatures.[14] Many studies in literature showed that vacuum frying of potato chips led to form less acrylamide compared to those of atmospheric pressure.[3,15–16] Although reduction of acrylamide in vacuum fried products is clear, the effect of vacuum on oil uptake is highly complex. According to Garayo and Moreira,[13] potato chips had 30% less fat content with vacuum frying than atmospheric frying, while the potato chips with similar color and textural properties obtained with both frying methods. In contrast to this study, Troncoso et al.,[8] found that vacuum frying resulted in an increase in oil content of potato chips compared to atmospheric frying.

The quality of frying oil is also an important parameter affecting the quality of the fried food. Limited number of studies have been in literature investigating the effect of vacuum application on quality of frying oil.[9,17] Crosa et al.,[9] investigated the effect of vacuum frying and traditional frying on sunflower oil degradation, fatty acid composition and alpha-tocopherol content. It was determined a significant increase in the usage time of the oil with vacuum frying process compared with atmospheric frying process. Similarly, Aladedunye and Przybylski,[17] reported that vacuum frying reduced the total polarity by 76% compared to atmospheric frying and lower oxidative degradation was observed. They also found that the rate of tocopherol degradation was three and twelve slower with vacuum frying than with other methods.

During frying, the texture of the fruits and vegetables becomes initial soft and then hard due to progressive development of a dehydration crust. In addition, there is less structural change with vacuum frying than with atmospheric frying.[14] Visual observations in apple slices showed that the surface of vacuum fried products was less expanded than atmospheric frying.[6] Dueik et al.,[18] determined that the maximum power of fried carrot chips is not affected by frying technology and temperature, so that vacuum fried chips have the same crispness as atmospheric fried ones. Da Silva and Moreira,[19] did not found significant differences in the textural parameters of sweet potato, mango and green beans between atmospheric and vacuum frying.

In this study, a vacuum cooking equipment having frying function was developed to investigate the effect of frying conditions in terms of temperature and time on physical, chemical and sensorial properties of French fries and frying oil. In order to determine the optimum frying conditions (temperature and time), optimization study was carried out according to Central Composite Rotatable Design (CCRD) and the effects of the temperature and time of vacuum frying were investigated.

2. Experimental

2. 1. Material

Frozen French fries and sunflower oil were obtained from a local supermarket in Izmir. Sunflower oil was selected as frying medium due to preferring mostly at home. Prior to frying process, frozen French fries were sorted with respect to their size (1 × 1 × 8 cm) and stored at –24 °C. The moisture and oil content of the frozen French fries were determined 71.7 ± 1.7% and 3.9 ± 0.5%, respectively.

2. 2. Developed Vacuum Frying Equipment

The vacuum frying equipment was designed to allow frying at wide range of temperature and vacuum pressure. Tomruk et al.[20] already gave the constructional and working details of the equipment used in this study. The developed equipment consisted of three parts that were vacuum vessel, condenser and vacuum pump as shown in Fig. 1. The vacuum vessel was capacity of 6 liter and a basket, which can be moved up and down, was added to the vacuum vessel and it was difference from Tomruk et al.[20]. Also, a thermocouple (PT 100) was placed in the vacuum vessel to determine temperature of frying oil. Electrical heater was 1.5 kW and the vacuum pump (0.55 Hp) was oily type. The condenser includes refrigerant (R-404a). In this developed equipment, while the vacuum level and cooking time were controlled by PLC system, the heater was programmed by PID control system.

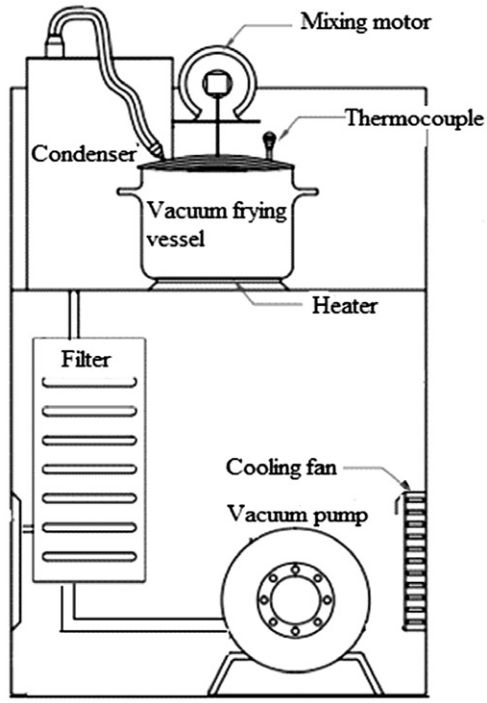


Fig. 1. Developed vacuum frying equipment

2. 3. Frying Process

In this study, French fries were fried under vacuum. French fries to sunflower oil ratio was 1:6 (w/v). Vacuum frying process was consisted of eight steps: (1) heating oil to selected temperature, (2) loading of French fries in a bas-

ket and closing the lid, (3) applying vacuum until 13.3 kPa, (4) immersing the French fries into the hot oil, (5) frying French fries for selected time, (6) lifting the basket from the oil, (7) waiting for 30 seconds to allow the surface oil flow down, (8) pressurizing the vessel.

The level of vacuum in this study was 13.3 kPa for all vacuum frying experiments. This level of vacuum was maximum vacuum pressure can be applied in the developed equipment.

For vacuum frying experiments, French fries were fried at 120–150 °C for 5–15 min according to Central Composite Rotatable Design (CCRD). Experimental CCRD design was given in Table 1. All the frying experiments were done in duplicate.

2. 4. French Fries Analysis

Moisture Content

For determination of moisture content in raw and fried French fries, samples were crushed with sand and dried in vacuum oven (Vacucell, U.S.A) at 65 °C for 24–48h until constant weight.[21]

Color

Color of the raw and fried French fries were determined with a Minolta Chroma Meter (Konica Minolta, CR-400, Osaka, Japan). Hunter L, a, and b values were recorded to calculate the browning index (BI) of French fries (Eq. 1).[22,23]

$$BI = ([100 * ((a + 1.75L)/(5.645L + + a - 3.012b) - 0.31)])/0.17 \quad (1)$$

Texture

The firmness of raw and fried French fries was measured by using the Texture Analyzer equipment (TA-XT2, Stable Micro Systems, UK) equipped with Multiple Chip Rig probe. Puncture test was simultaneously applied to 10 potato samples and the maximum power (N) was recorded. Puncture test was performed under these conditions: pre-test speed: 2 mm/s, test speed: 1 mm/s, post-test speed: 10 mm/s, distance: 5 mm and trigger force: 20 g.

Acrylamide content

Acrylamide content of French fries was analyzed with LC/MS-MS (ThermoFisher Scientific, USA). This method consisted of three sections, which were acrylamide standards preparation, sample preparation and purification.[23]

Oil content

Oil content of samples was gravimetrically determined by using hexane as the solvent with Soxhelet system.[21]

Microstructure

Microstructure of the raw and fried French fries were determined by using Micro Computer Tomography (Micro-CT) equipment (Scanco Medical μCT 50, Switzerland). 3D models were created with the images received cross-section of the sample by using X-rays. The average pore diameter (μm) of the raw and fried samples were also measured.[24]

Sensory evaluation

Sensory properties of fried French fries were evaluated in terms of appearance, color, texture, flavor (taste and smell) and overall acceptance. Sensory analysis was performed according to Altuğ and Elmacı,[25] with 10 panelists. All panelists were non-smokers. The intensity of the properties was determined using a 5–point scale (1 being the lowest and 5 being the highest).

2. 5. Frying Oil Analysis

Free Fatty Acids

Free fatty acids (FFA) content of frying oil was determined using a titrimetric method and expressed as free oleic acid percentage.[26]

Peroxide Value (PV)

Peroxide value (PV) expressed in milliequivalents of active oxygen per kilogram oil (mEq O2/kg oil), was determined. [26]

Total Polar Compounds (TPC)

Total polar compounds estimation was based on dielectric constant changes directly measured on hot oil with Deep Frying Oil Tester testoT270, when frying oil temperature was approximately 80 (± 5) °C.

Experimental Design and Statistical Analysis

Response surface methodology (RSM) was used to investigate the main effects of frying temperature and time on physical, chemical and sensorial properties of French fries fried under vacuum and optimize the responses. All experimental data were fitted to a second-order polynomial model and regression coefficients were obtained for each response. Significant terms in the models were found by analysis of variance (ANOVA). Design Expert Ver. 7.0.0 (Stat-Ease, 2005) and were used to fit response surfaces, where significant differences ($p < 0.05$) were detected.

All of the analysis were done in triplicates. Results are shown as mean ± standard deviation.

Optimization

Numerical methods (desirability function) were used for optimization. At least five attempts were carried out at the optimum point as determined by the model (the optimum process conditions) and the optimum point was confirmed experimentally. In this study, desirability functions were evaluated for the criteria of minimum oil content, 30–45 N in range of hardness, minimum acrylamide content and maximum overall preference. These criterions

were chosen according the literature data. Furthermore, response surface graphs and contour lines that helps to determine the optimum point is plotted using models obtained by regression analysis.

3. Results and Discussion

3. 1. Effect of Vacuum Frying on French Fries

The physical, chemical and sensorial properties of the French fries at different experimental conditions are given in Table 1.

ANOVA and regression analysis were evaluated to fit the model and determined the statistical significance of the model terms, as shown in Table 2. The quadratic polynomial model represented significantly the experimental values of responses at $p < 0.05$ level, besides the lack of fit of models were not significant. The counter plots of the predicted model of BI, hardness, oil content, acrylamide content, moisture content, overall acceptance, average pore diameter and peroxide value are given in Fig. 2.

Moisture content was an important quality criteria for fried foods due to its effect on final product texture, microstructure and sensorial acceptability.[27] The moisture content of fried foods varied with initial moisture content and dimensions of the product, and frying temperature and time.[24] The moisture content of French fries decreased with an increase in frying temperature and time as shown in Table 1. Garayo and Moreira,[13] explained this circumstance as follows; the boiling point of water reduced with a decrease in pressure, so the water in the potato begun to vaporize faster under vacuum. Lisinska and Golubowska,[28] have reported that French fries had a moisture content of 44.7% because of atmospheric frying at 180 °C for 7 min. Besides, Romani et al.,[29] observed that moisture content of French fries changed from 43.38% to 29.37% at 180 °C for 10 min depending on type of fryer and potato to oil ratio. These results were in consistent with our findings for vacuum frying. The ANOVA results also showed that, the moisture contents of French fries fried under vacuum significantly changed with frying temperature and time as shown in Table 2. In addition, it can be clearly seen in Fig.2.

The oil content of fried products was also one of the most important quality features in many ways such as number of calories supplied by the food and growing trend on consuming foods produced with healthier methods. Beside the health issues about oil consumption, it had specific functional effects on flavor, appearance and smooth mouthfeel, which contributes the sensorial quality of the product.[30] For this reason, many studies focused on producing fried products with low oil content that still protecting the desirable texture and flavor. Oil absorption was affected by the quality of frying oil, frying temperature, time and pressure, shape and chemical composition of food and applied pre-treatments.[4] In literature, critical

Table 1. Quality analysis results of vacuum fried French fries and frying oil at different temperatures and times

Temperature (°C)	Time (min)	BI (N)	Hardness diameter (μm)	Average pore (%)	Oil content content (%)	Moisture content (ppb)	Acrylamide acceptance	Overall (% oleic acid)	Free fatty acids (mEq O_2/kg oil)	Peroxide value compounds (%)	Total polar
124.4	6.5	28.65 ± 0.79	31.57 ± 0.86	116.8	12.88 ± 1.05	41.65 ± 0.36	44.0 ± 1.4	3.12 ± 0.20	0.0383 ± 0.0024	0.116 ± 0.004	8.33 ± 0.14
145.6	6.5	35.91 ± 0.08	32.77 ± 1.05	185.6	18.39 ± 0.29	35.51 ± 0.86	314.5 ± 9.2	3.80 ± 0.45	0.0377 ± 0.0012	0.401 ± 0.049	8.42 ± 0.12
124.4	13.5	43.72 ± 0.82	66.49 ± 2.12	207.3	18.40 ± 1.20	25.78 ± 0.81	96.0 ± 5.7	4.06 ± 0.56	0.0413 ± 0.0034	0.232 ± 0.004	8.08 ± 0.12
145.6	13.5	58.26 ± 1.07	68.77 ± 3.49	342.2	21.00 ± 0.54	20.06 ± 0.45	412.1 ± 5.8	3.25 ± 0.46	0.0486 ± 0.0008	0.459 ± 0.015	8.33 ± 0.04
120.0	10.0	41.40 ± 1.21	33.47 ± 2.12	171.4	19.00 ± 1.41	32.22 ± 0.21	42.0 ± 2.8	4.19 ± 0.37	0.0412 ± 0.0025	0.115 ± 0.035	8.83 ± 0.24
150.0	10.0	50.39 ± 0.84	46.35 ± 2.92	290.6	23.10 ± 1.26	25.40 ± 0.28	516.9 ± 5.5	4.40 ± 0.70	0.0341 ± 0.0006	0.481 ± 0.013	8.28 ± 0.12
135.0	5.0	25.32 ± 0.81	26.27 ± 1.25	143.6	12.15 ± 0.71	43.50 ± 0.32	116.0 ± 5.7	2.57 ± 0.69	0.0323 ± 0.0022	0.113 ± 0.007	8.25 ± 0.08
135.0	15.0	43.86 ± 0.75	66.15 ± 3.57	296.3	18.96 ± 1.89	16.28 ± 0.01	373.5 ± 9.2	2.86 ± 0.29	0.0348 ± 0.0001	0.246 ± 0.028	8.25 ± 0.10
135.0	10.0	38.11 ± 0.16	43.15 ± 2.55	232.0	19.86 ± 0.45	34.04 ± 0.34	320.0 ± 8.5	4.75 ± 0.16	0.0428 ± 0.0012	0.206 ± 0.052	8.83 ± 0.14
135.0	10.0	43.40 ± 0.66	37.18 ± 0.08	206.7	19.00 ± 1.50	26.26 ± 0.01	280.0 ± 11.3	4.57 ± 0.46	0.0375 ± 0.0036	0.226 ± 0.005	8.58 ± 0.12
135.0	10.0	41.35 ± 0.65	37.51 ± 1.78	-	18.94 ± 1.19	31.93 ± 0.22	322.0 ± 9.9	4.58 ± 0.23	0.0384 ± 0.0014	0.206 ± 0.012	8.25 ± 0.16
135.0	10.0	42.70 ± 0.07	36.36 ± 0.07	-	19.06 ± 0.86	29.69 ± 0.42	268.0 ± 11.3	4.58 ± 0.49	0.0441 ± 0.0002	0.283 ± 0.007	8.58 ± 0.11
135.0	10.0	40.41 ± 0.14	36.79 ± 1.56	-	18.00 ± 1.20	29.07 ± 0.68	300.0 ± 4.9	4.75 ± 0.42	0.0413 ± 0.0010	0.236 ± 0.001	8.25 ± 0.12

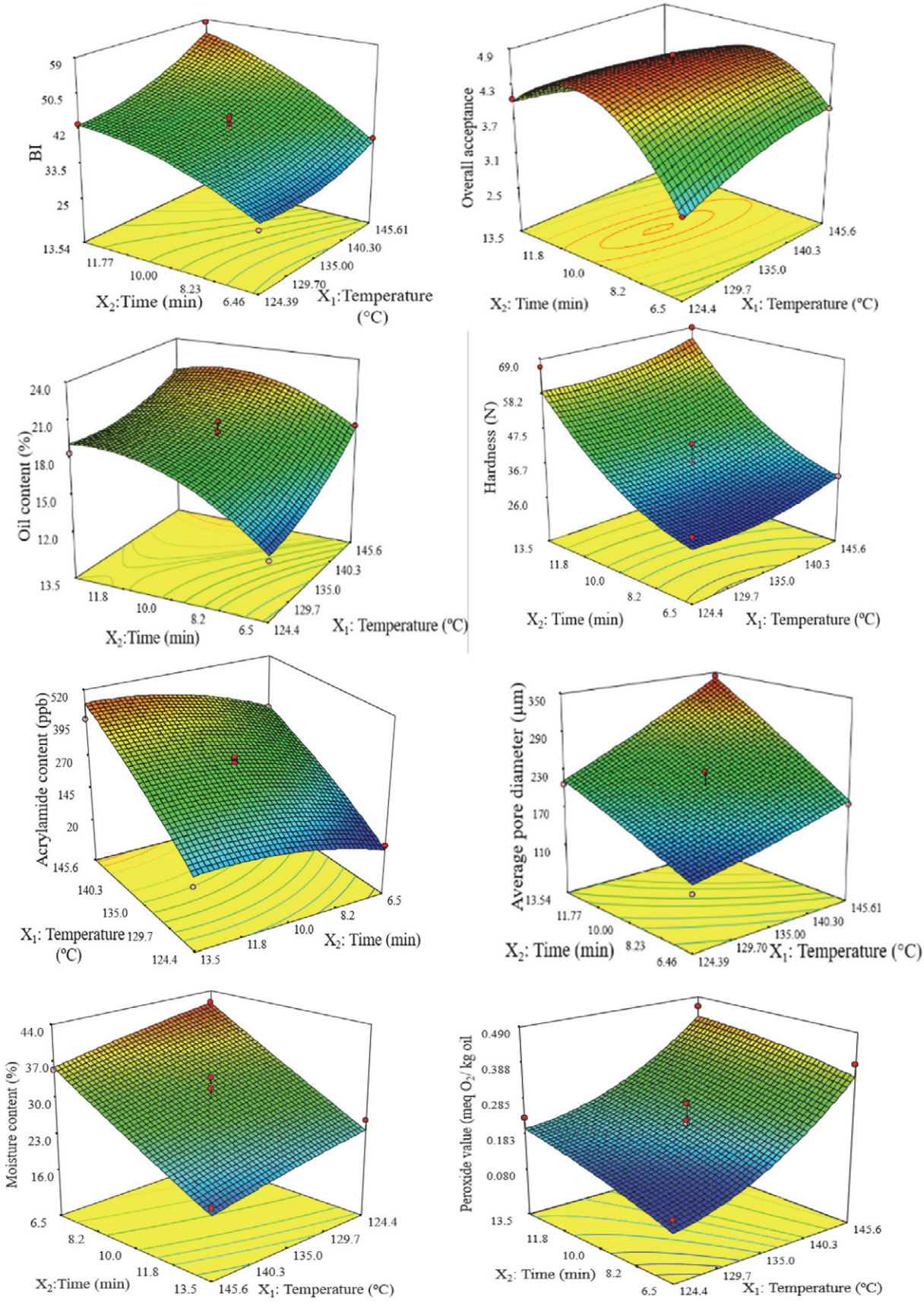


Fig. 2 Response surface graphics and isohips curves for the quality characteristic of vacuum fried French fries

Table 2. ANOVA results for quality analysis of vacuum fried French fries and frying oil

Variation Source	*p*- value BI	Hardness (N)	Average pore diameter (μm)	Oil content (%)	Moisture content (%)	Acrylamide content (ppb)	Overall acceptance	Free fatty acids (% oleic acid)	Peroxide value (meq O_2 /kg oil)	Total polar compounds (%)
Model	0.0001*	0.0007*	0.0017*	<0.0001*	0.0005*	0.0002*	<0.0001*	0.5710	0.0005*	0.6923
X_1	0.0013*	0.1727	0.0009*	0.0002*	0.0207*	<0.0001*	0.8834	0.8059	<0.0001*	0.3745
X_2	<0.0001*	<0.0001*	0.0004*	<0.0001*	<0.0001*	0.0040*	0.0085*	0.2216	0.0176*	0.6769
$X_1 X_2$	0.1430	0.9177	0.0933	0.0787	0.9377	0.6141	<0.0001*	0.4262	0.5051	0.7675
X_1^2	0.0277*	0.2223	0.7211	0.0134*	0.7357	0.2483	0.0024*	0.9545	0.0168*	0.7333
X_2^2	0.0236*	0.0204*	0.7090	0.0002*	0.8448	0.0535	<0.0001*	0.2574	0.5397	0.2136
Lack of fit	0.3094	0.0543	0.7088	0.3776	0.7489	0.0539	0.8370	0.0782	0.1799	0.3626

* Significant differences at 0.05 level X_1: Temperature (°C), X_2: Time (min)

temperatures for frying which were important for ensuring desirable structural and textural properties of the fried product were stated as 160 and 180 °C.[31] Pedreschi and Moyano,[32] found that increase in frying temperature resulted in a decrease in the oil absorption. This was occurred by the reason of that the surface of the food dried faster and a crust formed, which acted as a barrier to the absorption of oil at high temperature.[33]

The literature data indicated that vacuum frying decreased oil content, even though it occurred at low temperatures.[6,13,15] For vacuum frying, Fig. 2 showed that the oil content of French fries increased with increasing frying temperature and time. The lowest oil content (12.9%) was observed at 135 °C for 5 min (Table 1). Oil content of French fries was significantly affected by frying time and temperature ($p < 0.05$) (Table 2).

Troncoso et al.,[8] determined that oil content of vacuum fried potato chips was higher than atmospheric fried chips whereas Garayo and Moreira[13], Da Silva and Moreira[19] and Dueik et al.,[34] reported that vacuum fried potato chips contained less oil compared to atmospheric frying chips. Furthermore, it was determined that by centrifuging the fried product after vacuum frying process resulted in 70-81% reduction in oil content.[10,35]

Color of fried foods was also an important physical quality attribute generally considered when making a decision to consume the product. The color of French fries was developed as a result of Maillard reaction, which was mainly dependent on chemical composition of raw material and frying conditions in terms of temperature and time.[36] In this study, the color alternation of French fries caused by either frying conditions or frying methods was evaluated with Browning index (BI). Because the BI was considered as a reliable indicator of acrylamide concentration.[23] The results showed that the higher frying temperature and/or the longer frying time resulted in the higher BI. Because the color development mechanism for Frenchfries in thermal processing was dependent upon the rate of heat transfer. Vacuum fried vegetables and fruits had lower color changes and lighter color than atmospheric fried products.[6,8,16,19] In case of high heat rates in atmospheric frying, the color of French fries turned rapidly to brown.[37] However, in the vacuum frying method, low frying oil temperature resulted in slowing down the rate of heat transfer to the interior of food and the color of food products was preserved. Moreover, Moyano et al.,[38] found out that moisture content and color changes of French fries was highly correlated to each other. The similar results were also observed in BI and moisture content relations in this study.

The ANOVA results (Table 2) also showed that BI was significantly affected by frying temperature and frying time for vacuum frying ($p < 0.05$). Diamante et al.,[39] also observed the similar effect of frying temperature and time on BI value of vacuum fried gold kiwifruit slices. However, the effect of frying temperature on BI is limited for short frying

times in vacuum frying method (Fig. 2). The maximum value of BI (58.26) was observed at 145.6 °C for 13.5 min in vacuum fried French fries (Table 1). As far as BI results were concerned, vacuum frying protected the desired color of French Fries. Because the natural color and flavor of food product could be preserved during vacuum frying due to frying at low temperature and low oxygen content. Da Silva and Moreira,[19] studied with different fruits and vegetables to determine the effect of vacuum frying on their physical and chemical properties and they found out that most of the products retained their natural colors.

For frying process, the size of food is another important parameter affecting the oil content and colour of fried food. Studies have shown that the oil absorption increases as the thickness of the product decreases and the surface area increases.[40] The best example of this is that French fries absorb less oil than potato chips due to their smaller surface area / volume ratio.[41] Similarly, Guillaumin[42] and Krokida et al.[43] reported that there was a linear relationship between the thickness of potato chips and the amount of oil absorbed. Higher oil content as thickness decreases has been determined for potato chips. Also, the color change phenomenon gets more intense at smaller sample thickness. As thickness of French Fries was considered, lower thickness resulted in lower lightness and higher yellow color of the product.[43] There are no studies examining the effect of food size for vacuum frying in the literature, but studies for atmospheric frying are sufficient to understand the effect of food size.

The texture of French fries was analyzed considering hardness, which was the maximum force (N) needed to penetrate the probe into sample. The changes in the hardness of French fries with respect to frying temperature and time were given in Table 1 for vacuum frying. The hardness of French fries increased with increasing frying temperature and time. The hardness of French fries was only affected by frying time in vacuum frying ($p < 0.05$) (Table 2). The 3-D response surface graph of hardness also approved the sole effect of frying time on hardness of vacuum fried French fries (Fig 2).

In the literature, there were different results about the effect of frying methods mainly atmospheric and vacuum frying. Troncoso et al.,[8] studied on vacuum fried potato chips and determined that the values of hardness and crispiness of chips were decreased by vacuum frying. In contrast, Mir-Bel et al.,[12] indicated that vacuum fried dough had a much crunchier texture compared to atmospheric fried dough. However, Da Silva and Moreira,[19] Dueik et al.,[18] and Moreira et al.,[35] observed no significant differences in the texture of vegetables prepared by atmospheric and vacuum frying processes. In addition to frying method, the frying conditions, the chemical composition of fried sample, the size and thickness of fried sample, the kind of oil used as frying medium should also take a consideration during interpreting the texture of fried samples. Indeed, Kita and Lisinska,[44] found out that the type of frying medium significantly affected the texture of French fries.

As previously mentioned, the moisture content of French fries had directly effect on textural properties of French fries. The highest hardness value for vacuum fried sample (68.8 N) was observed at 145 °C for 13.5 min and this sample also had the lowest moisture content (20.1%). In order to highlight the effect of the moisture content on hardness, Pearson correlation tests were evaluated for vacuum frying. The results of these tests showed that hardness of vacuum fried French fries were inversely correlated with the moisture content, and the correlation coefficients (r) of vacuum fried French fries were found as –0.827.

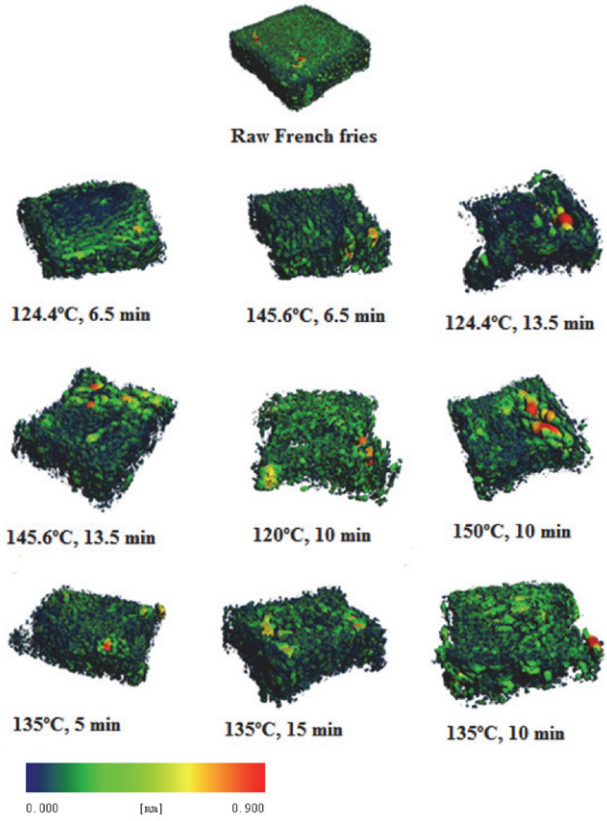


Fig. 3. Micro-CT images of vacuum fried French fries

The physical structure of fried products changed because of simultaneous heat and mass transfer during frying process. These changes played a key role in fat absorption and formation of textural structure.[45,46] That is why, the structural changes in French fries during frying was analyzed with Micro Computer Tomography (Micro-CT) in this study. Micro-CT images of vacuum fried French fries are shown in Fig. 3. In these images, the change of colors from blue to red indicated to enlarge the pore diameter of French fries. Alam and Takhar,[24] also found that the pore diameter of deep fat fried potato increased with increasing frying time while the total number of pores decreased.

The average pore diameters of vacuum fried French fries enlarged with increasing frying time and temperature, and ranged between 116.8 and 342.2 μm. As mentioned above, the microstructure namely average pore diameter had a key role on texture and oil absorption. Thus, Pearson correlation test was applied between the pore diameter values and the hardness and oil content of vacuum fried French fries. The correlation coefficient values (r) were 0.788 for hardness and 0.794 for oil content at vacuum frying. Bouchon et al.,[46] explained the oil absorption mechanism in deep fat frying of potato that was directly dependent upon microstructure as follow; suction of oil into the porous crust region after removing of potato from frying medium and the competition between capillary suction of oil into the crust region and drainage of oil along the surface of the product.

Using frozen or non-frozen potato in the frying process can cause some effect on the fried product. If non-frozen potatoes are used, the temperature difference between the oil and the product decreases and crust occurs slower than for the frozen ones. The slower crust formation causes the product to absorb more oil. Also, Grop[47] explained that one of the factors influencing acrylamide formation during frying is whether the food is fresh or frozen. French fries prepared from fresh potato contained more than the double the level of acrylamide compared with those from frozen potato.

Pedreschi et al.,[48] determined that acrylamide content of potatoes increased about 58 times due to an increase in the frying temperature from 120 °C to 150 °Cat atmospheric pressure. There were many studies indicating that increasing temperature caused higher acrylamide content during frying of potato products. [48]

The amount of acrylamide in vacuum fried French fries varied between 42.0 and 516.9 ppb under different operating conditions (Table 1). It could be clearly seen in Fig. 2 and ANOVA analysis (Table 2), the acrylamide content of French fries was significantly affected by the frying temperature and time ($p < 0.05$) and it increased with increasing frying temperature and time. Surdyk et al.,[49] and Brathen and Knutsen,[50] also observed a strong correlation between acrylamide formation and the baking temperature and time. The 3-D counter plot of acrylamide content also demonstrated the effect of frying temperature and time (Fig. 2). In addition, it has been determined that frying temperature was more effective on acrylamide content than frying time. The highest acrylamide content (516.9 ppb) was detected at the highest temperature (150 °C) for 10 min of frying time. This indicated that frying temperature was the most effective parameter for acrylamide formation.

Ölmez et al.,[51] investigated the acrylamide content of atmospheric fried foods in Turkey and stated that the highest acrylamide content was found in potato chips (59–2336 ppb) and the secondly was in French fries (355–436 ppb). Granda et al.,[15] examined the acrylamide content in potato chips fried at atmospheric (150, 165 and 180 °C) and vacuum frying conditions (118, 125 and 140 °C, 1.3 kPa). The acrylamide content of chips was found in the range of 358–5021 ppb at 165 °C for 4 minutes of atmospheric frying and 25–437 ppb at 118 °C for 8 minutes of vacuum frying. Similarly, reduction in acrylamide content with vacuum frying was determined as 39–60% while frying of shrimp compared to atmospheric frying.[16] In this study, the reduction in acrylamide content with vacuum frying of French fries was found between 36% and 96% at 10 min.

It is well known that the formation of acrylamide is related with Maillard browning reaction and content of reducing sugar and asparagine in the potato product.[52] Because of the relation of Maillard browning reaction and acrylamide formation, colour values can be utilized as an indicator of acrylamide formation. Many studies have pointed out that there was a correlation between the acrylamide content and colour of fried potatoes.[36,48,53] In our study, similar to literature, it was determined that as the browning index increased higher acrylamide content was determined in fried French fries. According to correlation analysis, the acrylamide content and the browning index gave a correlation of r = 0.64 in vacuum fried French fries.

In addition, there is a relationship between the acrylamide content and the moisture and oil contents and the pore diameters of the samples. The acrylamide content of the samples increased by increasing the oil content and decreased by the increase in moisture content. The increase in pore diameters of samples also showed a positive correlation with the increase of acrylamide content. As previously mentioned, the moisture content of the samples decreased after the frying process at high temperatures and long processing times, while the oil contents and pore diameters were growing. These changes in oil and moisture content and pore diameter were also effective on the acrylamide content of the samples. Acrylamide generally formed at high temperatures and low moisture conditions related with frying, baking, and roasting.[54] During the frying process, most of the heat energy transferred from oil to food in order to evaporate the moisture in the food. With the prolongation of the frying process, especially the moisture content of the food surface decreases, but the heat transfer from the oil to the food continues and the temperature of the food rises above the wet bulb temperature. Thus, the proteins and sugars that make up the dry matter of the food are exposed to high temperatures, and the formation of compounds such as acrylamide takes place. Gökmen et al.,[54] also reported that acrylamide formed even at temperatures below 120 °C when the moisture content becomes adequately low upon prolonged frying. At high temperature frying process, rapid evaporation on the surface of the food can provide the necessary conditions for acrylamide formation.

Depending on potato cultivars, there are difference in dry matter, starch, protein ratio, phosphorus com-

pounds, amylose, amylopectin ratio, total sugar, sucrose and ascorbic acid content. In previous studies, it was found that the oil content, acrylamide formation and colors of fried potato differ according to the potato cultivars.[55–56] The reducing sugars and asparagine, as acrylamide precursors, are very important for reducing the acrylamide content in fried potato products.[57] So, the selection of the potato cultivar is very important to reduce acrylamide formation.[58] Some cultivars are more suitable than others for frying, due to the low reducing sugar content. Yang et al.[56] evaluated three potato cultivars to investigate acrylamide formation during frying and they determined that the composition of the fresh potato cultivar is the primary factor in the formation of acrylamide. Additionally, fried potato color is the result of the Maillard reaction that depends on the content of reducing sugars and amino acids or proteins at the surface, and the temperature and time of frying. So, the cultivars of potato have effect on color of fried potatoes, as acrylamide content.[59] Moreover, dry matter content of potato can be change depending on cultivars and oil uptake of fried potato products is known to have a highly significant negative relationship with dry matter content. Kaur et al.[60] evaluated 5 different cultivars of potato and the cultivars with higher dry matter content showed lower oil uptake.

The consumer perceived the sensory quality as food quality. Sensory evaluation was used to determine the quality of both the raw material and the final product. In this study, the sensorial quality of vacuum fried French fries represented as overall acceptance, which was determined considering appearance, color, texture and taste of French fries.

The overall acceptance scores of vacuum fried French fries as sensorial quality are given in Table 1. It was found that the most effective independent variable on the overall acceptance values was frying temperature until 10 min; afterward the overall acceptance value decreased possibly due to the browning of the color, losses in texture and taste of burnt flavor in vacuum fried French fries (Fig. 2). The region where the response surface curves had a circular shape showing the highest score of the overall acceptance and it was determined as 4.75 score for frying at 135 °C for 10 min. Frying temperature did not have a significant effect on the overall acceptance of vacuum fried French fries compared to the frying time. This result was also coherent with ANOVA results (Table 2).

3. 2. Effect of Vacuum Frying on Frying Oil

During frying process, oil undergoes to chemical deterioration. This leads to the formation of more polar compounds than the triacylglycerol's of frying oil. These are called total polar material (TPM), and concentration of TPM is considered as an indicator of the quality of frying oil.[61] The amount of TPM depend on processing conditions as frying temperature, frying time, oxygen and water content of food.[62] Because TPM is harmful for human healthy, some countries have a limit of TPM in frying oil. The limit of TPM is 25% in France, Turkey, Belgium, Italy, Spain and South Africa, while it is 27% in Austria and Germany.[63,64] According to Table 1, the total polar material content of the frying oils obtained at the end of the frying process varies between 8.25% and 8.83%. Although different frying time and temperature were applied, the total polar material contents of frying oils were found to be very close to each other. According to ANOVA analysis, the effect of frying time and temperature was not significant statistically ($p > 0.05$). In addition, the frying oil has a polar substance content of 8.08 ± 0.20% before frying process, this was indicated that the vacuum frying process does not produce significant differences in the total polar material content. In our study, the results of the total polar material content were found to be in accordance with the current regulation of frying oil in all countries.

The free fatty acid content of the frying oil is widely used as an indicator of oil degradation. Free fatty acidity can be followed quickly and reliably during frying.[65] It is usually formed by the decomposition of triglycerides as a result of hydrolysis in the oil with the effect of air and humidity at high temperature.[66] According to the frying oil regulation in Turkey, the acids number can be maximum 2.5 mg KOH /g oil.[64] The acids number is equal to two times free fatty acids content. This limit value may vary between countries. The maximum permissible free fatty acid values of some countries are as follows; 1.25% in Austria , 2.5% in Belgium , 1% in Germany, 1.25% in Japan and 2.25% in the Netherlands.[67] In addition, frying oil is changed according to the free fatty acid content in the industry and the point determined for changing the oil varies depending on the product. This value is 0.5% for potato chips and 1% for French fries.

The effects of vacuum frying process variables on the free fatty acid content of frying oil were investigated and the free fatty acid content of frying oil were found between 0.0323% and 0.0486% oleic acids. These values were very close to each other. The free fatty acid content of the oil was determined as 0.0310 ± 0.0019% before frying process. It was observed that the free fatty acid content of the oil increased with the frying process, but the frying oil was suitable for reuse according to the regulations.

According to ANOVA analysis, the effect of vacuum frying process conditions on the free fatty acidity of frying oil could not be explained by the selected quadratic model ($p > 0.05$). This is because the values of free fatty acid of frying oils are very close to each other. Frying temperature and time did not have a significant effect on the free fatty acid content of vacuum frying oil (Table 2).

The peroxide value increases with the progression of primary oxidation in oil. As oxidation progresses, primary oxidation products (hydroperoxide) are broken down to

produce secondary oxidation products (aldehydes and ketones).[9] Therefore, while peroxide value give information about the quality of the oil, but it is insufficient in determining the usage period of the oil.

The peroxide value of the frying oil at different temperatures and times under vacuum, are given in Table 1. When the peroxide values were examined, it was determined that increasing in temperature and time increased the peroxide values, but the effect of time was very low. It was observed that the values of peroxide varied between 0.113 and 0.481 meq O_2 /kg and the highest value was reached in the condition at the highest temperature (150 °C). According to the results of variance analysis, the effect of temperature and time of the frying oil on the peroxide number was statistically significant ($p < 0.05$).

3. 3. Optimization

The results were evaluated by using Design Expert version 7.0-packaged software and optimum vacuum frying conditions targeting minimum oil content, 30–45 N in range of hardness, minimum acrylamide content and maximum overall preference.

Second-order polynomial model was used for each response for determining the optimum point. The desirability function approach was applied to obtain the optimum point solution given in Table 3. The optimum vacuum frying condition was selected as 124.39 °C of frying temperature and 8.36 min of frying time for French fries frying. The oil content, hardness, acrylamide content and overall preference at optimum conditions were predicted as 16.35%, 32.03 N, 87.4 ppb and 4.09, respectively. The results of the five validation experiments at optimum vacuum frying conditions are also given in Table 3, comparatively as average results and the estimated values. The oil content, hardness, acrylamide content and overall preference of the obtained samples were found to be significant ($p < 0.05$) different from the predicted values determined by Design Expert. It was determined that the hardness value was within the defined limits (30–45 N), but it was higher than the predicted value. Overall preference score was found to be higher than the predicted value, oil content and acrylamide content were obtained to be lower than the predicted values. These indicated a considerable increase in positive way.

4. Conclusion

Vacuum frying methods were applied to investigate the effect of frying conditions on physical, chemical and sensorial quality of French fries. That is why a vacuum frying equipment prototype was designed to work under both vacuum and atmospheric pressure. Effect of frying independent variables (temperature and time) on French fries and frying oil was investigated according to CCRD experimental design. In addition, vacuum frying process conditions in terms of frying temperature and time were optimized to produce French fries with targeting minimum oil content, 30–45 N in range of hardness, minimum acrylamide content and maximum overall preference. The optimum vacuum frying condition was selected as 124.39 °C of frying temperature and 8.36 min of frying time for French fries frying. The results showed that vacuum frying method protected the characteristic color, texture and sensorial quality of French fries, while the acrylamide content of French fries was low. The encountered problems, when targeted to achieve the desired color and texture in French fries frying at atmospheric frying, such as high acrylamide content, darkening of color and high oil content could be eliminated with vacuum frying. As a conclusion, vacuum frying can produce French fries containing low acrylamide content but having the same quality characteristics with those obtained under the atmospheric frying.

Acknowledgements

Funding provided by Ministry of Science, Industry and Technology, Republic of Turkey SAN- TEZ project (Project no: 0724.STZ.2014) and Arçelik A.Ş is appreciated.

4. References

1. R. G. Moreira, J. Palau, X. Sin, *J Food Process Eng.* **1995**, *18,* 307–320. **DOI:**10.1111/j.1745-4530.1995.tb00369.x
2. D. Dana, I. S. Saguy, *Adv Colloid Interfac*, **2006**, *128–130*, 267–272. **DOI:**10.1016/j.cis.2006.11.013
3. C. Granda, R. G. Moreira, *J Food Process Eng*, **2005**, *28,* 478–493. **DOI:**10.1111/j.1745-4530.2005.034.x
4. I. Saguy, D. Dana, *J Food Eng*, **2003**, *56,* 143–152. **DOI:**10.1016/S0260-8774(02)00243-1

Table 3. Results of statistical analysis for verification the optimization results

Responses	Predicted value	Experimental value[a]	SE[b]	Difference	% Error[c]	*p*-value
Hardness (N)	32.03	37.95 ± 1.38	0.619	5.92	15.60	0.001
Overall acceptance	4.09	4.51 ± 0.17	0.076	0.42	9.41	0.005
Acrylamide content (ppb)	87.4	65.1 ± 3.9	1.739	–22.32	34.28	0.000
Oil content (%)	16.35	13.18 ± 1.27	0.569	–3.16	24.01	0.005

[a] Experimental values were given as mean ± standard deviation [b] Mean standard error [c] % Error = $(|y_{exp} - y_{pre}|/ y_{exp}) * 100$

5. L. M. Diamante, S. Shi, A. Hellmann, J. Busch, *Int Food Res J*, **2015**, *22(1),* 15–22.
6. M. Mariscal, P. Bouchon, *Food Chem*, **2008**, *107,* 1561–1569. **DOI:**10.1016/j.foodchem.2007.09.031
7. R. G. Moreira, *Eur J Lipid Sci Technol*, **2014**, *116,* 723–734. **DOI:**10.1002/ejlt.201300272
8. E. Troncoso, F. Pedreschi, R. N. Zuniga, *LWT-Food Sci Technol*, **2009**, *42,* 187–195. **DOI:**10.1016/j.lwt.2008.05.013
9. M. J. Crosa, V. Skerl, M. Cadenazzi, L. Olazábal, R. Silva, G. Suburú, M. Torres, *Food Chem*, **2014**, *146,* 603–607. **DOI:**10.1016/j.foodchem.2013.08.132
10. A. Pandey, R. G. Moreira, *J Food Process Eng*, **2012**, *35,* 863–873. **DOI:**10.1111/j.1745-4530.2011.00635.x
11. J. Mir-Bel, R. Oria, M. L. Salvador, *J Food Eng*, **2009**, *95,* 416–422. **DOI:**10.1016/j.jfoodeng.2009.06.001
12. J. Mir-Bel, R. Oria, M. L. Salvador, *Int J Food Sci Technol*, **2013**, *48,* 2042–2049.
13. J. Garayo, R. Moreira, *J Food Eng*, **2002**, *55,* 181–191. **DOI:**10.1016/S0260-8774(02)00062-6
14. A. Andrés-Bello, P. García-Segovia, J. Martínez-Monzó, *Food Eng Rev*, **2011,** *3,* 63–78. **DOI:**10.1007/s12393-011-9037-5
15. C. Granda, R. G. Moreira, S. E. Tichy, *J Food Sci*, **2004**, *69,* 405–411. **DOI:**10.1111/j.1365-2621.2004.tb09903.x
16. G. Pan, H. Ji, S. Liu, X. He, *LWT-Food Sci Technol*, **2015**, *62,* 734–739. **DOI:**10.1016/j.lwt.2015.01.007
17. F. Aladedunye, R. Przybylski, *Eur J Lipid Sci Technol*, **2009**, *111(9)* 893–901. **DOI:**10.1002/ejlt.200900020
18. V. Dueik, P. Robert, P. Bouchon, *Food Chem*, **2010**, *119,* 1143–1149. **DOI:**10.1016/j.foodchem.2009.08.027
19. P. F. Da Silva, R. G. Moreira, *LWT-Food Sci Technol*, **2008**, *41,* 1758–1767. **DOI:**10.1016/j.lwt.2008.01.016
20. D. Tomruk, E. Devseren, M. Koç, Ö. Ö. Ocak, H. Karataş, F. Kaymak-Ertekin, *Agron Res*, **2016**, *14(S2),* 1475–1487.
21. AOAC, Association of official methods of analysis methods 950.46 and 960.39 (16th ed.). Arlington, Association of Official Analytical Chemists. Washington, DC, **1995**.
22. G. Dadalı, D. Kılıc-Apar, B. Ozbek, *Drying Technol*, **2007**, *25,* 925–936. **DOI:**10.1080/07373930701372296
23. H. Isleroglu, T. Kemerli, M. Sakin Yilmazer, G. Guven, O. Ozdestan, A. Uren, F. Kaymak-Ertekin, *J Food Sci*, **2012**, *77(10),* E257-E263. **DOI:**10.1111/j.1750-3841.2012.02912.x
24. T. Alam, P. S. Takhar, *J Food Sci*, **2006**, *81(3),* 651–664. **DOI:**10.1111/1750-3841.13219
25. T. Altuğ, Y. Elmacı, Gıdalarda duyusal değerlendirme. Meta press, İzmir, **2005**, p 130.
26. AOAC, Official Methods for Analysis, 15th ed. Vol. 2. Arlington, VA: Association of Official Analytical Chemists, **1990**.
27. R. G. Moreira, M. E. Castell-Perez, M. A. Barrufet, Deep- Fat Frying: Fundamentals and Applications. Aspen Publishers, Gaithersburg, MD, USA, **1999.**
28. G. Lisinska, G. Golubowska, *Food Chem*, **2005**, *93,* 681–687. **DOI:**10.1016/j.foodchem.2004.10.046
29. S. Romani, M. Bacchiocca, P. Rocculi, M. Dalla Rosa, *J Food Compos Anal*, **2009**, *22,* 582–588. **DOI:**10.1016/j.jfca.2008.10.001
30. M. H. Gamble, P. Rice, *LWT-Food Sci Technol*, **1988**, *21,* 62–65.
31. B. Baumann, F. Escher, *LWT-Food Sci Technol*, **1995**, *28,* 395–403. **DOI:**10.1016/0023-6438(95)90023-3
32. F. Pedreschi, P. Moyano, *LWT-Food Sci Technol*, **2005**, *38,* 599–604. **DOI:**10.1016/j.lwt.2004.08.008
33. P. Bouchon, *Adv Food Nutr Res*, **2009**, *57,* 210–334.
34. V. Dueik, M. C. Moreno, P. Bouchon, *J Food Eng*, **2012**, *111,* 528–536. **DOI:**10.1016/j.jfoodeng.2012.02.027
35. R. G. Moreira, P. F. Da Silva, C. Gomes, *J Food Eng*, **2009**, *92,* 297–304. **DOI:**10.1016/j.jfoodeng.2008.11.012
36. F. Pedreschi, K. Kaack, K. Granby, E. Troncoso, *J Food Eng*, **2007**, *79(4),* 1287–1294. **DOI:**10.1016/j.jfoodeng.2006.04.014
37. M. Yost, J. M. Abu-Ali, S.A. Barringer, *J Food Sci*, **2006**, *71(9),* 364–369. **DOI:**10.1111/j.1750-3841.2006.00171.x
38. P. C. Moyano, V. K. Rioseco, P. A. Gonzalez, *J Food Eng*, **2002**, *54,* 249–255. **DOI:**10.1016/S0260-8774(01)00211-4
39. L. M. Diamante, G. P. Savage, L. Vanhanen, *Inter J Food Sci Technol*, **2012**, *47,* 518–524. **DOI:**10.1111/j.1365-2621.2011.02872.x
40. M. H. Gamble, P. Rice, *Inter J Food Sci Technol*, **1987**, *22,* 535–548. **DOI:**10.1111/j.1365-2621.1987.tb00519.x
41. S. Paul, G. S. Mittal, *Crit Rev Food Sci Nutr*, **1997**, *37,* 635–662. **DOI:**10.1080/10408399709527793
42. R. Guillaumin, Kinetics of fat penetration in food. In Valera, A. E. Bender, I. D. Merlon,Frying of food. Chichester, UK: VCH, **1988.**
43. M. K. Krokida, V. Oreopoulou, Z. B. Maroulis, *J Food Eng*, **2000**, *44,* 39–46. **DOI:**10.1016/S0260-8774(99)00163-6
44. A. Kita, G. Lisinska, *J Sci Food Agric*, **2005**, *85,* 2600–2604. **DOI:**10.1002/jsfa.2319
45. F. Pedreschi, C. Cocio, P. Moyano, E. Troncoso, *J Food Eng*, **2008**, *87,* 200–212. **DOI:**10.1016/j.jfoodeng.2007.11.031
46. P. Bouchon, J. M. Aguilera, D. L. Pyle, *J Food Sci*, **2003**, *68,* 2711–2716. **DOI:**10.1111/j.1365-2621.2003.tb05793.x
47. K. Grob, *Food Addit Contam, Supplement,* **2007***, 24 (S1),* 71–81. **DOI:**10.1080/02652030701398509
48. F. Pedreschi, P. Moyano, K. Kaack, K. Granby, *Food Res Inter*, **2005**, *38,* 1–9. **DOI:**10.1016/j.foodres.2004.07.002
49. N. Surdyk, J. Rosén, R. Andersson, P. Åman, *J Agric Food Chem*, **2004**, *52(7),* 2047–2051. **DOI:**10.1021/jf034999w
50. E. Brathen, S. H. Knutsen*, Food Chem*, **2005**, *92(4),* 693–700. **DOI:**10.1016/j.foodchem.2004.08.030
51. H. Ölmez, F. Tuncay, N. Özcan, S. Demirel, *J Food Compos Anal*, **2008**, *21,* 564–568. **DOI:**10.1016/j.jfca.2008.04.011
52. F. Mestdagh, T. De Wilde, P. Castelein, O. Németh, C. Van Peteghem, B. De Meulenaer, *Euro Food Res Technoly*, **2008**, *227(1),* 69–76. **DOI:**10.1007/s00217-007-0694-9
53. F. Pedreschi, K. Kaack, K. Granby, *Food Res Interl*, **2006**, *39,* 40–46. **DOI:**10.1016/j.foodres.2005.06.001
54. V. Gökmen, T. K. Palazoğlu, H. Z. Şenyuva, *J Food Eng***, 2006**, *77(4),* 972–976. **DOI:**10.1016/j.jfoodeng.2005.08.030
55. T. Karadoğan, *Atatürk Ü Zir Fak Der*, **1994**, *25 (1),* 30–38.
56. Y. Yang, I. Achaerandio, M. Pujolà, *Food Control*, **2016**, *62,* 216–223. **DOI:**10.1016/j.foodcont.2015.10.028
57. T. K. Palazoğlu, D. Savran, V. Gökmen*, J Food Sci*, **2010**, *75(1),* E25–E29. **DOI:**10.1111/j.1750-3841.2009.01389.x
58. T. M. Amrein, S. Bachmann, A. Noti, M. Biedermann, M. F.

Barbosa, S. Biedermann-Brem, et al., *J Agric Food Chem*, **2003**, *51*(18), 5556–5560. **DOI:**10.1021/jf034344v
59. G. O. Abong, M. W. Okoth, J. K. Imungi, J. N. Kabira, *Am J Food Technol*, **2011**, *6(9),* 753–762.
60. A. Kaur, N. Singh, R. Ezekiel, *Int J Food Prop*, **2008**, *11:* 791–803. **DOI:**10.1080/10942910701622664
61. H. D. Isengard, *Lipid Technol*, **2010**, *22(6),* 134–136. **DOI:**10.1002/lite.201000019
62. R. Farhoosh, M. H. Tavassoli-Kafrani, *Food Chem*, **2010**, *122:* 381–385. **DOI:**10.1016/j.foodchem.2010.02.066
63. A. H. A. Tarmizi, K. Niranjan, *Food Bioprocess Technol*, **2013**, 6:2600–2608. **DOI:**10.1007/s11947-012-0921-7
64. Anonymous, **2012**, Kızartmada Kullanılmakta Olan Katı Ve Sıvı Yağlar İçin Özel Hijyen Kuralları Yönetmeliği, Retrieved from http://www.resmigazete.gov.tr/eskiler/2012/05/20120512-5.htm
65. A. H. Ahmad Tarmizi, L. İsmail, *J American Oil Chem Soc,* **2008**, *85(3),* 245–251. **DOI:**10.1007/s11746-007-1184-8
66. M. Bensmira, B. Jiang, C. Nsabimana, T. Jian, *Food Res Inter*, **2007**, *40(3),* 341–346. **DOI:**10.1016/j.foodres.2006.10.004
67. J. B. Rossell, Frying: Improving Quality. Woodhead Publishing Limited, Cambridge, **2001**, pp. 1–355. **DOI:**10.1201/9781439822951

Povzetek

Testirali smo različne pogoje vakuumskega cvrtja pomfrita in preverjali njegove fizikalne, kemijske in organoleptične lastnosti glede na uporabljeno olje ter trajanje in temperaturo cvrtja. Da bi določil optimalne pogoje cvrtja smo pri študiji uporabili načrt s centralno zasnovo z rotacijo. Optimalni pogoji so vključevali minimalno vsebnost olja, trdoto v območju 30–45 N, minimalno vsebnost akrilamida in celovito ustreznost. Optimalne rezultate cvrtja pomfrita smo dosegli s temperaturo 124.39 °C in trajanjem 8.36 min. Tako pripravljen pomfrit je ohranil željeno bravo, teksturne lastnosti in okus, vseboval pa je tudi malo olja in znižano tvorbo akrilamidov. Poleg tega se je pri vakuumskem cvrtju tudi ohranila kvaliteta olja.

Except when otherwise noted, articles in this journal are published under the terms and conditions of the Creative Commons Attribution 4.0 International License

Scientific paper

Extraction-Chromogenic System for Cobalt Based on 5-Methyl-4-(2-thiazolylazo) Resorcinol and Benzalkonium Chloride

Danail G. Georgiev Hristov,[1] Petya Vassileva Racheva,[1,2] Galya Konstantinova Toncheva[3] and Kiril Blazhev Gavazov[1,2,*]

[1] *Department of Chemical Sciences, Medical University of Plovdiv, 120 Buxton Brothers St., Plovdiv 4004, Bulgaria*

[2] *Research Institute at the Medical University of Plovdiv, 15A Vasil Aprilov Bld., Plovdiv, Bulgaria*

[3] *Department of General and Inorganic Chemistry with Methodology of Chemical Education, University of Plovdiv Paisii Hilendarski, 24 Tsar Assen St., Plovdiv 4000, Bulgaria*

** Corresponding author: E-mail: kgavazov@abv.bg*

Received: 04-14-2020

Abstract

The interaction between Co^{II} and 5-methyl-4-(2-thiazolylazo)-resorcinol (MTAR) was studied in a water-chloroform system, in the presence or absence of benzalkonium chloride (BZC) as a cationic ion-association reagent. The optimum pH, concentration of the reagents and extraction time for the extraction of Co were found. In the presence of BZC, the extracted ion-associate could be represented by the formula $(BZ^+)[Co^{III}(MTAR^{2-})_2]$, where MTAR is in its deprotonated form. The following extraction-spectrophotometric characteristics were determined: absorption maximum, molar absorptivity, Sandell's sensitivity, limit of detection, limit of quantification, constant of extraction, distribution ratio and fraction extracted. In the absence of BZC, the extraction is incomplete and occurs in a narrow pH range. The extracted chelate contains one deprotonated and one monoprotonated ligand: $[Co^{III}(MTAR^{2-})(HMTAR^-)]$.

Keywords: Cobalt; 4-(2-thiazolylazo)resorcinol; benzalkonium chloride; ternary complex; solvent extraction; spectrophotometry

1. Introduction

Cobalt is a group 9 transition metal that occupies position 27 in the periodic table. Because of its unique properties it is important for industry, agriculture, medicine and high technology development. As a highly wear- and corrosion-resistant metal which retains these properties even at high temperature, cobalt is an essential constituent of alloys for special uses.[1,2] It is also applied in the manufacture of sintered cutting tools, catalysts, permanent magnets, pigments, siccative's and rechargeable (e.g., lithium-ion) batteries. Since the need of these batteries increases, some business experts predict a 47x increase in global demand for cobalt in 2030 compared to 2017.[3]

Cobalt is a relatively rare element. It is present in rocks, soils and sea water at very low concentrations and its average content in the continental crust is approximately 17.3 mg/kg.[4] There are several commercially important cobalt-containing minerals, such as heterogenite, linnaeite, cobaltite, smaltite, erythrite, carrolite, skutterudite and asbolite. However, in most deposits, this element is not in sufficient quantity to be economically minable alone and is obtained as a by-product of the metallurgy of copper, nickel, silver, gold, lead and zinc.[1,4,5]

Cobalt is an essential trace element for all animals, including humans, and an active nutrient for bacteria, fungi and algae. It is utilized by animals only in the form of vitamin B-12, synthesized by certain bacteria and archaea in the presence of enough cobalt. Cobalt deficiency (or vitamin B-12 deficiency) in humans can lead to pernicious anemia and nerve damage.[6] On the other hand, excess cobalt can provoke numerous negative effects on central metabolism.[7,8] That is why its content in various samples should be monitored.[8–11]

There are many analytical methods for cobalt. Azo dyes such as 4-(2-pyridylazo)resorcinol (PAR)[12-23] and

4-(2-thiazolylazo)resorcinol (TAR)[24–27] have long been used for its preconcentration and subsequent determination. Due to the ability of these reagents to form anionic chelates with cobalt cations, analytical procedures are often associated with the addition of auxiliary reagents providing the necessary hydrophobicity and extraction characteristics.

The following cationic reagents have been used as components of Co-PAR and Co-TAR ternary complexes: diphenylguanidine,[15] dicyclohexyl-18-crown-6,[17] tetradecyl(trihexyl)phosphonium chloride,[21] xylometazoline hydrochloride,[19] tributylammonium bromide,[22] tetraphenylarsonium chloride,[28,29] tetraphenylphosphonium chloride,[28,29] nitron,[30] tetrazolium salts,[27,31–33] and quaternary ammonium salts.[16,18,20,34–36]

5-Methyl-4-(2-thiazolylazo)resorcinol (MTAR)[37] is a TAR derivative that has been used in our laboratory for the liquid-liquid extraction of $V^{IV,V}$ [38–42] and Ni^{II}.[43] Its interaction with Co^{II} in water-ethanol medium has been studied by Kiryukhina.[44] This reagent has also been used for the reversed-phase capillary high-performance liquid chromatographic determination of Co^{II}.[45] There are no reports on the liquid-liquid extraction of Co complexes with MTAR, nor on the ternary Co-MTAR complexes with auxiliary reagents.

The objective of this work was to investigate the complex formation and liquid-liquid extraction of Co with MTAR in the presence and absence of benzalkonium chloride (BZC). BZC (Figure 1) is a mixture of quaternary ammonium chlorides used in pharmaceuticals, cosmetics and cleaning products due to its valuable bacteriostatic, bactericidal, fungicidal, algicide, spermicide and surfactant properties.[46,47] Its ability to form ion-pairs with bulky anions has been used in liquid-liquid extraction methods for its determination.[48]

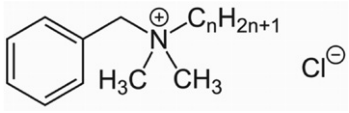


Fig. 1. Structural formula of BZC. The index n can be 8, 10, 12, 14, 16 or 18 (constituents with n = 12, 14, and 16 predominate).

2. Experimental

2. 1. Reagents and Apparatus

Cobalt standard solution (1000 mg dm^{-3}, $Co(NO_3)_2$) was obtained from Merck, Germany. Working solutions ($c_{Co} = 4.0 \times 10^{-4}$ mol dm^{-3}) were prepared by appropriate dilution. MTAR (95%) and BZC (≥ 95%) were also Merck products. Neutral or slightly basic aqueous solutions of MTAR (2.0×10^{-3} mol dm^{-3}) were prepared by the addition of KOH.[40,41] BZC was dissolved in water ($c_{BZC} = 2 \times 10^{-2}$ mol dm^{-3} and 4×10^{-4} mol dm^{-3}). Chloroform was redistilled and used repeatedly. The acidity of the aqueous phase was maintained constant by the addition of buffer solution, prepared by mixing 2 mol dm^{-3} aqueous solutions of acetic acid and ammonia. The resulting pH was checked by a WTW InoLab 720 pH-meter (Germany) with a precision of ±0.01 pH units. UV/vis spectrophotometers Ultrospec3300 pro and Camspec M508 UV-Vis (UK), equipped with 10-mm path-length cells, were employed for absorbance measurements. Distilled water was used in all experiments.

2. 2. General Procedure

Solutions of Co^{II}, buffer (pH 3.7–9.2), MTAR and BZC were sequentially transferred into a separatory funnel. Water was added to a total volume of 10 cm^3. Then 10 cm^3 of chloroform were buretted and the funnel was shaken for a fixed time interval. After a short wait for phase separation, a portion of the organic extract was transferred through a filter paper into the spectrophotometer cell. Absorbance was measured against chloroform or a simultaneously prepared blank.

2. 3. Determination of the Distribution Ratio and Fraction Extracted

The distribution ratio D was found from the equation $D = A_1/(A_3 - A_1)$, where A_1 is the absorbance measured after a single extraction under the optimum conditions in the presence of BZC (Table 1) and A_3 is the absorbance measured after a triple extraction under the same conditions. The total volume in both cases (single extraction and triple extraction) was 25 cm^3.[39-41] The fraction extracted was calculated from the equation $E(\%) = 100 \times D/(D+1)$.

3. Results and Discussion

3. 1. Absorption Spectra and Effect of pH

Kiryukhina[44] reported that Co^{II} reacts with MTAR in a water-ethanol medium to form a 1:2-complex with an

Table 1. Optimum extraction-spectrophotometric conditions.

Extraction system	λ_{max}, nm	pH	c_{MTAR}, mol dm^{-3}	c_{BZC}, mol dm^{-3}	Shaking time, min
Co – MTAR – water –chloroform	509	5.5	4.0×10^{-4}	–	3[a]
Co – MTAR – BZC– water –chloroform	550	7.5	1.6×10^{-4}	1.4×10^{-4}	3

[a] quantitative extraction cannot be achieved

absorption maximum λ_{max} = 520 nm. She found that the optimum pH for complex formation was 6 – 8 but did not pay attention to the change in spectral characteristics as the pH changed.

Our extraction studies have shown that the extracted into organic phase complex in the Co-MTAR-water-chloroform system has an absorption maximum at 509 nm (Figure 2, spectrum 1). In the presence of BZC, the absorption maximum shifts to the higher wavelengths (about 549 –550 nm; spectrum 2) and the optimum pH range widens significantly and shifts to higher pH values (Figure 3).

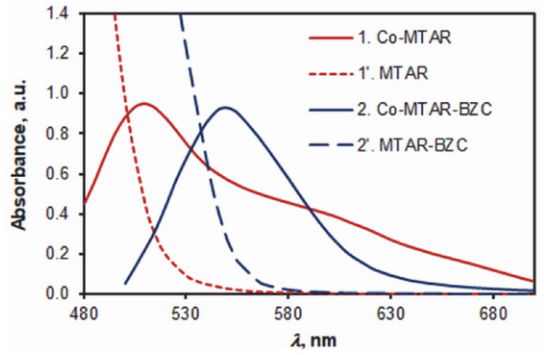


Figure 2. Absorption spectra in chloroform of the Co-MTAR binary complex (1) against blank (1') and Co-MTAR-BZC ternary complex (2) against corresponding blank (2'). $c_{Co} = 4 \times 10^{-5}$ mol dm^{-3}; t_{ex} = 3 min; $c_{MTAR} = 4.0 \times 10^{-4}$ mol dm^{-3} (1, 1') or 1.6×10^{-4} mol dm^{-3} (2, 2'); pH = 5.5 (1, 1') or 7.5 (2, 2'); $c_{BZC} = 1.4 \times 10^{-4}$ mol dm^{-3} (2, 2').

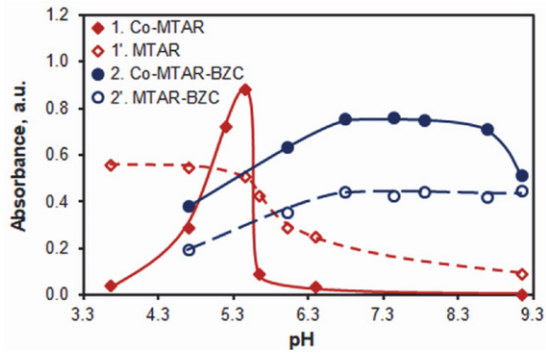


Figure 3. Absorbance of the Co-MTAR (1) and Co-MTAR-BZC (2) complexes and corresponding blanks (1' and 2') *vs* pH of the aqueous phase. $_{Co} = 4 \times 10^{-5}$ mol dm^{-3} (1, 2); $c_{MTAR} = 4 \times 10^{-4}$ mol dm^{-3} (1, 1', 2, 2'); $c_{BZC} = 1 \times 10^{-3}$ mol dm^{-3} (2, 2'); λ = 509 nm (1,1') or 550 nm (2,2'); t_{ex} = 3 min.

3. 2. Effect of MTAR Concentration and the MTAR-to-Co Molar Ratio

The effect of MTAR concentration on the absorbance at 509 and 550 nm is shown in Figure 4, curves 1a-c. Processing of the data received in the presence or absence of BZC by the straight-line method of Asmus[49] (Figure 5) showed that in both cases the MTAR-to-Co molar ratio is 2:1. When the concentration of MTAR increases in the

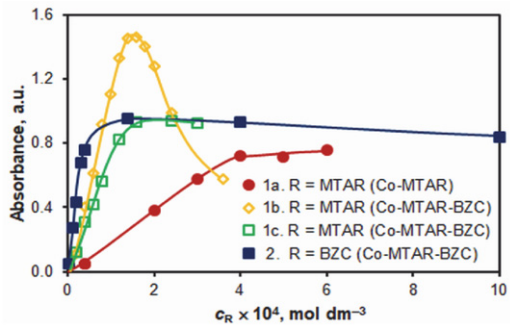


Figure 4. Effect of MTAR (1a,b,c) and BZC (2) concentration. (1a) $c_{Co} = 4 \times 10^{-5}$ mol dm^{-3}, pH 5.2, t_{ex} = 3 min, λ = 509 nm; (1b) $c_{Co} = 8.5 \times 10^{-5}$ mol dm^{-3}, $c_{BZC} = 4 \times 10^{-4}$ mol dm^{-3}, pH 6.0, t_{ex} = 3 min, λ = 509 nm; (1c) $c_{Co} = 4.0 \times 10^{-5}$ mol dm^{-3}, $c_{BZC} = 1.4 \times 10^{-4}$ mol dm^{-3}, pH 7.5, t_{ex} = 3 min, λ = 550 nm; (2) $c_{Co} = 4 \times 10^{-5}$ mol dm^{-3}, $c_{MTAR} = 2 \times 10^{-4}$ mol dm^{-3}, pH 7.5, t_{ex} = 3 min, λ = 550 nm.

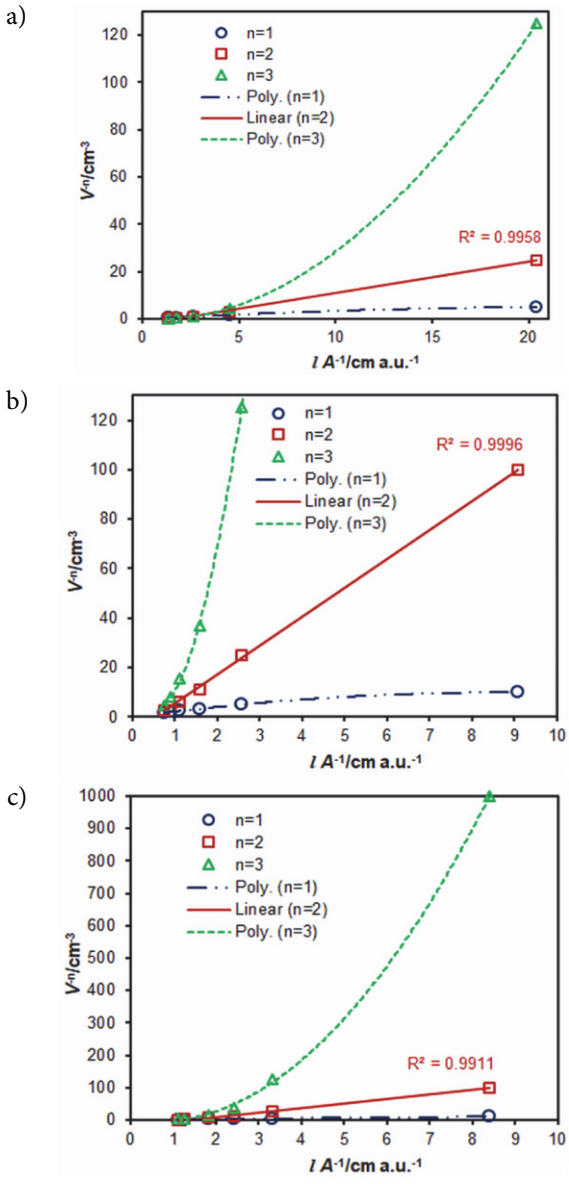


Figure 5. Determination of the MTAR-to-Co molar ratio by the straight-line method of Asmus. The experimental conditions are given in Figure 4, curves 1a-c, respectively.

presence of BZC, the absorption maximum shifts to lower wavelengths. This can be attributed to the simultaneous extraction of the binary Co–MTAR complex (λ_{max} = 509 nm).

3. 3. Effect of BZC Concentration and the BZC-to-Co Molar Ratio

The effect of BZC concentration is shown in Figure 4, curve 2. This curve allowed the BZC-to-Co molar ratio (1:1) to be determined by many methods: straight-line method of Asmus,[49] Bent and French limited logarithm method[50,51] (Figure 6), You and Jones method[52] (Figure 7) and mobile equilibrium method[53] (Figure 8). Successful determination of the composition by all these methods is rarely possible since they have certain limitations related to the stability of the species and the presence of side processes.[51,54]

In addition to the aforementioned methods, the composition was determined by the Job's method of continuous variations (Figure 9).[55] The obtained curve shows that the complex is rather stable.

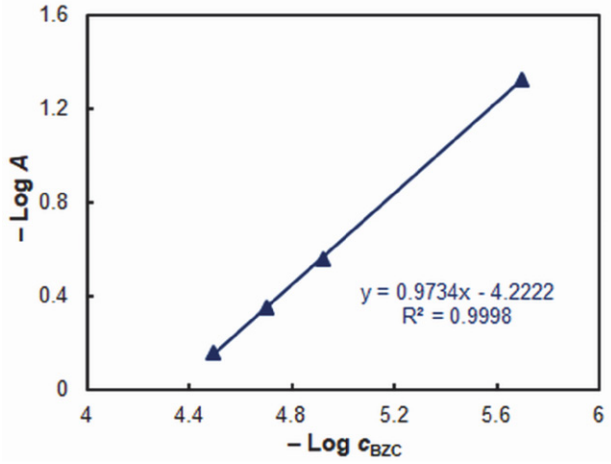


Figure 6. Determination of the BZC-to-Co molar ratio by the Bent-French limited logarithm method.

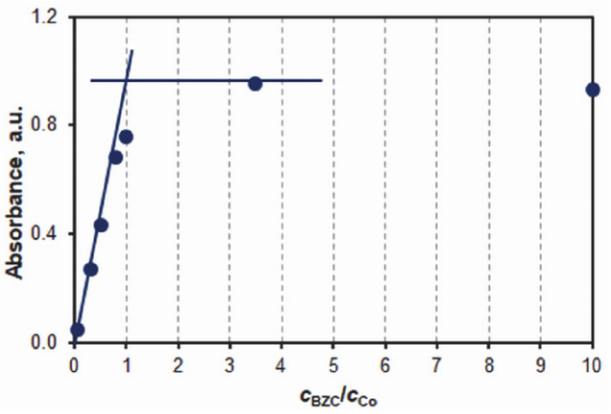


Figure 7. Determination of the BZC-to-Co molar ratio by the You and Jones method.

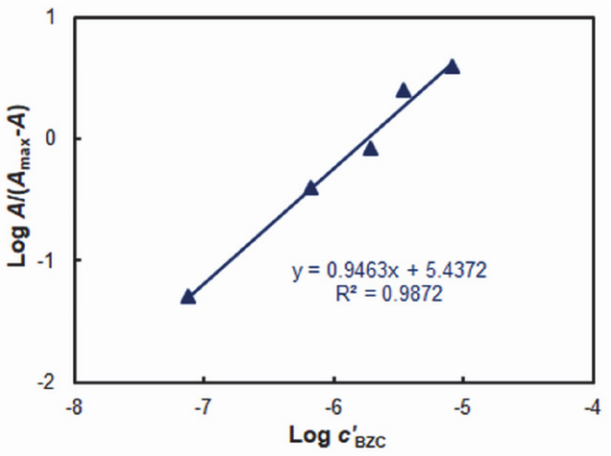


Figure 8. Determination of the BZC-to-Co molar ratio by the mobile equilibrium method.

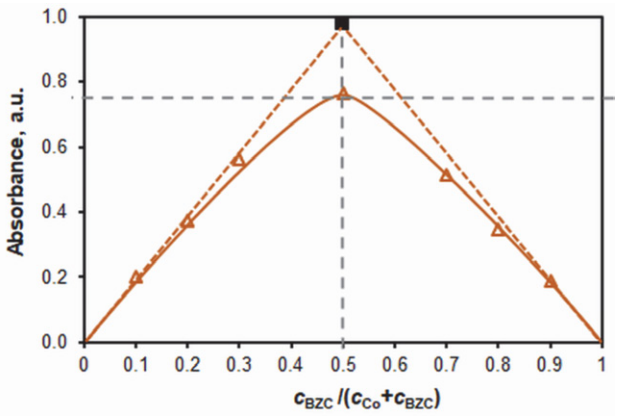


Figure 9. Determination of the BZC-to-Co molar ratio by the Job's method of continuous variations and K_{ex} by the Likussar-Boltz method. $k = c_{Co} + c_{BZC} = 8 \times 10^{-5}$ mol dm^{-3}, $c_{MTAR} = 2 \times 10^{-4}$ mol dm^{-3}, pH 7.5, λ = 547 nm.

3. 4. Suggested Chemical Formulae and Equations

In order to propose correct formulae for the extracted species, the data for their composition must be synchronized with the information accumulated in the literature for the possible oxidation of Co^{II} to Co^{III} by the atmospheric oxygen. Numerous studies in this area allow us to summarize that in the presence of azo dyes[17,27–31,56-61] such as PAR and TAR, (i) the oxidation proceeds rapidly (in seconds);[58,61] (ii) the oxidation is quantitative;[60] (iii) Co^{II} is oxidized even in the presence of reducing agents such as ascorbic acid, sulfite or hydrazine;[57,61] (iv) the protonation state of the azo dye in the complex can be estimated by the position and intensity of the spectral bands in the visible range.

The MTAR complex extracted in the absence of BZC has a composition of Co:MTAR = 1:2. Because of the requirement of electroneutrality, it is reasonable to assume that its formula is $[Co^{III}(HL^{-})(L^{2-})]^{0}$ (L^{2-} and HL^{-} are the deprotonated and monoprotonated forms of the ligand H_2L = MTAR). A similar Co-PAR complex has been isolat-

ed and studied by Mochizuki et al.[58] The chloroform-extracted (at pH close to 4) Co-TAR binary complex[29] can probably be represented by the same formula.

It can be seen from Figure 3 (curve 1) that the Co-MTAR binary complex is formed in a narrow pH range (about pH 5.5), which corresponds well with the onset of the decrease in absorbance (curve 1 ‘) associated with the conversion of the neutral MTAR into a monoanion:

$$H_2L^0 \rightleftarrows HL^- + H^+ \quad (1)$$

The course of curve 1’ is in good agreement with the pK_a value determined by Menek et al.[62] (Table 2; p$K_{p\text{-}OH}$ = 5.7), characterizing Eq. 1.

As the pH increases the neutral complex is transformed into an anionic complex with a bathochromically shifted absorption maximum:

$$[Co^{III}(HL^-)(L^{2-})]^0 \rightleftarrows [Co^{III}(L^{2-})_2]^- + H^+ \quad (2)$$

The anionic complex can also be formed by the direct interaction (Eq. 3) of the metal with the dominant form of the reagent under optimal conditions (i.e., HL^-).

$$Co^{II}_{(aq)} + 2\ HL^- \rightleftarrows [Co^{III}(L^{2-})_2] + 2H^+ + e^- \quad (3)$$

The formation of the ternary ion-association complex can be described by Eq. 4, in which BZ^+ is the cation of BZC.

$$[Co^{III}(L^{2-})_2]^- + BZ^+ \rightleftarrows (BZ^+)[Co^{III}(L^{2-})_2] \quad (4)$$

The overall process of complex formation and extraction at the optimum pH-range (see Figure 3, curve 2) is shown in Eq. 5.

$$Co^{II}_{(aq)} + 2\ HL^-_{(aq)} + BZ^+_{(aq)} \rightleftarrows \rightleftarrows (BZ^+)[Co^{III}(L^{2-})_2]_{(org)} + 2H^+_{(aq)} + e^- \quad (5)$$

It involves metal assisted deprotonation of the ligand HL^-, oxidation of the initially formed labile Co^{II}-complex to inert Co^{III}-complex in the presence of air,[16,58,63] and ion-association between BZ^+ and the anionic complex.[54,64] The spectral characteristics and composition of the ternary complex (Co:MTAR:BZC = 1:2:1), and the optimal pH-range of its existence suggests that it contains two deprotonated ligands, as in the literature concerning similar ternary PAR- and TAR-complexes.[27-31] These azo dyes have pK_a values (Table 2) that are close to those reported for MTAR.

3. 5. Extraction Characteristics

The conditional equilibrium constant characterizing Eq. 5 was calculated by the mobile equilibrium method[53] (Figure 8), Likussar-Boltz method[67] (Figure 9) and Holme-Langhmyir method.[68] The obtained values are given in Table 3, along with the values for fraction extracted (*E*) and distribution ratio (*D*).

Table 3. Extraction characteristics.

Extraction characteristic	Value
Extraction constant (Log K_{ex})	5.6 ± 0.2^a ($N = 3$) 5.7 ± 0.3^a ($N = 5$) 5.8 ± 0.1^c ($N = 5$)
Distribution ratio (Log *D*)	1.4 ± 0.2 ($N = 4$)
Fraction extracted (*E*), %	96 ± 2 ($N = 4$)

[a] Likussar-Boltz method. [b] Molar equilibrium method. [c] Holme-Langmyhr method.

3. 6. Beer’s Law and Analytical Characteristics

The relationship between the concentration of Co^{II} in the aqueous phase and the absorbance of the extracted ternary complex was studied under optimum conditions (Table 1). A good linearity was observed in the concentration range of 0.2 – 2.8 μg cm^{-3} ($R^2 = 0.9994$, $N = 7$). The linear regression equation was $A = 0.395\gamma + 0.004$, where A is the absorbance and γ is the concentration (μg cm^{-3}). The standard deviations of the slope and intercept were

Table 2. Dissociation constants of MTAR, TAR and PAR.

Azo dye	pK_{NH}	pK_a p$K_{p\text{-}OH}$	p$K_{o\text{-}OH}$	Conditions	Ref.
MTAR	–	5.7	11.8		62
TAR	1.25	6.0	9.3	0.1 mol dm^{-3} $NaClO_4$	65, 66
	0.96	6.23	9.44	0.1 mol dm^{-3} $NaClO_4$	
	–	6.16	9.59	I = 0.2	
	–	6.15	9.68		
PAR	2.7	5.83	12.5	0.1 mol dm^{-3} KNO_3	65, 66
	2.66	5.48	12.31	0.1 mol dm^{-3} $NaClO_4$	
	3.1	5.6	11.9	I = 0.1	
	2.57	6.2	11.5		

0.004 and 0.008, respectively. The limits of detection (LOD) and quantitation (LOQ), calculated as 3- and 10 times standard deviation of the intercept divided by the slope, were LOD = 0.058 μg cm^{-3} and LOQ = 0.193 μg cm^{-3}. The molar absorptivity (ε) and Sandell's sensitivity (*SS*) were $\varepsilon = 2.33 \times 10^4$ dm^3 mol^{-1} cm^{-1} and *SS* = 2.53×10^{-3} μg cm^{-2}, respectively.

4. Conclusions

The present investigations shed light on the complex formation of Co^{II} with MTAR in the presence or absence of BZC. The conditions for formation of two electroneutral complex species, $[Co^{III}L(HL)]$ and $(BZ^+)[Co^{III}(L)_2]$, were found. The first one contains one monoprotonated MTAR and one deprotonated MTAR. It is extracted in a narrow pH-range (about 5.5) and shows an absorption maximum at 509 nm. In the presence of BZC, a ternary ion-association complex (λ_{max} = 550 nm) is formed over a wider pH range (6.8–8.7). In both cases, the complex formation involves the oxidation of Co^{II} to Co^{III} by atmospheric oxygen.

Acknowledgements

This study is part of a project (DPDP-24) within the framework of a scientific competition "Doctoral and post-doctoral projects-2019" at the Medical University of Plovdiv.

5. References

1. K. K. Chatterjee, Uses of Metals and Metallic Minerals, New Age International (P) Ltd. Publishers, New Delhi, India, **2007**, pp. 272–275.
2. S. Gialanella, A. Malandruccolo, Aerospace Alloys, Springer, Cham, Switzerland, **2020**, pp. 267–386. **DOI:**10.1007/978-3-030-24440-8_6
3. T. Wilson, We'll all be relying on Congo to power our electric cars, https://www.bloomberg.com/news/articles/2017-10-26/battery-boom-relies-on-one-african-nation-avoiding-chaos-of-past, (assessed: March 31, 2020)
4. G. M. Mudd, Z. Weng, S. M. Jowitt, I. Turnbull, T. Graedel, *Ore Geol. Rev.* **2013**, *55*, 87–98. **DOI:**10.1016/j.oregeorev.2013.04.010
5. G. Rao, Nickel and Cobalt Ores: Flotation, in: Reference Module in Chemistry, Molecular Sciences and Chemical Engineering, Elsevier, **2014**, pp. 1–27. **DOI:**10.1016/B978-0-12-409547-2.10944-8
6. D. Linhares, A. Pimentel, C. Borges, J. V. Cruz, P. Garcia, A. dos Santos Rodrigues, *Sci. Total Environ.* **2019**, *684*, 715–721. **DOI:**10.1016/j.scitotenv.2019.05.359
7. S. J. Moore, M. J. Mayer, R. Biedendieck, E. Deery, M. J. Warren, *New Biotechnol.* **2014**, *31*, 553–561. **DOI:**10.1016/j.nbt.2014.03.003
8. A. Z. Zalov, Sh. A. K. Ibragimova, *Izv. Saratov Univ. (N. S.), Ser. Chemistry. Biology. Ecology*, **2019**, *19*, 379–386 (in Russian). **DOI:**10.18500/1816-9775-2019-19-4-379-386
9. L. Dospatliev, M. Ivanova, *Bulg. Chem. Commun.* **2017**, *49*, 787–791.
10. L. Dospatliev, Z. Yaneva, *Sci. Technol.* **2014**, *4*, 31–35.
11. A. Z. Zalov, K. A. Kuliev, S. M. Shiralieva, S. A. Mammadova, K. R. Aliyeva, S. N. Gahramanova, *J. Pharmacogn. Phytochem.* **2019**, *8*, 2612–2616.
12. T. Yotsuyanagi, R. Yamashita, K. Aomura, *Jpn. Anal.* **1970**, *19*, 981–982. **DOI:**10.2116/bunsekikagaku.19.981
13. R. Yamashita, T. Yotsuyanagi, K. Aomura, *Jpn. Anal.* **1971**, *20*, 1282–1288. **DOI:**10.2116/bunsekikagaku.20.1282
14. H. Okochi, *Jpn. Anal.* **1972**, *21*, 51–56. **DOI:**10.2116/bunsekikagaku.21.51
15. S. G. Mamuliya, I. V. Pyatnitskii, L. L. Kolomiets, K. I. Grigalashvili, *Zh. Anal. Khim.* **1980**, *35*, 1306–1309.
16. T. Okutani, A. Sakuragawa, M. Murakami, *Anal. Sci.* **1991**, *7*, 109–112. **DOI:**10.2116/analsci.7.Supple_109
17. A. G. Gaikwad, H. Noguchi, M. Yoshio, *Anal. Lett.* **1991**, *24*, 1625–1641. **DOI:**10.1080/00032719108052999
18. J. Dolezal and L. Sommer, *Collection Czech. Chem. Commun.* **1994**, *59*, 2209–2226. **DOI:**10.1135/cccc19942209
19. S. N. Bhadani, M. Tewari, A. Agrawal, C. Sekhar, *J. Indian Chem. Soc.* **1998**, *75*, 176–177.
20. K. Sato, T. Goto, *Jpn. Anal.* **1998**, *47*, 735–738. **DOI:**10.2116/bunsekikagaku.47.735
21. P. Berton, R. G. Wuilloud, *Anal. Methods* **2011**, *3*, 664–672. **DOI:**10.1039/c0ay00616e
22. M. H. Hosseini, F. Kaveh, H. Haddadi, E. Zolfonoun, *Sep. Sci. Technol.* **2017**, *52*, 2632–2640. **DOI:**10.1080/01496395.2017.1301955
23. M. A. Akl, W. S. Alharawi, *Egypt. J. Chem.* **2018**, *61*, 639–650. **DOI:**10.21608/ejchem.2018.3586.1300
24. K. Ueda, *Bull. Chem. Soc. Jpn.* **1979**, *52*, 1215–1216. **DOI:**10.1246/bcsj.52.1215
25. M. Soylak, E. Yilmaz, *J. Hazard. Mater.* **2010**, *182*, 704–709. **DOI:**10.1016/j.jhazmat.2010.06.089
26. V. Divarova, K. Stojnova, P. Racheva, V. Lekova, *Russ. J. Inorg. Chem.* **2018**, *63*, 974–977. **DOI:**10.1134/S0036023618070057
27. V. V. Divarova, P. V. Racheva, V. D. Lekova, K. B. Gavazov, A. N. Dimitrov, *J. Chem. Technol. Metall.* **2013**, *48*, 623–630.
28. M. Široki, L. Marić, Z. Štefanac, M. J. Herak, *Anal. Chim. Acta* **1975**, *75*, 101–109. **DOI:**10.1016/S0003-2670(01)81957-7
29. L. Marić, M. Široki, Z. Štefanac, M. J. Herak, *J. Inorg. Nucl. Chem.* **1981**, *43*, 3357–3361. **DOI:**10.1016/0022-1902(81)80115-7
30. P. V. Racheva, K. B. Gavazov, V. D. Lekova, A. N. Dimitrov, *J. Mater.* **2013**, *2013*, 7. **DOI:**10.1155/2013/897343
31. V. V. Divarova, K. B. Gavazov, V. D. Lekova and A. N. Dimitrov, *Chemija* **2013**, *24*, 81–87.
32. V. V. Divarova, V. D. Lekova, P. V. Racheva, K. T. Stojnova, A. N. Dimitrov, *Acta Chim. Slov.* **2014**, *61*, 813–818.
33. V. Divarova, K. Stojnova, P. Racheva, V. Lekova, *Acta Chim. Slov.* **2016**, *63*, 97–103. **DOI:**10.17344/acsi.2015.1987

34. J. B. Noffsinger, N. D. Danielson, *J. Liq. Chromatogr.* **1986**, *9*, 2165–2183. **DOI:**10.1080/01483918608074141
35. H. R. Pouretedal, P. Sononi, M. H. Keshavarz, A. Semnani, *Chemistry* **2009**, *18*, 22–34.
36. K. Ueda, *Analytical Letters* **1978**, *11*, 1009–1021. **DOI:**10.1080/00032717808067896
37. Y. Erdogdu, Ü. C. Başköse, S. Sağlam, *Chem. Pap.* **2019**, *73*, 1879–1891. **DOI:**10.1007/s11696-019-00739-4
38. K. B. Gavazov, T. S. Stefanova, *Croat. Chem. Acta* **2014**, *87*, 233–240. **DOI:**10.5562/cca2436
39. K. B. Gavazov, V. B. Delchev, K. T. Mileva, T. S. Stefanova, G. K. Toncheva, *Acta Chim. Slov.* **2016**, *63*, 392–398. **DOI:**10.17344/acsi.2016.2431
40. G. K. Toncheva, N. P. Milcheva, K. B. Gavazov, *Acta Chim. Slov.* **2018**, *65*, 847–852. **DOI:**10.17344/acsi.2018.4491
41. D. G. Hristov, N. P. Milcheva, K. B. Gavazov, *Acta Chim. Slov.* **2019**, *66*, 987–994. **DOI:**10.17344/acsi.2019.5244
42. K. B. Gavazov, V. B. Delchev, N. P. Milcheva, G. K. Toncheva, *Open Chem.* **2019**, *17*, 599–608. **DOI:**10.1515/chem-2019-0071
43. G. K. Toncheva, D. G. Hristov, N. P. Milcheva, K. B. Gavazov, *Acta Chim. Slov.* **2020**, *67*, 151–158. **DOI:**10.17344/acsi.2019.5299
44. N. N. Kiryukhina, *Tr. Perm. Med. Inst.* **1972**, *108*, 178–181.
45. Y. Chung, W. Chung, *Bull. Korean Chem. Soc.* **2003**, *24*, 1781–1784. **DOI:**10.5012/bkcs.2003.24.12.1781
46. L. Mastropasqua, L. Agnifili, R. Mastropasqua, V. Fasanella, *Curr. Opin. Pharmacol.* **2013**, *13*, 56–64. **DOI:**10.1016/j.coph.2012.10.002
47. R. C. Rowe, P. Sheskey, M. Quinn (Ed.): Handbook of pharmaceutical excipients, Pharmaceutical Press, London, UK, **2009**, pp. 56-58
48. J. Halvax, G. Wiese, J. Arp, J. Vermeer, W. Van Bennekom, A. Bult, *J. Pharmaceut. Biomed. Anal.* **1990**, *8*, 243–252. **DOI:**10.1016/0731-7085(90)80033-L
49. E. Asmus, *Fresenius' J. Anal. Chem.* **1960**, *178*, 104–116. **DOI:**10.1007/BF00467200
50. H. E. Bent, C. L. French, *J. Am. Chem. Soc.* **1941**, *63*, 568–572. **DOI:**10.1021/ja01847a059
51. M. I. Bulatov, I. P. Kalinkin, Practical Handbook on Photometric Methods of Analysis, Khimiya, Leningrad, Russia, **1976**.
52. J. H. Yoe, A. L. Jones, *Ind. Eng. Chem. Anal. Ed.* **1944**, *16*, 111–115. **DOI:**10.1021/i560126a015
53. Z. Zhiming, M. Dongsten, Y. Cunxiao, *J. Rare Earths* **1997**, *15*, 216–219.
54. K. B. Gavazov, Liquid-liquid extraction of ion-association complexes, in: J. C. Taylor (Ed.) Advances in Chemistry Research, Vol. 50, Nova Science Publishers, New York, **2019**, pp. 203–238.
55. P. Job, *Ann. Chim. (Paris)* **1928**, *9*, 113–134. **DOI:**10.3406/bmsap.1928.9218
56. A. Corsini, Q. Fernando, H. Freiser, *Inorg. Chem.* **1963**, *2*, 224–226. **DOI:**10.1021/ic50005a061
57. T. Iwamoto, M. Fujimoto, *Anal. Chim. Acta* **1963**, *29*, 282–284. **DOI:**10.1016/S0003-2670(00)88616-X
58. K. Mochizuki, T. Imamura, T. Ito, M. Fujimoto, *Bull. Chem. Soc. Jpn.* **1978**, *51*, 1743–1750. **DOI:**10.1246/bcsj.51.1743
59. K. Mochizuki, T. Ito, M. Fujimoto, *Bull. Chem. Soc. Jpn.* **1979**, *52*, 441–445. **DOI:**10.1246/bcsj.52.441
60. V. Cucinotta, R. Caruso, A. Giuffrida, M. Messina, G. Maccarrone, A. Torrisi, *J. Chromatogr. A* **2008**, *1179*, 17–23. **DOI:**10.1016/j.chroma.2007.09.063
61. I. Vyshcherevich, I. Kalinichenko, *J. Water Chem. Technol.* **2010**, *32*, 33–38. **DOI:**10.3103/S1063455X10010042
62. N. Menek, E. Eren, S. Topçu, *Dyes Pigm.*, **2006**, *68*, 205–210. **DOI:**10.1016/j.dyepig.2005.01.010
63. X.-Q. Luo, Q.-R. Liu, Y.-J. Han, L.-W. Xue, *Acta Chim. Slov.* **2020**, *67*, 159–166. **DOI:**10.17344/acsi.2019.5303
64. K. Tôei, *Anal. Sci.* **1987**, *3*, 479–488. **DOI:**10.2116/analsci.3.479
65. A. Hulanicki, S. Glab, G. Ackermann, *Pure and Applied Chemistry* **1983**, *55*, 1137–1230. **DOI:**10.1351/pac198355071137
66. K. Pytlakowska, V. Kozik, M. Dabioch, *Talanta* **2013**, *110*, 202–228. **DOI:**10.1016/j.talanta.2013.02.037
67. W. Likussar, D. F. Boltz, *Anal. Chem.* **1971**, *43*, 1265–1272. **DOI:**10.1021/ac60304a006
68. A. Holme, F. J. Langmyhr, *Anal. Chim. Acta* **1966**, *36*, 383–391. **DOI:**10.1016/0003-2670(66)80066-1

Povzetek

Proučevali smo interakcijo med Co^{II} in 5-metil-4-(2-tiazolilazo)-rezorcinolom (MTAR) v zmesi voda-kloroform, v prisotnosti ali odsotnosti benzalkonijevega klorida (BZC) kot kationskega iono-asociacijskega reagenta. Določili smo optimalni pH, koncentracijo reagentov in ekstrakcijski čas za ekstrakcijo Co. V prisotnosti BZC lahko ekstrahirani ionski kelat predstavimo s formulo $(BZ^{+})[Co^{III}(MTAR^{2-})_2]$, kjer je MTAR v deprotonirani obliki. Določili smo tudi naslednje ekstrakcijske in spektrofotometrične parametre: absorpcijski maksimum, molarno absorptivnost, Sandellovo občutljivost, mejo detekcije in kvantifikacije, konstanto ekstrakcije, porazdelitveno razmerje in delež ekstrakcije. V odsotnosti BZC je ekstrakcija nepopolna in poteka v ozkem območju pH. Ekstrahirani kelat vsebuje en deprotoniran in en monoprotoniran ligand, $[Co^{III}(MTAR^{2-})(HMTAR^{-})]$.

Except when otherwise noted, articles in this journal are published under the terms and conditions of the Creative Commons Attribution 4.0 International License

DOI: 10.17344/acsi.2020.6044 *Acta Chim. Slov.* **2021,** *68,* 44–50
creative commons

Scientific paper

Synthesis, Crystal Structures, Characterization and Catalytic Property of Copper(II) Complexes Derived from Hydrazone Ligands

Yao Tan* and Yan Lei*

School of Environmental and Chemical Engineering, Chongqing Three Gorges University, Chongqing 404000, P. R. China

** Corresponding author: E-mail: 18696838310@163.com (Yao Tan), leiyan222@126.com (Yan Lei)*

Received: 07-03-2020

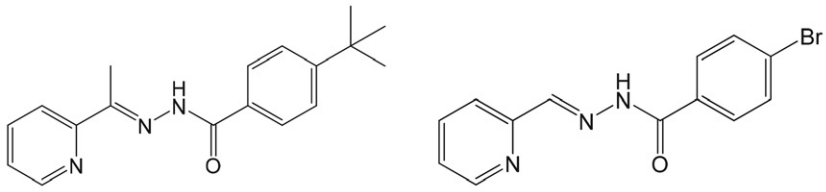
Abstract

A new bromido-coordinated mononuclear copper(II) complex $[Cu(HL^1)Br_2]$ (**1**), and a new mononuclear copper(II) complex $[CuL^2(HL^2)]ClO_4 \cdot 0.5H_2O$ (**2**), with the hydrazone ligands 4-*tert*-butyl-*N*'-(1-(pyridin-2-yl)ethylidene)benzohydrazide (HL^1) and 4-bromo-*N*'-(pyridin-2-ylmethylene)benzohydrazide (HL^2), have been synthesized and structurally characterized by physico-chemical methods and single crystal X-ray determination. X-ray analysis indicates that the Cu atom in complex **1** is in distorted square pyramidal coordination, and that in complex **2** is in octahedral coordination. The catalytic property for epoxidation of styrene by the complexes was evaluated.

Keywords: Copper complex; hydrazone ligand; crystal structure; catalytic property

1. Introduction

Hydrazone compounds, containing the typical -CH=N-NH-C(O)- groups, represent one of the most attractive series of ligands in coordination chemistry. The hydrazone ligands are capable of binding various transition and rare earth metal atoms to form complexes with versatile structures and properties.[1] To date, most hydrazone complexes have been reported to have interesting catalytic properties, such as asymmetric epoxidation, oxidation of sulfides, and various type of polymerization.[2] Among the complexes, those with Cu centers are of particular interest for their catalytic properties.[3] To date, a large number of metal complexes with the hydrazones derived from salicylaldehyde and its analogues are reported. This type of hydrazone ligands usually act as dianionic form during coordination.[4] However, the complexes with the hydrazones derived from 2-acetylpyridine and 2-pyridinecarboxaldehyde, which act as mono-anionic form in the complexes are rare.[5] Shaabani and coworkers have reported copper(II) complexes with the ligand pyridine-2-carboxaldehyde 4-hydroxy benzol hydrazone, and their interesting antibacterial activities.[6] In pursuit of new copper(II) complexes with mono-anionic hydrazone ligands, we report herein the syntheses, X-ray crystal structures, and catalytic properties of a new bromido-coordinated mononuclear copper(II) complex $[Cu(HL^1)Br_2]$ (**1**), and a new mononuclear copper(II) complex $[CuL^2(HL^2)]ClO_4 \cdot 0.5H_2O$ (**2**), with the hydrazone ligands 4-*tert*-butyl-*N*'-(1-(pyridin-2-yl)ethylidene)benzohydrazide (HL^1) and 4-bromo-*N*'- (pyridin-2-ylmethylene)benzohydrazide (HL^2) (Scheme 1).



Scheme 1. The preparation of the hydrazone ligands HL^1 and HL^2.

2. Experimental

2. 1. Materials

Copper bromide, copper perchlorate, 2-acetylpyridine, 2-pyridinecarboxaldehyde, 4-*tert*-butylbenzohydrazide, and 4-bromobenzohydrazide were purchased from Aldrich. All other reagents with AR grade were used as received without further purification.

Caution: Copper perchlorate is potentially explosive. Only small quantities should be used and handled with great care.

2. 2. Physical Measurements

Infrared spectra (4000–400 cm^{-1}) were recorded as KBr discs with a FTS-40 BioRad FT-IR spectrophotometer. The electronic spectra were recorded on a Lambda 35 spectrometer. Microanalyses (C,H,N) of the complex were carried out on a Carlo-Erba 1106 elemental analyzer. Solution electrical conductivity was measured at 298K using a DDS-11 conductivity meter. GC analyses were performed on a Shimadzu GC-2010 gas chromatograph.

2. 3. X-ray Crystallography

Crystallographic data of the complexes were collected on a Bruker SMART CCD area diffractometer with graphite monochromated Mo-Kα radiation (λ = 0.71073 Å) at 298(2) K. Absorption corrections were applied by using the multi-scan program.[7] The structures of the complexes were solved by direct methods and successive Fourier difference syntheses (SHELXS-97), and anisotropic thermal parameters for all nonhydrogen atoms were refined by full-matrix least-squares procedure against F^2 (SHELXL-97).[8] All non-hydrogen atoms were refined anisotropically. The hydrogen atoms were located at calculated positions, and refined isotropically with U_{iso}(H) values constrained to 1.2 U_{iso}(C) and 1.5 U_{iso}(O and methyl C). The perchlorate anion of complex **2** is disordered over two sites, with occupancies of 0.565(3) and 0.435(3), respectively. The Cl-O and O···O distances are restrained to 1.40(1) and 2.30(2) Å, respectively. The atoms of the disordered perchlorate anion are refined as isotropic behavior. The resolution and bond precision of complex **2** are low, which is due to the poor quality of the crystal. There is a large solvent accessible void in the structure of complex **2**, which might indicate the presence of solvent molecules. The crystallographic data and experimental details for the structural analysis are summarized in Table 1, and the selected bond lengths and angles are listed in Table 2.

2. 4. Synthesis of $[Cu(HL^1)Br_2]$ (1)

2-Acetylpyridine (1.0 mmol, 0.12 g) and 4-*tert*-butylbenzohydrazide (1.0 mmol, 0.19 g) were mixed and stirred in methanol (20 mL) for 30 min. Then, copper bromide (1.0 mmol, 0.22 g) was added to the mixture, and the final mixture was further stirred at room temperature for 30 min. The deep blue reaction solution was

Table 1. Crystallographic data for the single crystal of the complexes

	1	**2**
Empirical formula	$C_{72}H_{84}Br_8Cu_4N_{12}O_4$	$C_{52}H_{40}Br_4Cl_2Cu_2N_{12}O_{13}$
Formula weight	2074.95	1558.58
Temperature (K)	298(2)	298(2)
Crystal system	Monoclinic	Triclinic
Space group	$P2_1/c$	$P\bar{1}$
a (Å)	8.0883(11)	10.0284(10)
b (Å)	13.2359(13)	12.0977(11)
c (Å)	18.8467(12)	13.9005(15)
α (°)	90	83.955(2)
β (°)	101.400(2)	77.755(2)
γ (°)	90	89.579(2)
V (Å^3)	1977.8(4)	1638.7(3)
Z	1	1
F(000)	1028	772
Collected data	11413	9964
Unique data	3651	4390
Observed data [$I > 2\sigma(I)$]	2553	1551
Restraints	0	80
Parameters	230	431
Goodness-of-fit on F^2	1.022	0.903
R_1, wR_2 [$I > 2\sigma(I)$]	0.0456, 0.1013	0.0859, 0.1502
R_1, wR_2 (all data)	0.0773, 0.1142	0.1806, 0.2141

Table 2. Selected bond distances (Å) and bond angles (°) for the complexes

Bond	*d*, Å	Bond	*d*, Å
1			
Cu(1)–N(1)	2.010(4)	Cu(1)–N(2)	1.978(4)
Cu(1)–O(1)	2.037(3)	Cu(1)–Br(1)	2.5519(9)
Cu(1)–Br(2)	2.3801(9)		
N(2)–Cu(1)–N(1)	78.95(17)	N(2)–Cu(1)–O(1)	78.10(15)
N(1)–Cu(1)–O(1)	156.59(17)	N(2)–Cu(1)–Br(2)	145.42(13)
N(1)–Cu(1)–Br(2)	99.22(13)	O(1)–Cu(1)–Br(2)	97.01(11)
N(2)–Cu(1)–Br(1)	107.43(13)	N(1)–Cu(1)–Br(1)	97.18(13)
O(1)–Cu(1)–Br(1)	94.04(12)	Br(2)–Cu(1)–Br(1)	107.05(3)
2			
Cu(1)–N(1)	2.292(10)	Cu(1)–N(2)	2.005(10)
Cu(1)–N(4)	2.094(12)	Cu(1)–N(5)	1.849(13)
Cu(1)–O(1)	2.379(8)	Cu(1)–O(2)	2.048(9)
N(5)–Cu(1)–N(2)	177.6(5)	N(5)–Cu(1)–O(2)	78.4(5)
N(2)–Cu(1)–O(2)	99.3(4)	N(5)–Cu(1)–N(4)	79.2(5)
N(2)–Cu(1)–N(4)	103.1(5)	O(2)–Cu(1)–N(4)	157.3(4)
N(5)–Cu(1)–N(1)	105.4(5)	N(2)–Cu(1)–N(1)	74.2(4)
O(2)–Cu(1)–N(1)	100.2(3)	N(4)–Cu(1)–N(1)	89.5(4)
N(5)–Cu(1)–O(1)	108.7(4)	N(2)–Cu(1)–O(1)	71.7(4)
O(2)–Cu(1)–O(1)	86.1(3)	N(4)–Cu(1)–O(1)	97.4(4)
N(1)–Cu(1)–O(1)	145.9(3)		

evaporated to remove three quarters of the solvents under reduced pressure, yielding blue solid of the complex. Yield: 45%. Well-shaped single crystals suitable for X-ray diffraction were obtained by recrystallization of the solid from methanol. Elemental analysis found: C, 41.15; H, 4.23; N, 7.92%. $C_{72}H_{84}Br_8Cu_4N_{12}O_4$ calcd: C, 41.68; H, 4.08; N, 8.10%. IR data (KBr, cm^{-1}): 3453 (w, OH), 3183 (w, NH), 1635 (s, C=O), 1603 (s, CH=N), 1502, 1461, 1346, 1165, 1073, 963, 860, 637, 540, 515, 446. UV-Vis data (λ_{max}, nm): 276, 320, 375, 515, 681.

2. 5. Synthesis of $[CuL^2(HL^2)]ClO_4 \cdot 0.5H_2O$ (2)

2-Pyridinecarboxaldehyde (1.0 mmol, 0.11 g) and 4-bromobenzohydrazide (1.0 mmol, 0.21 g) were mixed and stirred in methanol (20 mL) for 30 min. Then, copper perchlorate hexahydrate (1.0 mmol, 0.37 g) was added to the mixture, and the final mixture was further stirred at room temperature for 30 min. The deep blue reaction solution was evaporated to remove three quarters of the solvents under reduced pressure, yielding blue solid of the complex. Yield: 37%. Well-shaped single crystals suitable for X-ray diffraction were obtained by recrystallization of the solid from methanol. Elemental analysis found: C, 40.23; H, 2.68; N, 10.71%. $C_{52}H_{40}Br_4Cl_2Cu_2N_{12}O_{13}$ calcd: C, 40.07; H, 2.59; N, 10.78%. IR data (KBr, cm^{-1}): 3482 (w, OH), 3197 (w, NH), 1638 (s, C=O), 1592 (s, CH=N), 1565, 1487, 1445, 1367, 1306, 1293, 1222, 1150, 1107, 1066, 1010, 919, 845, 777, 751, 671, 623, 580, 523, 476. UV-Vis data (λ_{max}, nm): 293, 378, 656.

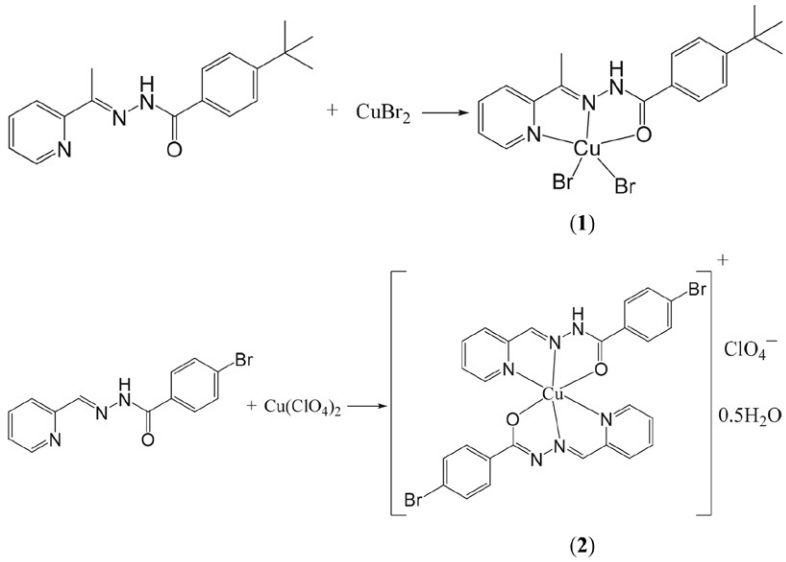
2. 6. Styrene Epoxidation

The epoxidation reaction was carried out at room temperature in acetonitrile under N_2 atmosphere with constant stirring. The composition of the reaction mixture was 2.00 mmol of styrene, 2.00 mmol of chlorobenzene (internal standard), 0.10 mmol of the complex (catalyst) and 2.00 mmol iodosylbenzene or sodium hypochlorite (oxidant) in 5.00 mL freshly distilled acetonitrile. When the oxidant was sodium hypochlorite, the solution was buffered to pH 11.2 with NaH_2PO_4 and NaOH. The composition of reaction medium was determined by GC with styrene and styrene epoxide quantified by the internal standard method (chlorobenzene). All other products detected by GC were mentioned as others. For each complex the reaction time for maximum epoxide yield was determined by withdrawing periodically 0.1 mL aliquots from the reaction mixture and this time was used to monitor the efficiency of the catalyst on performing at least two independent experiments. Blank experiments with each oxidant and using the same experimental conditions except catalyst were also performed.

3. Results and Discussion

3. 1. Chemistry

The hydrazones were readily prepared by condensation reaction of 2-acetylpyridine with 4-*tert*-butylbenzohydrazide, and 2-pyridinecarboxaldehyde with 4-bromobenzohydrazide, respectively, in methanol. The com-



Scheme 2. The preparation of the complexes.

plexes **1** and **2** were prepared by the reaction of the hydrazones with copper bromide (for **1**) and copper perchlorate hexahydrate (for **2**) in methanol (Scheme 2). The reaction progresses are accompanied by an immediate color change of the solution from colorless to deep blue. The molar conductivities (Λ_M = 28 Ω^{-1} cm^2 mol^{-1} for **1** and 153 Ω^{-1} cm^2 mol^{-1} for **2**) are consistent with the values expected for non-electrolyte and 1:1 electrolyte.[9]

3. 2. Crystal Structure Description of Complex 1

Single-crystal X-ray analysis reveals that compound **1** is a bromido-coordinated mononuclear copper(II) complex. The ORTEP plot of the complex is shown in Fig. 1. The copper atom is in a distorted square pyramidal geometry, which is coordinated by the N_2O donor atoms of the hydrazone ligand and one Br atom in the basal plane, and one Br atom at the apical position. The distortion of the square pyramidal coordination of the structure can be observed from the bond angles (Table 2) related to the Cu atom. The *cis*- and *trans*- angles related to the Cu atom at the basal plane are in the range of 78.10(15)–99.22(13)° and 145.42(13)–156.59(17)°, respectively. The bond angles among the apical and basal donor atoms are in the range of 94.04(12)–107.43(13)°. The bond lengths of Cu–O and Cu–N (Table 2) are close to those in other Cu complexes with Schiff base ligands.[9] The question arises as to whether the coordination polyhedron around the five-coordinated metal ion can be described as a distorted square pyramid or a distorted trigonal bipyramid. Further information can be obtained by determining the structural index τ which represents the relative amount of trigonality (square pyramid, τ = 0; trigonal bipyramid, τ = 1); $\tau = (\beta - \alpha)/60°$, α and β being the two largest angles

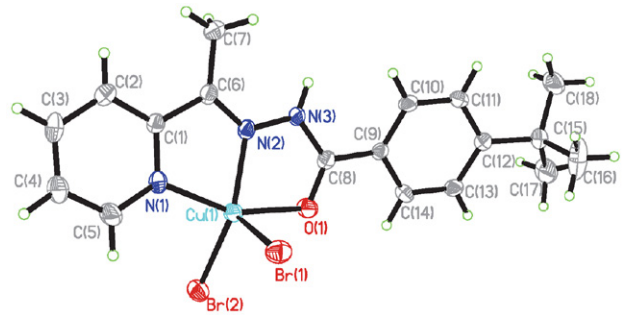


Fig. 1. ORTEP diagram of complex **1** with 30% thermal ellipsoid.

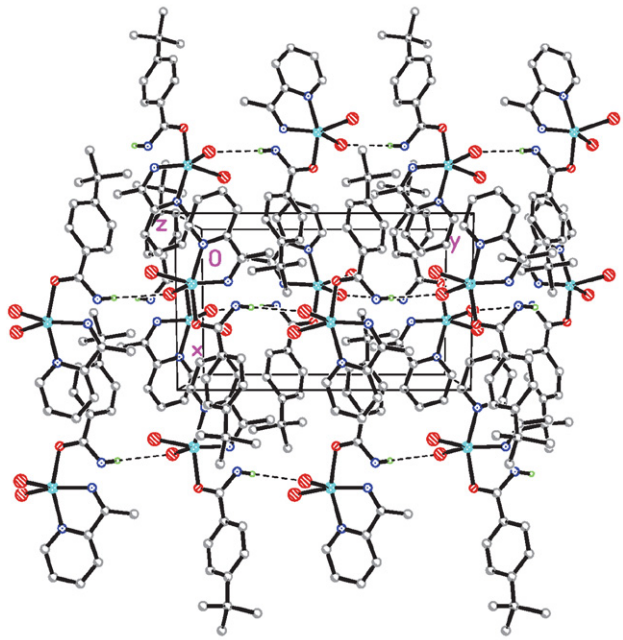


Fig. 2. Molecular packing structure of complex **1** linked by hydrogen bonds.

around the central atom.[10] The value of τ is 0.366. Thus, the coordination geometry of the copper atom is approximately described as a severely distorted square pyramid. The hydrazone ligand coordinates to the Cu atom through neutral state. The molecules are linked through N-H···Br hydrogen bonds (Table 3), to generate chains along the *y* axis (Fig. 2).

3. 3. Crystal Structure Description of Complex 2

Single-crystal X-ray analysis reveals that compound **2** is a mononuclear copper(II) complex. The ORTEP plot of the complex is shown in Fig. 3. The compound contains a [$CuL^2(HL^2)$] cation, a perchlorate anion and half water molecule of crystallization. The ORTEP plot of the complex is shown in Fig. 1b. The copper atom is in a distorted octahedral geometry, which is coordinated by the N_2O donor atoms of one neutral hydrazone ligand and one mono-anionic hydrazone ligand. The distortion of the octahedral coordination of the structure can be observed from the bond angles (Table 2) related to the Cu atom. The *cis*- and *trans*- angles related to the Cu atom are in the range of 74.2(4)–108.7(4)° and 145.9(3)–177.6(5)°, respectively. The bond lengths of Cu–O and Cu–N (Table 2) are close to those in other Cu complexes with Schiff base ligands.[9] The perchlorate anions are linked to the complex cations through N-H···O hydrogen bonds (Table 3; Fig. 4).

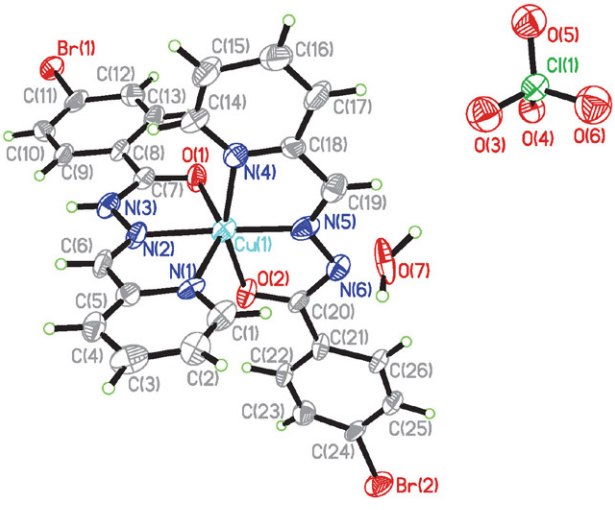


Fig. 3. ORTEP diagram of complex **2** with 30% thermal ellipsoid.

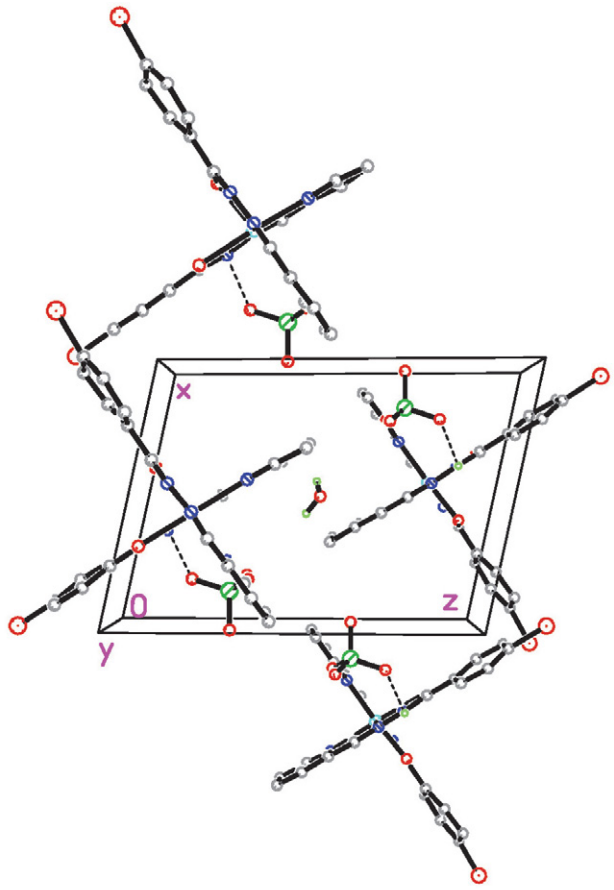


Fig. 4. Molecular packing structure of complex **2** linked by hydrogen bonds.

3. 4. IR and UV-vis Spectra of the Complexes

The weak and broad absorptions in the region 3350–3500 cm^{-1} are attributed to the O-H bonds of the water molecules. The weak absorptions at 3180–3200 cm^{-1} are assigned to the stretching vibration of the N–H groups. The intense bands at 1635 cm^{-1} for **1** and 1638 cm^{-1} for **2** are assigned to the vibration of the C=O groups. The typical bands for the azomethine groups, ν(C=N), are observed at 1595–1603 cm^{-1} for both complexes.[11] The in-

Table 3. Hydrogen bond distances (Å) and bond angles (deg) for the complexes

D–H···*A*	*d*(*D*–H)	*d*(H···*A*)	*d*(*D*···*A*)	Angle (*D*–H···*A*)
1				
N3–H3···Br2$^{\#1}$	0.86	3.05	3.910(4)	178(5)
2				
N3–H3A···O4$^{\#2}$	0.86	2.45	3.036(19)	126(5)

Symmetry codes: #1: 1 – *x*, –*y*, 1 – *z*; #2: *x*, –1 + *y*, *z*.

tense bands in the range of 1060–1110 cm^{-1} for the spectrum of complex **2** are due to the vibration of the perchlorate anion.[12] The weak bands in the range of 400–650 cm^{-1} are assigned to the vibrations of the Cu–O and Cu–N bonds.

In the UV-Vis spectra of the complexes, the bands at 375 nm for **1** and 378 nm for **2** are attributed to the azomethine chromophore π-π* transition. The bands at higher energy (276 and 320 nm for **1** and 293 nm for **2**) are associated with the benzene π-π* transition.[13] The weak and less well-defined bands at 681 nm for **1** and 656 nm for **2** are assigned to the *d*–*d* transitions.

3. 5. Catalytic Properties of the Complexes

The percentage of conversion of styrene, selectivity for styrene oxide, yield of styrene oxide and reaction time to obtain maximum yield using both the oxidants are given in Table 4. The data reveals that the complexes as catalysts convert styrene most efficiently in the presence of both oxidants. Nevertheless, the catalysts are selective towards the formation of styrene epoxides despite of the formation of by-products which have been identified by GC-MS as benzaldehyde, phenylacetaldehyde, styrene epoxides derivative, alcohols *etc.* From the data it is also clear that the complexes exhibit excellent efficiency for styrene epoxide yield. When the reactions are carried out with PhIO and NaOCl, styrene conversions of complexes **1** and **2** were about 87% and 75%, and 79% and 73%, respectively. It is evident that between PhIO and NaOCl, the former acts as a better oxidant with respect to both styrene conversion and styrene epoxide selectivity. The epoxide yields for the complexes **1** and **2** using PhIO and NaOCl as oxidants are 79% and 72%, and 70% and 65%, respectively.

4. Conclusion

Two new mononuclear copper(II) complexes derived from hydrazone ligands were prepared and characterized. Single crystal X-ray analysis indicates that the Cu atom in complex **1** is in distorted square pyramidal coordination, and that in complex **2** is in octahedral coordination. The complexes have effective catalytic property for the epoxidation of styrene, with conversions over 70% and selectivities over 90%.

Supplementary Material

CCDC 1858019 for **1** and 1858021 for **2** contain the supplementary crystallographic data for this paper. These data can be obtained free of charge *via* http://www.ccdc.cam.ac.uk/conts/retrieving.html, or from the Cambridge Crystallographic Data Centre, 12 Union Road, Cambridge CB2 1EZ, UK; fax: (+44) 1223-336-033; or e-mail: deposit@ccdc.cam.ac.uk.

Acknowledgments

This project was supported by the Scientific and Technological Research Program of Chongqing Municipal Education Commission (Grant No. KJQN201801222) and the Chunhui Project from Education Ministry of China (Grant No. Z2015140).

5. References

1. (a) Z. You, H. Yu, Z. Li, W. Zhai, Y. Jiang, A. Li, S. Guo, K. Li, C. Lv, C. Zhang, *Inorg. Chim. Acta* **2018**, *480*, 120–126; **DOI:**10.1016/j.ica.2018.05.020
(b) Z. You, H. Yu, B. Zheng, C. Zhang, C. Lv, K. Li, L. Pan, *Inorg. Chim. Acta* **2018**, *469*, 44–50; **DOI:**10.1016/j.ica.2017.09.011
(c) D. Sadhukhan, M. Maiti, E. Zangrando, S. Pathan, S. Mitra, A. Patel, *Polyhedron* **2014**, *69*, 1–9; **DOI:**10.1016/j.poly.2013.11.007
(d) Y. Tan, *Acta. Chim. Slov.* **2019**, *66*, 1002–1009.
(e) H.-Y. Liu, Y.-S. Yin, L.-J. Yang, X.-L. Zou, Y.-F. Ye, *Acta. Chim. Slov.* **2020**, *67*, 130–136.
(f) M. Liang, N. Sun, D.-H. Zou, *Acta. Chim. Slov.* **2018**, *65*, 964–969.
2. (a) B. Shaabani, A.A. Khandar, H. Mobaiyen, N. ramazani, S.S. Balula, L. Cunha-Silva, *Polyhedron* **2014**, *80*, 166–172; **DOI:**10.1016/j.poly.2014.03.033
(b) A.E.M.M. Ramadan, I.M. El-Mehasseb, *Transition Met. Chem.* **1998**, *23*, 183–189; **DOI:**10.1023/A:1006959513023
(c) M. Bagherzadeh, M. Amini, H. Parastar, M. Jalali-Heravi, A. Allern, L, K. Woo, *Inorg. Chem. Commun.* **2012**, *20*, 86–89; **DOI:**10.1016/j.inoche.2012.02.023
(d) Z. Ma, M. Sutradhar, A. V. Gurbanov, A. M. Maharramov, R. A. Aliyeva, F. S. Aliyeva, F. N. Bahmanova, V. I. Mardanova, F. M. Chyragov, K. T. Mahmudov, *Polyhedron* **2015**, *101*, 14–22. **DOI:**10.1016/j.poly.2015.07.054
3. (a) M. Sutradhar, E. C. Alegria, T. R. Barman, M. F. C. G. da Sil-

Table 4. Catalytic epoxidation results of complexes **1** and **2***

	1	**1**	**2**	**2**
Oxidant	PhIO	NaOCl	PhIO	NaOCl
Conversion (%)	87	79	75	73
Epoxide yield (%)	79	72	70	65
Selectivity (%)	91	92	93	90

* The time is 2 h for PhIO, and 3 h for NaOCl.

va, K. T. Mahmudov, F. I. Guseynov, A. J. L. Pombeiro, *Polyhedron* **2016**, *117*, 666–671; **DOI:**10.1016/j.poly.2016.07.002
(b) Z. Ma, A. V. Gurbanov, A. M. Maharramov, F. I. Guseinov, M. N. Kopylovich, F. I. Zubkov, K. T. Mahmudov, A. J. L. Pombeiro, *J. Mol. Catal. A Chem.* **2017**, *426*, 526–533; **DOI:**10.1016/j.molcata.2016.05.030
(c) H. Hosseini-Monfared, E. Pousaneh, S. Sadighian, S.W. Ng, E. R. T. Tiekink, *Z. Anorg. Allg. Chem.* **2013**, *639*, 435–442. **DOI:**10.1002/zaac.201200395

4. (a) R. Dinda, S. Ghosh, L. R. Falvello, M. Tomas, T. C. W. Mak, *Polyhedron* **2006**, *25*, 2375–2382; **DOI:**10.1016/j.poly.2006.02.002
(b) N. K. Ngan, K. M. Lo, C. S. R. Wong, *Polyhedron* **2011**, *30*, 2922–2932; **DOI:**10.1016/j.poly.2011.08.038
(c) W. Plass, H.-P. Yozgatli, *Z. Anorg. Allg. Chem.* **2003**, *629*, 65–70. **DOI:**10.1002/zaac.200390018
5. (a) N. R. Sangeetha, S. Pal, S. Pal, *Polyhedron* **2000**, *19*, 2713–2717; **DOI:**10.1016/S0277-5387(00)00595-7
(b) S. Mondal, S. Naskar, A. K. Dey, E. Sinn, C. Eribal, S. R. Herron, S. K. Chattopadhyay, *Inorg. Chim. Acta* **2013**, *398*, 98–105; **DOI:**10.1016/j.ica.2012.12.018
(c) R. Bikas, H. Hosseini-Monfared, L. Sieron, A. Gutierrez, *J. Coord. Chem.* **2013**, *66*, 4023–4031. **DOI:**10.1080/00958972.2013.858811
6. B. Shaabani, A. A. Khandar, H. Mobaiyen, N. Ramazani, S. S. Balula, L. Cunha-Silva, *Polyhedron* **2014**, *80*, 166–172. **DOI:**10.1016/j.poly.2014.03.033
7. G. M. Sheldrick, SHELXTL97, Program for refining crystal structure refinement, University of Göttingen: Germany, 1997.
8. W. J. Geary, *Coord. Chem. Rev.* **1971**, *7*, 81–122. **DOI:**10.1016/S0010-8545(00)80009-0
9. (a) J. Wang, D. Qu, J.-X. Lei, Z. You, *J. Coord. Chem.* **2017**, *70*, 544–555; **DOI:**10.1080/00958972.2016.1262538
(b) S. Guo, T. Wang, J. Xin, Q. Hu, S. Ren, G. Sheng, L. Pan, C. Zhang, K. Li, Z. You, *J. Coord. Chem.* **2017**, *70*, 3449–3458. **DOI:**10.1080/00958972.2017.1390569
10. A. W. Addison, T. N. Rao, J. Reedijk, J. Vanrijn, G. C. Verschoor, *J. Chem. Soc. Dalton Trans.* **1984**, *7*, 1349–1356. **DOI:**10.1039/DT9840001349
11. N. Zhang, C.-Y. Huang, D.-H. Shi, Z.-L. You, *Inorg. Chem. Commun.* **2011**, *14*, 1636–1639. **DOI:**10.1016/j.inoche.2011.06.027
12. J. Qian, J.-L. Tian, L. Feng, W. Gu, X.-J. Zhao, S.-P. Yan, *J. Coord. Chem.* **2009**, *62*, 3276–3283. **DOI:**10.1080/00958970903059984
13. Y.-M. Zhou, X.-R. Ye, F.-B. Xin, X.-Q. Xin, *Transition Met. Chem.* **1999**, *24*, 118–120. **DOI:**10.1023/A:1006989707001

Povzetek

Sintetizirali smo nov z bromidom koordiniran enojedrni bakrov(II) kompleks $[Cu(HL^1)Br_2]$ (**1**) in nov enojedrni bakrov(II) kompleks $[CuL^2(HL^2)]ClO_4 \cdot 0.5H_2O$ (**2**) s hidrazonskim ligandom 4-*t*-butil-*N*'-(1-(piridin-2-il)etiliden)benzohidrazidom (HL^1) in 4-bromo-*N*'-(piridin-2-ilmetilen)benzohidrazidom (HL^2). Kompleksa smo okarakterizirali s fiziko-kemijskimi metodami in monokristalno rentgensko difrakcijo. Strukturna analiza je razkrila, da ima Cu atom v kompleksu **1** popačeno kvadratno piramidalno geometrijo, v kompleksu **2** pa oktaedrično geometrijo. Določili smo tudi katalitične aktivnosti za epoksidacijo stirena.

Except when otherwise noted, articles in this journal are published under the terms and conditions of the Creative Commons Attribution 4.0 International License

Scientific paper

Multi-component Reactions of Cyclohexan-1,3-diketones to Produce Fused Pyran Derivatives with Antiproliferative Activities and Tyrosine Kinases and Pim-1 Kinase Inhibitions

Rafat Milad Mohareb,[1,*] Rehab Ali Ibrahim[2] and Ensaf Sultan Alwan[1,2]

[1] *Department of chemistry, Faculty of science, Cairo University, Giza, A. R. Egypt*

[2] *Higher Institute of Engineering and Technology, El-Tagammoe El-Khames, New Cairo, Egypt*

[3] *Department of Quality Assurance, Yemen Drug Company for Industry and Commerce (YEDCO), Sana'a, Yemen*

** Corresponding author: E-mail: raafat_mohareb@yahoo.com*

Received: 05-06-2020

Abstract

In this work the multi-component reactions of either of the arylhydrazocyclohexan-1,3-dione derivatives **3a–c** with either of benzaldehyde (**4a**), 4-chlorobenzaldehyde (**4b**) or 4-methoxybenzaldehyde (**4c**) and either malononitrile (**5a**) or ethyl cyanoacetate (**5b**) giving the 5,6,7,8-tetrahydro-4*H*-chromene derivatives **6a–r**, respectively, are presented. The reaction of two equivalents of cyclohexan-1,3-dione with benzaldehyde gave the hexahydro-1*H*-xanthene-1,8(2*H*)-dione derivative **7**. On the other hand, the multi-component reactions of compound **1** with dimedone and benzaldehyde gave **13**. Both of **7** and **13** underwent heterocyclization reactions to produce fused thiophene, pyran and thiazole derivatives. Selected compounds among the synthesized compounds were tested against six cancer cell lines where most of them gave high inhibitions; especially compounds **3b**, **3c**, **6b**, **6c**, **6d**, **6f**, **6i**, **6m**, **6n**, **8b**, **14a**, **15** and **16** being the most cytotoxic compounds. Further tests against the five tyrosine kinases c-Kit, Flt-3, VEGFR-2, EGFR, and PDGFR and Pim-1 kinase showed that compounds **3c**, **6c**, **6d**, **6f**, **6n**, **14a** and **15** were the most potent of the tested compounds toward the five tyrosine kinases and compounds **3c**, **6c**, **6d**, **6n** and **15** displayed the highest inhibitions toward Pim-1 kinase.

Keywords: Cyclohexan-1,3-dione; dimedone; thiophene; pyran; thiazole; antitumor activity; tyrosine kinases

1. Introduction

Pyran derivatives are known as important class of compounds that exist in nature and have many applications[1] especially fused pyrans are important core units comprising many natural products. Due to their various kinds of biological activities pyrans and their fused derivatives attracted the attention within the last few years. It was reported that benzo[*b*]pyran derivatives were excellent anticancer compounds that give good results at very low concentrations.[2] Many 2-amino-4*H*-pyran derivatives have various applications within industry like their uses as photoactive materials,[3] pigments,[4] and potentially biodegradable agrochemicals.[5] In addition, naphthopyrans have many application with optical studies due to their ability to generate a yellow color on being irradiated with UV light (van). In addition, pyranochalcones have many applications like antimutagenic, antimicrobial, antiulcer, and antitumor activities.[6–8] Pyrans and their fused derivatives showed different kinds of biological activities. The attachments of heterocyclic ring to the pyran ring improve many of the biological effects of the resulting molecules. Especially the 4*H*-pyran derivatives exhibited wide range of biological activities with great interests such as antimicrobial,[9] antiviral,[10,11] mutagenicity,[12] antiproliferative,[13] sex pheromone,[14] antitumor,[15] cancer therapy,[16] and central nervous system activity.[17] Some of these compounds were applied in industrial chemistry as they can be used in many cosmetic manufacturing and through the field of agrochemicals.[18] Such high importance of pyrans and their derivatives together with the ease of their synthesis with high yields direct many works through their synthesis.

This encouraged our research group to be attracted toward the synthesis of pyran derivatives through the uses of β-diketones. The produced compounds showed high anti-proliferative activities against cancer cell lines together with high inhibitions toward tyrosine kinases.[19–25] Through our present work we adopted multi-component reactions of either arylhydrazonocyclohexan-1,3-dione, aromatic aldehydes and cyanometylene derivatives together with using the produced molecule as a suitable starting material for subsequent heterocyclization to obtain a variety of fused derivatives. The anti-proliferative activities of the synthesized compounds and their inhibitions toward tyrosine kinases were determined.

2. Experimental

For newly synthesized compounds melting points were determined and are given as uncorrected values. For all compounds the IR spectra (KBr discs) were measured using a FTIR plus 460 or PyeUnicam SP-1000 spectrophotometer. The ^{1}H NMR spectra were measured using Varian Gemini-300 (300 MHz) and Jeol AS 500 MHz instruments. Measurements were performed in DMSO-d_6 as the solvent using TMS as the internal standard and chemical shifts are expressed as δ ppm. The MS spectra (EI) were measured using Hewlett Packard 5988 A GC/MS system and GCMS-QP 1000 Ex Shimadzu instruments. The microanalytical CHN data were obtained from the Micro-analytical Data Unit at Cairo University and were performed on Vario EL III Elemental analyzer. Screening of compounds against the cancer cell lines and tyrosine kinases were performed through The National Cancer Institute at Cairo University.

2. 1. Synthesis of the Arylhydrazone Derivatives 3a–c

A solution of either the diazonium salts (0.01 mol) [prepared by the addition of a solution of sodium nitrite (0.70 g, 0.01 mol) in water (10 mL) to a cold solution of either aniline (0.93 g, 0.01 mol), 4-methylaniline (1.07 g, 0.01 mol) or 4-chloroaniline (1.27 g, 0.01 mol) dissolved in concentrated hydrochloric acid (10 mL, 18 mol) with continuous stirring] was added to a cold solution of any of the compounds **1** (1.12 g, 0.01 mol), in ethanol (50 mL) containing sodium acetate (3.0 g) with stirring. The whole reaction mixture was left at room temperature for 2 h and the formed solid product was collected by filtration.

2-(2-Phenylhydrazono)cyclohexane-1,3-dione (3a)

Yellow crystals from ethanol, yield 1.51 g (70%). Mp 145–147 °C. IR (KBr) ν_{max} (cm^{-1}): 3472–3328 (NH), 3055 (CH, aromatic), 1705, 1688 (2C=O), 1640 (C=N), 1634 (C=C); ^{1}H NMR (DMSO-d_6, 300 MHz): δ 1.67–1.70 (m, 4H, 2CH_2), 2.38–2.45 (m, 2H, CH_2), 7.26–7.59 (m, 5H, C_6H_5), 8.36 (s, 1H, D_2O exchangeable, NH); ^{13}C NMR (DMSO-d_6, 75 MHz): δ 24.8, 34.6, 38.2, (3CH_2), 120.2, 122.4, 125.8, 127.6 (C_6H_5), 164.3 (C=N), 166.2, 168.6 (2C=O). Anal. Calcd. for $C_{12}H_{12}N_2O_2$: C, 66.56; H, 5.59; N, 12.96. Found: C, 66.80; H, 5.73; N, 13.06. MS: *m/z* 216 (M^+, 36%).

2-(2-(*p*-Tolyl)hydrazono)cyclohexane-1,3-dione (3b)

Brown crystals from ethanol, yield 1.51 g (66%). Mp 170–172 °C. IR (KBr) ν_{max} (cm^{-1}): 3493–3342 (NH), 3055 (CH, aromatic), 1703, 1689 (2C=O), 1638 (C=N), 1632 (C=C); ^{1}H NMR (DMSO-d_6, 300 MHz): δ 1.64–1.72 (m, 4H, 2CH_2), 2.36–2.43 (m, 2H, CH_2), 2.74 (s, 3H, CH_3), 7.26–7.59 (m, 4H, C_6H_4), 8.38 (s, 1H, D_2O exchangeable, NH); ^{13}C NMR (DMSO-d_6, 75 MHz): δ 24.5, 34.8, 38.6 (3CH_2), 39.4 (CH_3), 120.6, 123.8, 126.5, 128.3 (C_6H_4), 164.3 (C=N), 166.7, 168.4 (2C=O). Anal. Calcd. for $C_{13}H_{14}N_2O_2$: C, 67.81; H, 6.13; N, 12.17. Found: C, 68.21; H, 6.08; N, 12.36. MS: *m/z* 230 (M^+, 48%).

2-(2-(4-Chlorophenyl)hydrazono)cyclohexane-1,3-dione (3c)

Orange crystals from ethanol, yield 1.85 g (74%). Mp 180–183 °C. IR (KBr) ν_{max} (cm^{-1}): 3485–3326 (NH), 3055 (CH, aromatic), 1701, 1687 (2C=O), 1636 (C=N), 1634 (C=C); ^{1}H NMR (DMSO-d_6, 300 MHz): δ 1.62–1.70 (m, 4H, 2CH_2), 2.34–2.46 (m, 2H, CH_2), 7.24–7.40 (m, 4H, C_6H_4), 8.38 (s, 1H, D_2O exchangeable, NH); ^{13}C NMR (DMSO-d_6, 75 MHz): δ 24.5, 34.8, 38.6 (3CH_2), 39.4 (CH_3), 120.6, 123.8, 126.5, 128.3 (C_6H_4), 164.3 (C=N), 166.7, 168.4 (2C=O). Anal. Calcd. for $C_{12}H_{11}ClN_2O_2$: C, 57.49; H, 4.42; N, 11.17. Found: C, 57.62; H, 4.73; N, 11.29. MS: *m/z* 250 (M^+, 24%).

2. 2. General Procedure for the Synthesis of the 5,6,7,8-Tetrahydro-4*H*-chromene Derivatives 6a–r

Each of either benzaldehyde (1.06 g, 0.01 mol), 4-chlorobenzaldehyde (1.40 g, 0.01 mol) or 4-methoxybenzaldehyde (1.36 g, 0.01 mol) and either malononitrile (0.66 g, 0.01 mol) or ethyl cyanoacetate (1.13 g, 0.01 mol) were added to a solution of either **3a** (2.16 g, 0.01 mol), **3b** (2.30 g, 0.01 mol) or **3c** (2.50 g, 0.01 mol) in 1,4-dioxane (50 mL) containing triethylamine (1.00 mL). The whole reaction mixture was heated under reflux for 3 h then poured onto ice/water mixture containing a few drops of hydrochloric acid and the formed solid product was collected by filtration.

2-Amino-7-oxo-4-phenyl-8-(2-phenylhydrazono)-5,6,7,8-tetrahydro-4*H*-chromene-3-carbonitrile (6a)

Yellow crystals from 1,4-dioxane, yield 2.51 g (68%). Mp 95–98 °C. IR (KBr) ν_{max} (cm^{-1}): 3485–3341 (NH_2, NH), 3054 (CH, aromatic), 2220 (CN), 1689 (C=O), 1642 (C=N), 1636 (C=C); ^{1}H NMR (DMSO-d_6, 300 MHz): δ 2.83–2.94 (2t, 4H, 2CH_2), 4.82 (s, 2H, D_2O exchangeable NH_2), 5.08 (s, 1H, pyran H-4), 7.23–7.48 (m, 10H, 2C_6H_5),

8.28 (s, 1H, D_2O exchangeable, NH); ^{13}C NMR (DMSO-d_6, 75 MHz): δ 37.9, 42.1 ($2CH_2$), 51.2 (pyran C-4), 117.3 (CN), 120.4, 121.3, 121.8, 122.0, 123.6, 124.3,125.8, 126.8 ($2C_6H_5$), 130.2, 131.6, 134.8, 136.1 (pyran C), 166.8 (C=N), 167.2 (C=O). Anal. Calcd. for $C_{22}H_{18}N_4O_2$: C, 71.37; H, 4.90; N, 15.13.Found: C, 71.52; H, 5.13; N, 15.29. MS: *m/z* 370 (M^+, 28%).

2-Hydroxy-7-oxo-4-phenyl-8-(2-phenylhydrazono)-5,6,7,8-tetrahydro-4*H*-chromene-3-carbonitrile (6b)

Yellow crystals from 1,4-dioxane, yield 2.59 g (70%). Mp 117–120 °C. IR (KBr) ν_{max} (cm^{-1}): 3528–3330 (OH, NH), 3055 (CH, aromatic), 2220 (CN), 1688 (C=O), 1640 (C=N), 1632 (C=C); ^{1}H NMR (DMSO-d_6, 300 MHz): δ 2.81–2.98 (2t, 4H, $2CH_2$), 5.05 (s, 1H, pyran H-4), 7.25–7.46 (m, 10H, $2C_6H_5$), 8.26 (s, 1H, D_2O exchangeable, NH), 10.27 (s, 1H, D_2O exchangeable, OH); ^{13}C NMR (DMSO-d_6, 75 MHz): δ 37.6, 42.5 ($2CH_2$), 51.1 (pyran C-4), 116.3 (CN), 120.2, 120.6, 121.9, 122.3, 123.9, 125.2,125.5, 126.3 ($2C_6H_5$), 130.4, 131.1, 133.8, 136.5 (pyran C), 166.3 (C=N), 168.4 (C=O). Anal. Calcd. for $C_{22}H_{17}N_3O_3$: C, 71.15; H, 4.61; N, 11.31. Found: C, 70.93; H, 4.82; N, 11.42. MS: *m/z* 371 (M^+, 36%).

2-Amino-4-(4-chlorophenyl)-7-oxo-8-(2-phenylhydrazono)-5,6,7,8-tetrahydro-4*H*-chromene-3-carbonitrile (6c)

Yellow crystals from 1,4-dioxane, yield 3.21 g (79%). Mp 93–95 °C. IR (KBr) ν_{max} (cm^{-1}): 3468–3359(NH_2, NH), 3055 (CH, aromatic), 2220 (CN), 1688 (C=O), 1646 (C=N), 1630 (C=C); ^{1}H NMR (DMSO-d_6, 300 MHz): δ 2.81–2.97 (2t, 4H, $2CH_2$), 4.84 (s, 2H, D_2O exchangeable NH_2), 5.13 (s, 1H, pyran H-4), 7.24–7.58 (m, 9H, C_6H_5, C_6H_4), 8.32 (s, 1H, D_2O exchangeable, NH); ^{13}C NMR (DMSO-d_6, 75 MHz): δ 37.5, 42.3 ($2CH_2$), 51.6 (pyran C-4), 117.2 (CN), 120.1, 120.5, 121.5, 122.3, 123.8, 125.1,125.9, 126.3 (C_6H_5, C_6H_4), 130.4, 131.6, 133.8, 1358 (pyran C), 166.6 (C=N), 167.8 (C=O). Anal. Calcd. for $C_{22}H_{17}ClN_4O_2$: C, 65.27; H, 4.23; N, 13.84. Found: C, 65.42; H, 4.33; N, 14.09. MS: *m/z* 404 (M^+, 72%).

4-(4-Chlorophenyl)-2-hydroxy-7-oxo-8-(2-phenylhydrazono)-5,6,7,8-tetrahydro-4*H*-chromene-3-carbonitrile (6d)

Yellow crystals from1,4-dioxane, yield 2.63 g (65%). Mp 122–125 °C. IR (KBr) ν_{max} (cm^{-1}): 3542–3348 (OH, NH), 3055 (CH, aromatic), 2220 (CN), 1701 (C=O), 1645 (C=N), 1632 (C=C); ^{1}H NMR (DMSO-d_6, 300 MHz): δ 2.83–2.97 (2t, 4H, $2CH_2$), 5.07 (s, 1H, pyran H-4), 7.22–7.55 (m, 9H, C_6H_5, C_6H_4), 8.23 (s, 1H, D_2O exchangeable, NH), 10.29 (s, 1H, D_2O exchangeable, OH); ^{13}C NMR (DMSO-d_6, 75 MHz): δ 37.2, 42.8 ($2CH_2$), 51.6 (pyran C-4), 117.8 (CN), 120.4, 121.8, 122.2, 122.6, 124.3, 125.6, 125.8, 126.0 (C_6H_5, C_6H_4), 130.4, 132.8, 134.8, 135.2 (pyran C), 166.7 (C=N), 168.8 (C=O). Anal. Calcd. for $C_{22}H_{16}ClN_3O_3$: C, 65.11; H, 3.97; N, 10.35. Found: C, 65.29; H, 4.16; N, 10.53. MS: *m/z* 405 (M^+, 26%).

2-Amino-4-(4-methoxyphenyl)-7-oxo-8-(2-phenylhydrazono)-5,6,7,8-tetrahydro-4*H*-chromene-3-carbonitrile (6e)

Brown crystals from 1,4-dioxane, yield 2.40 g (60%). Mp 86–88 °C. IR (KBr) ν_{max} (cm^{-1}): 3478–3338 (NH_2, NH), 3055 (CH, aromatic), 2222 (CN), 1687 (C=O), 1643 (C=N), 1630 (C=C); ^{1}H NMR (DMSO-d_6, 300 MHz): δ 2.83–2.95 (2t, 4H, $2CH_2$), 3.70 (s, 3H, OCH_3), 4.86 (s, 2H, D_2O exchangeable NH_2), 5.09 (s, 1H, pyran H-4), 7.22–7.52 (m, 9H, C_6H_5, C_6H_4), 8.33 (s, 1H, D_2O exchangeable, NH); ^{13}C NMR (DMSO-d_6, 75 MHz): δ 37.3, 42.6 ($2CH_2$), 50.2 (OCH_3), 51.2 (pyran C-4), 117.4 (CN), 120.2, 121.0, 121.8, 122.7, 123.2, 125.3,125.6, 126.1 (C_6H_5, C_6H_4), 130.1, 132.8, 134.5, 136.2 (pyran C), 166.8 (C=N), 167.9 (C=O). Anal. Calcd. for $C_{23}H_{20}N_4O_3$: C, 68.99; H, 5.03; N, 13.99. Found: C, 68.79; H, 4.93; N, 14.27. MS: *m/z* 400 (M^+, 68%).

2-Hydroxy-4-(4-methoxyphenyl)-7-oxo-8-(2-phenylhydrazono)-5,6,7,8-tetrahydro-4*H*-chromene-3-carbonitrile (6f)

Yellow crystals from 1,4-dioxane, yield 3.00 g (75%). Mp 121–123 °C. IR (KBr) ν_{max} (cm^{-1}): 3552–3329 (OH, NH), 3054 (CH, aromatic), 2220 (CN), 1696 (C=O), 1642 (C=N), 1630 (C=C); ^{1}H NMR (DMSO-d_6, 300 MHz): δ 2.81–2.99 (2t, 4H, $2CH_2$), 3.69 (s, 3H OCH_3), 5.13 (s, 1H, pyran H-4), 7.24–7.59 (m, 9H, C_6H_5, C_6H_4), 8.24 (s, 1H, D_2O exchangeable, NH), 10.32 (s, 1H, D_2O exchangeable, OH); ^{13}C NMR (DMSO-d_6, 75 MHz): δ 37.5, 42.9 ($2CH_2$), 50.2 (OCH_3), 51.6 (pyran C-4), 116.9 (CN), 120.3, 121.6, 122.8, 123.4, 124.7, 125.4, 125.2, 126.4 (C_6H_5, C_6H_4), 130.7, 133.2, 134.5, 135.8 (pyran C), 166.8 (C=N), 168.9 (C=O). Anal. Calcd. for $C_{23}H_{19}N_3O_4$: C, 68.82; H, 4.77; N, 10.47. Found: C, 68.93; H, 4.80; N, 10.54. MS: *m/z* 401 (M^+, 34%).

2-Amino-7-oxo-4-phenyl-8-(2-(*p*-tolyl)hydrazono)-5,6,7,8-tetrahydro-4*H*-chromene-3-carbonitrile (6g)

Brown crystals from 1,4-dioxane, yield 2.84 g (74%). Mp 110–113 °C. IR (KBr) ν_{max} (cm^{-1}): 3492–3326 (NH_2, NH), 3055 (CH, aromatic), 2221 (CN), 1687 (C=O), 1641 (C=N), 1630 (C=C); ^{1}H NMR (DMSO-d_6, 300 MHz): δ 2.68–2.93 (2t, 4H, $2CH_2$), 2.80 (s, 3H, CH_3), 4.86 (s, 2H, D_2O exchangeable NH_2), 5.13 (s, 1H, pyran H-4), 7.24–7.58 (m, 9H, C_6H_5, C_6H_4), 8.33 (s, 1H, D_2O exchangeable, NH); ^{13}C NMR (DMSO-d_6, 75 MHz): δ 37.6, 42.8 ($2CH_2$), 36.8 (CH_3), 51.3 (pyran C-4), 117.3 (CN), 120.4, 121.5, 122.4, 122.9, 123.6, 125.8, 125.1, 126.4 (C_6H_5, C_6H_4), 130.1, 133.7, 134.8, 135.6 (pyran C), 166.5 (C=N), 167.8 (C=O). Anal. Calcd. for $C_{23}H_{20}N_4O_2$: C, 71.86; H, 5.24; N, 14.57. Found: C, 71.72; H, 5.43; N, 14.39. MS: *m/z* 384 (M^+, 42%).

2-Hydroxy-7-oxo-4-phenyl-8-(2-(*p*-tolyl)hydrazono)-5,6,7,8-tetrahydro-4*H*-chromene-3-carbonitrile (6h)

Dark brown crystals from1,4-dioxane, yield 2.31 g (60%). Mp 177–179 °C. IR (KBr) ν_{max} (cm^{-1}): 3539–3342

(OH, NH), 3055 (CH, aromatic), 2220 (CN), 1692 (C=O), 1645 (C=N), 1631 (C=C); ^{1}H NMR (DMSO-d_6, 300 MHz): δ 2.83–2.96 (2t, 4H, $2CH_2$), 2.72 (s, 3H CH_3), 5.11 (s, 1H, pyran H-4), 7.21–7.47 (m, 9H, C_6H_5, C_6H_4), 8.26 (s, 1H, D_2O exchangeable, NH), 10.31 (s, 1H, D_2O exchangeable, OH); ^{13}C NMR (DMSO-d_6, 75 MHz): δ 38.1, 42.3 ($2CH_2$), 36.2 (CH_3), 51.4 (pyran C-4), 117.8 (CN), 120.1, 120.9, 121.3, 122.8, 124.3, 125.6, 126.1, 126.8 (C_6H_5, C_6H_4), 130.9, 132.6, 134.8, 136.4 (pyran C), 166.7 (C=N), 168.5 (C=O). Anal. Calcd. for $C_{23}H_{19}N_3O_3$: C, 71.67; H, 4.97; N, 10.90. Found: C, 71.82; H, 4.74; N, 11.25. MS: *m/z* 385 (M^+, 40%).

2-Amino-4-(4-chlorophenyl)-7-oxo-8-(2-(*p*-tolyl)hydrazono)-5,6,7,8-tetrahydro-4*H*-chromene-3-carbonitrile (6i)

Pale brown crystals from 1,4-dioxane, yield 2.92 g (70%). Mp 114–116 °C. IR (KBr) ν_{max} (cm^{-1}): 3463–3351 (NH_2, NH), 3055 (CH, aromatic), 2220 (CN), 1689 (C=O), 1640 (C=N), 1630 (C=C); ^{1}H NMR (DMSO-d_6, 300 MHz): δ 2.65–2.91 (2t, 4H, $2CH_2$), 2.76 (s, 3H, CH_3), 4.88 (s, 2H, D_2O exchangeable NH_2), 5.08 (s, 1H, pyran H-4), 7.21–7.50 (m, 8H, $2C_6H_4$), 8.34 (s, 1H, D_2O exchangeable, NH); ^{13}C NMR (DMSO-d_6, 75 MHz): δ 37.8, 42.9 ($2CH_2$), 36.8 (CH_3), 51.6 (pyran C-4), 117.0 (CN), 120.6, 121.8, 122.1, 122.5, 123.4, 125.2, 125.5, 126.1 ($2C_6H_4$), 130.3, 132.6, 134.6, 136.1 (pyran C), 166.8 (C=N), 168.1 (C=O). Anal. Calcd. for $C_{23}H_{19}ClN_4O_2$: C, 65.95; H, 4.57; N, 13.38. Found: C, 65.73; H, 4.73; N, 13.42. MS: *m/z* 418 (M^+, 28%).

4-(4-Chlorophenyl)-2-hydroxy-7-oxo-8-(2-(*p*-tolyl)hydrazono)-5,6,7,8-tetrahydro-4*H*-chromene-3-carbonitrile (6j)

Yellow crystals from1,4-dioxane, yield 2.31 g (55%). Mp 153–155 °C. IR (KBr) ν_{max} (cm^{-1}): 3539–3342 (OH, NH), 3055 (CH, aromatic), 2221 (CN), 1692 (C=O), 1645 (C=N), 1631 (C=C); ^{1}H NMR (DMSO-d_6, 300 MHz): δ 2.83–2.96 (2t, 4H, $2CH_2$), 2.72 (s, 3H CH_3), 5.11 (s, 1H, pyran H-4), 7.21–7.47 (m, 8H, $2C_6H_4$), 8.26 (s, 1H, D_2O exchangeable, NH), 10.31 (s, 1H, D_2O exchangeable, OH); ^{13}C NMR (DMSO-d_6, 75 MHz): δ 38.4, 42.8 ($2CH_2$), 36.2 (CH_3), 51.2 (pyran C-4), 117.6 (CN), 120.0, 120.6, 122.8, 123.2, 125.0, 125.2, 126.0, 126.5 ($2C_6H_4$), 130.2, 132.8, 134.8, 136.5 (pyran C), 166.8 (C=N), 168.5 (C=O). Anal. Calcd. for $C_{23}H_{18}ClN_3O_3$: C, 65.79; H, 4.32; N, 10.01. Found: C, 65.81; H, 4.29; N, 9.82. MS: *m/z* 419 (M^+, 58%).

2-Amino-4-(4-methoxyphenyl)-7-oxo-8-(2-(*p*-tolyl)hydrazono)-5,6,7,8-tetrahydro-4*H*-chromene-3-carbonitrile (6k)

Brown crystals from 1,4-dioxane, yield 2.92 g (71%). Mp 93–95 °C. IR (KBr) ν_{max} (cm^{-1}): 3463–3351 (NH_2, NH), 3055 (CH, aromatic), 2220 (CN), 1689 (C=O), 1640 (C=N), 1630 (C=C); ^{1}H NMR (DMSO-d_6, 300 MHz): δ 2.65–2.91 (2t, 4H, $2CH_2$), 2.76 (s, 3H, CH_3), 3.72 (s, 3H, OCH_3), 4.88 (s, 2H, D_2O exchangeable NH_2), 5.08 (s, 1H, pyran H-4), 7.21–7.50 (m, 8H, $2C_6H_4$), 8.34 (s, 1H, D_2O exchangeable, NH); ^{13}C NMR (DMSO-d_6, 75 MHz): δ 37.8, 42.9 ($2CH_2$), 36.8 (CH_3), 50.8 (OCH_3), 51.6 (pyran C-4), 116.8 (CN), 120.6, 121.8, 122.1, 122.5, 123.4, 125.2, 125.5, 126.1 ($2C_6H_4$),130.3, 132.4, 134.8, 136.1 (pyran C), 166.8 (C=N), 168.1 (C=O). Anal. Calcd. for $C_{24}H_{22}N_4O_3$: C, 69.55; H, 5.35; N, 13.52. Found: C, 69.70; H, 5.72; N, 13.68. MS: *m/z* 414 (M^+, 44%).

2-Hydroxy-4-(4-methoxyphenyl)-7-oxo-8-(2-(*p*-tolyl)hydrazono)-5,6,7,8-tetrahydro-4*H*-chromene-3-carbonitrile (6l)

Orange crystals from1,4-dioxane, yield 2.82 g (68%). Mp 82–84 °C. IR (KBr) ν_{max} (cm^{-1}): 3548–3328 (OH, NH), 3055 (CH, aromatic), 2221 (CN), 1692 (C=O), 1641 (C=N), 1631 (C=C); ^{1}H NMR (DMSO-d_6, 300 MHz): δ 2.86–2.99 (2t, 4H, $2CH_2$), 2.75 (s, 3H CH_3), 3.67 (s, 3H, OCH_3), 5.08 (s, 1H, pyran H-4), 7.26–7.54 (m, 8H, 2 C_6H_4), 8.26 (s, 1H, D_2O exchangeable, NH), 10.30 (s, 1H, D_2O exchangeable, OH); ^{13}C NMR (DMSO-d_6, 75 MHz): δ 38.8, 42.7 ($2CH_2$), 36.8 (CH_3), 50.6 (OCH_3), 51.8 (pyran C-4),117.3 (CN), 120.3, 120.9, 122.6, 123.4, 124.8, 125.6, 126.4, 126.9 ($2C_6H_4$), 130.1, 133.2, 134.2, 136.4 (pyran C), 166.5 (C=N), 168.8 (C=O). Anal. Calcd. for $C_{24}H_{21}N_3O_4$: C, 69.39; H, 5.10; N, 10.11. Found: C, 69.52; H, 4.85; N, 9.96. MS: *m/z* 415 (M^+, 65%).

2-Amino-8-(2-(4-chlorophenyl)hydrazono)-7-oxo-4-phenyl-5,6,7,8-tetrahydro-4*H*-chromene-3-carbonitrile (6m)

Brown crystals from 1,4-dioxane, yield 2.86 g (71%). Mp 101–103 °C. IR (KBr) ν_{max} (cm^{-1}): 3480–3338 (NH_2, NH), 3055 (CH, aromatic), 2223 (CN), 1688 (C=O), 1643 (C=N), 1632 (C=C); ^{1}H NMR (DMSO-d_6, 300 MHz): δ 2.68–2.96 (2t, 4H, $2CH_2$), 4.82 (s, 2H, D_2O exchangeable NH_2), 5.13 (s, 1H, pyran H-4), 7.24–7.47 (m, 9H, C_6H_5, C_6H_4), 8.36 (s, 1H, D_2O exchangeable, NH); ^{13}C NMR (DMSO-d_6, 75 MHz): δ 37.4, 42.3 ($2CH_2$), 51.2 (pyran C-4), 116.8 (CN), 120.2, 120.9, 121.6, 122.8, 123.0, 124.6, 125.2, 126.8 (C_6H_5, C_6H_4), 130.4, 133.0, 134.6, 136.8 (pyran C), 167.2 (C=N), 168.8 (C=O). Anal. Calcd. for $C_{22}H_{17}ClN_4O_2$: C, 65.27; H, 4.23; N, 13.84. Found: C, 65.40; H, 4.32; N, 13.79. MS: *m/z* 404 (M^+, 60%).

8-(2-(4-Chlorophenyl)hydrazono)-2-hydroxy-7-oxo-4-phenyl-5,6,7,8-tetrahydro-4*H*-chromene-3-carbonitrile (6n)

Yellow crystals from 1,4-dioxane, yield 3.03 g (75%). Mp 107–110 °C. IR (KBr) ν_{max} (cm^{-1}): 3528–3358 (OH, NH), 3054 (CH, aromatic), 2223 (CN), 1696 (C=O), 1640 (C=N), 1633 (C=C); ^{1}H NMR (DMSO-d_6, 300 MHz): δ 2.83–2.98 (2t, 4H, $2CH_2$), 5.15 (s, 1H, pyran H-4), 7.23–7.50 (m, 9H, C_6H_5, C_6H_4), 8.28 (s, 1H, D_2O exchangeable, NH), 10.35 (s, 1H, D_2O exchangeable, OH); ^{13}C NMR (DMSO-d_6, 75 MHz): δ 38.5, 42.0 ($2CH_2$), 51.8 (pyran C-4), 117.6 (CN), 120.6, 120.8, 121.5, 122.7, 123.7, 124.9,

125.8, 126.2 (C_6H_5, C_6H_4), 130.4, 133.7, 134.0, 136.0 (pyran C), 166.9 (C=N), 168.6 (C=O). Anal. Calcd. for $C_{22}H_{16}ClN_3O_3$: C, 65.11; H, 3.97; N, 10.35. Found: C, 65.08; H, 4.16; N, 10.22. MS: *m/z* 405 (M^+, 48%).

2-Amino-4-(4-chlorophenyl)-8-(2-(4-chlorophenyl)hydrazono)-7-oxo-5,6,7,8-tetrahydro-4*H*-chromene-3-carbonitrile (6o)

Orange crystals from 1,4-dioxane, yield 2.76 g (63%). Mp 128–131 °C. IR (KBr) ν_{max} (cm^{-1}): 3489–3325 (NH_2, NH), 3053 (CH, aromatic), 2222 (CN), 1688 (C=O), 1641 (C=N), 1633 (C=C); ^{1}H NMR (DMSO-d_6, 300 MHz): δ 2.61–2.97 (2t, 4H, $2CH_2$), 4.87 (s, 2H, D_2O exchangeable NH_2), 5.15 (s, 1H, pyran H-4), 7.23–7.56 (m, 8H, $2C_6H_4$), 8.36 (s, 1H, D_2O exchangeable, NH); ^{13}C NMR (DMSO-d_6, 75 MHz): δ 37.3, 42.8 ($2CH_2$), 51.2 (pyran C-4), 117.7 (CN), 120.3, 121.5, 122.0, 122.9, 123.6, 124.1, 125.8, 126.6 ($2C_6H_4$), 130.6, 133.8, 134.2, 136.0 (pyran C), 166.9 (C=N), 168.4 (C=O). Anal. Calcd. for $C_{22}H_{16}Cl_2N_4O_2$: C, 60.15; H, 3.67; N, 12.75. Found: C, 59.79; H, 3.59; N, 12.90. MS: *m/z* 439 (M^+, 42%).

4-(4-Chlorophenyl)-8-(2-(4-chlorophenyl)hydrazono)-2-hydroxy-7-oxo-5,6,7,8-tetrahydro-4*H*-chromene-3-carbonitrile (6p)

Pale yellow crystals from 1,4-dioxane, yield 3.43 g (78%). Mp 181–184 °C. IR (KBr) ν_{max} (cm^{-1}): 3550–3329 (OH, NH), 3054 (CH, aromatic), 2222 (CN), 1689 (C=O), 1643 (C=N), 1633 (C=C); ^{1}H NMR (DMSO-d_6, 300 MHz): δ 2.80–2.96 (2t, 4H, $2CH_2$), 5.11 (s, 1H, pyran H-4), 7.25–7.56 (m, 8H, 2 C_6H_4), 8.29 (s, 1H, D_2O exchangeable, NH), 10.31 (s, 1H, D_2O exchangeable, OH); ^{13}C NMR (DMSO-d_6, 75 MHz): δ 38.5, 42.0 ($2CH_2$), 51.6 (pyran C-4), 117.9 (CN), 120.1, 120.6, 121.8, 122.7, 123.2, 124.3, 125.5, 126.8 ($2C_6H_4$), 130.5, 133.8, 134.8, 136.1 (pyran C), 166.6 (C=N), 168.9 (C=O). Anal. Calcd. for $C_{22}H_{15}Cl_2N_3O_3$: C, 60.02; H, 3.43; N, 9.54. Found: C, 60.19; H, 3.80; N, 9.69. MS: *m/z* 440 (M^+, 60%).

2-Amino-8-(2-(4-chlorophenyl)hydrazono)-4-(4-methoxyphenyl)-7-oxo-5,6,7,8-tetrahydro-4*H*-chromene-3-carbonitrile (6q)

Yellow crystals from 1,4-dioxane, yield 2.95 g (68%). Mp 86–88 °C. IR (KBr) ν_{max} (cm^{-1}): 3472–3351 (NH_2, NH), 3055 (CH, aromatic), 2224 (CN), 1689 (C=O), 1643 (C=N), 1636 (C=C); ^{1}H NMR (DMSO-d_6, 300 MHz): δ 2.60–2.99 (2t, 4H, $2CH_2$), 3.66 (s, 3H, OCH_3), 4.84 (s, 2H, D_2O exchangeable NH_2), 5.12 (s, 1H, pyran H-4), 7.24–7.59 (m, 8H, $2C_6H_4$), 8.34 (s, 1H, D_2O exchangeable, NH); ^{13}C NMR (DMSO-d_6, 75 MHz): δ 37.6, 42.4 ($2CH_2$), 50.3 (OCH_3), 51.4 (pyran C-4), 116.9 (CN), 120.1, 120.8, 121.6, 122.7, 123.4, 124.3, 124.9, 126.2 ($2C_6H_4$), 130.3, 133.7, 134.6, 136.0 (pyran C), 166.8 (C=N), 168.6 (C=O). Anal. Calcd. for $C_{23}H_{19}ClN_4O_3$: C, 63.52; H, 4.40; N, 12.88. Found: C, 63.71; H, 4.27; N, 12.73. MS: *m/z* 434 (M^+, 50%).

8-(2-(4-Chlorophenyl)hydrazono)-2-hydroxy-4-(4-methoxyphenyl)-7-oxo-5,6,7,8-tetrahydro-4*H*-chromene-3-carbonitrile (6r)

Pale yellow crystals from1,4-dioxane, yield 3.43 g (79%). Mp 85–87 °C. IR (KBr) ν_{max} (cm^{-1}): 3550–3329 (OH, NH), 3054 (CH, aromatic), 2223 (CN), 1689 (C=O), 1643 (C=N), 1633 (C=C); ^{1}H NMR (DMSO-d_6, 300 MHz): δ 2.80–2.96 (2t, 4H, $2CH_2$), 3.70 (s, 3H, OCH_3), 5.11 (s, 1H, pyran H-4), 7.25–7.56 (m, 8H, 2 C_6H_4), 8.29 (s, 1H, D_2O exchangeable, NH), 10.31 (s, 1H, D_2O exchangeable, OH); ^{13}C NMR (DMSO-d_6, 75 MHz): δ 38.5, 42.0 ($2CH_2$), 50.1 (OCH_3), 51.6 (pyran C-4), 118.0 (CN), 120.1, 120.6, 121.8, 122.7, 123.2, 124.3, 125.5, 126.8 ($2C_6H_4$), 130.7, 132.8, 134.8, 136.1 (pyran C), 166.6 (C=N), 168.9 (C=O). Anal. Calcd. for $C_{23}H_{18}ClN_3O_4$: C, 63.38; H, 4.16; N, 9.64. Found: C, 63.47; H, 3.93; N, 9.83. MS: *m/z* 435 (M^+, 58%).

2. 3. 9-Phenyl-3,4,5,6,7,9-hexahydro-1*H*-xanthene-1,8(2*H*)-dione (7)

Benzaldehyde (1.06 g, 0.01 mol) was added to a solution of compound **1** (2.24 g, 0.02 mol) in absolute ethanol (40 mL) containing piperidine (1.0 mL). The whole reaction mixture was heated under reflux for 3 h then poured onto ice/water mixture containing a few drops of hydrochloric acid and the formed solid product was collected by filtration.

White crystals from ethanol, yield 2.35 g (80%). Mp 214–217 °C. IR (KBr) ν_{max} (cm^{-1}): 3056 (CH, aromatic), 1702, 1689 (C=O), 1631 (C=C); ^{1}H NMR (DMSO-d_6, 300 MHz): δ 1.59–1.80 (m, 8H, $4CH_2$), 2.58–2.73 (m, 4H, $2CH_2$), 5.09 (s, 1H, pyran H-4), 7.25–7.41 (m, 5H, C_6H_5); ^{13}C NMR (DMSO-d_6, 75 MHz): δ 26.3, 28.4, 32.6 ($6CH_2$), 50.9 (pyran C-4), 120.6, 121.4, 123.6, 125.8 (C_6H_5), 168.9 (2C=O). Anal. Calcd. for $C_{19}H_{18}O_3$: C, 77.53; H, 6.16. Found: C, 77.80; H, 6.29. MS: *m/z* 294 (M^+, 100%).

2. 4. General Procedure for the Synthesis of the Dithieno[3,2-*a*:2',3'-*j*]xanthenes Derivatives 8a,b

Each of elemental sulfur (0.64 g, 0.02 mol) and either malononitrile (1.32 g, 0.02 mol) or ethyl cyanoacetate (2.26 g, 0.02 mol) were added to a solution of compound **7** (2.94 g, 0.01 mol) in 1,4-dioxane (40 mL) containing triethylamine (1.00 mL). The reaction mixture was heated under reflux for 3 h then poured onto ice/water mixture and the precipitated product was collected by filtration.

12,10-Diamino-12-phenyl-5,7,8,12-tetrahydro-4*H*-dithieno[3,2-*a*:2',3'-*j*]xanthene-1,11-dicarbonitrile (8a)

Orange crystals from 1,4-dioxane, yield 2.81 g (62%). Mp 144–146 °C. IR (KBr) ν_{max} (cm^{-1}): 3468–3369 (NH_2), 3055 (CH, aromatic), 2223, 2220 (2CN), 1630 (C=C); ^{1}H NMR (DMSO-d_6, 300 MHz): δ 2.84–3.39 (m, 8H, $4CH_2$), 4.89, 5.13 (2s, 4H, D_2O exchangeable, $2NH_2$), 5.12 (s, 1H,

pyran H-4), 7.26–7.43 (m, 5H, C_6H_5); ^{13}C NMR (DMSO-d_6, 75 MHz): δ 39.2, 45.8 ($4CH_2$), 116.8, 116.9 (2CN), 120.3, 120.5, 123.9, 125.3 (C_6H_5), 130.6, 131.6, 132.7, 134.6, 137.8, 139.2, 140.5, 141.2 (pyran, two thiophene C). Anal. Calcd. for $C_{25}H_{18}N_4OS_2$: C, 66.06; H, 3.99; N, 12.33; S, 14.11. Found: C, 65.93; H, 4.13; N, 12.29; S, 14.30. MS: *m/z* 454 (M^+, 58%).

Diethyl 2,10-Diamino-12-phenyl-5,7,8,12-tetrahydro-4*H*-dithieno[3,2-*a*:2',3'-*j*]xanthene-1,11-dicarboxylate (8b)

Orange crystals from 1,4-dioxane, yield 3.61 g (66%). Mp 118–121 °C. IR (KBr) ν_{max} (cm^{-1}): 3479–3339 (NH_2), 3055 (CH, aromatic), 1633 (C=C); ^{1}H NMR (DMSO-d_6, 300 MHz): δ 1.12, 1.14 (2t, 6H, J_1 = 5.90 Hz, J_2 = 6.48 Hz, two $OCH_2\underline{CH_3}$), 2.87–3.42 (m, 8H, $4CH_2$), 4.22, 4.24 (2q, 4H, J_1 = 5.90 Hz, J_2 = 6.48 Hz, two $O\underline{CH_2}CH_3$), 4.82, 5.14 (2s, 4H, D_2O exchangeable, $2NH_2$), 5.11 (s, 1H, pyran H-4), 7.25–7.42 (m, 5H, C_6H_5); ^{13}C NMR (DMSO-d_6, 75 MHz): δ 16.5, 16.8 (two OCH_2CH_3), 39.6, 45.5 ($4CH_2$), 50.8 (pyran C-4), 52.6, 52.9 (two OCH_2CH_3), 120.5, 120.3, 124.7, 125.8 (C_6H_5), 130.2, 131.6, 132.4, 132.8, 133.8, 137.2, 138.7, 140.3 (pyran, thiophene C). Anal. Calcd. for $C_{29}H_{28}N_2O_5S_2$: C, 63.48; H, 5.14; N, 5.14; S, 11.69. Found: C, 63.62; H, 5.41; N, 5.08; 11.73. MS: *m/z* 548 (M^+, 76%).

2,12-Diamino-4,10,14-triphenyl-5,6,8,9,10,14-hexahydro-4*H*-dipyrano[2,3-*a*:3',2'-*j*]xanthene-3,11-dicarbonitrile (9)

Each of benzaldehyde (2.12 g, 0.02 mol) and malononitrile (1.32 g, 0.02 mol) were added to a solution of compound **7** (2.94 g, 0.01 mol) in 1,4-dioxane (40 mL) containing triethylamine (1.00 mL). The reaction mixture was heated under reflux for 3 h then poured onto ice/water mixture and the precipitated product was collected by filtration.

Pale yellow crystals from 1,4-dioxane, yield 4.69 g (78%). Mp 189–202 °C. IR (KBr) ν_{max} (cm^{-1}): 3453–3326 (NH_2), 3055 (CH, aromatic), 2223, 2220 (2CN), 1630 (C=C); ^{1}H NMR (DMSO-d_6, 300 MHz): δ 2.82–3.42 (m, 8H, $4CH_2$), 4.95, 5.16 (2s, 4H, D_2O exchangeable, $2NH_2$), 5.08, 5.12, 5.14 (3s, 3H, pyran H-4), 7.22–7.58 (m, 15H, $3C_6H_5$); ^{13}C NMR (DMSO-d_6, 75 MHz): δ 39.2, 45.7 ($4CH_2$), 51.2, 51.6 (threepyran C-4), 116.6, 117.2 (2CN), 120.1, 120.8, 122.1, 122.5, 123.0, 123.5, 123.8, 124.2, 124.6, 125.3, 125.8, 126.8 ($3C_6H_5$), 130.3, 133.5, 134.6, 135.0, 136.7, 137.0, 137.6, 139.8 (three pyran C). Anal. Calcd. for $C_{39}H_{30}N_4O_3$: C, 77.72; H, 5.02; N, 9.30. Found: C, 77.90; H, 4.79; N, 9.42. MS: *m/z* 602 (M^+, 42%).

1,11,12-Triphenyl-4,5,7,8-tetrahydro-1*H*-xantheno[1,2-*d*:8,7-*d*']bis(thiazole)-2,10(11*H*,12*H*)-dithione (11)

Each of elemental sulfur (0.64 g, 0.02 mol) and phenylisothiocyanate (2.60 g, 0.02 mol) were added to a solution of compound **7** (2.94 g, 0.01 mol) in 1,4-dioxane (40 mL) containing triethylamine (1.00 mL). The reaction mixture was heated under reflux for 2 h then poured onto ice/water mixture and the precipitated product was collected by filtration.

Orange crystals from1,4-dioxane, yield 3.96 g (67%). Mp > 300 °C. IR (KBr) ν_{max} (cm^{-1}): 3055 (CH, aromatic), 1632 (C=C), 1208 (C=S); ^{1}H NMR (DMSO-d_6, 300 MHz): δ 2.96–3.41 (m, 8H, $4CH_2$), 5.08 (s, 1H, pyran H-4), 7.23–7.49 (m, 15H, $3C_6H_5$); ^{13}C NMR (DMSO-d_6, 75 MHz): δ 37.6, 42.5 ($2CH_2$), 51.1 (pyran C-4), 120.2, 120.8, 121.2, 121.6, 122.0, 122.3, 123.1, 123.9, 124.8, 125.1, 125.5, 126.8 ($3C_6H_5$), 130.2, 131.3, 132.6, 136.5, 139.4, 140.8 (pyran, two thiazole C), 180.3 (2C=S). Anal. Calcd. for $C_{33}H_{24}N_2OS_4$: C, 66.86; H, 4.08; N, 4.73; S, 21.64. Found: C, 66.93; H, 4.19; N, 4.90; S, 21.47. MS: *m/z* 592 (M^+, 18%).

3,3-Dimethyl-9-phenyl-3,4,5,6,7,9-hexahydro-1*H*-xanthene-1,8(2*H*)-dione (13)

Each of benzaldehyde (1.06 g, 0.01 mol) and dimedone (1.40 g, 0.01 mol) was added to a solution of compound **1** (1.12 g, 0.01 mol) in absolute ethanol (40 mL) containing piperidine (1.0 mL). The whole reaction mixture was heated under reflux for 1 h then poured onto ice/water mixture containing a few drops of hydrochloric acid and the formed solid product was collected by filtration.

White crystals from1,4-dioxane, yield 2.25 g (70%). Mp 149–152 °C. IR (KBr) ν_{max} (cm^{-1}): 3054 (CH, aromatic), 1704, 1689 (2C=O), 1635 (C=C); ^{1}H NMR (DMSO-d_6, 300 MHz): δ 1.06, 1.08 (2s, 6H, $2CH_3$), 1.68–1.96 (m, 6H, $3CH_2$), 2.79, 2.83 (2s, 4H, $2CH_2$), 5.13 (s, 1H, pyran H-4), 7.26–7.46 (m, 5H, C_6H_5); ^{13}C NMR (DMSO-d_6, 75 MHz): δ 24.4 ($2CH_3$), 26.5, 28.8, 32.9, 36.5, 42.1 ($5CH_2$), 50.8 (pyran C-4), 120.3, 121.8, 122.4, 124.2 (C_6H_5), 168.8, 170.3 (2C=O). Anal. Calcd. for $C_{21}H_{22}O_3$: C, 78.23; H, 6.88. Found: C, 78.40; H, 6.68. MS: *m/z* 322 (M^+, 60%).

2. 5. General Procedure for the Synthesis of the Dithieno[3,2-*a*:2',3'-*j*]xanthenes Derivatives 14a,b

Each of elemental sulfur (0.64 g, 0.02 mol) and either malononitrile (1.32 g, 0.02 mol) or ethyl cyanoacetate (2.26 g, 0.02 mol) were added to a solution of compound **13** (3.22 g, 0.01 mol) in 1,4-dioxane (40 mL) containing triethylamine (1.00 mL). The reaction mixture was heated under reflux for 3 h then poured onto ice/water mixture and the precipitated product was collected by filtration.

2,10-Diamino-4,4-dimethyl-12-phenyl-5,7,8,12-tetrahydro-4*H*-dithieno-[3,2-*a*:2',3'-*j*]xanthene-1,11-dicarbonitrile (14a)

Yellow crystals from 1,4-dioxane, yield 2.89 g (60%). Mp 138–141 °C. IR (KBr) ν_{max} (cm^{-1}): 3476–3337 (NH_2), 3055 (CH, aromatic), 2224, 2220 (2CN), 1633 (C=C); ^{1}H NMR (DMSO-d_6, 300 MHz): δ 1.06, 1.09 (2s, 6H, $2CH_3$),

2.86–3.42 (m, 4H, $2CH_2$), 3.62 (s, 2H, CH_2), 4.87, 5.15 (2s, 4H, D_2O exchangeable, $2NH_2$), 5.14 (s, 1H, pyran H-4), 7.28–7.40 (m, 5H, C_6H_5); ^{13}C NMR (DMSO-d_6, 75 MHz): δ 24.7 ($2CH_3$), 39.8, 44.6, 48.3 ($3CH_2$), 51.2 (pyran C-4),116.6, 117.3 (2CN), 120.2, 120.8, 123.3, 124.1 (C_6H_5), 132.3, 134.2, 135.1, 135.6, 136.3, 138.3, 138.7, 139.4, 140.2, 141.2, 142.0, 142.6 (pyran, two thiophene C). Anal. Calcd. for $C_{27}H_{22}N_4OS_2$: C, 67.19; H, 4.59; N, 11.61; S, 13.29. Found: C, 66.93; H, 4.75; N, 11.82; 13.05. MS: *m/z* 482 (M^+, 58%).

Diethyl 2,10-Diamino-12-phenyl-5,7,8,12-tetrahydro-4*H*-dithieno[3,2-*a*:2',3'-*j*]xanthene-1,11-dicarboxylate (14b)

Pale white crystals from 1,4-dioxane, yield 4.32 g (75%). Mp 175–179 °C. IR (KBr) ν_{max} (cm^{-1}): 3449–3326 (NH_2), 3055 (CH, aromatic), 11695, 1689 (2CO), 633 (C=C); ^{1}H NMR (DMSO-d_6, 300 MHz): δ 1.07, 1.09 (2s, 6H, $2CH_3$), 1.12, 1.13 (2t, 6H, J_1 = 6.77 Hz, J_2 = 6.92 Hz, two $OCH_2\underline{CH_3}$), 2.89–3.48 (2t, 4H, $2CH_2$), 3.70 (s, 2H, CH_2), 4.22, 4.23 (2q, 4H, J_1 = 6.77 Hz, J_2 = 6.92 Hz, two $O\underline{CH_2}CH_3$), 4.82, 5.14 (2s, 4H, D_2O exchangeable, $2NH_2$), 5.11 (s, 1H, pyran H-4), 7.25–7.42 (m, 5H, C_6H_5); ^{13}C NMR (DMSO-d_6, 75 MHz): δ 16.5, 16.8 (two $OCH_2\underline{CH_3}$),24.4 ($2CH_3$), 39.4, 45.8, 47.2 ($3CH_2$), 51.3 (pyran C-4), 52.6, 52.7(two $O\underline{CH_2}CH_3$),120.3, 122.8, 124.6, 125.7 (C_6H_5), 130.1, 131.8, 132.6, 131.1, 133.5, 136.6, 137.2, 138.9, 139.4, 140.3, 141.2, 142.6 (pyran, two thiophene C). Anal. Calcd. for $C_{31}H_{32}N_2O_5S_2$: C, 64.56; H, 5.59; N, 4.86; S, 11.12. Found: C, 64.41.; H, 5.79; N, 5.16; 11.30. MS: *m/z* 576 (M^+, 76%).

2,12-Diamino-5,5-dimethyl-4,10,14-triphenyl-5,6,8,9,10,14-hexahydro-4*H*-dipyrano[2,3-*a*:3',2'-*j*]xanthene-3,11-dicarbonitrile (15)

Each of benzaldehyde (2.12 g, 0.02 mol) and malononitrile (1.32 g, 0.02 mol) were added to a solution of compound **13** (3.22 g, 0.01 mol) in 1,4-dioxane (40 mL) containing triethylamine (1.00 mL). The reaction mixture was heated under reflux for 3 h then poured onto ice/water mixture and the precipitated product was collected by filtration.

Pale yellow crystals from1,4-dioxane, yield 4.69 g (78%). Mp 136–138 °C. IR (KBr) ν_{max} (cm^{-1}): 3453–3326 (NH_2), 3055 (CH, aromatic), 2223, 2220 (2CN), 1630 (C=C); ^{1}H NMR (DMSO-d_6, 300 MHz): δ 1.07, 1.08 (2s, 6H, $2CH_3$), 2.82–2.96 (2t, 4H, $2CH_2$), 3.11–3.42 (s, 2H, CH_2), 4.95, 5.16 (2s, 4H, D_2O exchangeable, $2NH_2$), 5.09, 5.11, 5.14 (3s, 3H, threepyran H-4), 7.22-7.58 (m, 15H, $3C_6H_5$); ^{13}C NMR (DMSO-d_6, 75 MHz): δ 24.5 ($2CH_3$), 39.2, 45.7 ($4CH_2$), 51.6 (pyran C-4), 116.6, 117.2 (2CN), 120.8, 122.5, 123.5, 123.8, 124.6,125.3, 125.8, 126.8 ($3C_6H_5$), 130.3, 131.2, 131.9, 132.3, 133.5, 134.6, 135.0, 136.7, 137.0, 137.6, 138.4, 139.8 (three pyran C). Anal. Calcd. for $C_{41}H_{34}N_4O_3$: C, 78.07; H, 5.43; N, 8.88. Found: C, 77.86; H, 5.60; N, 9.02. MS: *m/z* 630 (M^+, 32%).

4,4-Dimethyl-1,11,12-triphenyl-4,5,7,8-tetrahydro-1*H*-xantheno[1,2-*d*:8,7-*d*']bis(thiazole)-2,10(11*H*,12*H*)-dithione (16)

Each of elemental sulfur (0.64 g, 0.02 mol) and phenylisothiocyanate (2.60 g, 0.02 mol) were added to a solution of compound **13** (3.22 g, 0.01 mol) in 1,4-dioxane (40 mL) containing triethylamine (1.00 mL). The reaction mixture was heated under reflux for 2 h then poured onto ice/water mixture and the precipitated product was collected by filtration.

Yellowish white crystals from 1,4-dioxane, yield 4.24 g (68%). Mp 147–149 °C. IR (KBr) ν_{max} (cm^{-1}): 3054 (CH, aromatic), 1632 (C=C), 1209 (C=S); ^{1}H NMR (DMSO-d_6, 300 MHz): δ 1.05, 1.08 (2s, 6H, $2CH_3$), 2.82–2.98 (2t, 4H, $2CH_2$), 3.07–3.40 (s, 2H, CH_2), 5.12 (s, 1H, pyran H-4), 7.23–7.57 (m, 15H, $3C_6H_5$); ^{13}C NMR (DMSO-d_6, 75 MHz): δ 24.6 ($2CH_3$), 37.8, 42.7, 44.2 ($3CH_2$), 51.5 (pyran C-4), 120.1, 120.9, 121.1, 121.8, 122.3, 122.7, 123.5, 123.8, 124.3, 125.6, 126.0, 126.5 ($3C_6H_5$), 130.2, 131.3, 132.6, 136.5, 138.0, 139.4, 141.3, 142.6 (pyran, two thiazole C), 179.2, 180.1 (2C=S). Anal. Calcd. for $C_{35}H_{28}N_2OS_4$: C, 67.71; H, 4.55; N, 4.51; S, 20.66. Found: C, 67.80; H, 4.48; N, 4.72; S, 20.82. MS: *m/z* 620 (M^+, 32%).

2. 6. Biology Section

2. 6. 1. Cell Proliferation Assay

Most of the newly synthesized compounds were screened against the six cancer cell lines namely A549, HT-29, MKN-45, U87MG, SMMC-7721, and H460 using the standard MTT assay *in vitro*, with foretinib as the positive control.[26–28] Their anti-proliferative activities against the six cancer cell lines and the mean values of three independent experiments, expressed as IC_{50} values, are presented in Table 1. Most of the synthesized compounds exhibited potent anti-proliferative activity with IC_{50} values less than 30 μM. Generally, the variations of substituents within the thienopyridine moiety together with the heterocyclic ring being attached have a notable influence on the anti-proliferative activity.

2. 6. 2. Structure-Activity Relationship

Table 1 shows the cytotoxicity of most of the synthesized compounds toward the six cancer cell lines A549, H460, HT-29, MKN-45, U87MG, and SMMC-7721. The reaction of cyclohexan-1,3-dione with the aryldiazonium salts **2a**–**c** produced the arylhydrazono derivatives **3a**–**c**, respectively. The two compounds **3b** (X = CH_3) and **3c** (X = Cl) showed the highest cytotoxicity among these three compounds toward the six cancer cell lines. The multicomponent reactions of either of **3a**–**c** with either of the arylaldehydes **4a**–**c** and either malononitrile or ethyl cyanoacetate gave the 4*H*-chromenone derivatives **6a**–**r**, respectively. Eleven compounds of this series were selected for screening against the six cancer cell lines and their ac-

Table 1. *In vitro* growth inhibitory effects IC_{50} ± SEM (μM) of selected compounds of the synthesized compounds against cancer cell lines

Compound No	IC_{50} ± SEM (μM)					
	A549	H460	HT29	MKN-45	U87MG	SMMC-7721
3a	6.26 ± 2.86	8.36 ± 3.24	5.69 ± 1.39	6.58 ± 1.37	9.62 ± 3.15	6.43 ± 2.25
3b	0.28 ± 0.12	0.33 ± 0.18	0.53 ± 0.13	0.33 ± 0.17	0.61 ± 0.28	0.52 ± 0.16
3c	0.43 ± 0.31	0.51 ± 0.25	0.49 ± 0.28	0.63 ± 0.39	0.82 ± 0.27	0.93 ± 0.39
6b	1.38 ± 0.91	2.46 ± 1.16	1.52 ± 0.92	1.63 ± 0.78	1.54 ± 0.85	2.53 ± 1.06
6c	1.34 ± 0.79	2.41 ± 1.20	1.35 ± 0.84	1.52 ± 0.71	2.58 ± 1.23	2.63 ± 1.17
6d	0.56 ± 0.32	0.29 ± 0.26	0.48 ± 0.22	0.41 ± 0.26	0.35 ± 0.12	0.53 ± 0.23
6e	2.16 ± 1.02	3.27 ± 1.38	3.38 ± 1.80	2.80 ± 1.38	2.32 ± 1.09	4.64 ± 1.42
6f	1.64 ± 0.36	1.52 ± 0.85	1.43 ± 0.75	2.60 ± 0.89	1.46 ± 0.63	1.63 ± 0.45
6g	4.36 ± 1.20	3.45 ± 1.81	2.61 ± 1.59	6.83 ± 2.28	4.60 ± 1.52	6.50 ± 2.63
6h	3.28 ± 1.48	5.83 ± 1.39	4.60 ± 1.24	6.80 ± 1.79	5.53 ± 1.61	6.45 ± 2.23
6i	1.25 ± 1.06	2.34 ± 1.13	2.32 ± 1.16	2.29 ± 1.71	1.29 ± 0.47	1.36 ± 0.95
6m	1.37 ± 0.71	0.50 ± 0.29	1.96 ± 1.19	1.80 ± 0.88	1.69 ± 0.82	1.33 ± 0.86
6n	0.46 ± 0.09	0.73 ± 0.44	0.85 ± 0.34	0.63 ± 0.41	0.52 ± 0.24	0.30 ± 0.26
6o	4.41 ± 1.49	6.72 ± 1.53	6.41 ± 2.49	6.29 ± 2.17	8.09 ± 2.17	5.19 ± 1.29
6q	2.34 ± 1.21	3.63 ± 1.32	4.58 ± 1.56	6.28 ± 2.39	5.32 ± 2.43	3.36 ± 1.28
8a	3.48 ± 1.09	2.63 ± 1.19	3.64 ± 1.26	4.38 ± 0.84	2.48 ± 0.89	2.23 ± 1.27
8b	1.13 ± 0.59	2.28 ± 0.72	3.29 ± 1.85	2.26 ± 1.79	3.62 ± 1.29	1.81 ± 0.84
9	4.13 ± 1.29	5.09 ± 1.36	6.16 ± 2.93	6.92 ± 1.37	5.82 ± 1.39	7.27 ± 1.92
11	2.32 ± 1.18	2.35 ± 1.08	3.42 ± 1.26	2.46 ± 0.98	1.26 ± 0.63	2.39 ± 0.98
14a	1.29 ± 0.59	1.39 ± 0.79	2.42 ± 1.08	1.36 ± 0.62	1.72 ± 0.98	1.42 ± 0.63
14b	4.69 ± 1.22	5.48 ± 2.21	6.42 ± 2.20	5.37 ± 1.19	4.49 ± 1.28	6.52 ± 1.28
15	0.35 ± 0.22	0.44 ± 0.16	0.62 ± 0.26	0.35 ± 0.16	0.62 ± 0.45	0.38 ± 0.16
16	0.29 ± 0.03	0.46 ± 0.23	0.46 ± 0.26	0.33 ± 0.20	0.59 ± 0.29	0.48 ± 0.21
Foretinib	0.08 ± 0.01	0.18 ± 0.03	0.15 ± 0.023	0.03 ± 0.0055	0.90 ± 0.13	0.44 ± 0.062

tivites varied from moderate to high. Compounds **6b** (X = Y = H, R' = OH), **6c** (X = H, Y = Cl, R' = NH_2), **6f** (X = H, Y = OCH_3, R' = OH) and **6i** (X = CH_3, Y = Cl, R' = NH_2) showed moderate inhibitions. However, compounds **6d** (X = H, Y = Cl, R' = OH) and **6n** (X = Cl, Y = H, R' = OH) showed the highest inhibitions among the eleven compounds. On the other hand, compounds **6e**, **6g**, **6h**, **6o** and **6q** had declining inhibition activities. The reaction of compound **7** with two folds of elemental sulfur and either malononitrile or ethyl cyanoacetate gave the dithieno[3,2-*a*:2',3'-*j*]xanthene derivatives **8a**,**b**. It is obvious from Table 1 that compound **8b** (R = COOEt) was more cytotoxic than compound **8a** (R = CN); it seemsd that the oxygen content in **8b** was responsible for its high inhibition activity. Surprisingly, the dipyrano[2,3-*a*:3',2'-*j*]xanthene derivative **9** and the xantheno[1,2-*d*:8,7-*d*']bis(thiazole) derivative **11** exhibited low inhibition values. Considering the dithieno[3,2-*a*:2',3'-*j*] xanthene-2,10-diamine derivatives **14a** and **14b**, it is clear that compound **14a** (R = CN) showed higher inhibitions than **14b** (R = COOEt). Finally both of the 5,6,8,9,10,14-hexahydro-4*H*-dipyrano[2,3-*a*:3',2'-*j*]xanthene derivative **15** and the 4,5,7,8-tetrahydro-1*H*-xantheno[1,2-*d*:8,7-*d*']bis(thiazole)-2,10(11*H*,12*H*)-dithione derivative **16** exhibted high inhibitions against the six cancer cell lines. It is of great importance to note from Table 1 that compounds **3b**, **3c**, **6d**, **6n**, **15** and **16** showed the highest cytotoxicity among the tested compounds against the six cancer cell lines, while compounds **6b**, **6c**, **6f**, **6i, 6m**, **8b**, and **14a** exhibited moderate inhibitions. The high inhibition compounds together with those of moderate inhibitions were selected to be tested against tyrosine kinases.

2. 6. 3. Inhibitions of the Most Active Compounds Against Tyrosine Kinases

Compounds **3b**, **3c**, **6b**, **6c**, **6d**, **6f**, **6m**, **6n**, **14a**, **15** and **16** that showed from moderate to high inhibitions against the six cancer cell lines were further evaluated

Table 2. Inhibitions of tyrosine kinases [Enzyme IC_{50} (nM)] by compounds **3b**, **3c**, **6b**, **6c**, **6d**, **6f**, **6m**, **6n**, **14a**, **15** and **16**

Compound	c-Kit	Flt-3	VEGFR-2	EGFR	PDGFR
3b	2.83	3.25	2.16	0.73	0.52
3c	0.21	0.34	0.23	0.46	0.29
6b	1.32	1.08	1.69	0.43	1.02
6c	0.82	0.63	0.36	0.69	0.42
6d	0.25	0.31	0.47	0.24	0.29
6f	0.53	0.21	0.53	0.39	0.22
6m	1.16	0.29	0.42	1.80	2.01
6n	0.46	0.25	0.31	0.37	0.27
14a	0.82	0.29	0.37	0.44	0.29
15	0.33	0.21	0.47	0.35	0.26
16	2.09	1.28	1.62	1.59	2.42

against other five tyrosine kinases (c-Kit, Flt-3, VEGFR-2, EGFR, and PDGFR) using the same screening method (Table 2). These receptor tyrosine kinases (RTKs) have been implicated in vascular development by affecting the proliferation and migration of endothelial cells or pericytes. It is clear from Table 2 that compounds **3c**, **6c**, **6d**, **6f**, **6n**, **14a** and **15** were the most potent against the five tyrosine kinases. Compound **6b** showed high inhibitions towards EGFR kinase with IC_{50} 0.43 nM, while it showed moderate inhibition towards c-Kit, Flt-3, VEGFR-2 and PDGFR with IC_{50} 1.32, 1.08, 1.69 and 1.02 nM, respectively. Compound **6m** showed high inhibitions toward Flt-3 and VEGFR-2 tyrosine kinases with IC_{50} 0.29 and 0.42 nM, respectively. On the other hand, compound **3b** showed high inhibitions against EGFR and PDGFR kinases with IC_{50} 0.73 and 0.52 nM, respectively. Compounds **3c**, **6d** and **15** were the most active toward c-Kit tyrosine kinase with IC_{50} 0.21, 0.25 and 0.33 nM, respectively. Compounds **3b** and **16** showed the lowest potency among the tested compounds.

2. 6. 4. Inhibitions of Selected Compounds Against Pim-1 Kinase

Compounds **3c**, **6c**, **6d**, **6f**, **6n**, **14a** and **15** were selected to examine their Pim-1 kinase inhibition activity (Table 3) as these compounds showed high inhibition against the tested cancer cell lines at a range of 10 concentrations and the IC_{50} values were calculated. Compounds **3c**, **6c**, **6d**, **6n** and **15** most potently inhibited Pim-1 kinase with IC_{50} values of 0.24, 0.27, 0.24, 0.28 and 0.32 μM, respectively. On the other hand, compounds **6f** and **14a** were less effective (IC_{50} > 10 μM). These profiles in combination with cell growth inhibition data of compounds **3c**, **6c**, **6d**, **6f**, **6n**, **14a** and **15** are listed in Table 3, indicating that Pim-1 is a potential target of these compounds where SGI-1776 was used as the positive control with IC_{50} 0.048 μM in the assay.

Table 3. The inhibitions of compounds **3c**, **6c**, **6d**, **6f**, **6n**, **14a** and **15** against Pim-1 kinase.

Compound	Inhibition ratio at 10 μM	IC_{50} (μM)
3c	94	0.24
6c	90	0.27
6d	94	0.24
6f	20	> 10
6n	90	0.28
14a	31	>10
15	86	0.32
SGI-1776	–	0.048

2. 6. 5. Pan Assay Interference Compounds (PAINS)

Good antitumor drugs should give false positive results when evaluated within Pan Assay Interference Compounds (PAINS).[29,30] Compounds can be regarded as false positives due their binding interactions by forming aggregates[31–33] by being protein-reactive entities[34–36] or by directly interfering with assay signaling. Pan Assay Interference Compounds (PAINS) are chemical entities that are frequently false positive in HTS. PAINS have a tendency to non-specifically react with several biological targets moderately, then specifically disturbing one preferred target.[37] A number of disorderly functional groups are collected by numerous PAINS.[38] Unwanted compounds may negatively influence not only enzyme assays but also phenotypic

Table 4. Drug-like character of different compounds and standard drugs foretinib and SGI-1776

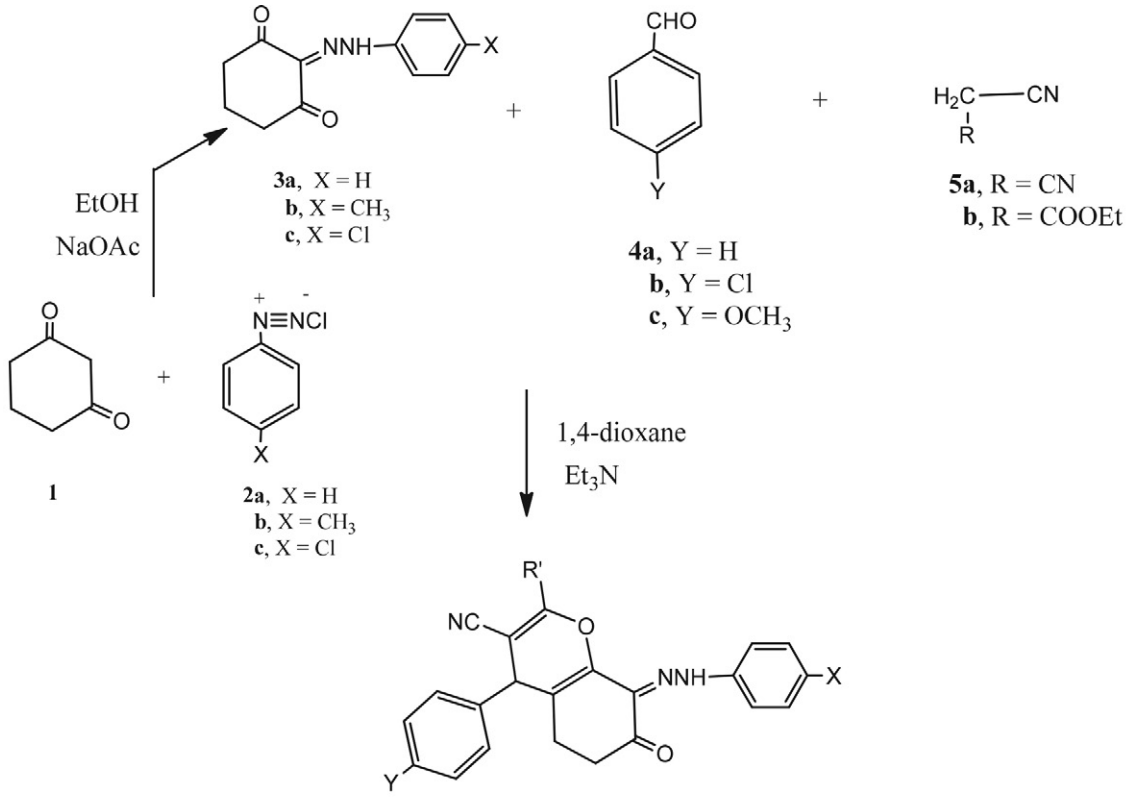
Compound	Drug-likeness Rule			Medicinal Chemistry Rules	
	Lvio.[a]/No. of vio.[a]	Vvio.[b]/No. of vio.[b]	Gvio.[c]/No. of vio.[c]	Lead likeliness /No. alert[d] of vio.	PAINS
3b	None	None	None	None	0
3c	None	None	None	None	0
6b	None	None	None	3	1
6c	None	None	None	2	0
6d	None	None	None	3	0
6f	None	None	None	None	0
6m	None	None	None	2	0
6n	None	None	None	3	0
14a	None	None	None	3	0
15	None	None	None	2	0
16	None	None	None	None	1
Foretinib	None	None	None	None	0
SGI-1776	None	None	None	None	0

[a] Lvio. = Lipinski's rule. [b] Vvio. = Veber Rules. [c] Gvio. = Ghose filter. [d] PAINS = Pan Assay Interference Compounds Analysis.

screens and show biological activity for the wrong reason.[39] PAINS violations of proposed compounds and reference drugs are given in Table 4. Almost all the compounds showed zero PAINS alert and can be used as good anticancer agents in the future without side effects.

3. Results and Discussion

Initially 2-arylhydrazonocyclohexan-1,3-dione was chosen as the model substrate for the synthesis of fused heterocyclic compounds through studying its multi-component reactions with aromatic aldehydes and cyanomethylene reagents to give biologically active fused pyran derivatives. The arylhydrazone derivatives **3a–c** were obtained through the coupling reaction between cyclohexane-1,3-dione (**1**) and either benzenediazonium chloride (**2a**), 4-methylbenzenediazonium chloride (**2b**) or 4-chlorobenzenediazonium chloride (**2c**) in ethanol solution containing the appropriate amount of sodium acetate. The multi-component reactions of either **3a**, **3b** or **3c** with either of benzaldehyde (**4a**), 4-chlorobenzaldehyde (**4b**) or

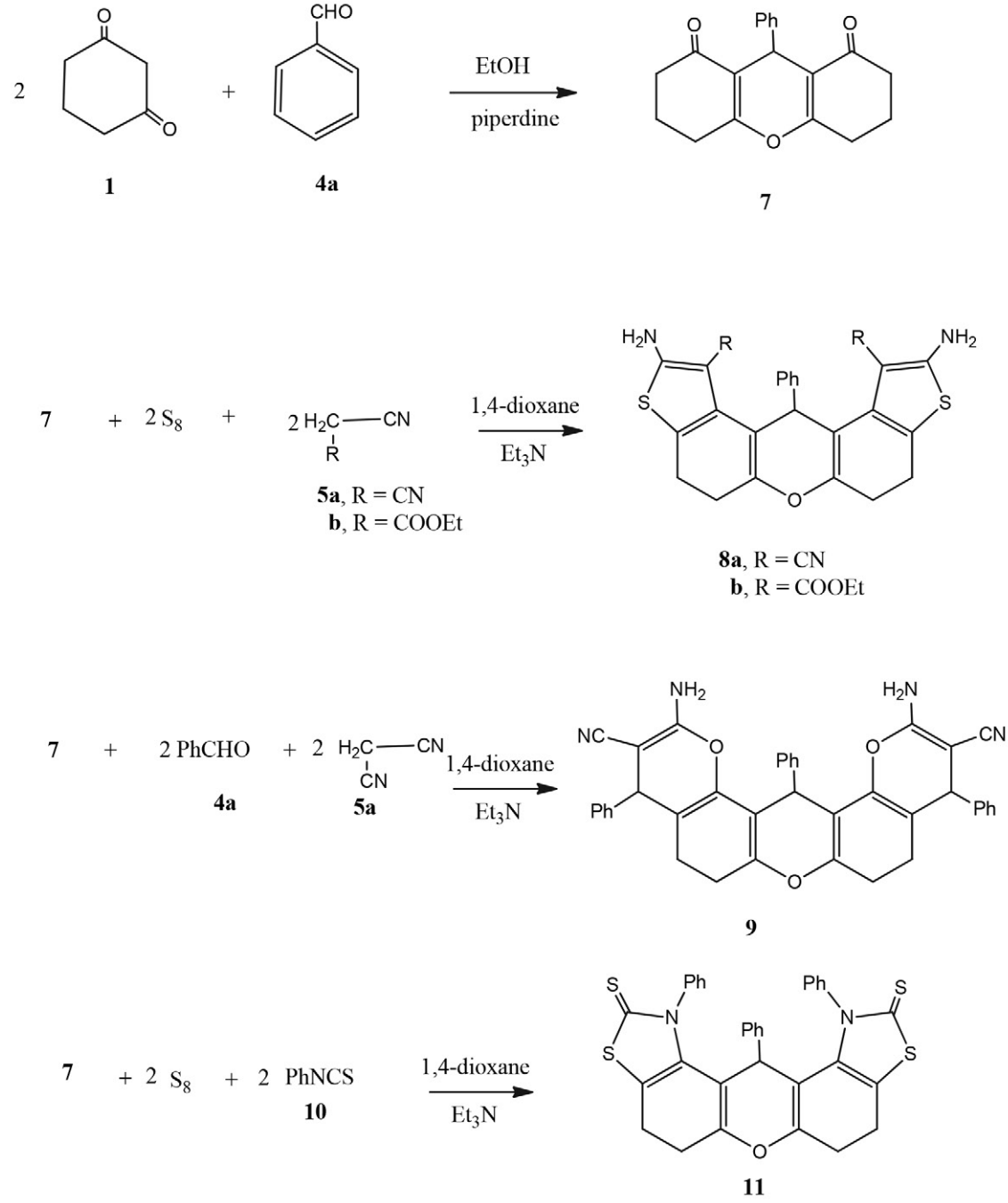


6	a	b	c	d	e	f	g	h	i
X	H	H	H	H	H	H	CH_3	CH_3	CH_3
Y	H	H	Cl	Cl	OCH_3	OCH_3	H	H	Cl
R'	NH_2	OH	NH_2	OH	NH_2	OH	NH_2	OH	NH_2
6	**j**	**k**	**l**	**m**	**n**	**o**	**p**	**q**	**r**
X	CH_3	CH_3	CH_3	Cl	Cl	Cl	Cl	Cl	Cl
Y	Cl	OCH_3	OCH_3	H	H	Cl	Cl	OCH_3	OCH_3
R'	OH	NH_2	OH	NH_2	OH	NH_2	OH	NH_2	OH

Sheme 1. Synthesis of compounds **3a–c** and **6a–r.**

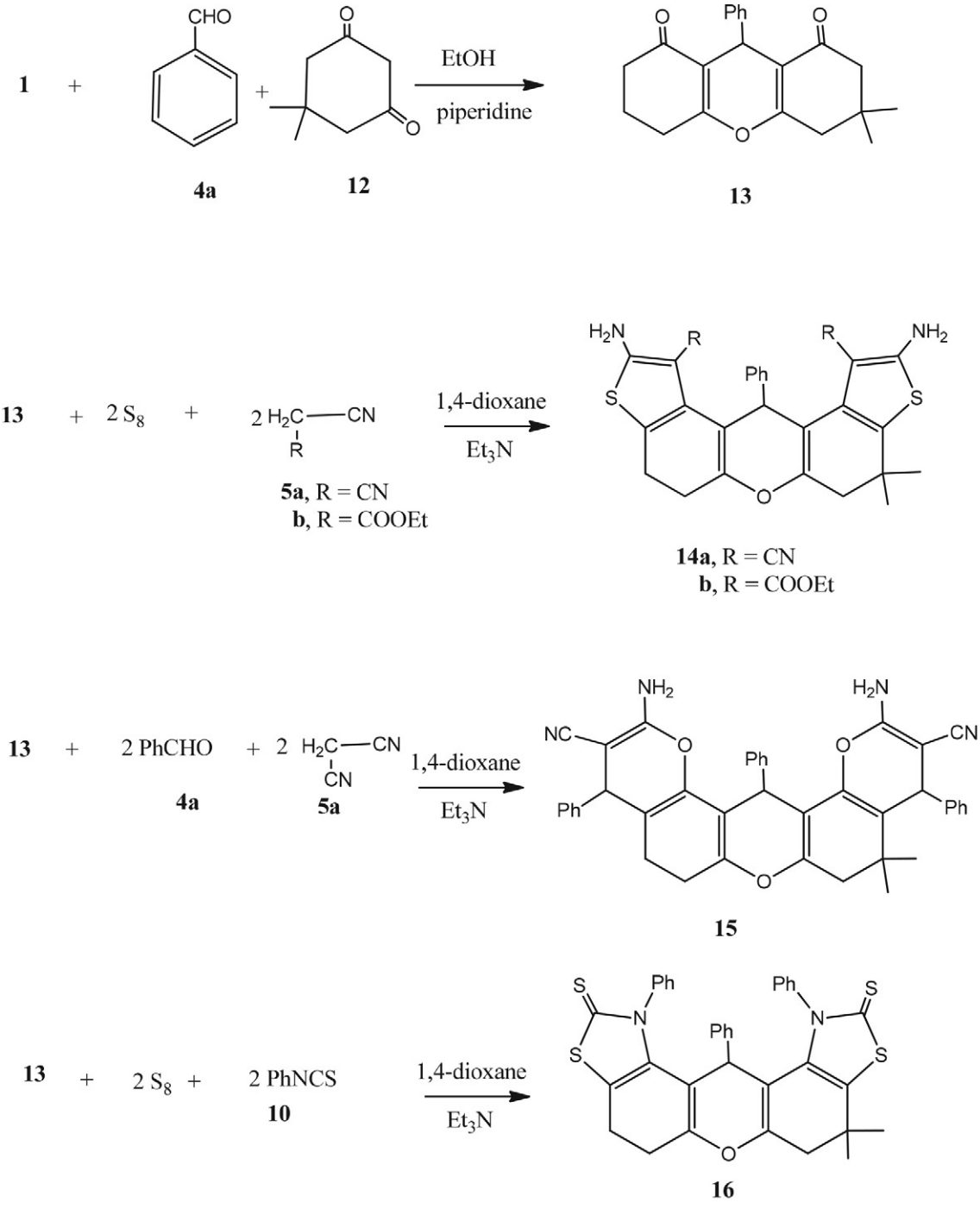
4-methoxybenzaldehyde (**4c**) and either malononitrile (**5a**) or ethyl cyanoacetate (**5b**) in 1,4-dioxane solution containing a catalytic amount of triethylamine gave the 5,6,7,8-tetrahydro-4*H*-chromene derivatives **6a**–**r**, respectively (Scheme 1). The chemical structures of new compounds were assured by spectral data (IR, ^{1}H, ^{13}C NMR, MS). Thus, the ^{1}H NMR spectrum of compound **6a** (as an example) showed (beside the expected signals) signals at δ 4.82 ppm (D_2O exchangeable) indicating the presence of the NH_2 group, a multiplet at δ 7.23–7.48 ppm for the two phenyl groups. In addition, the ^{13}C NMR spectrum revealed the presence of a signal at 51.2 due to the pyran C-4, one signal-at δ 117.3 for CN groups, signals at δ 130.2, 131.6, 134.8, 136.1 for the pyran carbons and two signals at δ 166.8 and 167.2 for the C=N and C=O groups.

Next, we studied the reaction of two-fold amount of cyclohexan-1,3-dione with benzaldehyde in ethanol containing a catalytic amount of triethylamine to give the 9-phenyl-3,4,5,6,7,9-hexahydro-1*H*-xanthene-1,8(2*H*)-dione (**7**). The analytical and spectral data of compound **7**



Sheme 2. Synthesis of compounds **7; 8a,b; 9** and **11.**

were in agreement with the proposed structure. Thus, the ^{1}H NMR spectrum showed the presence of two multiplets at δ 1.59–1.80 and 2.58–2.73 ppm equivalent to the six CH_2 groups, a singlet at δ 5.09 ppm for the pyran H-4 and a multiplet at δ 7.25–7.41 ppm corresponding to the C_6H_5 group. In addition, the ^{13}C NMR spectrum showed signals at δ 26.3, 28.4, 32.6 equivalent to the six CH_2 groups, signal at 50.9 due to the pyran C-4, four signals at δ 120.6, 121.4, 123.6 and 125.8 for the phenyl carbons and a signal at δ 168.9 for the two symmetric C=O groups. Compound **7** showed interesting reactivity toward heterocyclization reactions through its reactions with some reagents. It was ready to undergo Gewald's thiophene[40–42] reaction to produce biologically active fused thiophene derivatives. Thus, the reaction of compound **7** with two folds of either malononitrile (**5a**) or ethyl cyanoacetate (**5b**) and elemental sulfur gave the dithieno[3,2-*a*:2',3'-*j*]xanthene derivatives **8a** and **8b**, respectively. On the other hand, compound **7**



Sheme 3. Synthesis of compounds **13, 14a,b; 15** and **16.**

underwent multi-component reactions with two folds of benzaldehyde (**4a**) and malononitrile (**5a**) affording the hexahydro-4*H*-dipyrano[2,3-*a*:3',2'-*j*]xanthene derivative **9**. Its structure was established on the basis of its analytical and spectral data (see experimental section). In addition, the reaction of compound **7** with two folds of elemental sulfur and phenylisothiocyanate (**10**) in 1,4-dioxane solution containing a catalytic amount of triethylamine gave the xantheno[1,2-*d*:8,7-*d'*]bis(thiazole)-dithione derivative **11** (Scheme 2). Compounds **8**, **9** and **11** were obtained in pure state and high yields and promising structure identification were obtained thus encouraging us to carry similar reactions using cyclohexan-1,3-dione in one side and dimedone in the other side. Therefore, the multi-component reactions of cyclohexan-1,3-dione with benzaldehyde (**4a**) and dimedone gave the 3,3-dimethyl-9-phenyl-3,4,5,6,7,9-hexahydro-1*H*-xanthene-1,8(2*H*)-dione (**13**).

Compound **13** showed interesting reactivity toward heterocyclization reactions through its reactions with some reagents. Thus, the reaction of compound **13** with two folds of either malononitrile (**5a**) or ethyl cyanoacetate (**5b**) and elemental sulfur gave the 4,4-dimethyl-5,7,8,12-tetrahydro-4*H*-dithieno[3,2-*a*:2',3'-*j*]xanthenes derivatives **14a** and **14b**, respectively. On the other hand, compound **13** underwent multi-component reactions with two folds of benzaldehyde (**4a**) and malononitrile (**5a**) affording the 2,12-diamino-5,5-dimethyl-4,10,14-triphenyl-5,6,8,9,10,14-hexahydro-4*H*-dipyrano[2,3-*a*:3',2'-*j*]xanthene derivative **15**. In addition, the reaction of compound **13** with two folds of elemental sulfur and phenylisothiocyanates (**10**) in 1,4-dioxane solution containing a catalytic amount of triethylamine gave the 4,4-dimethyl-4,5,7,8-tetrahydro-1*H*-xantheno[1,2-*d*:8,7-*d'*]bis(thiazole)-dithione derivative **16** (Scheme 3).

4. Conclusion

The main result of these studies is the synthesis of a series of novel heterocyclic derivatives synthesized from arylhydrazonocyclohexan-1,3-dione followed by screening of the newly synthesized compounds against six cancer cell lines. Compounds **3b**, **3c**, **6b**, **6c**, **6d**, **6f**, **6m**, **6n**, **14a**, **15** and **16** were the most cytotoxic. Screening against the five tyrosine kinases c-Kit, Flt-3, VEGFR-2, EGFR, and PDGFR showed that compounds **3c**, **6c**, **6d**, **6f**, **6n**, **14a** and **15** were the most active compounds. On the other hand, inhibition against Pim-1 kinase indicated that compounds **3c**, **6c**, **6d**, **6n** and **15** were of the highest inhibitions.

5. References

1. T. Moriguchi, H. Matsuura, Y. Itakura, H. Katsuki, H. Saito, N. Nishiyama, *Life Sci.* **1997**, *61*, 1413–1420. **DOI:**10.1016/S0024-3205(97)00687-5
2. G. H. Abou El-Fotooh, O. I. Abd El-Salam, M. M. Ashraf, A. H. Nagla, *Ind. J. Chem.* **2005**, *44B*, 1887–1893.
3. D. Armesto, W. M. Horspool, N. Martin, A. Ramos, C. Seoane, *J. Org. Chem.***1989**, *54*, 3069–3072. **DOI:**10.1021/jo00274a021
4. J. A. Rideout, I. R. Smith, M. D. Sutherland, *Aust. J. Chem.* **1976**,*29*, 1087–1089. **DOI:**10.1071/CH9761087
5. D. Kumar, V. B. Reddy, S. Sharad, U. Dube, K. A. Suman, *Eur. J. Med. Chem.***2009**, *44*, 3805–3809. **DOI:**10.1016/j.ejmech.2009.04.017
6. Y. R. Lee, X. Wang, L. Xia, *Molecules* **2007**, *12*, 1420–1429. **DOI:**10.3390/12071420
7. M. M. Khafagy, A. H. F. El-Wahas, F. A. Eid, A. M. El-Agrody, *Il Farmaco* **2002**, *57*, 715–722. **DOI:**10.1016/S0014-827X(02)01263-6
8. W. P. Smith, L. S. Sollis, D. P. Howes, C. P. Cherry, D. I. Starkey, N. K. Cobley, H. Weston, J. Scicinski, A. Merritt, A. Whittington, P. Wyatt, N. Taylor, D. Green, R. Bethell, S. Madar, R. J. Fenton, P. J. Morley, T. Pateman, A. J. Beresford, *Med. Chem.* **1998**, *41*, 787–797. **DOI:**10.1021/jm970374b
9. A. G. Martinez, L. J.Marco, *Bioorg. Med. Chem. Lett.* **1997**, *7*, 3165–3170. **DOI:**10.1016/S0960-894X(97)10165-2
10. K. Hiramoto, A. Nasuhara, K. Michiloshi, T. Kato, K. Kikugawa, *Mutat. Res.***1997**, *395*,47–56. **DOI:**10.1016/S1383-5718(97)00141-1
11. C. P. Dell, C. W. Smith, *Eur. Pat. Appl.* **1993**, *537*, 949. *Chem. Abstr.* **1993**, *119*, 139102d.
12. G. Bianchi, A.Tava, *Agric. Biol. Chem.* **1987**, *51*, 2001–2002. **DOI:**10.1271/bbb1961.51.2001
13. S. J. Mohr, M. A. Chirigos, F. S. Fuhrman, J. W. Pryor, *Cancer Res.* **1975**, *35*, 3750–3754.
14. J. Skommer, D. Wlodkowic, M. Matto, M. Eray, J. Pelkonen, *Leukemia Res.* **2006**, *30*, 322–331. **DOI:**10.1016/j.leukres.2005.08.022
15. D. R. Anderson, S. Hegde, E. Reinhard, L. Gomez, W. F. Vernier, L. Lee, S. Liu, A. Sambandam, P. A. Snider, L. Masih, *Bioorg. Med. Chem. Lett.* **2005**, *15*, 1587–1590. **DOI:**10.1016/j.bmcl.2005.01.067
16. J. L. Wang, D. Liu, Z. Zhang, S. Shan, X. Han, S. M. Srinvasula, C. M. Croce, E. S. Alnemeri, Z. Huang, *Proc. Natl. Acad. Sci. USA* **2000**, *97*, 7124–7129. **DOI:**10.1073/pnas.97.13.7124
17. F. Eiden, F. Denk, *Arch. Pharm. (Weinheim, Germany)* **1991**, *324*, 353–354. **DOI:**10.1002/ardp.19913240606
18. E. A. A. Hafez, M. H. Elnagdi, A. G. A. Elagamey, F. M. A. El-Taweel, *Heterocycles* **1987**, *26*, 903–907. **DOI:**10.3987/R-1987-04-0903
19. R. M. Mohareb, N. Y. Abdo, K. A. EL-Sharkawy, *Anticancer Agent in Med. Chem.* **2018**, *18*, 1736–1749. **DOI:**10.2174/1871520618666180604091358
20. R. M. Mohareb, E. M. Samir, P. A. Halim, *Bioorg.Chem.* **2019**, *83*, 402–413. **DOI:**10.1016/j.bioorg.2018.10.067
21. R. M. Mohareb, K. A. El-Sharkawy, F. O. El-Farouk, *Med. Chem. Res.* **2019**, *28*, 1885–1900. **DOI:**10.1007/s00044-019-02421-6
22. R. M. Mohareb, A. E. M. Abdallah, M. A. Abelaziz, *Med. Chem. Res.* **2014**, *23*, 564–597. **DOI:**10.1007/s00044-013-0664-7

23. R. M. Mohareb, W. W. Wardakhan, F. I. Hamid, *Med. Chem. Res.* **2015**, *24*, 2043–2054. **DOI:**10.1007/s00044-014-1273-9
24. R. M. Mohareb, F. M. Manhi, A. Abdelwahab, *Acta Chim. Slov.* **2020**, *67*, 83–95. **DOI:**10.17344/acsi.2019.5224
25. R. M. Mohareb, P. A. Halim, *Acta Chim. Slov.* **2018**, *65*, 554–568. **DOI:**10.17344/acsi.2017.4146
26. L. Liu, A. Siegmund, N. Xi, P. Kaplan-Lefko, K. Rex, A. Chen, J. Lin, J. Moriguchi, L. Berry, L. Y. Huang, Y. Teffera, Y. J. Yang, Y. H. Zhang, S. F. Bellon, M. Lee, R. Shimanovich, A. Bak, C. Dominguez, M. H. Norman, J. C. Harmange, I. Dussault, T. S. Kim, *J. Med. Chem.* **2008**, *51*, 3688–3691. **DOI:**10.1021/jm800401t
27. M. L. Peach, N. Tan, S. J. Choyke, A. Giubellino, G. Athauda, T. R. Burke, M. C. Nicklaus, D. P. Bottaro, *J. Med. Chem.* **2009**, *52*, 943–951. **DOI:**10.1021/jm800791f
28. F. D. Bacco, P. Luraghi, E. Medico, G. Reato, F. Girolami, T. Perera, P. Gabriele, P. M. Comoglio, C. Boccaccio, *J. Natl. Cancer Inst.* **2011**, *103*, 645–661. **DOI:**10.1093/jnci/djr093
29. J. B. Bael, G. A. Holloway, *J. Med. Chem.***2010**, *53*, 2719–2740. **DOI:**10.1021/jm901137j
30. S. L. McGovern, E. Caselli, N. Grigorieff, B. K. Shoichet, *J. Med.Chem.* **2002**, *45*, 1712–1722. **DOI:**10.1021/jm010533y
31. S. L. McGovern, B. K. Shoichet, *J. Med. Chem.* **2003**, *46*, 1478–1483. **DOI:**10.1021/jm020427b
32. B. Y. Feng, A. Shelat, T. N. Doman, R. K. Guy, B. K. Shoichet, *Nat. Chem. Biol.* **2005**, *1*, 146–148. **DOI:**10.1038/nchembio718
33. B. Y. Feng, B. K. Shoichet, *J. Med. Chem.***2006**, *49*, 2151–2154. **DOI:**10.1021/jm060029z
34. J. T. Metz, J. R. Huth, P. J. Hajduk, *J. Computer-Aided Mol. Des.* **2007**, *21*, 139–144. **DOI:**10.1007/s10822-007-9109-z
35. J. R. Huth, D. Song, R. R. Mendoza, C. L. Black-Schaefer, J. C. Mack, S. A. Dorwin, U. S. Ladror, J. M. Severin, K. A.Walter, D. M. Bartley, P. Hajduk, *Chem. Res. Toxicol.* **2007**, *20*, 1752–1759. **DOI:**10.1021/tx700319t
36. B. B. Jonathan, A. W. Michael, *Nature* **2014**, *513*, 481–483. **DOI:**10.1038/513481a
37. L. D. Jayme, A. W. Michael, *Futu. Med.Chem.* **2014**, *6*, 1265–1290. **DOI:**10.4155/fmc.14.60
38. P. Martin, J. Stephane, *J. Med. Chem.* **2016**, 59, 497–503. **DOI:**10.1021/acs.jmedchem.5b00361
39. F. Cheng, A. W. Li, *J. Chem. Inf. Mod.***2012**, *52*, 3099–3105. **DOI:**10.1021/ci300367a
40. B. P. McKibben, C. H. Cartwright, A. L. Castelhano, *Tetrahedron Lett.* **1999**, *40*, 5471–5474. **DOI:**10.1016/S0040-4039(99)01108-9
41. R. Mishra, K. K. Jha, S. Kumar, I. Tomer, *A review Der Pharma Chemica* **2011**, *3*, 38–54.
42. K. Wang, D. Kim, A. Dömling, *J. Comb.Chem.* **2010**, *12*, 111–118. **DOI:**10.1021/cc9001586

Povzetek

V prispevku predstavljamo večkomponentne reakcije med arilhidrazocikloheksan-1,3-dionskimi derivati **3a**–**c** in benzaldehidom (**4a**), 4-klorobenzaldehidom (**4b**) ali 4-metoksibenzaldehidom (**4c**) ter malononitrilom (**5a**) ali etil cianoacetatom (**5b**), ki vodijo do nastanka 5,6,7,8-tetrahidro-4*H*-kromenskih derivatov **6a**–**r**. Pri reakciji dveh ekvivalentov cikloheksan-1,3-diona z benzaldehidom je nastal heksahidro-1*H*-ksanten-1,8(2*H*)-dionski derivat **7**. Po drugi strani pa večkomponentna reakcija med spojino **1** in dimedonom ali benzaldehidom daje produkt **13**. Obe spojini **7** in **13** lahko sodelujeta v reakcijah heterociklizacij, pri katerih nastanejo pripojeni tiofenski, piranski in tiazolski derivati. Izmed pripravljenih spojin smo nekatere uporabili za določevanje potencialne inhibitorne aktivnosti proti šestim rakavim celičnim linijam; rezultati so bili obetavni, spojine **3b**, **3c**, **6b**, **6c**, **6d**, **6f**, **6i**, **6m**, **6n**, **8b**, **14a**, **15** in **16** so se izkazale kot še posebej citotoksične. Nadaljnje testiranje na petih tirozin kinazah (c-Kit, Flt-3, VEGFR-2, EGFR in PDGFR) ter Pim-1 kinazi je pokazalo, da so spojine **3c**, **6c**, **6d**, **6f**, **6n**, **14a** in **15** najbolj aktivne proti prvim petim tirozin kinazam, medtem ko so spojine **3c**, **6c**, **6d**, **6n** in **15** najbolj aktivne proti Pim-1 kinazi.

Except when otherwise noted, articles in this journal are published under the terms and conditions of the Creative Commons Attribution 4.0 International License

Scientific paper

6-Bromo-2'-(2-chlorobenzylidene)nicotinohydrazide and 6-Bromo-2'-(3-bromo-5-chloro-2-hydroxybenzylidene) nicotinohydrazide Methanol Solvate: Synthesis, Characterization, Crystal Structures and Antimicrobial Activities

Hai-Yun Zhu

College of Energy and Chemical Engineering, Ningxia Vocational Technical College of Industry and Commerce, Yinchuan 750021, P. R. China

** Corresponding author: E-mail: zhuhaiyun76@126.com*

Received: 05-25-2020

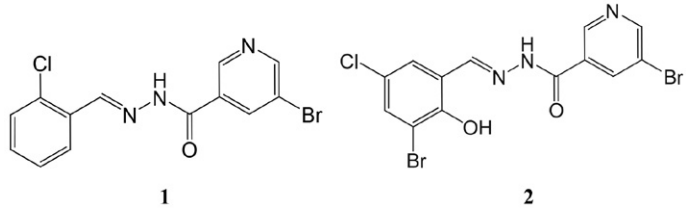
Abstract

Two newly synthesized nicotinohydrazones, 6-bromo-2'-(2-chlorobenzylidene)nicotinohydrazide (**1**) and 6-bromo-2'-(3-bromo-5-chloro-2-hydroxybenzylidene)nicotinohydrazide methanol solvate (**2**), have been obtained and structurally characterized by spectroscopic method and single crystal X-ray determination. The molecules in both compounds are in *E* configuration regarding to the azomethine groups. The molecules of compound **1** are linked *via* hydrogen bonds of N–H···O, generating one dimensional chains running along the *c*-axis direction. The hydrazone molecules of compound **2** are linked by methanol molecules *via* hydrogen bonds of N–H···O and O–H···N, generating dimers. The *in vitro* antimicrobial activities of these compounds indicate that they are interesting antibacterial agents.

Keywords: Hydrazone; synthesis; hydrogen bonding; X-Ray crystal structure; antimicrobial activity

1. Introduction

Hydrazones with the central group –CH=N–NH– are of great importance in biological fields, especially for the new drug investigation.[1] These compounds have been reported to show interesting biological activities like antimicrobial, antifungal, anticonvulsant, analgesic, antiplatelet, antitubercular, antiinflammatory, as well as antitumor.[2] Hydrazones are also a kind of interesting ligands in coordination chemistry.[3] The metal complexes with hydrazones are reported to have interesting biological activities.[4] Isoniazide is a front-line antituberculotic drug. The derivatives of isoniazide have been widely used as attractive drugs in the treatment of various deseases.[5] To date, a number of hydrazones derived from benzohydrazides were reported.[6] However, those derived from nicotinohydrazide are relatively rare. Moreover, the compounds bearing halide substituent such as F, Cl and Br usually possess effective antimicrobial activities.[7] We have reported on some hydrazone compounds with antimicrobial activities.[8] In pursuit of new antimicrobial agents, in this paper, two nicotinohydrazones, 6-bromo-2'-(2-chlorobenzylidene)nicotinohydrazide (**1**) and 6-bromo-2'-(3-bromo-5-chloro-2-hydroxybenzylidene)



Scheme 1. The nicotinohydrazones **1** and **2**

nicotinohydrazide methanol solvate (**2**), possessing simultaneously Cl, Br and isoniazide skeleton are presented (Scheme 1).

2. Experimental

2. 1. Materials and Methods

5-Bromonicotinohydrazide, 2-chlorobenzaldehyde and 3-bromo-5-chloro-2-hydroxybenzaldehyde were purchased from Bide Chemical Reagent Co. Ltd. The other chemicals with AR grade were obtained commercially and used as received. CHN elemental analyses were performed on a Perkin-Elmer 240C elemental analyzer. IR spectra were measured with a FT-IR 170-SX (Nicolet) spectrophotometer. ^{1}H NMR and ^{13}C NMR data were measured with a Bruker 500 MHz instrument.

2. 2. Synthesis of 6-Bromo-2'-(2-chlorobenzylidene)nicotinohydrazide (1)

5-Bromonicotinohydrazide (0.216 g, 1.0 mmol) and 2-chlorobenzaldehyde (0.140 g, 1.0 mmol) were mixed and stirred in methanol (50 mL) for 1 h at ambient temperature to give a colourless solution. The solution was left to slow evaporation of the methanol for a week, yielding colourless needle-shaped single crystals. The crystals were filtered out and washed with methanol. Yiled 0.28 g (83%). M.p. 173.2–174.5 °C. Analysis calculated for $C_{13}H_9BrClN_3O$: C, 46.1; H, 2.7; N, 12.4; found: C, 45.9; H, 2.7; N, 12.5. IR data (KBr, cm^{-1}): 3178 (w), 1654 (s), 1598 (m), 1561 (m), 1471 (w), 1437 (w), 1369 (w), 1303 (s), 1158 (w), 1031 (m), 963 (w), 927 (w), 745 (m). ^{1}H NMR (500 MHz, DMSO-d_6): δ 12.24 (s, 1H, NH), 9.05 (s, 1H, PyH), 8.92 (s, 1H, CH=N), 8.83 (s, 1H, PyH), 8.52 (s, 1H, PyH), 8.03 (d, 1H, ArH), 7.55 (d, 1H, ArH), 7.46 (m, 2H, ArH). ^{13}C NMR (126 MHz, DMSO-d_6): δ 160.26, 153.01, 147.34, 144.71, 137.64, 133.36, 131.78, 131.23, 130.48, 129.95, 127.66, 126.97, 120.05.

2. 3. Synthesis of 6-Bromo-2'-(3-bromo-5-chloro-2-hydroxybenzylidene) nicotinohydrazide methanol solvate (2)

5-Bromonicotinohydrazide (0.216 g, 1.0 mmol) and 3-bromo-5-chloro-2-hydroxybenzaldehyde (0.235 g, 1.0 mmol) were mixed and stirred in methanol (50 mL) for 1 h at ambient temperature to give a slight yellow solution. The solution was left to slow evaporation of the methanol for 2 days, yielding light yellow block-shaped single crystals. The crystals were filtered out and washed with methanol. Yiled 0.39 g (84%). M.p. 210.5–211.3 °C. Analysis calculated for $C_{14}H_{12}Br_2ClN_3O_3$: C, 36.1; H, 2.6; N, 9.0; found: C, 35.9; H, 2.7; N, 9.1. IR data (KBr, cm^{-1}): 3457 (w), 3190 (w), 1666 (s), 1600 (w), 1550 (w), 1443 (s), 1344 (m), 1294 (w), 1164 (s), 1078 (s), 955 (s), 861 (s), 734 (m). ^{1}H NMR (500 MHz, DMSO-d_6): δ 12.68 (s, 1H, OH), 12.39 (s, 1H, NH), 9.05 (s, 1H, PyH), 8.92 (s, 1H, CH=N), 8.52 (s, 1H, PyH), 8.50 (s, 1H, PyH), 7.72 (s, 2H, ArH). ^{13}C NMR (126 MHz, DMSO-d_6): δ 160.23, 153.31, 153.25, 147.98, 147.36, 137.71, 133.30, 129.63, 129.28, 123.39, 120.25, 120.07, 110.94.

2. 4. X-Ray Structure Analysis

X-Ray diffraction intensities were collected using a Bruker SMART 1000 CCD area detector equipped with graphite-monochromated Mo-Kα radiation (λ = 0.71073 Å) at 298(2) K. Absorption corrections were applied by SADABS.[9] The structures of the compounds were solved by direct methods and refined on F^2 by full-matrix least-squares methods with SHELXTL.[10] All non-hydrogen atoms were refined anisotropically. The amino and methanol H atoms in both compounds were located in difference Fourier maps and refined isotropically, with N–H and O–H distances restrained to 0.90(1) Å and 0.85(1) Å, respectively, and with U_{iso}(H) values fixed at 1.2U_{eq}(N) and 1.5U_{eq}(O). The other H atoms were placed in idealized positions and constrained to ride on their parent atoms. The Cl atoms in **1** is disordered over two sites, with occupancies of 0.84(2) and 0.16(2). The details of the crystallographic data are summarized in Table 1. Supplementary crystallographic data have been deposited at the Cambridge Crystallographic Data Center (CCDC 850161 and 2022935).

2. 5. Antimicrobial Test

Qualitative determination of antimicrobial activity was done using the disk diffusion method. Suspensions in sterile peptone water from 24 hour cultures of microorganisms were adjusted to 0.5 McFarland. Muller–Hinton Petri dishes of 90 mm were inoculated using these suspensions. Paper disks (6 mm in diameter) containing 10 μL of the substance to be tested (at a concentration of 2048 μg/mL in DMSO) were placed in a circular pattern in each inoculated plate. Incubation of the plates was done at 37 °C for 18–24 h. DMSO impregnated discs were used as negative controls. Toxicity tests of the solvent, DMSO, showed that the concentrations used in antimicrobial activity assays did not interfere with the growth of the microorganisms. Reading of the results was done by measuring the diameters of the inhibition zones generated by the test substance. Penicillin was used as a reference.

Determination of MIC was done using the serial dilutions in liquid broth method. The materials used were 96-well plates, suspensions of microorganism, Muller–Hinton broth and stock solutions of each substance to be tested (2048 μg/mL in DMSO). The following concentrations of the substances to be tested were obtained in the 96-well plates: 1024, 512, 256, 128, 64, 32, 16, 8, 4, 2, and

Table 1. Crystal data, data collection and structure refinement for the compounds

Compound	**1**	**2**
Molecular formula	$C_{13}H_9BrClN_3O$	$C_{14}H_{12}Br_2ClN_3O_3$
Molecular weight	338.6	465.5
Crystal system	Monoclinic	Monoclinic
Space group	$P2_1/c$	$C2/c$
Temperature (K)	298(2)	298(2)
a (Å)	11.482(2)	11.862(1)
b (Å)	14.034(3)	13.494(1)
c (Å)	8.443(2)	19.860(2)
β (°)	90.05(3)	95.485(1)
V (Å^3)	1360.5(5)	1562.1(5)
Z	4	8
D_{calc} (g cm^{-3})	1.653	1.954
Crystal dimensions (mm)	0.23 × 0.20 × 0.20	0.27 × 0.27 × 0.27
Absorption coefficient (mm^{-1})	3.212	5.309
Reflections measured	11289	7887
Total no. of unique data	2963 [R_{int} = 0.0409]	2890 [R_{int} = 0.0434]
No. of observed data, $I > 2\sigma(I)$	1825	1714
No. of variables	184	216
No. of restraints	4	2
Goodness of fit on F^2	1.001	0.961
R_1, wR_2 [I ³ $2\sigma(I)$]^a	0.0486, 0.1097	0.0324, 0.0639
R_1, wR_2 (all data)^a	0.0877, 0.1271	0.0754, 0.0757

$^aR_1 = \Sigma||F_o| - |F_c||/\Sigma|F_o|$, $wR_2 = [\Sigma w(F_o^2 - F_c^2)^2/\Sigma w(F_o^2)^2]^{1/2}$

1 μg/mL. After incubation at 37 °C for 18–24 h, the MIC for each tested substance was determined by microscopic observation of microbial growth. It corresponds to the well with the lowest concentration of the tested substance where microbial growth was clearly inhibited.

3. Results and Discussion

3. 1. Chemistry

The nicotinohydrazones **1** and **2** were facile prepared by the reaction of 1:1 molar ratio of 5-bromonicotinohydrazide with 2-chlorobenzaldehyde and 3-bromo-5-chloro-2-hydroxybenzaldehyde, respectively in methanol. The elemental analyses are in good agreement with the formulae proposed for the compounds determined by single crystal X-ray diffraction. The crystals of the compounds are stable in air at room temperature, and easily soluble in DMF, DMSO, methanol, ethanol, chloroform, dichloromethane, and acetonitrile.

Synthesis of the compounds was indicated in their IR spectra by the presence of bands for imine bonds, *i.e.* 1654 cm^{-1} for **1** and 1666 cm^{-1} for **2**. In ^{1}H NMR, the absence of NH_2 signals and the appearance of peaks for NH protons in the region δ 12.24–12.39 ppm and imine CH proton in the region δ 8.92 ppm confirmed the synthesis of the compounds. The aromatic proton signals were found in their respective regions with different multiplicities, confirming their relevant substitution pattern.

3. 2. Crystal Structure Description of 1 and 2

The molecular structures of compounds **1** and **2** are shown in Figures 1 and 2, respectively. Compound **2** contains a methanol molecule of crystallization. All the related bond lengths and angles (Table 2) in the compounds are similar, and within the ranges of the bond values observed in reported hydrazone compounds.[8a,11] The C7–N1 bond lengths of 1.278(5) Å in **1** and 1.243(4) Å in **2** indicate the double bond nature. The C8–N2 bond lengths of 1.339(4) Å in **1** and 1.335(4) Å in **2**, and the N1–N2 bonds (1.388(4) Å in **1** and 1.340(4) Å in **2**) are shorter than normal, suggesting the existence of delocalization in the molecules.

Table 2. Selected bond lengths (Å) and bond angles (°) for the compounds **1** and **2**

1			
C7–N1	1.278(5)	N1–N2	1.388(4)
N2–C8	1.339(4)	C8–O1	1.226(4)
C1–C7–N1	122.3(3)	C7–N1–N2	113.3(3)
N1–N2–C8	118.8(3)	N2–C8–C9	115.9(3)
N2–C8–O1	123.8(3)	O1–C8–C9	120.3(3)
2			
C7–N1	1.243(4)	N1–N2	1.340(4)
N2–C8	1.335(4)	C8–O1	1.185(4)
C1–C7–N1	118.6(3)	C7–N1–N2	119.3(3)
N1–N2–C8	115.2(3)	N2–C8–C9	115.8(4)
N2–C8–O1	122.7(4)	O1–C8–C9	121.5(3)

Table 3. Distances (Å) and angles (°) involving hydrogen bonding of the compounds **1** and **2**

D–H···A	*d*(*D*–H) (Å)	*d*(H···*A*) (Å)	*d*(*D*···*A*) (Å)	*Angle*(*D*–H···*A*) (°)
1				
N2–H2···O1^{i}	0.90(1)	2.02(2)	2.859(4)	157(4)
C7–H7···O1^{i}	0.93	2.32(2)	3.133(4)	146(4)
2				
O2–H2A···N1	0.82	1.81	2.518(4)	144(3)
N2–H2···O3	0.90(1)	1.93(1)	2.817(4)	168(4)
O3–H3···N3^{ii}	0.85(1)	1.96(1)	2.799(4)	172(4)

Symmetry code for i: *x*, 1/2 – *y*, 1/2 + *z*; ii: 1 – *x*, – *y*, 1 – *z*.

Table 4. π–π interactions

Cg	Distance between ring centroids (Å)	Dihedral angle (°)	Perpendicular distance of *Cg*(I) on *Cg*(J) (Å)	Perpendicular distance of *Cg*(J) on *Cg*(I) (Å)
1				
*Cg*1···*Cg*1^{iii}	3.9762	0	3.5858	3.5859
*Cg*1···*Cg*2^{iv}	4.1626	7.201	3.4858	–3.7417
*Cg*2···*Cg*2^{v}	3.8892	0	–3.4367	–3.4367
2				
*Cg*1···*Cg*2^{v}	3.6959	3.876	–3.4413	–3.5234
*Cg*1···*Cg*2^{vi}	4.8932	0	3.3600	3.3600

*Cg*1 and *Cg*2 are the centroids of the N3-C12-C11-C10-C9-C13 and C1-C2-C3-C4-C5-C6 rings, respectively. Symmetry codes: iii: 1 – *x*, 1 – *y*, 1 – *z*; iv: *x*, 1/2 – *y*, 1/2 + *z*; v: – *x*, – *y*, 1 – *z*; vi: 1/2 – *x*, 1/2 – *y*, 1 – *z*.

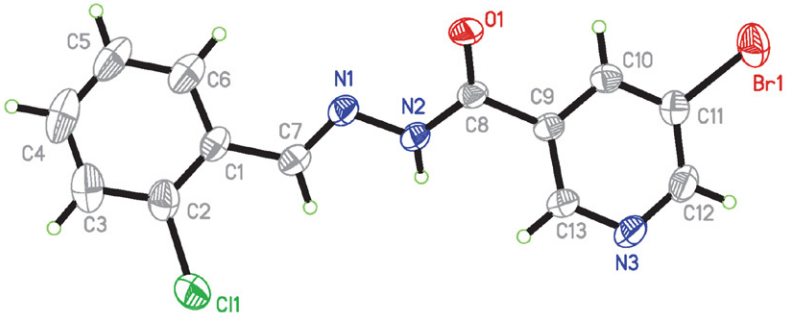


Figure 1. Molecular structure of **1** at 30% probability displacement. Only the major component of the disordered group is shown.

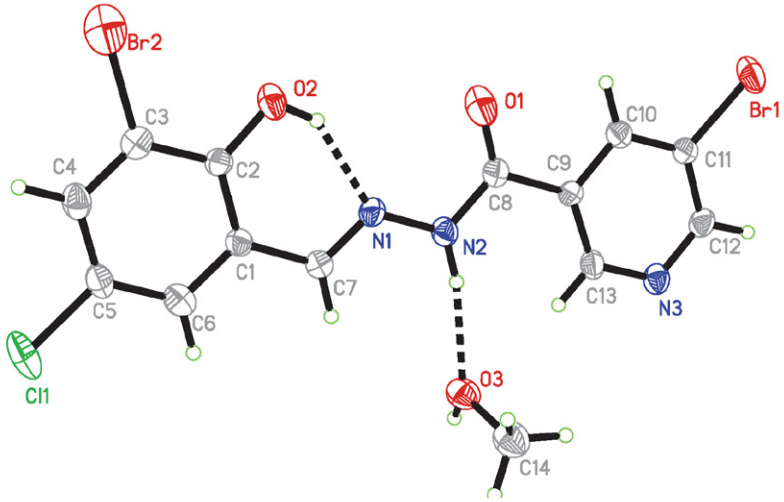


Figure 2. Molecular structure of **2** at 30% probability displacement. Intramolecular O–H···N and N–H···O hydrogen bonds are drawn as dashed lines.

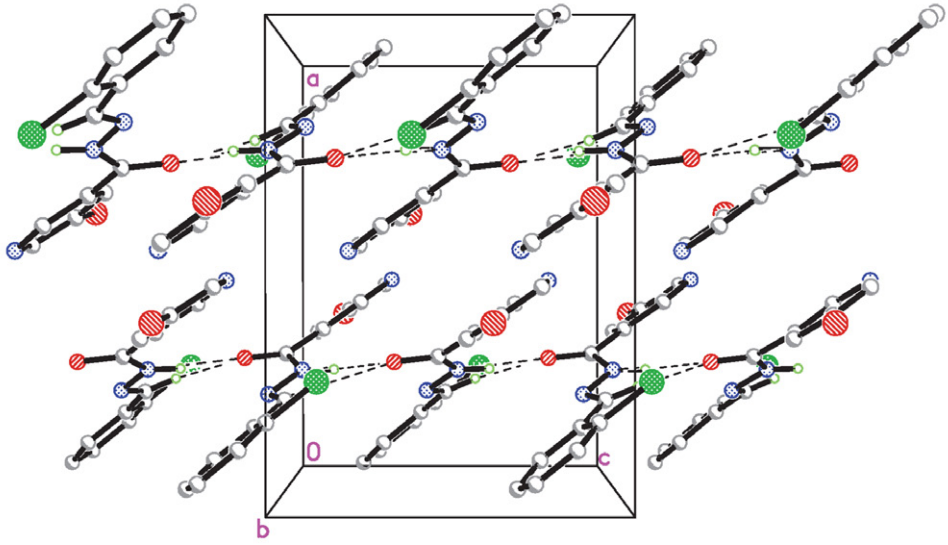


Figure 3. Molecular packing of **1**, viewed along the *b* axis. Hydrogen bonds are drawn as dashed lines.

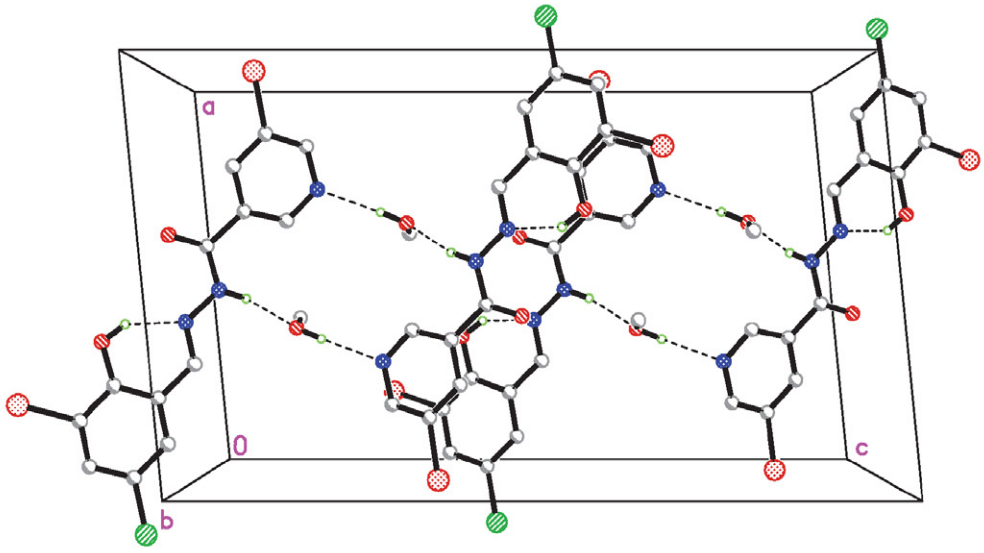


Figure 4. Molecular packing of **2**, viewed along the *b* axis. Hydrogen bonds are drawn as dashed lines.

The benzene ring and the pyridine ring form a dihedral angle of 6.4(4)° in **1** and 3.8(4)° in **2**.

In the crystal structure of **1**, the molecules are linked through hydrogen bonds of N2–H2···O1 and C7–H7···O1 (Table 3), generating one dimensional chains running along the *c*-axis direction (Figure 3). In the crystal structure of **2**, the adjacent two hydrazone molecules are linked by two methanol molecules through hydrogen bonds of N2–H2···O3 and O3–H3···N3 (Table 3), generating a dimer (Figure 4). In addition, in both compounds the presence of short π-electron ring – π-electron ring interactions with *Cg-Cg* distances < 6.0 Å and β < 60.0° that are specified in Table 4 was detected.[12]

3. 3. Antimicrobial Activity of the Compounds

The antimicrobial activities of the compounds against the organisms *Streptococcus pyogenes* (*S. pyogenes*), *Streptococcus agalactiae* (*S. agalactiae*), *Staphylococcus aureus* (*S. aureus*), *Bacillus anthracis* (*B. anthracis*), *Klebsiella pneumonia* (*K. pneumonia*) and *Pseudomonas aeruginosa* (*P. aeruginosa*) are summarized in Table 5. The results show that both compounds have effective antimicrobial activities against *S. pyogenes*, *S. agalactiae*, and *B. anthracis*, and have relatively poor or negative activities against other bacteria when compared to the Penicillin. Compounds **1** and **2** have similar activities against *S. agalactiae* and *B.*

anthracis. Interestingly, compound **2** has stronger activities against *S. pyogenes*, *K. pneumonia* and *P. aeruginosa* than compound **1**. This indicates that the Br and Cl substitunts are a good choice in the search for new antimicrobial agents. The activities of the nicotinohydrazone compounds in this work are stronger than the benzohydrazones with Br as substituent.[6a] The compounds are more active against *S. pyogenes*, *S. agalactiae*, *B. anthracis* and *P. aeruginosa* than the benzohydrazone compound with Br, NO_2 and Cl as the substituent.[13] Thus, the present compounds show promising activity against *S. pyogenes*, *S. agalactiae* and *B. anthracis*, which deserves further investigation for developing new antimicrobial drugs.

Table 5. Antimicrobial activities of the compounds as MIC values (μg/mL)

	1	**2**	**Penicillin**
S. pyogenes	32	16	230
S. agalactiae	8	8	65
S. aureus	> 1024	> 1024	250
B. anthracis	2	2	12
K. pneumonia	128	16	5
P. aeruginosa	256	64	> 1024

Acknowledgements

This work was supported by the applied research and development project of Ningxia Vocational Technical College of Industry and Commerce (nxgsyf201904).

4. References

1. (a) E. T. da Silva, G. F. de Andrade, A. D. da Silva, A. D. Almeida, E. S. Coimbra, M. V. N. de Souza, *Acta Parasitol.* **2020**, *65*, 203–207; **DOI:**10.2478/s11686-019-00146-5
(b) D. S. Cukierman, E. Accardo, R. G. Gomes, A. de Falco, M. C. Miotto, M. C. R. Freitas, M. Lanznaster, C. O. Fernandez, N. A. Rey, *J. Biol. Inorg. Chem.* **2018**, *23*, 1227–1241; **DOI:**10.1007/s00775-018-1606-0
(c) D. S. Cukierman, A. B. Pinheiro, S. L. P. Castineiras, A. S. P. da Silva, M. C. Miotto, A. de Falco, T. D. Ribeiro, S. Maisonette, A. L. M. C. da Cunha, R. A. Hauser-Davis, J. Landeira-Fermandez, R. Q. Aucelio, T. F. Outeiro, M. D. Pereira, C. O. Fernandez, N. A. Rey, *J. Inorg. Biochem.* **2017**, *170*, 160–168; **DOI:**10.1016/j.jinorgbio.2017.02.020
(d) D. S. Kalinowski, P. C. Sharpe, P. V. Bernhardt, D. R. Richardson, *J. Med. Chem.* **2008**, *51*, 331–344. **DOI:**10.1021/jm7012562
2. (a) S. H. Alotabi, *Arabian J. Chem.* **2020**, *13*, 4771–4784; **DOI:**10.1016/j.arabjc.2019.12.006
(b) S. A. Aly, S. K. Fathalla, *Arabian J. Chem.* **2020**, *13*, 3735–3750; **DOI:**10.1016/j.arabjc.2019.12.003
(c) S. Dasgupta, S. Karim, S. Banerjee, M. Saha, K. D. Saha, D. Das, *Dalton Trans.* **2020**, *49*, 1232–1240; **DOI:**10.1039/C9DT04636D
(d) M. X. Song, B. Liu, S. W. Yu, S. H. He, Y. Q. Liang, S. F. Li, Q. Y. Chen, X. Q. Deng, *Lett. Drug Des. Discov.* **2020**, *17*, 502–511; **DOI:**10.2174/1570180816666190731113441
(e) M. B. Muluk, A. S. Ubale, S. T. Dhumal, N. N. M. A. Rehman, P. P. Dixit, K. K. Kharat, P. B. Choudhari, K. P. Haval, *Synth. Commun.* **2019**, *50*, 243–255; **DOI:**10.1080/00397911.2019.1692870
(f) M. Cuccioloni, L. Bonfili, V. Cecarini, M. Nabissi, R. Pettinari, F. Marchetti, R. Petrelli, L. Cappellacci, M. Angeletti, A. M. Eleuteri, *ChemMedChem* **2019**, *15*, 105–113. **DOI:**10.1002/cmdc.201900551
3. (a) H.-Y. Liu, Y.-S. Yin, L.-J. Yang, X.-L. Zou, Y.-F. Ye, *Acta Chim. Slov.* **2020**, *67*, 130–136; **DOI:**10.17344/acsi.2019.5286
(b) Y. Tan, *Acta Chim. Slov.* **2019**, *66*, 1002–1009. **DOI:**10.17344/acsi.2019.5297
4. (a) C.-L. Zhang, X.-Y. Qiu, S.-J. Liu, *Acta Chim. Slov.* **2019**, *66*, 719–725; **DOI:**10.17344/acsi.2019.5241
(b) L.-H. Wang, X.-Y. Qiu, S.-J. Liu, *Acta Chim. Slov.* **2019**, *66*, 675–680; **DOI:**10.17344/acsi.2019.5117
(c) H.-Y. Qian, *Acta Chim. Slov.* **2019**, *66*, 995–1001. **DOI:**10.4149/neo_2019_190112N36
5. (a) E. D. Nunes, A. D. Villela, L. A. Basso, E. H. Teixeira, A. L. Andrade, M. A. Vasconcelos, L. G. D. Neto, A. C. S. Gondim, I. C. N. Diogenes, A. I. B. Romo, O. R. Nascimento, D. Zampieri, T. F. Paulo, I. M. M. de Carvalho, L. G. D. Lopes, E. H. S. Sousa, *Inorg. Chem. Front.* **2020**, *7*, 859–870; **DOI:**10.1039/C9QI01172B
(b) Y. Zou, Y. Zhang, L. W. Han, Q. X. He, H. R. Hou, J. A. Han, X. M. Wang, C. Y. Li, J. A. Cen, K. C. Liu, *J. Appl. Toxicol.* **2017**, *37*, 842–852; **DOI:**10.1002/jat.3432
(c) L. Negri, J. Le Grusse, P. Seraissol, M. Lavit, G. Houin, P. Gandia, *Therapie* **2014**, *69*, 509–516; **DOI:**10.2515/therapie/2014202
(d) N. Arshad, U. Yunus, S. Razzque, M. Khan, S. Saleem, B. Mirza, N. Rashid, *Eur. J. Med. Chem.* **2012**, *47*, 452–461. **DOI:**10.1016/j.ejmech.2011.11.014
6. (a) Z. F. Zhang, D. J. Chen, *CrystEngComm* **2020**, *22*, 1691–1694; **DOI:**10.1039/C9CE01978B
(b) M. Taha, N. H. Ismail, S. Imran, M. Selvaraj, A. Rahim, M. Ali, S. Siddiqui, F. Rahim, K. M. Khan, *Bioorg. Med. Chem.* **2015**, *23*, 7394–7404; **DOI:**10.1016/j.bmc.2015.10.037
(c) Q. Wang, K. J. Franz, *Bioorg. Med. Chem.* **2018**, *26*, 5962–5972. **DOI:**10.1016/j.bmc.2018.11.004
7. (a) M. Zhang, D.-M. Xian, H.-H. Li, J.-C. Zhang, Z.-L. You, *Aust. J. Chem.* **2012**, *65*, 343–350; **DOI:**10.1071/CH11424
(b) M. Gopalakrishnan, J. Thanusu, V. Kanagarajan, R. Govindaraju, *J. Enzym. Inhib. Med. Chem.* **2009**, *24*, 52–58; **DOI:**10.1080/14756360801906632
(c) L. Shi, H.-M. Ge, S.-H. Tan, H.-Q. Li, Y.-C. Song, H.-L. Zhu, R.-X. Tan, *Eur. J. Med. Chem.* **2007**, *42*, 558–564. **DOI:**10.1016/j.ejmech.2006.11.010
8. (a) H.-Y. Zhu, *Asian J. Chem.* **2012**, *24*, 558–560;
(b) H.-Y. Zhu, *Chinese J. Struct. Chem.* **2012**, *31*, 1075–1082;
(c) H.-Y. Zhu, *J. Chem. Crystallogr.* **2011**, *41*, 1785–1789.

DOI:10.1007/s10870-011-9982-0
9. G. M. Sheldrick, SADABS Program for Empirical Absorption Correction of Area Detector, University of Göttingen: Germany, **1996**.
10. G. M. Sheldrick, *Acta Crystallogr.* **2015**, *C71*, 3–8.
11. (a) V. Meenatchi, K. Muthu, M. Rajasekar, S. P. Meenakshisundaram, *Spectrochim. Acta A* **2014**, *124*, 423–428; **DOI:**10.1016/j.saa.2014.01.051
(b) B. Jeragh, M. S. Ali, A. A. El-Asmy, *Spectrochim. Acta A* **2015**, *145*, 295–301; **DOI:**10.1016/j.saa.2015.03.021
(c) N. Boonnak, S. Chantrapromma, P. Ruanwas, C. Sontimuang, H.-K. Fun, *Crystallogr. Rep.* **2017**, *62*, 1104–1108. **DOI:**10.1134/S1063774517070069
12. A. L. Spek, *Acta Crystallogr.* **2009**, *D65*, 148–155. **DOI:**10.1107/S090744490804362X
13. H.-Y. Zhu, *Chinese J. Struct. Chem.* **2011**, *30*, 724–730.

Povzetek

Pripravili smo dva nova predstavnika nikotinohidrazonov: 6-bromo-2'-(2-klorobenziliden)nikotinohidrazid (**1**) in 6-bromo-2'-(3-bromo-5-kloro-2-hidroksibenziliden)nikotinohidrazid metanolni solvat (**2**). Strukturi obeh produktov smo določili s spektroskopskimi metodami in z rentgensko difrakcijsko analizo monokristalov. Molekule obeh spojin imajo v azometinski skupini *E* konfiguracijo. Molekule v spojini **1** so povezane v enodimenzionalne verige vzdolž *c* osi z vodikovimi vezmi N–H···O. Hidrazonske molekule spojine **2** so z metanolnimi povezane v dimere preko vodikovih vezi N–H···O in O–H···N. Določitev *in vitro* antimikrobnih aktivnosti za ti dve spojini je pokazala, da bi lahko bili potencialno zanimivi antibakterijski učinkovini.

Except when otherwise noted, articles in this journal are published under the terms and conditions of the Creative Commons Attribution 4.0 International License

DOI: 10.17344/acsi.2020.6182 *Acta Chim. Slov.* **2021,** *68,* 72–87
creative commons

Scientific paper

New Approaches for the Synthesis of Heterocyclic Compounds Derived from Cyclohexan-1,3-dione with Anti-proliferative Activities

Rafat Milad Mohareb,[1] Yara Raafat Milad[2,3] and Ayat Ali Masoud[1]

[1] *Department of Chemistry, Faculty of Science, Cairo University, A. R. Egypt*

[2] *Jean Coutu, 531 Jarry Est, Montréal, Québec, Canada*

[3] *Department of Pharmaceutical Chemistry, Faculty of Pharmacy, Cairo University, Cairo, A. R. Egypt*

* *Corresponding author: E-mail: raafat_mohareb@yahoo.com*

Received: 06-11-2020

Abstract

In the present work a series of heterocyclization reactions were adopted using cyclohexan-1,3-dione through its reaction with either furan-2-carbaldehyde or thiophene-2-carbaldehyde to give the corresponding ylidene derivatives **3a**,**b**. The latter compounds underwent heterocyclization reactions to give thiophene and pyran derivatives **5a–d** and **6a–d**, respectively. Moreover, compounds **3a**,**b** reacted with elemental sulfur and phenyl isothiocyanate to give the fused thiazole derivatives **8a**,**b**. In addition, the reaction with either of hydrazine hydrate or phenylhydrazine has given the 4-hydrazono-4,5,6,7-tetrahydro-2*H*-indazole derivatives **10a–d**, respectively. Similarly, the reaction of either **3a** or **3b** with hydroxylamine hydrochloride gave the 6,7-dihydrobenzo[*c*]isoxazol-4(5*H*)-one oxime derivatives **12a** and **12b**, respectively. Other fused heterocyclic compounds were produced and their structures were elucidated. Evaluation of the synthesized compounds against selected cancer cell lines was performed. The most active compounds were further evaluated against tyrosine kinases and Pim-1 kinase inhibitions.

Keyword: Cyclohexan-1,3-dione, thiophene, pyrazole, isoxazole, cytotoxicity

1. Introduction

Within the last few years the synthesis of heterocyclic compounds attracted the attention due to the wide spectrum of their high biological activities. In addition, many compounds were considered as good synthons for fused systems that were characterized by different pharmaceutical applications.[1–10] Therefore, organic chemists have been making extensive efforts to produce heterocyclic compounds by developing new and efficient synthetic transformations. Within the field of pharmaceutical chemistry, many pyrazoles, thiophenes and thiazoles were reported with a wide spectrum of biological activities that included potent analgesic, anti-convulsant, anti-inflammatory and anti-bacterial, anti-pyretic, anti-tumor, anti-parasitic, anti-microbial, anti-histaminic (H1), anti-anexiety activities in tests in mice, anti-arrhythmic and as serotonin antagonists.[11–23] The present work is dealing with the current application of pyrazole, thiophene, pyrimidine and oxazine cores in the designing of anticancer agents within tumor progression. In our research it was possible to verify that such compounds are readily applicable to provide new insights and valuable inspiration in the research of new drugs and in their development as well as to contribute to the management of cancer. This encouraged our group to be attracted toward the synthesis of pyran derivatives research through the uses of b-diketones. The produced heterocyclic compounds showed high anti-proliferative activities against cancer cell lines together with high inhibitions toward tyrosine kinases.[24–26] Based on such importance of heterocyclic compounds, therefore, we studied the reaction of cyclohexane-1,3-dione with some heterocyclic aldehydes and cyanomethylene reagents followed by heterocyclization of the products. Additionally, the anti-tumor evaluations of the resulting compounds towards cancer cell lines are reported.

2. Experimental

2. 1. General

The melting points of the obtained compounds were determined using Electrothermal digital melting point apparatus and are uncorrected. IR spectra (KBr discs) were measured on an FTIR plus 460 or PyeUnicam SP-1000 spectrophotometer (PyeUnicam, UK, Cambridge). ^{1}H NMR spectra were obtained using Varian Gemini-300 (300 MHz, Varian UK) using DMSO-d_6 as the solvent and tetramethylsilane (TMS) as the internal standard; chemical shifts are expressed as δ ppm. The mass spectra were measured with Hewlett Packard 5988 A GC/MS system (Hewlett-Packard, Agilent, USA) instrument.

2. 1. 1. General Procedure for the Synthesis of the 2-Methylenecyclohexane-1,3-dione Derivatives 3a,b

Either of furan-2-carbaldehyde (0.96 g, 0.01 mol) of thiophene-2-carbaldehyde (1.12 g, 0.01 mol) was added to a solution of cyclohexane-1,3-dione (**1**) (1.12 g, 0.01 mol) in absolute ethanol (40 mL) containing piperdine (0.50 mL). The reaction mixture, in each case, was heated under reflux for 3 h then poured onto ice/water containing a few drops of hydrochloric acid and the formed solid product was collected by filtration.

2-(Furan-2-ylmethylene)cyclohexane-1,3-dione (3a)

Yellow crystals from ethanol, yield 1.46 g (77%), m.p. 185–188 °C. IR (KBr) ν_{max} (cm^{-1}) 3053 (CH, aromatic), 1704, 1687 (2 CO), 1632 (C=C); ^{1}H NMR (DMSO-d_6, 300 MHz) δ 1.45–1.69 (m, 2H, CH_2), 2.63–2.76 (m, 4H, $2CH_2$), 6.82 (s, 1H, CH), 6.80–7.83 (m, 3H, furan H); ^{13}C NMR (DMSO-d_6, 75 MHz) δ 16.4, 36.5, 39.2 ($3CH_2$), 112.4, 158.1 (C=CH), 135.8, 140.2, 142.6, 146.1 (furan C), 177.1, 179.4 (2CO). Anal. Calcd for $C_{11}H_{10}O_3$: C, 69.46; H, 5.30. Found: C, 69.31; H, 5.52. MS: *m/z* 190 (M^+, 28%).

2-(Thiophen-2-ylmethylene)cyclohexane-1,3-dione (3b)

Orange crystals from ethanol, yield 1.44 g (70%), m.p. 201–204 °C. IR (KBr) ν_{max} (cm^{-1}) 3055 (CH, aromatic), 1703, 1689 (2 CO), 1630 (C=C); ^{1}H NMR (DMSO-d_6, 200 MHz) δ 1.43–1.68 (m, 2H, CH_2), 2.61–2.74 (m, 4H, $2CH_2$), 6.80 (s, 1H, CH), 6.82–7.88 (m, 3H, thiophene H); ^{13}C NMR (DMSO-d_6, 75 MHz) δ 16.8, 36.2, 39.1 ($3CH_2$), 112.6, 158.8 (C=CH), 135.6, 140.5, 142.3, 146.2 (thiophene C), 177.6, 179.2 (2CO). Anal. Calcd for $C_{11}H_{10}O_2S$: C, 64.05; H, 4.89; S, 15.55. Found: C, 63.80; H, 4.73; 15.38. MS: *m/z* 206 (M^+, 32%).

2. 1. 2. General Procedure for the Synthesis of the 6,7-Dihydrobenzo[*b*]thiophen-5(4*H*)-one Derivatives 5a–d

Either malononitrile (0.66 g, 0.01 mol) or ethyl cyanoacetate (1.07 g, 0.01 mol) was added to a solution of either compound **3a** (1.90 g, 0.01 mol) or **3b** (2.06 g, 0.01 mol) in ethanol (40 mL) containing triethylamine (0.50 mL). The reaction mixture was heated under reflux for 3 h then poured onto ice/water mixture containing a few drops of hydrochloric acid and the formed solid product was collected by filtration.

2-Amino-4-(furan-2-ylmethylene)-5-oxo-4,5,6,7-tetrahydrobenzo[*b*]thiophene-3-carbonitrile (5a)

Pale yellow crystals from ethanol, yield 1.94 g (70%), m.p. 130–132 °C. IR (KBr) ν_{max} (cm^{-1}) 3482–3353 (NH_2), 3056 (CH, aromatic), 2220 (CN), 1686 (CO), 1630 (C=C); ^{1}H NMR (DMSO-d_6, 300 MHz) δ 2.62–2.78 (2t, 4H, $2CH_2$), 4.73 (s, 2H, D_2O exchangeable, NH_2), 6.84 (s, 1H, CH), 6.82–7.86 (m, 3H, furan H); ^{13}C NMR (DMSO-d_6, 75 MHz) δ 16.6, 36.3, 39.5 ($3CH_2$), 112.6, 158.4 (C=CH), 116.8 (CN), 135.4, 140.6, 141.4, 142.2, 142.7, 144.8, 145.6, 146.5 (thiophene, furan C), 179.3 (CO). Anal. Calcd for $C_{14}H_{10}N_2O_2S$: C, 62.21; H, 3.73; N, 10.36; S, 11.86. Found: C, 62.36; H, 3.80; N, 10.41; S, 12.04. MS: *m/z* 270 (M^+, 32%).

Ethyl 2-Amino-4-(furan-2-ylmethylene)-5-oxo-4,5,6,7-tetrahydrobenzo[*b*]thiophene-3-carboxylate (5b)

Yellow crystals from ethanol, yield 2.21 g (70%), m.p.125–127 °C. IR (KBr) ν_{max} (cm^{-1}) 3494–3368 (NH_2), 3058 (CH, aromatic), 2931, 2972 (CH_2, CH_3), 1689, 1688 (2 CO), 1630 (C=C); ^{1}H NMR (DMSO-d_6, 300 MHz) δ 1.12 (t, 3H, J = 7.28 Hz, CH_3), 2.68–2.74 (2t, 4H, $2CH_2$), 4.21 (q, 2H, J = 7.28 Hz, CH_2), 4.76 (s, 2H, D_2O exchangeable, NH_2), 6.86 (s, 1H, CH), 6.84–7.92 (m, 3H, furan H); ^{13}C NMR (DMSO-d_6, 75 MHz) δ 16.3 ($OCH_2\underline{CH_3}$), 16.4, 36.8, 39.3 ($3CH_2$), 52.8 ($O\underline{CH_2}CH_3$), 112.3, 158.6 (C=CH), 135.6, 18.0, 140.8, 141.6, 142.3, 143.5, 144.2, 146.7 (thiophene, furan C), 164.8, 178.3 (2CO). Anal. Calcd for $C_{16}H_{15}NO_4S$: C, 60.55; H, 4.76; N, 4.41; S, 10.10. Found: C, 60.80; H, 4.83; N, 4.60; S, 10.26. MS: *m/z* 317 (M^+, 38%).

2-Amino-5-oxo-4-(thiophen-2-ylmethylene)-4,5,6,7-tetrahydrobenzo[*b*]thiophene-3-carbonitrile (5c)

Orange crystals from ethanol, yield 1.94 g (68%), m.p. 202–205 °C. IR (KBr) ν_{max} (cm^{-1}) 3459–3342 (NH_2), 3058 (CH, aromatic), 2221 (CN), 1688 (CO), 1630 (C=C); ^{1}H NMR (DMSO-d_6, 300 MHz) δ 2.64–2.75 (2t, 4H, $2CH_2$), 4.74 (s, 2H, D_2O exchangeable, NH_2), 6.88 (s, 1H, CH), 6.80–7.87 (m, 3H, thiophene H); ^{13}C NMR (DMSO-d_6, 75 MHz) δ 16.3, 39.8 ($2CH_2$), 112.3, 158.8 (C=CH), 116.9 (CN), 134.2, 138.6, 140.3, 142.4, 143.1, 143.6, 145.2, 146.7 (two thiophene C), 179.8 (CO). Anal. Calcd for $C_{14}H_{10}N_2OS_2$: C, 58.72; H, 3.52; N, 9.78; S, 22.39. Found: C, 58.36; H, 3.80; N, 9.68; S, 22.41. MS: *m/z* 286 (M^+, 46%).

Ethyl 2-Amino-5-oxo-4-(thiophen-2-ylmethylene)-4,5,6,7-tetrahydrobenzo[*b*]thiophene-3-carboxylate (5d)

Pale yellow crystals from ethanol, yield 2.13 g (66%), m.p. 189–192 °C. IR (KBr) ν_{max} (cm^{-1}) 3486–3342 (NH_2), 3054 (CH, aromatic), 2938, 2893 (CH_2, CH_3), 1689, 1686 (2

CO), 1630 (C=C); ^{1}H NMR (DMSO-d_6, 300 MHz) δ 1.13 (t, 3H, J = 7.59 Hz, CH_3), 2.64–2.78 (2t, 4H, $2CH_2$), 4.23 (q, 2H, J = 7.59 Hz, CH_2), 4.79 (s, 2H, D_2O exchangeable, NH_2), 6.84 (s, 1H, CH), 7.29–7.85 (m, 3H, thiophene H); ^{13}C NMR (DMSO-d_6, 75 MHz) δ 16.1 ($OCH_2\underline{CH_3}$), 16.5, 36.4, 39.7 ($3CH_2$), 52.3 ($O\underline{CH_2}CH_3$), 112.1, 158.4 (C=CH), 135.3, 136.7, 138.3, 140.5, 141.5, 142.0, 143.8, 144.6, 146.8 (two thiophene C), 164.5, 178.9 (2CO). Anal. Calcd for $C_{16}H_{15}NO_3S_2$: C, 57.64; H, 4.53; N, 4.20; S, 19.23. Found: C, 57.80; H, 4.71; N, 4.38; S, 19.46. MS: *m/z* 333 (M^+, 26%).

2. 1. 3. General Procedure for the Synthesis of the 2*H*-Chromen-5-one Derivatives 6a–d

Either malononitrile (0.66 g, 0.01 mol) or ethyl cyanoacetate (1.13 g, 0.01 mol) was added to a solution of either compound **3a** (1.90 g, 0.01 mol) or **3b** (2.06 g, 0.01 mol) in absolute ethanol (40 mL) containing triethylamine (1.0 mL). The reaction mixture, in each case, was heated under reflux for 3 h then the excess solvent was removed under vacuum. The remaining product was triturated with diethyl ether and the formed solid product was collected by filtration.

2-Amino-4-(furan-2-yl)-5-oxo-5,6,7,8-tetrahydro-2*H*-chromene-3-carbonitrile (6a)

Pale yellow crystals from ethanol, yield 1.66 g (69%), m.p. 194–196 °C. IR (KBr) ν_{max} (cm^{-1}) 3470–3328 (NH_2), 3055 (CH, aromatic), 2220 (CN), 1632 (C=C); ^{1}H NMR (DMSO-d_6, 300 MHz) δ 1.41–1.66 (m, 4H, $2CH_2$), 2.61–2.76 (m, 4H, $2CH_2$), 4.71 (s, 2H, D_2O exchangeable, NH_2), 6.04 (s, 1H, pyran H-4), 6.87–7.83 (m, 3H, furan H); ^{13}C NMR (DMSO-d_6, 75 MHz) δ 16.1, 36.3, 37.2, 39.5 ($4CH_2$), 116.8 (CN), 134.3, 141.5, 141.8, 142.6, 1431.4, 143.8, 145.2, 146.4 (pyran, furan C), 178.4 (CO). Anal. Calcd for $C_{14}H_{14}N_2O_2$: C, 69.41; H, 5.82; N, 11.56. Found: C, 69.38; H, 5.92; N, 11.29. MS: *m/z* 242 (M^+, 28%).

4-(Furan-2-yl)-2-hydroxy-5-oxo-5,6,7,8-tetrahydro-4*H*-chromene-3-carbonitrile (6b)

Pale brown crystals from ethanol, yield 1.79 g (74%), m.p. 198–200 °C. IR (KBr) ν_{max} (cm^{-1}) 3568–3339 (OH), 3055 (CH, aromatic), 2222 (CN), 1630 (C=C); ^{1}H NMR (DMSO-d_6, 300 MHz) δ 1.32–1.68 (m, 4H, $2CH_2$), 2.63–2.74 (m, 4H, $2CH_2$), 6.02 (s, 1H, pyran H-4), 6.84–7.85 (m, 3H, furan H), 9.80 (s, 1H, D_2O exchangeable, OH); ^{13}C NMR (DMSO-d_6, 75 MHz) δ 16.3, 36.5, 37.1, 39.3 ($4CH_2$), 116.7 (CN), 134.1, 138.0, 140.2, 141.7, 142.3, 142.9, 143.3, 146.6 (furan, pyran C). Anal. Calcd for $C_{14}H_{13}NO_3$: C, 69.12; H, 5.39; N, 5.76. Found: C, 68.92; H, 5.42; N, 5.58. MS: *m/z* 243 (M^+, 36%).

2-Amino-4-(thiophen-2-yl)-5,6,7,8-tetrahydro-4*H*-chromene-3-carbonitrile (6c)

Brown crystals from ethanol, yield 1.85 g (72%), m.p. 211–214 °C. IR (KBr) ν_{max} (cm^{-1}) 3445–3372 (NH_2), 3055 (CH, aromatic), 2220 (CN), 1630 (C=C); ^{1}H NMR (DMSO-d_6, 200 MHz) δ 1.41–1.64 (m, 4H, $2CH_2$), 2.61–2.77 (m, 4H, $2CH_2$), 4.73 (s, 2H, D_2O exchangeable, NH_2), 6.07 (s, 1H, thiophene H-4), 6.91–7.73 (m, 3H, thiophene H); ^{13}C NMR (DMSO-d_6, 75 MHz) δ 16.3, 36.6, 37.2, 39.8 ($4CH_2$), 116.4 (CN), 134.6, 138.7, 140.2, 141.6, 142.3, 142.8, 143.6, 146.2 (thiophene, pyran C). Anal. Calcd for $C_{14}H_{14}N_2O_2S$: C, 65.09; H, 5.46; N, 10.84; S, 12.41. Found: C, 64.90; H, 5.62; N, 10.68; S, 12.58. MS: *m/z* 258 (M^+, 40%).

2-Hydroxy-4-(thiophen-2-yl)-5,6,7,8-tetrahydro-4*H*-chromene-3-carbonitrile (6d)

Orange crystals from ethanol, yield 1.96 g (76%), m.p. 177–179 °C. IR (KBr) ν_{max} (cm^{-1}) 3542–3329 (OH), 3055 (CH, aromatic), 2220 (CN), 1688 (CO), 1630 (C=C); ^{1}H NMR (DMSO-d_6, 300 MHz) δ 1.34–1.66 (m, 4H, $2CH_2$), 2.61–2.76 (m, 4H, $2CH_2$), 6.04 (s, 1H, pyran H-4), 6.76–7.89 (m, 3H, furan H), 9.83 (s, 1H, D_2O exchangeable, OH); ^{13}C NMR (DMSO-d_6, 75 MHz) δ 16.1, 36.3, 37.4, 39.6 ($4CH_2$), 116.9 (CN), 134.4, 139.2, 140.8, 141.5, 143.7, 144.3, 145.2, 146.8 (furan, pyran C), 178.6 (CO). Anal. Calcd for $C_{14}H_{13}NO_2S$: C, 64.84; H, 5.05; N, 5.40; S, 12.36. Found: C, 64.72; H, 5.24; N, 12.59. MS: *m/z* 259 (M^+, 42%).

2. 1. 4. General Procedure for the Synthesis of 2-Thioxohexahydrobenzo[*d*]thiazole Derivatives 8a,b

Each of elemental sulfur (0.32 g, 0.01 mol) and phenyl isothiocyanate (1.30 g, 0.01 mol) were added to a solution of either compound **3a** (1.90 g, 0.01 mol) or **3b** (2.06 g, 0.01 mol) in 1,4-dioxane (40 mL) containing triethylamine (1.0 mL). The reaction mixture was heated under reflux for 2 h then was left to cool and the formed solid product, in each case, was collected by filtration.

4-(Furan-2-ylmethylene)-3-phenyl-2-thioxo-2,3,6,7-tetrahydrobenzo[*d*]thiazol-5(4*H*)-one (8a)

Yellow crystals from ethanol, yield 2.50 g (74%), m.p. 168–169 °C. IR (KBr) ν_{max} (cm^{-1}) 3055 (CH, aromatic), 1688 (CO), 1630 (C=C), 1205 (C=S); ^{1}H NMR (DMSO-d_6, 300 MHz) δ 2.63–2.78 (2t, 4H, $2CH_2$), 6.87 (s, 1H, CH), 6.82–7.85 (m, 8H, C_6H_5, furan H); ^{13}C NMR (DMSO-d_6, 75 MHz) δ 16.1, 36.6, 39.5 ($3CH_2$), 112.1, 158.4 (C=CH), 120.3, 122.6, 124.8, 127.2, 134.6, 140.8, 142.2, 143.2, 143.8, 146.9 (C_6H_5, furan, thiazole C), 179.6 (CO), 181.3 (C=S). Anal. Calcd for $C_{18}H_{13}NO_2S_2$: C, 63.69; H, 3.86; N, 4.13; S, 18.89. Found: C, 63.80; H, 3.69; N, 4.32; S, 19.18. MS: *m/z* 339 (M^+, 48%).

3-Phenyl-4-(thiophen-2-ylmethylene)-2-thioxo-2,3,6,7-tetrahydrobenzo[*d*]thiazol-5(4*H*)-one (8b)

Pale yellow crystals from 1,4-dioxane, yield 2.84 g (80%), m.p. 222–225 °C. IR (KBr) ν_{max} (cm^{-1}) 3055 (CH, aromatic), 1689 (CO), 1630 (C=C), 1205 (C=S); ^{1}H NMR (DMSO-d_6, 300 MHz) δ 2.61–2.79 (2t, 4H, $2CH_2$), 6.88 (s, 1H, CH), 6.96–7.89 (m, 8H, C_6H_5, thiophene H); ^{13}C

NMR (DMSO-d_6, 75 MHz) δ 16.5, 39.7 ($2CH_2$), 112.4, 158.6 (C=CH), 120.7, 122.5, 124.3, 126.8, 136.2, 140.6, 141.3, 142.6, 143.4, 146.6 (C_6H_5, thiophene, thiazole C), 179.3 (CO), 181.3 (C=S). Anal. Calcd for $C_{18}H_{13}NOS_3$: C, 60.81; H, 3.69; N, 3.94; S, 27.06. Found: C, 60.69; H, 3.74; N, 4.12; S, 26.86. MS: *m/z* 355 (M^+, 59%).

2. 1. 5. General Procedure for the Synthesis of the 4-Hydrazono-4,5,6,7-tetrahydro-2*H*-indazole Derivatives 10a–d

Either hydrazine hydrate (0.1 mL, 0.02 mol) or phenylhydrazine (2.16 g, 0.02 mol) was added to a solution of either of compound **3a** (1.90 g, 0.01 mol) or **3b** (2.06 g, 0.01 mol) in 1,4-dioxane (40 mL). The reaction mixture was heated under reflux for 3 h then poured onto ice/water mixture containing a few drops of hydrochloric acid and the formed solid product was collected by filtration.

3-(Furan-2-yl)-4-hydrazono-4,5,6,7-tetrahydro-2*H*-indazole (10a)

Yellow crystals from ethanol, yield 1.55 g (72%), m.p. 158–161 °C. IR (KBr) ν_{max} (cm^{-1}) 3472–3328 (NH, NH_2), 3055 (CH, aromatic), 1658 (exocyclic C=N), 1630 (C=C); ^{1}H NMR (DMSO-d_6, 300 MHz) δ 1.32–1.64 (m, 2H, CH_2), 2.60–2.78 (m, 4H, $2CH_2$), 4.86 (s, 2H, D_2O exchangeable, NH_2), 7.14–7.84 (m, 3H, furan H), 8.28 (s, 1H, D_2O exchangeable, NH); ^{13}C NMR (DMSO-d_6, 75 MHz) δ 16.5, 36.3, 39.7 ($3CH_2$), 112.4, 158.6 (C=CH), 136.4, 138.0, 139.2, 140.3, 143.8, 146.2 (furan, pyrazole C), 168.3, 172.8 (2C=N). Anal. Calcd for $C_{11}H_{12}N_4O$: C, 61.10; H, 5.59; N, 25.91. Found: C, 60.93; H, 5.29; N, 25.77. MS: *m/z* 216 (M^+, 36%).

3-(Furan-2-yl)-2-phenyl-4-(2-phenylhydrazono)-4,5,6,7-tetrahydro-2*H*-indazole (10b)

Pale yellow crystals from 1,4-dioxane, yield 2.50 g (68%), m.p. 177–180 °C. IR (KBr) ν_{max} (cm^{-1}) 3463–3341 (NH), 3055 (CH, aromatic), 1652 (exocyclic C=N), 1630 (C=C); ^{1}H NMR (DMSO-d_6, 300 MHz) δ 1.31–1.67 (m, 2H, CH_2), 2.63–2.77 (m, 4H, $2CH_2$), 7.26–7.89 (m, 13H, $2C_6H_5$, furan H), 8.30 (s, 1H, D_2O exchangeable, NH); ^{13}C NMR (DMSO-d_6, 75 MHz) δ 16.2, 36.1, 39.4 ($3CH_2$), 120.2, 121.6, 123.2, 123.8, 124.0, 126.3, 128.3, 1290.1, 136.4, 140.3, 140.8, 141.2, 143.4, 146.8 ($2C_6H_5$, pyrazole, furan C), 176.2, 178.3 (2C=N). Anal. Calcd for $C_{23}H_{20}N_4O$: C, 74.98; H, 5.47; N, 15.21. Found: C, 75.19; H, 5.31; N, 15.02. MS: *m/z* 368 (M^+, 41%).

4-Hydrazono-3-(thiophen-2-yl)-4,5,6,7-tetrahydro-2*H*-indazole (10c)

Pale yellow crystals from 1,4-dioxane, yield 1.76 g (76%), m.p. 233–236 °C. IR (KBr) ν_{max} (cm^{-1}) 3458–3342 (NH, NH_2), 3055 (CH, aromatic), 1656 (exocyclic C=N), 1630 (C=C); ^{1}H NMR (DMSO-d_6, 300 MHz) δ 1.33–1.67 (m, 2H, CH_2), 2.62–2.75 (m, 4H, $2CH_2$), 4.80 (s, 2H, D_2O exchangeable, NH_2), 6.96–7.88 (m, 3H, thiophene H), 8.28 (s, 1H, D_2O exchangeable, NH); ^{13}C NMR (DMSO-d_6, 75 MHz) δ 16.5, 36.3, 39.7 ($3CH_2$), 112.4, 158.6 (C=CH), 136.6, 138.4, 139.2, 140.1, 143.5, 146.4 (thiphene, pyrazole C), 176.4, 178.6 (2C=N). Anal. Calcd for $C_{11}H_{12}N_4S$: C, 56.87; H, 5.21; N, 24.12; S, 13.80. Found: C, 56.93; H, 5.30; N, 24.31; S, 13.98. MS: *m/z* 232 (M^+, 28%).

2-Phenyl-4-(2-phenylhydrazono)-3-(thiophen-2-yl)-4,5,6,7-tetrahydro-2*H*-indazole (10d)

Orange crystals from ethanol, yield 2.61 g (68%), m.p. 180–184 °C. IR (KBr) ν_{max} (cm^{-1}) 3484–3326 (NH), 3055 (CH, aromatic), 1655 (exocyclic C=N), 1630 (C=C); ^{1}H NMR (DMSO-d_6, 300 MHz) δ 1.32–1.69 (m, 2H, CH_2), 2.60–2.78 (m, 4H, $2CH_2$), 7.23–7.85 (m, 13H, $2C_6H_5$, thiophene H), 8.29 (s, 1H, D_2O exchangeable, NH); ^{13}C NMR (DMSO-d_6, 75 MHz) δ 16.4, 36.6, 39.4 ($3CH_2$), 120.8, 122.2, 123.6, 123.9, 125.8, 126.6, 128.1, 129.7, 135.8, 140.6, 142.6, 142.9, 143.1, 146.5 ($2C_6H_5$, pyrazole, thiophene C), 176.4, 178.6 (2C=N). Anal. Calcd for $C_{23}H_{20}N_4S$: C, 71.85; H, 5.24; N, 14.57; S, 8.34. Found: C, 72.13; H, 5.42; N, 14.38; S, 8.62. MS: *m/z* 384 (M^+, 26%).

2. 1. 6. General Procedure for the Synthesis of the 6,7-Dihydrobenzo[*c*]isoxazol-4(5*H*)-one Oxime Derivatives 12a,b

Hydroxylamine hydrochloride (1.40 g, 0.02 mol) was added to a solution of either compound **3a** (1.90 g, 0.01 mol) or **3b** (2.06 g, 0.01 mol) in 1,4-dioxane (40 mL) containing sodium acetate (2.0 g). The reaction mixture was heated under reflux for 3 h then poured onto ice/water mixture and the formed solid product, in each case, was collected by filtration.

3-(Furan-2-yl)-6,7-dihydrobenzo[*c*]isoxazol-4(5*H*)-one Oxime (12a)

Yellow crystals from 1,4-dioxane, yield 1.52 g (70%), m.p. 177–180 °C. IR (KBr) ν_{max} (cm^{-1}) 3524–3376 (OH), 3055 (CH, aromatic), 1655 (exocyclic C=N), 1630 (C=C); ^{1}H NMR (DMSO-d_6, 300 MHz) δ 1.31–1.68 (m, 2H, CH_2), 2.63–2.77 (m, 4H, $2CH_2$), 6.93–7.81 (m, 3H, furan H), 10.29 (s, 1H, D_2O exchangeable, OH); ^{13}C NMR (DMSO-d_6, 75 MHz) δ 16.2, 36.3, 39.2 ($3CH_2$), 132.3, 135.1, 140.6, 141.5, 142.8, 143.6 (isoxazole, furan C), 176.1, 178.4 (2C=N). Anal. Calcd for $C_{11}H_{10}N_2O_3$: C, 60.55; H, 4.62; N, 12.84. Found: C, 60.39; H, 4.80; N, 12.93. MS: *m/z* 218 (M^+, 32%).

3-(Thiophen-2-yl)-6,7-dihydrobenzo[*c*]isoxazol-4(5*H*)-one Oxime (12b)

Pale yellow crystals from 1,4-dioxane, yield 1.52 g (65%), m.p. 222–225 °C. IR (KBr) ν_{max} (cm^{-1}) 3551–3349 (OH), 3055 (CH, aromatic), 1653 (exocyclic C=N), 1630 (C=C); ^{1}H NMR (DMSO-d_6, 300 MHz) δ 1.32–1.65 (m, 2H, CH_2), 2.61–2.74 (m, 4H, $2CH_2$), 7.22–7.80 (m, 3H,

thiophene H), 10.29 (s, 1H, D_2O exchangeable, OH); ^{13}C NMR (DMSO-d_6, 75 MHz) δ 16.4, 36.6, 39.8 ($3CH_2$), 132.1, 134.3, 138.8, 140.9, 141.6, 144.2 (isoxazole, thiophene C), 176.0, 178.6 (2C=N). Anal. Calcd for $C_{11}H_{10}N_2O_2S$: C, 56.39; H, 4.30; N, 11.96; S, 13.69. Found: C, 56.42; H, 4.49; N, 12.05; S, 13.83 MS: *m/z* 234 (M^+, 42%).

2. 1. 7. 2-(Ethoxymethylene)cyclohexane-1,3-dione (14)

Ethyl orthoformate (1.68 g, 0.01 mol) was added to a solution of cyclohexan-1,3-dione (1.12 g, 0.01 mol) in acetic acid (40 mL). The reaction mixture was heated under reflux for 2 h then evaporated in vacuum and the remaining product was triturated with ethanol and the formed solid product was collected by filtration.

Yellow crystals from ethanol, yield 1.27 g (76%), m.p. 282–258 °C. IR (KBr) ν_{max} (cm^{-1}) 2980 (CH_2), 1689, 1686 (CO), 1632 (C=C); ^1H NMR (DMSO-d_6, 300 MHz) δ 1.28 (t, 3H, *J* = 6.83 Hz, CH_3), 1.49–1.67 (m, 2H, CH_2), 2.65–2.73 (m, 4H, $2CH_2$), 3.89 (q, 2H, *J* = 6.83 Hz, CH_2), 6.79 (s, 1H, CH); ^{13}C NMR (DMSO-d_6, 75 MHz) δ 16.3 ($OCH_2\underline{CH_3}$), 16.2, 36.8, 39.0 ($3CH_2$), 62.8 ($O\underline{CH_2}CH_3$), 112.3, 158.2 (C=CH), 177.3, 179.2 (2CO). Analysis Calcd for $C_9H_{12}O_3$ (168.19): C, 64.27; H, 7.19%. Found: C, 64.08; H, 7.33%. MS: *m/z* 168 (M^+, 22%).

2. 1. 8. General Procedure for the Synthesis of the 2-(Aminomethylene)cyclohexane-1,3-dione Derivatives 16a–c

Equimolar amounts of aniline (0.93 g, 0.01 mol), 4-methylaniline (1.08 g, 0.01 mol) or 4-methoxyaniline (1.34 g, 0.01 mol) and compound **14** (1.68 g, 0.01 mol) in 1,4-dioxane (50 mL) were refluxed for 4 h. The reaction mixture was evaporated under vacuum and the remaining product was triturated with ethanol and the solid product formed, in each case, was collected by filtration.

2-((Phenylamino)methylene)cyclohexane-1,3-dione (16a)

Yellow crystals from ethanol, yield 1.24 g (58%), m.p. 165–167 °C. IR (KBr) ν_{max} (cm^{-1}) 3480–3363 (NH), 3055 (CH aromatic), 2980 (CH_2), 1688, 1686 (2CO), 1632 (C=C); ^1H NMR (DMSO-d_6, 300 MHz) δ 1.42–1.69 (m, 2H, CH_2), 2.63–2.75 (m, 4H, $2CH_2$), 6.05 (s, 1H, CH), 7.28–7.39 (s, 5H, C_6H_5), 8.28 (s, 1H, D_2O exchangeable, NH); ^{13}C NMR (DMSO-d_6, 75 MHz) δ 16.5, 36.8, 39.4 ($3CH_2$), 94.3 (CH), 120.3, 123.1, 124.8, 126.4 (C_6H_5), 177.1, 179.8 (2CO). Anal. Calcd for $C_{13}H_{13}NO_2$ (215.25): C, 72.54; H, 6.09; N, 6.51%. Found: C, 72.31; H, 6.29; N, 6.38%.%. MS: *m/z* 215 (M^+, 35%).

2-((Phenylamino)methylene)cyclohexane-1,3-dione (16b)

Yellow crystals from ethanol, yield 1.67 g (73%), m.p. 214–217 °C. IR (KBr) ν_{max} (cm^{-1}) 3459–3341 (NH), 3054 (CH aromatic), 2982, 2886 (CH_3, CH_2), 1688, 1686 (2CO), 1631 (C=C); ^1H NMR (DMSO-d_6, 300 MHz) δ 1.43–1.67 (m, 2H, CH_2), 2.61–2.76 (m, 4H, $2CH_2$), 2.88 (s, 3H, CH_3), 6.08 (s, 1H, CH), 7.24–7.45 (s, 4H, C_6H_4), 8.26 (s, 1H, D_2O exchangeable, NH); ^{13}C NMR (DMSO-d_6, 75 MHz) δ 16.3, 36.6, 39.5 ($3CH_2$), 23.8 (CH_3), 90.6 (CH), 120.8, 122.9, 123.4, 127.9 (C_6H_4), 177.3, 179.5 (2CO). Analysis Calcd for $C_{14}H_{15}NO_2$ (229.27): C, 73.34; H, 6.59; N, 6.11%. Found: C, 73.29; H, 6.41; N, 6.26%. MS: *m/z* 229 (M^+, 40%).

2-(((4-Methoxyphenyl)amino)methylene)cyclohexane-1,3-dione (16c)

Yellow crystals from 1,4-dioxane, yield 1.47 g (60%), m.p. 193–196 °C. IR (KBr) ν_{max} (cm^{-1}) 3463–3329 (NH), 3055 (CH aromatic), 2982, 2886 (CH_3, CH_2), 1689, 1686 (2CO), 1630 (C=C); ^1H NMR (DMSO-d_6, 300 MHz) δ 1.41–1.69 (m, 2H, CH_2), 2.61–2.78 (m, 4H, $2CH_2$), 3.68 (s, 3H, OCH_3), 6.06 (s, 1H, CH), 7.27–7.48 (s, 4H, C_6H_4), 8.28 (s, 1H, D_2O exchangeable, NH); ^{13}C NMR (DMSO-d_6, 75 MHz) δ 16.3, 36.6, 39.5 ($3CH_2$), 50.3 (OCH_3), 90.2 (CH), 120.3, 122.4, 125.6, 128.7 (C_6H_4), 177.1, 179.3 (2CO). Analysis Calcd for $C_{14}H_{15}NO_3$ (245.27): C, 68.56; H, 6.16; N, 5.71%. Found: C, 68.80; H, 6.24; N, 5.93%. MS: *m/z* 245 (M^+, 38%).

2. 1. 9. General Procedure for the Synthesis of the 6,7-Dihydrobenzo[*b*]thiophen-5(4*H*)-one Derivatives 17a–f

Either malononitrile (0.66 g, 0.01 mol) or ethyl cyanoacetate (1.07 g, 0.01 mol) was added to a solution of either compound **16a** (2.15 g, 0.01 mol), **16b** (2.29 g, 0.01 mol) or **16c** (2.45 g, 0.01 mol) in ethanol (40 mL) containing triethylamine (0.50 mL). The reaction mixture was heated under reflux for 3 h then poured onto ice/water mixture containing a few drops of hydrochloric acid and the formed solid product was collected by filtration.

2-Amino-5-oxo-4-((phenylamino)methylene)-4,5,6,7-tetrahydrobenzo[*b*]thiophene-3-carbonitrile (17a)

Pale yellow crystals from ethanol, yield 2.06 g (70%), m.p. 127–129 °C. IR (KBr) ν_{max} (cm^{-1}) 3472–3353 (NH_2, NH), 3055 (CH, aromatic), 2220 (CN), 1686 (CO), 1630 (C=C); ^1H NMR (DMSO-d_6, 300 MHz) δ 2.60–2.79 (2t, 4H, $2CH_2$), 4.78 (s, 2H, D_2O exchangeable, NH_2), 6.89 (s, 1H, CH), 7.26–7.42 (m, 5H, C_6H_5), 8.39 (s, 1H, D_2O exchangeable, NH); ^{13}C NMR (DMSO-d_6, 75 MHz) δ 36.0, 39.8 ($2CH_2$), 112.2, 158.4 (C=CH), 116.8 (CN), 121.6, 122.4, 124.8, 127.2, 132.7, 134.2, 138.0, 142.6 (C_6H_5, thiophene C), 179.6 (CO). Anal. Calcd for $C_{16}H_{13}N_3OS$: C, 65.06; H, 4.44; N, 14.23; S, 10.86. Found: C, 65.18; H, 4.60; N, 14.19; S, 11.17. MS: *m/z* 295 (M^+, 38%).

Ethyl 2-Amino-5-oxo-4-((phenylamino)methylene)-4,5,6,7-tetrahydrobenzo[*b*]thiophene-3-carboxylate (17b)

Yellow crystals from ethanol, yield 2.18 g (64%), m.p. 96–98 °C. IR (KBr) ν_{max} (cm^{-1}) 3486–3351 (NH_2), 3058

(CH, aromatic), 2930, 2972 (CH_2, CH_3), 1689, 1686 (2 CO), 1630 (C=C); ^{1}H NMR (DMSO-d_6, 300 MHz) δ 1.13 (t, 3H, *J* = 7.08 Hz, CH_3), 2.68–2.76 (2t, 4H, $2CH_2$), 4.22 (q, 2H, *J* = 7.08 Hz, CH_2), 4.77 (s, 2H, D_2O exchangeable, NH_2), 6.86 (s, 1H, CH), 7.22–7.40 (m, 5H, C_6H_5), 8.33 (s, 1H, D_2O exchangeable, NH); ^{13}C NMR (DMSO-d_6, 75 MHz) δ 16.3 ($OCH_2\underline{CH_3}$), 36.8, 39.6 ($2CH_2$), 52.5 ($O\underline{CH_2}CH_3$), 112.4, 158.8 (C=CH), 121.3, 123.6, 125.2, 126.8, 132.9, 133.3, 138.0, 142.7 (C_6H_5, thiohene C), 164.2, 179.8 (2CO). Anal. Calcd for $C_{18}H_{18}N_2O_3S$: C, 63.14; H, 5.30; N, 8.18; S, 9.36. Found: C, 62.91; H, 5.49; N, 8.25; S, 9.60. MS: *m/z* 342 (M^+, 27%).

2-Amino-5-oxo-4-((*p*-tolylamino)methylene)-4,5,6,7-tetrahydrobenzo-[*c*]thiophene-3-carbonitrile (17c)

Orange crystals from 1,4-dioxane, yield 2.31 g (75%), m.p. 177–179 °C. IR (KBr) ν_{max} (cm^{-1}) 3493–3323 (NH_2, NH), 3055 (CH, aromatic), 2220 (CN), 1688 (CO), 1630 (C=C); ^{1}H NMR (DMSO-d_6, 300 MHz) δ 2.62–2.77 (2t, 4H, $2CH_2$), 2.79 (s, 3H, CH_3), 4.77 (s, 2H, D_2O exchangeable, NH_2), 6.82 (s, 1H, CH), 7.28–7.46 (m, 4H, C_6H_4), 8.37 (s, 1H, D_2O exchangeable, NH); ^{13}C NMR (DMSO-d_6, 75 MHz) δ 36.0, 39.6 ($2CH_2$), 24.3 (CH_3), 112.0, 158.6 (C=CH), 116.9 (CN), 120.3, 123.7, 124.8, 128.9, 132.9, 134.7, 138.3, 142.2 (C_6H_4, thiophene C), 179.3 (CO). Anal. Calcd for $C_{17}H_{15}N_3OS$: C, 66.00; H, 4.89; N, 13.58; S, 10.36. Found: C, 65.85; H, 4.91; N, 13.70; S, 10.42. MS: *m/z* 309 (M^+, 24%).

Ethyl 2-Amino-5-oxo-4-((*p*-tolylamino)methylene)-4,5,6,7-tetrahydrobenzo[*b*]thiophene-3-carboxylate (17d)

Brown crystals from 1,4-dioxane, yield 2.45 g (69%), m.p. 203–206 °C. IR (KBr) ν_{max} (cm^{-1}) 3459–3337 (NH_2), 3055 (CH, aromatic), 2930, 2970 (CH_2, CH_3), 1689, 1687 (2 CO), 1630 (C=C); ^{1}H NMR (DMSO-d_6, 300 MHz) δ 1.12 (t, 3H, *J* = 6.59 Hz, CH_3), 2.65–2.78 (2t, 4H, $2CH_2$), 2.80 (s, 3H, CH_3), 4.24 (q, 2H, *J* = 6.59 Hz, CH_2), 4.79 (s, 2H, D_2O exchangeable, NH_2), 6.83 (s, 1H, CH), 7.21–7.45 (m, 4H, C_6H_4), 8.36 (s, 1H, D_2O exchangeable, NH); ^{13}C NMR (DMSO-d_6, 75 MHz) δ 16.1 ($OCH_2\underline{CH_3}$), 36.3, 39.7 ($3CH_2$), 23.9 (CH_3), 52.1 ($O\underline{CH_2}CH_3$), 112.2, 158.7 (C=CH), 120.1, 123.8, 124.9, 128.3, 134.8, 137.2, 140.2, 142.6 (C_6H_5, thiophene C), 164.3, 179.5 (2CO). Anal. Calcd for $C_{19}H_{20}N_2O_3S$: C, 64.02; H, 5.66; N, 7.86; S, 9.00. Found: C, 63.91; H, 5.53; N, 8.01; S, 9.26. MS: *m/z* 356 (M^+, 32%).

2-Amino-4-(((4-methoxyphenyl)amino)methylene)-5-oxo-4,5,6,7-tetrahydrobenzo[*b*]thiophene-3-carbonitrile (17e)

Yellow crystals from ethanol, yield 2.30 g (71%), m.p. 166–169 °C. IR (KBr) ν_{max} (cm^{-1}) 3474–3329 (NH_2, NH), 3055 (CH, aromatic), 2220 (CN), 1688 (CO), 1630 (C=C); ^{1}H NMR (DMSO-d_6, 300 MHz) δ 2.61–2.77 (2t, 4H, $2CH_2$), 3.68 (s, 3H, OCH_3), 4.75 (s, 2H, D_2O exchangeable, NH_2), 6.87 (s, 1H, CH), 7.24–7.46 (m, 4H, C_6H_4), 8.35 (s, 1H, D_2O exchangeable, NH); ^{13}C NMR (DMSO-d_6, 75 MHz) δ 16.1, 36.2, 39.4 ($3CH_2$), 50.2 (OCH_3), 112.5, 158.4 (C=CH), 116.7 (CN), 120.1, 122.9, 125.3, 127.6, 132.2, 134.7, 137.6, 143.3 (C_6H_4, thiophene C), 179.6 (CO). Anal. Calcd for $C_{17}H_{15}N_3O_2S$: C, 62.75; H, 4.65; N, 12.91; S, 9.85. Found: C, 62.53; H, 4.79; N, 12.83; S, 10.01. MS: *m/z* 325 (M^+, 32%).

Ethyl 2-Amino-4-(((4-methoxyphenyl)amino) methylene)-5-oxo-4,5,6,7-tetrahydrobenzo[*b*]-thiophene-3-carboxylate (17f)

Yellow crystals from ethanol, yield 2.40 g (65%), m.p. 203–206 °C. IR (KBr) ν_{max} (cm^{-1}) 3459–3337 (NH_2), 3055 (CH, aromatic), 2930, 2970 (CH_2, CH_3), 1689, 1687 (2 CO), 1630 (C=C); ^{1}H NMR (DMSO-d_6, 300 MHz) δ 1.13 (t, 3H, *J* = 7.59 Hz, CH_3), 2.62–2.75 (2t, 4H, $2CH_2$), 3.61 (s, 3H, OCH_3), 4.22 (q, 2H, *J* = 7.59 Hz, CH_2), 4.79 (s, 2H, D_2O exchangeable, NH_2), 6.83 (s, 1H, CH), 7.24–7.48 (m, 4H, C_6H_4), 8.34 (s, 1H, D_2O exchangeable, NH); ^{13}C NMR (DMSO-d_6, 75 MHz) δ 16.1 ($OCH_2\underline{CH_3}$), 36.3, 39.7 ($3CH_2$), 50.2 (OCH_3), 52.2 ($O\underline{CH_2}CH_3$), 112.2, 158.7 (C=CH), 120.2, 122.2, 124.3, 128.1, 134.6, 136.7, 138.1, 140.8 (C_6H_5, thiophene C), 164.1, 179.7 (2CO). Anal. Calcd for $C_{19}H_{20}N_2O_4S$: C, 61.27; H, 5.41; N, 7.52; S, 8.61. Found: C, 60.91; H, 5.23; N, 7.39; S, 8.59. MS: *m/z* 372 (M^+, 36%).

2. 1. 10. General Procedure for the Synthesis of the 6,7-Dihydrobenzo[*b*]thiophen-3-carboxamide Derivatives 19a–c

Either of compounds **18a** (1.12 g, 0.01 mol), **18b** (1.74 g, 0.01 mol) or **18c** (1.94 g, 0.01 mol) was added to a solution of cyclohexane-1,3-dione (**1**) (1.12 g, 0.01 mol) in 1,4-dioxane (40 mL) containing triethylamine (0.50 mL). The reaction mixture was heated under reflux for 3 h then poured onto ice/water mixture containing a few drops of hydrochloric acid and the formed solid product was collected by filtration.

2-Amino-5-oxo-*N*-phenyl-4,5,6,7-tetrahydrobenzo[*b*] thiophene-3-carboxamide (19a)

Pale yellow crystals from ethanol, yield 2.14 g (75%), m.p. 120–123 °C. IR (KBr) ν_{max} (cm^{-1}) 3484–3337 (NH_2, NH), 3055 (CH, aromatic), 2220 (CN), 1689, 1686 (2 CO), 1630 (C=C); ^{1}H NMR (DMSO-d_6, 300 MHz) δ 2.62–2.79 (2t, 4H, $2CH_2$), 3.02 (s, 2H, CH_2), 4.75 (s, 2H, D_2O exchangeable, NH_2), 7.28–7.40 (m, 5H, C_6H_5), 8.38 (s, 1H, D_2O exchangeable, NH); ^{13}C NMR (DMSO-d_6, 75 MHz) δ 16.3, 36.6, 40.3 ($3CH_2$), 116.6 (CN), 120.8, 122.2, 125.3, 127.3, 132.2, 134.5, 138.0, 142.9 (C_6H_5, thiophene C), 164.3, 179.6 (2CO). Anal. Calcd for $C_{15}H_{14}N_2O_2S$: C, 62.92; H, 4.93; N, 9.78; S, 11.20. Found: C, 63.22; H, 4.75; N, 9.59; S, 11.36. MS: *m/z* 286 (M^+, 42%).

2-Amino-5-oxo-*N*-(*p*-tolyl)-4,5,6,7-tetrahydrobenzo[*b*] thiophene-3-carboxamide (19b)

Yellow crystals from ethanol, yield 1.98 g (66%), m.p. 194–196 °C. IR (KBr) ν_{max} (cm^{-1}) 3449–3327 (NH_2, NH), 3055 (CH, aromatic), 2220 (CN), 1689, 1687 (2 CO), 1630 (C=C); ^{1}H NMR (DMSO-d_6, 300 MHz) δ 2.63–2.77 (2t, 4H, $2CH_2$), 2.80 (s, 3H, CH_3), 3.06 (s, 2H, CH_2), 4.78 (s, 2H, D_2O exchangeable, NH_2), 7.26–7.46 (m, 4H, C_6H_4), 8.38 (s, 1H, D_2O exchangeable, NH); ^{13}C NMR (DMSO-d_6, 75 MHz) δ 16.3, 36.6, 40.3 ($3CH_2$), 116.6 (CN), 120.8, 122.2, 125.3, 127.3, 132.7, 134.7, 138.4, 142.6 (C_6H_4, thiophene C), 164.3, 179.6 (2CO). Anal. Calcd for $C_{16}H_{16}N_2O_2S$: C, 63.98; H, 5.37; N, 9.33; S, 10.67. Found: C, 63.72; H, 5.75; N, 9.59; S, 10.36. MS: *m/z* 300 (M^+, 36%).

2-Amino-*N*-(4-chlorophenyl)-5-oxo-4,5,6,7-tetrahydrobenzo[*b*]thiophene-3-carboxamide (19c)

Brown crystals from 1,4-dioxane, yield 2.49 g (78%), m.p. 205–208 °C. IR (KBr) ν_{max} (cm^{-1}) 3473–3351 (NH_2, NH), 3055 (CH, aromatic), 2220 (CN), 1689, 1686 (2 CO), 1630 (C=C); ^{1}H NMR (DMSO-d_6, 300 MHz) δ 2.64–2.76 (2t, 4H, $2CH_2$), 3.06 (s, 2H, CH_2), 4.79 (s, 2H, D_2O exchangeable, NH_2), 7.23–7.48 (m, 4H, C_6H_4), 8.36 (s, 1H, D_2O exchangeable, NH); ^{13}C NMR (DMSO-d_6, 75 MHz) δ 16.1, 36.4, 40.6 ($3CH_2$), 116.9 (CN), 120.2, 123.5, 125.8, 128.6, 132.3, 134.7, 138.0, 142.7 (C_6H_4, thiophene C), 164.3, 179.8 (2CO). Anal. Calcd for $C_{15}H_{13}ClN_2O_2S$: C, 56.16; H, 4.08; N, 8.73; S, 10.00. Found: C, 56.29; H, 4.26; N, 8.93; S, 10.26. MS: *m/z* 320 (M^+, 28%).

2. 1. 11. General Procedure for the Synthesis of the Tetrahydrobenzo[*b*]thiophene-3-carboxamide Derivatives 20a–c

A mixture of either **19a** (2.86 g, 0.01 mol), **19b** (3.00 g, 0.01 mol) or **19c** (3.20 g, 0.01 mol) in *N*,*N*-dimethylformamide (30 mL) and ethyl cyanoacetate (1.07 g, 0.01 mL) was heated under reflux for 3 h. The solid product, formed in each case, produced upon pouring onto ice/water mixture, was collected by filtration.

2-(2-Cyanoacetamido)-5-oxo-*N*-phenyl-4,5,6,7-tetrahydrobenzo[*b*]thiophene-3-carboxamide (20a)

Dark brown crystals from ethanol, yield 3.28 g (78%), m.p 118–120 °C. IR (KBr) ν_{max} (cm^{-1}) 3469–3329 (NH), 3054 (CH, aromatic), 2256 (CN), 1690–1686 (3 CO), 1630 (C=C); ^{1}H NMR (DMSO-d_6, 300 MHz) δ 2.61–2.82 (2t, 4H, $2CH_2$), 3.08 (s, 2H, CH_2), 3.68 (s, 2H, CH_2), 7.29–7.42 (m, 5H, C_6H_5), 8.24, 8.34 (2s, 2H, D_2O exchangeable, 2NH); ^{13}C NMR (DMSO-d_6, 75 MHz) δ 16.6, 36.2, 40.5 ($3CH_2$), 60.3 (CH_2), 170.1 (CN), 120.3, 123.5, 125.9, 126.5, 132.8, 133.3, 138.6, 142.8 (C_6H_5, thiophene C), 164.3, 166.1, 179.6 (3CO). Anal. Calcd for $C_{18}H_{15}N_3O_3S$: C, 61.18; H, 4.28; N, 11.89; S, 9.07. Found: C, 61.31; H, 4.29; N, 11.68; S, 8.85. MS: *m/z* 353 (M^+, 20%).

2-(2-Cyanoacetamido)-5-oxo-*N*-phenyl-4,5,6,7-tetrahydrobenzo[*b*]thiophene-3-carboxamide (20b)

Brown crystals from ethanol, yield 2.27 g (62%), m.p 211–214 °C. IR (KBr) ν_{max} (cm^{-1}) 3453–3340 (NH), 3055 (CH, aromatic), 2256 (CN), 1693–1685 (3 CO), 1630 (C=C); ^{1}H NMR (DMSO-d_6, 300 MHz) δ 2.63–2.80 (2t, 4H, $2CH_2$), 2.70 (s, 3H, CH_3), 3.10 (s, 2H, CH_2), 3.62 (s, 2H, CH_2), 7.25–7.38 (m, 4H, C_6H_4), 8.23, 8.38 (2s, 2H, D_2O exchangeable, 2NH); ^{13}C NMR (DMSO-d_6, 75 MHz) δ 16.3, 36.4, 40.8 ($3CH_2$), 60.5 (CH_2), 168.3 (CN), 120.6, 122.1, 126.4, 127.1, 132.8, 134.2, 138.6, 142.9 (C_6H_4, thiophene C), 164.2, 166.1, 179.8 (3CO). Anal. Calcd for $C_{19}H_{17}N_3O_3S$: C, 62.11; H, 4.66; N, 11.44; S, 8.73. Found: C, 62.26; H, 4.48; N, 11.52; S, 8.90. MS: *m/z* 367 (M^+, 28%).

***N*-(4-Chlorophenyl)-2-(2-cyanoacetamido)-5-oxo-4,5,6,7-tetrahydrobenzo[*b*]thiophene-3-carboxamide (20c)**

White crystals from ethanol, yield 2.12 g (55%), m.p 118–121 °C. IR (KBr) ν_{max} (cm^{-1}) 3470–3338 (NH), 3055 (CH, aromatic), 2256 (CN), 1691–1685 (3 CO), 1630 (C=C); ^{1}H NMR (DMSO-d_6, 300 MHz) δ 2.62–2.82 (2t, 4H, $2CH_2$), 3.12 (s, 2H, CH_2), 3.62 (s, 2H, CH_2), 7.22–7.49 (m, 4H, C_6H_4), 8.26, 8.32 (2s, 2H, D_2O exchangeable, 2NH); ^{13}C NMR (DMSO-d_6, 75 MHz) δ 16.1, 36.6, 40.4 ($3CH_2$), 60.2 (CH_2), 168.9 (CN), 120.4, 124.2, 125.1, 128.6, 132.5, 134.9, 138.4, 142.6 (C_6H_4, thiophene C), 164.4, 166.3, 179.6 (3CO). Anal. Calcd for $C_{18}H_{14}ClN_3O_3S$: C, 55.74; H, 3.64; N, 10.83; S, 8.27. Found: C, 55.80; H, 3.80; N, 11.01; S, 8.38. MS: *m/z* 387 (M^+, 30%).

2. 1. 12. General Procedure for the Synthesis of the Phenylthioureido Derivatives 21a–c

Equimolar amounts of either **19a** (2.86 g, 0.01 mol), **19b** (3.00 g, 0.01 mol) or **19c** (3.20 g, 0.01 mol) and phenyl isothiocyanate (1.30 g, 0.01 mol) in ethanol (40 mL) containing triethylamine (1.0 mL) were heated under reflux for 3 h then left to cool. The formed solid crystals, in each case, were collected by filtration.

5-Oxo-*N*-phenyl-2-(3-phenylthioureido)-4,5,6,7-tetrahydrobenzo[*b*]thiophene-3-carboxamide (21a)

Yellow crystals from ethanol, yield 2.52 g (60%), m.p. 115–117 °C. IR (KBr) ν_{max} (cm^{-1}) 3464–3331 (NH), 3054 (CH, aromatic), 1689, 1687 (2 CO), 1632 (C=C), 1205 (C=S); ^{1}H NMR (DMSO-d_6, 300 MHz) δ 2.63–2.84 (2t, 4H, $2CH_2$), 3.66 (s, 2H, CH_2), 7.28–7.40 (m, 10H, $2C_6H_5$), 8.21, 8.23, 8.38 (3s, 3H, D_2O exchangeable, 3NH); ^{13}C NMR (DMSO-d_6, 75 MHz) δ 16.1, 36.6, 40.6 ($3CH_2$), 120.8, 122.4, 125.8, 126.0, 126.3, 127.5, 127.9, 128.2, 131.9, 133.8, 139.3, 142.9 ($2C_6H_5$, thiophene C), 164.2, 179.2 (2CO),180.2 (C=S). Anal. Calcd for $C_{22}H_{19}N_3O_2S_2$: C, 62.68; H, 4.54; N, 9.97; S, 15.21. Found: C, 62.77; H, 4.49; N, 10.21; S, 15.49. MS: *m/z* 421 (M^+, 32%).

5-Oxo-2-(3-phenylthioureido)-*N*-(*p*-tolyl)-4,5,6,7-tetrahydrobenzo[*b*]thiophene-3-carboxamide (21b)

Pale yellow crystals from 1,4-dioxane, yield 2.70 g (60%), m.p. 205–208 °C. IR (KBr) ν_{max} (cm^{-1}) 3485–3329 (NH), 3055 (CH, aromatic), 1689, 1687 (2 CO), 1638 (C=C), 1208 (C=S); ^{1}H NMR (DMSO-d_6, 300 MHz) δ 2.61–2.89 (2t, 4H, $2CH_2$), 2.80 (s, 3H, CH_3), 3.67 (s, 2H, CH_2), 7.23–7.48 (m, 9H, C_6H_5, C_6H_4), 8.26, 8.21, 8.36 (3s, 3H, D_2O exchangeable, 3NH); ^{13}C NMR (DMSO-d_6, 75 MHz) δ 16.5, 36.6, 40.6 ($3CH_2$), 30.6 (CH_3), 120.2, 121.6, 124.5, 126.7, 126.8, 128.1, 128.7, 129.3, 133.5, 135.2, 138.6, 142.6 (C_6H_5, C_6H_4, thiophene C), 164.6, 179.4 (2CO), 180.6 (C=S). Anal. Calcd for $C_{23}H_{21}N_3O_2S_2$: C, 63.42; H, 4.86; N, 9.65; S, 14.72. Found: C, 63.52; H, 4.68; N, 9.74; S, 14.80. MS: *m/z* 435 (M^+, 28%).

***N*-(4-Chlorophenyl)-5-oxo-2-(3-phenylthioureido)-4,5,6,7-tetrahydrobenzo[*b*]thiophene-3-carboxamide (21c)**

Yellow crystals from ethanol, yield 2.95 g (65%), m.p. 200–203 °C. IR (KBr) ν_{max} (cm^{-1}) 3442–3338 (NH), 3054 (CH, aromatic), 1689, 1685 (2 CO), 1630 (C=C), 1208 (C=S); ^{1}H NMR (DMSO-d_6, 300 MHz) δ 2.62–2.86 (2t, 4H, $2CH_2$), 3.68 (s, 2H, CH_2), 7.22–7.48 (m, 9H, C_6H_5, C_6H_4), 8.22, 8.25, 8.41 (3s, 3H, D_2O exchangeable, 3NH); ^{13}C NMR (DMSO-d_6, 75 MHz) δ 16.0, 36.6, 40.9 ($3CH_2$), 120.3, 124.6, 125.5, 126.6, 127.2, 128.3, 128.7, 128.9, 132.5, 134.7, 138.0, 142.6 (C_6H_5, C_6H_4, thiophene C), 164.5, 179.8 (2CO), 180.5 (C=S). Anal. Calcd for $C_{22}H_{18}ClN_3O_2S_2$: C, 57.95; H, 3.98; N,9.22; S, 14.06. Found: C, 57.63; H, 3.77; N, 9.39; S, 14.26. MS: *m/z* 455 (M^+, 28%).

2. 1. 13. General Procedure for the Synthesis of the Hexahydrobenzo[4,5]thieno[2,3-*d*]pyrimidin-6(5*H*)-one Derivatives 22a–c

A suspension of either compound **21a** (4.21 g, 0.01 mol), **21b** (4.35 g, 0.01 mol), **21c** (4.55 g, 0.01 mol) in sodium ethoxide [prepared through dissolving metallic sodium (0.46 g, 0.02 mol) in absolute ethanol (50 mL)] was heated in a boiling water bath for 6 h. The reaction mixture was poured onto ice/water mixture then triturated with hydrochloric acid (till pH 7) and the formed solid product was collected by filtration.

3-Phenyl-4-(phenylimino)-2-thioxo-1,2,3,4,7,8-hexahydrobenzo[4,5]thieno[2,3-*d*]pyrimidin-6(5*H*)-one (22a)

Yellow crystals from ethanol, yield 3.14 g (78%), m.p. 111–113 °C. IR (KBr) ν_{max} (cm^{-1}) 3458–3324 (NH), 3055 (CH, aromatic), 1688 (CO), 1632 (C=C), 1205 (C=S); ^{1}H NMR (DMSO-d_6, 300 MHz) δ 2.61–2.86 (2t, 4H, $2CH_2$), 3.68 (s, 2H, CH_2), 7.28–7.40 (m, 10H, $2C_6H_5$), 8.21 (s, 1H, D_2O exchangeable, NH); ^{13}C NMR (DMSO-d_6, 75 MHz) δ 16.1, 36.6, 40.6 ($3CH_2$), 120.8, 122.4, 125.8, 126.0, 126.3, 127.5, 127.9, 128.2, 132.2, 134.7, 137.2, 142.9 ($2C_6H_5$, thiophene C), 179.1 (CO), 180.3 (C=S). Anal. Calcd for $C_{22}H_{17}N_3OS_2$: C, 65.48; H, 4.25; N, 10.41; S, 15.89. Found: C, 65.63; H, 4.19; N, 10.32; S, 15.74. MS: *m/z* 403 (M^+, 38%).

3-Phenyl-2-thioxo-4-(*p*-tolylimino)-1,2,3,4,7,8-hexahydrobenzo[4,5]thieno[2,3-*d*]pyrimidin-6(5*H*)-one (22b)

Brown crystals from ethanol, yield 2.46 g (59%), m.p. 273–275 °C. IR (KBr) ν_{max} (cm^{-1}) 3479–3336 (NH), 3055 (CH, aromatic), 1688 (CO), 1631 (C=C), 1209 (C=S); ^{1}H NMR (DMSO-d_6, 300 MHz) δ 2.60–2.88 (2t, 4H, $2CH_2$), 2.93 (s, 3H, CH_3), 3.65 (s, 2H, CH_2), 7.22–7.45 (m, 9H, C_6H_5, C_6H_4), 8.25 (s, 1H, D_2O exchangeable, NH); ^{13}C NMR (DMSO-d_6, 75 MHz) δ 16.4, 36.8, 40.9 ($3CH_2$), 32.6 (CH_3), 120.2, 122.6, 125.5, 125.9, 126.9, 127.7, 127.3, 128.1, 132.2, 134.9, 137.6, 142.3 (C_6H_5, C_6H_4, thiophene C), 179.6 (CO), 180.8 (C=S). Anal. Calcd for $C_{23}H_{19}N_3OS_2$: C, 66.16; H, 4.59; N, 10.06; S, 15.36. Found: C, 66.39; H, 4.42; N, 10.15; S, 15.80. MS: *m/z* 417 (M^+, 42%).

4-((4-Chlorophenyl)imino)-3-phenyl-2-thioxo-1,2,3,4,7,8-hexahydrobenzo[4,5]thieno[2,3-*d*]pyrimidin-6(5*H*)-one (22c)

Pale yellow crystals from ethanol, yield 3.49 g (80%), m.p. 119–122 °C. IR (KBr) ν_{max} (cm^{-1}) 3459–3328 (NH), 3054 (CH, aromatic), 1688, 1685 (2CO), 1630 (C=C), 1210 (C=S); ^{1}H NMR (DMSO-d_6, 200 MHz) δ 2.62–2.88 (2t, 4H, $2CH_2$), 3.68 (s, 2H, CH_2), 7.22–7.48 (m, 9H, C_6H_5, C_6H_4), 8.22 (s, 1H, D_2O exchangeable, NH); ^{13}C NMR (DMSO-d_6, 75 MHz) δ 16.0, 36.6, 40.9 ($3CH_2$), 120.3, 124.6, 125.5, 126.6, 127.2, 128.3, 128.7, 128.9, 132.8, 134.3, 137.2, 142.9 (C_6H_5, C_6H_4, thiophene C), 164.8, 179.4 (2CO), 180.2 (C=S). Anal. Calcd for $C_{22}H_{16}ClN_3OS_2$: C, 60.33; H, 3.68; N, 9.59; S, 14.64. Found: C, 60.26; H, 3.49; N, 9.41; S, 14.52. MS: *m/z* 437 (M^+, 32%).

2. 2. Biology Section

2. 2. 1. Cell Proliferation Assay

Foretinib was used as the positive control[27–29] during measuring the anti-proliferative activities of the newly synthesized compounds (Table 1). The newly synthesized compounds were evaluated against the six cancer cell lines A549, HT-29, MKN-45, U87MG, and SMMC-7721 and H460 using the standard MTT assay *in vitro*.

The IC_{50} values were measured through three independent experiments and the data are shown in Table 1. It is clear that many of the tested compounds showed potent anti-proliferative activity with IC_{50} values less than 6.00 μM. Generally, the variations of substituents within the aryl moiety together with the heterocyclic ring being attached had a notable effect and a positive impact on the anti-proliferative activity.

Table 1. *In vitro* growth inhibitory effects IC_{50} ± SEM (μM) of the newly synthesized compounds against cancer cell lines

Compound	IC_{50} ± SEM (μM)					
	A549	H460	HT29	MKN-45	U87MG	SMMC-7721
3a	6.62 ± 2.34	5.42 ± 2.31	7.73 ± 2.59	6.72 ± 2.21	6.82 ± 1.73	5.01 ± 2.32
3b	0.40 ± 0.25	0.39 ± 0.17	0.29 ± 0.16	0.24 ± 0.16	0.19 ± 0.17	0.42 ± 0.23
5a	4.16 ± 1.49	4.18 ± 1.26	5.43 ± 2.71	5.32 ± 1.41	6.53 ± 251	6.80 ± 1.49
5b	1.07 ± 0.68	1.17 ± 0.63	2.04 ± 0.95	2.27 ± 1.33	1.95 ± 0.49	2.17 ± 0.52
5c	0.19 ± 0.07	0.26 ± 0.11	0.37 ± 0.21	0.26 ± 0.08	0.52 ± 0.23	0.62 ± 0.25
5d	0.39 ± 0.15	0.36 ± 0.21	0.27 ± 0.18	0.29 ± 0.17	0.36 ± 0.22	0.35 ± 0.18
6a	6.41 ± 2.26	5.73 ± 2.17	6.42 ± 2.31	8.92 ± 3.41	6.22 ± 2.73	5.82 ± 1.39
6b	1.08 ± 0.69	0.82 ± 0.26	0.63 ± 0.37	0.38 ± 0.26	1.82 ± 0.79	0.63 ± 0.31
6c	0.32 ± 0.21	0.37 ± 0.19	0.40 ± 0.15	0.25 ± 0.07	0.62 ± 0.14	0.51 ± 0.23
6d	0.32 ± 0.15	0.42 ± 0.26	0.16 ± 0.09	0.26 ± 0.14	0.37 ± 0.17	0.28 ± 0.08
8a	0.33 ± 0.12	0.28 ± 0.15	0.28 ± 3.19	6.28 ± 1.08	7.89 ± 2.63	9.39 ± 2.37
8b	0.65 ± 0.18	0.29 ± 0.12	0.43 ± 0.25	0.36 ± 0.19	0.26 ± 0.18	0.56 ± 0.18
10a	6.48 ± 1.54	7.60 ± 2.42	6.63 ± 2.29	6.16 ± 2.59	5.26 ± 1.83	6.29 ± 2.28
10b	2.48 ± 1.01	3.80 ± 1.18	2.47 ± 1.14	4.52 ± 2.16	0.93 ± 0.42	2.83 ± 1.02
10c	0.26 ± 0.18	0.43 ± 0.18	0.41 ± 0.20	0.38 ± 0.16	0.46 ± 0.26	0.38 ± 0.13
10d	0.65 ± 0.32	0.58 ± 0.21	1.08 ± 0.62	0.73 ± 0.32	0.46 ± 0.29	0.53 ± 0.25
12a	1.82 ± 0.78	1.06 ± 0.62	0.84 ± 0.38	0.61 ± 0.19	0.72 ± 0.36	0.59 ± 0.16
12b	0.22 ± 0.15	0.36 ± 0.12	0.43 ± 0.19	0.29 ± 0.16	0.42 ± 0.25	0.58 ± 0.24
14	8.68 ± 2.59	6.70 ± 2.63	7.28 ± 1.62	5.63 ± 1.26	6.92 ± 2.37	7.29 ± 2.62
16a	4.91 ± 1.56	5.41 ± 1.28	3.52 ± 1.15	3.30 ± 1.86	5.02 ± 2.80	4.69 ± 1.38
16b	6.53 ± 2.38	7.24 ± 2.49	6.80 ± 1.92	7.49 ± 2.63	5.60 ± 1.32	8.05 ± 3.26
16c	0.76 ± 0.39	0.68 ± 0.27	0.43 ± 0.26	0.51 ± 0.23	0.60 ± 0.29	0.39 ± 0.24
17a	4.83 ± 1.53	6.28 ± 2.54	6.22 ± 2.26	3.42 ± 1.60	5.23 ± 1.21	4.72 ± 1.38
17b	3.41 ± 1.25	4.61 ± 1.28	4.82 ± 1.52	2.16 ± 0.73	2.37 ± 1.29	3.42 ± 1.53
17c	3.42 ± 1.80	2.63 ± 1.03	4.81 ± 1.68	3.68 ± 1.29	3.62 ± 1.26	2.46 ± 1.82
17d	1.02 ± 0.71	1.65 ± 0.83	0.93 ± 0.42	0.85 ± 0.31	0.72 ± 0.29	0.69 ± 0.23
17e	0.82 ± 0.18	0.51 ± 0.23	0.42 ± 0.19	0.31 ± 0.25	0.39 ± 0.13	0.58 ± 0.13
17f	0.21 ± 0.09	0.33 ± 0.17	0.48 ± 0.31	0.35 ± 0.12	0.59 ± 0.23	0.23 ± 0.17
19a	7.28 ± 2.62	8.29 ± 2.17	6.39 ± 1.02	5.86 ± 2.23	7.43 ± 2.49	6.32 ± 2.34
19b	2.34 ± 1.14	2.28 ± 0.82	3.51 ± 1.50	3.46 ± 1.63	3.68 ± 1.23	2.18 ± 1.02
19c	0.24 ± 0.13	0.32 ± 0.17	0.48 ± 0.23	0.29 ± 0.36	0.26 ± 0.15	0.43 ± 0.29
20a	8.52 ± 3.50	7.62 ± 2.40	6.39 ± 3.60	7.80 ± 2.68	5.18 ± 2.70	6.48 ± 2.37
20b	4.26 ± 1.05	5.72 ± 2.83	6.93 ± 2.40	4.70 ± 1.52	5.94 ± 1.29	1.04 ± 0.89
20c	0.37 ± 0.16	0.35 ± 0.18	0.46 ± 0.261	0.51 ± 0.28	0.24 ± 0.63	0.28 ± 0.18
21a	8.24 ± 3.51	6.39 ± 2.73	4.46 ± 1.28	5.34 ± 1.60	6.70 ± 2.93	5.45 ± 1.69
21b	1.42 ± 0.98	1.64 ± 0.52	0.68 ± 0.31	1.25 ± 0.79	2.35 ± 1.06	3.36 ± 1.20
21c	6.43 ± 2.53	8.69 ± 2.64	7.16 ± 1.69	8.69 ± 2.26	8.53 ± 2.38	8.76 ± 2.49
22a	6.42 ± 2.26	8.25 ± 2.13	5.29 ± 2.30	3.27 ± 1.04	5.52 ± 1.31	4.50 ± 1.46
22b	2.43 ± 1.16	2.37 ± 1.28	3.45 ± 1.19	2.26 ± 1.16	4.58 ± 1.14	3.27 ± 3.16
22c	0.42 ± 0.23	0.29 ± 0.15	0.54 ± 0.29	0.19 ± 0.04	0.59 ± 0.31	0.42 ± 0.63
Foretinib	0.08 ± 0.01	0.18 ± 0.03	0.15 ± 0.023	0.03 ± 0.0055	0.90 ± 0.13	0.44 ± 0.062

2. 2. 2. Structure Activity Relationship

It is clear from Table 1 that most of the compounds exhibited high cyctotoxicities against the six cancer cell lines A549, HT-29, MKN-45, U87MG, and SMMC-7721 and H460. Where in the most of the cases the presence of electronegative substituents is responsible for the high inhibitions. Considering the 2-ylidenecyclohexane-1,3-dione derivatives **3a**,**b** it is clear that compound **3b** (X = S) showed higher cytotoxicities than compound **3a** (X = O). For the 4,5,6,7-tetrahydrobenzo[*b*]thiophene derivatives **5a**–**d**, compound **5a** (X = O, R = CN) exhibited relatively low inhibitions while compound **5b** (X = O, R = COOEt) showed moderate inhibitions. On the other side, compounds **5c** (X = S, R = CN) and **5d** (X = S, R = COOEt) showed extensively high inhibitions toward the six cancer cell lines. Similarly, for the 5,6,7,8-tetrahydro-4*H*-chromene derivatives **6a**–**d**, it is obvious that compound **6a** (X = O, Y = NH_2) showed low inhibitions, compound **6b** (X = O, Y = OH) displayed moderate inhibitions and compounds **6c** (X = S, Y = NH_2) and **6d** (X = S, Y = NH_2) showed high inhibitions. Considering the 2,3,6,7-tetrahydrobenzo[*d*]thiazole derivatives **8a**,**b**, where both of the two compounds exhibited high cytotoxicities, this is at-

tributed to the presence of the thiazole moiety in both compounds. For the 4,5,6,7-tetrahydro-2*H*-indazole derivatives **10a–d** it is clear that compound **10a** (X = O, R = H) showed low inhibitions, compound **10b** with high inhibition only toward U87MG cell line with IC_{50} = 0.93 μM and moderate inhibitions toward the other five cell lines A549, H460, HT29, MKN-45 and SMMC-7721. Compounds **10c** (X = S, R = H) and **10d** (X = S, R = Ph) revealed high inhibitions toward the six cancer cell lines. On the other hand, the 6,7-dihydrobenzo[*c*] isoxazole derivatives **12a** and **12b** showed high inhibitions. Compound **14** the 2-(ethoxymethylene)cyclohexane-1,3-dione showed low inhibitions toward the six cancer cell lines. Considering the 2-(arylamino)methylene)cyclohexane-1,3-dione derivatives **16a–c** where compound **16c** (X = OCH_3) showed the highest inhibitions among the three compounds although compound **16a** (X = H) showed relatively higher inhibitions than compound **16b** (X = CH_3). For the 6,7-dihydrobenzo[*b*]thiophene derivatives **17a–f**, it is clear from Table 1 that compounds **17a**, **17b** and **17c** showed low inhibitions while compounds **17d** (X = CH_3, R = COOEt), **17f** (X = OCH_3, R = CN) and **17d** (X = OCH_3, R = COOEt) showed high inhibitions. Within the 6,7-dihydrobenzo[*b*]thiophene derivatives **19a–c** and **20a–c**, compounds **19c** (Y = Cl) and **20c** (X= Cl) showed the highest inhibitions among the six compounds. Surprisingly, for compounds **21a–c** where compound **21b** (Y = CH_3) showed higher inhibitions than **21a** (Y = H) and **21c** (Y = Cl). Finally for the 1,2,3,4,7,8-hexahydrobenzo[4,5]thien[2,3-*d*]pyrimidine derivatives **22a–c**, where compound **22a** (Y = H) showed low inhibitions, compound **22b** (Y = CH_3) displayed moderate inhibitions and compound **22c** (Y = Cl) showed high inhibitions. It is of great value to mention that compounds **3b**, **5c**, **5d**, **6b**, **6c**, **6d**, **8a**, **8b**, **10c**, **10d**, **12a**, **12b**, **16c**, **17d**, **17e**, **17f**, **19c**, **20c** and **22c** were the most cytotoxic compounds among the tested compounds.

2. 2. 3. Inhibition of Tyrosine Kinases

Compounds **3b**, **5c**, **5d**, **6b**, **6c**, **6d**, **8a**, **8b**, **10c**, **10d**, **12a**, **12b**, **16c**, **17d**, **17e**, **17f**, **19c**, **20c** and **22c** were selected for inhibition of the five tyrosine kinases c-Kit, Flt-3, VEGFR-2, EGFR, and PDGFR. It is clear from Table 2 that compounds **3b**, **5d**, **6b**, **6d**, **8a**, **8b**, **10c**, **12a**, **12b**, **16c**, **17e**, **17f** and **19c** were the most potent of the tested compounds towards the five tyrosine kinases. Compound **5c** showed high potency towards the two kinases c-EGFR and PDGFR with IC_{50} 0.96 and 0.68 nM, respectively. In addition the 2-(((4-methoxyphenyl)amino)methylene)cyclohexane-1,3-dione (**16c**) showed activity towards the five kinases with IC_{50} 0.14, 0.32, 0.21, 0.36 and 0.40 nM, respectively. Compounds **6c**, **10d**, **20c** and **22c** showed the lowest potency among the tested compounds.

Table 2. Inhibition of tyrosine kinases (enzyme IC_{50} in nM) by compounds **3b**, **5c**, **5d**, **6b**, **6c**, **6d**, **8a**, **8b**, **10c**, **10d**, **12a**, **12b**, **16c**, **17d**, **17e**, **17f**, **19c**, **20c** and **22c**

Compound	c-Kit	Flt-3	VEGFR-2	EGFR	PDGFR
3b	0.80	0.37	0.42	0.58	0.38
5c	1.03	2.63	1.82	0.96	0.68
5d	0.23	0.26	0.42	0.69	0.72
6b	0.48	0.27	0.62	0.49	0.52
6c	1.42	2.58	1.61	1.80	2.31
6d	0.16	0.24	0.57	0.34	0.28
8a	0.58	0.42	0.38	0.27	0.19
8b	0.29	0.48	0.68	0.52	0.40
10c	0.16	0.13	0.28	0.31	0.28
10d	2.07	1.24	1.30	1.28	1.72
12a	0.36	0.24	0.62	0.18	0.24
12b	0.18	0.53	0.61	0.53	0.42
16c	0.14	0.32	0.21	0.36	0.40
17d	1.85	1.64	1.52	2.83	1.18
17e	0.26	0.23	0.37	0.28	0.46
17f	0.55	0.80	0.92	0.16	0.27
19c	0.26	0.42	0.31	0.50	0.62
20c	1.27	1.43	2.60	2.88	1.69
22c	2.49	2.61	1.96	2.37	3.39

2. 2. 4. Inhibition of Selected Compounds Towards Pim-1 Kinase

Compounds **3b**, **5d**, **6b**, **6d**, **8a**, **8b**, **10c**, **12a**, **12b**, **16c**, **17e**, **17f** and **19c** were selected to examine their Pim-1 kinase inhibition activity (Table 3) as these compounds showed high inhibition towards the tested cancer cell lines at a range of 10 concentrations and the IC_{50} values were calculated. Compounds **5d**, **6b**, **6d**, **10c**, **12a**, **17e** and **17f** were the most potent to inhibit Pim-1 activity with IC_{50} values of 0.24, 0.41, 0.30, 0.28, 0.45, 0.23 and 0.25 μM, respectively. On the other hand, compounds **3b**, **8a, 8b**, **12b**, **16c**, and **19c** were less effective (IC_{50} > 10 μM). SGI-1776 was used as the positive control with IC_{50} 0.048 μM in the assay. These profiles in combination with cell growth inhibition data of compounds **3b**, **5d**, **6b**, **6d**, **8a**, **8b**, **10c**, **12a**, **12b**, **16c**, **17e**, **17f** and **19c** are listed in Table 3 indicating that Pim-1 is a potential target of these compounds.

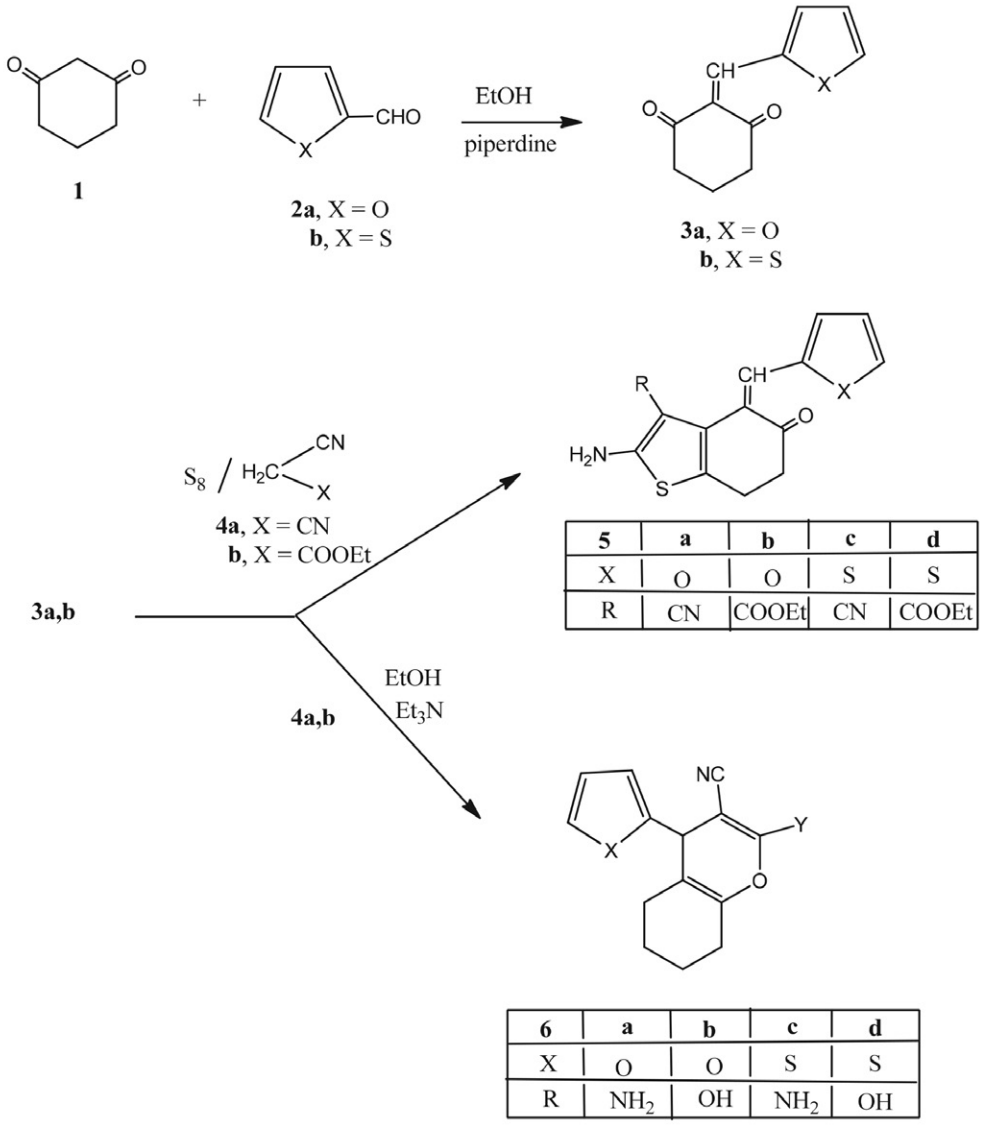
3. Results and Discussion

The synthesis of the 2-(hetero-2-ylmethylene)cyclohexane-1,3-dione derivatives **3a**,**b** has been accomplished as outlined in Scheme 1 starting from cyclohexan-1,3-dione (**1**). Compounds **3a** and **3b** were obtained through the reaction of **1** with either of furan-2-carbaldehyde or thiophene-2-carbaldehyde. The reaction of either of compound **3a** or **3b** with elemental sulfur and either of malononitrile (**4a**) or ethyl cyanoacetate (**4b**) gave the 6,7-dihydrobenzo[*b*]thiophen-5(4*H*)-one derivatives **5a–**

Table 3. The inhibitory activity of compounds **3b**, **5d**, **6b**, **6d**, **8a**, **8b**, **10c**, **12a**, **12b**, **16c**, **17e**, **17f** and **19c** toward Pim-1 kinase.

Compound	Inhibition ratio at 10 μM	IC_{50} (μM)
3b	16	> 10
5d	96	0.24
6b	90	0.41
6d	89	0.30
8a	26	> 10
8b	24	> 10
10c	92	0.28
12a	0.88	0.45
12b	28	> 10
16c	26	> 10
17e	92	0.23
17f	90	0.25
19c	18	> 10
SGI-1776	–	0.048

d, respectively. The structures of the latter products were established on the analytical and spectral data. Thus, the ^{1}H NMR spectrum of compound **5a** (as an example) showed the presence of two triplets at δ 2.62–2.78 ppm for the two CH_2 groups, a singlet at δ 4.73 ppm (D_2O exchangeable) indicating the presence of the NH_2 group, a singlet at δ 6.84 for the pyran *H*-4 and a multiplet at δ 6.82–7.86 ppm for the furan protons. In addition, the ^{13}C NMR spectrum revealed three signals at δ 16.6, 36.3 and 39.5 equivalent to the three CH_2 groups, two signals at δ 112.6 and 158.4 for the C=CH group, a signal at δ 116.8 for the CN group, eight signals at δ 135.4, 140.6, 141.4, 142.2, 142.7, 144.8, 145.6, 146.5 for the thiophene and furan carbons and a signal at δ 179.3 indicating the CO group. The reaction of either compound **3a** or **3b** with either of malononitrle (**4a**) or ethyl cyanoacetate (**4b**) in ethanol containing a catalytic amount of triethylamine gave the 2*H*-chromen-5-one derivatives **6a**–**d**, respectively (Scheme 1).



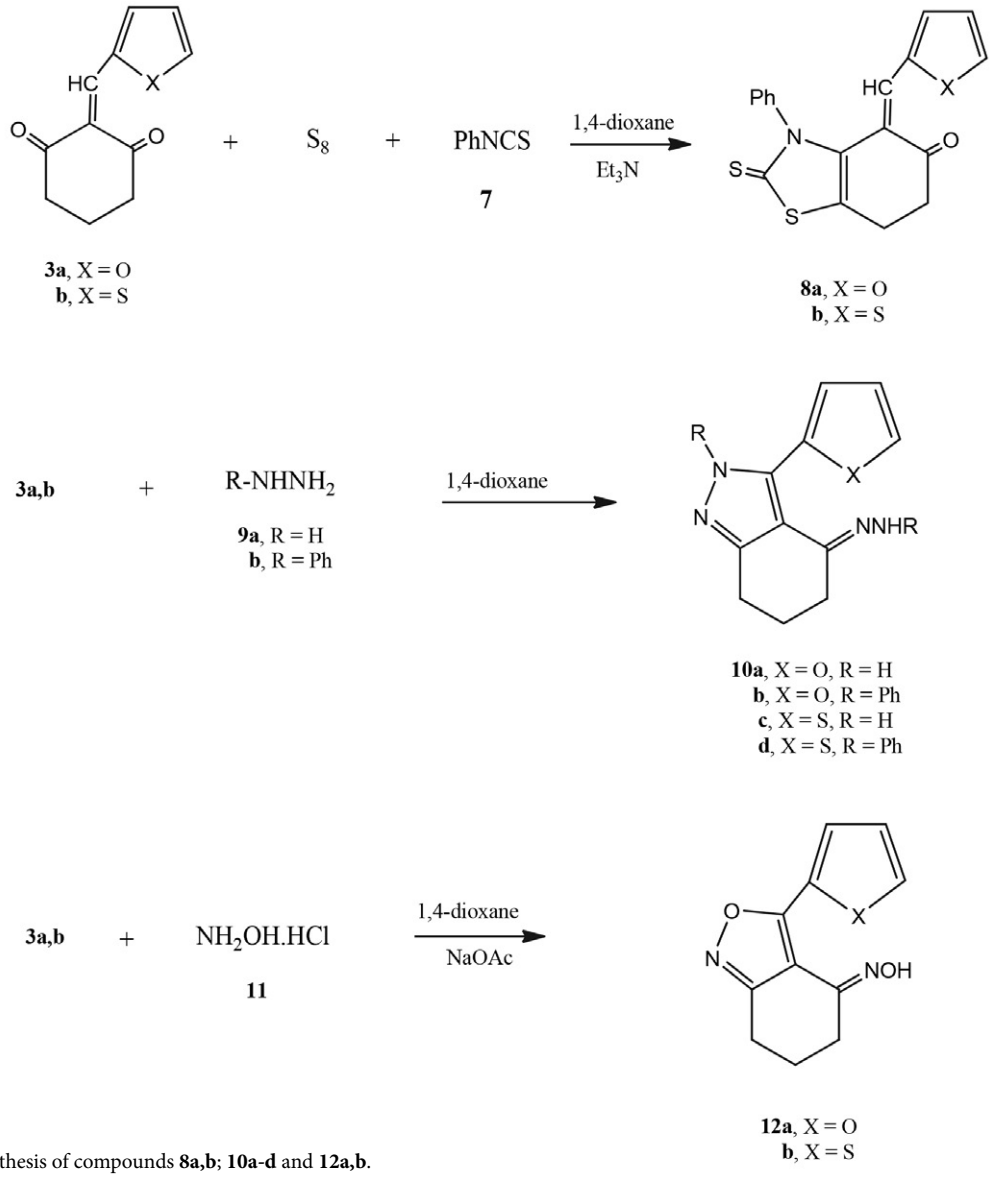
Scheme 1. Synthesis of compounds **3a,b**; **5a-d** and **6a-d**.

The reactivity of compounds **3a** and **3b** toward thiazole synthesis was studied. Thus, the reaction of either compound **3a** or **3b** with elemental sulfur and phenyl isothiocyanate (**7**) gave the 2-thioxohexahydrobenzo[*d*]thiazole derivatives **8a** and **8b**, respectively.

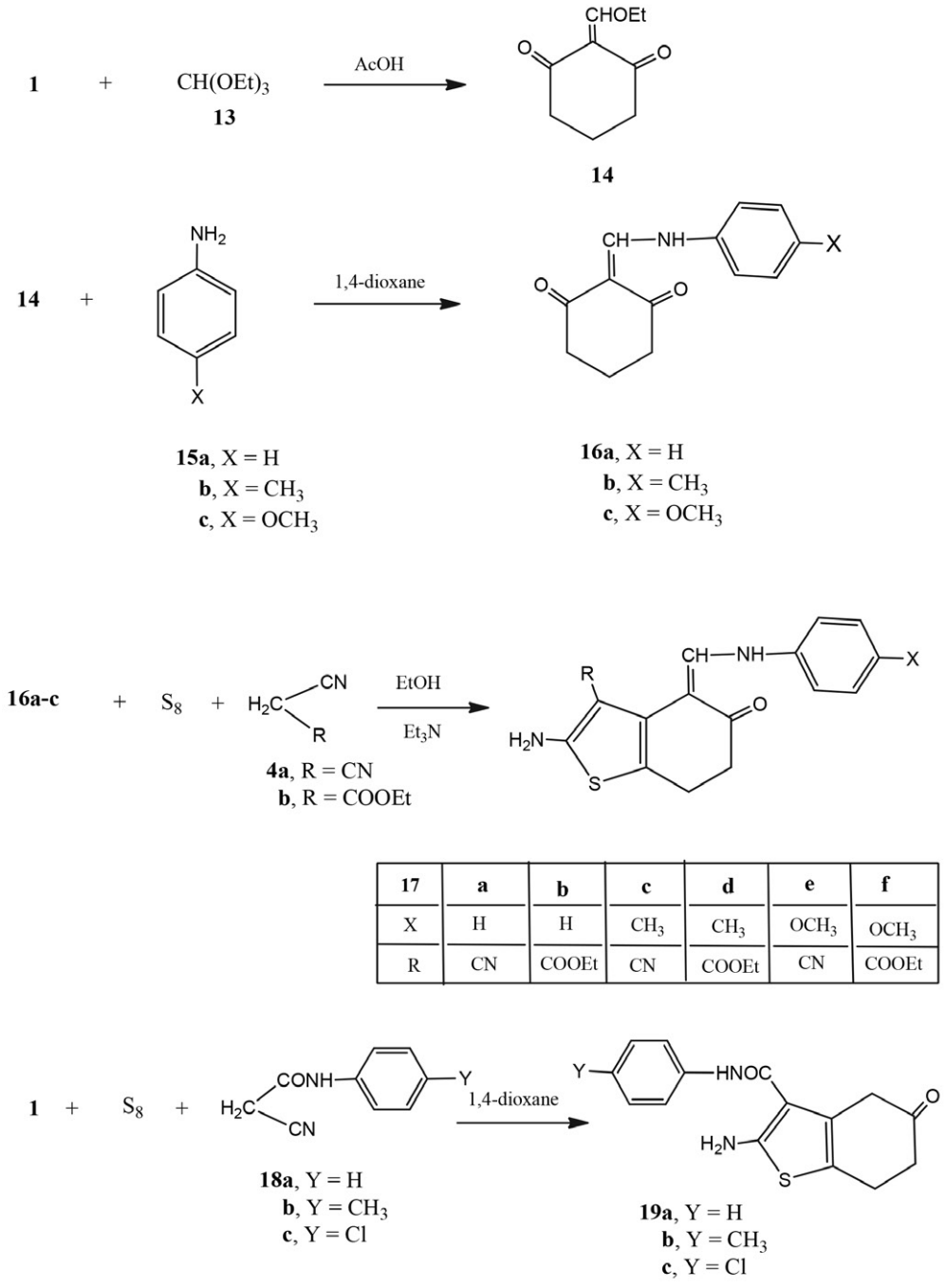
The reaction of either of compound **3a** or **3b** with either hydrazine hydrate (**9a**) or phenylhydrazine (**9b**) gave the 4-hydrazono-4,5,6,7-tetrahydro-2*H*-indazole derivatives **10a–d**, respectively. Similarly, the reaction of either **3a** or **3b** with hydroxylamine hydrochloride (**11**) gave the 6,7-dihydrobenzo[*c*]isoxazol-4(5*H*)-one oxime derivatives **12a** and **12b**, respectively (Scheme 2).

Next, we moved toward studying the use of 2-(ethoxymethylene)cyclohexane-1,3-dione (**14**), obtained according to the reported work[30] *via* the reaction of cyclohexane-1,3-dione (**1**) with ethyl orthoformate in acetic acid solution, through different heterocyclization reactions. Thus, the reaction of compound **3** with any of the aromatic amines namely aniline (**15a**), 4-methylaniline (**15b**) or 4-methoxyaniline (**15c**) gave the 2-(aminomethylene) cyclohexane-1,3-dione derivatives **16a–c**, respectively. Structures of compounds **16a–c** were confirmed on the basis of their respective analytical and spectral data (see experimental section). Compounds **16a–c** were used to synthesize thiophene derivatives using the Gewald's thiophene synthesis.[31–33] Thus, the reaction of any of compounds **16a**, **16b** or **16c** with elemental sulfur and either of malononitrile (**4a**) or ethyl cyanoacetate (**4b**) gave the 6,7-dihydrobenzo[*b*]thiophene derivatives **17a–f**, respectively.

The reaction of cycohexane-1,3-dione (**1**) with elemental sulfur and any of cyanoacetanilide (**19a**), cyano-4-methylacetanilide (**19b**) or cyano-4-methoxyacetanilide (**19c**) gave the 6,7-dihydrobenzo[*b*]thiophene



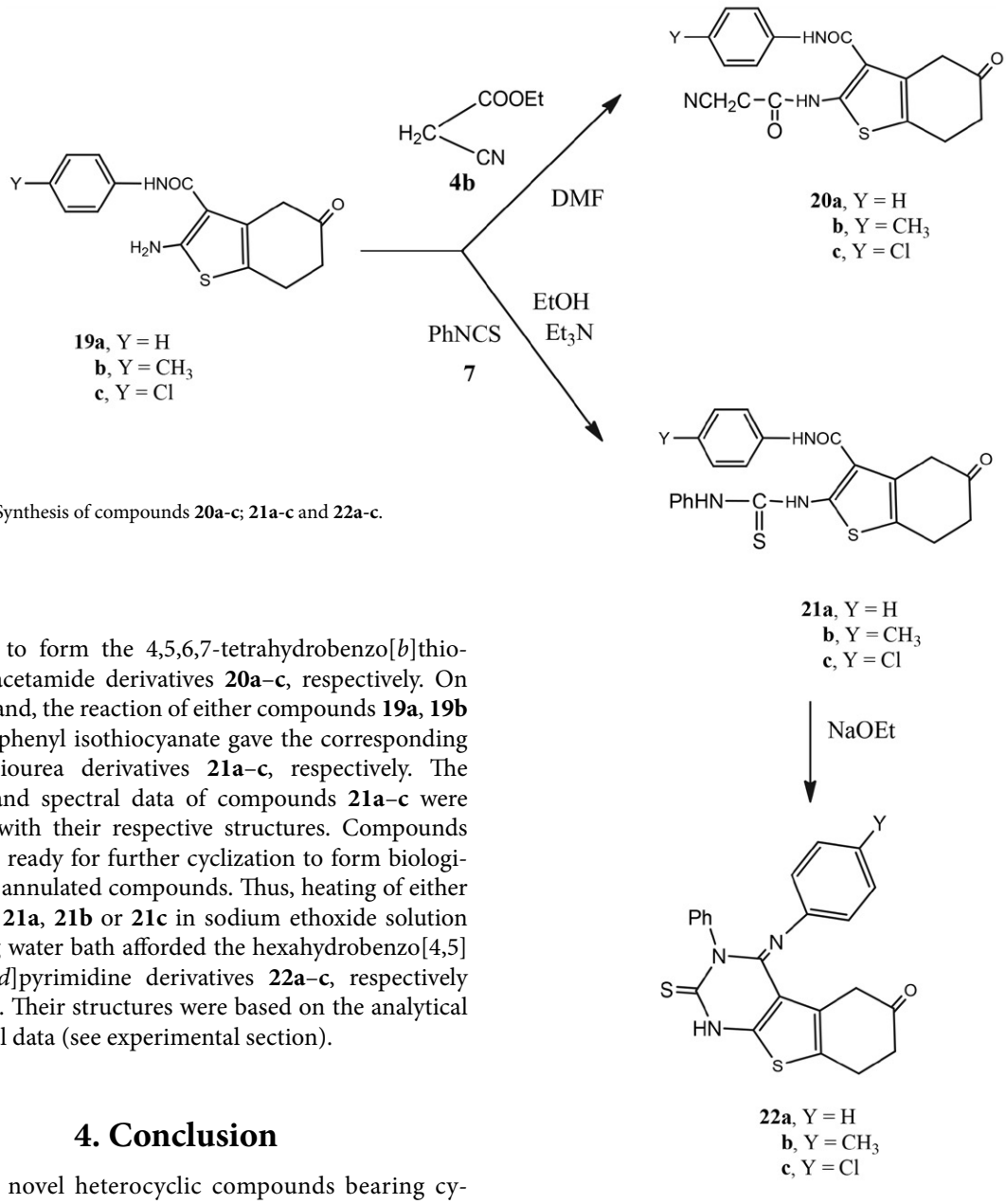
Scheme 2. Synthesis of compounds **8a,b**; **10a-d** and **12a,b**.



Scheme 3. Synthesis of compounds **14, 16a-c**; **17a-f** and **19a-c**.

derivatives **19a–c**, respectively (Scheme 3). The analytical and spectral data of the latter compounds were consistent with their respective structures. Thus, the ^{1}H NMR of compound **19a** showed the presence of two triplets at δ 2.62–2.79 ppm equivalent to the two CH_2 groups, a singlet for the third CH_2 group, a singlet at δ 4.75 ppm (D_2O exchangeable) for the NH_2 group, a multiplet at δ 7.28–7.40 ppm for the phenyl protons and a singlet at δ 8.38 ppm (D_2O exchangeable) indicating the NH group. Moreover, the ^{13}C NMR spectrum showed the presence of three signals at δ 16.3, 36.6, 40.3 corresponding to the three CH_2 groups, a signal at δ 116.6 indicating the presence of the CN group, signals at δ 120.8, 122.2, 125.3, 127.3, 132.2, 134.5, 138.0, 142.9 for the C_6H_5 and thiophene carbons and two signals at δ 164.3, 179.6 confirming the presence of two CO groups.

Compounds **19a–c** were ready to form amide derivatives through their reactions with cyanomethylene esters. Thus, the reaction of either compounds **19a–c** with ethyl cyanoacetate in *N*,*N*-dimethylformamide solution



Scheme 4. Synthesis of compounds **20a-c**; **21a-c** and **22a-c**.

took place to form the 4,5,6,7-tetrahydrobenzo[*b*]thiophen-2-yl)acetamide derivatives **20a**–**c**, respectively. On the other hand, the reaction of either compounds **19a**, **19b** or **9c** with phenyl isothiocyanate gave the corresponding *N*-phenylthiourea derivatives **21a**–**c**, respectively. The analytical and spectral data of compounds **21a**–**c** were consistent with their respective structures. Compounds **20a**–**c** were ready for further cyclization to form biologically active annulated compounds. Thus, heating of either compound **21a**, **21b** or **21c** in sodium ethoxide solution in a boiling water bath afforded the hexahydrobenzo[4,5]thieno[2,3-*d*]pyrimidine derivatives **22a**–**c**, respectively (Scheme 4). Their structures were based on the analytical and spectral data (see experimental section).

4. Conclusion

Forty novel heterocyclic compounds bearing cyclohexanone moiety were designed and synthesized. Their structures were confirmed by multiple techniques. The synthesized compounds were screened for cytotoxic activity against a panel of six human cancer cell lines using MTT assay. Some intriguing structure-activity relationships were found and discussed and the most active compounds were selected for further screening against tyrosine kinases, Pim-1 kinase and the results indicated that these compounds are good condidates as anti-cancer agents that will encourange further work in the future.

Human and Animal Rights

No Animals/Humans were used for studies that are basis of this research.

Consent for Publication

This work is consent for publication through the Journal formats.

Conflict of Interest

The authors declare no conflict of interest, financial or otherwise.

5. References

1. W. Pfau, H. Marquardt, *Toxicology* **2001**, *166*, 25–30. **DOI:**10.1016/S0300-483X(01)00435-8

2. V. P. Boyarskiy, K. V. Luzyanin, V. Y. Kukushkin, *Coord. Chem. Rev.* **2012**, *256*, 2029–2056. **DOI:**10.1016/j.ccr.2012.04.022
3. R. K. Singh, N. Sinha, S. Jain, M. Salman, F. Naqvi, N. Anand, *Tetrahedron* **2005**, *61*, 8868–8874. **DOI:**10.1016/j.tet.2005.07.018
4. V. Frenna, G. Macaluso, G. Consiglio, B. Cosimelli, D. Spinelli, *Tetrahedron* **1999**, *55*, 12885–12896. **DOI:**10.1016/S0040-4020(99)00762-0
5. B. S. Jursic, F. Douelle, K. Bowdy, E. D. Stevens, *Tetrahedron Lett.* **2002**, *43*, 5361–5365. **DOI:**10.1016/S0040-4039(02)00799-2
6. K. V. Padoley, S. N. Mudliar, R. A. Pandey, *Bioresour. Technol.* **2008**, *99*, 4029–4043. **DOI:**10.1016/j.biortech.2007.01.047
7. A. W. Erian, S. M. Sherif, A. A. Alassar, Y. M. Elkholy, *Tetrahedron* **1994**, *50*,1877–1884. **DOI:**10.1016/S0040-4020(01)80859-0
8. J. Bergman, S. Bergman, T. Brimert, *Tetrahedron* **1999**, *55*, 10447–10466. **DOI:**10.1016/S0040-4020(99)00570-0
9. J. Fuentes,W. Moreda, C. Ortiz, I. Robina, C. Welsh, *Tetrahedron* **1992**, *48*, 6413–6424. **DOI:**10.1016/S0040-4020(01)88231-4
10. S. Buscemi, A. Pace, I. Pibiri, N. Vivona, T. Caronna, *J. Fluor. Chem.* **2004**, *125*, 165–173. **DOI:**10.1016/j.jfluchem.2003.07.006
11. M. R. Shaaban, T. S. Saleh, A. S. Mayhoub, A. Mansour, A. M. Farag, *Bioorg. Med. Chem.* **2008**, *16*, 6344–6352. **DOI:**10.1016/j.bmc.2008.05.011
12. M. G. Rimoli, L. Avallone, P. de Caprariis, E. Luraschi, E. Abignente, W. Filippelli, L. Berrino, F. Rossi, *Eur. J. Med. Chem.* **1997**, *32*, 195–203. **DOI:**10.1016/S0223-5234(97)83971-2
13. L. Feng, K. W. Yang, L. S. Zhou, J. M. Xiao, X. Yang, L. Zhai, Y. L. Zhang, M. W. Crowder, *Bioorg. Med. Chem. Lett.* **2012**, *22*, 5185–5189. **DOI:**10.1016/j.bmcl.2012.06.074
14. S. Günal, N. Kaloğlu, S. I. Özdemir, I. D. Özdemir, *Inorg. Chem. Comm.* **2012**, *21*, 142–146. **DOI:**10.1016/j.inoche.2012.04.033
15. S. K. Srivastava, W. Haq, P. M. S. Chauhan, *Bioorg. Med. Chem. Lett.* **1999**, *9*, 965–966. **DOI:**10.1016/S0960-894X(99)00128-6
16. D. Z. Li,Y. Li, X. G. Chen, C. G. Zhu, J. Yang, H. Y. Liu, X. D. Pan, *Chin. Chem. Lett.* **2007**, *18*, 1335–1338. **DOI:**10.1016/j.cclet.2007.09.014
17. Z. Li, Q. Yang, X. Qian, *Bioorg. Med. Chem.* **2005**, *13*, 3149–3155. **DOI:***10.1016/j.bmc.2005.02.045*
18. R. J. Pagliero, S. Lusvarghi, A. B. Pierini, R. Brun, M. R. Mazzieri, *Bioorg. Med. Chem.* **2010**, *18*, 142–150. **DOI:**10.1016/j.bmc.2009.11.010
19. S. Barbuceanu, G. Saramet, G. L. Almajan, C. Draghici, F. Barbuceanu, G. Bancescu, *Eur. J. Med. Chem.* **2012**, *49*, 417–423. **DOI:**10.1016/j.ejmech.2012.01.031
20. A. Da Settimo, G. Primofiore, F. Da Settimo, L. Calzolari, P. Cazzulani, A. Passoni, O. Tofanetti, *Eur. J. Med Chem.* **1992**, *27*, 395–400. **DOI:**10.1016/0223-5234(92)90153-R
21. A. E. Amr, M. H. Sherif, M. G. Assy, M. A. Al-Omar, I. Ragab, *Eur. J. Med. Chem.* **2010**, *45*, 5935–5942. **DOI:**10.1016/j.ejmech.2010.09.059
22. T. Bányász, J. Magyar, A. Varró, A. Kovács, I. Gyönös, G. Szénási, P. Nánási, *Vasc. Pharmacol.* **1999**, *32*, 329–333. **DOI:**10.1016/S0306-3623(98)00197-9
23. D. M. Swanson, C. R. Shah, B. Lord, K. Morton, L. K. Dvorak, C. Mazur, R. Apodaca, W. Xiao, J. D. Boggs, M. Feinstein, S. Wilson, A. J. Barbier, P. Bonaventure, T. W. Lovenberg, N. I. Carruthers, *Eur. J. Med. Chem.* **2009**, *44*, 4413–4425. **DOI:**10.1016/j.ejmech.2009.06.007
24. R. M. Mohareb, R. A. Ibrahim, E. S. Alwan, *Acta Chim. Slov.* **2020**, *in press*. **DOI:**10.17344/acsi.2020.6090
25. R. M. Mohareb, F. M. Manhi, A. Abdelwahab, *Acta Chim. Slov.* **2020**, *67*, 83–95. **DOI:**10.17344/acsi.2019.5224
26. R. M. Mohareb, P. A. Halim, *Acta Chim. Slov.* **2018**, *65*, 554–568. **DOI:**10.17344/acsi.2017.4146
27. L. Liu, A. Siegmund, N. Xi, P. Kaplan-Lefko, K. Rex, A. Chen. J. Lin, J. Moriguchi, L. Berry, L. Y. Huang, Y. Teffera, Y. J. Yang, Y. H. Zhang, S. F. Bellon, M. Lee, R. Shimanovich, A. Bak, C. Dominguez, M. H. Norman, J. C. Harmange, I. Dussault, T. S. Kim, *J. Med. Chem.* **2008**, *51*, 3688–3691. **DOI:**10.1021/jm800401t
28. M. L. Peach, N. Tan, S. J. Choyke, A. Giubellino, G. Athauda, T. R. Burke, M. C. Nicklaus, D. P. Bottaro, *J. Med. Chem.* **2009**, *52*, 943–951. **DOI:**10.1021/jm800791f
29. F. D. Bacco, P. Luraghi, E. Medico, G. Reato, F. Girolami, T. Perera, P. Gabriele, P. M. Comoglio, C. Boccaccio, *J. Natl. Cancer Inst.* **2011**, *103*, 645–661. **DOI:**10.1093/jnci/djr093
30. R. M. Mohareb, K. M. H. Hilmy, Y. A. Elshehawy, *Bull. Chem. Soc. Ethiop.* **2018**, *32*, 285–308. **DOI:**10.4314/bcse.v32i2.9
31. B. P. McKibben, C. H. Cartwright, A. L. Castelhano, *Tetrahedron Lett.* **1999**, *40*, 5471–5474. **DOI:**10.1016/S0040-4039(99)01108-9
32. K. Wang, D. Kim, A. Dömling, *J. Comb. Chem.* **2010**, *12*, 111–118. **DOI:**10.1021/cc9001586
33. R. Mishra, K. K. Jha, S. Kumar, I. Tomer, *Der Pharma Chem.* **2011**, *3*, 38–54.

Povzetek

V prispevku opisujemo serijo heterociklizacijskih reakcij, ki smo jih izvedli na cikloheksan-1,3-dionu s furan-2-karbaldehidom ali tiofen-2-karbaldehidom pri čemer sta nastala ustrezna ilidenska derivata **3a**,**b**; ti dve spojini sta bili izhodišče za nadaljnje heterociklizacijske reakcije, ki so vodile do tiofenskih in piranskih derivatov **5a**–**d** oz. **6a**–**d**. Ob reakciji spojin **3a**,**b** z elementarnim žveplom in fenil izotiocianatom sta nastala pripojena tiazolska derivata **8a**,**b**. Pri reakciji s hidrazin hidratom ali fenilhidrazinom pa so nastali 4-hidrazono-4,5,6,7-tetrahidro-2*H*-indazolski derivati **10a**–**d**. Podobno sta pri reakciji med **3a** ali **3b** s hidroksilamin hidrokloridom nastala 6,7-dihidrobenzo[*c*]izoksazol-4(5*H*)-on oksima **12a** in **12b**. Pripravili smo še več drugih heterocikličnih spojin in določili njihove strukture. Pripravljenim spojinam smo določili citotoksične aktivnosti na izbrane celične linije raka. Za najbolj aktivne spojine smo v nadaljevanju določili še inhibitorne lastnosti proti tirozin kinazam in Pim-1 kinazi.

Except when otherwise noted, articles in this journal are published under the terms and conditions of the Creative Commons Attribution 4.0 International License

DOI: 10.17344/acsi.2020.6183 *Acta Chim. Slov.* **2021,** *68,* 88–101
creative commons

Scientific paper

Synthesis, Crystallographic Structure, Hirshfeld Surface Analysis, Drug-likeness Properties and Molecular Docking Studies of New Oxime-pyridine Compounds

Tufan Topal*

Department of Chemistry, Pamukkale University, 20020, Denizli, Turkey,

** Corresponding author: E-mail: tufantopal@hotmail.com*
Phone: +90 258 2963457, fax: +90 258 2963535

Received: 06-11-2020

Abstract

A detailed description of the two new pyridine ligands, (2E,3Z)-3-[2-(3-chloropyridin-2-yl)hydrazinylidene]-N-hydroxybutan-2-imine and 3-chloro-2-{(2Z)-2-[1-(4 nitrophenyl)ethylidene]hydrazinyl}, is reported. The synthesized compounds were characterized by spectroscopic studies, spectral features were performed by TD-DFT calculations. New-generation pyridine ligand of HL_2 was also determinate by single-crystal X-ray diffraction and Hirshfeld surface analysis with two-dimensional fingerprint plots was used to analyze intermolecular interactions in crystals. Molecular-docking was performed to investigate the binding areas of chemical compounds, and the results showed the inhibitory activity of the studied HL_1 and HL_2 against *E. coli***.** The results of the current study revealed the drug-likeness and bioactive properties of the ligands.

Keywords: Pyridine-oxime; molecular electrostatic potential (MEP); Drug-likeness; E. Coli; Hirshfeld surface analysis; X-ray diffraction

1. Introduction

For biological activities, pyridine compounds are widely used as antibacterial, antifungal, and anticancer agents.[1–3] Several studies have been conducted on biological compounds in health-related journals and books. Accordingly, pyridine derivatives cause interactions with high binding capacity by targeting enzymes, proteins, and deoxyribonucleic acid (DNA) that create biological problems.[4] With the discovery of new compounds, several studies were performed in the last decade to inhibit antibacterial drug resistance and reduce associated adverse effects on human health.[5] It is clear that new types of viruses and bacteria affect the lives of humans worldwide in a variety of ways. Accordingly, this places immense responsibility on researchers and chemists who work to develop new materials to decrease the effects of viruses and bacteria as well as biologists and physicians who test the new compounds on animals and humans. Requiring extensive research, conducting in vitro studies is costly and time-consuming; accordingly, one of the most important advantages of the current study was the contribution to perform *in silico* studies inactivating viruses, bacteria, and cancer cells by the production of ligands with medicinal potential. Pyridine and oxime compounds have a high interference of hydrogen bond in electrostatic potential capacity. Intramolecular and intermolecular hydrogen bonds play a major role in the interacting and binding of biological molecules. In addition, pyridine and oxime compounds have been selected particularly for their ability to easily transfer the electrons of nitrogen atoms participating in the aromatic ring and C=N groups into the donor–acceptor system.[6–11] Due to their high levels of antibacterial properties and bioactive multizones, nitrogenous organic or inorganic compounds are reported to have positive effects on *Escherichia coli.*[12] The reason for the investigation of *E. coli* pathogens in molecular-docking studies is this bacterium's resistance against some medications and its high binding capacity.[5] Furthermore, *E. coli,* also known as the most-common human pathogen, causes different types of infections, such as kidney, gallbladder, skin, and respiratory infections in addition to meningitis in neonates.[13,14] The physicochemical properties of compounds affect bioavailability, including electrostatic potential, molar absorptivity, stability, solubility, structure, intracellular absorption, hydrogen bonds, and bonding energy.[15,16] The theoretical method such as Density Functional Theory (DFT) in the computational chemistry is

important tool to predict the assignment of specific electronic transitions in the UV-Vis spectra. In the present study, oxime and pyridine derivative compounds were synthesized and characterized by X-ray and spectroscopic methods. In addition, the surface analysis was performed to analyze their chemical properties, and molecular electrostatic potential was calculated to determine the nucleophilic and electrophilic zones. Molecular-docking was conducted to investigate the hydrogen-binding interactions of *E. coli* DNA gyrase subunit B (GyrB) and *E. coli* beta-ketoacyl-acyl carrier protein synthase III (FabH) and determined pharmacokinetic and pharmacological properties.

2. Materials and Methods

2. 1. Materials and Physical Measurements

The chemicals and solvents: methanol, acetonitrile, 3-chloro-2-hydrazinopyridine, 2,3 butanedione monoxime, 4′-nitroacetophenone were obtained from Sigma–Aldrich. BRUKER BIOSPIN NMR AVANCE Spectrometer III 400MHz model spectrometer was used for ^{1}H-NMR and ^{13}C-NMR analysis. Elemental analysis were determined using a Costech Elemental analysis device ECS 4010 Model analyzer. IR spectrums were recorded in the 400–4000 cm^{-1} on Perkin Elmer FTIR-Spectrometer Spectrum Two Model and Mass Spectra (ESI) on TSQ Fortis™ Triple Quadrupole Mass Spectrometer. Melting points of ligands were determined by Stuart SMP10. The mains water was passed through the Thermo Scientific Smart2pure device to make it pure water. Absorption spectra was carried out using Shimadzu UV-1800 UV-VIS spectrophotometer. Single-crystal X-ray structure was determined using an Agilent SuperNova Dual CCD detector diffractometer eguipped with graphite-monochromated MoKα radiation (λ = 0.71073 °A) at room temperature.

2. 2. Synthesis of Ligands HL_1, HL_2

Chemical preparation of (2*E*,3*Z*)-3-[2-(3-chloropyridin-2-yl)hydrazinylidene]-*N*-hydroxybutan-2-imine HL_1 and 3-chloro-2-{(2*Z*)-2-[1-(4-nitrophenyl)ethylidene]hydrazinyl}pyridine HL_2.

3-chloro-2-hydrazinopyridine (1 mmol, 0.1435 g) in acetonitrile solution (10 ml) was added 2,3 butanedione monoxime (1 mmol, 0.1011 g) HL_1 and 4′-Nitroacetophenone (1 mmol, 0.1651 g) HL_2 in 10 ml of acetonitrile respectively (Fig.1). The both solution stirred for 24 h at room temperature and were kept aside for slow evaporation of solvent for about 5 days. The HL_2 crystal was obtained from slow evaporation technique by dissolving the product in acetonitrile.

$C_9H_{11}ClN_4O$ (HL_1), Crem; Yield 87%. m.p.:194 °C. ^{1}H-NMR (400 MHz, Chloroform-d_6, ppm): δ 9.83 (s, 1H, O-H), δ 8.45 (s, 1H, -NH), δ 8.37 (d, 1H, Ar-H), δ 7.62 (d, 1H, Ar-H), δ 6.84 (t, 1H, Ar-H), δ 2.34 (s, 3H, -CH_3), δ 2.23 (s, 3H, -CH_3). ^{13}C-NMR (100 MHz, Chloroform-d_6, ppm): δ 157.39 (-C=N-OH), δ 157.32 (-C=N-), δ 150.00, 147.12, 137.32, 116.50, 115.35 (C-$Ar_{pyridine}$), δ 10.03 (-CH_3), δ 9.53 (-CH_3).[17] LC/MS-MS, (ESI) m/z= 226.66284 $[M+1]^+$ (100%). Calcd. for $C_9H_{11}ClN_4O$: C, 47.69; H, 4.89; N, 24.72%; found: C, 47.71; H, 4.86; N, 24.69%. IR (KBr) cm^{-1}: 3357 (N-H), 3112 (O-H), 2981 (C-H_{Ar}), 1596 (C=N)$_{pyridine}$, 1561 (C=N)$_{imine}$, 1516 (C=N)$_{oxime}$, 935 (N-O).

$C_{13}H_{11}ClN_4O_2$ (HL_2), Orange; Yield 86%. m.p.:169 °C. ^{1}H-NMR (400 MHz, Chloroform-d_6, ppm): δ 8.48 (s, 1H, -NH), δ 8.30 (d, 1H, Ar-H), δ 8.20 (d, 2H, Ar-H), δ 8.01 (d, 2H, Ar-H), δ 7.61 (d, 1H, Ar-H), 6.84 (t, 1H, Ar-H), δ 2.38 (s, 3H, -CH_3), ^{13}C-NMR (100 MHz, Chloroform-d_6, ppm): δ 149.92, δ 147.61 (C-$Ar_{pyridine}$), δ 147.17 (-C=N-), δ 144.49, 144.42 (C-Ar), δ 137.33 (C-$Ar_{pyridine}$), δ 126.89, 126.89, 123.64, 123.64 (C-Ar), δ 116.97, 115.49 (C-$Ar_{pyridine}$), δ 12.53 (-CH_3). LC/MS-MS, (ESI) m/z= 290.70558

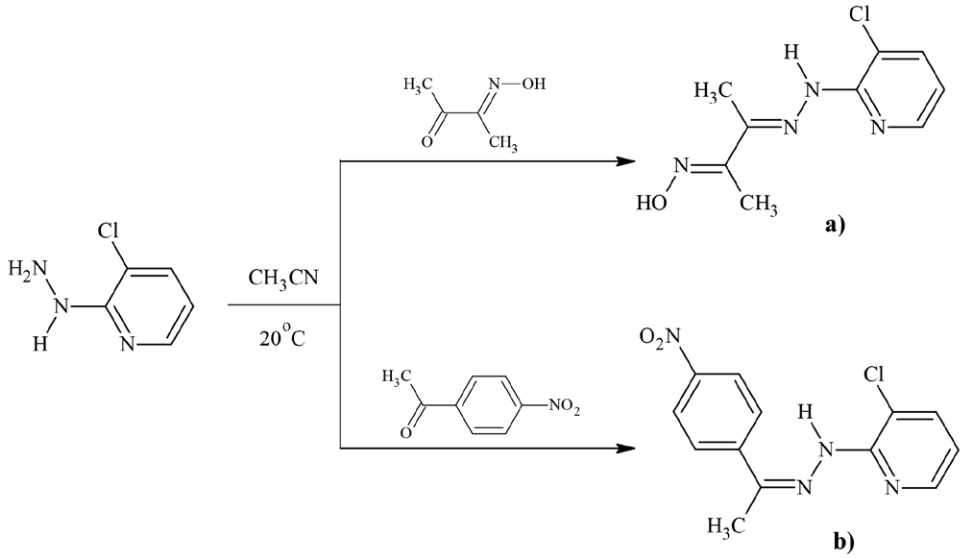


Fig. 1. Structure of compounds a) HL_1 and b) HL_2

$[M+1]^+$ (100%). Calcd. for $C_{13}H_{11}ClN_4O_2$: C, 53.71; H, 3.81; N, 19.27%; found: C, 53.73; H, 3.79; N, 19.22%. IR (KBr) cm^{-1}: 3378 (N-H), 2922 (C-H_{Ar}), 1585 (C=N) $_{pyridine}$, 1557 $(C=N)_{imine}$, 1392 (NO_2).[18]1H NMR and UV-Vis spectra. Reaction of 1:1 stoichiometric proportion of HL with Na2[PdCl4] in methanol affords a mononuclear palladium(II

2. 3. X-ray Crystallography Analysis

Orange crystal of the $C_{13}H_{11}ClN_4O_2$ compound was obtained in acetonitrile solution through slow evaporation for 5 days at room temperature. The data set of reflections were collected using an Agilent SuperNova X-Ray diffractometer with MoKα (λ = 0.71073) at 293 K. The data reduction and data correction were performed by Olex2 software (version 1.3).[19,20] Refinements were obtained by the Full-Matrix method on F^2 using the Olex2 software, and crystal packing diagrams were created by Mercury 4.3.0 software. All the nonhydrogen atoms were anisotropically refined using the riding model approximation.[21] Tables 1 and 2, a summary of the experimental details of HL_2.[22–24] CCDC DOI: 10.5517/ccdc.csd.cc24rlzh and number 1988897 contains the supplementary rystallographic data for this work. This data can be obtained from The Cambridge Crystallographic Data Centre via www.ccdc.cam.ac.uk/data_ request/cif.

Table 1. Crystal data and structure refinement for HL_2.

CCDC number	1988897
Empirical formula	$C_{13}H_{11}ClN_4O_2$
Formula weight	290.71
Temperature/K	293(2)
Crystal system	monoclinic
Space group	$P2_1/c$
a/Å	11.7767(7)
b/Å	14.4529(7)
c/Å	7.9073(4)
α/°	90
β/°	91.381(5)
γ/°	90
Volume/$Å^3$	1345.49(12)
Z	4
$\rho_{calc}g/cm^3$	1.435
μ/mm^1	0.291
F(000)	600.0
Crystal size/mm^3	0.14 × 0.13 × 0.12
Radiation	Mo Kα (λ = 0.71073)
2Θ range for data collection/°	6.756 to 49.996
Index ranges	$-8 \le h \le 14$, $-16 \le k \le 16$, $-8 \le l \le 9$
Reflections collected	4286
Independent reflections	2343 [R_{int}=0.0161, R_{sigma} = 0.0302]
Data/restraints/parameters	2343/0/182
Goodness-of-fit on F^2	1.047
Final R indexes [I>=2σ (I)]	R_1 = 0.0548, wR_2 = 0.1338
Final R indexes [all data]	R_1 = 0.0790, wR_2 = 0.1491
Largest diff. peak/hole / e $Å^{-3}$	0.21/-0.41

3. Results and Discussion

3. 1. Description of the Crystal Structures and Hydrogen Bonding

Slow evaporation technique was used to make the sample suitable for X-ray structure analysis. The HL_2 crystallizes in the centrosymmetric space group $P2_1/c$ of monoclinic system with a unit cell volume of 1345.49(12) $Å^3$, the cell dimensions are: a = 11.7767(7) Å, b = 14.4529(7)

Table 2. Selected Bond Lengths/Å, Angles/° and Torsion/° for HL_2.

Atom	Atom	Length	Atom	Atom	Atom	Angle	Atom	Atom	Atom	Atom	Torsion
N7	N8	1.355(3)	C9	N8	N7	117.57(19)	N7	N8	C9	C10	–1.6(3)
N8	C9	1.287(3)	N8	N7	C2	121.4(2)	N8	N7	C2	N1	–1.4(4)
N1	C2	1.329(3)	C2	N1	C6	117.2(3)	C2	N1	C6	H6	–179.5(4)
N1	C6	1.333(4)	C13	C12	C9	120.2(2)	C13	C12	C9	N8	8.3(3)
C9	C12	1.474(3)	C17	C12	C9	122.1(2)	C9	N8	N7	H7	–4.3(4)
C12	C13	1.397(3)	C17	C12	C13	117.7(2)	C2	N7	N8	C9	175.7(2)
C12	C17	1.391(3)	N1	C2	C3	122.5(2)	C6	N1	C2	N7	–177.6(3)
C3	C2	1.394(4)	C4	C3	C2	118.7(3)	C6	N1	C2	C3	2.4(4)
C9	C10	1.505(3)	C12	C9	C10	120.8(2)	C10	C9	C12	C13	–170.9(2)
C14	C13	1.375(3)	N8	C9	C12	115.0(2)	N8	C9	C12	C17	–172.1(2)
C17	C16	1.369(4)	N8	C9	C10	124.2(2)	C10	C9	C12	C17	8.7(3)
C15	C14	1.379(4)	N7	C2	C3	118.7(2)	N8	C9	C10	10HA	–55.3
C4	C3	1.375(4)	C16	C17	C12	122.0(2)	N8	C9	C10	10HB	–175.3
C6	C5	1.368(5)	N1	C2	N7	118.9(2)	N8	C9	C10	10HC	64.7
C5	C4	1.371(5)	N1	C6	C5	124.2(3)	C12	C9	C10	10HA	123.9
N7	C2	1.371(3)	C14	C15	N18	119.1(3)	C12	C9	C10	10HB	3.9
C16	C15	1.361(4)	C14	C13	C12	120.6(2)	C12	C9	C10	10HC	–116.1

Å, c = 7.9073(4) Å, β = 91.381(5)° and Z = 4. The full data collection was done for indices h, k and l with ranges of -8 ≤ h ≤ 14, −16 ≤ k ≤ 16, −8 ≤ l ≤ 9 and R value of R_1 = 0.0548, wR_2 = 0.1338. Carbon and hydrogen atoms have been geometrically positioned.

The bond lengths between the atoms N8=C9 1.287(3) Å, N7-N8 1.355(3) Å, C9-C12 1.474(3) Å, C12-C13 1.397(3) Å and C12-C17 1.391(3) Å were found. In literature 1.28(14) Å, 1.35(3) Å, 1.49(14) Å, 1.39(15) Å and 1.38(16) Å are similar with our values of atomic lengths.[25–27] The N8=C9 bond was shorter than the N8-N7 bond and it confirms that N8=C9 shows a double bond character. In HL_2, pyridyl N1-C2 and N1-C6 bond distances were 1.329(3) and 1.333(4) Å, bond angle C2-N1-C6 117.2(3)° and torsion angle C2-N1-C6-H6 -179.5(4)° were found and this torsion value is competible with the expected 180°.[11,28] Torsion angles of atoms between pyridyl and benzene ring have been observed C13-C12-C9-N8 8.3(3)°, N8-N7-C2-N1 −1.4(4)° and N7-N8-C9-C10 −1.6(3)°. The ORTEP-3 drawn with 35% probability is given in Fig. 2.

Basically 3 pairs of hydrogen bond interactions are observed in the structure, these are C-H···O, C-H···N and C-H···Cl intramolecular and intermolecular hydrogen bonds.[29,30] Selected hydrogen bond distances and angles are listed in Table 3. In HL_2, carbon atom C10 acts as a donor to N1 atom at C(10)-H(10A)···N(1) (x,1.5-y,-1/2+z),

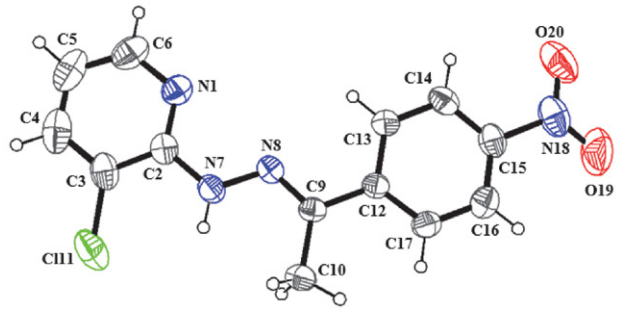


Fig. 2. Molecular structure of the HL_2. Thermal ellipsoids are shown at 35% probability level

developing the capped stick style and two-dimensional chain along the crystallographic axis as depicted in Fig. 3a.

As illustrated in Fig. 3b, in HL_2, C-H···O intermolecular hydrogen bonding interactions were used to generate a three-dimensional (3D) supramolecular network along the c axis. All the figures were drawn in Mercury software. Other hidrogen bonds were C(10)-H(10A)···Cl(11) (1-x,2-y,1-z), C(5)-H(5)···O(20) (1-x,1-y,1-z), C(10)-H(10B)···O(19) (2-x,-1/2 + y,1/2-z), C(17)-H(17) ···O(20) (2-x,-1/2 + y,1/2-z), C(5)-H(5)···O(19) (-1 + x,y,1 + z), C(10)-H(10B)···O(20) (2-x,-1/2 + y,1/2-z), C(13)- H(13)···Cl(11) (1-x,2-y,1-z).[31]

Table 3. Selected hydrogen bond distances (Å), symmetry and angles (°) for HL_2.

D-H···Å	d (D-H)	d (H···Å)	d(D-H···Å)	Symmetry codes	∠D–H···Å
C(10)-H(10A)···Cl(11)	0.960	3.174	3.882	1-x,2-y,1-z	131.90
C(10)-H(10A) ···N(1)	0.960	2.768	3.602	x,1.5-y, -1/2+z	145.68
C(5)-H(5)···O(20)	0.930	3.019	3.606	1-x,1-y,1-z	122.57
C(10)-H(10B)···O(19)	0.960	2.730	3.417	2-x, -1/2+y,1/2-z	129.08
C(17)-H(17)···O(20)	0.930	2.460	3.322	2-x, -1/2+y,1/2-z	154.19
C(13)-H(13) ···Cl(11)	0.930	2.941	3.764	1-x,-1/2+y,1.5-z	148.37
C(5)-H(5)···O(19)	0.930	2.909	3.747	-1+x,y,1+z	150.54
C(10)-H(10B)···O(20)	0.960	3.057	3.978	2-x, -1/2+y,1/2-z	161.22

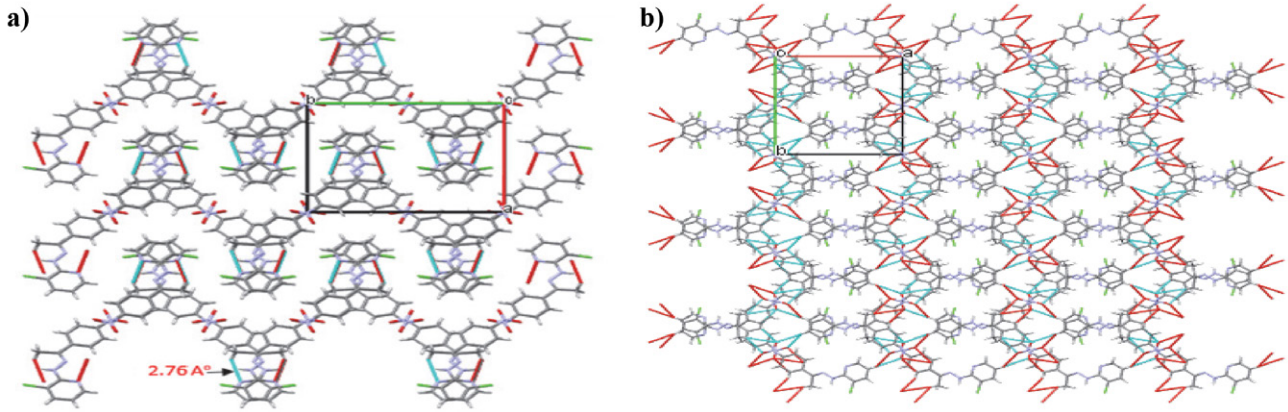


Fig. 3. a) Two-dimensional self-assembling; b) three-dimensional supramolecular frameworks of $C_{13}H_{11}ClN_4O_2$ and hydrogen bonds

3. 2. ^{1}H NMR Studies

^{1}H-NMR spectrum of HL_1 is shown in Fig. 4. ^{1}H-NMR spectrum of the HL_1 ligand oxime (N–OH) group of the proton (H13) was observed at 9.83 ppm as a singlet peak. The NH proton (H8) generated a signal at 8.45 ppm. The spectrum of the (2*E*,3*Z*)-3-[2-(3-chloropyridin-2-yl)hydrazinylidene]-*N*-hydroxybutan-2-imine ligand observed at singlet peaks 2.23 ppm (H14A, H14B, H14C) and 2.34 ppm (H15A, H15B, H15C) methylene group of protons. While H1 proton signal appeared at d 8.37 ppm, the signals at d 7.62 and d 6.84 ppm were due to H3 and H2 of pyridinium moiety, respectively.[32] In HL_2, the NH proton (H7) generated a sharp signal at 8.48 ppm, as a singlet peak. The peaks were observed at range 8.30–6.84 ppm were assignable to the protons of aromatic rings as multiplet peaks. The spectrum of the 3-chloro-2-{(2*Z*)-2-[1-(4-nitrophenyl)ethylidene]hydrazinyl}pyridine ligand observed at singlet peaks 2.38 ppm (H10A, H10B, H10C) methylene group of protons. The signal at d 8.30 ppm was attributed at to (H6) aromatic proton of pyridine. The proton signal appearing at d 8.20 and d 8.01 ppm were due to (H13, H17, H16, H14) of aromatic moiety respectively. Aromatic protons of pyridine moiety produced a broad signal at d 7.61 and t 6.84 ppm (H5, H4).[11,18,33] It was observed that the obtained results were exactly compatible with the structure.

3. 3. ^{13}C NMR Studies

^{13}C-NMR spectrum of HL_1 is shown in Fig. 5. ^{13}C-NMR spectrum HL_1 observed a single resonance at 157.39 and 157.32 ppm, respectively which showed that the oxime (C=NOH) and hydrazone (-NHN=CH) (C11,C10) carbon atoms. All the signals were assigned to the aromatic carbons (C1-C5) of the pyridine at the range of 150.00–115.35 ppm. The signals observed at 10.03 and 9.53 ppm are attributable to the carbon atom of methyl group (C15,C14). For HL_2, aromatic carbons of pyridine and benzene rings gave different signals in their resonance. Hence the signals at 149.92, 147.61, 137.33, 116.97, 115.49 ppm were due to carbon (C2-C6) while (C12-C17) presented in different signals at 144.49, 144.42, 126.89, 126.89, 123.64, 123.64 ppm in the aromatic moiety of ligand. Two equivalent para carbons (C13,C17) and (C14,C16) brought out a signals at d 126.89 and 123.64 ppm in the spectrum. The signal at 147.17 ppm was due to the (C9) carbon of the imine group of moiety. The signal observed at 12.53 ppm is attributable to the carbon atom of methyl group (C10).[25,32,33]

3. 4. UV-Vis Absorption Spectra and TD-DFT Calculations

UV-Vis calculations were performed by TD-DFT/B3LYP method with 6-31G basis set using Gaussian 09

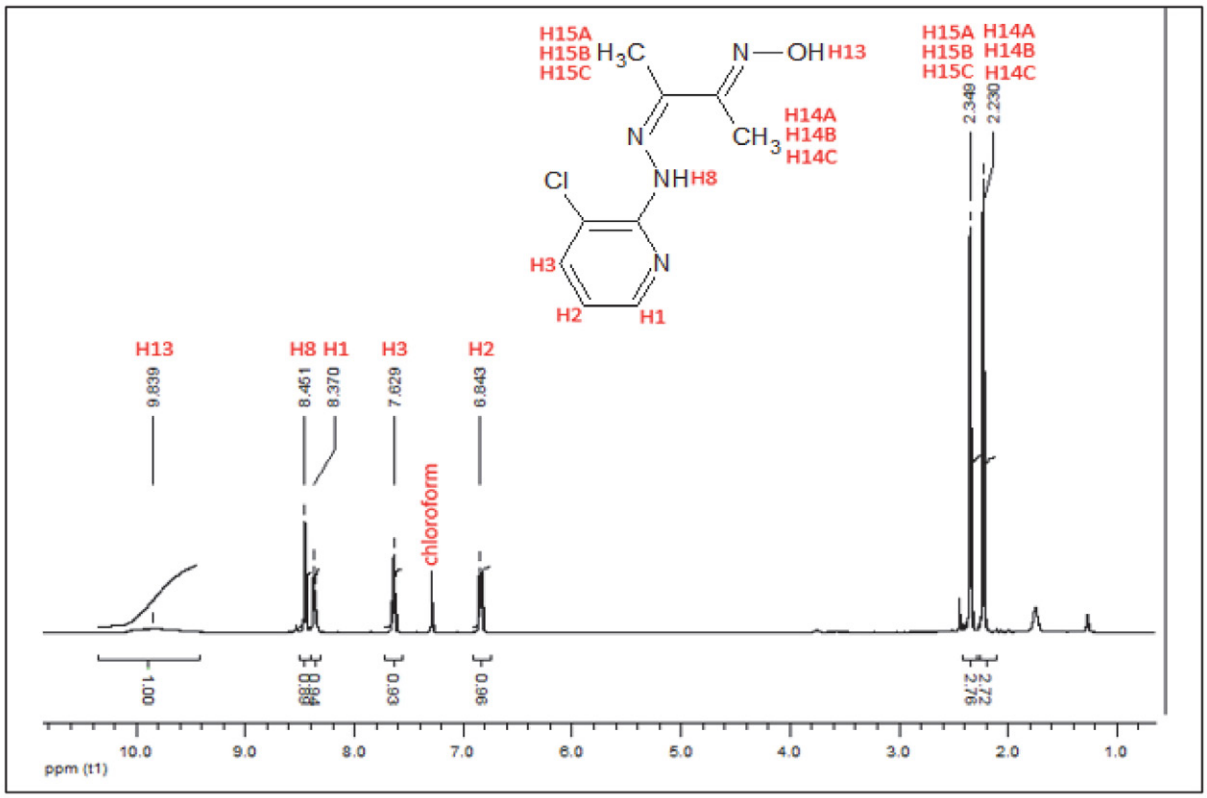


Fig. 4. ^{1}H-NMR spectrum of HL_1

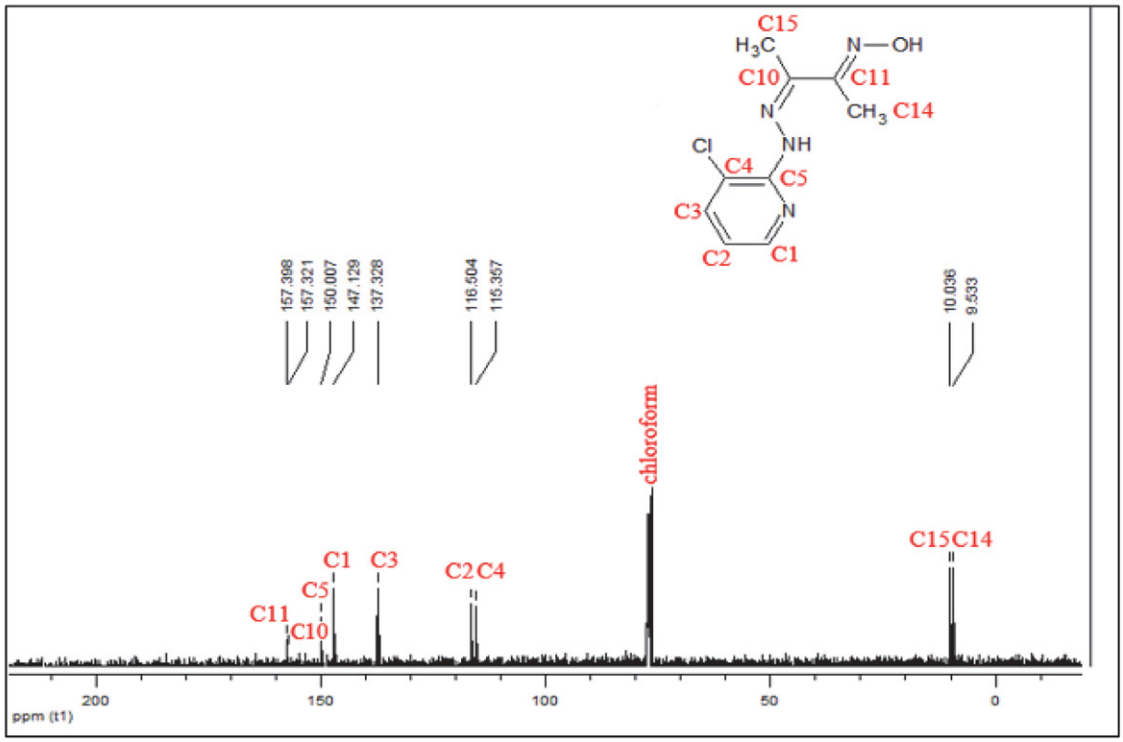


Fig. 5. ^{13}C-NMR spectrum of HL_1

program.[34,35] The electronic absorption spectra of the ligands, along with the molar extinction coefficient, were obtained in a 5 × 10^{-5} mol L^{-1} chloroform solution in the wavelength zone (240–480 nm) using the spectroscopic method.[23] The electron transition possibilities of different compounds were compared using ultraviolet-visible spectroscopy. For HL_1 and HL_2, slightly different absorption peaks centered at 322, 285 nm and 362, 312 nm (ε = 42800, 41100 and 34520, 26300 mol^{-1} L cm^{-1}), respectively. The experimental UV-Vis spectra of the HL_1 compund and corresponding theoretical calculations are plotted in Fig. 6. Theoretical calculations predicted two peaks at 307, 287 nm and 364, 331 nm which indicated formation of the HL_1 and HL_2.[36] The calculated excitation energy, excitation wavelength, oscillator strength with the aid of TD-DFT/B3LYP method are given in Table 4. The electronic absorption spectra of the ligands were defined with two sharp absorption bands. These two bands were observed at 285-312 and 322–362 nm indicative of the π-π* and n-π* transitions, respectively.[37] While the π-π* transitions of the ligands originated from the electrons of the pyridine ring, the n-π* band occurred due to hydrazone groups (-NHN=CH) of atoms.[38]

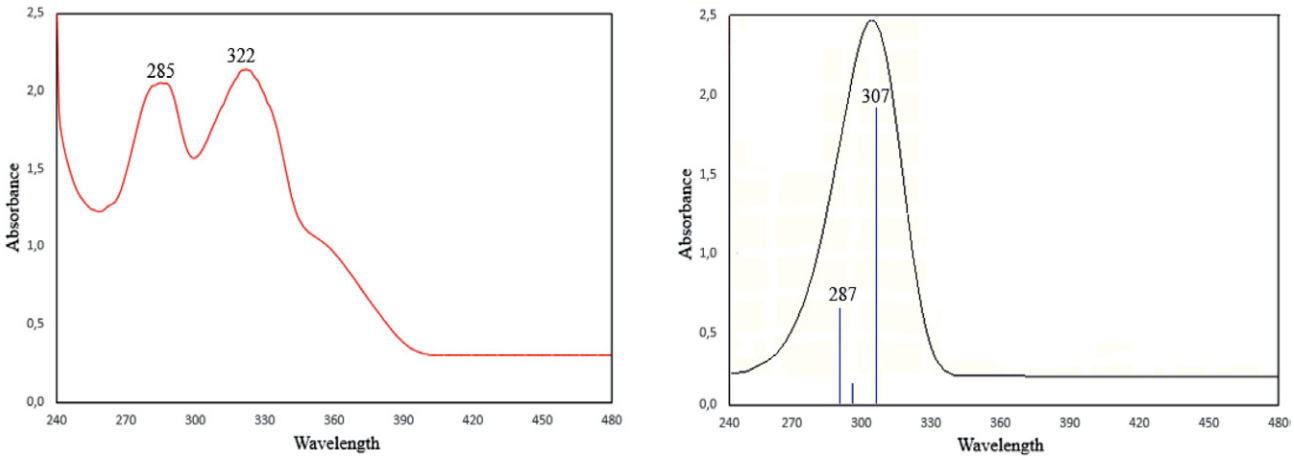


Fig. 6. The (left) experimental and (right) calculated spectrum and observed UltravioleteVisible spectra of the HL_1 in CH_2Cl_2 solution at room temperature

Table 4. The experimental and calculated UV-Vis spectral parameters for HL_1 and HL_2 ligand with its assignments.

Compounds	Experimental λ(nm)	Calculated λ(nm)	E (eV)	f	Assignment
HL_1	285	287	4.36	0.18	π-π*
	322	307	4.03	0.03	n-π*
HL_2	312	331	3.73	0.02	π-π*
	362	364	2.56	0.06	n-π*

3. 5. Mass and FT-IR Spectra

Mass spectral datas of ligands were obtained by electrospray ionization (ESI) method. The mass exhibited the molecular ion at m/z 226.66284 $[M+1]^+$ and 290.70558 $[M+1]^+$ which indicated formation of the HL_1 and HL_2 (Fig. S1). The moleculer peak of both ligands have a 100% relative abundance.[32]

Generally compunds are characterized by three IR absorption bands such as ν(O–H), ν(C=N) and ν(N–O) stretching vibrations. FT-IR spectrum of the HL_1 ligand showed (C=N) imine (C=N) oxime peaks at 1596 cm^{-1} and 1516 cm^{-1} (Fig. S2).[39] The bands 3361 cm^{-1} and 3377 cm^{-1} were due to (N-H) vibrations for HL_1 and HL_2 respectively. Also (O-H) band of oxime group peak was observed at 3111 cm^{-1}.[33] But this peak was not seen at HL_2 ligand. At the same time, the bands at 935 cm^{-1} and 1392 cm^{-1} assignable to (N-O) and (NO_2) vibrations, respectively. The FT-IR spectrum of ligands displayed bands at 2981 cm^{-1} and 2972 cm^{-1} which assignable to ($C\text{-}H_{Ar}$) protons. The medium bands observed at 553 cm^{-1} and 546 cm^{-1} assigned to pyridyl rings. For HL_1 and HL_2, the bands 1454–1451 cm^{-1}, 1394–1392 cm^{-1}, 1044–1032 cm^{-1} and 1012–1032 cm^{-1} assignable to the aromatic pyridine ring.[40] FT-IR analysis give us the preliminary information about whether this structure is formed or not. Our datas are in agreement with similar oxime and pyridine ligands in the literature.[41]

3. 6. Hirshfeld Surface Analysis

The surface analysis method is the best way to identify crystal packing and intermolecular interacting in a structure. For this reason, the Hirshfeld surface analysis was performed using CrystalExplorer software (version 17.5).[42,43] Accordingly, the close correlations between the fragments were quantitatively analyzed. Furthermore, it is one of the computer calculation programs to investigate the mechanism of molecular interactions in proteins and with which intermolecular interactions they could bond to a receptor. In addition, it helps to identify the intermolecular hydrogen bond as well as π-π, C-H···X (X=halogens) interactions with great importance in crystal package arrangement and stabilization of the molecule. Therefore, C(17)-H(17)···O(20) and C(13)-H(13)···Cl(11) interactions are illustrated in Fig. 7.

Intermolecular interactions of HL_2 ligand is presented in Fig. 8 as 2D fingerprints plot.[44] Blue zone shows intermolecular interaction areas whereas grey zone shows outside of the this interaction area. According to fingerplots studies results of for HL_2; Cl···H 11,4%, H···H 28,7%, N···C 6,4%, N···H 6,5%, O···H 18,3%, Cl···N 2,5%, C···C 3,8%, C···H 15,2%.[22–24] Other bondings constituted all interactions by making small contributions on the surface. The highest H···H interaction rate (28.7%) was shown to be derived from the abundance of the H···H interactions in aromatic rings (Fig. S3).[4]

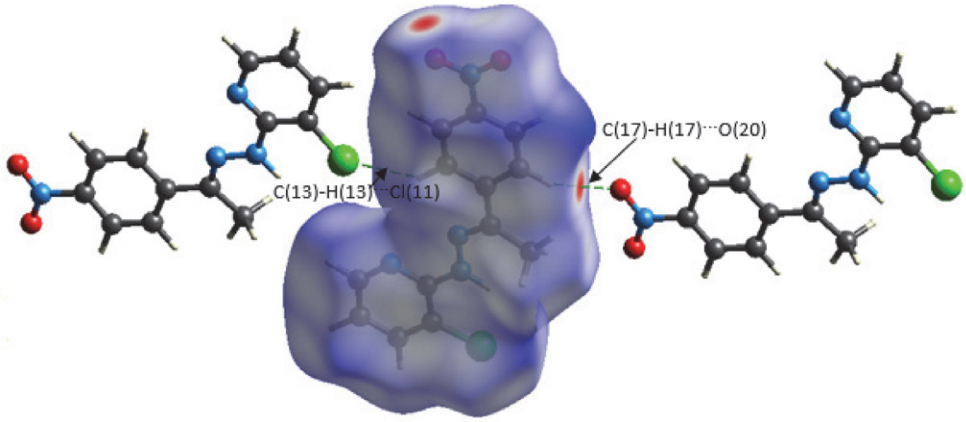


Fig. 7. Close contact of C(17)-H(17)···O(20) and C(13)-H(13)···Cl(11) interactions determined by Hirshfeld surface analysis over dnorm of HL_2

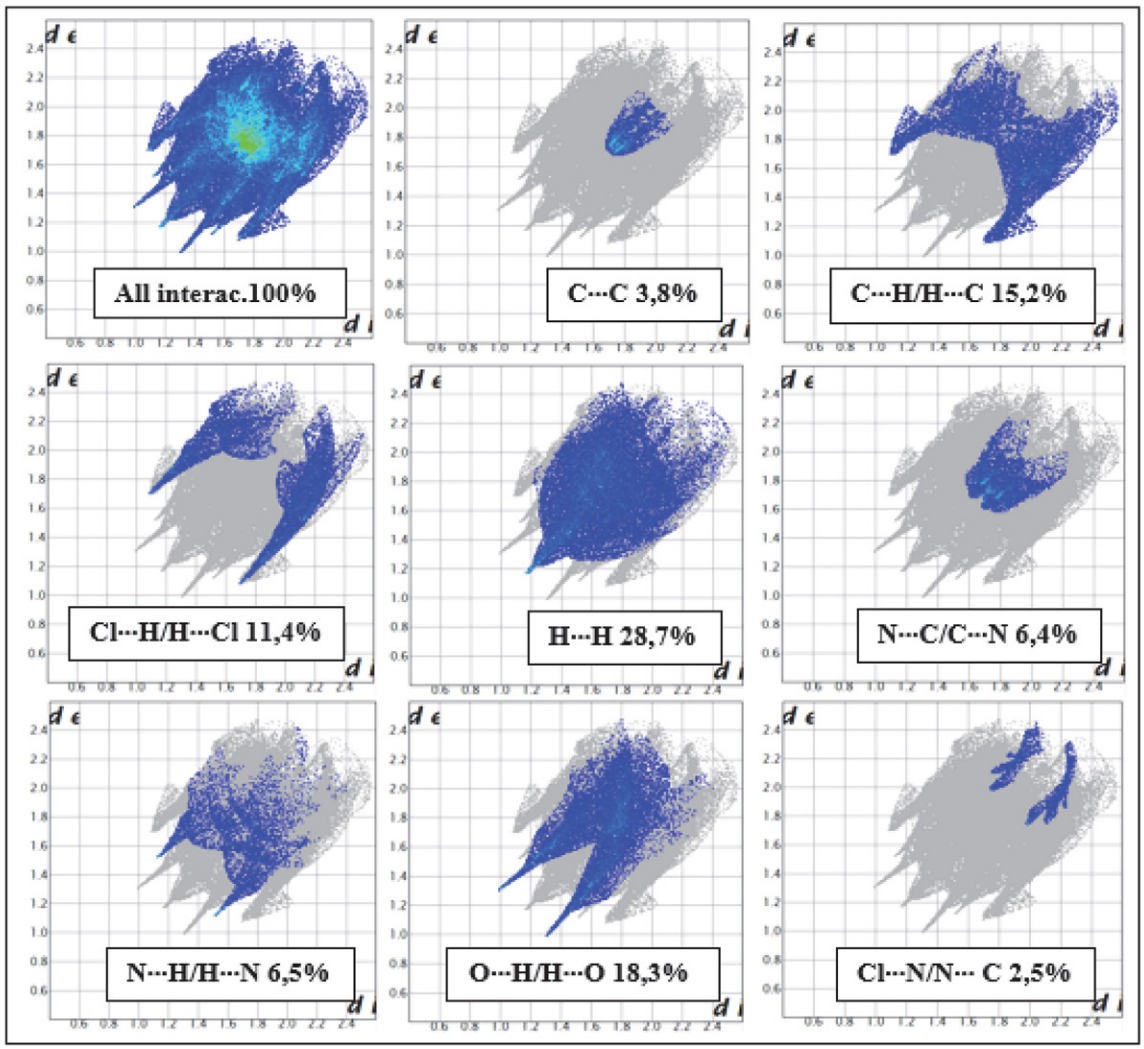


Fig. 8. The 2D fingerprint plos of the HL_2

3. 7. Molecular Electrostatic Potential Analysis

Molecular electrostatic potential mapping is a method for the observation of the interactions of molecules with each other based on their charge distribution on 3D diagrams. This is an auxiliary method that estimates electrophilic and nucleophilic reactive sites of ligands leading to investigate protein binding and medicine developing by defining hydrogen bond interactions.[4,45] Electrostatic po-

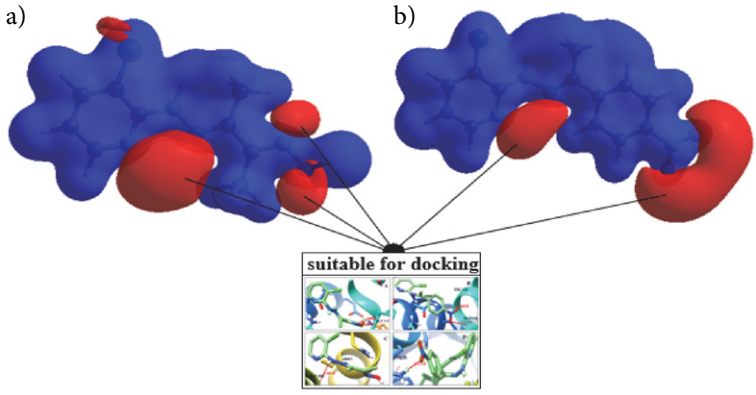


Fig. 9. Electrostatic potential maps of a) $C_9H_{11}ClN_4O$ and b) $C_{13}H_{11}ClN_4O_2$

tential (3D) diagrams of ligands were mapped using the Hartree-Fock theory Slater type orbital-3G base set of Hirshfeld surface analysis by CrystalExplorer software as depicted in Fig. 9. The input file of the geometry was obtained using Tonto.[46,47] Surface qualification values were set –0,025–0,025 au and high resolution was selected. When it was performed, the molecule was taken to transparency mode and atoms were made clear. The red color represents the negative electrostatic potential regions and acceptor hydrogen bonds. Moreover, the blue color represents the positive electrostatic potential regions and donor hydrogen bonds.[48,49] In addition, blue-colored zones are the preferred regions for the nucleophilic attack, while red-colored negative zones are susceptible to electrophilic attack.[11] Furthermore, red-colored regions have electron-rich atoms or atom groups; therefore, they can easily interact with amino acid residues. Based on the findings of molecular docking studies, hydrogen bond interactions between donor-acceptor confirmed the results of the electrostatic potential analysis as depicted in Fig. 11.

3. 8. Molecular Docking Studies

In silico docking calculations are of great importance in drug design and medical chemistry fields. Molecular docking is commonly used in the studies carried out on target medicine designing by estimating the binding mechanisms of small molecules on target biologic proteins.[50,51] Donor-acceptor binding mechanisms create complexations with hydrophobic hydrogen bond and electrostatic interactions.[52] The current study examined the ligands creating intramolecular hydrogen bonds by targeting the active zones of *E. coli* DNA GyrB (PDB Code:4WUB) and *E. coli* FabH (PDB Code:1HNJ) amino acid residues. The protein-related data were obtained from Research Collaboratory for Structural Bioinformatics Protein Data Bank https://www.pdb.org. Molecular docking studies analyzed binding energy, hydrogen bonding, and interactions between the ligands and bacteria.[53–56] Furthermore, by the calculation of the ligands' lowest binding energy to aminoacids residues, it was determined that which structure has stronger hydrogen bonding and higher binding energy score.[57] Ligands SMILES formats were created at page https://www.cheminfo.org; it is C/C(=N\O)/C(C)=N/Nc1ncccc1Cl for HL_1 and C/C(=N/Nc1nccc1Cl)c2ccc(N(=O)=O)cc2 for HL_2.

Molecular docking studies were performed Autodock vina program (https://www.vina.scripps.edu). Ligands were converted into mol2 format and prepared for molecular docking at Chimera software program with receptors (*E.coli* FabH and GyrB) (https://www.cgl.ucsf.edu/chimera/).[58] In the Dock Prep method, firstly, all nonstandarts and solvents were selected and refined from receptors. Then, protein models were added by the selection of all hydrogen atoms (also considered H-bonds) and Gasteiger charges. Docking studies were conducted by targeting ligand receptors and binding the most convenient coordinates.[59] While defining an approximate donor and acceptor binding zone in in-silico studies, docking parameters are of great importance. Different types of grid box values were applied for the best and most accurate binding. The application of target protein binding zones (as a great scale) in a cubic box resulted in the best binding; however, this method requires a long computer calculation.[60,61] The grid box values of ligands applied to *E. coli* GyrB receptor were 10, 25, –10 at the center with a grad spacing of 0.375 Å including default the sizes of 40, 40, 40 for HL_1 and HL_2. The same method was employed to *E. coli* FabH receptor reporting the values of 30, 15, 30 at the center with the sizes of 30, 30, 30 for HL_1 and HL_2. In addition, default values were used for other parameters. Root-mean-square deviation were selected as minumum value. The binding energy values of –7.9 and –8.8 kcal/mol were applied by HL_1 and HL_2 ligands to the GyrB receptor, respectively. Fig. 10 illustrates the hydrophobicity surface area of HL_1 inside GyrB and FabH proteins. The binding energy values

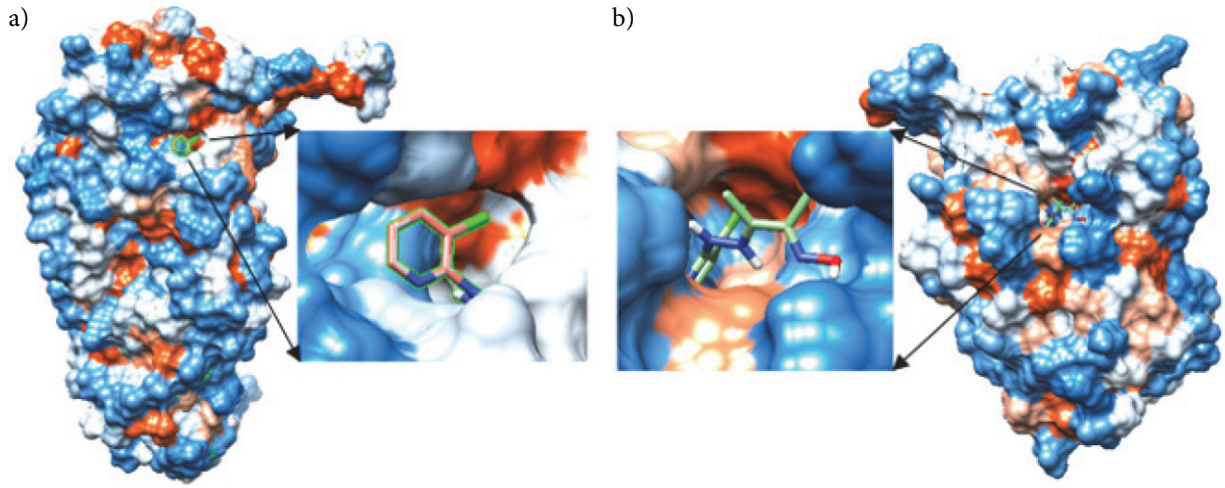


Fig. 10. Illustration of hydrophobicity surface area of HL_1 inside a) gyrase subunit B and b) beta-ketoacyl-acyl carrier protein synthase III proteins

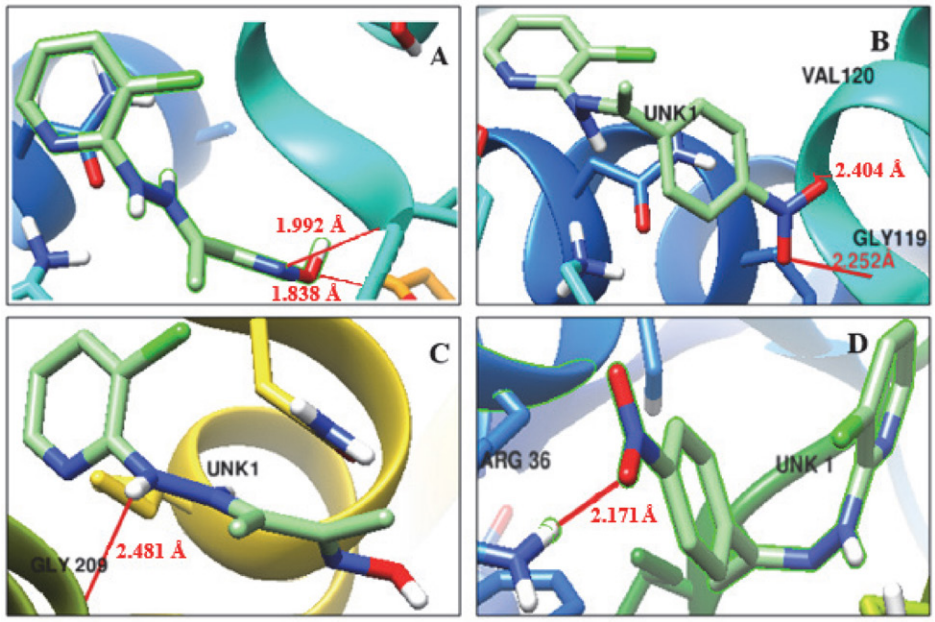


Fig. 11. Results of molecular docking for a) HL_1-gyrase subunit B (GyrB) (4WUB), b) HL_2-GyrB (4WUB), c) HL_1- beta-ketoacyl-acyl carrier protein synthase III (FabH) (1HNJ), and d) HL_2-FabH (1HNJ)

of –6.1 and –6.8 kcal/mol were applied by HL_1 and HL_2 ligands to the FabH receptor, respectively. The binding interactions and docking poses are depicted in Fig. 11. Since the ligands bind to the GyrB receptor with higher binding energy than that reported for the FabH receptor, there was a better docking to the ligands-GyrB complex. While there were two hydrogen bonds in the complex that ligands made with 4WUB protein, 1HNJ protein had one hydrogen bond. This finding proved that this effect increases the binding energy value. As the binding energy value enhances, the binding score increases indicating a better docking.[41,62] Therefore, the binding energy of HL_2 was higher than that reported for HL_1 which is considered a better docking. The other reason behind that is believed to be the electron density and unpaired electron couples of two oxygen atoms that bond to the nitrogen atom of HL_2.[63] In a study carried out by Fathima et al. (2018), docking results were observed to be –8.4 and –8.5 kcal/mol for 2ABP2C-1HNJ and 2ABHB-1HNJ, respectively.[54]

The HL_1 created a hydrogen bond to GLY 117 and GLN 335.A HE22 amino acid residues of 4WUB protein with N12 and O13 atoms and binding lengths were observed as 1.992 Å and 1.838 Å, respectively. The HL_2 bonded to GLY 119 and VAL 120 amino acid residues of 4WUB proteins with O19 and O20 atoms and binding lengths were observed as 2.252 Å and 2.404 Å. In another study conducted by Metelytsia et al. (2020), the binding of ligands to the regions of amino acid residues were reported as GLY 119 and His 116. This finding is similar to the results of docking investigations in the current study in terms of attachment regions.[52] The HL_1 and HL_2 created a hydrogen bond to GLY 209, ARG 36.A HH22 amino acid residues of 1HNJ receptor with N8 and O19 atoms and binding lengths were observed as 2.481 Å and 2.171 Å, respectively. Donor and acceptor hydrogen binding interactions are shown as Table 5.[64] The findings of docking studies confirmed that the results and interactions of molecular electrostatic potential generally occur in red regions. The

Table 5. AutoDock results showing Compound-Protein name, Binding site of protein, Binding site of Ligand, Type of interactions, Bond length, Binding energy.

Compound-Protein name	Binding site of protein	Binding site of Ligand	Type of interaction	Bond length (Å)	Binding energy (Kcal/Mol)
HL_1-4WUB	GLY 117	UNK1-N12 atom	Hydrogen bond	1.992	–7.9
	GLN 335.A HE22	UNK1-O13 atom	Hydrogen bond	1.838	
HL_2-4WUB	GLY 119	UNK1-O19 atom	Hydrogen bond	2.252	–8.8
	VAL 120	UNK1-O20 atom	Hydrogen bond	2.404	
HL_1- 1HNJ	GLY 209	UNK1-N8 atom	Hydrogen bond	2.481	–6.1
HL_2- 1HNJ	ARG 36.A HH22	UNK1-O19 atom	Hydrogen bond	2.171	–6.8

findings of docking studies also revealed that ligands are potential inhibitors against *E. coli* DNA GyrB and *E. coli* FabH.[65]

3. 9 Drug-Likeness and Biological Activity

Drug-likeness and bioactivity of ligands were obtained from molinspiration (https://www.molinspiration.com/cgi-bin/properties). Although the parameters of druglikeness cannot estimate the biological activity of each compound, it is one of the most successful and efficient methods for the analysis of compounds with medicinal potential through the determination of pharmacokinetic characteristics. Based on Table 6, the parameters of drug-likeness and biologic activity for the compounds in the present study (miLogP, TPSA, nAtoms, MW, nON, nOHNH, nviolations, and rotb) and (enzyme inhibitor, protease inhibitor, nuclear receptor ligand, kinase inhibitor, ion channel modulator, and GPRC ligand). The aforementioned findings have been the first obtained data regarding the medicinal potential of the compounds.[66] The values of drug-likeness were determined in this study, and the ligands were examined regarding midicinal potential with the consideration of these values. In this sense, the miLogP parameter, which is the capacity of penetrating the cell membrane, is expected to be under 5. In this regard, the values of miLogP parameter were reported as 1.81 and 3.37 for HL_1 and HL_2, respectively. The polar surface area (TPSA) represents the hydrogen bonding potential of a compound. Accordingly, the TPSA values were observed as 69.88 and 83.11 A^2 for HL_1 and HL_2, respectively. These values were below the 160 A^2 limit defined for TPSA and at a good performance.[67–70] Although miLogP and TPSA are not sufficient criteria for the investigation of druglikeness, they are two important parameters to represent oral absorption in cells.[71] The number of acceptor hydrogen bonds was set to nON ≤ 10, and the number of donor hydrogen bonds was set to nOHNH ≤ 5. In this study, the obtained results were below the aforementioned values.[72] Low molecule weight is important in terms of easy transport, diffusion, and absorption of the molecule. The values of molecular weight are expected to be < 500 Da. In this study, the molecular weights of the ligands were lower than the aforementioned value. The ligands were reported with successful results according to Lipinski's rule of five. Based on Fig. 12, the red column shows Lipinski's rule of five, and the green and red columns depict the druglikeness score of the ligands.[68]

If the value of violations equals 0, it shows that crystallized compounds can easily bond to the receptor. This value was reported as 0 for the compounds of the present study. The number of rotatable bonds is a simple topological value and measurement of flexibility.[73] If the bioactivity results of the compounds are > 0, –5.0-0.0, and < –5.0, they are considered active, medium active, and not active, respectively. All the results of biological activity parameters were within the range of –5.0–0.0; therefore, the ligandswere regarded as medium active.[74] As a result, it was concluded that the ligands of the current study obtained satisfactory druglikeness scores and properties to be considered medicine potential agents.

Table 6. Calculated drug-likeness parametres and Bioactivity Score of ligands.

	HL_1	HL_2
$miLog_P$	1.81	3.37
TPSA	69.88	83.11
natoms	15	20
MW	226,67	290.71
nON	5	6
nOHNH	2	1
nviolations	0	0
nrotb	3	4
GPCR ligand	–0.78	–0.70
Ion channel modulator	–0.62	–0.70
Kinase inhibitor	–0.74	–0.55
Nuclear receptor ligand	–1.32	–0.94
Protease inhibitor	–1.32	–1.02
Enzyme inhibitor	–0.43	–0.49

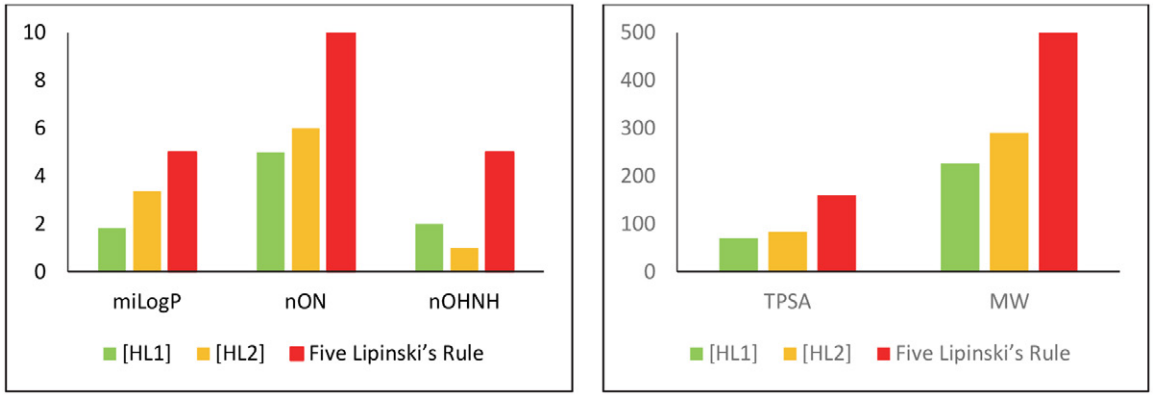


Fig. 12. Druglikeness scores of ligands according to Lipinski's rule of five

4. Conclusion

In this work, the new (2*E*,3*Z*)-3-[2-(3-chloropyridin-2-yl)hydrazinylidene]-*N*-hydroxybutan-2-imine and 3-chloro-2-{(2*Z*)-2-[1-(4-nitrophenyl)ethylidene]hydrazinyl}pyridine ligands were synthesized and characterized by elemental analysis, LC/MS-MS, FT-IR, ^{1}H-NMR, ^{13}C-NMR and UV-Vis. HL_2 was also determinated by single-crystal X-ray diffraction (XRD) and crystallized in the space group $P2_1/c$ of with Z=4 and was linked into (3-D) network by C-H···O intermoleculer hydrogen bonding interactions. Additionally, Cl···H 11,4%, H···H 28,7%, N···C 6,4%, N···H 6,5%, O···H 18,3%, Cl···N 2,5%, C···C 3,8%, C···H 15,2% reciprocal influence were revealed by Hirshfeld Surface Analysis. The mass spectra of the ligands showed the main peaks that corresponding to $[M+1]^+$. UV-Vis studies demonsrated that the π-π* and n-π* transitions appearing at 285, 312 nm and 322, 362 nm, respectively. The obtained experimental results of the present study were fully compatible with the theoretical results. The binding energy values of –7.9 and –8.8 kcal/mol were applied by HL_1 and HL_2 ligands to the GyrB receptor, respectively. Moreover, the binding energy values of –6.1 and –6.8 kcal/mol were applied by HL_1 and HL_2 ligands to the FabH receptor. The increase at binding energy values is resulted with a better docking. Therefore, HL_2 has a better docking ability than HL_1. The synthesized ligands are compatible with Lipinski's rule of five and have features to be a good drug-likeness scores. The bioactivity scores of the ligands are within the range of –5.0-0.0; consequently, the pharmacokinetic and pharmacological properties of the ligands are appropriate leading to be considered potential drug agents.

5. References

1. H. Mansouri-Torshizi, M. Moghadam, A. Divsalar and A. Saboury, *Acta Chim. Slov.*, **2011**, *58*, 811–822.
2. E. Gina Vasile Scăet, M. C. Chifiriuc, C. Bleotu, C. Kamerzan, T. Luminița Măru, C. G. Daniliuc, C. Maxim, L. Calu, R. Olar and M. Badea, *Molecules*, **2018**, *23*, 1–18. **DOI:**10.3390/molecules23010157
3. B. A. V Lima, A. E. Graminha, A. Kuznetsov, J. Ellena, F. R. Pavan, C. Q. F. Leite and A. A. Batista, *J. Braz. Chem. Soc.*, **2016**, *27*, 30–40. **DOI:**10.5935/0103-5053.20150237
4. M. Venkateshan, R. V. Priya, M. Muthu, J. Suresh and R. R. Kumar, *Chem. Data Collect.*, **2019**, *23*, 100262. **DOI:**10.1016/j.cdc.2019.100262
5. L. Metelytsia, D. Hodyna, I. Dobrodub, I. Semenyuta, M. Zavhorodnii, V. Blagodatny, V. Kovalishyn and O. Brazhko, *Comput. Biol. Chem.*, **2020**, *85*, 107224. **DOI:**10.1016/j.compbiolchem.2020.107224
6. S. S. Kumar, S. Athimoolam and B. Sridhar, *Spectrochim. Acta. A. Mol. Biomol. Spectrosc.*, **2015**, *146*, 204–213. **DOI:**10.1016/j.saa.2015.02.104
7. A. M. Netto, S. M. C. M. Bicalho, C. L. Filgueiras and J. C. Machado, *Chem. Phys. Lett.*, **1985**, *119*, 507–510. **DOI:**10.1016/0009-2614(85)85378-1
8. N. Wazzan, *Asian J. Chem.*, **2015**, *27*, 4641–4656. **DOI:**10.14233/ajchem.2015.19304
9. G. Vadivelan, M. Saravanabhavan, V. Murugesan and M. Sekar, *Spectrochim. Acta. A. Mol. Biomol. Spectrosc.*, **2015**, *145*, 461–466. **DOI:**10.1016/j.saa.2015.03.045
10. K. M, S. Saxena, R. S and V. R, *Curr. Med. Chem. - Anti-Infective Agents*, **2003**, *2*, 269–286. **DOI:**10.2174/1568012033483015
11. S. Madhankumar, P. Muthuraja and M. Dhandapani, *J. Mol. Struct.*, **2020**, *1201*, 127151. **DOI:**10.1016/j.molstruc.2019.127151
12. M. Akram, S. Niaz, M. Adeel, M. N. Tahir, I. Ullah, M. A. Ullah, S. Subashchandrabose and G. Uddin, *J. Mol. Struct.*, **2019**, 127448. **DOI:**10.1016/j.molstruc.2019.127448
13. L. K. McLellan and D. A. Hunstad, *Trends Mol. Med.*, **2016**, *22*, 946–957. **DOI:**10.1016/j.molmed.2016.09.003
14. V. L. Tchesnokova, L. L. Ottley, K. Sakamoto, J. Fierer, E. Sokurenko and M. A. Liss, *Urology*, **2015**, *86*, 1200–1205. **DOI:**10.1016/j.urology.2015.07.008
15. Y. Zhang, X. Zhang, L. Qiao, Z. Ding, X. Hang, B. Qin, J. Song and J. Huang, *J. Mol. Struct.*, **2019**, *1176*, 335–345. **DOI:**10.1016/j.molstruc.2018.08.069
16. K. M. Hillgren, A. Kato and R. T. Borchardt, *Med. Res. Rev.*, **1995**, *15*, 83–109. **DOI:**10.1002/med.2610150202
17. N. Srinivasan, S. Thirumaran and S. Ciattini, *J. Mol. Struct.*, **2009**, *936*, 234–238. **DOI:**10.1016/j.molstruc.2009.08.001
18. B. Guhathakurta, C. Biswas, J. P. Naskar, L. Lu and M. Zhu, *J. Chem. Crystallogr.*, **2011**, *41*, 1355–1359. **DOI:**10.1007/s10870-011-0103-x
19. O. V Dolomanov, L. J. Bourhis, R. J. Gildea, J. A. K. Howard and H. Puschmann, *J. Appl. Crystallogr.,* **2009**, *42*, 339–341. **DOI:**10.1107/S0021889808042726
20. L. Palatinus, S. J. Prathapa and S. van Smaalen, *J. Appl. Crystallogr.*, **2012**, *45*, 575–580. **DOI:**10.1107/S0021889812016068
21. C. F. Macrae, I. J. Bruno, J. A. Chisholm, P. R. Edgington, P. McCabe, E. Pidcock, L. Rodriguez-Monge, R. Taylor, J. Van De Streek and P. A. Wood, *J. Appl. Crystallogr.*, **2008**, *41*, 466–470. **DOI:**10.1107/S0021889807067908
22. E. Matamala-Cea, F. Valenzuela-Godoy, D. González, R. Arancibia, V. Dorcet, J. R. Hamon and N. Novoa, *J. Mol. Struct.*, **2020,** *1201*, 127139. **DOI:**10.1016/j.molstruc.2019.127139
23. Y. Y. Cai, L. Y. Xu, L. Q. Chai and Y. X. Li, *J. Mol. Struct.*, **2020**, *1204*, 127552. **DOI:**10.1016/j.molstruc.2019.127552
24. Q. Wu, Y. Tang and Q. Zi, *Polyhedron*, **2019**, *166*, 123–129. **DOI:**10.1016/j.poly.2019.03.021
25. N. Bandyopadhyay, A. B. Pradhan, S. Das, L. Lu, M. Zhu, S. Chowdhury and J. P. Naskar, *J. Photochem. Photobiol. B Biol.*, **2016**, *160*, 336–346. **DOI:**10.1016/j.jphotobiol.2016.04.026
26. S. Chantrapromma, P. Jansrisewangwong and H.-K. Fun, *Acta Crystallogr. Sect. E. Struct. Rep. Online*, **2010**, *66*, o2994-5. **DOI:**10.1107/S1600536810043266

27. T. Karakurt, S. Meral, A. A. Agar, *Süleyman Demirel Univ. J. Nat. Appl. Sci.,* **2019**, *23*, 505–514. **DOI:**10.19113/sdufenbed.530279
28. E. Szłyk, A. Wojtczak, A. Surdykowski and M. Goździkiewicz, *Inorganica Chim. Acta*, **2005**, *358*, 467–475. **DOI:**10.1016/j.ica.2004.07.065
29. L. Chai, Y. Zhang, J. Tong and G. Liu, *Z. Naturforsch.,* **2013**, *68b*, 239–244. **DOI:**10.5560/znb.2013-2301
30. P. Pattanayak, J. L. Pratihar, D. Patra, P. Brandão and V. Felix, *Inorganica Chim. Acta*, **2014**, *418*, 171–179. **DOI:**10.1016/j.ica.2014.04.021
31. H. Wang, H. Xiao, N. Liu, B. Zhang and Q. Shi, *Open J. Inorg. Chem.*, **2015**, *05*, 63–73. **DOI:**10.4236/ojic.2015.53008
32. T. Topal, E. Karapınar, *J. Turkish Chem. Soc. Sect. A Chem.*, **2018**, *5*, 785–802. **DOI:**10.18596/jotcsa.324878
33. T. Topal, H. H. Kart, P. Tunay Taşlı and E. Karapınar, *Opt. Spectrosc.,* **2015**, *118*, 897–912. **DOI:**10.1134/S0030400X15060223
34. M. J. Frisch *et al.,* G16_B01. *Gaussian 16, Revision B.01* Gaussian, Inc., Wallingford CT, **2016**.
35. J. B. Foresman, A. E. Frisch., Exploring chemistry with electronic structure methods. *Gaussian, Inc.,* **1996**.
36. R. Mohamed Asath, R. Premkumar, T. Mathavan and A. Milton Franklin Benial, *Spectrochim. Acta - Part A Mol. Biomol. Spectrosc.*, **2017**, *175*, 51–60. **DOI:**10.1016/j.molstruc.2017.04.117
37. E. Erdem, M. Akarsu, R. Kılınçarslan, İ. Kayağil, İ. Kara and S. Söyleyici, *Croat. Chem. Acta,* **2016**, *89*, 55–64. **DOI:**10.5562/cca2820
38. S. Shit, M. Nandy, C. Rizzoli and S. Mitra, *J. Chem. Sci.,* **2016**, *128*, 913–920. **DOI:**10.1007/s12039-016-1082-4
39. E. Karapinar, O. Karabulut and N. Karapinar, *Hindawi Publ. Corp. J. Chem.* **2013**, 2013. **DOI:**10.1155/2013/256983
40. H. Briseño-Ortega, L. Juárez-Guerra, S. Rojas-Lima, L. H. Mendoza-Huizar, R. A. Vázquez-García, N. Farfán, R. Arcos-Ramos, R. Santillan and H. López-Ruiz, *J. Mol. Struct.,* **2018**, *1157*, 119–126. **DOI:**10.1016/j.molstruc.2017.12.059
41. R. Mohamed Asath, R. Premkumar, T. Mathavan and A. Milton Franklin Benial, *Spectrochim. Acta - Part A Mol. Biomol. Spectrosc.*, **2017**, *175*, 51–60. **DOI:**10.1016/j.saa.2016.11.037
42. P. Muthuraja, M. Sethuram, T. Shanmugavadivu and M. Dhandapani, *J. Mol. Struct.*, **2016**, *1122*, 146–156. **DOI:**10.1016/j.molstruc.2016.05.083
43. M. A. Spackman and D. Jayatilaka, *CrystEngComm*, **2009**, *11*, 19–32. **DOI:**10.1039/B818330A
44. J. J. McKinnon, M. A. Spackman and A. S. Mitchell, *Acta Crystallogr. Sect. B.*, **2004**, *60*, 627–668. **DOI:**10.1107/S0108768104020300
45. R. Daengngern and N. Kungwan, *J. Lumin.*, **2015**, *167*, 132–139. **DOI:**10.1016/j.jlumin.2015.06.001
46. J. J. McKinnon, D. Jayatilaka and M. A. Spackman, *Chem. Commun.*, **2007**, 3814–3816. **DOI:**10.1039/b704980c
47. D. Jayatilaka and D. J. Grimwood, *Comput. Sci. ICCS,* **2003**, 142–151. **DOI:**10.1007/3-540-44864-0_15
48. M. A. Spackman, J. J. McKinnon and D. Jayatilaka, *CrystEngComm*, **2008**, *10*, 377–388. **DOI:**10.1039/b715227b
49. S. M. Kumar, B. C. Manjunath, G. S. Lingaraju, M. M. M. Abdoh and M. P. Sadashiva, *Cryst. Struct. Theory Appl.* **2013**, *2013*, 124–131. **DOI:**10.4236/csta.2013.23017
50. S. Vilar, G. Cozza and S. Moro, *Curr. Top. Med. Chem.*, **2008**, *8*, 1555–1572. **DOI:**10.2174/156802608786786624
51. R. Thomsen and M. H. Christensen, *J. Med. Chem.*, **2006**, *49*, 3315–3321. **DOI:**10.1021/jm051197e
52. P. Sjoberg and P. Politzer, *J. Phys. Chem.*, **1990**, *94*, 3959–3961. **DOI:**10.1021/j100373a017
53. E. G. Sağlam, E. Bulat, C. T. Zeyrek, H. Dal and T. Hökelek, *J. Mol. Struct.*, **2019**, *1178*, 112–125. **DOI:**10.1016/j.molstruc.2018.09.084
54. K. S. F. M. Sathiyendran, K. Anitha, *Mater. Sci. Eng. C.*, **2018**, *91*, 103–114. **DOI:**10.1016/j.msec.2018.05.035
55. I. Ali, M. N. Lone, Z. A. Alothman and A. Alwarthan, *J. Mol. Liq.*, **2017**, *234*, 391–402. **DOI:**10.1016/j.molliq.2017.03.112
56. M. M. Silva, F. C. Savariz, E. F. Silva-JÃ\textordmasculinenior, T. M. de Aquino, M. H. Sarragiotto, J. C. C. Santos and I. M. Figueiredo, *J. Braz. Chem. Soc.*, **2016**, *27*, 1558–1568.
57. M. K. Bhattacharyya, D. Dutta, S. M. Nashre-ul-Islam, A. Frontera, P. Sharma, A. K. Verma and A. Das, *Inorganica Chim. Acta*, **2020**, *501*, 119233. **DOI:**10.1016/j.ica.2019.119233
58. R. S. Soderquist and A. Eastman, *Mol. Cancer Ther.*, **2016**, *15*, 2011–2017. **DOI:**10.1158/1535-7163.MCT-16-0031
59. N. Shahabadi and M. Falsafi, *Spectrochim. Acta - Part A Mol. Biomol. Spectrosc.*, **2014**, *125*, 154–159. **DOI:**10.1016/j.saa.2014.01.066
60. W. P. Feinstein and M. Brylinski, *J. Cheminform.*, **2015**, *7*. **DOI:**10.1186/s13321-015-0067-5
61. D. Plewczynski, M. Lazniewski, R. Augustyniak and K. Ginalski, *J. Comput. Chem.*, **2011**, *32*, 742–755. **DOI:**10.1002/jcc.21643
62. B. Kurt, H. Temel, M. Atlan and S. Kaya, *J. Mol. Struct.,* **2020**, *1209*, 127928. **DOI:**10.1016/j.molstruc.2020.127928
63. N. Das, P. K. Jena and S. K. Pradhan, *Heliyon*, 2020, **6**, e02693. **DOI:**10.1016/j.heliyon.2019.e02693
64. A. De, H. P. Ray, P. Jain, H. Kaur and N. Singh, *J. Mol. Struct.*, **2020**, *1199*, 126901. **DOI:**10.1016/j.molstruc.2019.126901
65. M. Parveen, A. Aslam, A. Ahmad, M. Alam, M. R. Silva and P. S. P. Silva, *J. Mol. Struct.*, **2020**, *1200*, 127067. **DOI:**10.1016/j.molstruc.2019.127067
66. S. M. Hiremath, A. S. Patil, C. S. Hiremath, M. Basangouda, S. S. Khemalapure, N. R. Patil, S. B. Radder, S. J. Armaković and S. Armaković, *J. Mol. Struct.*, **2019**, *1178*, 1–17. **DOI:**10.1016/j.molstruc.2018.10.007
67. C. A. Lipinski, F. Lombardo, B. W. Dominy and P. J. Feeney, *Adv. Drug Deliv. Rev.* **2001**, *46*, 3–26. **DOI:**10.1016/S0169-409X(00)00129-0
68. C. A. Lipinski, *Drug Discov. Today. Technol.*, **2004**, *1*, 337–341. **DOI:**10.1016/j.ddtec.2004.11.007
69. A. Verma, *Asian Pac. J. Trop. Biomed.*, **2012**, *2*, 1735–1737. **DOI:**10.1016/S2221-1691(12)60486-9
70. P. Ertl, B. Rohde and P. Selzer, *J. Med. Chem.*, **2000**, *43*, 3714–3717. **DOI:**10.1021/jm000942e

71. S. Nadeem, M. Sirajuddin, S. Ahmad, S. A. Tirmizi, M. I. Ali and A. Hameed, *Alexandria J. Med.*, **2016**, *52*, 279–288. **DOI:**10.1016/j.ajme.2015.10.003
72. S. Deswal, Naveen, R. K. Tittal, D. Ghule Vikas, K. Lal and A. Kumar, *J. Mol. Struct.*, **2020**, *1209*, 127982. **DOI:**10.1016/j.molstruc.2020.127982
73. D. F. Veber, S. R. Johnson, H.-Y. Cheng, B. R. Smith, K. W. Ward and K. D. Kopple, *J. Med. Chem.*, **2002**, *45*, 2615–2623. **DOI:**10.1021/jm020017n
74. N. Dege, A. S. Aydın, E. Ağar, S. Kansız, S. JoseKavitha, K. BalaSubramani, M. Hemamalini and V. Rajakannan, *Chem. Data Collect.*, **2020**, *25*, 100320. **DOI:**10.1016/j.cdc.2019.100320

Povzetek

A detailed description of the two new pyridine ligands, (2E**,**3Z**)**-3-[2-(3-chloropyridin-2-yl)hydrazinylidene]-N-hydroxybutan-2-imine and 3-chloro-2-{(2Z)-2-[1-(4 nitrophenyl)ethylidene]hydrazinyl}, is reported. The synthesized compounds were characterized by spectroscopic studies, spectral features were performed by TD-DFT calculations. New-generation pyridine ligand of HL_2 was also determinate by single-crystal X-ray diffraction and Hirshfeld surface analysis with two-dimensional fingerprint plots was used to analyze intermolecular interactions in crystals. Molecular-docking was performed to investigate the binding areas of chemical compounds, and the results showed the inhibitory activity of the studied HL_1 and HL_2 against *E. coli***.** The results of the current study revealed the drug-likeness and bioactive properties of the ligands.

Podan je podroben opis dveh novih piridinskih ligandov, (2E,3Z)-3-[2-(3-kloropiridin-2-il) hidraziniliden]-N-hidroksibutan-2-imina in 3-kloro-2-{(2Z)-2-[1-(4nitrofenil)etiliden] hidrazinila}. Sintetizirane spojine so bile okarakterizirane s spektroskopskimi študijami, spektralne značilnosti pa so bile ovrednotene z izračuni TD-DFT. Nova generacija piridinskih ligandov HL2 je bila določena tudi z žarkovno rentgensko difrakcijo, za analizo medmolekularnih interakcij v kristalih pa je bila uporabljena Hirshfeldova površinska analiza s specifičnimi dvodimenzionalnimi prikazi. Za proučitev vezavnih površin kemijskih spojin smo izvedli molekularno sidranje, pri čemer so rezultati pokazali inhibitorno aktivnost proučevanih HL_1 in HL_2 spojin napram *E. coli*. Rezultati sedanje študije kažejo na potencialne zdravilne in bioaktivne lastnosti ligandov.

Except when otherwise noted, articles in this journal are published under the terms and conditions of the Creative Commons Attribution 4.0 International License

DOI: 10.17344/acsi.2020.6205 *Acta Chim. Slov.* **2021,** *68,* 102–108
creative commons

Scientific paper

Copper(II) and Zinc(II) Complexes Derived from *N,N'*-Bis(4-bromosalicylidene)propane-1,3-diamine: Syntheses, Crystal Structures and Antimicrobial Activity

Yu-Mei Hao

Department of Chemistry, Baicheng Normal University, Baicheng 137000, P.R. China

** Corresponding author: E-mail: jyxygzb@163.com*

Received: 06-19-2020

Abstract

A mononuclear copper(II) complex, [CuL] (**1**), and a phenolato-bridged trinuclear zinc(II) complex, $[Zn_3Cl_2L_2(DMF)_2]$ (**2**), where L is the deprotonated form of *N,N'*-bis(4-bromosalicylidene)propane-1,3-diamine (H_2L), have been prepared and characterized by elemental analyses, IR and UV-Vis spectroscopy, and single crystal X-ray diffraction. The Cu atom in complex **1** is in square planar coordination, while the terminal and central Zn atoms in complex **2** are in square pyramidal and octahedral coordination, respectively. The antibacterial activities of the complexes have been tested on the bacteria *Staphylococcus aureus* and *Escherichia coli*, and the yeast *Candida parapsilosis*.

Keywords: Schiff base; copper complex; zinc complex; crystal structure; antibacterial property

1. Introduction

Schiff bases have been extensively used as multi-dentate ligands to construct metal complexes with versatile structures due to their easy formation and strong metal-binding ability.[1] The increasing interest in the synthesis and structural studies of Schiff bases is due to their bioactivity and coordination properties. Schiff base with donors (N, O, S, *etc.*) have structure similarities with neutral biological systems. Most of the Schiff bases and their complexes with transition metals have a broad range of applications in biological and pharmaceutical fields.[2] A number of Schiff bases have been reported for their remarkable biological activities, such as antibacterial, antifungal, antimalarial, anti-proliferative, anti-inflammatory, antiviral and antipyretic activities.[3] Copper(II) and zinc(II) Schiff base complexes have been studied extensively and are considered as excellent alternatives for classic organic antibacterial agents.[4] Despite the presence of considerable research on the antibacterial properties of such complexes, it is still necessary to search for new complexes to find more effective agents as well as to better understand the mechanism of the action of this class of compounds. With an interest in the chemistry of biologically active Schiff bases and their metal complexes, this study aimed to synthesize copper(II) and zinc(II) complexes. The newly synthesized complexes, [CuL] (**1**) and $[Zn_3Cl_2L_2(DMF)_2]$ (**2**), where L is the deprotonated form of *N,N'*-bis(4-bromosalicylidene)propane-1,3-diamine (H_2L), were structurally characterized, and examined for their antimicrobial activities.

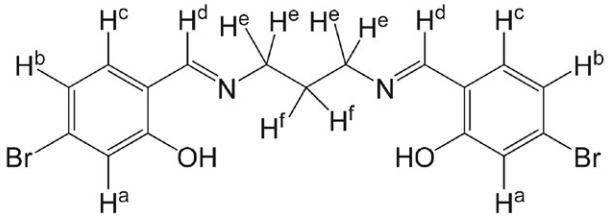
2. Experimental

2. 1. Materials and Methods

1,3-Diaminopropane and 4-bromosalicylaldehyde were purchased from TCI. $CuCl_2 \cdot 2H_2O$ and $ZnCl_2$ were purchased from Aladdin Chemical Reagent Co. Ltd. The solvents methanol and DMF were purchased from Kemiou Chemical Reagent Co. Ltd. Elemental analyses were performed on a Perkin-Elmer 240C elemental analyzer. IR spectra were recorded on a Jasco FT/IR-4000 spectrometer as KBr pellets in the 4000–400 cm^{-1} region. UV-Vis spectrum was recorded on a Lambda 900 spectrometer. ^1H and ^{13}C NMR were determined with a Bruker 500 MHz instrument. Single crystal X-ray diffraction was carried out on a Bruker SMART 1000 CCD diffractometer.

2. 2. Syntheis of H_2L

1,3-Diaminopropane (0.15 g, 2.0 mmol) was diluted by methanol (20 mL). Then, it was added dropwise to the methanol solution (30 mL) of 4-bromosalicylalde-



Scheme 1. The Schiff base H_2L, showing the H atoms.

hyde (0.84 g, 4.0 mmol). The reaction mixture was stirred and heated to reflux for 30 min. The solvent was removed by evaporation under reduced pressure. The yellow solid was recrystallized from ethanol to give yellowish crystalline product. Yield: 0.72 g (82%). ^{1}H NMR (500 MHz, DMSO-d^6; Scheme 1) δ /ppm: 8.58 (s, 2H, CH^d=N), 7.50 (s, 2H, ArH^c), 7.33 (t, 2H, ArH^a), 7.14 (d, 2H, ArH^b), 3.72 (t, 4H, CH^e_2), 2.07 (t, 2H, CH^f_2). ^{13}C NMR (126 MHz, DMSO-d^6) δ /ppm: 165.12, 153.13, 133.27, 124.54, 123.27, 122.02, 115.57, 54.78, 30.73. IR (KBr, cm^{-1}): 3449, 2980, 2921, 1632, 1471, 1385, 1287, 1231, 1096, 930, 845, 646, 451. UV-Vis λ_{max}/nm (1.13×10^{-5} mol L^{-1}, MeOH; ε, L mol^{-1} cm^{-1}): 230 (27,300), 270 (13,800), 330 (7,120), 420 (4,520). Anal. Calcd. (%) for $C_{17}H_{16}Br_2N_2O_2$: C, 46.39; H, 3.66; N, 6.36. Found (%): C, 46.22; H, 3.75; N, 6.43.

2. 3. Synthesis of [CuL] (1)

H_2L (44 mg, 0.10 mmol) and $CuCl_2{\cdot}2H_2O$ (34 mg, 0.20 mmol) were mixed in methanol (30 mL). The mixture was stirred at room temperature for 30 min to give a blue solution. Single crystals of the complex, suitable for X-ray diffraction, were obtained after 8 days. Yield: 31 mg (62%). IR data (cm^{-1}): 2925, 2853, 1608, 1514, 1407, 1289, 1192, 1126, 1060, 973, 913, 853, 777, 600, 543, 451. UV-Vis (1.03×10^{-5} mol L^{-1}, MeOH; ε, L mol^{-1} cm^{-1}): 230 (23,500), 247 (24,100), 280 (16,320), 355 (7,135). Anal. Calcd. (%) for $C_{17}H_{14}Br_2CuN_2O_2$: C, 40.70; H, 2.81; N, 5.58. Found (%): C, 40.86; H, 2.92; N, 5.47.

2. 4. Synthesis of $[Zn_3Cl_2L_2(DMF)_2]$ (2)

H_2L (44 mg, 0.10 mmol) and $ZnCl_2$ (27 mg, 0.20 mmol) were mixed in methanol (30 mL). The mixture was stirred at room temperature for 30 min to give a white precipitate. DMF (5 mL) was added to the mixture until the precipitate dissolved. Single crystals of the complex, suitable for X-ray diffraction, were obtained after 17 days. Yield: 27 mg (42%). IR data (cm^{-1}): 2917, 2849, 1632, 1615, 1581, 1533, 1460, 1390, 1276, 1198, 1112, 1071, 978, 911, 863, 800, 677, 602, 539, 464. UV-Vis (1.30×10^{-5} mol L^{-1}, MeOH; ε, L mol^{-1} cm^{-1}): 230 (22,370), 245 (23,920), 272 (12,100), 350 (7,630). Anal. Calcd. (%) for $C_{40}H_{42}Br_4Cl_2N_6O_6Zn_3$: C, 37.26; H, 3.28; N, 6.52. Found (%): C, 37.43; H, 3.35; N, 6.44.

2. 5. X-ray Crystallography

Single crystal X-ray data for the complexes were collected on a Bruker SMART 1000 CCD diffractometer using the SMART/SAINT software.[5] Intensity data were collected using graphite-monochromatized MoK_α radiation (0.71073 Å) at 298(2) K. The structures were solved by direct methods using SHELX.[6] Empirical absorption corrections were applied with SADABS.[7] All non-hydrogen atoms were refined with anisotropic displacement coefficients. The hydrogen atoms bonded to carbon were included in geometric positions and given thermal parameters equivalent to 1.2 and 1.5 times those of the atom to which they were attached. The C8-C9-C10 group of the Schiff base ligand in complex **1** is disordered over two sites, with occupancies of 0.5 and 0.5 due to the symmetry. The distances of C8–C9 and C9–C10 are restrained to 1.51(1) Å. The atoms C8, C9 and C10 were refined using ISOR instruction. The thermal factors of atoms C8 and C10 were constrained to be equal. Crystallographic data and refinement parameters are given in Table 1, and important interatomic distances and angles are given in Table 2.

Table 1. Crystallographic data and refinement parameters for the complexes

	1	**2**
Chemical Formula	$C_{17}H_{14}Br_2CuN_2O_2$	$C_{40}H_{42}Br_4Cl_2N_6O_6Zn_3$
Fw	501.66	1289.45
T (K)	298(2)	298(2)
Crystal system	Monoclinic	Monoclinic
Space group	*C*2/*c*	*P*2/*c*
a (Å)	23.0385(16)	11.9976(12)
b (Å)	8.0706(11)	12.9584(12)
c (Å)	9.0741(12)	16.0855(13)
α (°)	90	90
β (°)	93.0960(10)	107.2880(10)
γ (°)	90	90
V (Å^3)	1684.7(3)	2387.8(4)
Z	4	2
μ (Mo Kα) (cm^{-1})	6.052	5.003
D_c (g cm^{-3})	1.978	1.793
Reflections/ parameters	1543/117	4457/278
Unique reflections	955	3272
Restraints	21	0
Goodness of fit on F^2	1.039	1.043
R_{int}	0.0597	0.0360
R_1, wR_2 [$I \geq 2\sigma(I)$]	0.0617, 0.1442	0.0517, 0.1302
R_1, wR_2 (all data)	0.1064, 0.1641	0.0744, 0.1436

2. 6. Biological Assay

The antibacterial property of the complexes was evaluated by a macro-dilution method using *Staphylococcus aureus*, *Escherichia coli*, and the yeast *Candida parapsi-*

Table 2. Selected bond distances (Å) and angles (°) for the complexes

1			
Cu(1)–O(1)	1.902(5)	Cu(1)–N(1)	1.964(7)
O(1)–Cu(1)–O(1A)	87.4(3)	O(1)–Cu(1)–N(1)A	154.1(2)
O(1)–Cu(1)–N(1)	92.5(3)	N(1)–Cu(1)–N(1)A	98.6(4)
2			
Zn(2)–O(2)	2.075(4)	Zn(2)–O(1)	2.101(4)
Zn(2)–O(3)	2.109(4)	Zn(1)–O(2)	2.059(4)
Zn(1)–O(1)	2.064(4)	Zn(1)–N(1)	2.078(5)
Zn(1)–N(2)	2.080(5)	Zn(1)–Cl(1)	2.2902(18)
O(2)–Zn(2)–O(2A)	169.0(2)	O(2)–Zn(2)–O(1A)	95.80(14)
O(2)–Zn(2)–O(1)	76.08(14)	O(1)–Zn(2)–O(1A)	86.5(2)
O(2)–Zn(2)–O(3)	91.16(15)	O(2)–Zn(2)–O(3A)	96.71(15)
O(1)–Zn(2)–O(3A)	172.65(15)	O(1)–Zn(2)–O(3)	92.91(16)
O(3)–Zn(2)–O(3A)	88.6(2)	O(2)–Zn(1)–O(1)	77.24(14)
O(2)–Zn(1)–N(1)	142.30(17)	O(1)–Zn(1)–N(1)	87.16(17)
O(2)–Zn(1)–N(2)	86.45(18)	O(1)–Zn(1)–N(2)	155.07(18)
N(1)–Zn(1)–N(2)	94.7(2)	O(2)–Zn(1)–Cl(1)	107.19(12)
O(1)–Zn(1)–Cl(1)	100.25(12)	N(1)–Zn(1)–Cl(1)	109.28(14)
N(2)–Zn(1)–Cl(1)	102.55(15)		

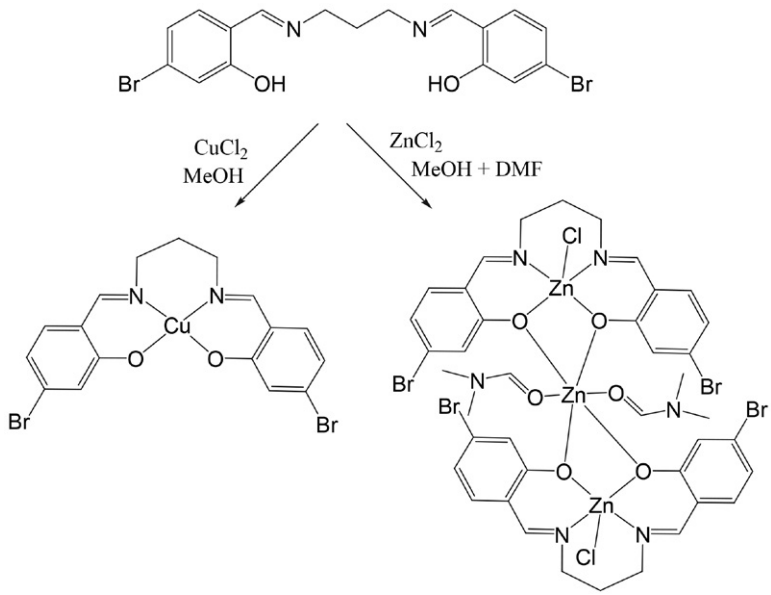
Symmetry code for A: 1 – *x*, *y*, ½ – *z*.

losis. The cultures of bacteria and yeasts were incubated under vigorous shaking. The compounds were dissolved in small amount of DMSO. Concentration of the tested compounds ranging from 0.010 to 2.5 mmol L^{-1} for the bacteria and yeasts was used in all experiments. The antibacterial activity was characterized by IC_{50} and MIC values. MIC experiments on subculture dishes were used to assess the minimal microbicidal concentration (MMC). Subcultures were prepared separately in Petri dishes containing competent agar medium and incubated at 30 °C for 48 h. The MMC value was taken as the lowest concentration, which showed no visible growth of microbial colonies in the subculture dishes.

3. Results and Discussion

3. 1. Chemistry

The complexes **1** and **2** were facile prepared by the reaction of the Schiff base H_2L with copper chloride and



Scheme 2. The synthetic procedure of the complexes

zinc chloride, respectively, in methanol (Scheme 2). Single crystals of the complexes were formed by slow evaporation of the solvent at room temperature.

3. 2. Crystal Structure Description

The molecular structure of complex **1** is shown in Fig. 1. The complex is a mononuclear copper(II) species. Molecule of the complex possesses a crystallographic two-fold rotation axis symmetry. The Cu(1) atom is coordinated by the two imine nitrogen and two phenolate oxygen of the Schiff base ligand, forming a tetrahedrally distorted square planar geometry, which is evidenced by the *trans* bond angles of 154.1(2)° and the *cis* angles of 87.4(3)–98.6(4)°. The distortion of the square planar coordination results in the deflection of the two benzene rings, which has a dihedral angle of 35.2(3)°. Similarly, the dihedral angle between the two six-membered chelate rings Cu(1)-N(1)-C(7)-C(1)-C(2)-O(1) and Cu(1)-N(1A)-C(7A)-C(1A)-C(2A)-O(1A) is 33.8(3)°. The coordinate bond lengths in the complex are comparable to those observed in the copper(II) complexes with Schiff bases.[8] In the crystal structure, the molecules are linked *via* Br···Br interactions, with a distance of 3.659(4) Å, to form zigzag chains along the *x* axis (Fig. 2).

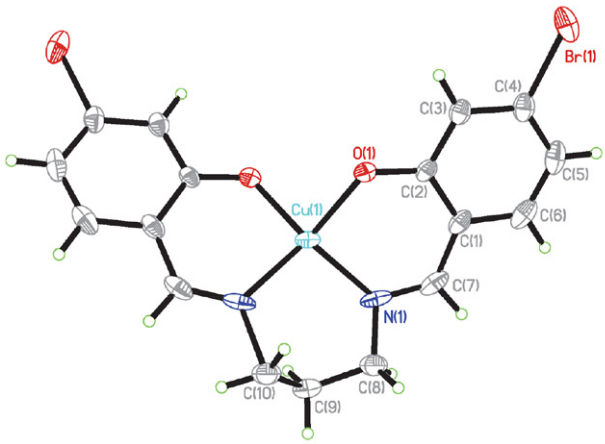


Fig. 1. A perspective view of the molecular structure of complex **1** with the atom labeling scheme. Thermal ellipsoids are drawn at the 30% probability level.

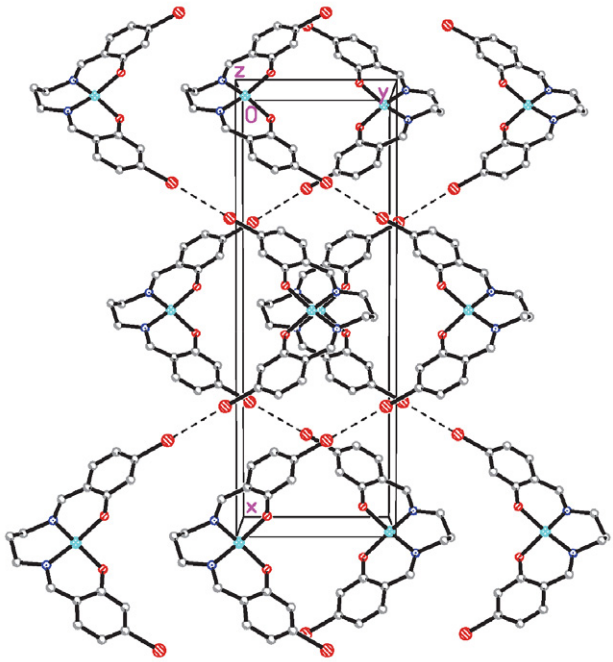


Fig. 2. Packing structure for complex **1** viewed along the *z* axis. Dashed lines represent Br···Br interactions forming zigzag chains along the *x* axis.

The molecular structure of complex **2** is shown in Fig. 3. The complex is a phenolate-bridged trinuclear zinc(II) species, with the two [ZnClL] units connected by the central Zn atom (Zn(2)). Molecule of the complex possesses a crystallographic two-fold rotation axis symmetry. The Zn···Zn distance is 3.227(2) Å. The terminal Zn atom (Zn(1)) shows a distorted square pyramidal coordination geometry, with the two phenolate oxygen atoms (O(1) and O(2)) and the two imine nitrogen atoms (N(1) and N(2)) occupying the basal coordination site, and with a Cl atom occupies the apical position. The Zn(1) atom deviates from the best coordination plane defined by the atoms N(1), N(2), O(1) and O(2) by 0.532(2) Å in direction of the apical Cl atom. The *cis* and *trans* bond angles in the basal plane are in the range of 77.24(14)–94.7(2)° and 142.30(17)–155.07(18)°, and those between the apical and basal donor atoms are in the range of 100.25(12)-109.28(14)°. Thus, the coordination is distorted from the ideal geometry of a square pyramid. The bond lengths related to Zn(1) atom

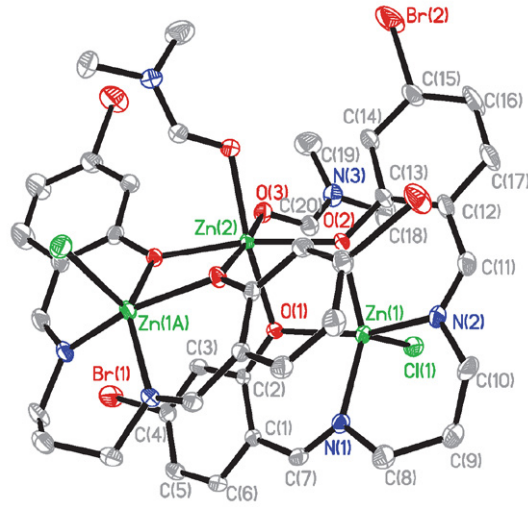


Fig. 3. A perspective view of the molecular structure of complex **2** with the atom labeling scheme. Thermal ellipsoids are drawn at the 30% probability level. The carbon hydrogens are omitted for clarity. Atoms labelled with the suffix A or unlabelled are at the symmetry position 1 – *x*, *y*, ½ – *z*.

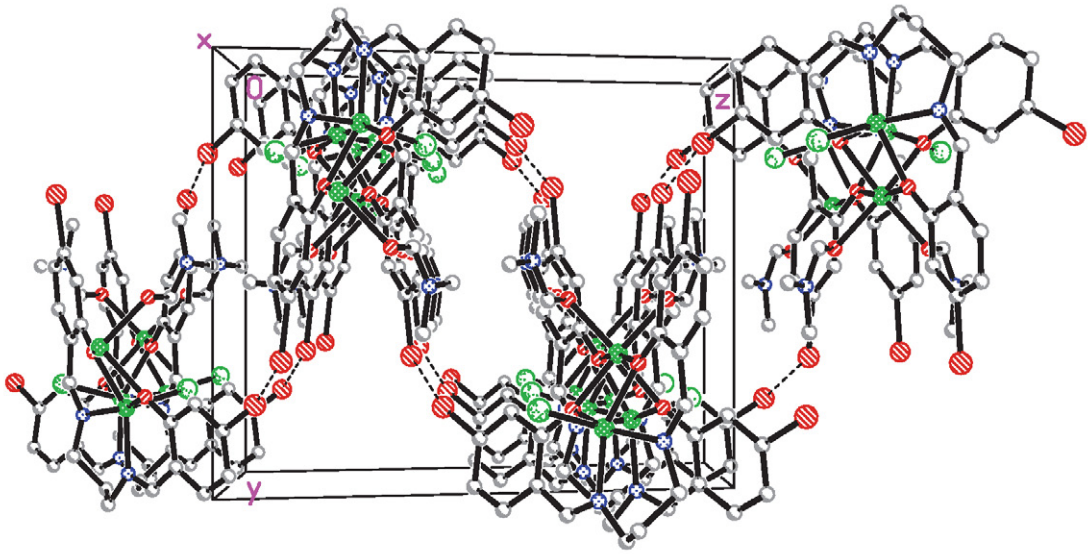


Fig. 4. Packing structure for complex **2** viewed along the *x* axis. Dashed lines represent Br···Br interactions forming zigzag chains along the *z* axis.

are 2.06 Å for Zn–O, 2.08 Å for Zn–N and 2.29 Å for Zn–Cl, which are comparable to those observed in Schiff base zinc complexes with square pyramidal coordination.[9] The central Zn atom (Zn(2)), located at the two-fold rotation axis, shows a distorted octahedral coordination geometry. The donor atoms come from two Schiff base ligands (O(1), O(2), O(1A), O(2A)), and two DMF ligands (O(3), O(3A)). The *cis* and *trans* bond angles related to Zn(2) are 76.08(14)–96.71(15)° and 169.0(2)–172.65(15)°, respectively. Thus, the coordination is distorted from the ideal geometry of an octahedron. The Zn–O bond lengths related to Zn(2) atom are 2.07–2.11 Å, which are comparable to those observed in Schiff base zinc complexes with octahedral coordination.[10] The [ZnClL] unit is butterfly shaped, with the dihedral angle between the two benzene rings of 33.1(3)°. The bond lengths are also similar to the trinuclear zinc complexes with square pyramidal and octahedral coordination.[11] In the crystal structure, the molecules are linked *via* Br···Br interactions,[12] with a distance of 3.871(3) Å, to form zigzag chains along the *z* axis (Fig. 4).

3. 3. IR and UV-Vis Spectra

The medium and broad absorption centered at 3449 cm^{-1} in the spectrum of H_2L substantiates the presence of O–H groups. The intense band indicative of the C=O groups of the DMF ligands of complex **2** are observed at 1632 cm^{-1}. The strong absorption band at 1632 cm^{-1} for H_2L is assigned to the azomethine groups, ν(C=N),[13] which is shifted to lower wave numbers 1608 cm^{-1} for complexes **1** and 1615 cm^{-1} for complex **2**.[14] The weak bands in the low wave numbers 450–550 cm^{-1} are due to the vibration of the Cu-O and Cu-N bonds.[15]

In the electronic spectra of complexes **1** and **2** measured in methanol, the intense bands observed at about 230–280 nm for the complexes are assigned to intra-ligand π–π^* transitions. The complexes displayed bands centered at 270–280 nm, which can be assigned to the n–π^* transition.[16] The charge transfer LMCT bands are located in the range of 350 nm.[17]

3. 4. Antibacterial Activity

The antibacterial results are summarized in Table 3. The Schiff base H_2L showed activity against *E. coli*, while no activity on *S. aureus* and *C. parapsilosis*. Both the copper and the zinc complexes have higher activities than the free Schiff base. The copper complex showed strong activity against *S. aureus* and *E. coli*, and weak activity against *C. parapsilosis*. The zinc complex showed medium activity against *S. aureus*, and weak activities against *E. coli* and *C. parapsilosis*. Obviously, the copper complex is more effective than the zinc complex. The copper complex has the most activity against *S. aureus*, with IC_{50} and MIC values of 0.16 and 0.27 mmol L^{-1}, which deserves further study. As a comparison, the copper complex has similar antibacterial activities against *S. aureus* and *E. coli* to the Schiff base manganese(III) complex[18] and the Schiff base copper(II) complexes.[19] However, it has weaker activity against the the yeast *C. para-*

Table 3. Antibacterial property of the Schiff base and the complexes

Compound	*S. aureus*		*E. coli*		*C. parapsilosis*	
	IC_{50}*	MIC*	IC_{50}	MIC	IC_{50}	MIC
H_2L	>2.50	>2.50	1.63	2.50	>2.50	>2.50
1	0.27	0.16	0.56	0.32	2.17	1.25
2	1.15	0.62	1.83	1.25	3.39	2.50

* mmol L^-

psilosis when compared with the manganese and copper complexes.

4. Conclusion

In summary, with the bis-Schiff base *N,N'*-bis(4-bromosalicylidene)propane-1,3-diamine a mononuclear copper(II) complex and a phenolato-bridged trinuclear zinc(II) complex were synthesized. The complexes were characterized by physic-chemical methods, and their structures were confirmed by single crystal X-ray determination. The Schiff base ligand coordinates to the metal atoms through the phenolate oxygen and imine nitrogen. The complexes have significant antibacterial activities on the bacteria *Staphylococcus aureus* and *Escherichia coli*, and the yeast *Candida parapsilosis*.

Supplementary Mateiral

CCDC 2007656 (**1**) and 2007657 (**2**) contain the supplementary crystallographic data for this paper. These data can be obtained free of charge at http://www.ccdc.cam.ac.uk/const/retrieving.html or from the Cambridge Crystallographic Data Centre, 12 Union Road, Cambridge CB2 1EZ, UK; fax: +44(0)1223-336033 or email: deposit@ccdc.cam.ac.uk.

5. References

1. (a) A. Bhanja, R. Herchel, Z. Travnicek, D. Ray, *Inorg. Chem.* **2019**, *58*, 12184–12198; **DOI:**10.1021/acs.inorgchem.9b01517
   (b) R. Ogawa, T. Suzuki, M. Hirotsu, N. Nishi, Y. Shimizu, Y. Sunatsuki, Y. Teki, I. Kinoshita, *Dalton Trans.* **2019**, *48*, 13622–13629; **DOI:**10.1039/C9DT03007G
   (c) S. Yadamani, A. Neamati, M. Homayouni-Tabrizi, S. Yadamani, A. Javdani-Mallak, S. A. Beyramabadi, *Appl. Biochem. Biotech.* **2020**, *190*, 997–1009; **DOI:**10.1007/s12010-019-03118-7
   (d) M. S. S. Adam, O. M. El-Hady, F. Ullah, *RSC Advances* **2019**, *9*, 34311–34329; **DOI:**10.1039/C9RA06816C
   (e) L.-W. Xue, Q.-L. Peng, P.-P. Wang, H.-J. Zhang, *Acta Chim. Slov.* **2019**, *66*, 694–700; **DOI:**10.17344/acsi.2019.5151
   (f) C.-L. Zhang, X.-Y. Qiu, S.-J. Liu, *Acta Chim. Slov.* **2019**, *66*, 484–489. **DOI:**10.17344/acsi.2019.5019
2. (a) K. Venkateswarlu, N. Ganji, S. Daravath, K. Kanneboina, K. Rangan, Shivaraj, *Polyhedron* **2019**, *171*, 86–97; **DOI:**10.1016/j.poly.2019.06.048
   (b) S. C. Manna, S. Mistri, A. Patra, M. K. Mahish, D. Saren, R. K. Manne, M. K. Santra, E. Zangrando, H. Puschmann, *Polyhedron* **2019**, *171*, 77–85; **DOI:**10.1016/j.poly.2019.06.049
   (c) M. Aidi, H. Keypour, A. Shooshtari, M. Mahmoudabadi, M. Bayat, Z. Ahmadvand, R. Karamian, M. Asadbegy, S. Tavatli, R. W. Gable, *Polyhedron* **2019**, *167*, 93–102; **DOI:**10.1016/j.poly.2019.02.030
   (d) I. Mondal, K. Ghosh, S. Chattopadhyay, *Inorg. Chim. Acta* **2019**, *494*, 123–131; **DOI:**10.1016/j.ica.2019.05.003
   (e) D.-L. Peng, N. Sun, *Acta Chim. Slov.* **2018**, *65*, 895–901. **DOI:**10.17344/acsi.2018.4543
3. (a) S. Ali, T. Ara, M. Danish, S. Shujah, A. M. Z. Slawin, *Russ. J. Coord. Chem.* **2019**, *45*, 889–898; **DOI:**10.1134/S1070328419120017
   (b) S. Mandal, T. Sen, U. Mandal, D. Bhunia, C. Rizzoli, D. Bandyopadhyay, *J. Coord. Chem.* **2019**, *72*, 3614–3624; **DOI:**10.1080/00958972.2019.1704275
   (c) H. Keypour, F. Forouzandeh, S. Salehzadeh, F. Hajibabaei, S. Feizi, R. Karamian, N. Ghiasi, R. W. Gable, *Polyhedron* **2019**, *170*, 584–592; **DOI:**10.1016/j.poly.2019.06.023
   (d) H. Y. Qian, N. Sun, *Transition Met. Chem.* **2019**, *44*, 501–506; **DOI:**10.1007/s11243-018-00296-x
   (e) M. H. Esfahani, H. Iranmanesh, J. E. Beves, M. Kaur, J. P. Jasinski, M. Behzad, *J. Coord. Chem.* **2019**, *72*, 2326–2336. **DOI:**10.1080/00958972.2019.1643846
4. (a) L. Saghatforoush, K. Moeini, S. A. Hosseini-Yazdi, Z. Mardani, A. Bakhtiari, A. Hajabbas-Farshchi, S. Honarvar, M. S. M. Abdelbaky, *Polyhedron* **2019**, *170*, 312–324; **DOI:**10.1016/j.poly.2019.05.057
   (b) M. S. S. Adam, L. H. Abdel-Rahman, A. M. Abu-Dief, N. A. Hashem, *Inorg. Nano-Met. Chem.* **2020**, *50*, 136–150; **DOI:**10.1080/24701556.2019.1672735
   (c) K. Dankhoff, M. Gold, L. Kober, F. Schmitt, L. Pfeifer, A. Durrmann, H. Kostrhunova, M. Rothemund, V. Brabec, R. Schobert, B. Weber, *Dalton Trans.* **2019**, *48*, 15220–15230; **DOI:**10.1039/C9DT02571E
   (d) Y. N. Guo, X. B. Hu, X. L. Zhang, X. H. Pu, Y. Wang, *RSC Advances* **2019**, *9*, 41737–41744. **DOI:**10.1039/C9RA07298E
5. *SMART/SAINT*, Madison (WI, USA): Bruker AXS, Inc., **2004**.
6. G. M. Sheldrick, *Acta Crystallogr.* **2015**, *C71*, 3–11.
7. G. M. Sheldrick, *SADABS*, Göttingen (Germany): Univ. of Göttingen, **1999**.
8. (a) L. S. Ghomi, M. Behzad, A. Tarahhomi, A. Arab, *J. Mol. Struct.* **2017**, *1150*, 214–226; **DOI:**10.1016/j.molstruc.2017.08.089
   (b) H. Barfeie, G. Grivani, V. Eigner, M. Dusek, A. D. Khalaji, *Polyhedron* **2018**, *146*, 19–25; **DOI:**10.1016/j.poly.2018.02.012
   (c) S. Bharti, M. Choudhary, B. Mohan, S. P. Rawat, S. R. Sharma, K. Ahmad, *J. Mol. Struct.* **2017**, *1149*, 846–861. **DOI:**10.1016/j.molstruc.2017.07.101
9. (a) D. M. Gonzalez, J. Cisterna, I. Brito, T. Roisnel, J. R. Hamon, C. Manzur, *Polyhedron* **2019**, *162*, 91–99; **DOI:**10.1016/j.poly.2019.01.043
   (b) S. Shit, M. Nandy, D. Saha, L. Zhang, W. Schmitt, C. Rizzoli, T. N. G. Row, *J. Coord. Chem.* **2016**, *69*, 2403–2414; **DOI:**10.1080/00958972.2016.1197390
   (c) A. H. Mirza, M. H. S. A. Hamid, S. Aripin, M. R. Karim, M. Arifuzzaman, M. A. Ali, P. V. Bernhardt, *Polyhedron* **2014**, *74*, 16–23. **DOI:**10.1016/j.poly.2014.02.016
10. (a) S. S. Qian, X. S. Cheng, J. Q. Ren, Z. L. You, H. L. Zhu, *Russ. J. Coord. Chem.* **2013**, *39*, 836–843;

DOI:10.1134/S1070328413110080
(b) K. Das, A. Jana, S. Konar, S. Chatterjee, T. K. Mondal, A. K. Barik, S. K. Kar, *J. Mol. Struct.* **2013**, *1048*, 98–103; **DOI:**10.1016/j.molstruc.2013.05.020
(c) Z. H. Chohan, M. Hanif, *Appl. Organomet. Chem.* **2011**, *25*, 753–760.

11. (a) D. Ulku, L. Tatar, O. Atakol, M. Aksu, *Acta Crystallogr.* **2001**, *57*, 273–274; **DOI:**10.1107/S0108270100019983
(b) M. Escarcega-Bobadilla, E. C. Escudero-Adan, M. M. Belmonte, E. Martin, A. W. Kleij, *Chem. Eur. J.* **2013**, *19*, 2641–2648; **DOI:**10.1002/chem.201204132
(c) X.-X. Zhou, H.-C. Fang, Y.-Y. Ge, Z.-Y. Zhou, Z.-G. Gu, X. Gong, G. Zhao, Q.-G. Zhan, R.-H. Zeng, Y.-P. Cai, *Cryst. Growth Des.* **2010**, *10*, 4014–4022; **DOI:**10.1021/cg100612b
(d) T. Z. Yu, K. Zhang, Y. L. Zhao, C. H. Yang, H. Zhang, L. Qian, D. W. Fan, W. K. Dong, L. L. Chen, Y. Q. Qiu, *Inorg. Chim. Acta* **2008**, *361*, 233–240. **DOI:**10.1016/j.ica.2007.07.012
12. I. Mondal, K. Ghosh, A. Franconetti, A. Frontera, S. Chatterjee, S. Chattopadhyay, *J. Coord. Chem.* **2019**, *72*, 3237–3247. **DOI:**10.1080/00958972.2019.1688311
13. R. W. Handel, H. Willms, G. B. Jameson, K. J. Berry, B. Moubaraki, K. S. Murray, S. Brooker, *Eur. J. Inorg. Chem.* **2010**, *21*, 3317–3327. **DOI:**10.1002/ejic.201000288
14. G. Marinescu, A. M. Madalan, S. Shova, M. Andruh, *J. Coord. Chem.* **2012**, *65*, 1539–1547. **DOI:**10.1080/00958972.2012.675435
15. A. Ray, D. Sadhukhan, G. Rosair, C. J. Gomez-Garcia, S. Mitra, *Polyhedron* **2009**, *28*, 3542–3550. **DOI:**10.1016/j.poly.2009.07.017
16. A. Jayamani, M. Sethupathi, S. O. Ojwach, N. Sengottuvelan, *Inorg. Chem. Commun.* **2017**, *84*, 144–149. **DOI:**10.1016/j.inoche.2017.08.013
17. B. Sarkar, M. G. B. Drew, M. Estrader, C. Diaz, A. Ghosh, *Polyhedron* **2008**, *27*, 2625–2633. **DOI:**10.1016/j.poly.2008.05.004
18. Y.-M. Hao, *Russ. J. Coord. Chem.* **2015**, *41*, 25–30. **DOI:**10.1134/S1070328415010030
19. A. Valent, M. Melnik, D. Hudecova, B. Dudova, R. Kivekas, M. R. Sundberg, *Inorg. Chim. Acta* **2002**, *340*, 15–20. **DOI:**10.1016/S0020-1693(02)01062-9

Povzetek

Sintetizirali smo enojedrni bakrov(II) kompleks [CuL] (**1**) in trijedrni cinkov(II) kompleks s fenolatnim mostom $[Zn_3Cl_2L_2(DMF)_2]$ (**2**), kjer je L deprotonirana oblika *N,N'*-bis(4-bromosaliciliden)propan-1,3-diamina (H_2L), ter ju okarakterizirali z elementno analizo, IR in UV-Vis spektroskopijo in rentgensko monokristalno analizo. Cu atom v kompleksu **1** ima kvadratno planarno koordinacijo, medtem ko imata terminalna Zn atoma v kompleksu **2** kvadratno piramidalno koordinacijo in centralni Zn atom oktaedrično koordinacijo. Protimikrobno aktivnost kompleksov smo testirali na bakterijah *Staphylococcus aureus* in *Escherichia coli* ter na glivi *Candida parapsilosis*.

Except when otherwise noted, articles in this journal are published under the terms and conditions of the Creative Commons Attribution 4.0 International License

Scientific paper

Ultrasound-Assisted Synthesis, Antioxidant Activity and Computational Study of 1,3,4-Oxadiazol-2-amines

Hamid Beyzaei,[1]* Soheila Sargazi,[2] Ghodsieh Bagherzade,[2] Ashraf Moradi,[1] and Elahe Yarmohammadi[1]

[1] *Department of Chemistry, Faculty of Science, University of Zabol, Zabol, Iran*

[2] *Department of Chemistry, Faculty of Science, University of Birjand, Birjand, Iran*

* *Corresponding author: E-mail: hbeyzaei@yahoo.com and hbeyzaei@uoz.ac.ir*
Tel: +98 5431232186 / Fax: +98 5431232180

Received: 06-19-2020

Abstract

Development of synthetic procedures for the preparation of 1,3,4-oxadiazole derivatives has always been in the interest of researchers as a result of their widespread biological activities. In this study, an ultrasound-assisted procedure was proposed for the synthesis of 1,3,4-oxadiazol-2-amines form the reaction of hydrazides and cyanogen bromide. They were efficiently produced in 81–93% yields in the presence of ethanol and potassium bicarbonate as the reaction media and the base, respectively. Their antioxidant properties were determined *via* DPPH free radical scavenging method as one of the most basic steps in identifying other related biological effects. IC_{50} values were in the range of from 0.237 to 0.863 mM. The synthesized 1,3,4-oxadiazoles are protective agents against oxidative stress, and can be used in the treatment of cancer, candidiasis, diabetes, neurodegenerative and inflammatory diseases. Furthermore, bond dissociation energies (BDEs) and electron densities based NCI (non-covalent interactions) were calculated using density-functional theory (DFT) to understand the observed reactivities. It was found that reversible dipole-dipole forces play a key role in most interactions.

Keywords: 1,3,4-Oxadiazole; Antioxidant activity; DPPH; Ultrasound irradiation; NCI; DFT

1. Introduction

Antioxidants are synthetic or natural compounds that inhibit the oxidation reactions *via* free radical scavenging. Free radicals are unstable and reactive atoms or molecules containing one unpaired electron that can begin a propagation sequence in the chain reactions leading to cell damage.[1] Vitamins C and E as two essential nutrients are well known for being potent antioxidants. Ascorbic acid, known as vitamin C, is a water-soluble biologically active compound which should be provided to humans through food especially fresh vegetables and citrus fruits. Lack of vitamin C is accompanied by early symptoms of weakness and fatigue which can lead to anemia, hair loss, bleeding gum and skin, and scurvy disease in the acute cases.[2] Vitamin C is required for the proper functioning of some enzymes and immune system, tissue regeneration and the enzymatic production.[3–5] Oil-soluble vitamin E includes four tocopherols as well as four tocotrienols. It is found in cereals, vegetable oils, meat, poultry, fruits and eggs, and its deficiency damages the nervous system.[6]

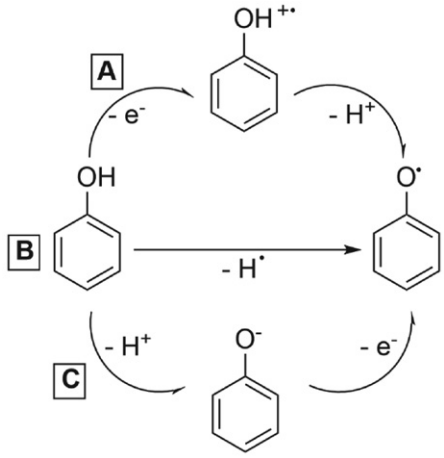
It has been understood that there is a significant relationship between the antioxidant capacity of compounds and some of their biological activities. Mendonca *et al.* have evaluated antioxidant and antiproliferative potentials of muscadine grape extracts on breast cancer cell lines; a strong positive correlation was observed between total phenolic content of extracts and their inhibitory activities against African American breast cancer cells.[7] There are complex and often positive connections between oxidative stress with the inflammatory response given as a result of tissue injury and infection.[8] Guava leaves are used as traditional medicines for the treatment of diabetes; they lowered levels of cholesterol, sugar, triglycerides, malonaldehyde and glycated serum protein in the blood of streptozotocin-induced diabetic mice according to their ABTS, OH and DPPH free radical scavenging capabilities.[9] Reactive oxygen species are one of the main causes of Alzheimer disease, as a result, any agent that blocks their generation, can be useful in treating the disease.[10]

1,3,4-Oxadiazole derivatives have attracted a great deal of interest due to their diverse biological properties

such as antioxidant, antiproliferative, anticonvulsant, antimicrobial and anti-Alzheimer.[11–15] Synthetic approaches of 1,3,4-oxadiazoles were reviewed in several literatures.[16–18] Hypervalent iodine mediated reaction of *N´*-arylidene acetohydrazides, intracyclocondensation of thiosemicarbazides prepared from the reaction of aryl hydrazides with ammonium thiocyanate using *N*,*N*,*N´*,*N´*-tetramethyl-*O*-(benzotriazol-1-yl)uronium tetrafluoroborate (TBTU) or *N*,*N´*-diisopropylcarbodiimide (DIC), and simultaneous reaction of 1-chloroketones, *N*-isocyaniminotriphenylphosphorane and aryl carboxylic acids are examples of recent methods proposed to synthesize 1,3,4-oxadiazole derivatives.[19–21]

Theoretical calculations can be performed to justify experimental observations. However, it is possible that a logical relationship between experimental data and theoretical parameters cannot be found in all cases. The thermodynamics of free radical scavenge of some 1,3,4-oxadiazole derivatives were studied by DFT method in gas and aqueous phases to predict their action mechanisms; it was found that the selected reaction pathway is completely dependent on the reaction medium.[22]

It has been shown that phenolic compounds act as antioxidants in three ways (Scheme 1):



Scheme 1. Antioxidant mechanism of phenolic compounds: (**A**) Single Electron Transfer Followed by Proton Transfer (SET-PT); (**B**) Hydrogen Atom Transfer (HAT); (**C**) Sequential Proton Loss Electron Transfer (SPLET).

Computational studies can be applied to calculate values of bond dissociation enthalpy, ionization potential and proton dissociation enthalpy, proton affinity and electron transfer enthalpy to determine the predominant path.[23] DPPH free radical scavenging activity of some synthesized 1,2,4-triazole-3-thiones containing phenolic substituents was evaluated by Ivanović *et al.*; DFT calculations proved synergistic effects of 1,2,4-triazole-3-thione rings and predicted SPLET pathway as the action mechanism in methanol.[23]

In order to expand library of small organic biomolecules, some 5-alkyl/aryl/heteroaryl-1,3,4-oxadiazol-2-amine derivatives were synthesized *via* a new procedure under ultrasound irradiation. Antioxidant activities of the synthesized 1,3,4-oxadiazoles were assessed against DPPH to predict their other possible biological capabilities. Bond dissociation energy and electron density of all synthesized heterocycles were calculated to establish the probable relation to the observed antioxidant activities.

2. Experimental

2. 1. Chemicals

All chemicals, solvents and aluminium thin-layer chromatography (TLC) plates pre-coated with silica gel containing fluorescent indicator F254 were purchased from Merck and Sigma-Aldrich companies. The melting points were determined with Kruss KSP1N melting point apparatus, and are uncorrected. Bruker Tensor-27 FT-IR spectrometer was applied to record the FT-IR spectra of compounds. ^{1}H and ^{13}C NMR spectra were registered using a Bruker 300 MHz NMR spectrometer. Chemical shifts are provided as δ values (ppm) and coupling constants *J* (Hz). Elemental analyses for C, H, N and S atoms were performed on a Termo Finnigan Flash EA microanalyzer. Ultrasonic irradiation was supplied by Backer vCLEAN1-L03 (40 kHz frequency and 100 W output power).

2. 1. 1. General Procedure for the Synthesis of 5-Substituted 1,3,4-Oxadiazol-2-amines 3a–h

A 25 mL round-bottom flask containing 5 mmol of each hydrazides **1a**–**h**, cyanogen bromide (**2**) (0.53 g) and potassium bicarbonate (0.50 g) in 10 mL absolute ethanol was subjected to an ultrasonic bath. The reaction progress was checked by TLC with different volumetric ratios of methanol and dichloromethane as the desired mobile phase. The reaction content was added to 20 g of crushed ice containing an excess of salt. The solid phase was filtered out, washed respectively with water (5 mL) and ethanol (5 mL), and oven-dried at 70 °C to give pure 1,3,4-oxadiazoles **3a**–**h**.

5-Methyl-1,3,4-oxadiazol-2-amine (3a).

Yellow powder; yield 0.40 g (81%); m.p. 172–174 °C (lit. m.p. 176–180 °C[24]); IR (KBr) *ν* 3420, 3352 (NH_2), 3120, 2359, 1666 (C=N), 1595, 1383, 1254, 1123 (C–O), 1005 (N–N), 781, 626 cm^{-1}; ^{1}H NMR (300 MHz, DMSO-d_6) *δ* 6.85 (s, 2H, NH_2), 2.27 (s, 3H, CH_3); ^{13}C NMR (75 MHz, DMSO-d_6) *δ* 10.9 (CH_3), 156.6 (C-5 oxadiazole), 164.0 (C-2 oxadiazole). Anal. Calcd. for $C_3H_5N_3O$: C, 36.36; H, 5.09; N, 42.41. Found: C, 36.31; H, 5.11; N, 42.43.

5-Phenyl-1,3,4-oxadiazol-2-amine (3b).

White powder; yield 0.74 g (92%); m.p. 243–245 °C (lit. m.p. 239–242 °C[25]); IR (KBr) *ν* 3476, 3413 (NH_2), 2924, 2358, 1613 (C=N), 1452, 1113 (C–O), 1027 (N–N), 620, 478 cm^{-1}; ^1H NMR (300 MHz, DMSO-d_6) *δ* 7.25 (s, 2H, NH_2), 7.80–7.78 (m, 2H, H-2′,6′ Ph), 7.51–7.49 (m, 3H, H-3′,4′,5′ Ph); ^{13}C NMR (75 MHz, DMSO-d_6) *δ* 124.8 (C-1′ Ph), 125.4 (C-2′,6′ Ph), 129.6 (C-3′,5′ Ph), 130.7 (C-4′ Ph), 157.8 (C-5 oxadiazole), 164.3 (C-2 oxadiazole). Anal. Calcd. for $C_8H_7N_3O$: C, 59.62; H, 4.38; N, 26.07. Found: C, 59.59; H, 4.35; N, 26.11.

5-(4-Nitrophenyl)-1,3,4-oxadiazol-2-amine (3c).

Yellow powder; yield 0.91 g (88%); m.p. 265–267 °C (lit. m.p. 267–270 °C[25]); IR (KBr) *ν* 3436, 3375 (NH_2), 2924, 2358, 1652 (C=N), 1598 (N–O), 1527, 1389, 1344, 1116 (C–O), 1037 (N–N), 858, 620 cm^{-1}; ^1H NMR (300 MHz, DMSO-d_6) *δ* 7.52 (brs, 2H, NH_2), 8.32 (d, *J* = 8.7 Hz, 2H, H-3′,5′ Ar), 7.98 (d, *J* = 8.7 Hz, 2H, H-2′,6′ Ar); ^{13}C NMR (75 MHz, DMSO-d_6) *δ* 124.9 (C-3′,5′ Ar), 126.4 (C-2′,6′ Ar), 130.2 (C-1′ Ar), 148.3 (C-4′ Ar), 156.5 (C-5 oxadiazole), 165.0 (C-2 oxadiazole). Anal. Calcd. for $C_8H_6N_4O_3$: C, 46.61; H, 2.93; N, 27.18. Found: C, 46.66; H, 2.93; N, 27.15.

5-(4-(*tert*-Butyl)phenyl)-1,3,4-oxadiazol-2-amine (3d).

Pink powder; yield 1.01 g (93%); m.p. 262–264 °C (lit. m.p. 256–258 °C[25]); IR (KBr) *ν* 3434, 3358 (NH_2), 3127, 2963, 2358, 1655 (C=N), 1609, 1391, 1118 (C–O), 1042 (N–N), 836, 621, 561 cm^{-1}; ^1H NMR (300 MHz, DMSO-d_6) *δ* 7.55 (brs, 2H, NH_2), 7.83 (d, *J* = 8.5 Hz, 2H, H-2′,6′ Ar), 7.63 (d, *J* = 8.5 Hz, 2H, H-3′,5′ Ar), 1.34 (s, 9H, 3 × CH_3); ^{13}C NMR (75 MHz, DMSO-d_6) *δ* 31.1 (C($\underline{C}H_3$)$_3$), 35.0 ($\underline{C}$(CH_3)$_3$), 121.4 (C-3′,5′ Ar), 125.0 (C-2′,6′ Ar), 127.2 (C-1′ Ar), 152.6 (C-4′ Ar), 157.5 (C-5 oxadiazole), 164.3 (C-2 oxadiazole). Anal. Calcd. for $C_{12}H_{15}N_3O$: C, 66.34; H, 6.96; N, 19.34. Found: C, 66.30; H, 6.98; N, 19.36.

3-(5-Amino-1,3,4-oxadiazol-2-yl)phenol (3e).

White powder; yield 0.73 g (83%); m.p. 240–242 °C (lit. m.p. 244–245 °C[26]); IR (KBr) *ν* 3554 (OH), 3458, 3413 (NH_2), 3145, 2924, 2360, 2341, 1643 (C=N), 1601, 1568, 1493, 1384, 1320, 1309, 1221, 1126 (C–O), 1064 (N–N), 1035, 994, 876, 799, 739, 701, 688, 669, 617, 450 cm^{-1}; ^1H NMR (300 MHz, DMSO-d_6) *δ* 9.90 (s, 1H, OH), 7.35–7.26 (m, 5H, NH_2, H-2′,5′,6′ Ar), 6.91 (d, *J* = 6.9 Hz, 1H, H-4′ Ar); ^{13}C NMR (75 MHz, DMSO-d_6) *δ* 112.0 (C-2′ Ar), 116.3 (C-4′ Ar), 118.0 (C-6′ Ar), 125.8 (C-1′ Ar), 130.8 (C-5′ Ar), 157.9 (C-3′ Ar), 158.2 (C-5 oxadiazole), 164.2 (C-2 oxadiazole). Anal. Calcd. for $C_8H_7N_3O_2$: C, 54.24; H, 3.98; N, 23.72. Found: C, 54.19; H, 3.96; N, 23.75.

5-(3-Methoxyphenyl)-1,3,4-oxadiazol-2-amine (3f).

Yellow powder; yield 0.86 g (90%); m.p. 193–194 °C (lit. m.p. 192–195 °C[27]); IR (KBr) *ν* 3415, 3386 (NH_2), 3109, 2359, 1654 (C=N), 1489, 1390, 1322, 1284, 1215, 1106 (C–O), 1040 (N–N), 875, 786, 748, 683, 621 cm^{-1}; ^1H NMR (300 MHz, DMSO-d_6) *δ* 7.48–7.38 (m, 2H, H-5′,6′), 7.31–7.30 (m, 3H, NH_2, H-2′ Ar), 7.10 (d, *J* = 7.0 Hz, 1H, H-4′ Ar), 3.83 (s, 3H, CH_3); ^{13}C NMR (75 MHz, DMSO-d_6) *δ* 55.7 (CH_3), 110.3 (C-2′ Ar), 116.8 (C-4′ Ar), 117.8 (C-6′ Ar), 126.6 (C-1′ Ar), 130.9 (C-5′ Ar), 157.7 (C-3′ Ar), 160.0 (C-5 oxadiazole), 164.3 (C-2 oxadiazole). Anal. Calcd. for $C_9H_9N_3O_2$: C, 56.54; H, 4.75; N, 21.98. Found: C, 54.59; H, 4.74; N, 21.95.

5-(3-Bromophenyl)-1,3,4-oxadiazol-2-amine (3g).

White powder; yield 1.10 g (92%); m.p. 246–248 °C (lit. m.p. 240–243 °C[27]); IR (KBr) *ν* 3451, 3413 (NH_2), 3116, 2358, 1654 (C=N), 1604, 1557, 1392, 1112 (C–O), 1044 (N–N), 794, 681 cm^{-1}; ^1H NMR (300 MHz, DMSO-d_6) *δ* 7.91 (m, 1H, H-6′), 7.80 (d, *J* = 7.8 Hz, 1H, H-4′ Ar), 7.71 (d, *J* = 7.7 Hz, 1H, H-2′ Ar), 7.50 (t, *J* = 7.5 Hz, 1H, H-5′ Ar), 7.38 (s, 2H, NH_2); ^{13}C NMR (75 MHz, DMSO-d_6) *δ* 122.7 (C-3′ Ar), 124.4 (C-6′ Ar), 126.9 (C-1′ Ar), 127.7 (C-4′ Ar), 131.9 (C-5′ Ar), 133.4 (C-2′ Ar), 156.4 (C-5 oxadiazole), 164.5 (C-2 oxadiazole). Anal. Calcd. for $C_8H_6BrN_3O$: C, 40.03; H, 2.52; N, 17.50. Found: C, 40.01; H, 2.50; N, 17.47.

5-(Pyridin-4-yl)-1,3,4-oxadiazol-2-amine (3h).

Brown powder; yield 0.68 g (84%); m.p. 260–261 °C (lit. m.p. 262–264 °C[25]); IR (KBr) *ν* 3417, 3383 (NH_2), 2358, 1665 (C=N), 1538, 1391, 1340, 1123 (C–O), 1043 (N–N), 837, 682, 620 cm^{-1}; ^1H NMR (300 MHz, DMSO-d_6) *δ* 8.74 (d, *J* = 7.7 Hz, 2H, H-2′,6′ Ar), 7.71 (d, *J* = 7.7 Hz, 2H, H-3′,5′ Ar), 7.58 (brs, 2H, NH_2); ^{13}C NMR (75 MHz, DMSO-d_6) *δ* 119.2 (C-3′,5′ Ar), 131.6 (C-4′ Ar), 151.1 (C-2′,6′ Ar), 156.2 (C-5 oxadiazole), 165.0 (C-2 oxadiazole). Anal. Calcd. for $C_7H_6N_4O$: C, 51.85; H, 3.73; N, 34.55. Found: C, 51.89; H, 3.75; N, 34.51.

2. 2. Half Maximal Inhibitory Concentration (IC_{50}) Identification

DPPH free radical scavenging activities of prepared 1,3,4-oxadiazoles were evaluated and compared to those of ascorbic acid.[28] 1 mL of any oxadiazole at concentrations 25, 50, 75, and 100 μg mL^{-1} in methanol was added to 4 mL of 0.004% (w/v) methanolic solution of DPPH. The mixed solutions were stored at room temperature for 30 min in darkness. Then, the absorbance of the solutions was read against the blank at λ_{max} 517 nm. The inhibition percentage (*I*%) was calculated according to the following equation:

$$I\% = \frac{A(blank) - A(sample)}{A(blank)} \cdot 100$$

Wher *A*(blank) and *A*(sample) are the absorbance of control and sample solutions, respectively. A graph of *I*% (*y*-axis) *vs.* concentration (*x*-axis) was plotted. The IC_{50} is

x in the equation of a straight line $y = mx + b$, while $y = 50$. Finally, the μg mL^{-1} units were converted to the mM units.

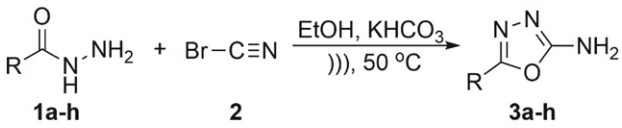
2. 3. Computational Details

All the geometries were optimized in the gas phase and frequency calculations confirmed the nature of the stationary points. The methanol solvent was modelled using C-PCM as implemented in Gaussian 09 program package at the B3LYP level of density functional theory using the 6-311++G (d) basis set.[29–32] NCI analysis was performed by the NCIPlot software.[33]

3. Results and Discussion

3. 1. Synthesis and Spectroscopic Characterization of 1,3,4-Oxadiazol-2-amines 3a–h

5-Substituted 1,3,4-oxadiazol-2-amine derivatives **3a**–**h** were synthesized *via* reaction of hydrazides **1a**–**h** and cyanogen bromide (**2**) under ultrasonic irradiation (Scheme 2). Potassium bicarbonate and absolute ethanol were applied as the base and the solvent, respectively.



R = a: CH_3; b: C_6H_5; c: 4-O_2N-C_6H_4; d: 4-$(H_3C)_3C$-C_6H_4; e: 3-HO-C_6H_4; f: 3-H_3CO-C_6H_4; g: 3-Br-C_6H_4; h: 4-Pyridinyl

Scheme 2. Reaction scheme of the synthesis of 1,3,4-oxadiazol-2-amines **3a**–**h**.

The interaction of 1 mmol of both benzhydrazide (**1b**) and cyanogen bromide was selected as the model reaction for the preparation of 1,3,4-oxadiazoles (Table 1). Water and hydrous solvents were not used as a result of hydrolysis of cyanogen bromide to hypobromous acid and hydrogen cyanide. Absolute ethanol as a green, nontoxic, readily available, low-cost, water soluble, nonexplosive, easily removable, and recoverable solvent was selected and preferred to the toxic methanol. 2 mL of ethanol was used in all processes as the minimum solvent required to dissolve the most reactants and perform the reaction. Only nucleophilic attack of NH_2 group of hydrazide to cyano group of cyanogen bromide occurred at room temperature (Table 1, entry 1). Intramolecular cyclization to **3b** occurred at temperatures above 60 °C (Table 1, entry 2). The product yield and the reaction time were improved under refluxing conditions due to the increased solubility of the hydrazide and effective interactions between the reagents (Table 1, entry 3). Higher yields were achieved at similar times in the presence of bases such as potassium bicarbonate (1 mmol) and potassium carbonate (0.5 mmol); increasing basicities had no effect on the yield and time. They only neutralized hydrogen bromide produced during the process so that it would not react with the hydrazide. Relative cyanogen bromide cleavage was observed in the presence of potassium hydroxide. The reaction progress was checked in the presence of $KHCO_3$ as a nontoxic and inexpensive base under ultrasound irradiation at 50 °C. 1,3,4-Oxadiazole **3b** was afforded in the shortest time with the highest yield under these conditions (Table 1, entry 7).

Table 1. Optimization of reaction conditions in the synthesis of 5-phenyl-1,3,4-oxadiazol-2-amine (**3b**).

Entry	Base	*T* (°C)	Time (h)	Yield (%)
1	–	r.t.	3	–
2	–	60	9	68
3	–	reflux	7	72
4	$KHCO_3$	reflux	5	81
5	K_2CO_3	reflux	5	81
6	KOH	reflux	5	75
7	**$KHCO_3$**	**))), 50**	**3.5**	**92**

1,3,4-Oxadiazoles **3a**–**h** were synthesized under optimized conditions. The results are given in the Table 2.

Table 2. The data of ultrasonic-assisted reactions of hydrazides **1a**–**h** and cyanogen bromide in ethanol yielding 1,3,4-oxadiazoles **3a**–**h**.

Product	R	Time (h)	Yield (%)
3a	CH_3	7	81
3b	C_6H_5	3.5	92
3c	4-O_2N-C_6H_4	4.5	88
3d	4-$(H_3C)_3C$-C_6H_4	5	93
3e	3-HO-C_6H_4	6	83
3f	3-H_3CO-C_6H_4	6	90
3g	3-Br-C_6H_4	3.5	92
3h	4-Pyridinyl	2.5	84

The chemical structure of all synthesized 1,3,4-oxadiazoles **3a**–**h** was determined by spectral data. Recorded melting points are already in agreement with previously reported findings.[24–27] The absorption bands around 1120 and 1660 cm^{-1} attributed respectively to C–O and C=N stretching vibrations confirmed the formation of 1,3,4-oxadiazole rings. In ^{1}H NMR spectra, singlet or broads peaks in the range of 6.85 to 7.58 ppm belong to amino groups. In ^{13}C NMR spectra, signals corresponding to the asymmetric 2- and 5-carbons of 1,3,4-oxadiazole ring have appeared in the 156.2–165.0 ppm range.

The reaction between hydrazides **1** and cyanogen bromide is a straightforward method to synthesize 1,3,4-oxadiazole derivatives **3**. Several procedures were developed for this purpose. Faizi *et al.* prepared 1,3,4-oxadiazole **3b** in 62% yield from the reaction of benzhydrazide and a 1.22 molar excess of cyanogen bromide in boiling methanol for 4 h.[34] Some 1,3,4-oxadiazol-2-amine derivatives were synthesized *via* the stirring of mixture including hydrazides and 1.5 molar excess of both cyanogen bromide and potassium bicarbonate in acetonitrile water mixture (v/v 6.25:93.75) for 1 day at room temperature.[35] Katritzky *et al.* proposed a convenient method for the preparation of 1,3,4-oxadiazole **3b**; the mixture of symmetric and asymmetric di(benzotriazolyl)methanimines prepared from 1,2,3-benzotriazole and cyanogen bromide was reacted with benzhydrazide in THF under reflux for 3 h to afford **3b** in 94% yield.[36]

3. 2. Antioxidant Evaluation of the Synthesized Compounds

Free radical scavenging activity of all 1,3,4-oxadiazoles **3a–h** was assessed against DPPH. The inhibitory effects were calculated as IC_{50} values and are reported in Table 3.

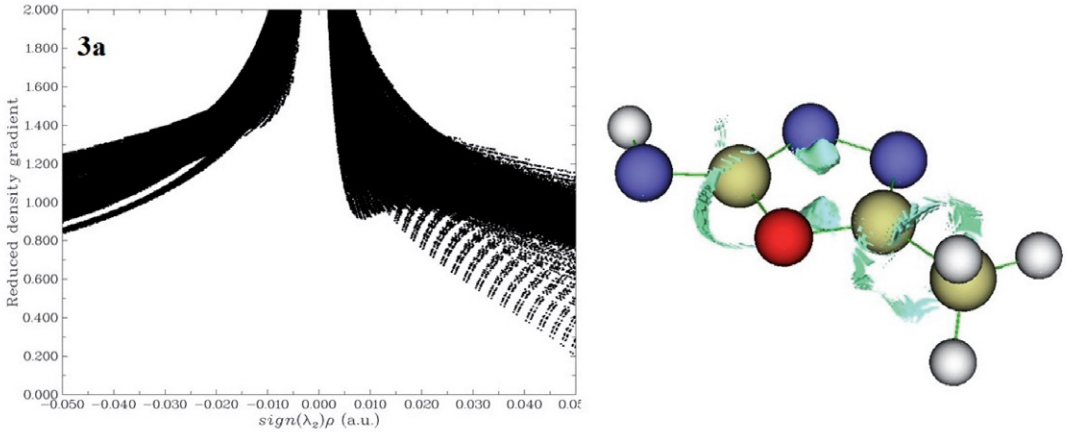
1,3,4-Oxadiazole derivatives **3a–h** exhibited antioxidant activities in the following order: **3c** > **3h** > **3a** > **3e** > **3f** > **3b** > **3g** > **3d** which, were less than that of vitamin C. No antioxidant property was observed with derivative **3d** containing 5-(4-(*tert*-butyl)phenyl) substituent. Unlike 3-(5-amino-1,3,4-oxadiazol-2-yl)phenol (**3e**), 1,3,4-oxadiazoles **3c** and **3h** with electron-withdrawing nitro and pyridinyl groups exhibited significant effects. Methylation of hydroxy group of derivative **3e** did not significantly alter its antioxidant properties; this probably indicates a lack of hydrogen-atom donation of OH substituent in **3e**.

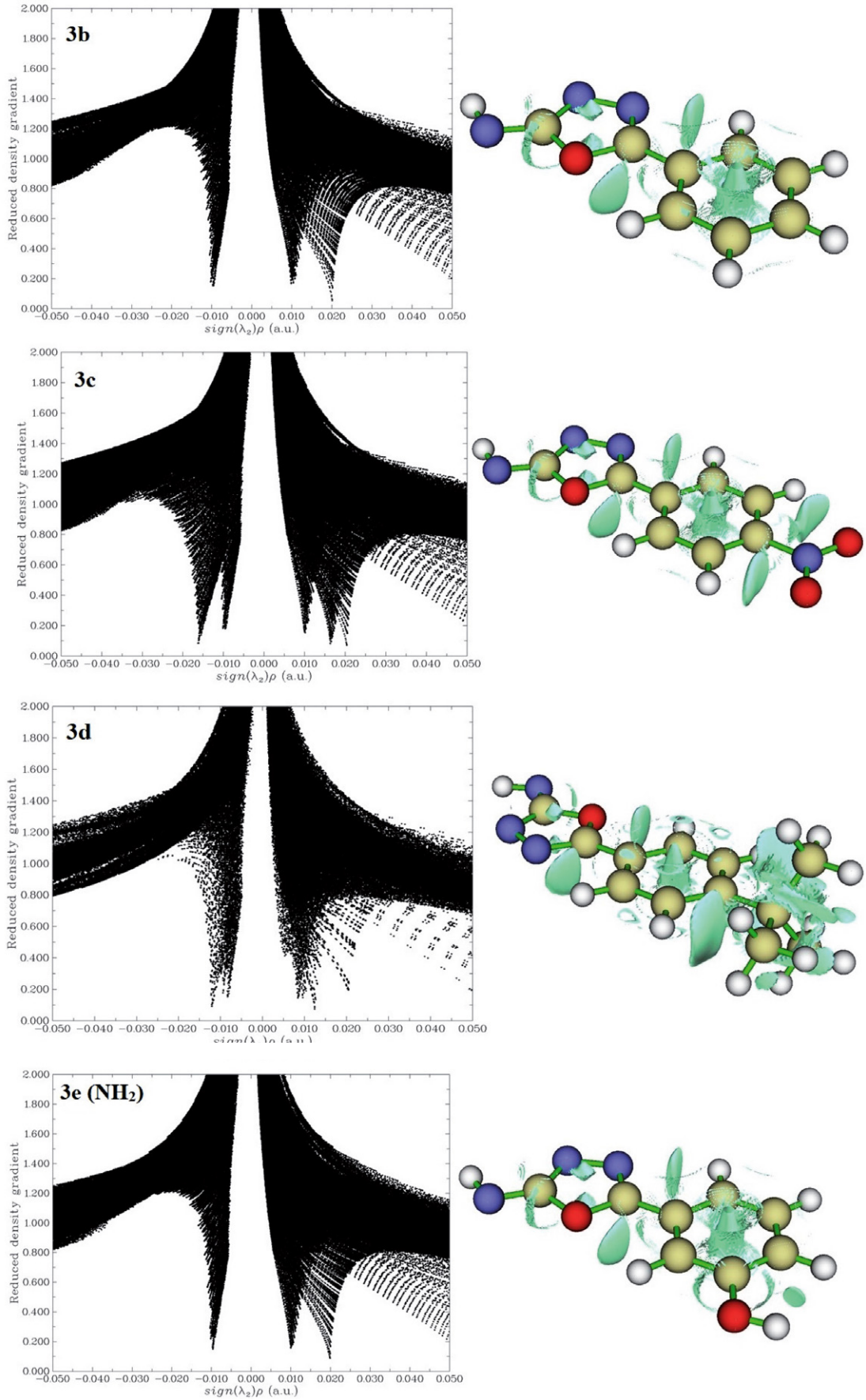
3. 3. Non-Covalent Interactions (NCI) Analysis

We have also used NCI index, while it is a visualization index based on the electron density (ρ) and the reduced density gradient (s). It is based on the empirical observation that NCI can be associated with the regions of small reduced density gradient at low electronic densities. In quantum chemistry, the NCI index is used to visualize non-covalent interactions in three-dimensional space. Its visual representation arises from the isosurfaces of the reduced density gradient colored by a scale of strength. The strength is usually estimated through the product of the electron density and the second eigenvalue (λ_H) of the Hessian of the electron density at each point of the isosurface, with the attractive or repulsive character being determined by the sign of λ_H. This allows for a direct representation and characterization of non-covalent interactions in the three-dimensional space, including hydrogen bonds and steric clashes. Being based on the electron density and derived scalar fields, NCI indexes are invariant with respect to the transformation of molecular orbitals. Furthermore, the electron density of a system can be calculated by X-ray diffraction experiments as well as theoretical wavefunction calculations (Figure 1).[37–39]

Table 3. Antioxidant activity of 1,3,4-oxadiazole derivatives 3a–h.

Products	**3a**	**3b**	**3c**	**3d**	**3e**	**3f**	**3g**	**3h**	**Vitamin C**
IC_{50} (mM)	0.237	0.306	0.114	0	0.273	0.284	0.863	0.222	0.022




3b
3c
3d
3e (NH2)
Reduced density gradient
sign(λ2)ρ (a.u.)

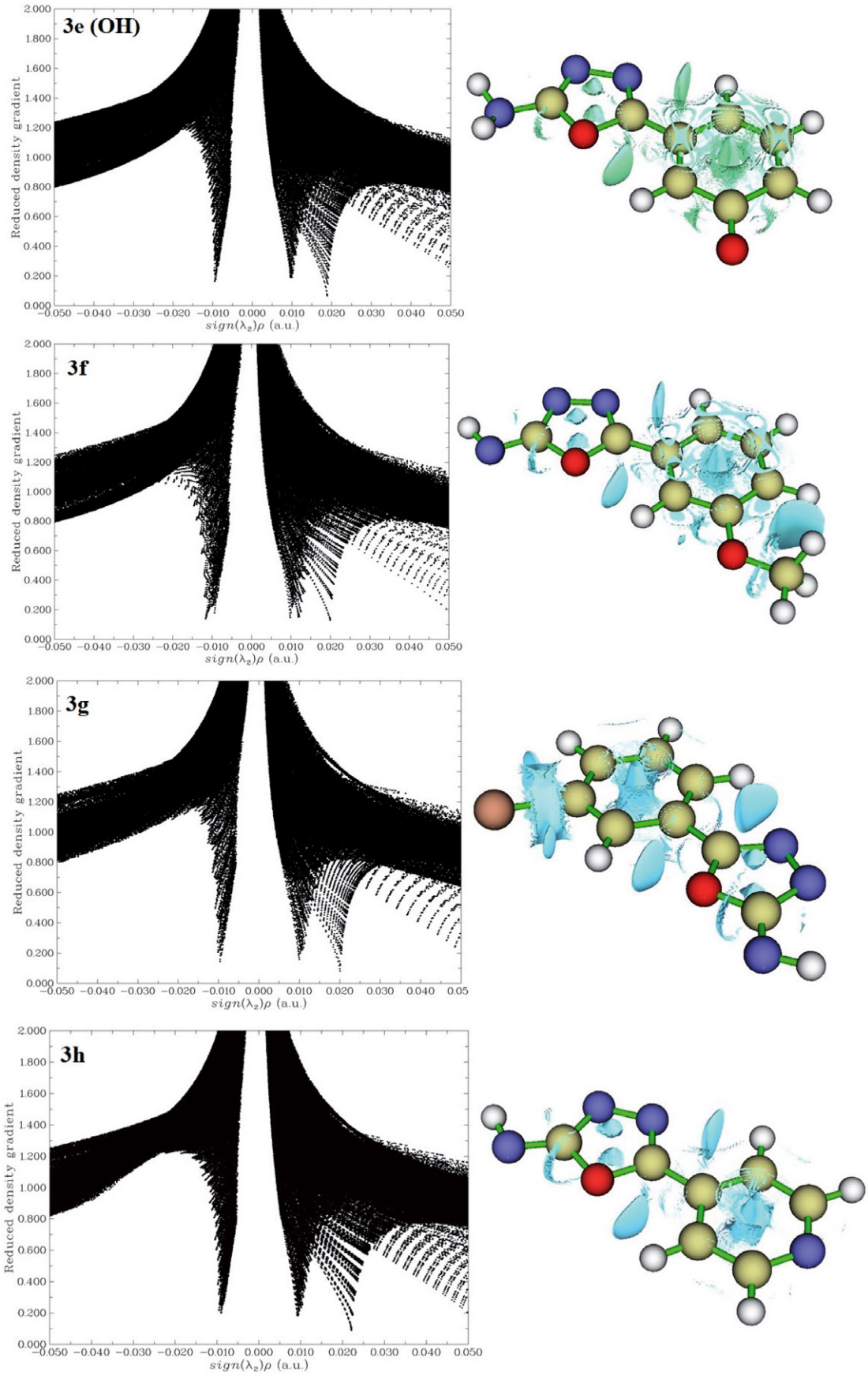


Figure 1. Plots of the reduced density gradient (RDG) versus sign (λ_2 ρ and NCI isosurface (isovalue = 0.8 au) of compounds **3a**–**h**.

The reduced density gradient (s) is a scalar field of the electron density (ρ) that can be defined as:

$$s(r) = \frac{|\nabla\rho(r)|}{2(3\pi^2)^{1/3}\,\rho(r)^{4/3}}$$

3. 4. Radicalization Energy and BDE Theory

The BDE of radicals generated from compounds **3a**–**h** were calculated and are reported in Table 4, they were arranged according to the increasing BDEs in moving from the top to the bottom on this table. Based on calculations and BDE theory, the stability of free radicals decreases as we go from left to right across the periodic table.[40] Accordingly, the product **3e** tends to form radical from nitrogen side; oxygen atom is more electronegative than nitrogen atom and its partially empty orbital is being held more closely to the positively charged nucleus. Thus, radical **3e(NH$_2$)** is more stable than radical **3e(OH)** by about 4 kcal mol^{-1}. Mesomeric and/or inductive electron-withdrawing groups such as nitro destabilize free radicals; as radical **3c** is about 3 kcal mol^{-1} less stable than radical **3b**. Radical **3g** containing 3-bromophenyl substituent is about 1 kcal mol^{-1} more stable than radical **3b**; this slight energy difference may be due to the dual nature of the halogen atoms (electron-withdrawing inductive effects versus electron-donating mesomeric effects). Unexpectedly, the replacement of C-4 in benzene with one nitrogen atom (4-pyridyl ring instead of a phenyl ring) in **3h** can increase the stability of corresponding radical.

Table 4. Calculation of energy opt + frq of compounds **3a**–**h** using DFT method in 6-311++G (d) basis set.

Compounds	Reactants (a.u.)	Radicals (a.u)	BDE (kcal mol^{-1})
3h	–564.5609986	–563.9221562	400.88
3e(OH)	–623.7550404	–623.1156937	401.20
3d	–705.7909084	–705.1461778	404.57
3b	–548.5353695	–547.8896743	405.18
3e(NH$_2$)	–623.7550392	–623.1091857	405.28
3f	–663.0593888	–662.4135282	405.28
3g	–3119.639242	–3118.991964	406.17
3a	–356.7947813	–356.1463463	406.90
3c	–753.0392	–752.38958	407.64

4. Conclusions

In this study, a new and efficient procedure was proposed for the synthesis of 1,3,4-oxadiazol-2-amines. They were prepared in good to excellent yields under ultrasound irradiation as promotion of the reaction between hydrazides and cyanogen bromide. Hydrogen-atom-donating abilities of all synthesized heterocycles were evaluated against DPPH radical. Acceptable to good antioxidant properties of the derivatives candidate them as potent antidiabetic, antiproliferative, anti-inflammatory and anti-neurodegenerative agents. The trend observed in the stability of radicals was not in complete agreement with the theoretical data suggesting that other mechanisms should be involved in the formation of all or some of them.

Acknowledgements

This study was funded by the University of Zabol (grant No. UOZ-GR-9718-9).

6. References

1. S. Goodarzi, S. Rafiei, M. Javadi, H. Khadem Haghighian, S. Noroozi, *J. Food Nutr. Sec.* **2018**, 3, 106–112.
2. R. Gallizzi, M. Valenzise, S. Passanisi, G. B. Pajno, F. De Luca, G. Zirilli, *J. Med. Case Rep.* **2020**, 14, 18. **DOI:**10.1186/s13256-020-2341-z
3. P. Tozatti, E. J. Hopkins, C. Briggs, P. Hucl, M. T. Nickerson, *Food Sci. Technol. Int.* **2020**, *26*, 614–628. **DOI:**10.1177/1082013220915363
4. T. Chaitrakoonthong, R. Ampornaramveth, P. Kamolratanakul, *Int. J. Dent.* **2020**, *2020*, 4706418. **DOI:**10.1155/2020/4706418
5. A. Boretti, B. K. Banik, *PharmaNutrition* **2020**, *12*, 100190. DOI:10.1016/j.phanu.2020.100190
6. Y. Baghcheghi, S. Mansouri, F. Beheshti, M. N. Shafei, H. Salmani, P. Reisi, A. Anaeigoudari, A. E. Bideskan, M. Hosseini, *Int. J. Vitam. Nutr. Res.* **2020**, *90*, 156–168. **DOI:**10.1024/0300-9831/a000533
7. P. Mendonca, A. G. Darwish, V. Tsolova, I. El-Sharkawy, K. F. A. Soliman, *Anticancer Res.* **2019**, *39*, 4043–4053. **DOI:**10.21873/anticanres.13560
8. M. Allegra, *Antioxidants* **2019**, *8*, 549. **DOI:**10.3390/antiox8110549
9. Y. Luo, B. Peng, W. Wei, X. Tian, Z. Wu, *Molecules* **2019**, *24*, 1343. **DOI:**10.3390/molecules24071343
10. A. Badrul, H. Ekramul, *Iran. J. Pharm. Res.* **2011**, *7*, 49–56.
11. M. M. El Sadek, S. A. Magd, S. Y. Hassan, M. Mostafa, G. Yacouat, *Iran. J. Chem. Chem. Eng.* **2019**, *38*, 229–242.
12. Z. M. M. Alzhrani, M. M. Alam, T. Neamatallah, S. Nazreen, *J. Enzyme Inhib. Med. Chem.* **2020**, *35*, 1116–1123. **DOI:**10.1080/14756366.2020.1759581
13. S. Nazar, N. Siddiqui, O. Alam, *Arch. Pharm. (Weinheim)* **2020**, e1900342. **DOI:**10.1002/ardp.201900342
14. D. Zeng, M. W. Wang, M. Xiang, L. W. Liu, P. Y. Wang, Z. Li, S. Yang, *Pest. Manag. Sci.* **2020**, *76*, 2681–2692. **DOI:**10.1002/ps.5814
15. A. Tripathi, P. K. Choubey, P. Sharma, A. Seth, P. N. Tripathi, M. K. Tripathi, S. K. Prajapati, S. Krishnamurthy, S. K. Shrivastava, *Eur. J. Med. Chem.* **2019**, *183*, 111707. **DOI:**10.1016/j.ejmech.2019.111707
16. C. S. De Oliveira, B. F. Lira, J. M. Barbosa-Filho, J. G. F. Loren-

zo, P. F. De Athayde-Filho, *Molecules* **2012**, *17*, 10192-10231. **DOI:**10.3390/molecules170910192
17. K. D. Patel, S. M. Prajapati, S. N. Panchal, H. D. Patel, *Synth. Commun.* **2014**, *44*, 1859–1875. **DOI:**10.1080/00397911.2013.879901
18. P. N. Khatale, T. Sivakumar, *Indian J. Heterocycl. Chem.* **2014**, *24*, 47–50.
19. J. Chauhan, M. K. Ravva, S. Sen, *Org. Lett.* **2019**, *21*, 6562–6565. **DOI:**10.1021/acs.orglett.9b02542
20. F. Golmohammadi, S. Balalaie, F. Hamdan, S. Maghari, *New J. Chem.* **2018**, *42*, 4344–4351. **DOI:**10.1039/C7NJ04720G
21. A. Ramazani, D. Zamanesazi, Y. Ahmadi, P. Azimzadeh Asiabi, A. Souldozi, S. J. Woo, *J. Appl. Chem. Res.* **2017**, *11*, 76–85.
22. I. O. Alisi, A. Uzairu, S. E. Abechi, *Helion* **2020**, *6*, e03683. **DOI:**10.1016/j.heliyon.2020.e03683
23. N. Ivanović, L. Jovanović, Z. Marković, V. Marković, M. D. Joksović, D. Milenković, P. T. Djurdjević, A. Ćirić, L. Joksović, *ChemistrySelect* **2016**, *1*, 3870–3878. **DOI:**10.1002/slct.201600738
24. I. Pibiri, L. Lentini, R. Melfi, M. Tutone, S. Baldassano, P. Ricco Galluzzo, A. Di Leonardo, A. Pace, *Eur. J. Med. Chem.* **2018**, *159*, 126–142. **DOI:**10.1016/j.ejmech.2018.09.057
25. R. Kapoorr, S. N. Singh, S. Tripathi, L. D. S. Yadav, *Synlett* **2015**, *26*, 1201–1206. **DOI:**10.1055/s-0034-1380493
26. H. Rajak, B. Singh Thakur, A. Singh, K. Raghuvanshi, A. K. Sah, R. Veerasamy, P. C. Sharma, R. Singh Pawar, M. D. Kharya, *Bioorg. Med. Chem. Lett.* **2013**, *23*, 864–868. **DOI:**10.1016/j.bmcl.2012.11.051
27. M. Zender, T. Klein, C. Henn, B. Kirsch, C. K. Maurer, D. Kail, C. Ritter, O. Dolezal, A. Steinbach, R. W. Hartmann, *J. Med. Chem.* **2013**, *56*, 6761–6774. **DOI:**10.1021/jm400830r
28. H. Beyzaei, M. Kamali Deljoo, R. Aryan, B. Ghasemi, M. M. Zahedi, M. Moghaddam-Manesh, *Chem. Cent. J.* **2018**, *12*, 114. **DOI:**10.1186/s13065-018-0488-0
29. M. J. Frisch, G. W. Trucks, H. B. Schlegel, G. E. Scuseria, M. A. Robb, J. R. Cheeseman, G. Scalmani, V. Barone, B. Mennucci, G. A. Petersson, H. Nakatsuji, M. Caricato, X. Li, H. P. Hratchian, A. F. Izmaylov, J. Bloino, G. Zheng, J. L. Sonnenberg, M. Hada, M. Ehara, K. Toyota, R. Fukuda, J. Hasegawa, M. Ishida, T. Nakajima, Y. Honda, O. Kitao, H. Nakai, T. Vreven, J. A. Montgomery, J. E. Peralta, F. Ogliaro, M. Bearpark, J. J. Heyd, E. Brothers, K. N. Kudin, V. N. Staroverov, R. Kobayashi, J. Normand, K. Raghavachari, A. Rendell, J. C. Burant, S. S. Iyengar, J. Tomasi, M. Cossi, N. Rega, J. M. Millam, M. Klene, J. E. Knox, J. B. Cross, V. Bakken, C. Adamo, J. Jaramillo, R. Gomperts, R. E. Stratmann, O. Yazyev, A. J. Austin, R. Cammi, C. Pomelli, J. W. Ochterski, R. L. Martin, K. Morokuma, V. G. Zakrzewski, G. A. Voth, P. Salvador, J. J. Dannenberg, S. Dapprich, A. D. Daniels, O. Farkas, J. B. Foresman, J. V. Ortiz, J. Cioslowski, D. J. Fox, Gaussian 09, Revision A 02, Gaussian, Inc., Wallingford CT, USA, **2009**.
30. S. J. A. Pople, *J. Comput. Chem.* **2004**, *25*, fmv–viii. **DOI:**10.1002/jcc.20049
31. M. J. S. Dewar, E. G. Zoebisch, E. F. Healy, J. J. P. Stewart, *J. Am. Chem. Soc.* **1985**, *107*, 3902–3909. **DOI:**10.1021/ja00299a024
32. J. J. P. Stewart, *J. Comput. Chem.* **1989**, *10*, 209–220. **DOI:**10.1002/jcc.540100208
33. J. Contreras-García, E. R. Johnson, S. Keinan, R. Chaudret, J. P. Piquemal, D. N. Beratan, W. Yang, *J. Chem. Theory Comput.* **2011**, *7*, 625–632. **DOI:**10.1021/ct100641a
34. M. Faizi, S. Dabirian, H. Tajali, F. Ahmadi, E. Rezaee Zavareh, S. Shahhosseini, S. A. Tabatabai, *Bioorg. Med. Chem.* **2015**, *23*, 480–487. **DOI:**10.1016/j.bmc.2014.12.016
35. G. D. Fallon, C. L. Francis, K. Johansson, A. J. Liepa, R. C. J. Woodgate, *Aust. J. Chem.* **2005**, *58*, 891-900. **DOI:**10.1071/CH05070
36. A. R. Katritzky, B. V. Rogovoy, V. Y. Vvedensky, K. Kovalenko, P. J. Steel, V. I. Markov, B. Forood, *Synthesis* **2001**, *2001*, 897–903. **DOI:**10.1055/s-2001-13400
37. E. Pastorczak, C. Corminboeuf, *J. Chem. Phys.* **2017**, *146*, 120901. **DOI:**10.1063/1.4978951
38. E. R. Johnson, S. Keinan, P. Mori-Sánchez, J. Contreras-García, A. J. Cohen, W. Yang, *J. Am. Chem. Soc.* **2010**, *132*, 6498-6506. **DOI:**10.1021/ja100936w
39. J. Contreras-García, W. Yang, E. R. Johnson, *J. Phys. Chem. A* **2011**, *115*, 12983–12990. **DOI:**10.1021/jp204278k
40. I. Hamlaoui, R. Bencheraiet, R. Bensegueni, M. Bencharif, *J. Mol. Struct.* **2018**, *1156*, 385–389. **DOI:**10.1016/j.molstruc.2017.11.118

Povzetek

Razvoj sinteznih postopkov za pripravo 1,3,4-oksadiazolskih derivatov je bil vedno v središču pozornosti raziskovalcev, saj tovrstni heterocikli izkazujejo množico uporabnih bioloških aktivnosti. V tej *študiji* smo z reakcijo med različnimi hidrazidi in cianogen bromidom s pomočjo ultrazvočnega valovanja, ob prisotnosti etanola kot topila in kalijevega hidrogenkarbonata kot baze, uspešno sintetizirali serijo 1,3,4-oksadiazol-2-aminov, ki smo jih izolirali z 81–93 % izkoristki. Antioksidativne lastnosti pripravljenih spojin smo določili s pomočjo metode lovljenja DPPH prostih radikalov; to je ena izmed najbolj osnovnih stopenj pri identifikaciji povezanih bioloških učinkov. Izmerjene IC_{50} vrednosti so bile v območju 0.237 to 0.863 mM. Sintetizirani 1,3,4-oksadiazoli lahko služijo kot spojine, ki *ščitijo* pred oksidativnim stresom, in se lahko uporabljajo za zdravljenje raka, kandidiaze, sladkorne bolezni ter nevrodegenerativnih in inflamatornih obolenj. S pomočjo teorije gostotnega polja (DFT) smo izračunali energije disociacije vezi (BDE) in elektronske gostote, ki temeljijo na nekovalentnih interakcijah (NCI). Ugotovili smo, da reverzibilne sile dipol-dipol igrajo ključno vlogo pri večini interakcij.

Except when otherwise noted, articles in this journal are published under the terms and conditions of the Creative Commons Attribution 4.0 International License

DOI: 10.17344/acsi.2020.6212 *Acta Chim. Slov.* **2021,** *68,* 118–127
creative commons

Scientific paper

Antidiabetic Potential of Stem Bark Extract of *Enantia chlorantha* and Lack of Modulation of Its Therapeutic Efficacy in Diabetic Rats Co-Administered with Lisinopril

Latifat Bolanle Ibrahim, Patience Funmilayo Idowu, Opemipo Adekanye Moses, Mutiu Adewunmi Alabi* and Emmanuel Oladipo Ajani

Department of Medical Biochemistry and Pharmacology, Faculty of Pure and Applied Sciences, Kwara State University, Malete, P. M. B. 1530, Ilorin, Nigeria

** Corresponding author: E-mail: mutiu.alabi@kwasu.edu.ng*
Phone: +234-7030428661

Received: 08-18-2020

Abstract

This study validates the antidiabetic efficacy of *Enantia chlorantha* stem bark and the possible therapeutic implications of the co-administration of lisinopril and *E. chlorantha* in type 2 diabetic rats. *E. chlorantha* stem bark was extracted by cold maceration. The inhibitory effect of the plant on carbohydrate metabolizing enzymes and its antioxidative potentials were assessed *in vitro.* The extract exhibited α-amylase and α-glucosidase inhibitory activities and also showed antioxidative properties *in vitro*. Administration of the extract normalized fasting hyperglycemia *in vivo* by showing 47.24% reduction in blood glucose levels relative to untreated diabetic rats. Co-administration of *E. chlorantha* and lisinopril restored serum glucose and serum lipid profile levels. *E. chlorantha* stem bark displayed antidiabetic potentials as compared with a standard antidiabetic drug (metformin). The study also showed that the plant contained some bioactive compounds which we hypothesize might be responsible for the observed activities. Co-administration of the plant with lisinopril conferred no significant therapeutic advantage on the serum glucose level and lipid profile.

Keywords: Antidiabetic; Antioxidants; Co-administration*; Enantia chlorantha*; Hyperglycemia

1. Introduction

Diabetes mellitus is a chronic metabolic disorder that affects the metabolism of carbohydrates, fats and proteins. It is characterized by hyperglycemia which can result from, the pancreas not producing enough insulin or cells of the body not responding properly to the insulin produced. Diabetes mellitus can cause long-term complications such as heart disease, stroke and dysfunction and failure of various organs.[1] The three main types of diabetes are type 1, type 2 and gestational diabetes. Both women and men can develop diabetes at any age. Diabetes is associated with major abnormalities in fatty acid metabolism.[2] The most common lipid pattern in type 2 diabetes consists of hypertriglyceridemia, low High-Density Lipoprotein Cholesterol (HDL-C) and normal plasma levels of Low-Density Lipoprotein Cholesterol (LDL-C).[3,4] Type 2 diabetes is one of the primary threats to human health due to its increased prevalence and associated complications.

Many and diverse therapeutic strategies for the treatment of type 2 diabetes are known. The conventional treatments for diabetes include the reduction of the body's demand for insulin, stimulation of endogenous insulin secretion, enhancement of the action of insulin at the target tissues and the inhibition of degradation of oligo and disaccharides by enzyme inhibitors.[5,6] Currently, metformin is considered the initial medication of choice for hyperglycemia in type 2 diabetes due to its effectiveness. Metformin is a biguanide class of antihyperglycemic drug which acts primarily by enhancing the action of insulin in the liver to reduce the rate of hepatic glucose production, to decrease glucose absorption and to increase target cell

insulin sensitivity.[7] Improvements in insulin action in skeletal muscle also contribute to the therapeutic actions of metformin, mainly resulting in increased non-oxidative glucose disposal.[8] Together, these actions reduce blood glucose in the setting of hyperglycemia, with very little potential for inducing hypoglycaemia.[9] Moreover, the enzymes alpha-glycosidase, is responsible for the breakdown of oligosaccharides, disaccharides and/or polysaccharides to monosaccharides and α-amylase degrades starch to more simple sugars (dextrin, maltotriose, maltose and glucose).[10] The inhibitory action of these enzymes leads to a decrease of blood glucose level, because the monosaccharides are the form of carbohydrates which are absorbed through the mucosal border in the small intestine. However, many of the synthetic hypoglycemic agents have their limitations; are non-specific, produce serious side effects and fail to alleviate diabetic complications. The main side effects of these agents are gastrointestinal i.e. bloating, abdominal discomfort, diarrhea, and flatulence.[11]

There is need to develop effective, safe and cheap drugs for diabetes management because of the side effects associated with the present antidiabetic drugs. Drugs from medicinal plants are effective, safe and cheap for the management of diabetes. Many clinical studies have supported the view that utilization of herbal medicines could be a reliable alternative to manage diabetes effectively with little or no adverse effect.[12,13]

Enantia chlorantha belongs to Annonaceae family. This plant is commonly known as African yellow wood. Among the Yoruba in Nigeria it is known as Awopa.[14] In traditional medicine, this plant has been used for a long time in many parts of the African continent to treat various ailments of the human body. Many of these uses are supported by several studies.[15–18] For example, it was reported that a decoction of 500 g of stem bark in 3 l of water for 20 min may be used to treat malaria symptoms, aches, wounds, boils, vomiting, yellow fever, chills, sore, spleen in children and hepatitis.[15]

Lisinopril is an oral long-acting angiotensin converting enzyme (ACE) inhibitor. ACE inhibitors (ACE-Is) are a family of drugs commonly prescribed to combat hypertension. The primary vasodilatory action of ACE-Is is the blockage of ACE and thus preventing the formation of angiotensin II.[19] With long-term administration, ACEIs lower blood pressure, even in patients with low renin hypertension. This thus suggests that effect of lisinopril may be independent of a decrease in angiotensin II. The appropriate blood pressure control in diabetes trial found that diabetic patients treated with ACE-Is had lower incidence of myocardial infarction (MI) and overall cardiac events. ACE-Is have been used for years to reduce the rate of diabetic nephropathy progression in patients with type 2 diabetes.[19] Thus, this drug may be efficacious in treatment of patients with type 2 diabetes.

Herb-Drug interactions (HDIs) are either pharmacodynamic (PD) or pharmacokinetic (PK) in nature. For the former, this occurs when co-administered substances enhance or negate each other's effects as a result of similar or disparate pharmacological activities, respectively.[20] Such interactions may render the drug less effective or change its activity and producing adverse effect. PK interactions on the other hand arise from the ability of the substance to modulate the absorption, distribution, metabolism and/or excretion (ADME) of the drug.[20]

Despite the fact that *E. chlorantha* is commonly used among the local communities in Nigeria in the management of diabetes, scientific data in support of this local medicinal use in diabetes is lacking in the literatures. Moreover, whereas, the general practice in the management of diabetes in Nigeria is to combine the use of antidiabetic and antihypertensive agents, no study has reported on the therapeutic implications of combining *E. chlorantha* with any hypertensive agent. In view of the foregoing, the present study investigates the anti-diabetic properties of *E. chlorantha* stem bark extract and the thermodynamic implications of its co-administration with lisinopril. In addition, the study investigated the phytochemical constituents of the plant to identify the bioactive components that may be responsible for the pharmacological antidiabetic properties and the possible mechanism for its pharmacological action.

2. Materials and Methods

2. 1. Materials

Streptozocin was a product of Sigma-Aldrich, USA. Metformin (Glucophage 500 mg) was manufactured by Merck Santé, France and Lisiofil (Lisinopril 5 mg) was manufactured by Fourrts India Laboratories Pvt Ltd., India. All the reagent kits used for bioassay were sourced from Randox Laboratories Ltd., Crumlin, UK. All other chemicals were of analytical grade.

2. 2. Methods

2. 2. 1. Plant Collection, Identification and Crude Extract Preparation

The stem bark of *E. chlorantha* was collected in June 2018. The plant sample was identified and authenticated and a voucher number UIH/001/1356 was assigned. Thereafter, a sample specimen was deposited at the herbarium of the University of Ilorin, Ilorin, Nigeria. The stem bark was cleaned to remove adhering dirt, air-dried for two weeks and ground into powder using an electric blender. Extraction was carried out by cold maceration of 800 g of the coarse powder with 5 L of 70% ethanol for 72 h, with constant shaking. The resultant mixture was filtered using Whatman filter paper (No.1) and the filtrate was concentrated using a rotary evaporator at 40 °C. The extract was weighed, and the final yield was 12.5%. The dried extract was finally reconstituted in distilled water for use in the study.

2. 2. 2. Qualitative and Quantitative Phytochemical Screening

Qualitative phytochemical analysis of the extract was carried out using the method previously described[21] to identify phytochemicals while quantitative phytochemical screening was carried out using different method previously described, for saponins,[22] tannins,[23] alkaloids[24] and flavonoids.[25]

2. 3. Antioxidant Assay

2. 3. 1. 1,1-Diphenyl-2-picryl-hydrazyl Radical Inhibition

The method previously described[26] was used to evaluate the 1,1-diphenyl-2-picryl-hydrazyl (DPPH) radical scavenging potential of the extract. One (1) ml of different concentrations (0.2–1.0 mg/ml) of the extract or vitamin C (reference) were added to 1 ml of 0.2 mM methanolic solution of DPPH. Similarly, sterile distilled water (1 ml) was mixed with an aliquot (1 ml) of 0.2 mM methanolic DPPH and used as control. Following incubation (30 min, 25 °C) in each case, the absorbance was read against blank at 516 nm using a spectrophotometer (Beckman, DU 7400, USA). The inhibitory effect (I%) of EOAE on DPPH radical was estimated as follow:

$$\text{Inhibitory effect (I\%)} = \frac{\text{A control} - \text{A test}}{\text{A control}} \times 100 \quad (1)$$

where A control is the absorbance of the control and A test is the absorbance of the test sample. Thereafter, the concentration of the extract eliciting 50% inhibitory (IC_{50}) effect on the DPPH radical was calculated from a standard curve.

2. 3. 2. Hydrogen Peroxide Inhibition

This was estimated using the adapted method previously described.[27] Briefly 0.6 ml of 40 mM H_2O_2 was mixed with 3.4 ml of phosphate-buffered (pH 7.4) solution (0.2–1.0 mg/ml) concentrations of either the extract or vitamin C and incubated at 25 °C for 10 min. Sterile distilled water replaced the extract for the control sample. The absorbance was read spectrophotometrically at 230 nm. The H_2O_2 inhibitory potential of the extract was calculated as follow:

$$\%\ H_2O_2\ \text{scavenged} = \frac{\text{A test} - \text{A sample}}{\text{A control}} \times 100 \quad (2)$$

Where, A control is the absorbance of the control; A test and A sample represent the absorbance of the mixture with the extract and that of the extract alone, respectively. The IC_{50} value was estimated from the standard curve.

2. 3. 3. Hydroxyl Radical ($OH^{\cdot}$) Inhibition

The $OH^{\cdot}$ inhibitory effect of the extract was determined as previously described.[28] In brief, 2 ml at 0.2–1.0 mg/ml of the extract or vitamin C (reference) were mixed with 0.6 ml of ferrous sulfate (8 mM), 0.5 ml of H_2O_2 (20 mM), and 2 ml of salicylic acid (3 mM). After 30 min of incubation (37 °C), distilled water (0.9 ml) was added and the resulting mixture centrifuged (Beckman and Hirsch, Burlington, IO, USA) at 4472 g for 10 min. For the control, sterile distilled water was used. The absorbance was read at 510 nm, and the IC_{50} value was calculated subsequent to determination of inhibitory capacity of the extract against $OH^{\cdot}$ using the expression:

$$\%\ \text{hydroxyl radical scavenged} = \\ = \frac{\text{A test} - \text{A sample}}{\text{A control}} \times 100 \quad (3)$$

Where, A control, A test, and A sample represent the absorbance of the control, mixture with the extract, and that of the extract alone, respectively.

2. 3. 4. Reducing Power Activity

The reducing power of extract was determined by previously described method.[29] One (1) ml of extracts or gallic acid (reference) was mixed with 2.5 ml of phosphate buffer (200 mM, pH 6.6) and 2.5 ml of 1% potassium ferricyanide. The mixtures were incubated for 20 min at 50 °C. After incubation, 2.5 ml of 10% trichloroacetic acid were added to the mixtures, followed by centrifugation at 4000 rpm for 10 min. The upper layer (5 ml) was mixed with 5 ml of distilled water and 1 ml of 0.1% ferric chloride and the absorbance of the resultant solution were measured at 700 nm.

2. 4. *In vitro* Carbohydrate-Metabolizing Enzymes' Inhibitory Assay

2. 4. 1. Alpha-Amylase Inhibition Assay

The alpha amylase inhibitory assay was performed as previously described method.[30] Briefly, concentrations (50-200 mg/ml) of the extract or acarbose (standard) were prepared and 50 µl of the extract or acarbose was added to 500 µl of 20 mM sodium phosphate buffer (pH, 6.9, with 6 mM NaCl) containing porcine pancreatic alpha-amylase (0.5 mg/ml) and incubated at 25 °C for 10 min. One unit of the enzyme will liberate 1.0 mg of maltose from starch in 3 min. Then, 500 µl of 1% starch solution in 20 mM sodium phosphate buffer (pH 6.9, with 6 mM NaCl) was added to each tube. The reaction mixture was incubated at 25 °C for 10 min and stopped with 1.0 ml of 3,5-dinitrosalicylic acid colour reagent. Thereafter, the mixture was incubated in a boiling water bath for 5 min and cooled to room temperature. The reaction mixture was then diluted by adding 10 ml of distilled water, and absorbance was measured at 540 nm. The control experiment was performed without the test sample, and the α-amylase inhibi-

tory activity was expressed as percentage inhibition using the following equation:

$$\% \text{ Inhibition} = \frac{\Delta A_{control} - \Delta A_{extract}}{\Delta A_{control}} \times 100 \quad (4)$$

Where $\Delta A_{extract}$ and $\Delta A_{control}$ are the respective changes in absorbance of the extract sample and control. The IC_{50} of the extract against α-amylase activity was thereafter calculated from a standard calibration plot.

2. 4. 2. Alpha-Glucosidase Inhibition Assay

The assay was performed as previously described.[31] Briefly, known concentrations (50–200 mg/ml) of the extract or acarbose (standard) were prepared and 50 µl of the extract or acarbose was added to 100 µl of alpha-glucosidase solution (1.0 U/ml) in 0.1 M phosphate buffer (pH, 6.9) and incubated at 25 ºC for 10 min. One unit of the enzyme will liberate 1.0 µmol of D-glucose from p-nitrophenyl-α-D-glucoside per min. Then, 50 µl of 5 mM p-nitrophenyl-α-D-glucopyranoside solution in 0.1M phosphate buffer (pH 6.9) was added. The mixture was incubated at 25 °C for 5 min, and the absorbance was measured at 405 nm. The control experiment was performed without the test sample, and the α-glucosidase inhibitory activity was expressed as percentage inhibition using the following equation:

$$\% \text{ Inhibition} = \frac{\Delta A_{control} - \Delta A_{extract}}{\Delta A_{control}} \times 100 \quad (5)$$

Where $\Delta A_{extract}$ and $\Delta A_{control}$ are the respective changes in absorbance of the extract sample and control. The IC_{50} of the extract against α- glucosidase activity was thereafter calculated from a standard calibration plot.

2. 5. Experimental Protocols

2. 5. 1. Experimental Animals

The experiment was carried out on healthy forty-nine (49) male Wistar rats of about 10–12 weeks old and weighing an average of 169 ± 6 g. The rats were housed in metallic cages at the animal house. The rats were acclimatized for fourteen days and fed with commercial diets and water *ad libitum*. They were all maintained at 25 ± 2 °C light and dark cycle of 12/12 hr, respectively.

2. 5. 2. Induction of Diabetes

Type 2 diabetes was induced by the previously described method.[32] The rats were first fed 15% fructose solution (w/v) for four weeks, after which they were fasted overnight and thereafter administered streptozotocin (40 mg/kg i.p.) freshly prepared in 0.1 M sodium citrate buffer. The diabetic state was confirmed 72 h after streptozotocin injection. Specifically, rats having fasting blood glucose levels greater than 200 mg/dl were considered diabetic.

2. 5. 3. Animal Grouping/Administration

Forty-two (42) diabetic male Wistar rats were divided into six (6) groups consisting of seven (7) rats each: Diabetic groups consisted of DC - Diabetic Control group; treatment groups (T1 - *E. chlorantha* (200 mg/kg b.w.), T2 - Metformin (7.14 mg/kg b.w.), T3 - *E. chlorantha* + lisinopril (200 mg/kg b.w. and 0.14 mg/kg b.w. respectively), T4 - Metformin + lisinopril (7.14 mg/kg b.w. and 0.14 mg/kg b.w. respectively) and T5 – lisinopril (0.14 mg/kg b.w.)) and another seven (7) non-diabetic male rats acted as the Normal control group. All administrations were carried out orally as a single dose daily for four weeks using a gavage needle. The rats were housed in cages in the Department Animal Facility Center maintained at 25 ± 2 °C light and dark cycles of 12/12 hr. The chosen dose of the extract and the route of administration were informed by both the results of our ethnobotanical survey on the use of the plant in the management of diabetic and the reported minimum effective (ME) and maximum safe (MS) dose of the plant.[33,34] The rats were maintained in accordance with the principles of laboratory animal care guidelines.[35] The weight of the rats was determined every week throughout the experiment period. The experiment was designed according to the Department Animal Ethics Committee guidelines and approval certificate (KSUMB/005/01/013) was given.

2. 5. 4. Monitoring of Blood Glucose Level during Treatment

All blood samples for monitoring of blood glucose level *in situ* were taken from the tail vein of the rats using 24 gauge needles at intervals of 0, 5, 10, and 15 days. Blood glucose levels were determined by the glucose oxidase method using reactive strips and a single touch glucometer (Accu-Chek Active, Roche Diagnostics, Mannheim, Germany). Results were recorded in mg/dl. Percentage reduction in fasting blood glucose was calculated as:

$$\% \text{ Reduction of FBS} = \frac{\text{Initial value} - \text{Final value}}{\text{Initial value}} \times 100 \quad (6)$$

2. 6. Biochemical Assay

Twenty-four hours after the last treatment, under mild diethylether anesthesia, the animals were sacrificed, and blood was obtained via jugular puncture and serum was obtained by centrifugation. Isolated serum was analyzed for total cholesterol, HDL- cholesterol (HDL-C), LDL-cholesterol (LDL-C) and total glycerides (TG) colorimetrically using Randox diagnostic kits.

2. 7. Data Analysis

All data were presented as mean ± standard error of mean (S.E.M) of seven replicates. One-way analysis of variance (ANOVA) using SPSS software package for windows (Version 16) for differences between means was used to detect differences between the treatment groups ($\alpha < 0.05$) followed by the Tukey post hoc test using R statistical software.

3. Results and Discussion

3. 1. Screening and Detection of Phytoconstituents

E. chlorantha stem bark gave positive results for some major constituents; alkaloids, saponins, flavonoids, coumarins, anthocyanins and phenolics (Table 1). Terpenes, terpenoids, steroids and glycosides were not detected. The Table also showed that flavonoid concentration was the highest (114.92 ± 0.36 mg/kg) while saponin concentration was the lowest (40.50 ± 0.71 mg/kg).

3. 2. Antioxidant Assay

Presented in Table 2 and Table 3 are the results of the *in vitro* antioxidant assay of the stem bark extract of *E. chlorantha*. The extract showed a significant inhibition of DPPH radical with an IC_{50} of 62 mg/ml. The extract also showed a strong scavenging capacity of H_2O_2 and $OH^{\cdot}$. In addition, the extract demonstrated Ferric Reducing Antioxidant Power (FRAP).

Table 2. % DPPH (2,2-diphenyl-1-picrylhydrazyl) inhibition of *E. chlorantha* extract

Concentration (mg/ml)	*E. Chlorantha* (%)	Vitamin C (%)
20	31.781 ± 0.085[a]	35.474 ± 0.969[a]
40	61.791 ± 0.040[a]	67.540 ± 0.085[a]
60	62.025 ± 0.064[a]	70.590 ± 0.180[a]
80	69.990 ± 0.000[a]	80.720 ± 0.270[b]
100	79.850 ± 0.085[a]	90.590 ± 0.200[b]

Data are presented as mean ± SEM of 3 replicates. Value on the same row with similar superscripts are not significantly (P>0.05) different from each other.

3. 3. Effect of Treatment with *E. chlorantha* on Blood Glucose and Total Body Weight

Figure 1 is the result of the effect of treatment on the body weight changes. There was no significant difference in the body weight of all the rats between the groups before treatment. Body weights of rats in diabetic control group were observed to be lower than those in other groups after the treatment period.

Table 1. Qualitative and quantitative phytochemical screening of *E. chlorantha*

Phytochemical group	Reagent used	Observations	Result	Concentrations (mg/kg)
Alkaloids	Wagner's reagent	A reddish-brown precipitate	+	82.12 ± 0.02
Triterpenes	Acetic anhydride	No blue green colour	–	ND
Glycosides	Fehling's solution	No brick red precipitate	–	ND
Saponins	Frothing test	Frothing precipitate	+	40.50 ± 0.71
Tannins	KOH	No dirty white precipitate	–	ND
Phlobatannin	HCl	Absence of red precipitate	–	ND
Steroids	Salakowsti test	No red colouration	–	ND
Flavonoids	Ferric chloride	Yellow colour after HCl	+	114.92±0.36
Coumarin			+	ND
Anthocyanins			+	ND
Terpenoids	Liberman Burchard	No reddish-brown boundary	–	ND
Phenolics	$FeCl_3$	A greenish precipitate	+	ND

+ = detected, - = not detected; ND = not determined

Table 3. Percentage OH^-, H_2O_2 and FRAP Scavenging Activity of *E. chlorantha* Extract

Agent	$OH^{\cdot}$ (%)	H_2O_2 (%)	FRAP (%)
E. chlorantha	102.650 ± 0.939[a]	42.347 ± 3.002[a]	148.240 ± 6.912[a]
Reference	118.727 ± 0.000[a]	67.364 ± 0.000[b]	168.273 ± 0.000[a]

Data are presented as mean ± SEM of 3 replicates. Value on the same row with similar superscripts are not significantly (P > 0.05) different from each other.

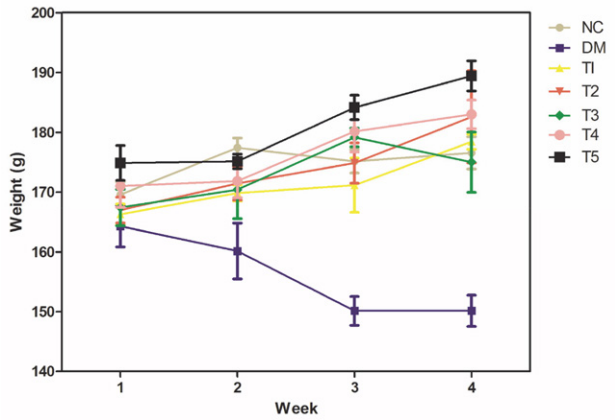


Fig. 1. Effect of treatment on Total Body Weight of Rats. NC – normal control group, DM – diabetic control group, T1 – *E. chlorantha* treated group, T2 - Metformin treated group, T3 - *E. chlorantha* + lisinopril treated group, T4 - Metformin + lisinopril treated group and T5 – Lisinopril treated group.

Table 4 presents the result of the fasting blood glucose level. Fructose -STZ administration exhibited a significant increase in fasting blood glucose (235.80 ± 18.94 mg/dl) as compared to the normal control group (95.12 ± 0.45 mg/dl). Before the commencement of treatment (Day 0), the blood glucose levels of all the treatment groups were not different from that of the diabetic non treated group. On day 5, the fasting blood glucose of the *E. chlorantha* treated rat (183.6 ± 9.31 mg/dl) was observed to be significantly lower than that of the diabetic untreated group (299.20 ± 6.46 mg/dl). Similar results were obtained in the rats co -treated with *E. chlorantha* and lisinopril and the group treated with lisinopril only. At day 15, the blood glucose levels of all the treatment groups were observed not to be significantly different from each other but were significantly lower than that of the diabetic untreated group. They were also observed to be significantly higher than that of the normal control group (96.53 ± 0.73 mg/dl).

The results also showed that the highest percentage reduction in blood glucose after 15th day of treatment relative to day 0 was observed in the group co-treated with metformin and lisinopril (60.64%). This was followed by the group co-treated with the *E. chlorantha* and lisinopril (52.70%). The percentage glucose reduction of the group treated with *E. chlorantha* alone was 47.24. There was no reduction in the glucose level of the normal and diabetic control groups.

Table 5 shows the inhibitory potential of *E. chlorantha* extract on the specific activities of α-amylase and alpha-glycosidase. The result revealed a dose-related inhibitory effect. The alpha-amylase IC_{50} values for *E. chlorantha* extract and acarbose were 90 and 65 mg/ml, respectively. The Table also showed an alpha-glucosidase IC_{50} of 145 and 125 mg/ml for the extract and acarbose respectively

Table 4. Effect of treatments on fasting blood glucose levels

Group	Treatment	Fasting Blood glucose level (mg/dl) Day 0	Day 5	Day10	Day 15	Total % reduction
Control	Distilled water	95.12 ± 0.45^a	95.56 ± 0.56^a	95.08 ± 0.62^a	96.53 ± 0.73^a	–
Diabetic control	STZ-fructose + distilled water	294.00 ± 2.31^b	299.20 ± 6.46^b	300.80 ± 6.67^b	301.60 ± 6.93^b	–
T1	Extract	235.80 ± 18.94^b	183.6 ± 9.31^c	135.80 ± 5.60^c	124.40 ± 2.35^c	47.24%
T2	Metformin	305.40 ± 21.55^b	287.60 ± 2.54^b	207.00 ± 8.25^d	152.80 ± 5.83^c	50.09%
T3	Extract + Lisinopril	272.80 ± 11.56^b	200.60 ± 3.26^c	151.40 ± 6.12^c	129.60 ± 2.08^c	52.70%
T4	Metformin + lisinopril	271.80 ± 18.33^b	268.60 ± 9.60^b	182.60 ± 6.14^d	146.80 ± 8.09^c	60.64%
T5	Lisinopril only	248.33 ± 14.52^b	199.83 ± 9.06^c	171.00 ± 4.80^d	151.00 ± 7.55^c	39.10%

Data are presented as mean ± SEM of 7 determinations. Values in the same column with the same superscripts are not significantly ($P > 0.05$) different from each other.

Table 5. Inhibitory potential of *E. chlorantha* ethanolic extract on the activity of α amylase and α glucosidase (n = 3, mean ± SD).

Concentrations (mg/ml)	% Inhibition α- Amylase		α- Glucosidase	
	Acarbose	*E. chlorantha*	Acarbose	*E. chlorantha*
50	32.87 ± **3.00**	44.52 ± 5.41	20.72 ± 0.18	18.67 ± 0.06
100	54.11 ± **4.01**	60.89 ± 0.24	31.32 ± 0.25	34.96 ± 1.01
150	62.35 ± **2.91**	74.22 ± 2.13*	54.70 ± 4.13	64.96 ± 3.09
200	67.21 ± **0.79**	84.44 ± 2.14*	73.42 ± 0.13	87.93 ± 2.04*
IC_{50}	65.00	90.00*	125.00	145.00*

Data are presented as mean ± SEM of 3 replicates. *indicates that value differ significantly ($P < 0.05$) from the respective reference (acarbose).

3. 4. Effect of Treatment on Serum Lipid Profile

The effect of treatments on serum lipid profile (Table 6) showed a significant increase in serum total cholesterol, total glycerides and LDL-C level and a decrease in the serum HDL-C level in the diabetic group when compared with the control group. Treatment with the extract restored the serum lipid levels. The serum levels of the lipids obtained in the rats treated with the extract alone were not significantly different from those of the diabetic rats treated with metformin but were different from diabetic rats treated with the metformin and lisinopril and the rats co-treated with the extract and lisinopril. The Table also showed that the concentration obtained in the diabetic rats treated with lisinopril alone was different from that of the control group and that of the diabetic control group.

3. 5. Discussion

The currently available drugs for management of diabetes mellitus have certain drawbacks and therefore, there is a need to find safer and more effective antidiabetic drugs. Result from this study indicates that *E. chlorantha* stem bark extract is efficacious as an antidiabetic agent in rats and that the efficacy of the extract was not significantly altered when *E. chlorantha* was co-administered with lisinopril suggesting that combined administration of the plant with lisinopril does not increase its therapeutic indications.

Medicinal plants received much attention due to presence of important bioactive secondary metabolites such as phenolics.[36] Result of our phytochemical screening showed that *E. chlorantha* stem bark consist of a large proportion of phytochemicals which may play a role as antidiabetic. We reported in this study, that the bioactive compounds contained in the stem bark of the plant belong to the group of alkaloids, saponins, flavonoids, coumarins, anthocyanin and phenolics. The flavonoids were detected to be of highest concentration. Similar studies have also reported the presence of saponins, flavonoids, alkaloids and phenols in aqueous extract of *E. chlorantha*.[37] However, it was reported that alkaloids had the highest content (46.26%).[37] These phytochemicals could act in a number of potential mechanisms to show their antidiabetic activities. Some of the potential mechanisms include increase in insulin secretion and action, decreases in hepatic glucose output, regulation of certain enzymes involved in carbohydrate metabolism i.e. α-amylase and α-glucosidase, modulation of certain regulation molecules such as PPARγ (Peroxisome Proliferator Activated Receptor-γ), hypolipidemic activities, antioxidant effects, enhancement of the expression of glucose transporters etc.[38,39,40]

Both flavonoids and alkaloids had been widely implicated in antidiabetic properties of plants. It was noted that some alkaloids e.g. nuciferine promotes glucose stimulated insulin secretion in rats' pancreatic islets, probably via a pathway involving hepatic nuclear factor 4α or by closing potassium-adenosine triphosphate channels.[41] Some alkaloids (i.e. mescaline, pyrrole, pyridine, tropane, aporphine, and quercetin) have been reported to have antioxidant and antimicrobial properties.[42,43] Studies on the antidiabetic potential of flavonoids from plants showed that flavonoids regenerate pancreatic islets and increase insulin secretion in streptozotocin (STZ)-induced diabetic rats.[44] It also stimulates insulin release and enhance glucose uptake from isolated islet cells.[45]

Streptozotocin (STZ)-fructose type 2 diabetes model shares a number of features with human type 2 diabetes mellitus (TDM2) both histologically and metabolically and is characterized by moderate stable hyperglycemia.[46,47] This is why in this study, STZ-fructose induced diabetes model was used. Streptozotocin injection caused β cells degeneration in rats, resulting in decrease in the release of insulin by the pancreas. Furthermore, high fructose ingestion causes insulin resistance (IR). This contributes negatively to blood glucose homeostasis thereby inducing hyperinsulinemia which predispose to type 2 diabetes. Result of fasting blood glucose of ≥ 200 mg/dl obtained in this study following STZ-fructose administration confirms induction of type 2 diabetes. This is similar to report from previous findings.[48,49,50]

Our study also showed that changes in body weight of fructose-streptozotocin-induced diabetes is associated with characteristic loss of body weight. This we hypothesized may due to increased muscle wasting and possibly

Table 6. Effect of treatments on serum lipid profiles

Group	Treatment	LDL-C (mg/dl)	HDL-C(mg/dl)	TG (mg/dl)	TC (mg/dl)
Control	Distilled water	1.26 ± 0.02^{a}	1.26 ± 0.82^{b}	0.78 ± 0.82^{a}	0.87 ± 0.97^{a}
Model	STZ-fructose + distilled water	6.09 ± 0.95^{c}	0.56 ± 0.07^{a}	1.50 ± 0.47^{b}	1.66 ± 0.48^{b}
T1	Extract	2.08 ± 0.41^{ab}	0.97 ± 0.40^{b}	0.89 ± 0.50^{a}	0.98 ± 0.09^{a}
T2	Metformin	2.83 ± 0.06^{ab}	1.10 ± 0.63^{b}	0.93 ± 0.29^{a}	1.06 ± 0.79^{a}
T3	Extract + Lisinopril	1.73 ± 1.00^{ab}	1.07 ± 0.55^{b}	0.77 ± 0.93^{a}	0.85 ± 0.16^{a}
T4	Metformin + lisinopril	2.36 ± 0.71^{ab}	1.18 ± 0.70^{b}	0.81 ± 0.03^{a}	0.96 ± 0.30^{a}
T5	Lisinopril only	3.08 ± 0.56^{b}	0.97 ± 0.17^{b}	1.07 ± 0.20^{a}	1.08 ± 0.91^{a}

Data are presented as mean ± SEM of 7 determinations. Values in the same column with the same superscripts are not significantly different ($p > 0.05$) from each other.

loss of tissue proteins which is similar to the previous observations.[50,51] As expected in the diabetic control group, the body weight of rats was progressively reduced whereas, in all the *E. chlorantha* treated rats and those co-administered with lisinopril there was a progressive improvement in the body weight. This indicates that treatment prevented muscle tissue damage associated with hyperglycemic condition.

In the management of diabetes mellitus, alpha-glucosidase and alpha-amylase enzymes represent the most crucial of the pharmacological targets.[52,53] These enzymes facilitate hydrolysis of starch to glucose with consequential increase in the systemic concentration of glucose. Hence, the inhibition of these enzymes activities delays glucose absorption and moderates postprandial blood sugar level.[53] In this study, the *in vitro* alpha-amylase inhibitory activities of the ethanol extract of *E. chlorantha* were investigated. The extract (50–200 mg/ml) exhibited potent α-amylase inhibitory activity in a dose dependent manner. This was similar to what was obtained with acarbose. The IC_{50} obtained with acarbose was lower than that of *E. chlorantha* extract. Furthermore, the alpha-glycosidase inhibitory assay of the ethanolic extract of *E. chlorantha* stem bark revealed a significant inhibitory action of alpha-glucosidase enzyme. The percentage inhibition at 50-200 mg/ml concentrations of *E. chlorantha* extract also showed a dose dependent increase with an IC_{50} of 145 mg/ml. Similarly, acarbose showed alpha-glucosidase inhibitory activity with an IC_{50} value of 125 mg/ml. The result indicates that the ethanolic extract of *E. chlorantha* is a potent alpha-amylase and alpha-glucosidase inhibitor similar to acarbose. Previous reports had noted that alpha-amylase and alpha-glucosidase are the main pharmacological targets in the management of diabetes.[52] These enzymes facilitate hydrolysis of starch to glucose with consequential increase in the systemic concentration of glucose in diabetes. This increased hyperglycemia may constitute a significant risk factor for diabetic complications. Our study suggests that *E. chlorantha* stem bark may be used as starch blockers indicating that the plant may prevent or slow the absorption of starch in to the body mainly by blocking the hydrolysis of 1,4-glycosidic linkages of starch and other oligosaccharides into maltose, maltriose and other simple sugars. Administration of *E. chlorantha* stem bark extract to diabetic rats caused significant reduction of blood glucose level compared to the control and diabetic untreated group.

Many previous studies have provided evidence that oxidative stress resulting from increased reactive oxygen species (ROS) is a key factor in the pathogenesis of diabetes.[53,54] Our study showed that *E. chlorantha* elicited marked antioxidant potentials suggesting that the plant has the capacity to regulate or stall free radicals chain reactions associated with diabetes complications, which is in agreement with previous report.[53] Natural products are the major source of antioxidants which delay the development of diabetes.[40]

The role of dyslipidemia in the development of diabetes macrovascular complications has been reported.[1,4] In this study, the STZ-fructose model of type 2 diabetes exhibited abnormalities in lipid metabolism as evidenced by the significant elevation of serum TC, TG, LDL-C and reduction of HDL-C levels. A previous study reported that treatment with metformin significantly reduced the TC, TG, LDL-C level and increased HDL-C levels in diabetic rats.[55] The extract was shown to improve the condition of diabetic mellitus as indicated by the lipid profile monitored in the study, thus showing its good antidiabetic activity in STZ-fructose-induced hyperglycemic rats. Lisinopril, an angiotensin converting enzyme inhibitor (ACE-I) acts by preventing the formation of Ang II, which has also been implicated in insulin resistance by inhibiting insulin receptor dependent PI3K signaling.[56] Therefore, the blockade of this substance is important in affecting insulin sensitivity. The co-administration of lisinopril and the extract did not show any difference from that achieved with the extract alone. Serum total cholesterol, LDL cholesterol and triglycerides decreased in all the treated groups when compared with the model group. No significant difference was however observed in all these parameters when compared among the treatment groups. Serum HDL cholesterol was also observed to increase in all treatment groups compared with the model group, but no difference was observed when compared among the treatment groups. In previous study, inhibitors of the renin angiotensin system, such as angiotensin converting enzyme (ACE) inhibitors was reported to ameliorate the lipid abnormalities to a substantial extent.[57]

4. Conclusion

The use of *E. chlorantha* in the management of diabetes is a common practice among some local communities in Nigeria. Data obtained from this study indicates that *E. chlorantha* is efficacious as antidiabetic agent and that combined administration of *E. chlorantha* and lisinopril does not in any way influence the efficacy of *E. chlorantha* stem bark as an antidiabetic agent. The study identified phytoconstituents belonging to the phenolics, flavonoids, saponins and alkaloids as some of the bioactive compounds which may be responsible for this pharmacological property. Study has just been concluded in our laboratory to evaluate the toxicological implication of the combined administration of these agents.[58]

Abbreviations

HDL-C: High-Density Lipoprotein Cholesterol
LDL-C: Low-Density Lipoprotein Cholesterol
ACE: Angiotensin converting enzyme
HDI: Herb-Drug interactions
DPPH: 1,1-diphenyl-2-picryl-hydrazyl

TDM2: Human type 2 diabetes mellitus
ROS: Reactive Oxygen Species
PPARγ : Peroxisome Proliferator Activated Receptor-γ

5. References

1. G. Keerthana, M. K. Kalaivani, A. Sumathy, *Asian J. Pharm. Clin. Res*., **2013**, *6*, 32–36.
2. G. H. Tomkin, *Diabetes Care*, **2008**, *31*, S241–S248. **DOI:**10.2337/dc08-s260
3. B. A. Salau, O. Osilesi, G. O. Idowu, S. Musa, E. O. Ajani, *Afr. J. Med. Pharm. Sci.*, **2003**, *7*, 6–11.
4. L. A. Leiter, J. Genest, S. B. Harris, G. Lewis, *Can. J. Diabetes*., **2006**, *30*, 230–240. **DOI:**10.2337/diacare.21.1.160
5. J. Thrasher, *Am. J. Med.*, **2017**, *130*, S4–S17. **DOI:**10.1016/j.amjmed.2017.04.004
6. A. Rawshani, A. Rawshani, S. Franzen, N. Sattar, B. Eliasson, A. M. Svensson, B. Zethelius, M. Miftaraj, D. K. McGuire, A. Rosengren, S. Gudbjornsdottir, *N. Engl. J. Med.*, **2018**, *379*, 633–644. **DOI:**10.1056/NEJMoa1800256
7. American Diabetes Association, *Diabetes Care*, **2018**, 41, S13–S27. **DOI:**10.2337/dc18-S002
8. M. J. Davies, D. A. D'Alessio, J. Fradkin, W. N. Kernan, C. Mathieu, G. Mingrone, P. Rossing, A. Tsapas, D. J. Wexler, J. B. Buse, *Diabetes Care*, **2018**, *41*, 2669–2701. **DOI:**10.2337/dci18-0033
9. American Diabetes Association, *Diabetes Care*, **2019**, *42*: S90–S102. **DOI:**10.2337/dc19-S009
10. V. Nivetha, V. Subramaniyan, G. Manikandan, M. Divya Bharathi, T. Krishna Prasanth, K. Manjula, *J. Pharmacogn. Phytochem.*, **2019**, *8*, 1060–1064.
11. M.S. Hashim, V. Lincy, V. Remya, M. Teena, L. Anila, *Food Chem*., **2005**, *92*, 653–660. **DOI:**10.1016/j.foodchem.2004.08.027
12. A. B. Medagama, R. Bandara, *Nutr. J.*, **2014**, *13***,** 102. **DOI:**10.1186/1475-2891-13-102
13. H. Choudhury, M. Pandey, C. K. Hua, C. S. Mun, J. K. Jing, L. Kong, L. Y. Ern, N. A. Ashraf, S. W. Kit, T. S. Yee, M. R. Pichika. *J. Tradit. Complement. Med*., **2018**, *8*, 361–376. **DOI:**10.1016/j.jtcme.2017.08.012
14. A. A. Adesokan, M. T. Yakubu, B. V. Owoyele, M. A. Akanji, A. O. Soladoye, O. K. Lawal, *Afr. J. Biochem. Res*., **2008**, *2*, 65–169. **DOI:**10.5897/AJBR2008.
15. N. Tsabang, P. V. Fokou, L. R. Tchokouaha, B. Noguem, I. Bakarnga-Via, M. S. Nguepi, B.A. Nkongmeneck, F. F. Boyom, *J. Ethnopharmacol*., **2012**, 139, 171–180. **DOI:**10.1016/j.jep.2011.10.035
16. O. E. Adebiyi, M. O. Abatan, *Interdiscip Toxicol*., **2013**, *6*, 145–151. **DOI:**10.2478/intox-2013-0023
17. M. N Djimeli, J. M. N. Mendimi, S. P. C. Fodouop, C. Fokunang, S. S. Atsafack, O. Dogmo, M. Guewo-Fokeng, D. Gatsing, *Am. J. Pharmacol. Ther*., **2017**, *1*, 020–027.
18. R. M. E. Etame, R. S. Mouokeu, F. S. M. Poundeu, I. K. Voukeng, C. L. P. Cidjeu, A. T. Tiabou, A. J. G. Yaya, R. A. N. Ngane, J. R. Kuiate, F. X. Etoa, *BMC Complement Altern Med*., **2019**, *19*, 56. **DOI:**10.1186/s12906-019-2459-y
19. J. Coyle, S. Gardner, C. M. White, *Ann. Pharmacother*. **2004**, *38*, 1731–1738. **DOI:**10.1345/aph.1E182
20. M. de Lima, S. Toccafondo, S. M. Vieira, *Planta Medica*, **2004**, *78*, 1400–1415. **DOI:**10.1055/s-0032-1315145
21. O. O. Odebiyi, E. A. Sofowora, *IIoydia*, **1978**, *41*, 234–246.
22. J. H. Brunner, *Anal. Chem*., **1984**, *34*, 1314–1326. **DOI:**10.1007/BF02844409
23. T. Swain, Herbivores: Their Interaction with Secondary Plant Metabolites, Academic Press, London, **1979**, pp. 657–682.
24. M. Plummer, D. T. Plummer, in Introduction to Practical Biochemistry, Tata McGraw Hill Publishing Company Limited, India, 2001.
25. B. I. Faridha, R. Mohankumar, M. Jeevan, K. Ramani, *Indian J. Microbiol*., **2016**, *56*, 426–432. **DOI:**10.1007/s12088-016-0609-1
26. A. Turkoglu, M. E. Duru, N. Mercan, I. Kivrak, K. Gezer, *Food Chem*., **2007**, *101*, 267–273. **DOI:**10.1016/j.foodchem.2006.01.025
27. R. J. Ruch, S. J. Cheng, J. E. Klaunig, *Carcinogenesis*, **1989**, 10, 1003. **DOI:**10.1093/carcin/10.6.1003
28. N. Smirnoff, Q. J. Cumbes, *Phytochem*., **1989**, *28*, 1057–1060. **DOI:**10.1016/0031-9422(89)80182-7
29. C. C. Yen, P. D. Duh, *J. Am. Oil Chem. Soc*., **1993**, *70*, 383–386. **DOI:**10.1007/BF02552711
30. G. Oboh, A. J. Akinyemi, A. O. Ademiluyi, A.S. Adefegha, *J. Food Nutr. Res*., **2010**, *49*, 14–20.
31. E. Apostolidis, Y. I. Kwon, K. Shetty, *Innov. Food Sci. Emerg. Technol.*, **2007**, *8*, 46–54. **DOI:**10.1016/j.ifset.2006.06.001
32. R. D. Wilson, M. S. Islam, *Pharmacol. Rep.*, **2012**, 64, 129–139. **DOI:**10.1016/S1734-1140(12)70739-9
33. T. M. M. Kuissu, E. G. Enow-Orock, C. Mezui, Z. E. Nkwengoua, V.P. Tan, B. Nyasse, *Br. J. Pharm. Res*., **2015**, *8*, 1–13. DOI :10.9734/BJPR/2015/19035.
34. T. T. Olivier, N. T. Francis, J. S. Armel, *Edorium J. Med*., **2016**, *3*, 12–18.
35. National Research Council, Guide for the Care and Use of Laboratory Animals, National Academic Press, Washington, **2011**, pp. 37–103.
36. E. O. Ajani, S. Sabiu, M. Zakari, N. Olanipekun, J. K. Akintunde, F. A. Bamisaye, *J. Biol. Active Prod.*, **2017**, *7*, 166–170. **DOI:**10.1080/22311866.2017.1329667
37. A. A. Adesokan, M. A. Akanji, M. T. Yakubu, *Afr. J. Biotechnol.*, **2007**, *6*, 2502-2505.
38. O. Elekofehinti, J. P. Kamdem, I. J. Kade, J. B. T. Rocha, I. G. Adanlawo, *S. Afr. J. Bot*., **2013**, *88*, 56–61. **DOI:**10.1016/j.sajb.2013.04.010
39. D. Y. Kwon, Y. S. Kim, S. Y. Ryu, M. R. Cha, G. H. Yon, H. J. Yang, M. J. Kim, S. Kang, S. Park, *Eur. J. Nutr*., **2012**, *51*, 529–540. **DOI:**10.1007/s00394-011-0236-x
40. C. N. Kunyanga, J. K. Imungi, M. Okoth, C. Momanyi, H. K. Biesalski, V. Vadivel, *J. Food Sci.*, **2011,** *76*, 560–567. **DOI:**10.1111/j.1750-3841.2011.02116.x
41. Z. Q. Wang, F. E. Lu, S. H. Leng, X. S. Fang, G. Chen, Z. S.

Wang, L. P. Dong, Z. Q. Yan, *World J. Gastroenterol*., **2008**, *4*, 6004–11. **DOI:**10.3748/wjg.14.6004
42. K. Akter, E. C. Barnes, J. J Brophy, D. Harrington, Y. Community Elders, S.R. Vemulpad, J. F. Jamie, *Evid. Based Complement. Alternat. Med.,* **2016**, *2016*, 4683059. **DOI:**10.1155/2016/4683059
43. L. Othman, A. Sleiman, R. M. Abdel-Massih, *Front. Microbiol*., **2019** 10, 911. **DOI:**10.3389/fmicb.2019.00911
44. M. Vessal, M. Hemmati, M. Vasei, *Comp. Biochem. Physiol.,* **2003**, *135*, 357–364. **DOI:**10.1016/S1532-0456(03)00140-6
45. R. Singh, A. Tasleem, K. Imran, S. Poonam, *J. Biomed. Ther. Sci*., **2014**, *1*, 1–33. **DOI:**10.1155/2014/741785
46. R. D. Wilson, M. S. Islam, *Pharmacol. Rep*., **2012**, *64*, 129–139. **DOI:**10.1016/S1734-1140(12)70739-9
47. R. K. Suman, I. Ray Mohanty, M. K. Borde, U. Maheshwari, Y. A. Deshmukh, *Adv. Pharmacol. Sci*., **2016**, 9463476. **DOI:**10.1155/2016/9463476
48. G. J. Litherland, E. Hajduch, G. W. Gould, H.S. Hundal, *Mol. Cell Biochem*., **2004**, *261*, 23–33. **DOI:**10.1023/B:MCBI.0000028734.77867.d2
49. R. D. Wilson, M. S. Islam, *Acta Pol. Pharm*., **2015**, *72*, 153–160
50. K. Chandan, K. Raj, N. Shamshun, *Int. J. Pharm. Res. Allied Sci*., **2014**, *3*, 195–202.
51. D. Cheng, B. Liang, Y. Li. *Biomed. Res. Int*., **2013**, *2013*, 162724. **DOI:**10.1155/2013/162724
52. A. J. Krentz, C. J. Bailey, *Drugs.* **2005**, *65*, 385–411. **DOI:**10.2165/00003495-200565030-00005
53. S. Sabiu, A. O. T. Ashafa, *S. Afr. J. Bot.*, **2016**, *105*, 264–269. **DOI:**10.1016/j.sajb.2016.04.007
54. T. J. Makhafola, E. E. Elgorashi, L. J. McGaw, M. D. Awouafack, L. Verschaeve, J. N. Eloff, *BMC Compliment. Altern. Med*., **2017**, 17, *446*. **DOI:**10.1186/s12906-017-1935-5
55. T. A. Ismail, M. M. Soliman, M. A. Nassan, *Exp. Ther. Med*., **2015**, *9*, 1921–1930. **DOI:**10.3892/etm.2015.2354
56. A. Ribeiro-Oliveira, A. I. Nogueira, R. M. Pereira, W. W. Boas, R. A. Dos Santos, A. C. Simoes, *Vasc. Health Risk Manag*., **2008**, *4*, 787–803. **DOI:**10.2147/VHRM.S1905
57. T. Keilani, W. A. Schlueter, D. C. Levin, *Ann. Intern. Med*., **1983**, *118*, 246–254. **DOI:**10.7326/0003-4819-118-4-199302150-00002
58. E. O. Ajani, L. B. Ibrahim. *Clin. Phytosci*., **2020,** *6*, **DOI:**10.1186/s40816-020-00174-z

Povzetek

Ta študija potrjuje protidiabetično učinkovanje lubja *Enantia chlorantha* in morebitne terapevtske posledice sočasne uporabe lizinoprila in *E. chlorantha* pri podganah s sladkorno boleznijo tipa 2. Lubje *E. chlorantha* je bilo ekstrahirano s hladno maceracijo. Inhibitorni učinek rastline na encime, ki presnavljajo ogljikove hidrate, in njene antioksidativne potenciale so bili ovrednoteni *in vitro*. Ekstrakt je izkazoval inhibitorno delovanje na α-amilazo in α-glukozidazo ter antioksidativne lastnosti in vitro. Aplikacija ekstrakta in vivo je normalizirala hiperglikemijo na tešče, tako da je znižala raven glukoze v krvi v primerjavi z nezdravljenimi diabetičnimi podganami za 47,24 %. Sočasna uporaba *E. chlorantha* in lizinoprila je normalizirala nivo glukoze v serumu in nivo serumskega lipidnega profila. Lubje *E. chlorantha* je pokazalo antidiabetični potencial v primerjavi s standardnim antidiabetikom (metformin). Študija je pokazala tudi, da je rastlina vsebovala nekatere bioaktivne spojine, za katere domnevamo, da bi lahko bile odgovorne za opažene učinke. Sočasna uporaba rastline z lizinoprilom ni prinesla pomembnega terapevtskega izboljšanja ravni glukoze v serumu in lipidnega profila.

Except when otherwise noted, articles in this journal are published under the terms and conditions of the Creative Commons Attribution 4.0 International License

DOI: 10.17344/acsi.2020.6225 *Acta Chim. Slov.* **2021,** *68,* 128–136
creative commons

Scientific paper

Application of Silica Supported Calix[4]arene Derivative as Anti-reversion Agent in Tire Tread Formulation

Hediye Mohamadi,[1] Fereshteh Motiee,[1,*] Saeed Taghvaei-Ganjali[1] and Mandana Saber-Tehrani[1]

[1] *Chemistry Department, IA-University, North Tehran Branch, Tehran 1651153311, Iran*

* *Corresponding author: E-mail: f_motiee@iau-tnb.ac.ir*
Phone: +9877009800

Received: 06-27-2020

Abstract

In this research the influence of the silica supported calix[4]arene derivative (SS-Calix) on the reversion resistance, mechanical properties and thermal behavior of NR/BR tire tread formulation was investigated by the oscillating disc rheometer, FTIR, TGA and tensile testing. The results revealed that the reversion behavior of NR/BR vulcanizate is affected by SS-Calix. The data obtained from curing characteristics and thermal stability of test pieces indicate that, SS-Calix acts as an anti-reversion for rubbery materials that are exposed to thermal shock in the early stages of temperature rise. It's predicted that these results are due to the interaction between the OH groups present in the SS-Calix surface and the carbon of the polymer chains. The broad peak observed in the IR spectrum around 1824 cm^{-1} which is referred to C=O bond, confirms this prediction. In addition, the presence of SS-Calix in compound causes to increase modulus and hardness but reduce elongation and resilience.

Keywords: Mechanical properties; rubber; thermal properties; tire tread formulation; silica supported calix[4]arene; perkalink900.

1. Introduction

Reversion refers to the loss of crosslink density. It occurs especially in compound containing natural rubber (NR) and some synthetic rubber (Isoprene Rubber) when polysulphidic crosslinks are exposed to temperature – time procedure which causes breakdown of polysulphidic crosslinks to di-sulfides and mono-sulfides crosslinks. This occurrence leads to a reduction in crosslink density and consequently loss of functional properties of rubber products.

The best method for evaluation of the reversion is based on rheometer torque curves. In this curves, the negative slope indicates the reversion phenomenon.[1,2] Since reversion decline modulus and mechanical properties of the compound, there are some approaches in the industry to reduce it. One of these methods is the applying of efficient (EV) and semi-efficient (Semi-EV) vulcanization systems. The crosslinks created by these curing systems are usually mono-sulfide and disulfide type which has a higher thermal stability compared to polysulfide crosslinks.[3,4] Efficient (EV) and semi-efficient (Semi-EV) vulcanization systems improved mechanical properties and thermal aging characteristics, but because the length of the mono and disulfide bonds is less than the polysulfide, the flexibility and fatigue life of rubber compounds are reduced.[5] Also in such curing systems due to faster cure rates and lower total sulphur levels the adhesion of rubber to metal and rubber to fabric is very low.[6] One of the approaches used to control the reversion phenomenon is the employing of anti-reversion agent. Perkalink900 (1, 3-bis-citraconimidomethyl benzene) is the most commonly used anti reversion agent in the rubber industry. Perkalink900 prevents loss crosslink density by creating new crosslinks through the well-known Diels-Alder reaction (Figure 1).[7,8]

In recent years, there have been numerous studies on the reversion and its kinetic.[9,10] In 2019, Nah et al. vulcanized chlorobutyl rubber and applied 4, 4'-bis (maleimido) diphenyl methane (BMDM) as a crosslinking agent. They examined rheometric curves and reported that

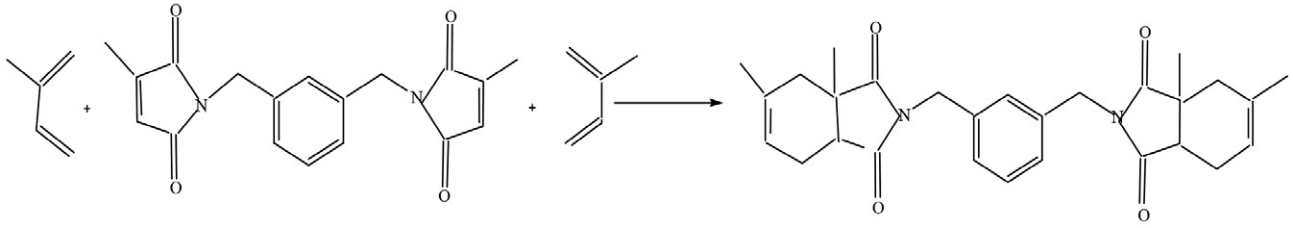


Figure 1. Creating new crosslinks by Perkalink900 [8]

BMDM significantly enhanced the reversion resistance.[11] In 2016, they applied BMDM in NR vulcanized with sulphur and described that the presence of 5 phr of BMDM significantly improves reversion resistance without adversely affecting the scorch time and cure rate. It also enhancement crosslink density and drops compression set value.[12] In 2017, Sousa et al. revealed that the presence of devulcanized rubber chain in the compound has a deleterious effect on the mechanical properties of curing blends.[13] In 2015, Milani et al. invented new approach to determine reversion kinetic constants.[14]

Calixarenes is a macromolecule with hydrophobic cavities which represent one of the most studied host systems known as host-guest chemistry. Calixarenes and their derivatives have many applications in membrane electrodes, construction of polyurethane foams and composites, remove ions, sensors, catalyst, adsorption, binders, detection and extraction.[15-21] In rubber industry, they used as filler,[22] coupling agent,[23] tackifier resin,[24] adsorbent of CBS, DPG[25] and antioxidant.[26]

Prevent the reversion phenomenon using anti-reversion agents has been investigated by different researchers, while the possible influence of calixarenes as anti-reversion element have not been properly studied in the existing literature. In this project, attempt has been made to investigate the role of silica supported calix[4]arene (SS-Calix) as an anti-reversion agent in tire tread formulation based on NR/BR blends. The SS-Calix was prepared according to available source[22,27] and applied as an anti-reversion agent in rubber specimens. The anti-reversion value of vulcanized samples was assessed by comparing the rheometric curves of blends containing SS-Calix and Perkalink900.

2. Experimental

2. 1. Materials

NR (SMR-20) was provided from Teh Ah Yau Rubber Factory (Malaysia). BR (High Cis-96%) was purchased by Shazand Petrochemical Company (Iran). Carbon Black 660 was supplied by Doodeh Sanati Pars Company (Iran). The commercial Silica (Ultrasil VN3) was supplied by Evonik Company (Germany). Aromatic oil was purchased from Iranol Co. (Tehran, Iran). Silane (Si69) was supplied by Shin-Etsu (japan). ZnO was provided from Shokohiye zinc oxid (Iran). Stearic Acid was supplied by AcidChem Company (Malaysia). Sulfur (OT-20) and other ingredients including accelerators were purchased from Taizhou Huangyan Donghai Chemical Co., Ltd. (China). Wax was provided from behran Factory (Iran). Perkalink 900 was supplied by RheinChemie Company (Germany). 25, 26, 27, 28 – tetrahydroxy – 5, 11, 17, 23 – tetrakis [cholorosulfonyl] calix[4]arene (SS-Calix) was prepared according to the literature.[22,27] Para tert-butyl phenol, hydrochloric acid, diethyl ether, sodium hydroxide, chloro sulfonic acid, di chloro methane, di phenyl ether were provided from Merck company (Germany) and formaldehyde, acetic acid, ethyl acetate, xylene and acetone were purchased from Mojalali company (Iran).

2. 2. Preparation of Rubber Compounds

The SS-Calix was introduced to the blends as a novel anti-reversion agent, along with accelerated sulfur for the Semi-EV vulcanization of NR/BR compound. The tire tread formulation of the rubbery samples which has been used in this study is shown in Table 1.

The compound that contains silica as filler, silane as coupling agent is designated as SP1 and it is used as control. The specimen that contains silica as filler, silane as coupling agent and Perkalink900 as anti-reversion agent is designated as SP2. SS-Calix is introduce to SP3 compound as filler, coupling agent and anti-reversion agent. Mixing was performed in a laboratory size two roll mixing according to ASTM D3184.

SP1 sample preparation: Natural rubber was initially masticated for 2 minutes then Butadiene Rubber was loaded into the roll mixing. Silica, Si69, aromatic oil and carbon black were added and mixed. Subsequently, the other ingredients: ZnO, stearic acid, TMQ, 6PPD and wax were added and mixed. In the second stage, sulfur, TBBS were added to the compound.

SP2 sample preparation: Preparation of SP2 sample is similar to SP1 sample. Only in the final stage, perkalink 900, in addition to sulfur and TBBS, were added to the blend.

Although, in samples SP1 and SP2, the amount of carbon black (46 phr) is higher (almost 3 times) than silica, however, in order to ensure the salinization of the blend, the mixing operation was performed for a longer period of time and at the maximum possible temperature compared to sample SP3

Table 1. Compound Formulations

Ingredient (phr*)	Sample SP1	SP2	SP2
NR	70	70	70
BR	30	30	30
Carbon Black 660	46	46	46
Aromatic Oil	15	15	15
ZnO	3	3	3
Silica Ultrasil VN3	17	17	–
Si69	0.5	0.5	–
Perkalink900	–	1	–
SS-Calix	-	–	17
Stearic Acid	1	1	1
TMQ	1	1	1
6PPD	1	1	1
Wax	2	2	2
TBBS	1.75	1.75	1.75
Sulphur	1.4	1.4	1.4

*phr represented the mass parts per 100 mass parts of NR/BR blend

SP3 sample preparation: In the first stage, natural rubber and butadiene rubber was masticated by laboratory two roll-mills of 8 inch diameter and 20 inch length. Following the compounding process, SS-Calix and carbon black added to the blend, then other components (aromatic oil, wax, stearic acid, zinc oxide, TMQ, 6PPD) except curing agents mixed with performing ingredients. Finally, the curatives (sulfur, TBBS) were added to the compound.

The compounding of this sample at a maximum temperature of 75 °C lasted approximately 30 minutes.

At all stages, the materials that falls on the tray under the rollers was collected by the brush and added again to the compounds. After mixing, in order to rest the compounds and control the expansion or shrinkage of polymer chain, samples were stored at room temperature for 24 h.

2. 3. Measurements

2. 3. 1. Determination of Crosslink Density

The swelling tests were used to calculate the crosslink density of three different rubber vulcanisates according to ASTM D471. The rubber pieces were cut from the compression-molded rubber sample weighting about 0.2–0.25 g, and swollen in toluene to reach equilibrium, which took 72 hours at room temperature. The cured test pieces were taken out from the liquid, the toluene was removed from the sample surfaces wiped with tissue paper, the weight after swelling were measured. The samples were then dried in the oven until constant weights were obtained. The swelling results were used to calculate the crosslink density by applying the Flory-Rehner manner [equation (1)].[28]

$$v = \frac{-\ln(1-v_2)+v_2+\lambda {v_2}^2}{v_1({v_2}^{\frac{1}{3}}-(\frac{v_2}{2}))} \quad (1)$$

Where V_1 is the molar volume of the solvent and V_2 is the volume fraction of rubber in the swollen. λ is an interaction parameter between the polymer and the swelling agent.

2. 3. 2. Cure Characteristics

The curing behavior of specimens was investigated from the torque curves generated by a Monsanto Moving Die Rheometer HIWA900 MDR (HIWA, Iran) at 160 °C.

2. 3. 3. Mechanical Properties

Specimens were cut from vulcanized blends with 2 mm thickness. The tensile strength and tear resistance test were carried out by using a tensile tester (Testometric M350) at room temperature according to ISO37. Hardness of the vulcanized was determined according to the ASTM D2240 method by ShoreA (Bareiss, Germany). Resilience was measured by Hiwa300 (HIWA, Iran) according to DIN 53512.

2. 3. 4. Thermal Gravimetric Analysis (TGA)

In order to understand the thermal stability of samples, thermo gravimetric analysis was performed on the TGA-SF1 (Mettler, Switzerland) apparatus using 15mg samples in the temperature range 25–800 °C and under nitrogen atmosphere, at a heating rate of 10 °C/min.

2. 3. 5. Fourier Transform Infrared Spectroscopy (FTIR)

Fourier transform infrared spectroscopy (FTIR) was obtained by Bruker FTIR spectrometer (Germany).

3. Result and Discussion

3. 1. Crosslink Density

The crosslink densities of the NR/BR composite were designated by the Flory–Rehner manner [equation (1)]. The results are presented in Table 2. As it can be seen the SP3 specimen have the most great crosslink density. This observation is due to the role of SS-Calix as filler and coupling agent and form more crosslinks. This is due to the interaction between the OH groups present in the SS-Calix structure and the rubber chains. The formation of C=O bonds observed in the IR spectrum of the samples is the evidence of this incident.

Table 2. The results of crosslink density of three different samples

	Sample SP1	SP2	SP3
Crosslink Density (× 10^{-4} mol/cm^3)	2.0812	2.596	2.9395

3. 2. Cure Characteristics

The best well-known compounding method to minimize reversion is the application of anti-reversion agents, thereby diminishing the number of polysulphidic crosslinks and generating reversion resistant mono and disulphidic crosslinks. The curing behavior of three various resulting materials is displayed in Figure 2. The cure rate index (CRI), the difference between maximum and minimum torque (ΔM = MH-ML), scorch time (ts_2) and optimum cure time (tc_{90}) are listed in Table 3 and Figure 3. The start time of the reversion is reported in Table 4 and its value at different times is shown in Table 4 and Figure 4.

The role of ZnO as activator depends on the type of rubber matrix and accelerator. The mechanism of zinc catalyzed sulfur vulcanization is very complex, but zinc-based complexes play a main role in determining the nature of the cross-linked products.

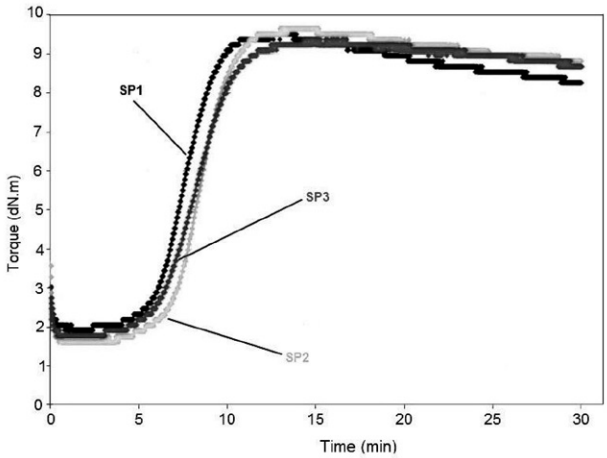


Figure 2. The curing curve of compounds based on NR/BR for SP1, SP2, and SP3

Table 3. The results of curing behavior of three different samples

	Sample		
	SP1	**SP2**	**SP3**
ts_2(Min)	6.69	7.09	7.55
tc_{90} (Min)	9.32	10.59	10.13
CRI	35.52	28.58	7.59
ΔM	7.59	7.59	8.01

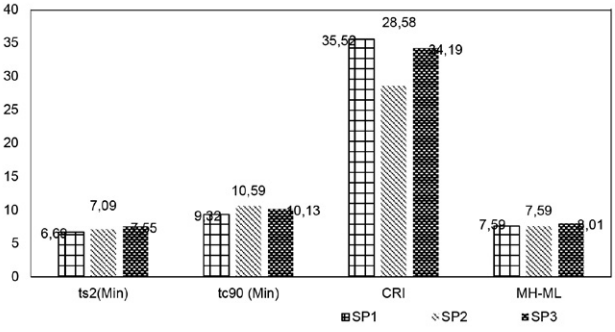


Figure 3. The curing characteristics of NR/BR blends

Table 4. Time to start the reversion and the value of reversion at different times for three various samples

	Sample		
	SP1	**SP2**	**SP3**
TSR* (min)	14	15	15
Revt14 (dN.m)	0.14	0.00	0.00
Revt15 (dN.m)	0.28	0.14	0.14
Revt16 (dN.m)	0.28	0.14	0.14
Revt17 (dN.m)	0.42	0.28	0.14
Revt18 (dN.m)	0.42	0.28	0.28
Revt20 (dN.m)	0.69	0.28	0.42
Revt22 (dN.m)	0.83	0.28	0.42
Revt24 (dN.m)	0.97	0.41	0.56
Revt26 (dN.m)	1.11	0.55	0.69
Revt28 (dN.m)	1.11	0.55	0.69
Revt30 (dN.m)	1.24	0.69	0.83

*TSR: The start time of Rev (min)

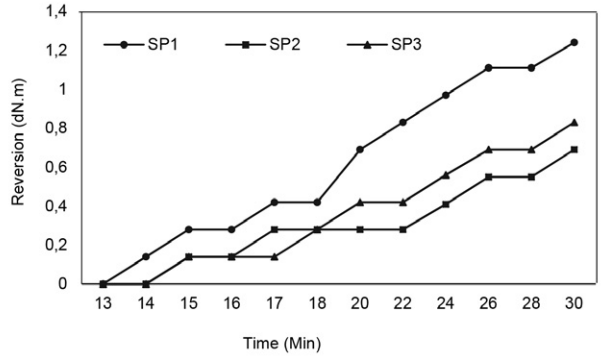


Figure 4. The reversion value of NR/BR blends at different times

Formation rate of zinc-accelerator complex determines scorch time of rubbery materials.[1] As shown in Figure 3, the maximum scorch time value is related to SP3 compound which treated by SS-Calix as an anti-reversion agents. The reason for this increase could be the physical interact of accelerators with the SS-Calix cavities.[22] Because of this, the formation of zinc-accelerator complex has delay and it caused to increases the scorch time. Another result of the rheometer's curve is 5% increase of ΔM in the SP3 specimen over the other two compounds and it indicates despite delayed, accelerator act its effect as good as before. ΔM indirectly indicates the crosslink density of rubber samples, an increase in ΔM and crosslink density in SP3 compound demonstrates an improvement in the curing properties of test pieces. As can be seen, the tc_{90} in SP3 and SP1 compounds are approximately equal but in SP2 (contain Perkalink900), tc_{90} has increased so the cure rate index (CRI) has drastically decreased. This decrement in curing rate can be attributed to the negative effect of Perkalink900 on the rate of vulcanization.

Another important and delicate point that can be considered from the torque curve of these three compounds is their reversion behavior which is significantly different at a certain time. The onset of reversion and its relationship with increasing curing time can be seen in Table 4 and Figure 4 for all samples.

As the rheometer curves displayed the onset of reversion in SP1 sample is earlier than two other samples. In SP2 and SP3, the reversion begins simultaneously, but then it behaves differently. As can be seen from the results, at t_{17} of curing, the lowest amount of reversion (0.14 dN.m) is related to SP3. At the same time, the reversion of SP1 and SP2 is three times and twice that of SP3, respectively.

However, at $t_{18,}$ reversion of SP1 and SP3 increases, but the value of this phenomenon in SP2 remains unchanged up to t_{22}. At this point SP2 and SP3 samples have the same reversion resistant. The reversion of SP1 and SP3 will be increased after t_{20}. The highest value of reversion is related to SP1 and the lowest is belonging to SP2 blends. This trend is continued and indicated the anti-reversion behavior of three samples as fallowed (Figure 4): SP2>SP3>SP1

As Figure 4 shows, the point to consider in this phenomenon is the performance of SS-Calix in SP3 blend as an anti-reversion agent in a certain curing temperature range (t_{15}-t_{17}). It seems that SS-Calix, in addition to being reinforcing filler that does not require a coupling agent [22], it can be act as anti-reversion agent in rubbery materials that exposed to thermal shock. In fact, it acts as an anti-reversion in the early stages of temperature rise for rubbery materials that are exposed to thermal shock.

It is predicted that at the first 2 minutes of reversion, the polymer chains which crosslinks have been broken and radicalized by the reversion phenomenon form new positive interaction with the radicals created in the SS-Calix. As a result, it reduces the reversion. Because a limited number of calix moieties are bonded to the silica surface, over time, the number of calixarenes radicals on the silica surface are finished and the radical reaction of SS-Calix with elastomer chains are quenched. As a result, the anti-reversion effect of SS-Calix decreases through the time. In general, it can be suggested that the ability of Perkalink900 as an anti-reversion is slightly higher than the SS-Calix agent. In Table 5 the influence of the type of anti-reversion agents on the mechanical properties of resulting materials is shown.

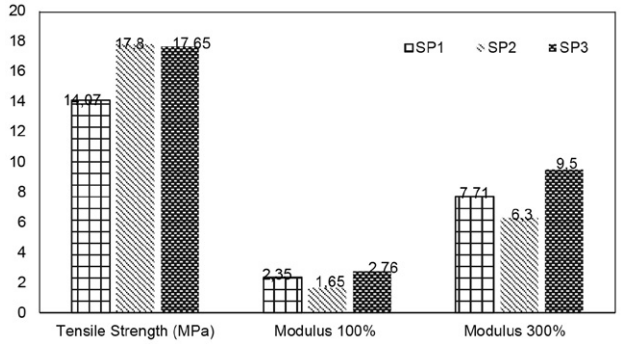


Figure 5a. Results of tensile strength, modulus100% and modulus 300% for SP1, SP2 and SP3

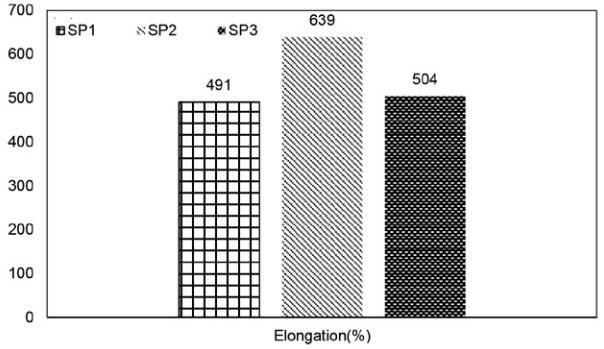


Figure 5b. Results of the elongation for SP1, SP2 and SP3

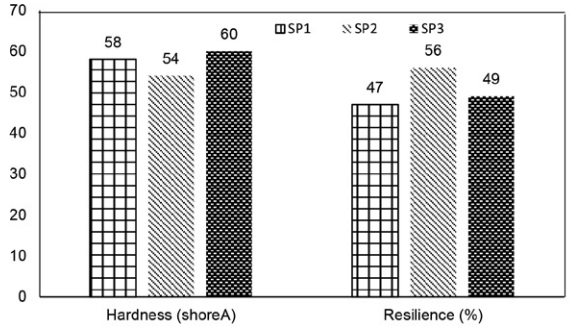


Figure 6. Results of hardness and resilience for SP1, SP2 and SP3

The results of the tensile strength, modulus100%, modulus 300% are displayed in Figure 5a and the result of the elongation is shown in Figure 5b. Hardness and resilience tests for all compounds are shown in Figure 6.

As Figure 5a shows the tensile strength of both SP3 and SP2 compounds increase in comparison with SP1 and

Table 5. The results of tensile, hardness and resilience properties of three different samples

Sample	Tensile Strength (MPa)	Modulus100% (MPa)	Modulus 300% (MPa)	Elongation (%)	Hardness (Shore A)	Resilience (%)
SP1	14.07	2.35	7.71	491	58	47
SP2	17.80	1.65	6.30	639	54	56
SP3	17.65	2.76	9.50	504	60	49

they are not significantly different from each other. So Perkalink900 and SS-Calix have the same effect on tensile strength of rubber products. It seems that due to the macromolecule structure of the SS-Calix and the presence of many hydroxyl groups and cavities in this system, polymer chains have been interacted with SS-Calix. As a result, the compound structure has become tighter, therefore the tensile strength has increased in comparison with SP1 compound. Figures 5a and 6 show that the highest modulus and hardness is related to SP3 rubbery compound and the lowest modulus and hardness is related to SP2. In fact, Perkalink900 has a negative effect on modulus and hardness. The increase in modulus and hardness in SP3 blend is due to the increase in crosslink density in this compound. Increasing the density of crosslinks also reduces the elongation and resilience of SP3 (Figures 5b and 6). It should be noted that the crosslink density effect on the tensile strength, modulus, elongation at break, resilience and hardness.[29–31]

3. 3. The Thermal Gravimetric Analysis

In order to investigate the thermal resistance of three different compounds thermal gravimetric was performed. Figure 7 show the weight loss behavior for all compounds.

The data of thermal analysis for all samples are summarized in Table 6. The results show that the onset temperature of degradation of SP2 is lower than that of SP3 and this process continues up to 45% of degradation. After that, the destruction temperature of both samples up to 90% is almost the same. However, due to chemical and physical interactions between SS-Calix and SP3 blend it

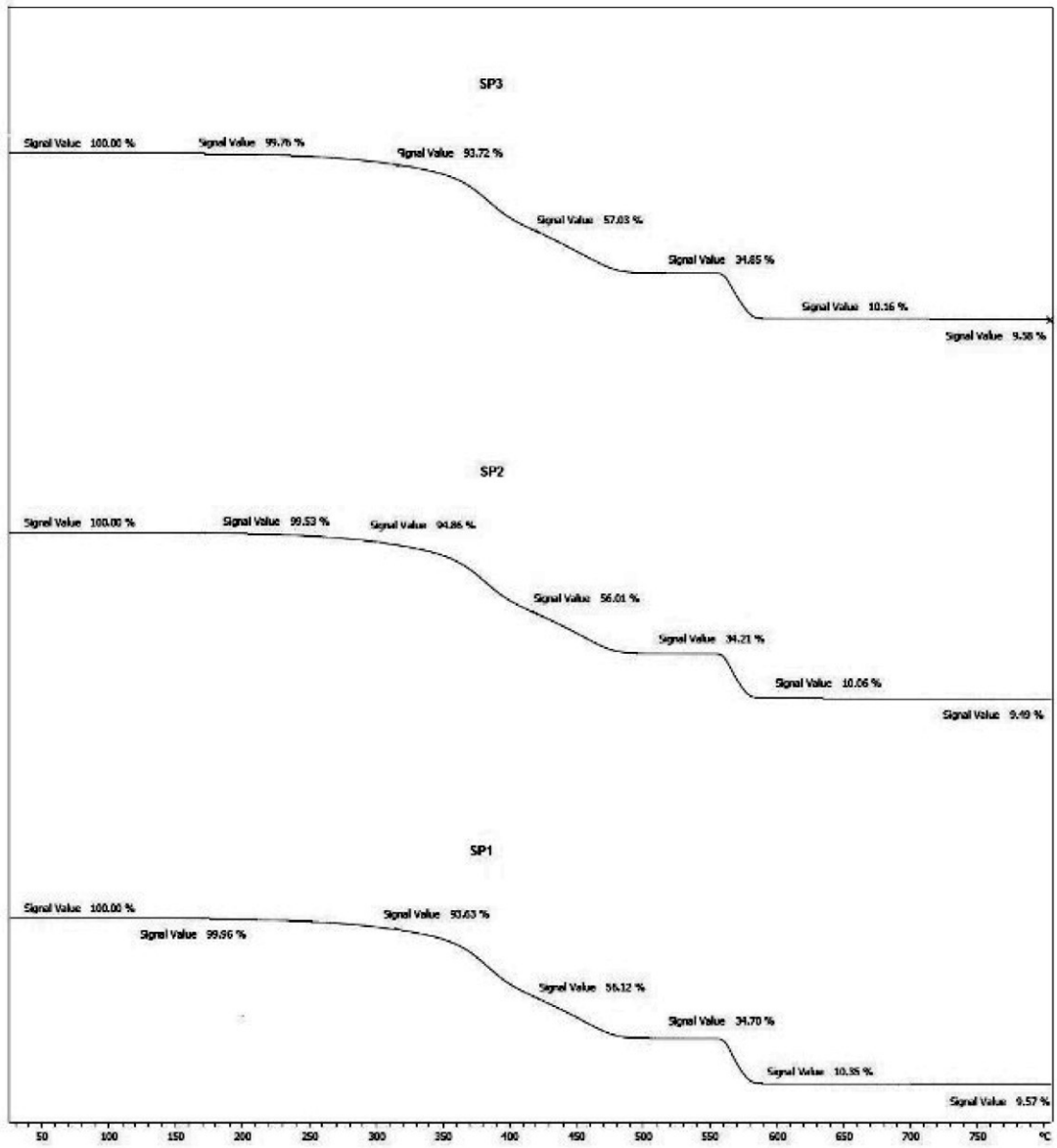


Figure 7. The weight loss behavior of SP1, SP2 and Sp3 specimens

Table 6. The TGA data for three different samples

	Sample		
	SP1	SP2	SP3
T_{in} (°C)	320	290	320
$T_{5\%}$ (°C)	329	310	329
$T_{15\%}$ (°C)	370	360	380
$T_{25\%}$ (°C)	386	378	388
$T_{35\%}$ (°C)	402	392	408
$T_{45\%}$ (°C)	431	419	435
$T_{50\%}$ (°C)	442	442	445
$T_{55\%}$ (°C)	461	451	452
$T_{65\%}$ (°C)	561	480	482
$T_{75\%}$ (°C)	570	569	570
$T_{85\%}$ (°C)	580	573	580
$T_{95\%}$ (°C)	582	580	582

seems reasonable that the thermal resistance of SP3 is higher than that of SP2.

3. 4. Fourier Transform Infrared Spectroscopy (FTIR)

The FTIR for all compounds were showed in Figure 8.

The Fourier transform infrared spectroscopy was performed to evaluate the anti-reversion behavior of SP3 blend. Since the interpretation of the FTIR spectrum of rubber samples is so complex, only strong bands were considered in this study.

The absorption curves of the SP3 blend showed that in addition to the bands characteristic for calix[4]arenes,[27] there is a broad peak around 1824 cm^{-1} which is referred to C=O bond.[32] As we know, the most important feature of SS-Calix is the position of the OH stretching bond in the 3100–3500 cm^{-1} region. The considerably weaker C=O bond for SP1 and SP2 blends is attributed to the fact that the oxygen of hydroxyl groups of the calixarene surface forms a C=O with the carbon in the polymer chain.[33]

3. 5. The Conversion Rate of Vulcanization

By using equation (2), the conversion rate of vulcanization at various times had evaluated for all compounds (Table 7).[34]

$$Xt = \frac{Mt-ML}{MH-ML} \quad (2)$$

In this equation, Xt indicate the conversion rate at the given time t. Mt, MH, ML and MH-ML represent torque at the given time t, the maximum Torque, the Minimum Torque and the difference between maximum and minimum Torque, respectively.

The value of X_5 indicate the delay in scorch time for SP3 specimen compared to SP2. The conversion ratio of SP1 and SP3 at X_{13} equaled 1, which revealed that Mt=MH

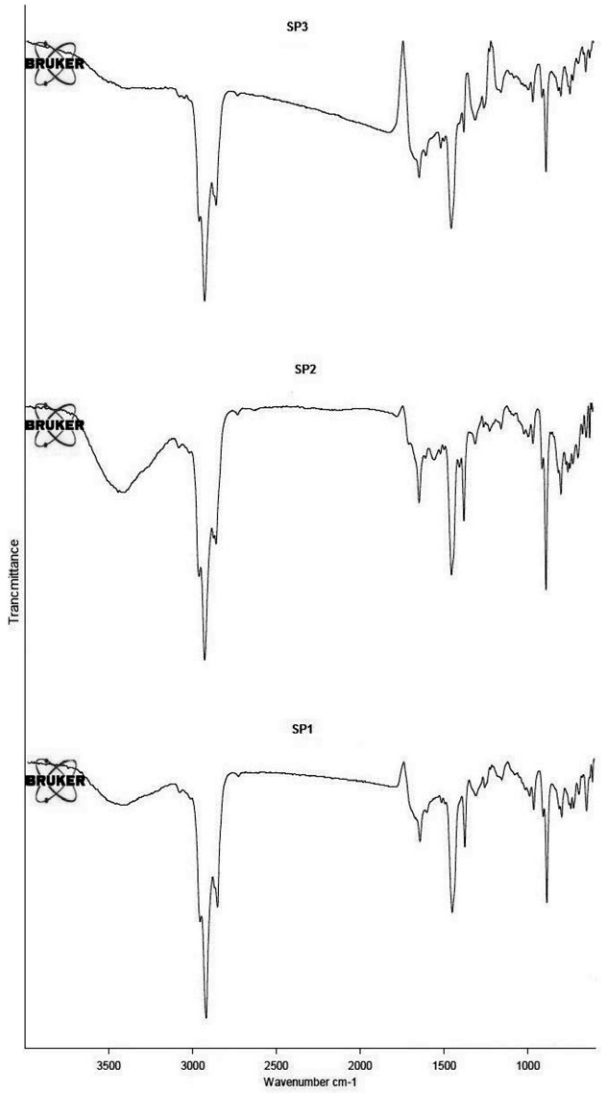


Figure 8. The FTIR for SP1, SP2 and Sp3 specimens

Table 7. The conversion rate of vulcanization at various times for all compounds

	Sample		
	SP1	SP2	SP3
X_5	0.05	0.05	0.03
X_{10}	0.95	0.85	0.86
X_{13}	1.00	0.98	1.00
X_{14}	0.98	1.00	1.00
X_{15}	0.96	0.98	0.98
X_{16}	0.96	0.98	0.98
X_{17}	0.94	0.96	0.98
X_{18}	0.94	0.96	0.96
X_{20}	0.91	0.96	0.95
X_{22}	0.89	0.96	0.95
X_{24}	0.87	0.94	0.93
X_{26}	0.85	0.93	0.91
X_{28}	0.85	0.93	0.91
X_{30}	0.84	0.91	0.90

and the 90% of curing is done, for SP2 sample it happened in the X_{14}, While for SP3 sample in X_{14} still remains 1. The SP3 conversion rate up to X_{17} almost is more than SP2 (Table 7). These findings predicted that;

I: The reversion resistance of SP3 up to about X_{17} is more than SP2 and SP1.

II: The second important point is that after X_{17} up to X_{30}, less reversion occurs for SP2.

III: The SP3 rubber sample exhibits high thermal resistance in a short time.

These outcomes confirm the result from curing behavior of three different samples.

4. Conclusion

Since the reversion has an undesirable effect on the performance properties of the rubber compounds, this study investigated the influence of the presence of SS-Calix as a novel anti-reversion on the reversion resistance of rubber blend based on NR/BR. Its anti-reversion properties were also compared with perkalink900. Finally, the following results are obtained:

- The presence of SS-Calix in compound based on NR/BR increase the modulus and hardness also decrease the resilience and the elongation.
- In a few minutes after the start of reversion the reversion resistance effect of the SS-Calix was much better than perkalink900.
- The presence of SS-Calix increases the formation of C=O bonds in SP3 sample that cause to increase reversion resistance in the early minutes after the start of reversion.
- Application of the SS-Calix to NR/BR rubber products subject to thermal shock is recommended.
- In NR/BR rubber compound that contains SS-Calix the initial temperature degradation until $T_{45\%}$ are more than perkalink900.

Based on these findings, it can be predicted that this feature of calix[4]arene can be applied in the preparation of rubber products that must have high thermal resistance in a short time.

5. Reference

1. B. Rodgers, (Ed.): Rubber Compounding Chemistry and Application, Marcel Dekker, New York , **2004**, p.512. **DOI:**10.1201/9781420030464
2. K. Boonkerd, CH. Deeprasertkul , K. Boonsomwong, *Rubber. Chem. Technol.* **2016**, *89, 3,* 450–464. **DOI:**10.5254/rct.16.85963
3. E. Leroy, A. Souid, A. Sarda, R. A. Deterre, *Polym. Test*. **2013**, *32, 1,* 9–14. **DOI:**10.1016/j.polymertesting.2012.08.012
4. P. M Visakh, S. Thomas, A. K. Chandra, A. P. Mathew, (Ed.): Advances in Elastomers I Blends and Interpenetrating Networks, Springer, Heidelberg, New York Dordrecht London, **2013**, pp. 121. **DOI:**10.1007/978-3-642-20925-3
5. S. Rabiei, A. Shojaei, *Eur. Polym.* **2016**, 81, 98–113. **DOI:**10.1016/j.eurpolymj.2016.05.021
6. N. R. Kumar, A. K. Chandra, R. Mukhopadhyay, *J. Mater. Sc.* **1997**, *32,* 3717–3725. **DOI:**10.1023/A:1018655102644
7. R. N. Datta, N. M. Huntink, S. Datta, A.G. Talma, *Rubber. Chem. Technol.* **2007**, *80, 3,* 436-480. **DOI:**10.5254/1.3548174
8. Sh. G. Sathi, J. Jeon, J. Won, Ch. Nah, *J. Polym. Res*. **2018**, 25.
9. E. Leroy, A. Souid, R. Deterre, *Polym. Test*. 2013, *32, 3,* 575–582. **DOI:**10.1016/j.polymertesting.2013.01.003
10. G. Milani, E. Leroy, F. Milani, R. Deterre, *Polym. Test*. 2013, *32, 6,* 1052–1063. **DOI:**10.1016/j.polymertesting.2013.06.002
11. Sh. Gopisathi, Ch. Park, Y. I. Huh, J. Jeon, Ch. H. Yun, J. Won, K.U. Jeong, Ch. Nah, *Rubber. Chem. Technol.* **2019**, *92, 1,* 110–128. **DOI:**10.5254/rct.18.82605
12. G. S. Shibulal, J.Y. Jang, H. Ch. Yu, Y. I. Huh, Ch. Nah, *J. Polym. Res*. **2016**, *23*. **DOI:**10.1007/s10965-016-1128-9
13. F. D. B. de Sousa, A. Zanchet, C. H. Scuracchio, *J. Appl. Polym. Sci*. **2017**, 134, 41. **DOI:**10.1002/app.45325
14. G. Milani, G. Milani, F. Milani, *J. Math. Chem*. **2015**, *53,* 1363–1379. **DOI:**10.1007/s10910-015-0493-7
15. S. Taghvaei-Ganjali, R. Zadmard, M. Zeyaei, K. Rahnama, F. Faridbod, M. R. Ganjali, *Lett. Org. Chem*. **2009**. **DOI:**10.1155/2009/601089
16. M. Hosseini, M. Rahimi, H. Bagheri Sadeghi, S. Taghvaei-Ganjali, Sh. Dehghan Abkenar, M. R. Ganjali, *Intern. J. Environ. Anal. Chem*. **2009**, *89, 6,* 407–422. **DOI:**10.1080/03067310802713195
17. M.S. Mirmoeini, M. M. Alavi Nikje, M. Rasouli-Saniabadi, S. Taghvaei-Ganjali, *Macromol. Symp*. **2017**, 373. **DOI:**10.1002/masy.201600101
18. S. Taghvaei-Ganjali, M. Rasouli-Saniabadi, M.S. Mirmoeini, *J. Inc. Phenom. Macro*. **2015**, *83,* 45–52. **DOI:**10.1007/s10847-015-0539-2
19. M. Nouri, Sh. Mozafari, S. Taghvaei-Ganjali, *Iran. JOC*. **2011**, *3, 4,* 807–809.
20. K. D. Daze, C. E. Jones, B. J. Lilgert, C. S. Beshara, F. Hof, *Can. J. Chem*. **2013**, *91,* 1072–1076. **DOI:**10.1139/cjc-2013-0186
21. T. T. Pang, L. M. Du, H. L. Liu, Y. L. Fu, *Can. J. Chem*. **2014**, *92,* 1139–1144. **DOI:**10.1139/cjc-2014-0150
22. H. Mohamadi, F. Motiee, M. Saber-Tehrani, S. Taghvaei-Ganjali, *Russ. J. App. Chem*. **2019**, *92,* 809–816. **DOI:**10.1134/S1070427219060107
23. M. Malekzadeh, H. Nouri, M. Farahani, *JACR*. **2010**, *3,* 41–45.
24. H. Margharian Pekachaki, S. Taghvaei-Ganjali, F. Motiee, M. Saber-Tehrani, Rubb. *Chem. Technol.* **2019**, 92, *3,* 467–480. **DOI:**10.5254/rct.19.81510
25. Z. Servati, M. Saber-Tehrani, S. Taghvaei-Ganjali, R. Zadmard, *J. Porous. Mater*. **2018**, *25,* 1463–1474. **DOI:**10.1007/s10934-018-0559-6
26. H. Li, Y. Zhong, W. Wu, L. Zhang, X. Lai, X. Zeng, *J. Appl. Polym. Sci*. **2017**, *134,* 31.

27. S. Taghvaei-Ganjali, R. Zadmard, M. Saber-Tehrani, *Appl. Surf. Sci*. **2012**, 258, *16,* 5925–5932. **DOI:**10.1016/j.apsusc.2011.09.019
28. P. J. Flory, J. Rehner, *J. Chem. Phys*. **1943**, *11,* 521–526. **DOI:**10.1063/1.1723792
29. L. M. Polgar, G. Fortunato, R. Araya-Hermosilla, M. van Duin, A. Pucci, F. Picchioni, *Eur. Polym. J.* **2016**, *82,* 208–219. **DOI:**10.1016/j.eurpolymj.2016.07.018
30. S. S. Choi, H. M. Kwon, Y. Kim, E. Ko, K. S. Leeb, *Polym. Int.* **2018**, 67, *3,* 340–346. **DOI:**10.1002/pi.5515
31. I. Surya, H. Ismail, A.R. Azura, *Polym. Test.* **2015**, *42,* 208–214. **DOI:**10.1016/j.polymertesting.2014.12.009
32. M. Fan, Y. Zhang, X. Li, B. Zeng, Sh. Chen, W. Zhu, Sh. Wang, J. Xu, N. Feng, *Polym. Advan. Technol*. **2019**, *30,* 5. **DOI:**10.1002/pat.4555
33. C. D. Gutsche, in: Calixarenes, Royal Society of chemistry, Cambridge, **2008**, p.70.
34. K. Chawla, A. P. S. Chauhan, A. Pandey, *Plast. Rubber. Compos*. **2016**, *45,* 6. **DOI:**10.1080/14658011.2016.1178969

Povzetek

Raziskali smo vpliv silikatnega nosilca ojačanega s kaliks [4] arenskim drivatom (SS-Calix) na zmanjševanje zamreženja, mehanske lastnosti in termično obnašanje NR/BR pnevmatik s pomočjo reometra z oscilacijskim diskom, FTIR, TGA in napetostnega testa. Rezultati so pokazali, da je zmanjševanje zamreženja NR/BR vulkanizata odvisno od dodatka SS-Calix-a. Rezultati pridobljeni iz meritev značilnosti zamreževanja in termične stabilnosti testiranih vzorcev so pokazali, da SS-Calix deluje kot preprečevalec zmanjševanja zamreženja za gumijaste materiale izpostavljene termičnemu šoku v zgodnjih fazah naraščanja temperature. Predpostavljamo, da so opažene lastnosti posledica interakcij med OH skupinami prisotnimi na SS-Calix-u in ogljikom v polimernih verigah. Širok vrh opažen na IR spektru okoli 1824 cm^{-1}, ki je značilen za C=O vez, potrjuje to predpostavko. Poleg tega prisotnost SS-Calix-a povečuje napetostni modul in trdoto a hkrati zmanjšuje raztegljivost in odpornost.

Except when otherwise noted, articles in this journal are published under the terms and conditions of the Creative Commons Attribution 4.0 International License

Scientific paper

Physicochemical Properties of Octane Isomers in View of the Structural Numbers

Anton Perdih

Faculty of Chemistry and Chemical Technology, University of Ljubljana (retired)
Večna pot 113, 1000 Ljubljana, Slovenia

** Corresponding author: E-mail: a.perdih@gmail.com*

Received: 06-07-2020

Abstract

The structural features of octane isomers were quantified with help of the Structural Numbers. A Mutually Optimized Contribution of the Structural Numbers (MOC_{SN}) was used to calculate which parts of information regarding branching contribute the tested Structural Numbers. Besides the known Structural Numbers, two Asymmetry Numbers were developed in order to quantify the asymmetry of the octane isomers, one regarding the asymmetry along the main chain of the molecule and the other one regarding the asymmetry perpendicular to the main chain of the molecule. Their correlation to the values of 29 tested physicochemical properties of octanes was low, $|R| < 0.6$. After optimization of the Mutually Optimized Contribution of the Structural Numbers, the Information Content of the Mutually Optimized Contribution of the Structural Numbers ranged from 34.3% to 89.0% of the information contained in the physicochemical properties. The Structural Numbers enable the first step of the structural interpretation of physicochemical properties of octane isomers. In 17 out of 29 cases the most of information contained in the physicochemical properties is presented among the Structural Numbers by the Number of Branches, in 8 cases by the Peripheral Number, in 3 cases by an Asymmetry Number and in 1 case by the Distance Number.

Keywords: Octanes; asymmetry number; distance number; number of branches; peripheral number; size of the largest branch; structural interpretation.

1. Introduction

In order to estimate the unknown values of the physicochemical properties (PCP) of alkanes, Wiener[1] started the development of the numerical measures of their structure, later named the topological indices.[2,3] In the structure of alkanes, the branching of their molecules is obvious. Branching of molecules is easily apprehended. It comprises several structural variables, for example the number of branches, their valencies, their distances apart, their distance from the graph center, the lengths of branches, etc.[4] However, any definition of branching must rest on an intuitive basis.[5] Bonchev and Trinajstić[6] presented several rules representing branching. Later, these rules were improved.[7] In that time, branching was attempted to be defined using few topological indices,[8] either the Wiener[1] index or the largest eigenvalue of the adjacency matrix.[9,10] As a new basis for the definition of branching the largest eigenvalue of the path matrix was provided.[8] There was also stressed the dilemma, whether a branching index should correlate well with physicochemical properties of alkanes or should it serve its own purpose to index branching regardless the correlation with the physicochemical properties. The attention was focused on the definition of branching, rather than to the application of it.[8] Randić and Wilkins[11] demonstrated the ordering of structures based on path indices. There have been presented also the intuitively derived sequences of octanes of increasing branching as well as some topological indices, which order the octane isomers into such sequences. Topological indices, which order the octane isomers into sequences of increasing branching, were, however, not good indices of the physicochemical properties of octanes.[12]

Later on,[13] based on physicochemical properties of octanes, which correlated to $R > 0.9$ to an intuitively derived sequence of octanes of increasing branching,[12] there was introduced the concept and the values of Branching Degrees of octane isomers. There were defined some Structural Numbers as well. Besides the previously known Number of Branches (N_{br}), also the values of the Peripheral Number (N_{per}), the Distance Number (N_d), as well as the

Size of the Largest Branch (L_{br}) were defined and their correlation to a number of physicochemical properties of octanes was determined.[13]

In a previous trial, it has been noticed that the symmetry of molecules has some importance in the Principal Component Analysis of physicochemical properties of alkanes, where the axis PC4 separates first of all the elongated and flat molecules from the spherical ones and among the former ones the symmetric from the asymmetric ones. However, the variance contained in the axis PC4 was low (3% or less). In the case of tested topological indices, it was hardly noticeable.[14]

To test the importance of symmetry of octanes regarding their physicochemical properties (PCP) in a different way, in present paper two measures of symmetry of octane molecules, i.e two Asymmetry Numbers were developed. They were tested alone as well as in combination with other Structural Numbers. The Structural Numbers are not another type of topological indices. They are the quantification of the structural features of alkanes. In present paper is performed the test, which part of information contained in the physicochemical properties of octanes can be explained using the mutually optimized contribution of the Structural Numbers. For other groups of alkanes, the Structural Numbers of them are to be derived and used using the approach described below.

2. Notation and Physicochemical Properties of Octane Isomers

Notations and physicochemical properties of octane isomers were presented in a previous paper.[15]

3. Calculations

The software for statistics calculations included in the program package MS Excel was used.

The definitions of the Structural Numbers are as follows.[13] The Peripheral Number N_{per} was defined as $N_{per} = \Sigma d_{sy}$, where d_{sy} is the distance of a branch from the axis of symmetry of the main chain of the molecular graph. The Distance Number N_d was defined as the distance between two branches. The Size of the Largest Branch L_{br} was equal to the number of vertices in the branch.

Here are defined as a new Structural Number two types of the Asymmetry Number: $N_{asym\leftrightarrow}$ and $N_{asym\perp}$.

As measures of the goodness of correlation were used the correlation coefficient, *R*, the standard error, *S*, and the information content regarding branching,[15] *IC*.

4. Results

The definitions of the Asymmetry Numbers $N_{asym\leftrightarrow}$ and $N_{asym\perp}$ are as follows:

$N_{asym\leftrightarrow}$ is the difference of distances of branches from the symmetry axis of the main chain of the octane molecule.

$N_{asym\perp}$ is the difference of the distances of vertices in branches perpendicular to the main chain of the octane molecule.

The Asymmetry Numbers are the inverse measures of the symmetry of molecules. For symmetrical molecules any $N_{asym} = 0$, whereas for non-symmetrical ones any $N_{asym} > 0$. Their values are presented in Table 1.

The Asymmetry Numbers were correlated to the physicochemical properties of octanes. At $N_{asym\leftrightarrow}$, the absolute values of the correlation coefficient, $|R|$, range from 0.004 to 0.419, whereas at $N_{asym\perp}$ the range is $0.016 < |R| < 0.602$. This is in line with an earlier observation[14] that on the Principal Component Analysis the variance contained in the axis PC4, which separates the symmetric molecules from the asymmetric ones, was low.

The highest correlations with the Asymmetry Numbers were observed at the physicochemical properties Solubility Parameter, Cohesive Energy Density, the Antoine parameter B and Surface Tension. These are the physicochemical properties of low correlation with other Structural Numbers.[15] They correlate negatively with the Asymmetry Numbers indicating that their values are higher among the more symmetrical molecules of octanes.

Table 2. Correlation of the Asymmetry Numbers with the number of branches (N_{br}), with the peripheral number (N_{per}), with the distance number (N_d), with the size of the largest branch (L_{br}), as well as with the branching degrees of octane isomers (Br. Deg.V_L).

Struct. No.	$R\ N_{asym\leftrightarrow}$	$R\ N_{asym\perp}$
N_{per}	0.451	0.166
L_{br}	0.031	0.385
N_d	–0.296	–0.113
N_{br}	0.000	0.067
Br. Deg.V_L	–0.017	0.087

Br. Deg.V_L – Branching degrees derived from the values of the index V_L(–0.126, –0.139, –0.270).[11]

Table 1. Asymmetry Numbers of octane isomers.

	Oct	2M7	3M7	4M7	3Et6	25M6	24M6	23M6	34M6	3Et2M5	22M6	33M6	3Et3M5	234M5	224M5	223M5	233M5	2233M4
$N_{asym\perp}$	0	2	1	0	1	0	1	2	0	1	3	1	0	0	1	2	1	0
$N_{asym\leftrightarrow}$	0	1	1	1	2	0	2	0	0	2	2	2	1	1	3	1	1	0

The correlation of the Asymmetry Numbers with other Structural Numbers are presented in Table 2.

In present stage, there is defined also the Mutually Optimized Contribution of the Structural Numbers (MOC_{SN}) containing the Structural Numbers N_{br}, N_{per}, N_d, L_{br}, $N_{asym\leftrightarrow}$, and $N_{asym\perp}$.

$MOC_{SN} = k_{Nbr} \times N_{br} + k_{Nper} \times N_{per} + k_{Nd} \times N_d + k_{Lbr} \times L_{br} + k_{\leftrightarrow} \times N_{asym\leftrightarrow} + k_{\perp} \times N_{asym\perp}$

In MOC_{SN} there is $\Sigma|k_{Ni}| = 1$.

MOC_{SN} was optimized to each physicochemical property of octanes separately.

The results are presented in Table 3 for the case of the tested physicochemical properties of octanes.

The positive value of a coefficient k_{Ni} means that with increasing value of N_i the value of that physicochemical property increases, whereas the negative value of a coefficient k_{Ni} indicates the decrease.

The optimized MOC_{SN} represents 89.0% of the information regarding branching of octanes contained in Tc/Pc, whereas it represents only 34.3% of the information regarding branching of octanes contained in the critical property αc.

The highest correlation with the optimized MOC_{SN} have the physicochemical properties ($R = 0.994$, $IC \sim 90$) > Tc/Pc > Tc^2/Pc > RON > ($R = 0.990$) > BON > BP/Tc > Pc > ω > ($R = 0.980$, $IC \sim 80$).

The lowest correlation have the critical properties ($R = 0.86$, $IC \sim 50$) > Vc > dc > Zc > αc > ($R = 0.75$, IC ~ 30).

In slightly more than half of tested cases, *i.e.* in 16 out of 29 cases, $|k_{\perp}| > |k_{\leftrightarrow}|$ indicating that the asymmetry perpendicular to the main chain has a higher influence on the value of a physicochemical property of octanes then the asymmetry along the main chain.

This can be observed for Solubility Parameter, the Cohesive Energy Density, the Antoine constant B and ΔHv. In other cases, especially at the critical properties αc, dc and Vc the reverse is true.

As estimated by the absolute value of the factor $|k_{Ni}|$, the contribution of N_{br} is higher than the contribution of other structural features at ($|k_{Nbr}| = 0.7$) > ω > RON > BON > Tc^2/Pc > C > ($|k_{Nbr}| = 0.6$) > MON > BP/Tc > Tc/Pc > R^2 > ΔHv > ($|k_{Nbr}| = 0.5$) > S > Pc > ($|k_{Nbr}| = 0.4$) > d > Vm > ($|k_{Nbr}| = 0.3$) > n_D > A > Zc > ($|k_{Nbr}| = 0.25$).

Table 3. Results of the optimization of the correlation between the MOC_{SN} and the values of tested physicochemical properties of octanes sorted by the Information Content regarding branching,[15] *IC*.

PCP	k_{Nbr}	k_{Nper}	k_{Nd}	k_{Lbr}	$k_{\leftrightarrow}$	$k_{\perp}$	*R*	*S*	*IC* (%)
Tc/Pc	−0.541	0.231	0.003	−0.158	−0.043	0.024	0.9939	0.093	89.0
Tc^2/Pc	−0.635	0.088	−0.031	−0.138	−0.007	−0.101	0.9921	55.791	87.4
RON	0.694	−0.079	−0.006	0.150	0.059	−0.012	0.9916	4.753	87.1
BON	0.640	−0.090	0.023	0.171	0.052	0.024	0.9896	4.944	85.6
BP/Tc	−0.596	0.201	0.066	−0.082	−0.028	0.027	0.9870	0.001	83.9
Pc	0.429	−0.263	−0.027	0.144	0.049	−0.088	0.9858	0.208	83.2
ω	−0.698	0.152	0.075	−0.031	−0.010	−0.034	0.9821	0.007	81.2
MON	0.598	−0.066	−0.017	0.262	0.048	0.009	0.9786	6.945	79.4
d	0.305	−0.256	−0.044	0.192	0.053	−0.150	0.9634	0.003	73.2
Vm	−0.302	0.257	0.045	−0.191	−0.055	0.150	0.9627	0.716	72.9
n_D	0.288	−0.225	−0.086	0.192	0.043	−0.166	0.9616	0.001	72.5
ΔHv	−0.507	−0.086	−0.034	0.124	0.024	−0.225	0.9566	0.064	70.9
BP	−0.240	−0.305	−0.011	0.109	0.086	−0.249	0.9554	1.862	70.5
ST	0.113	−0.343	−0.062	0.199	0.046	−0.237	0.9552	0.269	70.4
Tc	0.197	−0.350	−0.048	0.126	0.081	−0.198	0.9493	2.751	68.6
C	0.608	0.018	−0.180	0.033	−0.119	0.042	0.9488	1.300	68.4
S	−0.498	−0.075	0.200	−0.067	0.106	0.054	0.9440	1.535	67.0
R^2	−0.513	0.073	−0.127	−0.222	0.019	−0.046	0.9402	0.064	65.9
CED	−0.072	−0.247	−0.098	0.252	0.033	−0.298	0.9398	0.001	65.8
Sol.par.	−0.071	−0.246	−0.098	0.253	0.033	−0.299	0.9392	0.001	65.7
B	−0.008	−0.218	−0.221	0.178	−0.068	−0.307	0.9371	9.183	65.1
MR	−0.278	0.299	−0.083	−0.163	−0.090	0.087	0.9028	0.085	60.2
ΔHf°g	0.195	0.343	−0.148	−0.107	−0.124	0.083	0.9055	0.548	57.6
A	−0.260	0.101	−0.189	0.120	−0.145	−0.185	0.9041	0.013	57.2
logVP	0.141	−0.101	0.261	−0.170	0.115	0.212	0.8840	0.083	53.3
Vc	−0.264	0.284	−0.085	−0.157	−0.159	−0.051	0.8551	0.008	48.2
dc	0.262	−0.287	0.085	0.152	0.163	0.051	0.8460	0.005	46.7
Zc	0.257	0.189	−0.170	−0.051	−0.202	−0.131	0.7697	0.005	36.2
αc	−0.243	0.250	−0.219	−0.056	−0.184	−0.048	0.7540	0.095	34.3

The contribution of N_{per} is higher than the contribution of other structural features at ($|k_{Nper}| = 0.4$) > Tc > ΔHf°g > ST > BP > ($|k_{Nper}| = 0.3$) > MR > dc > Vc > αc > ($|k_{Nper}| = 0.2$), thus at the most of the critical properties of octanes.

The contribution of $N_{asym\perp}$ is higher than the contribution of other structural features at B > Sol. par. > CED, all ($|k_{Nasym\perp}| \sim 0.3$).

The contribution of N_d is higher than the contribution of other structural features at logVP only.

The MOC_{SN} was optimized also to some well-known topological indices of octanes in order to see the situation among them. The results are presented in Table 4.

The optimized MOC_{SN} represents 88.2% of the information regarding branching of octanes contained in the Branching degrees[13] derived from the values of index V_L(–0.126, –0.139, –0.270). It represents 87.9% of the information regarding branching of octanes contained in the Wiener[1] index W, whereas it represents only 50.8% of the information regarding branching of octanes contained in the index p4.

5. Discussion

Interestingly, the best correlation to the individually optimized MOC_{SN} has the physicochemical property Tc/Pc (R = 0.9939, IC = 89.0%), closely followed by the Branching Degrees[13] derived from the values of the index V_L(–0.126, –0.139, –0.270) (R = 0.9930, IC = 88.2%), the Wiener[1] index W (R = 0.9926, IC = 87.9%), the index[16] RW (R = 0.9924, IC = 87.7%), and index[18] p2/w2 (R = 0.9910, IC = 86.6%), whereas the Randić[17] index χ correlates to R = 0.9764, IC = 78.4% and the Hosoya[2] index Z to R = 0.9755, IC = 78.0% . Among the path indices,[18] the correlation to the individually optimized MOC_{SN} is p3 > p2 > p5 > p4, and p2/w2 > p3/w3 > p5/w5 > p4/w4 as well as p2/w2 > p2, p3 > p3/w3, p4/w4 > p4, p5 > p5/w5.

Whereas at Tc/Pc the magnitude of the optimized factors $|k_{Ni}|$ is $|k_{Nbr}| > |k_{Nper}| > |k_{Lbr}| > |k_{Nasym\leftrightarrow}| > |k_{Nasym\perp}| > |k_{Nd}|$, at V_L(–0.126, –0.139, –0.270) it is $|k_{Nbr}| > |k_{Nper}| > |k_{Nasym\leftrightarrow}| > k_{Nd}| > |k_{Lbr}| > |k_{Nasym\perp}|$, at W it is $|k_{Nbr}| > |k_{Lbr}| \sim |k_{Nper}| > |k_{Nasym\perp}| > |k_{Nasym\leftrightarrow}| > |k_{Nd}|$, at RW it is $|k_{Nbr}| > |k_{Nper}| > |k_{Lbr}| > k_{Nd}| > |k_{Nasym\perp}| > |k_{Nasym\leftrightarrow}|$, at the Randić[17] index χ it is $|k_{Nbr}| > |k_{Lbr}| \sim |k_{Nper}| > |k_{Nd}| > |k_{Nasym\perp}| > |k_{Nasym\leftrightarrow}|$ and at the Hosoya[2] index Z it is $|k_{Nbr}| > |k_{Lbr}| > |k_{Nper}|| > |k_{Nasym\perp}| > |k_{Nd}> |k_{Nasym\leftrightarrow}|$.

Information contribution of the Structural Numbers N_{br}, N_{per}, N_d, L_{br}, $N_{asym\leftrightarrow}$, and $N_{asym\perp}$ to the values of physicochemical properties of octanes as measured by the product $IC\times|k_{Ni}|$ (%) is presented in Table 4 and illustrated in Figure 1.

In Table 4 and Figure 1 we can see that in the case of octanes the highest observed contributions of tested Structural Numbers are as follows. The Number of Branches contributes up to 60.4% of the Information Content (the case of RON). The Peripheral Number contributes up to 24.1% of the Information Content (the case of surface tension). The Size of the Largest Branch contributes up to 20.8% of the Information Content (the case of MON). The Asymmetry Number $N_{asym\perp}$ contributes up to 20.0% of the Information Content (the case of the Antoine constant B). The Asymmetry number $N_{asym\leftrightarrow}$, on the other hand, contributes only up to 8.3% of the Information Content (the case of the Antoine constant A). The maximum contributions are thus at $N_{br} >> N_{per} > L_{br} > N_{asym\perp} > N_d > N_{asym\leftrightarrow}$.

The contributions in particular physicochemical properties are quite varying. The Number of Branches in octanes contributes the most to the values of physicochemical properties (in %; total IC = 100%): 61 > RON > ω > Tc^2/Pc > BON > BP/Tc > 50, and the least to the values of physicochemical properties: 10 > Zc > αc > Surface Tension > logVP > CED > Sol. par. > B > 0.5. The Peripheral number contributes in general much less, the most to the values of physicochemical properties (in %): 25 > Surface Tension > Tc > Pc > BP > Tc/Pc > 20, and the least to the

Table 4. Results of optimization of the correlation between the MOC_{SN} and the values of some topological indices of octanes. The values of topological indices of octanes were taken from Ref. [1,2,13,16-18]

Index	k_{Nbr}	k_{Nper}	k_{Nd}	k_{Lbr}	$k_{Nasim\leftrightarrow}$	$k_{Nasim\perp}$	R	S	IC (%)
Br. Deg.V_L	0.669	–0.108	–0.063	0.053	0.082	0.025	0.9930	0.062	88.2
W	–0.554	0.181	0.003	–0.188	0.015	–0.059	0.9926	0.808	87.9
RW	0.634	–0.163	–0.053	0.085	0.021	0.044	0.9924	0.070	87.7
χ	–0.552	–0.141	0.118	0.145	0.007	0.037	0.9764	0.037	78.4
Z	–0.459	–0.152	0.075	0.190	0.032	–0.092	0.9755	1.009	78.0
p2	0.689	0.005	–0.154	–0.102	–0.015	0.035	0.9704	0.365	75.8
p3	0.321	–0.273	0.015	0.194	0.082	–0.115	0.9765	0.334	78.5
p4	–0.363	0.083	0.168	–0.030	–0.060	0.296	0.8703	0.657	50.8
p5	–0.471	0.326	–0.021	0.021	–0.030	–0.131	0.9351	0.505	64.6
p2/w2	0.781	0.012	–0.098	–0.066	–0.008	–0.035	0.9910	0.007	86.6
p3/w3	0.232	–0.284	0.035	0.231	0.095	–0.123	0.9561	0.017	70.7
p4/w4	–0.356	–0.093	0.172	0.175	0.015	0.189	0.9024	0.014	56.9
p5/w5	–0.472	0.316	–0.032	0.027	–0.028	–0.125	0.9287	0.008	62.9

Table 4. Information contribution of the Structural Numbers N_{br}, N_{per}, N_d, L_{br}, $N_{asym\leftrightarrow}$, and $N_{asym\perp}$ to the values of physicochemical properties of octanes as measured by the product $IC\times|k_{Ni}|$ (%) and sorted by *IC*.

PCP	$IC\times\|k_{Nbr}\|$	$IC\times\|k_{Nper}\|$	$IC\times\|k_{Nd}\|$	$IC\times\|k_{Lbr}\|$	$IC\times\|k_{Nasym\leftrightarrow}\|$	$IC\times\|k_{Nasym\perp}\|$	*IC* (%)
Tc/Pc	48.2	20.6	0.3	14.1	3.8	2.1	89.0
Tc^2/Pc	55.5	7.7	2.7	12.1	0.6	8.8	87.4
RON	60.4	6.9	0.5	13.1	5.1	1.0	87.1
BON	54.8	7.7	2.0	14.6	4.5	2.1	85.6
BP/Tc	50.0	16.9	5.5	6.9	2.3	2.3	83.9
Pc	35.7	21.9	2.2	12.0	4.1	7.3	83.2
ω	56.7	12.3	6.1	2.5	0.8	2.8	81.2
MON	47.5	5.2	1.4	20.8	3.8	0.7	79.4
d	22.3	18.7	3.2	14.1	3.9	11.0	73.2
Vm	22.0	18.7	3.3	13.9	4.0	10.9	72.9
n_D	20.9	16.3	6.2	13.9	3.1	12.0	72.5
ΔHv	35.9	6.1	2.4	8.8	1.7	15.9	70.9
BP	16.9	21.5	0.8	7.7	6.1	17.5	70.5
ST	8.0	24.1	4.4	14.0	3.2	16.7	70.4
Tc	13.5	24.0	3.3	8.6	5.6	13.6	68.6
C	41.6	1.2	12.3	2.3	8.1	2.9	68.4
S	33.4	5.0	13.4	4.5	7.1	3.6	67.0
R^2	33.8	4.8	8.4	14.6	1.3	3.0	65.9
CED	4.7	16.3	6.5	16.6	2.2	19.6	65.8
Sol.par.	4.7	16.2	6.4	16.6	2.2	19.6	65.7
B	0.5	14.2	14.4	11.6	4.4	20.0	65.1
MR	16.7	18.0	5.0	9.8	5.4	5.2	60.2
ΔHf°g	11.2	19.7	8.5	6.2	7.1	4.8	57.6
A	14.9	5.8	10.8	6.9	8.3	10.6	57.2
logVP	7.5	5.4	13.9	9.1	6.1	11.3	53.3
Vc	12.7	13.7	4.1	7.6	7.7	2.5	48.2
dc	12.2	13.4	4.0	7.1	7.6	2.4	46.7
Zc	9.3	6.8	6.1	1.8	7.3	4.7	36.2
αc	8.3	8.6	7.5	1.9	6.3	1.6	34.3

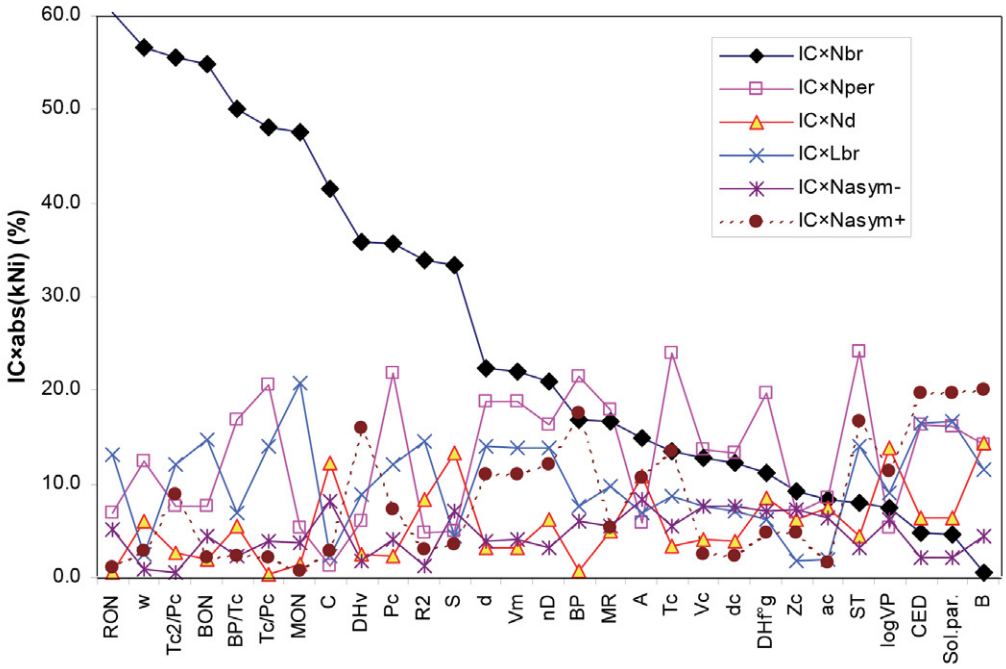


Figure 1. Information contribution of the Structural Numbers N_{br}, N_{per}, N_d, L_{br}, $N_{asym\leftrightarrow}$, and $N_{asym\perp}$ about the values of physicochemical properties of octanes as measured by the product $IC\times|k_{Ni}|$ (%) and sorted by the contribution of the Number of Branches.

values of physicochemical properties: 6 > A > logVP > MON > S > R^2 > C > 1. The Distance number contributes less, the most to the values of physicochemical properties (in %): 15 > B > logVP > S > C > A > 10, and the least to the values of physicochemical properties: 2 > BON > MON > BP > RON > Tc/Pc > 0.1.

The Size of the Largest Branch contributes the most to the values of physicochemical properties (in %): 21 > MON > Sol. par. > CED > 15, and the least to the values of physicochemical properties: 7 > BP/Tc > A > ΔHf°g > S > ω > C > αc > Zc > 1.

The Asymmetry number $N_{asym\leftrightarrow}$ contributes the most to the values of physicochemical properties (in %): 9 > A > C > Vc > dc > Zc > ΔHf°g > S > 7, and the least to the values of physicochemical properties: 3 > BP/Tc > CED > Sol. par. > ΔHv > R^2 > ω > Tc^2/Pc > 0.5.

The Asymmetry number $N_{asym\perp}$ contributes the most to the values of physicochemical properties (in %): 20 > B > Sol. par. > CED > BP > Surface Tension > ΔHv > 15, and the least to the values of physicochemical properties: 2.5 > Vc > dc > BP/Tc > Tc/Pc > BON > αc > RON > MON > 0.5.

In most cases (with exception of Tc/Pc, Tc^2/Pc, and RON) the structural numbers in form of the optimized MOC_{SN} do not suffice the criterion that for a useful correlation, $R > 0.99$ must be obtained.[19]

To obtain better correlations, the mutually optimized combinations of vertex-degree vertex-distance weighted elements of the Universal matrix and vertex-degree weighted path indices are to be used.[15,20-22]

As shown above, the values of the mutually optimized factors k_{Ni} as well as of products $IC\times|k_{Ni}|$ are useful for the structural interpretation of the values of physicochemical properties of octanes, as well. Whereas in the best case, i.e. at Tc/Pc there they explain 89.0% of the information regarding branching of octanes (48.2% is explained by N_{br}, 20.6% by N_{per}, 14.1% by L_{br}, 3.8% by $N_{asym\leftrightarrow}$, 2.1% by $N_{asym\perp}$, and only 0.3% by N_d), in the worst observed case, i.e. at the critical property αc there is explained only 34.3% of the information regarding branching of octanes (8.6% is explained by N_{per}, 8.3% by N_{br}, 7.5% by N_d, 6.3% by $N_{asym\leftrightarrow}$, 1.9% by L_{br}, and 1.6% by $N_{asym\perp}$).

The mutually optimized factors k_{Ni} as well as the products $IC\times|k_{Ni}|$ contribute thus to the structural interpretation of the values of physicochemical properties of octanes to different extents at different physicochemical properties of octanes. After determining their contribution, in most cases additional factors are to be sought for.

The situation for physicochemical properties of octanes Tc/Pc, d, MR, dc, and Tc is illustrated in Figure 2. It is presented as the difference between the experimental values of the physicochemical properties of octanes and the values calculated using mutually optimized contribution of all the tested Structural features reduced by the average of the experimental values of physicochemical properties of octanes.

In the case of Tc/Pc, for example, where IC = 89.0%, there remains open the question why at the octane isomers 3M7, 3Et6, 24M6, 3Et2M5, 22M6, 234M5, and 2233M4 the calculated values almost fit the experimental ones,

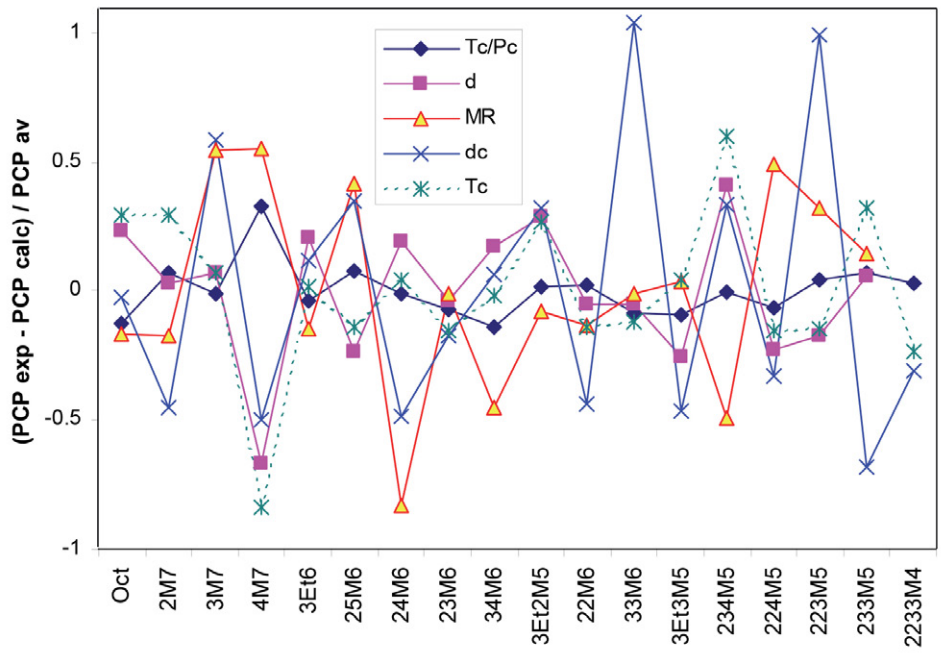


Figure 2. Reduced differences between the experimental values of the physicochemical properties of octanes and the values calculated using mutually optimized contribution of all the tested Structural features.

whereas at 4M7, 25M6, 233M5 the experimental values are higher than the calculated ones, and at Oct, 34M6, 33M6, 3Et3M5, and 224M5 they are lower.

Another example is e.g. dc, where *IC* = 46.7%. There remains open the question why at the octane isomers the calculated values almost fit the experimental ones only at Oct and 34M6, whereas at 3M7, 25M6, 2Et3M5, and especially at 33M6 and 223M5 the experimental values are higher than the calculated ones, and at 2M7, 4M7, 24M6, 22M6, 3Et3M5, 224M5, and 233M5 they are lower. This situation calls for additional study.

5. References

1. H. Wiener, *J. Am. Chem. Soc.* **1947**, *69*, 17–20. **DOI:**10.1021/ja01193a005
2. H. Hosoya, *Bull. Chem. Soc. Jpn*. **1971**, *44*, 2332–2339. **DOI:**10.1246/bcsj.44.2332
3. H. Hosoya, *Internet Electron. J. Mol. Des.* **2002**, *1*, 428–442.
4. E. C. Kirby, *J. Chem. Inf. Comput. Sci.* **1994**, *34*, 1030–1035. **DOI:**10.1021/ci00021a001
5. D. H. Rouvray, *J. Comput. Chem.* **1987**, *8*, 470–480. **DOI:**10.1002/jcc.540080427
6. D. Bonchev, N. Trinajstić, *J. Chem. Phys.* **1977**, *67*, 4517–4533. **DOI:**10.1063/1.434593
7. D. Bonchev, *J. Mol. Struct. (Theochem)* **1995**, *336*, 137–156. **DOI:**10.1063/1.434593
8. M. Randić, *Acta Chim. Slov.* **1997**, *44*, 57–77.
9. L. Lovasz, J. Pelikan, *Period Math Hung.* **1973**, *3*, 175–182. **DOI:**10.1007/BF02018473
10. D. M. Cvetković, I. Gutman, *Croat. Chem. Acta* **1977**, *49*, 115–121.
11. M. Randić, C. L. Wilkins, *J. Phys. Chem.* **1979**, *83,* 1525–1540. **DOI:**10.1021/j100474a032
12. A. Perdih, *Indian J. Chem.* **2003**, *42A*, 1246–1257.
13. A. Perdih, *Acta Chim. Slov*. **2016**, *63*, 411–415. **DOI:**10.17344/acsi.2015.1607
14. A. Perdih, M. Perdih, *Acta Chim. Slov*. **2000**, *47*, 231–259. **DOI:**10.17344/acsi.2015.1607
15. A. Perdih, *Acta Chim. Slov.* **2015**, *62*, 879–888. **DOI:**10.17344/acsi.2015.1607
16. M.V. Diudea, *J. Chem. Inf. Comput. Sci.* **1997**, *37*, 292–299. **DOI:**10.1021/ci960037w
17. M. Randić, *J. Am. Chem. Soc.* **1975**, *97*, 6609–6615. **DOI:**10.1021/ja00856a001
18. M. Randić, *J. Chem. Inf. Comput. Sci.* **2001**, *41*, 607–613. **DOI:**10.1021/ci0001031
19. Z. Mihalić, N. Trinajstić, *J. Chem. Educ.* **1992**, *69*, 701–712. **DOI:**10.1021/ed069p701
20. A. Perdih, *Acta Chim. Slov.* **2016**, *63*, 88–96. **DOI:**10.17344/acsi.2015.1975
21. A. Perdih, *Acta Chim. Slov.* **2016**, *63*, 411–415. **DOI:**10.17344/acsi.2016.2361
22. A. Perdih, *Acta Chim. Slov.* **2019**, *66*, 726–731. **DOI:**10.17344/acsi.2019.5346

Povzetek

S strukturnimi števili so bile kvantificirane strukturne značilnosti izomer oktana. Za ugotovitev, kolikšen del vsebine podatkov o fizikokemijskih lastnosti oktanov nam dajejo strukturna števila, je bil razvit način, kako določiti hkratno optimiziran doprinos strukturnih števil (MOC_{SN}). Poleg drugih strukturnih števil predstavljenih prej, sta uvedeni še števili, ki predstavljata merili za nesimetričnost izomer oktana. Eno predstavlja nesimetričnost vzdolž glavne osi molekule, drugo pa nesimetričnost pravokotno nanjo. Njuni korelaciji z vrednostmi 29 fizikokemijskih lastnosti oktanov sta nizki, $|R| < 0.6$. Po optimizaciji vsebuje MOC_{SN} od 34.3 % do 89.0 % informacije vsebovane v fizikokemijskih lastnostih oktanov. Strukturna števila omogočajo prvi korak k strukturni razlagi fizikokemijskih lastnosti oktanov. V 17 od 29 primerov največ informacij poda število vej, v 8 primerih periferno število, v 3 primerih eno od števil nesimetričnosti in v enem primeru število razdalj med vejami.

Except when otherwise noted, articles in this journal are published under the terms and conditions of the Creative Commons Attribution 4.0 International License

DOI: 10.17344/acsi.2020.6237 *Acta Chim. Slov.* **2021,** *68,* 144–150
creative commons

Scientific paper

Structure of Biologically Active Benzoxazoles: Crystallography and DFT Studies

Una Glamočlija,[1,2,*] Selma Špirtović-Halilović,[3] Mirsada Salihović,[4] Iztok Turel,[5] Jakob Kljun,[5] Elma Veljović,[3] Selma Zukić[3] and Davorka Završnik[3]

[1] *Department for Biochemistry and Clinical Analysis, Faculty of Pharmacy, University of Sarajevo, Zmaja od Bosne 8, 71000 Sarajevo, Bosnia and Herzegovina*

[2] *School of Medicine, University of Mostar, Zrinskog Frankopana 34, Mostar 88000, Bosnia and Herzegovina*

[3] *Department of Pharmaceutical Chemistry, Faculty of Pharmacy, University of Sarajevo, Zmaja od Bosne 8, 71000 Sarajevo, Bosnia and Herzegovina*

[4] *Department of Natural science, Faculty of Pharmacy, University of Sarajevo, Zmaja od Bosne 8, 71000 Sarajevo, Bosnia and Herzegovina*

[5] *Faculty of Chemistry and Chemical Technology, University of Ljubljana, Večna pot 113, 1000 Ljubljana, Slovenia*

* *Corresponding author: E-mail: una.glamoclija@ffsa.unsa.ba,*

Received: 07-02-2020

Abstract

Using X-ray single crystal diffraction, the crystal structures of biologically active benzoxazole derivatives were determined. DFT calculation was performed with standard 6-31G*(d), 6-31G** and 6-31+G* basis set to analyze the molecular geometry and compare with experimentally obtained X-ray crystal data of compounds.

The calculated HOMO-LUMO energy gap in compound **2** (2-(2-hydroxynaphtalen-1-yl)-4-methyl-7-isopropyl-1,3-benzoxazol-5-ol) is 3.80 eV and this small gap value indicates that compound **2** is chemically more reactive compared to compounds **1** (4-methyl-2-phenyl-7-isopropyl-1,3-benzoxazol-5-ol) and **3** (2-(4-chlorophenyl)-4-methyl-7-isopropyl-1,3-benzoxazol-5-ol). The crystal structures are stabilized by both intra- and intermolecular hydrogen bonds in which an intermolecular O–H···N hydrogen bond generates N3 and O7 chain motif in compounds **1**, **2**, and **3**, respectively. The calculated bond lengths and bond angles of all three compounds are remarkably close to the experimental values obtained by X-ray single crystal diffraction.

Keywords: Benzoxazole; X-ray diffraction; DFT calculation

1. Introduction

Benzoxazoles are compounds with a wide range of biological activities and represent a very important structural motif in medicinal chemistry. Benzoxazole ring can be found in natural and synthetic compounds used as pharmaceuticals.[1] Caboxamycin (Figure 1a) is a new antibiotic of the benzoxazole family produced by the deep-sea strain *Streptomyces* sp. NTK 937.[2] Figure 1b presents the synthetic compound with a two times better *Pseudomonas aeruginosa* inhibitory activity than ampicillin and streptomycin.[3] Benzoxazoles have anti-inflammatory,[4] antimicrobial,[5–7] and antitumor[6–10] activities.

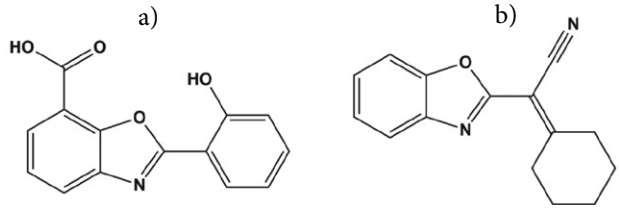
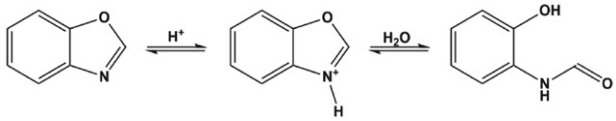


Figure 1. Structure of Caboxamycin (a) and (b) a synthetic derivative of benzoxazole.

Benzoxazoles have a certain structural similarity with nucleic bases such as adenine and guanine, and they interact with biopolymers in living organisms.[2] The mole-

cule is planar with conjugated sextets of π electrons in the cyclic system.[11] They have aromatic properties and are quite stable. Benzoxazoles are sensitive to hydrolysis which leads to ring-opening. Depending on substituents, different conditions of media and pH values lead to hydrolysis.[11–14] While unsubstituted benzoxazole is resistant to hydrolysis in alkaline medium, rapid hydrolysis occurs in acidic medium, probably due to nucleophilic attack (Scheme 1).[11] Hydrolysis can be seen *in vivo*, as Bray *et al.* (1952) have shown in experiments on rabbits. They evaluated the metabolism of benzoxazole, 2-methylbenzoxazole, and 2-phenylbenzoxazole and found that the stability of the ring depends on substituents. Benzoxazole and 2-methylbenzoxazole mainly hydrolyzed in organisms while the ring in 2-phenylbenzoxazole is stable and mainly metabolized by hydroxylation of phenyl group at the position 2'.[12]



Scheme 1. Hydrolysis of benzoxazole ring in acidic conditions.

Hydrolysis of drugs containing benzoxazole rings can have pharmaceutical importance. It can result in the formation of active compounds that can be directly delivered to the site of interest.[13] The stability and reactivity of benzoxazoles are crucial for their medicinal applications. Density functional theory (DFT) is a very common computational method used to solve Schrödinger and Dirac equations.[15]

In our previous paper,[16] a library of thymoquinone-derived benzoxazoles has been synthesized and their antiproliferative activities were reported. The starting compound for synthesis was thymoquinone that reacted with sodium azide to obtain aminothymoquinone (ATQ). ATQ reacted with aromatic aldehydes to obtain benzoxazoles. Out of the 10 novel compounds prepared,[16] in this paper, the structures of three compounds: **1** (4-methyl-2-phenyl-7-isopropyl-1,3-benzoxazole-5-ol), **2** (2-(2-hydroxynaphtalen-1-yl)-4-methyl-7-isopropyl-1,3-benzoxazole-5-ol), and **3** (2-(4-chlorophenyl)-4-methyl-isopropyl-1,3-benzoxazole-5-ol) are in the focus. Synthetic details, analytical and spectroscopic data of compounds can be found in our previous paper.[16]

The simultaneous approach of X-ray crystallography and DFT calculation is used. This approach takes advantage of the great interpretive power of theoretical studies and the precision of the experimental method. We report the crystal structure of benzoxazole derivatives, as well as results of theoretical studies using the DFT(B3LYP) method and standards 6-31G*(d), 6-31G** and 6-31+G* basis set. The aim of the present work was to describe and characterize the molecular structure and some electronic structure properties of the biologically active benzoxazole derivatives by using two approaches: experimental, using X-ray crystallography, and theoretical, using DFT calculation. Finally, the results of the two approaches are compared.

2. Experimental

2. 1. Crystallographic Data Collection

X-ray diffraction data for all compounds was collected on an Oxford Diffraction SuperNova diffractometer with Cu microfocus X-ray source with mirror optics and an Atlas detector. The structures were solved by direct methods implemented in SHELXT[17] and refined by a full-matrix least-squares procedure based on F^2 using SHELXL[18] within the Olex2 program pack.[19] All non-hydrogen atoms were refined anisotropically. The hydrogen atoms were placed at calculated positions and treated using appropriate riding models. The programs Platon and Mercury were used for data analysis and figure preparation.[20,21] The crystal structures have been submitted to the CCDC and have been allocated the deposition numbers 1586630, 1985495, 1985496.

2. 2. Computational Details

The molecular structures of compounds **1**, **2** and **3** were subjected to quantum chemical density functional calculation using the Becke-3Lee-Yang-Parr (B3LYP) hybrid functional with the standards 6-31G*(d), 6-31G** and 6-31+G* basis set. The computations were performed using Spartan 14. The structures are minima on potential energy surface. The calculated values were compared with the obtained experimental results.

3. Results and Discussion

The crystal data and structure refinement of compounds **1**, **2** and **3** are given in Table 1 and shown in Figure 2. The selected geometric parameters of the same compounds are given in Table 2. The structural parameters were calculated and are presented in Table 3. The crystal structure of compound **1** (4-methyl-2-phenyl-7-isopropyl-1,3-benzoxazole-5-ol) has been determined by X-ray diffraction in our previous paper.[16] Previous crystallographic results for this compound are used in this paper for comparison with the DFT results.

The calculated bond lengths and bond angles of **1**, **2** and **3** are remarkably close to the experimental values obtained by X-ray crystal diffraction.

3. 1. Geometrical Parameters Analysis

Bond lengths of compounds **1, 2** and **3** are in the normal range.[22] The experimentally obtained value of av-

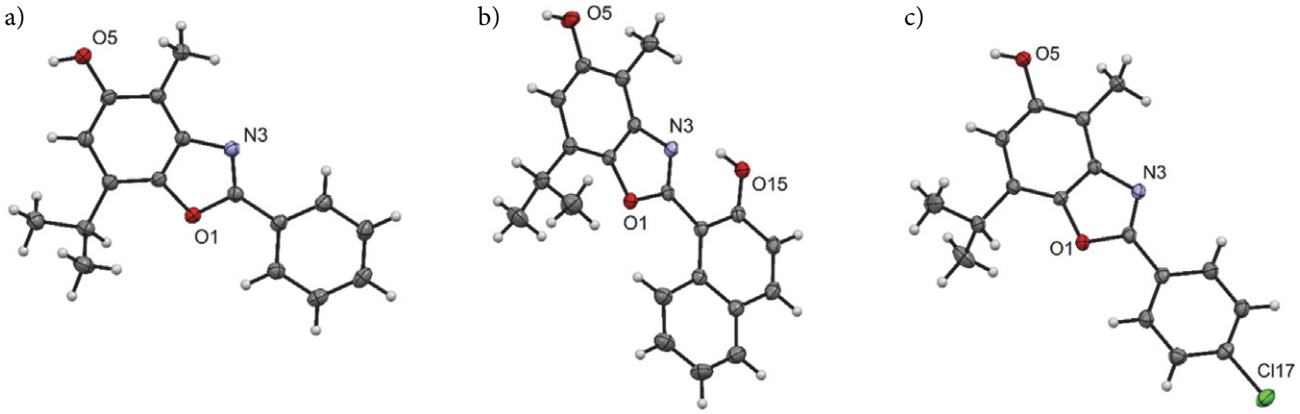


Figure 2. Crystal structures of compounds **1** (a),[16] **2** (b), and **3** (c) with heteroatom labelling. Thermal ellipsoids are drawn at 50% probability level.

erage mean bond distances were of C–C = 1.425 Å, C–O =1.373 Å, C–N = 1.353 Å, for compound **1**,[16] C–C = 1.424 Å, C–O =1.366Å, C–N = 1.348 Å, for compound **2** and C–C = 1.424 Å, C–O =1.373Å, C–N = 1.355 Å, for compound **3** respectively, shown in Table 3. The bond distances of C2=N3 are 1.302 Å, 1.307 Å and 1.303 Å for compounds **1**, **2** and **3**, respectively. They are comparable with the reported double bond lengths.[23] The theoretically obtained value of average mean bond distances were of C–C = 1.433 Å, C–O =1.373 Å, C–N = 1.347 Å, for compound **1**, C–C = 1.433 Å, C–O =1.366 Å, C–N = 1.353 Å, for compound **2** and C–C = 1.432 Å, C–O =1.376 Å, C–N = 1.346 Å, for compound **3**, respectively (Table 3). Experimentally obtained bond distances of C2=N3 show 1.302 Å (cal. 1.302 Å), 1.307 Å (cal. 1.318 Å) and 1.303 Å (cal. 1.301 Å), for compounds **1**, **2** and **3**, respectively. In addition to that, all three compounds display the electron delocalization over the atoms of O1–C2–N3. In all three compounds, the sum of bond angles around the C2 atom of the benzoxazole ring (O1–C2–N3, O1–C2–C14, and N3–C2–C14 = 359.99° (cal. 360.01°) for compound **1**, 359.98° (cal. 359.99°) for compound **2** and 359.98° (cal. 360.00°) for compound **3**) indicates sp^2 hybridization and the bond an-

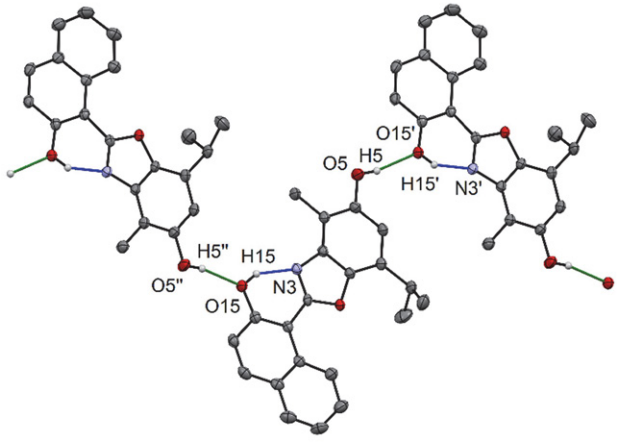


Figure 3. Hydrogen bond network in the crystal structure of 2. The hydroxyl group in position 5 forms intermolecular hydrogen bonds (green) with the O15 oxygen on the naphthyl group (O5–H5···O15') which in turn forms an intramolecular hydrogen bond (blue) with the neighboring benzoxazole N3 nitrogen atom (O15–H15···N3). Thermal ellipsoids are drawn at 50% probability level and non-relevant hydrogen atoms are omitted.

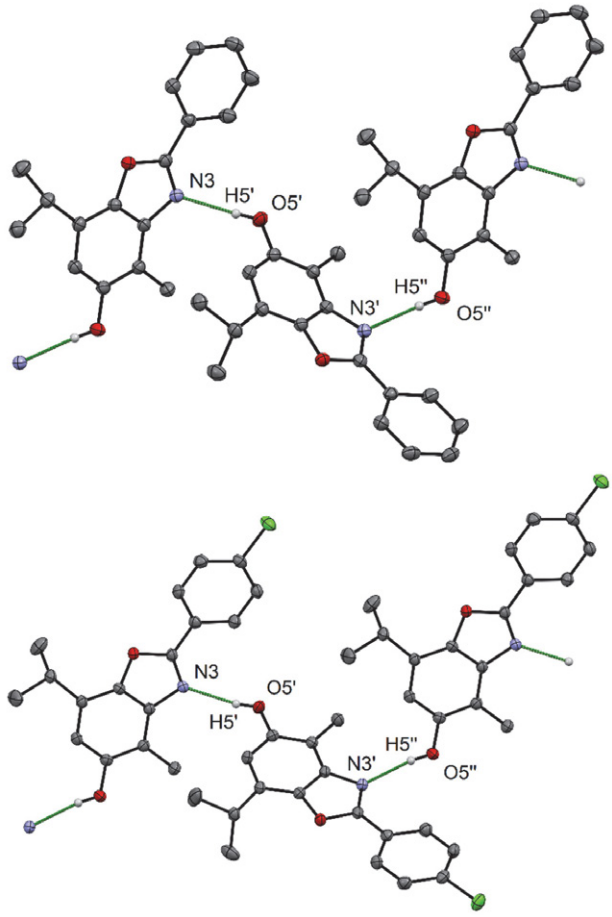


Figure 4. Hydrogen bond network in the crystal structures of compounds **1** (top) and **3** (bottom). The hydroxyl group in position 5 forms intermolecular hydrogen bonds (green) with the benzoxazole N3 nitrogen (O5'–H5'···N3). Thermal ellipsoids are drawn at 50% probability level and non-relevant hydrogen atoms are omitted.

Table 1. Crystal data and structure refinement summary of compounds **2** and **3**

Compound	2	3
Empirical formula	$C_{21}H_{19}NO_3$	$C_{17}H_{16}ClNO_2$
M_w	333.37	301.76
T, K	150(2)	150(2)
Crystal system	monoclinic	monoclinic
Space group	$P\,2_1/n$	$P\,2_1/n$
a, Å	6.7961(2)	8.3718(2)
b, Å	15.9766(4)	16.2112(1a)
c, Å	15.7268(4)	11.7098(1a)
α, deg.	90	90
β, deg.	97.488(2)	110.472(2)
γ, deg.	90	90
V, Å^3	1693.03(8)	1488.85(6)
Z	4	4
D_{calc}, g/cm^3	1.308	1.346
μ, mm^{-1}	0.705	2.300
F(000)	704	632
Crystal size, mm	0.60×0.10×0.10	0.20×0.20×0.20
Color	colorless	yellow
Data collected / unique	5939 / 3190	5382 / 5382
R_{int}/R_{sigma}	0.0359 / 0.0452	0.0195 / 0.0249
Restraints / parameters	0 / 231	0 / 194
S	1.059	1.043
R_1, wR_2 [I > 2σ(I)]	0.0595 / 0.1431	0.0371 / 0.1010
R_1, wR_2 (all data)	0.0690 / 0.1558	0.0404 / 0.1047
Larg. diff. peak/hole (e·Å^{-3})	0.35 / –0.58	0.28 / –0.33

gle of C2–N3–O1, C9–C8–C7, and C8–C9–C4 deviates from 120° due to the presence of substituents.

3. 2. Intra- and Intermolecular Interactions and Crystal Packing Analysis

The crystal structures of compounds **1**, **2** and **3** are stabilized *via* intramolecular O–H···N hydrogen bond and intermolecular O–H···N, O–H···O, and O–H···N hydrogen bonds (Table 2). The crystal structure of compound **2** is stabilized by intramolecular O15–H15···N3 hydrogen bond, in which the hydroxylic O15 acts as a donor and makes a hydrogen bond with imine N3 with the bond length of 2.477 Å (Figure 3).

The crystal packing is stabilized by one intramolecular O15–H15···N3 hydrogen bond with the bond distances of 2.477 Å (cal. 2.640 Å), whereas in compounds **1**, **2** and **3**, three intermolecular hydrogen bonds contribute to crystal packing such as O5–H5···N3 with the bond distances of 2.811 Å (2.850 Å), O15–H15···O15 2.711 Å (cal. 2.900 Å) and O5–H5···N3 2.800 Å (2.850 Å), respectively. Atom N3 acts as a hydrogen bond acceptor for O–H···N [O5–H5···N3] contacts (Figure 4).

Crystal data and structure refinement summary of compounds **2** and **3** are given in Table 1.

The same data for compound **1** are presented in our previous paper.[16]

Table 2. Selected distances and angles

Compound	Cpd (D–H···A)	type	d(D–H) (Å)		d(D···A) (Å)		d(H···A) (Å)		φ(D–H···A) (°)	
			Exp.	Calc.	Exp.	Calc.	Exp.	Calc.	Exp.	Calc.
1	(O5–H5···N3)	inter	0.84	0.90	2.8105	2.8500	1.97	1.90	175	172.9
2	(O5–H5···O15)	inter	0.84	0.90	2.7108	2.9000	1.88	2.00	168	166.5
2	(O15–H15···N3)	*intra*	0.84	0.90	2.4772	2.6400	1.72	1.74	149	147.0
3	(O5–H5···N3)	inter	0.84	0.90	2.8004	2.8500	1.97	1.87	170	174.0

Table 3. Bond lengths [A] and angles [deg] of compounds 1, 2 and 3

Bond length and angles	Compound 1			Compound 2			Compound 3		
	Exp.	Cal.		Exp.	Cal.		Exp.	Cal.	
	6-31G(d)	6-31G**	6-31+G*	6-31G(d)	6-31G**	6-31+G*	6-31G(d)	6-31G**	6-31+G*
O(1)-C(2)	1.364	1.370	1.371	1.369	1.363	1.365	1.362	1.367	1.370
O(5)-C(5)	1.368	1.371	1.372	1.371	1.361	1.369	1.370	1.366	1.369
C(9)-N(3)	1.403	1.395	1.394	1.396	1.388	1.387	1.389	1.406	1.400
C(2)-N(3)	1.302	1.302	1.303	1.301	1.307	1.308	1.307	1.303	1.301
C(2)-C(14)	1.461	1.460	1.461	1.360	1.458	1.454	1.455	1.457	1.456
O(5)-C(5)-C(4)	116.53	115.90	115.92	115.95	116.44	115.80	115.83	116.44	120.01
C(8)-C(9)-N(3)	108.29	108.89	108.90	108.91	107.76	107.95	107.96	108.22	108.80
C(4)-C(9)-N(3)	130.16	129.63	129.65	129.67	129.42	130.09	130.10	130.42	129.90
N(3)-C(2)-O(1)	114.97	114.89	114.90	114.91	113.79	113.53	113.55	114.83	114.87
N(3)-C(2)-C(14)	127.83	127.51	127.53	127.55	123.26	124.73	124.74	128.55	127.73
O(1)-C(2)-C(14)	117.19	117.60	117.61	117.59	122.93	121.99	122.00	116.60	117.56

Table 4. Calculated HOMO and LUMO energy values in compounds **1**, **2** and **3**

Parameters	Compound								
	1			**2**			**3**		
	6-31G*(d);	6-31G**;	6-31+G*	6-31G*(d);	6-31G**;	6-31+G*	6-31G*(d);	6-31G**;	6-31+G*
E_{HOMO} (eV)	−5.61	−5.61	−5.62	−5.40	−5.42	−5.44	−5.71	−5.73	−5.74
E_{LUMO} (eV)	−1.33	−1.34	−1.35	−1.61	−1.62	−1.63	−1.55	−1.57	−1.58
Energy gap (Δ)	4.28	4.27	4.27	3.79	3.80	3.81	4.16	4.16	4.16

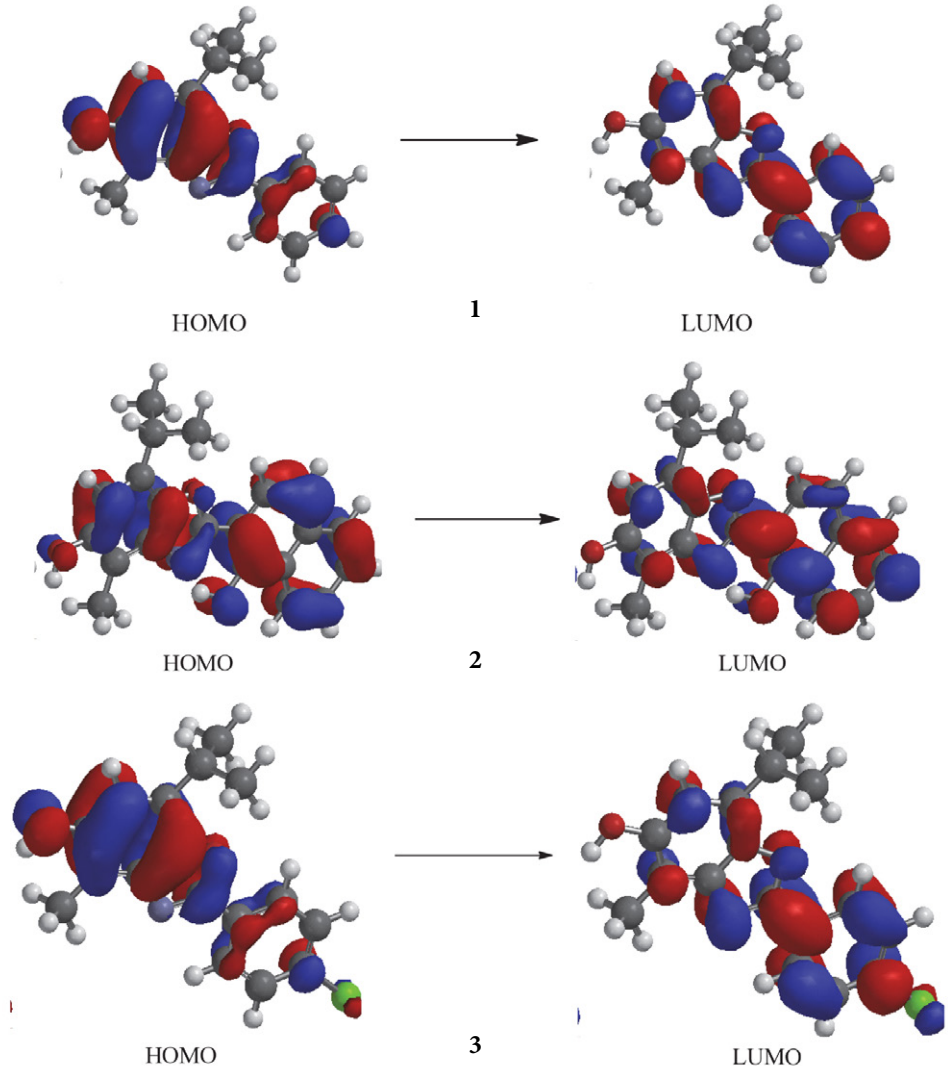


Figure 5. Atomic orbitals of HOMO to LUMO transition of the compounds **1**, **2** and **3**

3. 3. Molecular Orbital Analysis

The HOMO-LUMO energy gap of a molecule will play a crucial role in deciding its bioactive properties and is a very important parameter for quantum chemistry. The HOMO energy distinguishes the capacity of electron donor, whereas LUMO energy characterizes the capacity of electron acceptor, and the gap distinguishes the chemical stability.[24]biologically active methylxanthines were investigated. All calculations were performed at B3LYP/6-31G* level of theory. The electronic chemical potential, highest occupied molecular orbital (HOMO The HOMO-LUMO energy gap for the compounds **1**, **2** and **3** was calculated by 6-31G*(d) basis set and the values are 4.27 eV for compound **1**, 3.80 eV for compound **2** and 4.15 eV for compound **3**. The energies of HOMO and LUMO and the HOMO-LUMO energy gap are given in Table 4. The HOMO-LUMO orbital scheme of compounds **1**, **2** and **3** are shown in Figure 5 (positive phases are red and the negatives ones are blue). The value of the HOMO and LUMO energy gap in compound **2** is the smallest, indicating that the molecule is more stable compared to

compounds **3** and **1**. The lower value of the HOMO and LUMO energy gap explains the eventual charge transfer interaction taking place within the molecules.[25] The HOMO to LUMO transition indirectly explains the descriptor of electron donor and acceptor in order to understand their interacting ability with their target molecules. Compound **2**, which is the most chemically reactive, showed the lowest antitumor activity in our previous study.[16]

4. Conclusions

We presented the structural details of benzoxazole compounds, **1** ($C_{17}H_{17}NO_2$), **2** ($C_{21}H_{19}NO_3$) and **3** ($C_{17}H_{16}ClNO_2$), by using single crystal X-ray diffraction data. DFT calculation was performed with a standards 6-31G*(d), 6-31G** and 6-31+G* basis set to analyze the molecular geometry and compare with experimentally available X-ray crystal data of investigated compounds. The calculated HOMO-LUMO energy gap in compound **2** for basis set 6-31G*(d) is 3.79, for 6-31G** is 3.8, and 6-31+G* is 3.8. This small gap value indicates that compound **2** is chemically more reactive compared to compounds **1** and **3**. Chemical reactivity values, such as chemical hardness, chemical potential electronegativity and electrophilicity index and HOMO-LUMO energy gap obtained theoretically, can be used to understand the biological activity of the title compound. Further, the crystal structure is stabilized by both intra- and intermolecular hydrogen bonds in which intermolecular N–H···O hydrogen bond generates N3 and O7 chain motif in compounds **1**, **2** and **3**, respectively. The calculated bond lengths and bond angles of **1**, **2** and **3** show good agreement to the experimental values obtained by X-ray crystal diffraction. The values obtained theoretically show some correlations with previous results of biological activity testing.

Acknowledgements

The authors are grateful to financial support from Federal Ministry of education and science in Bosnia and Herzegovina (grant number: 05-39-3629-1/14, Most: Završnik D. "Modeliranje i doking studije novih potentnih azometinskih derivata timokinona i njihovih organometalnih kompleksa". Ministarstvo za obrazovanje, nauku, kulturu i sport FBiH, 2014–2015. godine (Mostar, 22.12.2014. godine, Ugovor broj: 05-39-3629-1/14).

We thank EN-FIST Centre of Excellence, Trg OF 13, 1000 Ljubljana, Slovenia for using SuperNova diffractometer and Slovenian Research Agency for financial support (P1-0175).

5. References

1. C. S. Demmer, L. Bunch, *Eur. J. Med. Chem.* **2015**, *97*, 778–785. **DOI:**10.1016/j.ejmech.2014.11.064
2. S. Laeeq, A. K. Sirbaiya, H. H. Siddiqui, *Indo. Am. J. Pharm. Res.* **2013**, *3*, 1660–1682.
3. H. Song, C. Rao, Z. Deng, Y. Yi, J. H. Naismith, *Angew. Chem. Int. Ed Engl.*, **2020**, *59*, 6054–6061. **DOI:**10.1002/anie.201915685
4. K. Seth, S. K. Garg, R. Kumar, P. Purohit, V. S. Meena, R. Goyal, U. C. Banerjee, A. K. Chakraborti, *ACS Med. Chem. Lett.*, **2014**, *5*, 512–516. **DOI:**10.1021/ml400500e
5. C. Sheng, X. Che, W. Wang, S. Wang, Y. Cao, J. Yao, Z. Miao, W. Zhang, *Eur. J. Med. Chem.*, **2011**, *46*, 1706–1712. **DOI:**10.1016/j.ejmech.2011.01.075
6. S. M. Rida, F. A. Ashour, S. A. M. El-Hawash, M. M. ElSemary, M. H. Badr, M. A. Shalaby, *Eur. J. Med. Chem.*, **2005**, *40*, 949–959. **DOI:**10.1016/j.ejmech.2005.03.023
7. C. Hohmann, K. Schneider, C. Bruntner, E. Irran, G. Nicholson, A. T. Bull, A. L. Jones, R. Brown, J. E. M. Stach, M. Goodfellow, W. Beil, M. Krämer, J. F. Imhoff, R. D. Süssmuth, H.-P. Fiedler, *J. Antibiot. (Tokyo)*, **2009**, *62*, 99–104. **DOI:**10.1038/ja.2008.24
8. E. Oksuzoglu, B. Tekiner-Gulbas, S. Alper, O. Temiz-Arpaci, T. Ertan, I. Yildiz, N. Diril, E. Sener-Aki, I. Yalcin, *J. Enzyme Inhib. Med. Chem.*, **2008**, *23*, 37–42. **DOI:**10.1080/14756360701342516
9. D. Kumar, M. R. Jacob, M. B. Reynolds, S. M. Kerwin, *Bioorg. Med. Chem.*, **2002**, *10*, 3997–4004. **DOI:**10.1016/S0968-0896(02)00327-9
10. Y. An, E. Lee, Y. Yu, J. Yun, M. Y. Lee, J. S. Kang, W.-Y. Kim, R. Jeon, *Bioorg. Med. Chem. Lett.*, **2016**, *26*, 3067–3072. **DOI:**10.1016/j.bmcl.2016.05.017
11. N. Aggarwal, A. Kaur, K. Anand, H. Kumar, S. R. Wakode, *Int. J. Pharm. Sci. Res.*, **2017**, *2*, 01–05.
12. H. G. Bray, R. C. Clowes, W. V. Thorpe, *Biochem. J.*, **1952**, *51*, 70–78. **DOI:**10.1042/bj0510070
13. C. J. McElhinny, A. H. Lewin, S. W. Mascarella, S. Runyon, L. Brieaddy, F. I. Carroll, *Bioorg. Med. Chem. Lett.*, **2012**, *22*, 6661–6664. **DOI:**10.1016/j.bmcl.2012.08.109
14. M. Ono, K. Yamakawa, H. Kobayashi, I. Itoh, *ChemInform*, **1988**, *19*, 92–93.
15. R. Haunschild, A. Barth, W. Marx, *J. Cheminformatics*, **2016**, *8*, 1–12. **DOI:**10.1186/s13321-016-0166-y
16. U. Glamočlija, S. Padhye, S. Špirtović-Halilović, A. Osmanović, E. Veljović, S. Roca, I. Novaković, B. Mandić, I. Turel, J. Kljun, S. Trifunović, E. Kahrović, S. Kraljević Pavelić, A. Harej, M. Klobučar, D. Završnik, *Molecules*, **2018**, *23*, 3297. **DOI:**10.3390/molecules23123297
17. G. M. Sheldrick, *Acta Crystallogr. Sect. Found. Adv.*, **2015**, *71*, 3–8. **DOI:**10.1107/S2053273314026370
18. G. M. Sheldrick, *Acta Crystallogr. Sect. C Struct. Chem.*, **2015**, *71*, 3–8. **DOI:**10.1107/S2053229614024218
19. O. V. Dolomanov, L. J. Bourhis, R. J. Gildea, J. A. K. Howard, H. Puschmann, *J. Appl. Crystallogr.*, **2009**, *42*, 339–341. **DOI:**10.1107/S0021889808042726
20. A. L. Spek, *Acta Crystallogr. D Biol. Crystallogr.*, **2009**, *65*, 148–155. **DOI:**10.1107/S090744490804362X
21. C. F. Macrae, P. R. Edgington, P. McCabe, E. Pidcock, G. P. Shields, R. Taylor, M. Towler, J. van de Streek, *J. Appl. Crystal-*

logr., **2006**, *39*, 453–457. **DOI:**10.1107/S002188980600731X
22. F. H. Allen, O. Kennard, D. G. Watson, L. Brammer, A. G. Orpen, R. Taylor, *J. Chem. Soc. Perkin Trans. 2*, **1987**, S1–S19. **DOI:**10.1039/p298700000s1
23. M. W. Schmidt, K. K. Baldridge, J. A. Boatz, S. T. Elbert, M. S. Gordon, J. H. Jensen, S. Koseki, N. Matsunaga, K. A. Nguyen, S. Su, T. L. Windus, M. Dupuis, J. A. Montgomery, *J. Comput. Chem.*, **1993**, *14*, 1347–1363. **DOI:**10.1002/jcc.540141112
24. M. Salihović, Š. Huseinović, S. Špirtović-Halilović, A. Osmanović, A. Dedić, Z. Ašimović, D. Završnik, *Bull. Chem. Technol. Bosnia Herzeg.*, **2014**, 31–36.
25. A. A. H. Kadhum, A. A. Al-Amiery, A. Y. Musa, A. B. Mohamad, *Int. J. Mol. Sci.*, **2011**, *12*, 5747–5761. **DOI:**10.3390/ijms12095747

Povzetek

Z rentgensko difrakcijo na monokristalih smo določili kristalne strukture biološko aktivnih derivatov benzoksazola. Z DFT izračuni, pri katerih smo uporabili standardne bazne sete 6-31G*(d), 6-31G** in 6-31+G*, smo analizirali molekulsko geometrijo in primerjali rezultate računskih modelov z eksperimentalno določenimi kristalnimi strukturami spojin. Izračunana HOMO-LUMO energijska vrzel v spojini **2** (2-(2-hidroksinaftalen-1-il)-4-metil-7-izopropil-1,3-benzoksazol-5-ol) je 3,80 eV, kar je najmanj med preučevanimi spojinami in nakazuje na večjo kemijsko reaktivnost spojine v primerjavi s spojinama **1** (4-metil-2-fenil-7-izopropil-1,3-benzoksazol-5-ol) in **3** (2-(4-klorofenil)-4-metil-7-izopropil-1,3-benzoksazol-5-ol). Kristalne strukture so stabilizirane z intra- in intermolekularnimi vodikovimi vezmi, pri čemer se v vseh strukturah spojin **1**, **2** in **3** pojavi verižni strukturni motiv O–H···N vodikovih vezi. Računski modeli dolžin in kotov kemijskih vezi se izjemno dobro skladajo z eksperimentalno določenimi vrednostmi eksperimenta rentgenske difrakcije na monokristalih.

Except when otherwise noted, articles in this journal are published under the terms and conditions of the Creative Commons Attribution 4.0 International License

Scientific paper

Apoptotic Effect of Homobrassinin and Thiazino[6,5-b]indol is Associated with Downregulation of Heat Shock Proteins in Human Ovarian Adenocarcinoma Cells

Zuzana Solárová,[1] Martin Kello[1] and Peter Solár[2,*]

[1] *Institute of Pharmacology, Faculty of Medicine, P. J. Šafárik University in Košice, SK-04154 Košice, Slovak Republic*

[2] *Institute of Medical Biology, Faculty of Medicine, P. J. Šafárik University in Košice, SK-04154 Košice, Slovak Republic*

* *Corresponding author: E-mail: peter.solar@upjs.sk*

Received: 09-04-2020

Abstract

Phytoalexins are substances with antimicrobial properties produced by plants after being attacked by microorganisms, especially phytopathogenic fungi and viruses. They are also currently being studied for their antitumor effect. We aimed to study the apoptosis-stimulating effect of homobrassinin and thiazino[6,5-b]indol in human ovarian adenocarcinoma A2780 and A2780cis cells via flow cytometric analysis of annexin V/PI, caspase 3 and 9 activity, cytochrome C release, and smac-diablo accumulation. Using the western blot technique, we also monitored the effect of both indoles on the response of heat shock proteins in these cells. Thiazino[6,5-b]indol showed more pronounced sensitizing and/or pro-apoptotic effect compared to homobrassinin accompanied by increased smac-diablo accumulation at earlier time intervals and pronounced externalization of phosphatidylserine at 72 h in A2780cis compared to A2780 cells. The apoptosis stimulating effect of thiazino[6,5-b]indol in A2780cis cells was associated with significant irreversible downregulation of HSP70 and HSP90 and partly with a decrease of HSP40. On the other hand, cisplatin-induced the apoptosis of sensitive A2780 cells with reversible downregulation of HSP40 and HSP57. In conclusion, the effect of thiazino[6,5-b]indol on resistant A2780cis cells could have a great utility in both the potential prevention and the treatment of other cisplatin-resistant tumor cells.

Keywords: Homobrassinin; thiazino[6,5-b]indol; cisplatin resistance; apoptosis; heat shock proteins; human ovarian adenocarcinoma cells

1. Introduction

Ovarian cancer has the highest mortality rate of all gynecologic neoplasms among women in Western Europe and the United States. Women who have one first-degree relative with ovarian cancer have an increased risk (5%) of developing ovarian cancer even without known genetic mutation (the average woman's lifetime risk is 1.4%).[1] For most women, the standard of care remains surgery and platinum-based cytotoxic chemotherapy. Platinum-based drugs are the most active and effective treatment option for most patients with early-stage disease. Women with advanced disease will develop many episodes of recurrent disease with progressively shorter disease-free intervals. Eventually, the tumor is declared platinum resistant. Although paclitaxel chemotherapy has improved over the last two decades, the progression to free survival has remained fairly constant at about 18 months. Significant advances in the treatment over the last decade led to a significant prolongation of 5-year survival while the incidence of the disease has remained constant.[2]

Platinum resistance can occur in almost all patients with recurrent ovarian cancer. However, many patients with "platinum-resistant" disease respond to further platinum-based treatment. Platinum, either cisplatin or carboplatin, is given weekly with the addition of etoposide or paclitaxel.[3] or in combination with gemcitabine for two out of three weeks.[4] Paclitaxel is one of the most active nonplatinum drugs used in this setting. Progression to free survival and overall survival increases significantly with paclitaxel administered weekly.[5] In women with platinum-resistant ovarian cancer, antiangiogenic agents, like

bevacizumab, may also play an important role. Indeed, these agents have been used as a monotherapy or in combination with low dose cyclophosphamide.[6] Other drugs, such as aflibercept (VEGF trap), have been found effective in controlling ascites.[7]

Other than anticancer chemotherapeutics, synthetic analogs of several natural substances with antitumor effects, such as indole phytoalexins, were also tested at our institute. Phytoalexins are substances with antimicrobial properties produced by plants after being attacked by microorganisms, especially phytopathogenic fungi and viruses. We tested indole phytoalexins on both cisplatin-sensitive human ovarian adenocarcinoma cell line A2780 (parental) as well as its cisplatin-resistant derivative A2780cis and compared their response to indoles to determine the rate of the resistance of A2780cis cells. Surprisingly, we found that A2780cis cells are only 3.2 times more resistant to thiazino[6,5-b]indol (K157) compared to the parental cell line, as opposed to cisplatin, where A2780cis cells revealed 18 times lower sensitivity.[8] Thus, the fold resistance of A2780cis cells compared to parental ones was surprisingly low, suggesting that A2780cis cells have much lower resistance to K157 than to cisplatin.

In the current work, we aimed to study the sensitizing effect of two indoles, homobrassinin (K1) and K157, on parental A2780 and cisplatin-resistant A2780cis cells. In addition to the apoptosis-stimulating effect of indoles, we were also interested in their effect on the response of selected heat shock proteins in these cells.

2. Experimental

2. 1. Cell Culture and Treatment

Human ovarian adenocarcinoma cell lines A2780 and A2780cis were obtained from European Collection of Animal Culture (ECAC, Salisbury, UK). Cells were grown as monolayers in RPMI1640 medium with L-glutamine (GibcoBRL, Paisley, UK) supplemented with 10% fetal calf serum (GibcoBRL) and antibiotic/antimycotic solution (100 U/ml of penicillin, 100 μg/ml of streptomycin and 0.25 μg/ml of amphotericin B; GibcoBRL) and were maintained under standard tissue culture conditions at 37 °C and 5% humidified atmosphere of CO2. The acquired resistance of A2780cis cells was maintained by supplementation of media with 1mM of cisplatin (Sigma-Aldrich Co., St. Louis, MI, USA) every second passage. IC_{50} concentrations of homobrassinin (K1; N-[2-(indol-3-yl)ethyl] -S-methyldithiocarbamate), thiazino[6,5-b]indol (K157; 2-(4′-fluorphenylamino)-4H-1,3-tiazino[6,5-b]indol) (Fig. 1) and cisplatin determined in our previous studies[11,8] on resistant A2780cis cells were applied in all assays.

2. 2. Flow Cytometric Analysis (FCM)

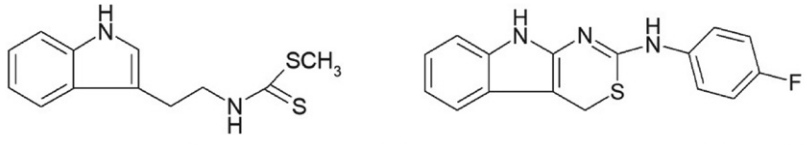
Human ovarian adenocarcinoma cells A2780 and A2780cis (1×10^6) were seeded for FCM analyses in Petri dishes and treated with homobrassinin, thiazino[6,5-b]indol and cisplatin at IC_{50} concentrations for 24, 48 or 72 h depending on experimental scheme. Floating and adherent cells were harvested, washed in PBS, divided for particular analysis and stained prior to analysis. Fluorescence was detected after 15–30 min incubation at room temperature in the dark using a BD FACSCalibur flow cytometer (Becton Dickinson, San Jose, CA, USA). A minimum of 1×10^4 cells were analysed per analysis. All experiments were performed in triplicate.

2. 3. Apoptosis Detection Via Annexin V/PI Staining

For apoptosis detection, floating and adherent A2780 and A2780cis cells (1×10^6) were harvested 24, 48 and 72 h after homobrassinin, thiazino[6,5-b]indol and cisplatin treatment (IC50 concentrations). Complete cell population was washed in PBS and stained using annexin V Alexa Fluor® 647 conjugate (Thermo Fisher, Waltham, MA, USA) for 15 min at room temperature in the dark followed by incubation with propidium iodide (PI; Sigma-Aldrich, Saint-Louis, MO, USA) and analysed by flow cytometer (BD FACSCalibur).

2. 4. Detection of Active Caspase 3

Activation of executioner caspases (such as caspase 3) subsequently impacts the main structural proteins and activates other enzymes, leading to apoptosis. The changes in caspase 3 activation were analysed with FCM using active Caspase-3 PE Mab (Cell Signaling Technology, Danvers, MA, USA). The cells were harvested 24, 48 and 72 h after homobrassinin, thiazino[6,5-b]indol and cisplatin treatment (IC_{50} concentrations). The cell population was stained with phycoerythrin (PE) conjugated antibody and incubated for 30 min at room temperature in the dark. The cells



homobrassinin 2-(4′-fluorphenylamino)-4H-1,3-tiazino[6,5-b]indole

Figure 1. Structure of homobrassinin (K1; N-[2-(indol-3-yl)ethyl]-S-methyldithiocarbamate) and thiazino[6,5-b]indol (K157; 2-(4′- fluorphenylamino)-4H-1,3-tiazino[6,5-b]indol).

were then washed twice with PBS, resuspended in 500 μM of the total volume, and analysed (1×10^4 cell per sample).

2. 5. Detection of Mitochondrial Apoptotic Pathway Associated Proteins

Cytochrome c release, Smac/DIABLO accumulation and caspase-9 activity were analysed with FCM using Cytochrome c antibody (6H2) FITC conjugate; Smac/Diablo Rabbit mAb + goat anti-rabbit IgG (H + L) secondary antibody Alexa Fluor 488 and cleaved Caspase- 9 (Asp315) rabbit mAb PE conjugate. The A2780 and A2780cis cells were harvested 24, 48 and 72 h after homobrassinin, thiazino[6,5-b]indol and cisplatin treatment (IC50 concentrations). Cell population was stained with conjugated antibody and incubated for 30 min at room temperature in the dark or stained with primary antibody (30 min), followed by secondary conjugated antibody staining (15 min in dark). The cells were then washed with PBS, resuspended in 500 μL of the total volume in PBS, and analysed (1×10^4 cells per sample) by a BD FACSCalibur flow cytometer.

2. 6. Western Blotting

Western blot analysis were carried out according to the standard protocol.[12] The protein sample was separated on 10% SDS-PAGE, electroblotted onto Immobilon-P transfer membrane (Millipore Co., Billerica, MA, USA) and incubated using primary antibodies shown below: anti-HSP40 (#4868, 1:1000; Cell Signaling, Danvers, MA, USA), anti-protein disulfide isomerase (anti-HSP57; #3501, 1:1000; Cell Signaling Technology, Danvers, MA, USA), anti- HSP60 (#12165, 1:1000; Cell Signaling, Danvers, MA, USA), anti-HSP70 (#4873, 1:1000; Cell Signaling Technology, Danvers, MA, USA), anti-HSP90 (#4877, 1:1000; Cell Signaling Technology, Danvers, MA, USA)

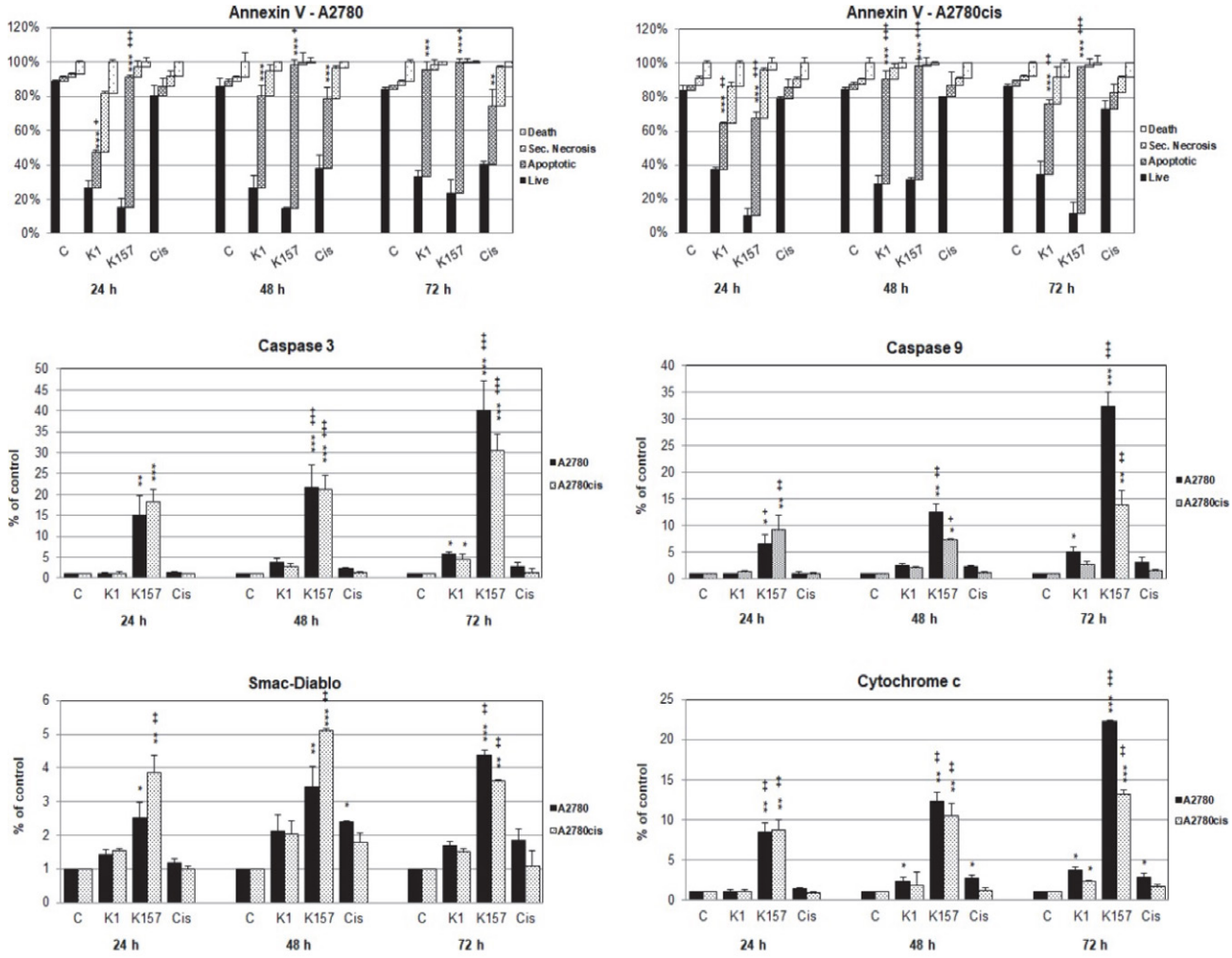


Figure 2. Effects of IC50 concentrations of homobrassinin (K1), thiazino[6,5-b]indol (K157), and cisplatin (Cis) on annexin V, caspase 3, caspase 9, smac-diablo, and cytochrome C in A2780 and A2780cis cell lines. The cells were grown in standard growth media for 24 h and then treated with mentioned above substances for 24, 48, and 72 h (untreated control - C). *p<0.05; **p<0.01***p<0.001 vs. C and +p<0.05; ++p<0.01; +++p<0.001 vs. Cis (three independent experiments)

and anti-α-tubulin (sc-5286, 1:200; Santa Cruz Biotechnology, Dallas, Texas, USA). Subsequently, the membranes were incubated with secondary horseradish peroxidase-conjugated antibodies (PI-31461, 1:10.000, goat anti-rabbit IgG F(AB')2 or PI-31436, 1:10.000, goat anti-mouse IgG F(AB')2; Thermo Fisher Scientific, Waltham, MA, USA) for 1 h, and the antibody reactivity was visualized with ECL Western blotting substrate (PI-32106, Thermo Fisher Scientific) using Kodak Biomax films (#1788207, Sigma-Aldrich Co.).

2. 7. Statistical Analysis

Data were processed using scientific graphing and ORIGIN analysis software (OriginLab Co., Northampton, MA, USA) and statistically analysed using one-way ANOVA followed by Tukey's multiple comparison tests.

3. Results and Discussion

Both indoles induced strong apoptosis in A2780 and A2780cis cells at 24 h compared to cisplatin that showed a pro-apoptotic effect later (at 48 and 72 h) but only in A2780, not A2780cis cells (Fig. 2). Annexin V increased in A2780 and A2780cis cells 24 h after the addition of both indoles (Fig. 2). In this regard, K157 induced more pronounced externalization of phosphatidylserine in A2780cis cells compared to parental ones at 72 h time point. Changes in other selected markers of apoptosis, such as caspase 3 and 9, smac-diablo, and cytochrome C, confirmed the pro-apoptotic potential of both indoles tested, which was more pronounced in the case of K157 than in K1 (Fig. 2). Indeed, K157 increased both caspase 3 and 9 activities, increased the accumulation of smac-diablo, and induced the release of cytochrome C in both cell lines and at all time points monitored (Fig. 2). Interestingly, K157 increased smac-diablo accumulation in A2780cis cells at earlier time intervals (Fig. 2). On the other hand, cisplatin-induced the release of cytochrome C only in A2780 cells, not in A2780cis cells (Fig. 2). This effect of cisplatin correlated well with the mentioned externalization of phosphatidylserine (annexin V/PI staining) and apoptosis in A2780 cells (Fig. 2).

Moreover, indoles reduced the level of HSP40, protein disulfide isomerase (HSP57), HSP70, and HSP90 in A2780 cells irreversibly and HSP40 and HSP57 in A2780cis cells reversibly (Fig. 3A, B; Tab. 1A, B). In this regard, indole K1 downregulated HSP70 in both cell lines at 24 h and HSP40 and HSP90 in A2780 cells at 48 h (Fig. 3A, B; Tab. 1A, B). On the other hand, indole K157 downregulated HSP40 and HSP70 in both A2780 and A2780cis cells and HSP57 and HSP90 in A2780 cells at 24 h (Fig. 3A, B; Tab. 1A, B). Cisplatin did sufficiently modify the level of monitored HSPs in A2780 cells (Fig. 3A, B; Tab. 1A, B) and downregulated both HSP40 and HSP57 in A2780 cells reversibly at 48 h and 24 h, respectively (Fig. 3A; Tab. 1A) and HSP57 in A2780cis cells at 48h (Fig. 3B; Tab. 1B). The level of only HSP60 did not change in A2780 or A2780cis cells after the indole or cisplatin administration (Fig. 3A, B; Tab. 1A, B). In general, the reduction in the level of HSPs in A2780 cells compared to A2780cis cells was more significant (Fig. 3A, B; Tab. 1A, B).

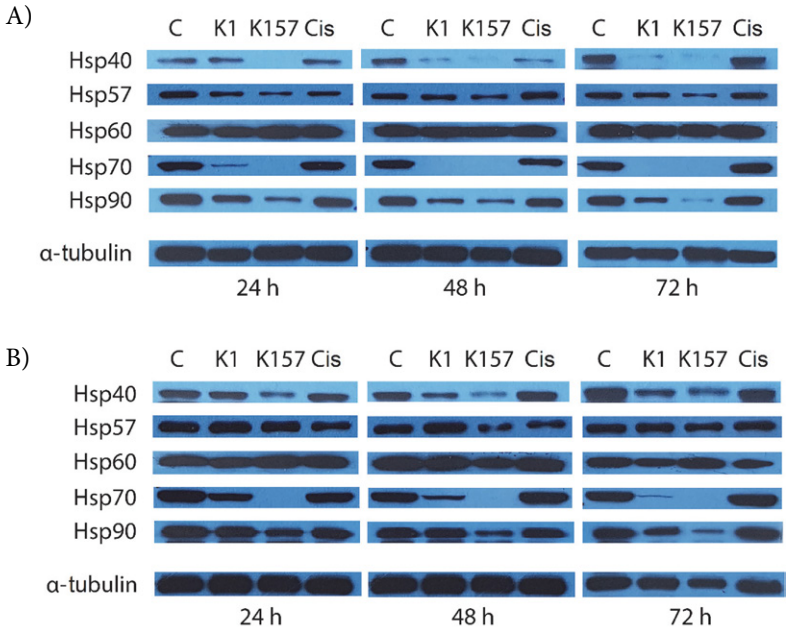


Figure 3. Effects of IC50 concentrations of homobrassinin (K1), thiazino[6,5-b]indol (K157), and cisplatin (Cis) on HSP40, HSP57 (PDI), HSP60, HSP70, and HSP90 in A2780 (A) and A2780cis (B) cell lines. The cells were grown in standard growth media for 24 h and then treated with the substances mentioned above for 24, 48, and 72 h (untreated control – C). The detection of α-tubulin confirmed equal loading. A representative image of three independent experiments is shown.

Table I. Effects of IC50 concentrations of homobrassinin (K1), thiazino[6,5-b]indol (K157), and cisplatin (Cis) on HSP40, HSP57 (PDI), HSP60, HSP70, and HSP90 in A2780 (A) and A2780cis (B) cell lines. Ratios ± standard deviation from quantitative densitometric analysis of HSP40, HSP57, HSP60, HSP70, and HSP90 were normalized to α-tubulin. Ratios at untreated control (C) were arbitrarily set to 1. *p<0.05; **p<0.01 vs. C (three independent experiments; one-way ANOVA tests).

A		**Hsp40**	**Hsp57**	**Hsp60**	**Hsp70**	**Hsp90**
24 h	C	1.0 ± 0.1	1.0 ± 0.1	1.0 ± 0.2	1.0 ± 0.1	1.0 ± 0.1
	K1	1.3 ± 0.3	0.7 ± 0.3	1.3 ± 0.2	0.1 ± 0.1**	0.7 ± 0.3
	K157	0.0 ± 0.1**	0.3 ± 0.1*	1.3 ± 0.3	0.0 ± 0.1**	0.1 ± 0.1**
	Cis	1.6 ± 0.3	0.5 ± 0.1*	1.1 ± 0.1	0.8 ± 0.3	0.7 ± 0.3
		Hsp40	**Hsp57**	**Hsp60**	**Hsp70**	**Hsp90**
48 h	C	1.0 ± 0.1	1.0 ± 0.2	1.0 ± 0.3	1.0 ± 0.2	1.0 ± 0.1
	K1	0.0 ± 0.1**	1.0 ± 0.3	1.1 ± 0.2	0.0 ± 0.1**	0.0 ± 0.1**
	K157	0.0 ± 0.2**	0.9 ± 0.1	1.3 ± 0.2	0.5 ± 0.1*	0.3 ± 0.1*
	Cis	0.1 ± 0.1**	1.2 ± 0.3	1.0 ± 0.3	0.7 ± 0.3	1.1 ± 0.3
		Hsp40	**Hsp57**	**Hsp60**	**Hsp70**	**Hsp90**
72 h	C	1.0 ± 0.1	1.0 ± 0.1	1.0 ± 0.2	1.0 ± 0.2	1.0 ± 0.1
	K1	0.0 ± 0.1**	0.9 ± 0.2	1.1 ± 0.3	0.0 ± 0.1**	0.5 ± 0.1*
	K157	0.0 ± 0.2**	0.4 ± 0.1*	0.8 ± 0.2	0.0 ± 0.1**	0.0 ± 0.1**
	Cis	1.1 ± 0.1	0.8 ± 0.3	0.9 ± 0.2	1.1 ± 0.3	0.9 ± 0.3
B		**Hsp40**	**Hsp57**	**Hsp60**	**Hsp70**	**Hsp90**
24 h	C	1.0 ± 0.1	1.0 ± 0.2	1.0 ± 0.2	1.0 ± 0.1	1.0 ± 0.2
	K1	0.8 ± 0.2	1.1 ± 0.3	0.9 ± 0.2	0.6 ± 0.3	0.8 ± 0.2
	K157	0.5 ± 0.1*	1.1 ± 0.2	1.3 ± 0.3	0.0 ± 0.1**	0.7 ± 0.2
	Cis	0.8 ± 0.3	0.7 ± 0.2	1.2 ± 0.2	0.7 ± 0.2	0.7 ± 0.2
		Hsp40	**Hsp57**	**Hsp60**	**Hsp70**	**Hsp90**
48 h	C	1.0 ± 0.1	1.0 ± 0.2	1.0 ± 0.2	1.0 ± 0.1	1.0 ± 0.1
	K1	0.6 ± 0.2	1.3 ± 0.3	1.0 ± 0.3	0.4 ± 0.1*	1.0 ± 0.2
	K157	0.4 ± 0.1*	0.6 ± 0.2	0.8 ± 0.2	0.0 ± 0.1**	0.5 ± 0.1*
	Cis	1.3 ± 0.3	0.7 ± 0.2	1.0 ± 0.3	1.0 ± 0.2	0.9 ± 0.2
		Hsp40	**Hsp57**	**Hsp60**	**Hsp70**	**Hsp90**
72 h	C	1.0 ± 0.2	1.0 ± 0.3	1.0 ± 0.2	1.0 ± 0.1	1.0 ± 0.1
	K1	1.0 ± 0.3	1.0 ± 0.3	1.0 ± 0.3	0.0 ± 0.1**	0.8 ± 0.2
	K157	1.0 ± 0.2	1.4 ± 0.3	1.8 ± 0.4	0.1 ± 0.1**	0.4 ± 0.1*
	Cis	1.0 ± 0.1	1.0 ± 0.2	0.7 ± 0.2	1.4 ± 0.2	1.1 ± 0.3

Homobrassinin (K1) had the most pronounced antiproliferative activity of the seven tested brassinin derivatives.[13] This compound accumulated human colorectal adenocarcinoma Caco2 cells in the G2/M phase of the cell cycle and inhibited microtubule formation through the dysregulation of α-tubulin, α 1-tubulin, and β 5 -tubulin expression.[13] Moreover, the apoptosis of Caco2 cells induced by K1 was associated with DNA fragmentation, loss of mitochondrial membrane potential, and intracellular reactive oxygen species production.[13] Our results demonstrated that K1 induced the apoptosis of cisplatin-sensitive human ovarian adenocarcinoma A2780 cells and cisplatin-resistant derivative A2780cis cells, both associated with annexin V/PI positivity, increased caspase 3 activity, and released cytochrome C. K157 showed even more pronounced apoptosis-stimulating effect compared to K1, with increased annexin V/PI positivity, caspase 3 and 9 activities, the accumulation of smac-diablo, and the release of cytochrome C in both cisplatin-sensitive as well as cisplatin-resistant cells in a time-dependent manner. The K157-induced apoptosis of A2780cis cells has already been confirmed by a lower concentration than IC_{50} and through the detection of increased pro-apoptotic Bad protein.[8] Cisplatin increased the release of cytochrome C and the externalization of phosphatidylserine but only in the sensitive A2780 cells, not in the resistant ones.

Hsp90 is one of the most abundant molecular chaperones and highly conserved proteins, the association of which is required for the stability and function of multiple mutated, chimeric, and overexpressed signaling proteins that promote the growth and/or survival of cancer cells.[14] Interestingly, antiproliferative and pro-apoptotic effects of

K157 were potentiated by HSP90 inhibitor 17-DMAG in A2780cis cells, which suggests a new strategy in cancer resistance therapy.[8] Similarly, combined exposure of A2780cis cells to HSP90 inhibitor geldanamycin and cisplatin yielded greater than the additive cytotoxic effect.[11] We have already shown that cisplatin-resistant CP70 and C200 cells (derivatives of parental A2780 cells) revealed significantly higher expression of HSPCA (HSP90α) and TRA1 (GRP94) proteins.[15] Overexpressed GRP94 and HSP90α might protect CP70 and C200 cells from cisplatin toxicity and render them more resistant.[15] Indeed, the role of HSPs in cisplatin resistance has been demonstrated in a previous study,[16] where HSP27, mtHSP75, and HSP70 were upregulated in the cisplatin-resistant ovarian tumor cell line 2008/C13*5.25 in contrast to the sensitive 2008 one. Therefore, in the present study, we decided to test the effect of indoles on the level of selected HSPs, which can have significant cytoprotective effects in pathological conditions through the initiation of protein folding, repair, refolding of misfolded peptides, and possible degradation of irreparable proteins.[17] Although some HSPs are produced constitutively, most are molecular chaperones that are normally overexpressed by cells in response to inducible signals that may lead to protein denaturation.[18] HSPs appear to have a large number of functions in apoptosis itself, which, in most cases, leads to suppression of apoptotic pathways.[17] In our case, the apoptosis-stimulating effects of indoles were associated with an irreversible decrease in HSP90 and HSP70 in both A2780 as well as A2780cis cells. At the same time, cisplatin did not cause any change in HSP90 and HSP70.

Moreover, Beere et al.[19] demonstrated that Hsp70, together with its co-chaperone Hsp40, inhibits nitric oxide-induced apoptosis in ATPase- and chaperoning-dependent manner by blocking the mitochondrial translocation of Bax, a pro-apoptotic member of the Bcl-2 family.[19] HSP70 and HSP40 were irreversibly downregulated as a result of the effect of both K1 and K157 indoles on A2780 and A2780cis cells. On the other hand, HSP40 protein was reversibly downregulated as a result of cisplatin in A2780 cells. Indeed, downregulation of HSP70 and/or HSP40 correlated well with the apoptosis induced by either indole in both cell lines or cisplatin in A2780 cells. Despite all the negative functions of HSPs in attenuating apoptosis, Hsp60, found in mitochondria complexed with Hsp10, is involved in a signaling complex that leads to pro-caspase-3 activation and cytochrome-dependent apoptosis. In addition, several studies have shown that cytosolic Hsp60 is associated with the pro-apoptotic protein Bax, leading to its activation as well as to apoptosis mediated by this protein.[20,21] Indeed, neither indoles nor cisplatin caused a change in the level of HSP60 protein, and they are unlikely to be related to the process of apoptosis induced by indoles or cisplatin in A2780 or A2780cis cells.

HSP57 (PDI) protein is highly expressed in many tumor cell types, including melanoma, prostate, lung, renal, brain, male germ cell tumors, and ovarian.[22] Conversely, decreased PDI levels are also associated with higher survival rates in patients with breast cancer and glioblastoma.[23] Although PDI promotes cancer cell survival, its silencing causes greater cytotoxicity in human breast cancer and neuroblastoma cell lines due to caspase activation.[24] The suppression of apoptosis by PDI itself serves a mechanism to promote tumor growth and metastasis. In this regard, K157 induced both irreversible and reversible downregulation of HSP57 in A2780 and A2780cis cells, respectively, while cisplatin caused a reversible decrease in HSP57 in both cell lines monitored.

4. Conclusions

Our results signify more pronounced sensitizing and/or proapoptotic potential of thiazino[6,5-b]indol compared to homobrassinin accompanied by increased smac-diablo accumulation at earlier time intervals and pronounced externalization of phosphatidylserine at 72 h in A2780cis compared to A2780 cells. The apoptosis-stimulating effect of thiazino[6,5-b]indol in A2780cis cells was associated with significant irreversible downregulation of HSP70 and HSP90 and partly with a decrease of HSP40. On the other hand, cisplatin induced the apoptosis of sensitive A2780 cells with reversible downregulation of HSP40 and HSP57. In conclusion, the effect of thiazino[6,5-b]indol on resistant A2780cis cells could have a great utility in both the potential prevention and the treatment of other cisplatin-resistant tumor cells.

Conflict of Interest

There is no conflict of interest.

Acknowledgments

This study was supported (50%) by the project Medicínsky univerzitný park v Košiciach (MediPark, Košice) ITMS: 26220220185 (95%) supported by Operational Programme Research and Development (OPVaV-2012/2.2/08-RO) (Contract No. OPVaV/12/2013). We would like to thank also the Slovak Grant Agency for Science (Grant No. 1/0536/19) for financial support of this work. The authors are grateful to Mgr. Marián Čurda for drawing the chemical structures of indoles.

5. References

1. Thomsen, L. H.; Schnack, T. H.; Buchardi, K.; Hummelshoj, L.; Missmer, S. A.; Forman, A.; Blaakaer, J., Risk factors of epithelial ovarian carcinomas among women with endometriosis: a systematic review. *Acta Obstet Gynecol Scand* **2017,** *96* (6), 761–778. **DOI:**10.1111/aogs.13010

2. Luvero, D.; Milani, A.; Ledermann, J. A., Treatment options in recurrent ovarian cancer: latest evidence and clinical potential. *Ther Adv Med Oncol* **2014,** *6* (5), 229–39. **DOI:**10.1177/1758834014544121
3. Sharma, R.; Graham, J.; Mitchell, H.; Brooks, A.; Blagden, S.; Gabra, H., Extended weekly dose- dense paclitaxel/carboplatin is feasible and active in heavily pre-treated platinum-resistant recurrent ovarian cancer. *Br J Cancer* **2009,** *100* (5), 707–12. **DOI:**10.1038/sj.bjc.6604914
4. Rose, P. G.; Mossbruger, K.; Fusco, N.; Smrekar, M.; Eaton, S.; Rodriguez, M., Gemcitabine reverses cisplatin resistance: demonstration of activity in platinum- and multidrug-resistant ovarian and peritoneal carcinoma. *Gynecol Oncol* **2003,** *88* (1), 17–21. **DOI:**10.1006/gyno.2002.6850
5. Katsumata, N.; Yasuda, M.; Isonishi, S.; Takahashi, F.; Michimae, H.; Kimura, E.; Aoki, D.; Jobo, T.; Kodama, S.; Terauchi, F.; Sugiyama, T.; Ochiai, K.; Japanese Gynecologic Oncology, G., Long-term results of dose-dense paclitaxel and carboplatin versus conventional paclitaxel and carboplatin for treatment of advanced epithelial ovarian, fallopian tube, or primary peritoneal cancer (JGOG 3016): a randomised, controlled, open-label trial. *Lancet Oncol* **2013,** *14* (10), 1020–6. **DOI:**10.1016/S1470-2045(13)70363-2
6. Garcia, A. A.; Hirte, H.; Fleming, G.; Yang, D.; Tsao-Wei, D. D.; Roman, L.; Groshen, S.; Swenson, S.; Markland, F.; Gandara, D.; Scudder, S.; Morgan, R.; Chen, H.; Lenz, H. J.; Oza, A. M., Phase II clinical trial of bevacizumab and low-dose metronomic oral cyclophosphamide in recurrent ovarian cancer: a trial of the California, Chicago, and Princess Margaret Hospital phase II consortia. *J Clin Oncol* **2008,** *26* (1), 76–82. **DOI:**10.1200/JCO.2007.12.1939
7. Gotlieb, W. H.; Amant, F.; Advani, S.; Goswami, C.; Hirte, H.; Provencher, D.; Somani, N.; Yamada, S. D.; Tamby, J. F.; Vergote, I., Intravenous aflibercept for treatment of recurrent symptomatic malignant ascites in patients with advanced ovarian cancer: a phase 2, randomised, double-blind, placebo-controlled study. *Lancet Oncol* **2012,** *13* (2), 154–62. **DOI:**10.1016/S1470-2045(11)70338-2
8. Solarova, Z.; Kello, M.; Varinska, L.; Budovska, M.; Solar, P., Inhibition of heat shock protein (Hsp) 90 potentiates the antiproliferative and pro-apoptotic effects of 2-(4'fluoro-phenylamino)-4H- 1,3-thiazine[6,5-b]indole in A2780cis cells. *Biomed Pharmacother* **2017,** *85*, 463–471. **DOI:**10.1016/j.biopha.2016.11.052
9. Banerjee Mustafi, S.; Chakraborty, P. K.; Raha, S., Modulation of Akt and ERK1/2 pathways by resveratrol in chronic myelogenous leukemia (CML) cells results in the downregulation of Hsp70. *PLoS One* **2010,** *5* (1), e8719. **DOI:**10.1371/journal.pone.0008719
10. Pilatova, M.; Sarissky, M.; Kutschy, P.; Mirossay, A.; Mezencev, R.; Curillova, Z.; Suchy, M.; Monde, K.; Mirossay, L.; Mojzis, J., Cruciferous phytoalexins: antiproliferative effects in T-Jurkat leukemic cells. *Leuk Res* **2005,** *29* (4), 415–21. **DOI:**10.1016/j.leukres.2004.09.003
11. Solar, P.; Horvath, V.; Kleban, J.; Koval, J.; Solarova, Z.; Kozubik, A.; Fedorocko, P., Hsp90 inhibitor geldanamycin increases the sensitivity of resistant ovarian adenocarcinoma cell line A2780cis to cisplatin. *Neoplasma* **2007,** *54* (2), 127–30.
12. Mahmood, T.; Yang, P. C., Western blot: technique, theory, and trouble shooting. *N Am J Med Sci* **2012,** *4* (9), 429–34. **DOI:**10.4103/1947-2714.100998
13. Kello, M.; Drutovic, D.; Chripkova, M.; Pilatova, M.; Budovska, M.; Kulikova, L.; Urdzik, P.; Mojzis, J., ROS-dependent antiproliferative effect of brassinin derivative homobrassinin in human colorectal cancer Caco2 cells. *Molecules* **2014,** *19* (8), 10877–97. **DOI:**10.3390/molecules190810877
14. Neckers, L., Hsp90 inhibitors as novel cancer chemotherapeutic agents. *Trends Mol Med* **2002,** *8* (4 Suppl), S55–61. **DOI:**10.1016/S1471-4914(02)02316-X
15. Solar, P.; Sytkowski, A. J., Differentially expressed genes associated with cisplatin resistance in human ovarian adenocarcinoma cell line A2780. *Cancer Lett* **2011,** *309* (1), 11–8. **DOI:**10.1016/j.canlet.2011.05.008
16. Yamamoto, K.; Okamoto, A.; Isonishi, S.; Ochiai, K.; Ohtake, Y., Heat shock protein 27 was up- regulated in cisplatin resistant human ovarian tumor cell line and associated with the cisplatin resistance. *Cancer Lett* **2001,** *168* (2), 173–81. **DOI:**10.1016/S0304-3835(01)00532-8
17. Ikwegbue, P. C.; Masamba, P.; Oyinloye, B. E.; Kappo, A. P., Roles of Heat Shock Proteins in Apoptosis, Oxidative Stress, Human Inflammatory Diseases, and Cancer. *Pharmaceuticals (Basel)* **2017,** *11* (1). **DOI:**10.3390/ph11010002
18. Srivastava, P., Roles of heat-shock proteins in innate and adaptive immunity. *Nat Rev Immunol* **2002,** *2* (3), 185–94.
19. Beere, H. M., "The stress of dying": the role of heat shock proteins in the regulation of apoptosis. *J Cell Sci* **2004,** *117* (Pt 13), 2641–51. **DOI:**10.1242/jcs.01284
20. Samali, A.; Cai, J.; Zhivotovsky, B.; Jones, D. P.; Orrenius, S., Presence of a pre-apoptotic complex of pro-caspase-3, Hsp60 and Hsp10 in the mitochondrial fraction of jurkat cells. *EMBO J* **1999,** *18* (8), 2040–8. **DOI:**10.1093/emboj/18.8.2040
21. Gupta, S.; Knowlton, A. A., Cytosolic heat shock protein 60, hypoxia, and apoptosis. *Circulation* **2002,** *106* (21), 2727–33.
22. Xu, S.; Sankar, S.; Neamati, N., Protein disulfide isomerase: a promising target for cancer therapy. *Drug Discov Today* **2014,** *19* (3), 222–40. **DOI:**10.1016/j.drudis.2013.10.017ww

Povzetek

Fitoaleksini so snovi s protimikrobnimi lastnostmi, ki jih rastline proizvajajo po napadu mikroorganizmov, zlasti fitopatogenih gliv in virusov. Trenutno jih preučujejo tudi zaradi njihovih protitumorskih učinkov. Naš cilj je bil proučiti apoptozo-stimulirajoče delovanje homobrassinina and thiazino[6,5-b]indola v celicah človeškega ovarijskega adenokarcinoma A2780 and A2780cis s pomočjo pretočne citometrične analize aneksina V/PI, aktivnosti kaspaz 3 in 9, sproščanja citokroma C in kopičenja smac-diablo. S tehniko prenosa po westernu smo spremljali tudi učinek obeh indolov na odziv proteinov toplotnega šoka v teh celicah. Thiazino [6,5-b]indol je v primerjavi s homobrassininom pokazal izrazitejši senzibilizacijski in/ali proapoptotični učinek, ki ga je spremljalo povečano kopičenje smac-diabla v zgodnejših časovnih intervalih in izrazita eksternalizacija fosfatidilserina po 72 urah v A2780cis celicah v primerjavi s celicami A2780. Učinek tiazino [6,5-b] indola, ki je stimuliral apoptozo, je bil v celicah A2780cis povezan z značilnim nepovratnim zmanjšanem HSP70 in HSP90, ter deloma z zmanjšanjem HSP40. Po drugi strani pa je cisplatin povzročil apoptozo občutljivih celic A2780 z reverzibilnim zmanjšanjem HSP40 in HSP57. Skratka, učinek tiazino [6,5-b]indola na odporne celice A2780cis bi bil lahko zelo koristen pri potencialnem preprečevanju in zdravljenju drugih tumorskih celic, odpornih na cisplatin.

Except when otherwise noted, articles in this journal are published under the terms and conditions of the Creative Commons Attribution 4.0 International License

Scientific paper

Characterization of Hydration Behaviour and Modeling of Film Formulation

Arunima Pramanik,[1] Rudra Narayan Sahoo,[1,2] Souvik Nandi,[1] Ashirbad Nanda[1] and Subrata Mallick[1,*]

[1] *Department of Pharmaceutics, School of Pharmaceutical Sciences, Siksha 'O' Anusandhan (Deemed to be University), Bhubaneswar 751003, Odisha, India.*

[2] *Centurion University of Technology and Management, Odisha, India.*

* *Corresponding author: E-mail: profsmallick@gmail.com (Telephone: +91-674-2386209; fax: +91-674 2386271*

Received: 07-26-2020

Abstract

Hydration behavior of hydrogel-based polymeric film possesses great importance in mucosal drug delivery. Modified Lag phase sigmoid model was used for the investigation of hydration of the film. Kaolin incorporated HPMC K100LVCR (H_L) and K100M (H_H) films containing dexamethasone as a model drug have been prepared for studying swelling kinetics. Swelling of H_L and H_H films was decreased with the gradual increase of kaolin content and H_H of higher viscosity has shown higher value than H_L matrix. Kaolin also inhibited the film erosion process. Mathematically modified lag phase sigmoid model demonstrated similarity of the predicted swelling content with the observed value. High R^2 and small RMSE value confirmed the successful fitting of the modified lag phase sigmoid model to the experimental data of swelling content. τ value similar to the observed one was obtained. This modified model could be reliable enough for estimating hydration process in food grains, food packaging films etc.

Keywords: Hydration phenomenon; water diffusion; swelling kinetic model; modified lag phase.

1. Introduction

Swelling behavior of polymer films possesses a significant importance in hydrogel-based transmucosal drug delivery systems and diverse application in biomolecular electronics and sensors, wound dressings, adsorption of chemical materials and contact lenses.[1,2] Matrix film of hydrophilic polymer is susceptible to environmental moisture and water due to the presence of hydrophilic groups in the macromolecule chains.[3] Swelling of polymer network is affected by the cross-linking degree of polymer, solvent-polymer compatibility and polymer nature.[4] In the process of swelling, the solvent molecules get in contact with the polymer and diffuse into the polymer materials. Diffusion of solvent molecules into the polymer network, expansion of network, and relaxation of polymer chain are the three steps of dynamic hydration process. [5] Thus swelling is responsible for the polymer chain relaxation and facilitates the patterned release of drug. Swelling develops bioadhesion through the intimate contact between polymer and mucosal tissue due to the entanglement of polymer and mucin chains of mucosal membrane lining.[6] For transmucosal drug delivery amlodipine, budesonide, diclofenac film formulations were developed in our laboratory wherein dynamic hydration process has been described.[6–8] The mucoadhesion between the mucus layer and the natural and synthetic polymers covered the mucosal epithelial surface. Further, the controlled drug release is affected by the interaction capability of polymer with mucus layer.[9] Swelling gets much attention as an important mechanism of controlled drug delivery system.[10,11] For hydrogel film, the dynamic process of solvent penetration can be interpreted from swelling. Based on this knowledge, the drug release pattern can be adjusted by modifying the swelling of polymer matrix.[5]

The incorporation of clay minerals into the polymer matrix reduces the strain of polymer matrix due to their intercalation properties[12] and increments significant property.[13] Silicate clay, such as montmorrilonite, has been characterized for the improvement of the biodegradability and mechanical properties of polymeric film.[14,15] Kaolin, a

phyllosilicate (1:1) crystalline clay has the cation exchange capacity.[16] It consists of a tetrahedral silica sheet and an alumina octahedral sheet, and the layers are bonded together with hydrogen bonds.[17] Incorporation of kaolin in drug delivery design is promoted due to its characteristic features such as chemical inertness, rheological properties, high specific area, swelling capacity and sorption capacity. The effect of kaolin incorporation in the film on the quality and functionality of swelling of film could be investigated by applying the mathematical model. This type of utilization of mathematical models is almost unavailable in the literature. The water diffusion and swelling behaviour of the polymeric film was previously studied by several researchers.[18–21] In literature, the kinetic model for absorbent gels swelling was constructed by Tanaka and Filmore.[22] After that, Li and Tanaka[23] included some new approaches regarding swelling of gel and that was implemented by Chi Wu and Chui-Ying Yan[24] for the gelatin of film swelling. Hans Schott described the swelling kinetics of gelatin film using second order kinetics.[25] Peleg model has been utilized to describe the swelling kinetics of acrylamide-sodium acrylate hydrogel[26] and water sorption process of food packaging films as well.[27] The cellulose polymer contains hydroxyl group and it is used in different fields due to their hydrophilic and hygroscopic nature.[28] Hydroxypropyl methylcellulose (HPMC) contains many hydroxyl groups and is widely used in pharmaceutical industry and other fields.[29] Kinetics of food grain hydration process has already been studied by several researchers earlier using lag phase sigmoid model and other kinetic models.[30–32] In this study, lag phase sigmoid model and also the modified version of this model has been applied to investigate the swelling of the films. In our knowledge, no such modification of model was used to describe the swelling kinetics of any polymeric film. Mathematical modification of lag phase sigmoid model has been described as:

$$S_t = \frac{S_E}{1+\exp(-k(t-\tau))} \qquad (1)\text{(Lag phase model)}$$

Modification:

$$\frac{S_E}{S_t} = 1 + \exp(-k(t-\tau)$$

$$\frac{S_E}{S_t} - 1 = \exp(-k(t-\tau)$$

$$Ln\left(\frac{S_E - S_t}{S_t}\right) = k\tau - kt \qquad (2)$$

S_E is the equilibrium swelling, k (min^{-1}) is the swelling rate constant and τ is the time to obtain half of the swelling sat-ration (i. e. $S_t = S_E/2$ at $t = \tau$). The swelling rate constant (k) can be determined from the slope of $Ln\left(\frac{S_E - S_t}{S_t}\right)$ vs. t linear plot.

2. Experimental

2.1. Materials

Dexamethasone (DXM) was received as gift sample (Sigma Company). Kaolin, HPMC K100LVCR (H_L) and HPMC K100M (H_H), triethanolamine were purchased from Qualikems, Burgoyne, Burbidges & co., Merck specialities Pvt Ltd (Mumbai) respectively. Ethanol was bought from MERCK (Germany).

2. 2. Preparation of Hydrogel Film

The polymers (H_L and H_H) were swelled in distilled water overnight and stirred continuously for 24 hours at room temperature to prepare homogenous polymeric dispersion. Simultaneously, kaolin clay dispersion (10 wt. %) was prepared separately without any treatment by dispersing kaolin clay in distilled water and stirring for 24 h. This dispersion was centrifuged at 2500 rpm for 15 min and the thin nano-dispersion layer from the upper part was separated for film formulation. It was established that this process of dispersion in distilled water may be capable of reducing the average particle size to nano size clay particle.[33] Kaolin dispersion in different amount (25, 50, 75 or 100 mg content) was gradually added into the H_L or H_H polymer dispersion (800 mg) and stirred continuously for 1 h with a magnetic stirrer. Dexamethasone (model drug, 100 mg) and triethanolamine (15 % of polymer as plasticizer) were dissolved in 5 ml of ethanol and incorporated in each polymeric kaolin dispersion with continuous stirring for 3 h. According to solvent casting and solvent evaporation method, final dispersion into the petri dish was spread and dried in an incubator for 24 h at 60 °C until constant weight. The prepared films were subjected to the following characterizations. At least three repetitions of the following experiments were done and mean ± SD values were calculated.

2. 3. Water Sorption Studies

Films were accurately weighed (W_1) at room temperature (30 °C) and placed in desiccators containing activated silica gel. After 24 h films were discarded from desiccators and weighed (W_2) until constant weight achieved. Water content was estimated from the difference between initial and final weight with respect to final weight (W_2). For water sorption analysis each film was weighed (W_1) after removal from desiccators over silica gel and placed in the desiccators to maintain 65, 75, and 84 % relative humidity with 100 ml super saturated solution of sodium nitrite, sodium chloride and potassium chloride, respectively. After about 24 h or more films were weighed (W_2) till three resulted weights of each film were same. Moisture uptake was determined from the difference between final and initial weight with respect to initial weight (W_1) and expressed as percentage.

2. 4. FTIR Spectroscopy

The possible interaction between the components was interpreted from FTIR analysis. The FTIR characterization of pure drug and the film formulations (DH_HK_0, DH_HK_1, DH_HK_2, DH_HK_3, and DH_HK_4) was performed using JASCO FT/IR-4100 spectra. To prepare sample pellets, KBr pressed-disk method was used (ratio of sample to KBr is 1:20) and then sample pellet was placed in FTIR spectrometer. FTIR spectra were obtained in the range of 400–4000 cm^{-1} and at a resolution of 4 cm^{-1} as transmission mode by accumulating 80 scans.

2. 5. Scanning Electron Microscopy (SEM)

SEM images were utilized to visualize the morphology of pure drug, kaolin and film formulations (DH_LK_4, and DH_HK_4) of highest kaolin content. Samples were gold sputter-coated under argon atmosphere and placed in JEOL/EO $ CM_VERSION 1.0 Scanning Electron Microscope model no (JSM-6390) (operating at 5 kV) for imaging.

2. 6. Hydration and Swelling Studies

Films were cut into small pieces and weighed (W_0). Then the small pieces of film were immersed into each petri plate containing 25 ml of pH 7.4 phosphate buffer saline at room temperature. After predetermined time interval samples were taken out from the petri plate and excess buffer was soaked in filter paper. Then the final weight (W_t) was recorded and this process was continued up to 6 h. Swelling content was calculated by using the following equation,[34]

$$S = \frac{W_t - W_0}{W_0} \tag{3}$$

S is the swelling content (g water/ g dry film), W_t is the weight of film after time t, and W_0 is the weight of dry film.

Erosion of film can also be analyzed from swelling studies. After 6 h of swelling study, films were dried at 40 °C in hot air oven. Films were removed from the oven after 24 h and reweighed (W_e) and erosion (E) was calculated as follow,

$$E = \frac{W_0 - W_e}{W_0} \tag{4}$$

W_e is the weight of the eroded film after drying in oven.

Swelling of polymer involved diffusion of water and necessitated the understanding of mechanism of solvent diffusion. The swelling kinetics and diffusion of polymer structure can be explained by basic law of Peppas law.[24]

$$F = \frac{S_t}{S_{max}} = Kt^n \tag{5}$$

where, F is the fraction of swelling content, S_{max} i the maximum swelling content of the formulation, S_t the swelling content of the formulation at any time, K the gel network structure constant, and n the diffusion exponential of solvent. The 'n' value of Peppas equation was utilized to determine the diffusion type. Coefficient of diffusion, an important parameter, was also evaluated from the swelling kinetics. It can be calculated for the square shape film from the following equation which was derived by re-arranging the Fick's II law.

$$D = a^2 \left(\frac{K}{4}\right)^{1/n} \tag{6}$$

where D is the diffusion coefficient expressed in cm^2s^{-1}, and "a" is the side of square film in cm.

In order to determine the swelling kinetics of films, lag phase sigmoid model was exploited in this study. The lag phase sigmoid equation has been modified to generalize the swelling kinetics study and also to compare it with the original lag phase sigmoid model.

Kaptso et al also proposed a sigmoid model and described the swelling of film.[36] The equation of this sigmoid model, comprised of an exponential rate of decay term, is accounted for an initial lag phase. The model is expressed as the following equation

$$S_t = \frac{S_E}{1 + \exp(-k(t - \tau))} \tag{7}$$

S_E is the equilibrium swelling, k (min^{-1}) is the swelling rate constant and τ is the time to obtain half of the swelling saturation (i. e. $S_t = S_E/2$ at $t = \tau$).

2. 7. Statistical Analysis

The model was statistically fitted with the experimental data and analyzed in Origin Pro 8.0 (OriginLab, Northampton, MA) software[37] by the nonlinear regression analysis. Model fitness to the experimental data has been assessed using R^2, χ^2, and root mean square error (RMSE) of statistical analysis data. χ^2 and RMSE can be calculated as

$$\chi^2 = \frac{\sum_{i=1}^{N} (S_{exp,i} - S_{pre,i})^2}{N - z} \tag{8}$$

$$RMSE = \left[\frac{1}{N}\sum_{i=1}^{N}\left(SR_{pre,i} - SR_{exp,i}\right)^2\right]^{1/2} \tag{9}$$

3. Results and Discussion

3. 1. Water Sorption Properties

The moisture content and moisture uptake of DXM film composed of HPMC and kaolin were measured at

Table 1. Water sorption properties of the film formulations.

Formulation	DXM : kaolin	% Water uptake at RH (mean ± SD, n = 3) 65 %	75 %	85 %	Water content (%) (mean ± SD, n = 3)
DH_LK_0	–	4.50 ± 0.02	12.61 ± 0.03	21.62 ± 0.03	2.80 ± 0.01
DH_LK_1	1 : 0.25	4.31 ± 0.03	12.06 ± 0.03	19.82 ± 0.03	2.58 ± 0.01
DH_LK_2	1 : 0.5	3.81 ± 0.02	11.45 ± 0.03	19.08 ± 0.02	2.34 ± 0.01
DH_LK_3	1 : 0.75	3.42 ± 0.02	10.28 ± 0.03	17.00 ± 0.03	2.06 ± 0.01
DH_LK_4	1 : 1	3.40 ± 0.03	10.20 ± 0.04	16.57 ± 0.03	1.14 ± 0.02
DH_HK_0	–	6.76 ± 0.04	14.28 ± 0.08	24.81 ± 0.11	3.87 ± 0.02
DH_HK_1	1 : 0.25	5.81 ± 0.05	13.95 ± 0.09	22.09 ± 0.10	3.52 ± 0.02
DH_HK_2	1 : 0.5	5.22 ± 0.05	13.43 ± 0.08	19.40 ± 0.10	3.22 ± 0.01
DH_HK_3	1 : 0.75	4.65 ± 0.05	12.79 ± 0.06	19.76 ± 0.06	2.68 ± 0.02
DH_HK_4	1 : 1	4.57 ± 0.06	11.76 ± 0.07	18.30 ± 0.03	2.40 ± 0.02

25 °C, and at 65, 75, and 85 % relative humidity. Table 1 displays the gradual depletion of both water content and water uptake while kaolin content increases in the film. It is also seen that moisture uptake of all respective formulations is progressively increasing with increasing RH from 65 to 85 %. The highest kaolin content in the film resulted in the decreased percent moisture uptake from 4.50 ± 0.02 to 3.40 ± 0.03 and 6.76 ± 0.04 to 4.57 ± 0.06 at 65 % RH for H_L and H_H matrices respectively in comparison with the absence of kaolin film. Percent moisture content of film has also been reduced from 2.80 ± 0.004 to 1.14 ± 0.02 and from 3.87 ± 0.02 to 2.40 ± 0.02 for H_L and H_H matrices respectively in the presence of kaolin (1:1) compared to the kaolin free films. The observed result indicated that the water resistance of both the matrix formulations was increased when kaolin was present in the film. In presence of triethanolamine as plasticizer, fine kaolin particles in the HPMC matrix enhanced the HPMC-kaolin interactions and left less free hydroxyl groups available for water binding. Thus, increased kaolin content gradually enhanced the barrier effect for the water uptake.[38,39]

3. 2. FTIR

The analysis of the chemical constituent of pharmaceutical solids has been carried out by the FTIR spectroscopy. The drug-excipient interaction nature was also confirmed from the changes in the IR spectra. The changes in drug-excipient interactions are displayed as the disappearance of existing bands and appearance of new bands in the IR spectra, and also as intensity alteration and absorption band broadening. Figure 1 shows the IR spectra of kaolin, pure DXM and formulations. The characteristic absorption peaks of DXM in IR spectra that appear at 3000–2800 cm^{-1}, 885 cm^{-1}, 1718 cm^{-1}, 1665 cm^{-1} and 1621 cm^{-1}, are assigned to CH_2 group, axial deformation of C-F group,

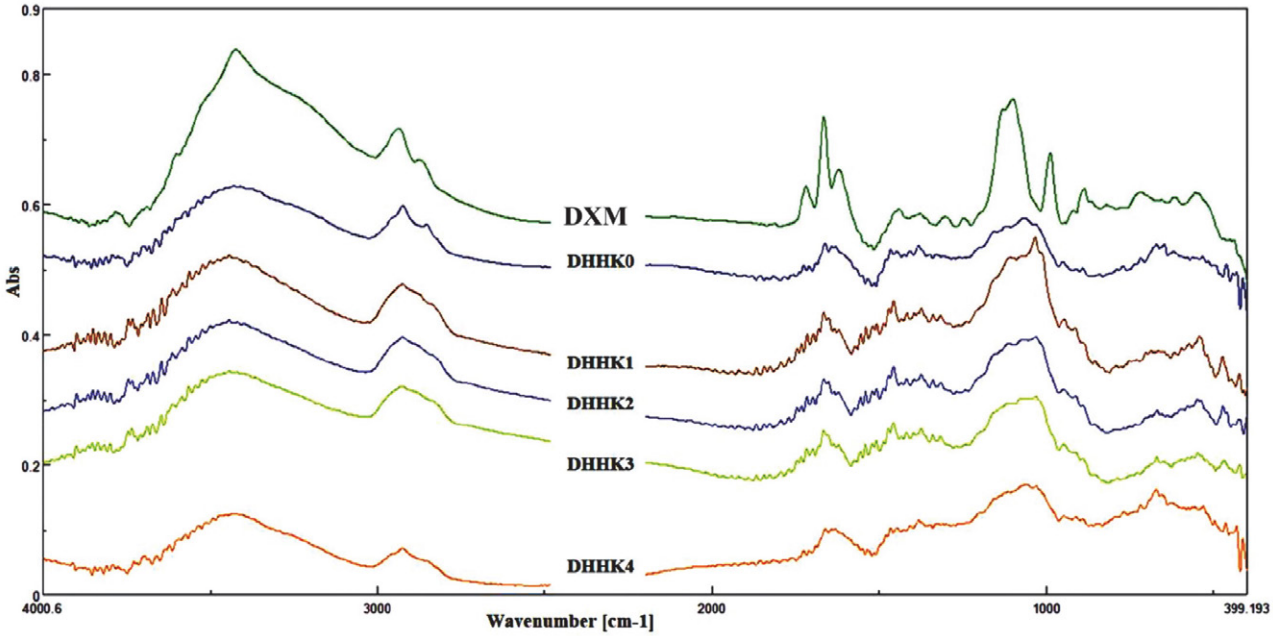


Figure 1. FTIR spectra of pure DXM and of the prepared film formulations (DH_HK_0, DH_HK_1, DH_HK_2, DH_HK_3, and DH_HK_4).

carbonyl group (C=O) of aliphatic ester and ketone,[40] and C=C group, respectively.[41] IR spectrum of pure kaolin demonstrated absorption peak at 1032 cm^{-1} with high intensity due to Si-O stretching in kaolin.[42] Kaolin contains hydroxyl groups at different position, i.e. outer hydroxyl groups (OuOH, positioned in the upper unshared plan) and inner hydroxyl groups (InOH, positioned in the lower unshared plan of octahedral sheet). Kaolin spectra showed peaks at 3693, 3669, 3649 cm^{-1} and at 3619 cm^{-1} due to the stretching of OuOH and stretching of InOH in Al-OH.[43] The broadening of absorption band at 3000–2800 cm^{-1} appeared due to the presence of polymer in the film. The successful incorporation of DXM in films has been confirmed by the presence of the main characteristic absorption peak

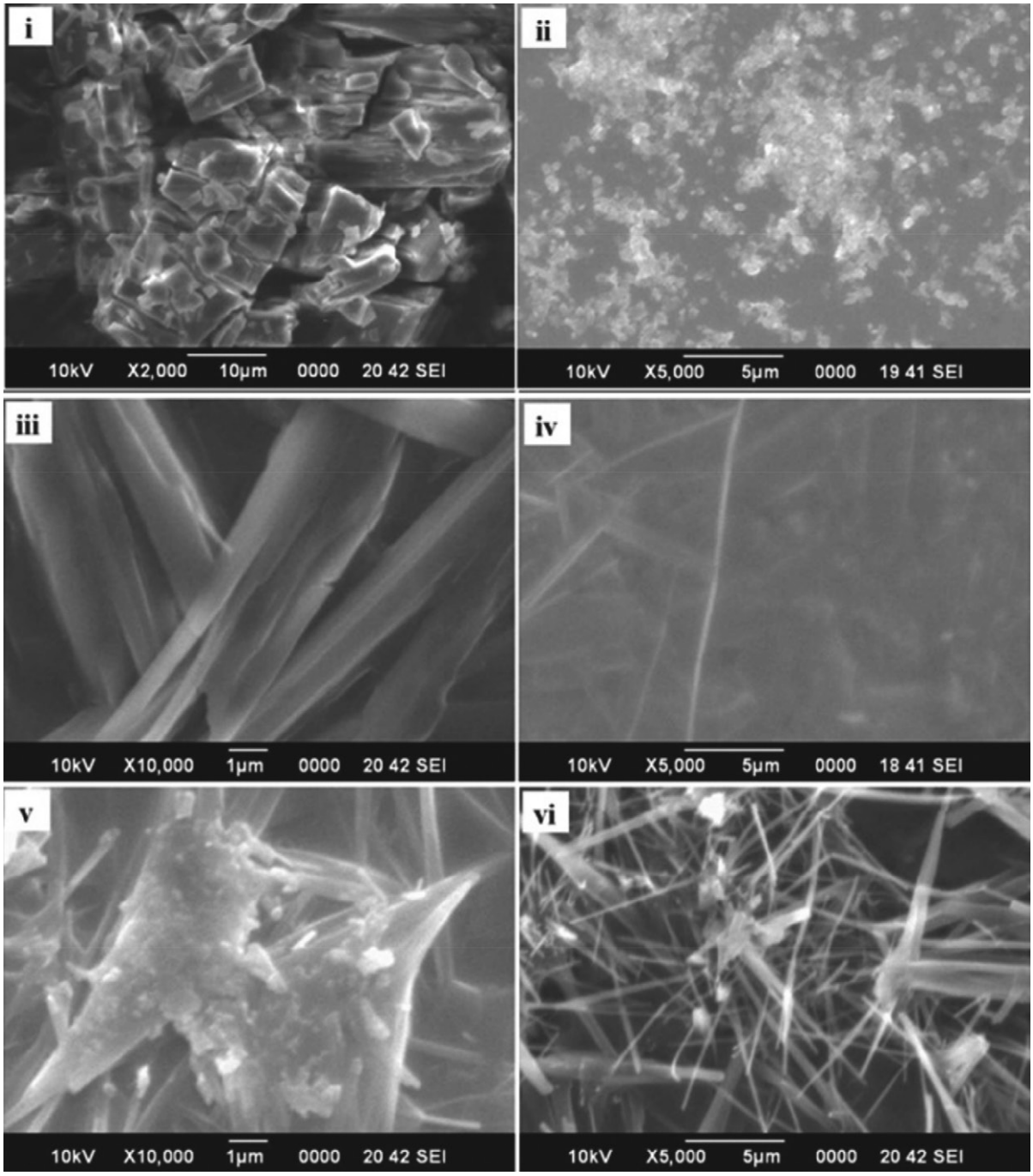


Figure 2. Scanning electron micrograph of pure DXM (magnification 2,000) (i); kaolin (magnification 5,000) (ii); films with kaolin (magnification 10,000) (iii), (magnification 5,000) (iv) of HPMC K100 LVCR; and films with kaolin (magnification 10,000) (v), (magnification 5,000) (vi) of HPMC K100 M matrices.

at 1665 cm^{-1}. This result suggested that the chemical properties of DXM have remained the same in the films. Interaction between DXM and kaolin in the film formulations has been confirmed by the shifting of the peak at 1032 cm^{-1}. The formation of hydrogen bond can be concluded as a result of this band shifting. The broadening of the characteristic peak at 1032 cm^{-1} was observed in the wide range in IR spectra of films containing higher kaolin content. This result indicates stronger binding between DXM and kaolin with the corresponding increase of kaolin content in the films.

3. 3. Scanning Electron Microscopy

The surface morphology of pure DXM, kaolin, and films of both HPMC K100 LVCR and HPMC K100 M matrices is demonstrated in Figure 2 by the scanning electron micrographs. The SEM images of Figure 2(i) demonstrate the geometric plate shaped microstructure of pure DXM and Figure 2(ii) that of nanosized kaolin. Figure 2(iii & iv) and (v & vi) represent the SEM images of films with higher kaolin content of both H_L and H_H matrices, respectively. The SEM images of films with added kaolin demonstrate the distinct distribution of nano-sized kaolin particles in the film. It can also be observed that the crystalline shape of DXM has almost disappeared in the films. In the presence of triethanolamine, the growth of drug crystal in HPMC film was not adequately noticed in the SEM micrographs due to the interfacial adhesion between the polymer phases and drug.[44] The crystal growth is also inhibited by HPMC in the matrix.[45]

3. 4. Hydration Behavior

The biological characteristic of hydrogel-based transmucosal drug delivery system significantly depended on the swelling of polymer present. Swelling capacity and swelling content of the film formulations were investigated in phosphate buffer saline (pH 7.4) at the laboratory ambient conditions. Swelling process included water uptake followed by the process of erosion of polymer matrix. The change of swelling content of film of both H_L and H_H matrix with varied kaolin content is depicted in Figure 3 and Figure 4 respectively. Graphs display that film of H_L and H_H matrices exhibited maximum swelling at 60 min and 6 h respectively. Decreased swelling content was observed while kaolin content increased in the film. The water resistance ability of kaolin resulted in sustaining swelling of polymer-based film matrix. Water resistance ability has been improved by increasing the kaolin content and gradually sustained the swelling of the film. Water uptake, the main basis for swelling, depends on the hydrophilicity and other parameter such as morphology (macro voids), free volume, and crystal size. Hence, swelling may also be dependent on these parameters. Kaolin produced a tortuous pathway and also formed a denser cross-linking network due to its certain level of hydrophilicity.[46,47] Thus kaolin had the capability of reducing the length of free pathway for water uptake into matrix, which led to sustained swelling of the film matrix.

In film formulations (H_L and H_H) swelling content was increased with the time of swelling. Higher swelling was found in the initial stage followed by a slower swelling at the later stages, known as hyperbolic form.[25] The form of difference in swelling content in the graphs (between H_L and H_H) is related probably to the polymer viscosity and molecular weight, because high molecular weight polymers exhibit high viscosity in the swelling stage.[48] The result of swelling content demonstrated higher value for the film of HPMC K100 M matrix compared with the film of HPMC K100LVCR matrix. This result suggests that the polymer viscosity and molecular weight play a role in the process of film swelling. The water uptake process did not easily empower through higher viscosity polymer of HPMC K100 M matrix. High molecular weight polymer increased the impact resistance due to higher degree of entanglement for rupturing more polymer bonds. In a fully hydrated state polymer chain disentanglement occured when there was no polymer-polymer interactions and higher viscosity induced greater chain entanglement than lower viscosity. Praveen et al.[49] also described in their report that the polymer chain disentanglement is affected by the polymer viscosity. Film of H_H matrix with maximum kaolin content showed higher swelling index, which suggests decreased movement of DXM molecules from the film matrix to the medium.

Erosion of film matrix is the process that follows after swelling and proceeds slowly. In this process, drug molecules diffuse through the micropores of polymer after

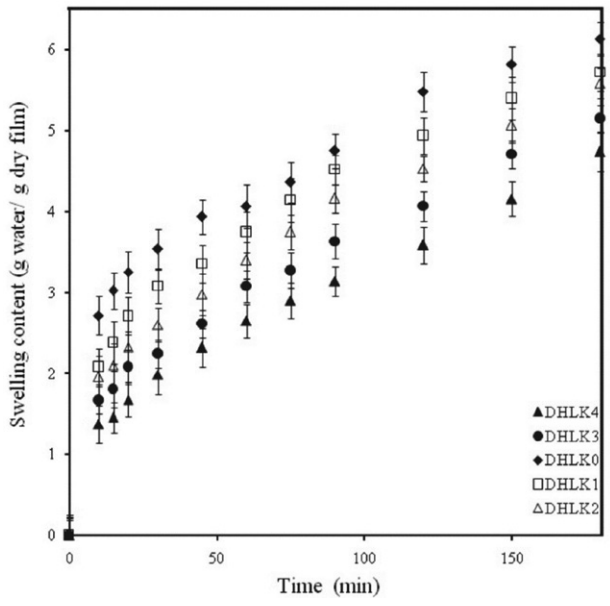


Figure 3. Swelling content of film of HPMC K100 LVCR (H_L) matrix with varied kaolin content.

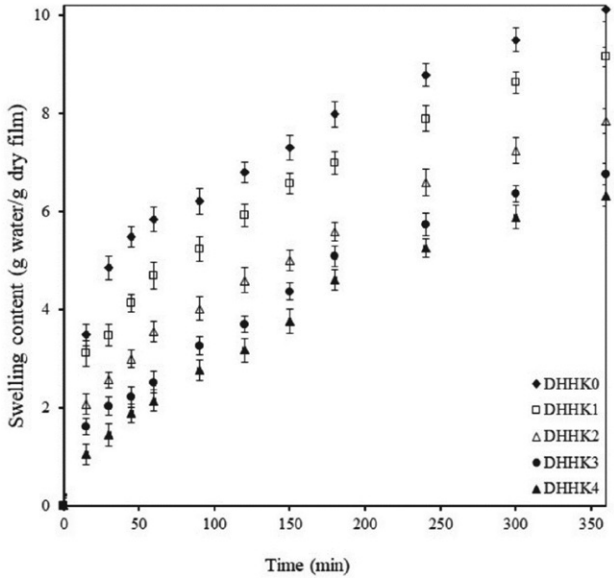


Figure 4. Swelling content of film of HPMC K100 M (H_H) matrix with varied kaolin content.

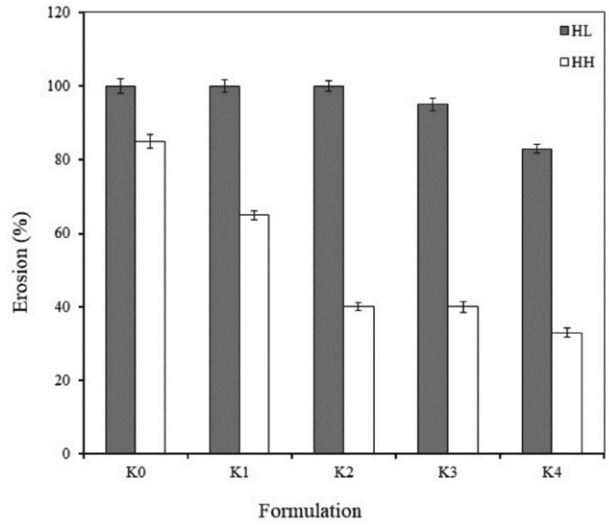


Figure 5. Erosion of film of HPMC K100 LVCR (H_L) and HPMC K100 M (H_H) matrix with varied kaolin content.

water uptake of the matrix.[6] After 6 h of the swelling study, erosion of films has been measured in pH 7.4 phosphate buffer saline. Figure 5 shows the progressive decrease in erosion with gradually increased kaolin content in the film. Presence of kaolin in the film hinders the process of erosion of film due to the entrapment of kaolin in the HPMC matrix networks. Higher kaolin content in the film has developed relatively stronger affinity between kaolin and polymer. Thus, the film with higher kaolin content shows more resistance for erosion. More resistance to the film erosion was also seen due to greater viscosity of H_H compared to H_L.

3. 5. Diffusion of Water

The predicted swelling value is similar with the experimental swelling value, when the swelling kinetics of films has been described by the Peppas model (RMSE = 0.016–0.02 for H_L matrix film and 0.016–0.02 for H_H matrix film). The diffusion exponential (n), k, R^2, reduced chi-square (χ^2) and RMSE values of all matrix films are demonstrated in Table 2. In order to investigate the water diffusion mechanism into hydrogel DXM film, Peppas equation was utilized. On the basis of the n value, the diffusion type of swelling was determined.[50] Fickian and non-Fickian diffusion are identified by the n values of 0.5 and 1.0, respectively. The ranges of swelling exponent values of films of H_L and H_H matrix are 0.28–0.43 and 0.31–0.59 respectively. According to the calculated n value, the diffusion mechanism of swelling of films of H_L and H_H matrix was Fickian and anomalous diffusion, respectively. Diffusion coefficient (D) is an important factor that describes how quickly water can diffuse through the polymeric matrix film. The results revealed that the D value increased with the increased kaolin content in the film

Table 2. Estimated swelling parameters of the film as per Peppas model and the diffusion coefficient of water.

Formulation	Parameter of Peppas model					
	k	n	R^2	χ^2	*RMSE*	D (cm^2s^{-1})
DH_LK_0	0.23	0.28	0.98	3.17E-04	0.016	$1.32*10^{-4}$
DH_LK_1	0.16	0.35	0.99	8.81E-05	0.008	$4.04*10^{-4}$
DH_LK_2	0.14	0.37	0.99	3.61E-04	0.017	$4.59*10^{-4}$
DH_LK_3	0.12	0.39	0.98	4.93E-04	0.020	$5.54*10^{-4}$
DH_LK_4	0.10	0.43	0.99	4.44E-04	0.019	$7.31*10^{-4}$
DH_HK_0	0.16	0.31	0.98	3.19E-04	0.016	$1.23*10^{-4}$
DH_HK_1	0.12	0.36	0.99	2.98E-04	0.016	$2.24*10^{-4}$
DH_HK_2	0.08	0.43	0.99	2.76E-04	0.015	$4.12*10^{-4}$
DH_HK_3	0.06	0.49	0.98	0.00101	0.029	$6.30*10^{-4}$
DH_HK_4	0.03	0.59	0.99	4.04E-04	0.018	$10.89*10^{-4}$

(Table 2). With the gradual increase in the kaolin content, water penetration becomes faster in both the polymers (H_L and H_H). The calculated diffusion coefficient increases from 1.32 *10^{-4} cm^2s^{-1} to 7.31 *10^{-4} cm^2s^{-1} for H_L matrix and 1.23 *10^{-4} to 10.89 *10^{-4} for H_H matrix.

3. 6. Evaluation of Lag Phase Model and Modified Lag Phase Model

The fitting of lag phase sigmoid model on the swelling data of film of both matrices (H_L and H_H) is shown in Figure 6 & Figure 7, respectively. The swelling data fitting with modified lag phase sigmoid model is depicted in Figure 8 & Figure 9 of H_L and H_H, respectively. The parameters (R^2, k, τ, $S_{obs.eq}$, RMSE, χ^2) of this model are presented in Table 3 for all films. These parameters describe the kinetics of all films with lower RMSE and χ^2 value and high correlation coefficient indicating appropriate fitting of model on swelling data. The time to obtain half of the swelling saturation (τ) is increased by higher kaolin content in the film. The predicted equilibrium swelling content and τ show higher value for H_H compared to H_L matrix film. Predicted equilibrium swelling content is similar to the experimentally obtained equilibrium moisture content. Modified lag phase sigmoid model demonstrates the increasing order of observed τ (17.6 to 105.7 and 38.4 to 283.1) and decreasing or almost similar order of k (20.3 to 12.4 and 9.4 to 6.3) with increased kaolin content in the film of both matrices (H_L and H_H matrix). Lag phase sigmoid model rate constant (k) decreases with increasing kaolin content in the film of both matrices supporting the effect of kaolin on prolonged swelling of the film. Kaptso et al [25] also described that the increased sigmoid model rate constant is due to increased mass transfer rate. However,

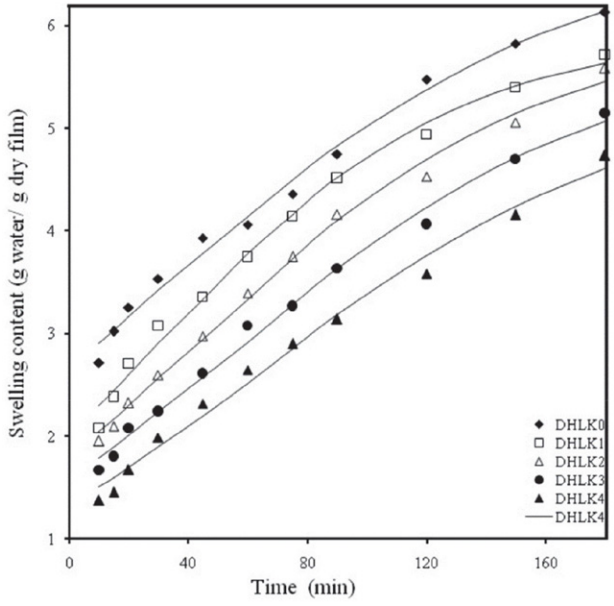


Figure 6. Fitting of the Lag phase sigmoid model of films of HPMC K100LVCR (H_L) matrix with varied kaolin content.

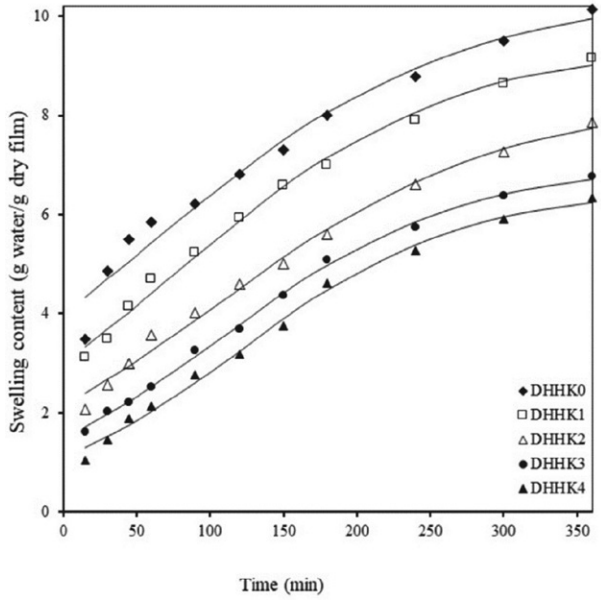


Figure 7. Fitting of the Lag phase sigmoid model of films of HPMC K100 M (H_H) matrix with varied kaolin swelling content.

Table 3. Estimated parameters of the modified Lag phase model.

Formulation	Parameter of the modified lag phase model						
	$S_{obs.eq}$	Obs τ (min)	Predicted τ (min)	$k \times 10^3$ (min^{-1})	R^2	RMSE	χ^2
DH_LK_0	6.32	17.6	24.3	20.3	0.951	0.174	0.03
DH_LK_1	6.38	37.2	41.6	16.1	0.984	0.138	0.01
DH_LK_2	6.70	55.2	64.3	14.1	0.996	0.119	0.01
DH_LK_3	6.75	80.6	84.5	13.0	0.999	0.121	0.01
DH_LK_4	6.77	105.7	107.1	12.4	0.998	0.145	0.01
DH_HK_0	10.62	38.4	57.7	9.4	0.964	0.338	0.03
DH_HK_1	11.02	103.6	115.4	7.1	0.994	0.290	0.02
DH_HK_2	11.14	173.3	196.2	6.5	0.999	0.321	0.02
DH_HK_3	11.33	219.7	253.1	6.3	0.995	0.412	0.04
DH_HK_4	11.70	283.1	287.3	6.9	0.989	0.485	0.06

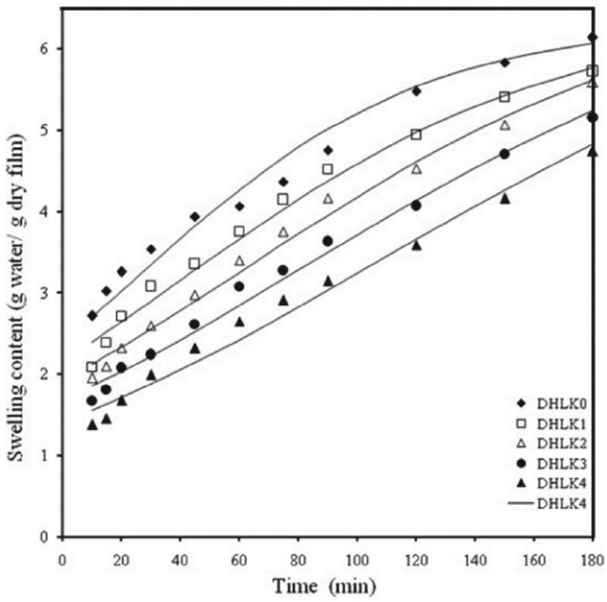


Figure 8. Fitting of the modified Lag phase sigmoid model of films of HPMC K100LVCR matrix with varied kaolin content.

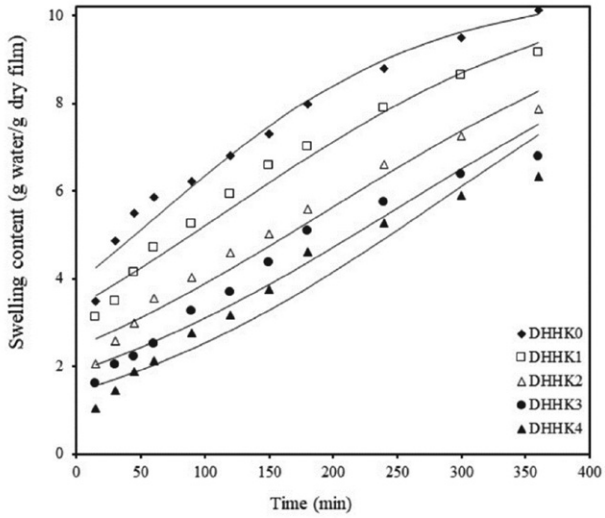


Figure 9. Fitting of the modified Lag phase sigmoid model of films of HPMC K100 M (H_H) matrix with varied kaolin swelling content.

the predicted value of τ increased from 24.26 to 107.10 and from 57.75 to 287.29 min for H_L and H_H, respectively. Correspondingly, *k* value decreased from 0.02 to 0.012 and from 0.009 to 0.006 min^{-1} for H_L and H_H, respectively. The fitting of this model is justified by the small RMSE and high R^2 value. Hence, the proposed modified Lag phase sigmoid model may be acceptable in the hydration study.

4. Conclusion

Kaolin incorporated HPMC films containing dexamethasone as a model drug have been prepared for characterization of hydration behaviour utilizing modified lag phase model. In this study, the effect of kaolin on swelling of H_L and H_H hydrogel films was investigated. Gradually decreased water content and water uptake were observed with increased kaolin content in the film. Distribution of nano-sized kaolin particles in the films was noticed in the SEM images. Swelling of both the matrices (H_L and H_H) has been decreased with increasing the kaolin content in the film, while H_H has shown higher value because of higher viscosity compared to the H_L matrix. Presence of kaolin in the film inhibited the erosion process of the film due to the entrapment of kaolin in the HPMC matrix networks. Greater viscosity of H_H also resulted in more resistance to the film erosion compared to H_L. Increasing diffusion coefficient value indicated that water penetration became faster in presence of kaolin in the film. The calculated value of diffusion coefficient increased with increasing kaolin content in both the matrices. Swelling kinetics of the films with varied kaolin content was investigated by the lag phase sigmoid mathematical model. The predicted swelling content value from the modified lag phase sigmoid model was similar to the observed value. This modified lag phase sigmoid model was successfully fitted to the experimental data, as confirmed by R^2 and lower RMSE value. The modified Lag phase sigmoid model resulted in τ values almost equal to the observed τ. Hence, we suggest that the modified version of the lag phase sigmoid model is also reliable enough to calculate kinetics in different food products.

Acknowledgements

We are very much grateful to the president, Siksha 'O' Anusandhan (Deemed to be University) Prof. (Dr) Manoj Ranjan Nayak for financial support and laboratory facility. Authors are also expressing our gratitude to the Pharmacia and Upjohn Company and Birla Institute of Technology, Mesra, Ranchi, for their gift sample and instrumental facility respectively.

5. References

1. A. S. Hoffman, *Adv. Drug Deliv. Rev.* **2002**, *54*, 3–12. **DOI:**10.1016/S0169-409X(01)00239-3
2. N. A. Peppas, K. B. Keys, M. Torres-Lugo, A. M. Lowman, *J. Control. Release.***1999**, *62*, 81–87. **DOI:**10.1016/S0168-3659(99)00027-9
3. K. Xu, J. Wang, Q. Chen, Y. Yue, W. Zhang, P. Wang, *J. Colloid Interf. Sci.* **2008**, *321*, 272–278. **DOI:**10.1016/j.jcis.2008.02.024
4. A. Martinez-Ruvalcaba, J. C. Sanchez-Diaz, F. Becerra, L. E. Cruz-Barba, A. Gonzalez-Alvarez, *Express Polym. Lett.* **2009**, *3*, 25–32. **DOI:**10.3144/expresspolymlett.2009.5
5. Y. Tang, J. R. Lu, A. L. Lewis, T. A.Vick, P. W. Stratford, *Macromolecules.* **2001**, *34*, 8768–8776. **DOI:**10.1021/ma010476i

6. B. Panda, R. Subhadarsini, S. Mallick, *Expert Opin. Drug* Del. **2016**, *13*, 633–643. **DOI:**10.1517/17425247.2016.1154038
7. S. Pattanaik, S. Nandi, R. N. Sahoo, A. Nanda, R. Swain, S. Das, S. Mallick, *Rev. Chim.* **2020**, *71*, 332–345. **DOI:**10.37358/RC.20.6.8200
8. R. Mohapatra, S. Senapati, C. Sahoo, S. Mallick, *Colloids Surf. B: Biointerfaces,* **2014**, *123*, 170–180. **DOI:**10.1016/j.colsurfb.2014.09.012
9. M. Birsan, I. C. Cojocaru, M. I. Stamate, V. Teodor, C. Tuchilus, *Rev. Chim.* **2016**, *67*, 1385–1388.
10. N. A. Peppas, A. R. Khare, *Adv. Drug Deliv. Rev.* **1993**, *11*, 1–35. **DOI:**10.1016/0169-409X(93)90025-Y
11. P. Colombo, *Adv. Drug Deliv. Rev*. **1993**, *11*, 37–57. **DOI:**10.1016/0169-409X(93)90026-Z
12. H. Hosseinzadeh, M. Sadeghi, *Asian J. Chem*. **2012**, *24*, 85–88.
13. M. Pannirselvam, A. Genovese, M. C. Jollands, S. N. Bhattacharya, R. A. Shanks, *Express Polym. Lett.* **2008**, *2*, 429–439. **DOI:**10.3144/expresspolymlett.2008.52
14. M. Alexandre, P. Dubois, *Mat. Sci. Eng.* R. **2000**, *28*, 1–63. **DOI:**10.1016/S0927-796X(00)00012-7
15. S. S. Ray, M. Bousmina, *Prog. Mater. Sci.* **2005**, *50*, 962–1079. **DOI:**10.1016/j.pmatsci.2005.05.002
16. M. I. Carretero, *App. Clay Sci*. **2002**, *21*, 155–163. **DOI:**10.1016/S0169-1317(01)00085-0
17. E. Cortes-Trivino, I. Martinez, *Express Polym. Lett.* **2018**, *12*, 616–627. **DOI:**10.3144/expresspolymlett.2018.52
18. W. Thakhiew, P. Waisayawan, S. Devahastin, *Dry. Technol.* **2011**, *29*, 1396–403. **DOI:**10.1080/07373937.2011.588816
19. D. Moreau, C. Chauvet, F. Etienne, F. P. Rannou, L. Corté, *Proc Natl Acad Sci.* **2016**, *113*, 13295–13300. **DOI:**10.1073/pnas.1609603113
20. M. Gagliardi, *Macromol Theor Simul.* **2019**, *28*, 1800063. **DOI:**10.1002/mats.201800063
21. H. R. Lee, Y. D. Lee, *Chem. Eng. Sci*. **1991**, *46*, 1771–1779. **DOI:**10.1016/0009-2509(91)87023-6
22. T. Tanaka, D. J. Filmore, *J. Chem. Phys*. **1979**, *70*, 1214–1218. **DOI:**10.1063/1.437602
23. Y. Li, T. Tanaka, *J. Chem. Phys.* **1990**, *92*, 1365–1371. **DOI:**10.1063/1.458148
24. C. Wu, C. Yan, *Macromol.* **1994**, *27*, 4516–4520. **DOI:**10.1021/ma00094a013
25. H. J. Schott, *Macromol. Sci.* B. **1992**, *31*, 1–9. **DOI:**10.1080/00222349208215453
26. A. S. Kipcak, O. Ismail, I. Doymaz, S. Piskin, *J. Chem.* **2014**, *2014*, 1–9. **DOI:**10.1155/2014/281063
27. S. H. Othman, N. R. A. Kechik, R. A. Shapi'i, R. A. Talib, I. S. M. A. Tawakkal, J Nanomater, vol. 2019, Article ID 3843949, 12 pages, 2019. **DOI:**10.1155/2019/3843949
28. Y. Cao, *Express Polym. Lett.* **2018**, *12*, 768–780. **DOI:**10.3144/expresspolymlett.2018.66
29. M. Grassi, G. Grassi, *Curr. Drug Deliv.* **2005**, *2*, 97–116. **DOI:**10.2174/1567201052772906
30. P. V. Pramiu, R. L. Rizzi, N. V. Do Prado, S. R. Coelho, P. Z. Bassinello, *J. Food Eng.* **2015**, *165*,112–23. **DOI:**10.1016/j.jfoodeng.2015.05.020
31. K. G. Kaptso, Y. N. Njintang, A. E. Komnek, J. Hounhouigan, J. Scher, C. M. F. Mbofung, *J. Food Eng*. **2008**, *86*, 91–99. **DOI:**10.1016/j.jfoodeng.2007.09.014
32. B. C. Marques, L. M. de Matos Jorge, R. M. Jorge, *J. Cereal Sci.* **2016**, *71*, 93–98. **DOI:**10.1016/j.jcs.2016.08.005
33. Lagaly, G., Olphen, H. Van, An Introduction to Clay Colloid Chemistry. Second ed. John Wiley and Sons, New York London, Sydney, Toronto (**1977**).
34. F. C. H. Pinto, A. Silva-Cunha, G. A. Pianetti, E. Ayres, R. L. Orefice, G. R. Da Silva, *J Nanomater*. **2011**, *2011*, Article ID 528628. **DOI:**10.1155/2011/528628
35. N. A. Peppas, P. Bures, W. Leobandung, H. Ichikawa, *Eur. J. Pharm. Biopharm*. **2000**, *50*, 27–46. **DOI:**10.1016/S0939-6411(00)00090-4
36. K. G. Kaptso, Y. N. Njintang, A. E. Komnek, J. Hounhouigan, J. Scher, C. M. F. Mbofung, *J. Food Eng*. 2008, **86**, 91–99. **DOI:**10.1016/j.jfoodeng.2007.09.014
37. http://www.originlab.com/OriginProLearning.aspx
38. S. Mallick, S. Pattnaik, K. Swain, P. K. De, A. Saha, G. Ghosal, A. Mondal, *Eur. J. Pharm. Biopharm*. **2008**, *68*, 346–351. **DOI:**10.1016/j.ejpb.2007.06.003
39. J. A. Mbey, S. Hoppe, F. Thomas, *Carbohyde. Polym.* **2012**, *88,* 213–222. **DOI:**10.1016/j.carbpol.2011.11.091
40. G. R. Silva, A. Silva-Cunha, F. Behar-Cohen, E. Ayres, R. L. Orefice, *Mater. Sci. Eng. C*. **2011**, *31*, 414–422. **DOI:**10.1016/j.msec.2010.10.019
41. M. M. Doile, A. K. Fortunato, I. C. Schhücker, S. K. Schucko, M. A. Silva, P. O. Rodrigues, *AAPS Pharm. Sci. Tech*. **2008**, *9*, 314–321. **DOI:**10.1208/s12249-008-9042-z
42. B. J. Saikia, G. J. Parthasarathy, *Mod. Phys*. **2010**, *1*, 206–210. **DOI:**10.4236/jmp.2010.14031
43. J. Kristo, R. L. Frost, A. Felinger, J. Mink, *J. Mol. Struct*. **1997**, *410–411*, 119–122. **DOI:**10.1016/S0022-2860(96)09488-4
44. F. S. Aleanizy, F. Alqahtani, A. O. Gohary, E. E. Tahir, R. A. Shalabi, *Saudi Pharm. J*. **2015**, *23*, 167–176. **DOI:**10.1016/j.jsps.2014.06.006
45. R. Mohapatra, S. Mallick, A. Nanda, R. N. Sahoo, A. Pramanik, A. Bose, D. Das, L. Pattnaik, *RSC Adv.* **2016**, *6*, 31976–31987. **DOI:**10.1039/C6RA03604J
46. A. Saada, B. Siffert, E. Papirer, *J Colloid Interf. Sci.***1995**, *174*, 185–190. **DOI:**10.1006/jcis.1995.1381
47. A.Ghebaur, S. A. Garea, S.Cecoltan, H. Iovu, *Mater. Plast*. **2017**, *54*, 8–13. **DOI:**10.37358/MP.17.1.4774
48. https://polymerdatabase.com/polymer%20physics/Solution_Viscosity.html
49. S. P. Hiremath, N. R. Saha, *AAPS Pharm. Sci. Tech*. **2008**, *9*, 1171–1178. **DOI:**10.1208/s12249-008-9159-0
50. N. A. Peppas, L. Brannon-Peppas, *J. Food Eng.***1994**, *22*, 189–210. **DOI:**10.1016/B978-1-85861-037-5.50015-1

Povzetek

Hidracijsko obnašanje polimernega filma na osnovi hidrogela ima velik pomen pri dostavi zdravil v sluznico. Za raziskovanje hidracije filma je bil uporabljen modificirani sigmoidni model na osnovi faznega zamika. Za preučevanje kinetike nabrekanja so bili pripravljeni filmi s kaolinom z vgrajenim HPMC K100LVCR (H_L) in K100M (H_H), ki so vsebovali deksametazon kot modelno zdravilo. Nabrekanje H_L in H_H filmov se je s postopnim povečevanjem vsebnosti kaolina zmanjšalo, H_H z višjo viskoznostjo pa je kazal večjo vrednost kot H_L. Kaolin je zaviral tudi postopek erozije filma. Spremenjen matematični sigmoidni model faznega zamika je pokazal podobnost med predvideno in opaženo vsebnostjo nabrekanja. Visoka vrednost R^2 in majhna vrednost RMSE sta potrdili uspešno prilagajanje modela eksperimentalnim podatkom za obseg nabrekanja. Tudi dobljena vrednost τ je bila podobna opaženi. Ta spremenjeni model bi lahko bil dovolj zanesljiv za oceno postopka hidracije v zrnih živil, filmih za pakiranje hrane itd.

Except when otherwise noted, articles in this journal are published under the terms and conditions of the Creative Commons Attribution 4.0 International License

DOI: 10.17344/acsi.2020.6299 *Acta Chim. Slov.* **2021,** *68,* 170–177
creative commons

Scientific paper

4-(4,5-Diphenyl-1H-imidazole-2-yl)phenol: Synthesis and Estimation of Nonlinear Optical Properties using Z-Scan Technique and Quantum Mechanical Calculations

Fatemeh Mostaghni

Department of Chemistry , Payam Noor University, P.O. BOX 19395-4697 Tehran, Iran

** Corresponding author: E-mail: mostaghnif@yahoo.com*

Received: 10-26-2020

Abstract

In this study, 4-(4,5-Diphenyl-1H-imidazole-2-yl) phenol is successfully synthesized, and its nonlinear optical properties (NLO) are investigated both experimentally and theoretically. Theoretical investigations have been done by using TD-DFT and B3LYP functional with usual 6-31+G(d,p) basis set. The results of HOMO-LUMO and NBO analysis show the low energy gap, high total dipole moment, and hyperpolarizabilities (β, γ) as well as the presence of dipolar excited states with relatively significant dipole-moment changes which are linked to the nonlinearity. The z-scan technique confirmed the NLO properties of title compound. The nonlinear absorption coefficient, refractive index, and third-order susceptibility were found to be 4.044×10^{-1} cmW^{-1}, 2.89×10^{-6} cm^{2}W^{-1} and 2.2627×10^{-6} esu, respectively. The negative sign of n_2 indicated the occurrence of self-defocusing nonlinearity. The results show that the title compound can been used as potential NLO material.

Keywords: Nonlinearity; z-scan technique; hyperpolarizabilities; triaryl imidazoles.

1. Introduction

The development of photonic technology, nonlinear optical materials have received widespread attention both from the research as well as industrial point of view.[1–3] In recent years, many studies have been reported by researchers to find new compounds with high nonlinear optical properties. The essential requirements of suitable photonic materials are their high nonlinearity, fast response time, chemical stability, and ease of molecular design.[4–8]

In this context, π-conjugated organic materials have received more attention due to their high nonlinearity and fast response times resulting from the ease of polarizability of the extended mobile π-electron clouds across the molecule.[9–13]

Unlike inorganic materials in which band structure phenomena cause nonlinear phenomena, in organic materials and polymers, these phenomena arise from the transition of an electron from the highest occupied molecular orbital (HOMO) to the lowest unoccupied molecular orbital (LUMO) that caused a transition of the dipole moment from the ground state to the excited state.[14–18]

Different types of organic compounds with extensive conjugated π system are expected to exhibit nonlinear optical properties because of π–π interactions that allow an intramolecular charge transfer (ICT).[19–29] Moreover, ICT is responsible for the broadening of the absorption spectrum, and the reduction of the optical bandgap.[30–32]

Over the past two decades, small organic molecules have been a subject of increasing research interest for their potential applications in organic electronics.[33] Furthermore, it was shown that the π-conjugated bridges based on heterocyclic rings had improved stability relative to other polyenes.[34–37]

Among these, various types of imidazole derivatives have received widespread attention due to their piezoelectric, photochromic, and thermochromic properties. They are widely used in optoelectronics, superconductors, molecular photonics, sensors, and optical data storage devices.[37–39]

In this study, 4-(4,5-Diphenyl-1H-imidazole-2-yl) phenol was synthesized by one-pot three-component syn-

thesis using $CoFe_2O_4$. Then for the first time, the nonlinear optical properties of this molecule are measured by the Z-scan technique and quantum mechanical methods. The results showed that the title compound could be a good candidate with the potential application in optoelectronic devices.

2. Experimental

All chemicals were analytical grade and purchased from Sigma-Aldrich. Deionized water served as reacting medium. The melting point was measured by an Electrothermal-9200 melting point apparatus. IR spectra were measured on the FTIR-6300 spectrometer (KBr). ^{1}HNMR spectra were recorded on Bruker ADVANC DRX 400 spectrometer, using DMSO as solvent.

2. 1. Synthesis of 4-(4,5-Diphenyl-1H-imidazole-2-yl) Phenol

To the solution of benzoin (1 mM), 2-hydroxy benzaldehyde (1 mM), ammonium acetate (4mM) in ethanol (10 mL) was added 5 mol% $CoFe_2O_4$ nanocatalyst. The mixture was reflux in 50 °C, and the progress of the reaction was controlled by TLC using the mixture eluent (n-Hexane: Ethyl acetate 4:1). After completion of the reaction (30 minutes), the catalyst was separated by an external magnet, and the reaction mixture was allowed to cool. Then the precipitate was collected by filtration, washed with water, and recrystallized using ethanol.

The product (figure 1) was characterized by FTIR and ^{1}H NMR and Mass spectroscopy. Yield 87%; purity > 96%; mp: 278 °C (275–276 °C).[40]

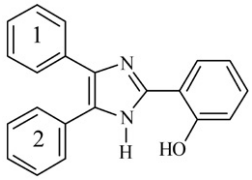


Figure 1. Molecular structure of 4-(4,5-Diphenyl-1H- imidazole-2-yl) phenol

IR (KBr, cm^{-1}): ν/cm^{-1} : 3598, 3445, 2996, 2468, 1643, 1613, 1546, 1506, 1490, 1240, 764, 698, ^{1}H NMR: δ_H(ppm) (300 MHz, $CDCl_3$): 8.03 (s, 1H, NH), 7.63–7.66 (m, 2H), 7.43–7.45 (m, 2H), 7.22–7.26 (m, 4H), 7.07–7.09 (d, 2H), 6.77–6.86 (m, 4H), GC-MS (IE, 70 eV) *m/z* (%) 312 (M+, 100.0), 208, 165, 89, 77, 51, 41.

2. 2. UV-Vis Absorption Spectrum

The UV-Vis absorption spectrum of the sample was recorded using a spectrometer (Jenway model 6310). The sample was dissolved in DMF and measured in quartz cell in the range of 320 to 1000 nm (Figure 2). The spectrum showed absorption peaks at 340 nm, and 406 nm.

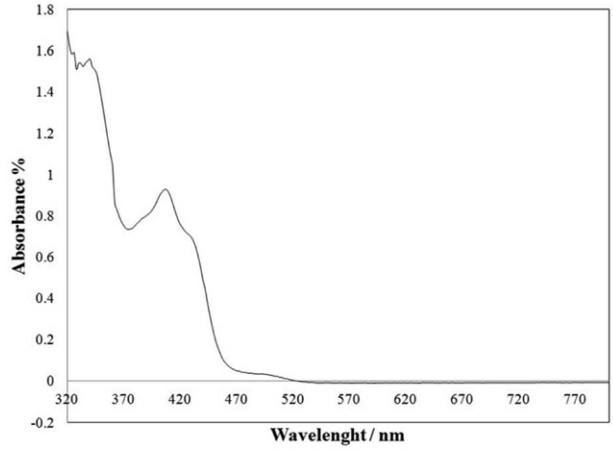


Figure 2. UV-Vis absorption spectra of 4-(4,5-Diphenyl-1H- imidazole-2-yl) phenol

2. 3. Z-Scan Measurement

The determining of the third-order nonlinear optical properties of the sample was carried out using the z-scan technique as a standard method. In this method, a very thin sample of matter is exposed to a laser beam while the sample was translated across the focal zone along the z-axis. The light passing through the sample is recorded as a function of the sample position relative to the beam focal point. The Z-Scan method is used to determine the nonlinear refractive index and absorption coefficient in close and open aperture configurations, respectively.

2. 4. Computational Method

I performed density functional theory (DFT) and time-dependent DFT (TD-DFT) calculations on the title compound using the Gaussian 09 suite of software.[41] The calculations were carried out by using TD-DFT and B3LYP functional.[42,43] The usual 6-31G+(d,p) basis set was employed in the calculations. Numerous quantities including molecular structures, ionization potentials, electronegativity, HOMO-LUMO energies, and the HOMO-LUMO energy gap, dipole moments, polarizability, and hyperpolarizability Have been measured and discussed.

3. Results and Discussion

3. 1. UV-Vis Absorption Spectrum

As can be seen in Figure 2, this sample has shown the absorption bands in the UV-Vis region between 340–470 nm. The absorption observed at 406 nm due to the $\pi \rightarrow \pi^*$ transition. The wide transparency of the sample in the vis-

ible region enables it for the second harmonic generation that required for all NLO materials.

The band gap energy was determined using the Tauc relation.[44] The band gap value obtained using the direct transition. Extrapolating the linear part of the curves to the X axis yield the bandgap equal to 2.54 eV (Figure 3).

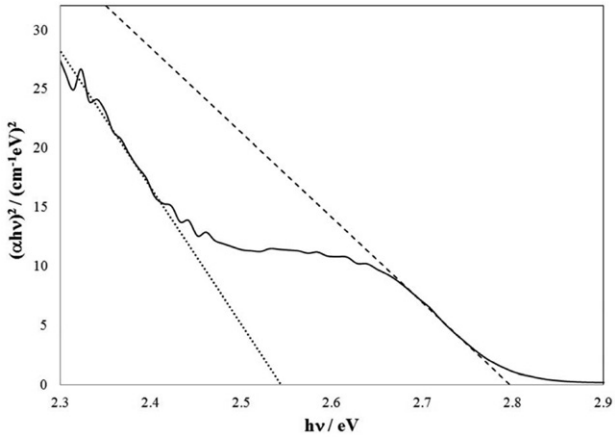


Figure 3. Plot $(\alpha h\nu)^2$ vs. photon energy

3. 2. Nonlinear Absorption Coefficient

The nonlinear absorption coefficient, the nonlinear susceptibility, and imaginary part of $\chi^{(3)}$ were determined from open aperture z-scan data. For this purpose, the normalized transmittance of open aperture Z-scan at wavelengths 532 nm was plotted as a function of sample position (Figure 4).

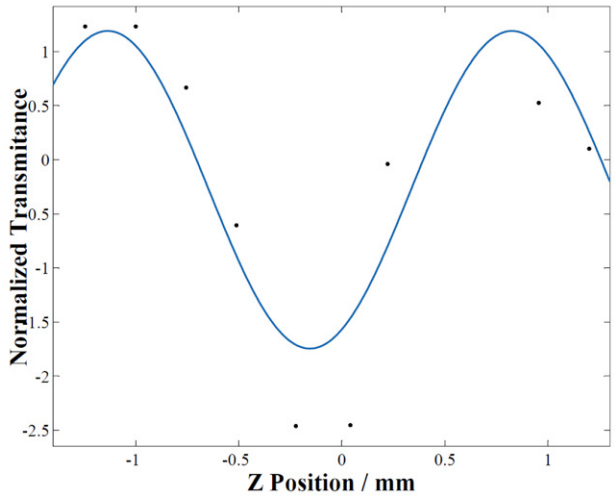


Figure 4. Open aperture Z-Scan data for 4-(4,5-Diphenyl- 1H-imidazole-2-yl) phenol solution.

As can be seen from Figure 4, the curve shows a valley shape, indicating a positive nonlinear absorption coefficient resulting from the two-photon absorptions (TPA) whereby a molecule simultaneously absorbs two photons that are inherently weak at low intensities of light.

The nonlinear absorption coefficient β was calculated by the following equations:[45]

$$T(z,s=1)=\sum_{m=0}^{\infty}\frac{\left[\frac{\beta I_0 L_{eff}}{1+\left(\frac{Z}{Z_0}\right)^2}\right]^m}{(m+1)^{\frac{3}{2}}} \quad (1)$$

$$Z_0=\frac{K\omega_0^2}{2} \quad (2)$$

$$L_{eff}=\frac{[1-exp(-\alpha L)]}{\alpha} \quad (3)$$

$$\alpha=-\frac{1}{L}ln\left(\frac{P}{P_0}\right) \quad (4)$$

Where I_0 is peak on-axis irradiation at the focal point, Z is the sample position at the minimum transmittance, Z_0 is diffraction length, T is the total transmittance, L_{eff} is the effective thickness of the sample and β is NLA coefficient. The nonlinear absorption coefficient is tabulated in table 1.

3. 3. Nonlinear Refractive Index

The sign and magnitude of the nonlinear refractive index, and real part of χ(3) were determined from the closed aperture z-scan data. The normalized transmittance of the sample as a function of distance from the focus point is plotted in Figure 5.

As figure 5 shows a peak-valley configuration, the nonlinear refractive index is negative and indicates self defocusing nonlinearity.

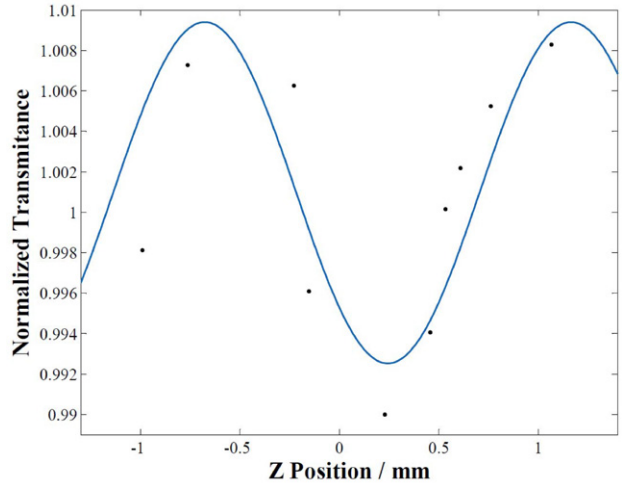


Figure 5. Closed aperture Z-Scan data for 4-(4,5-Diphenyl- 1H-imidazole-2-yl) phenol solution

However, ΔT_{p-v} is related to the nonlinear refractive index n_2 by the following equations:[46]

$$\Delta T_{p-v} = 0.406(1-S)^{0.27}\left(\frac{2\pi}{\lambda}\right) n_2 I_0 L_{eff} \quad (5)$$

$$I_0 = \frac{2p}{\pi\omega^2} \quad (6)$$

$$S = 1 - exp\left(\frac{-2r_a^2}{\omega_a^2}\right) \quad (7)$$

In the above equation, ΔT_{p-v} is the distance between the peak and valley transmittance which is obtained from figure 5, I_0 is the intensity in the focused sample, r_a is the radius of aperture, ω_a is the radius of the beam at the aperture, S is the linear transition, and n_2 is the nonlinear refractive index.

Besides, changes in the induction reflectance index were determined by the following equation.

$$\Delta n = n_2 I \quad (8)$$

3. 4. Third Order Susceptibility $\chi^{(3)}$

The real and imaginary parts of the third-order susceptibility are related to the nonlinear refractive index n_2 and the nonlinear absorption coefficient β respectively.

Where the imaginary part of the third-order susceptibility is calculated from the nonlinear absorption coefficient using the following equation.

$$Im\chi^{(3)}(esu) = \left(\frac{10^{-2}\varepsilon_0 c^2 n_0^2 \lambda}{4\pi^2}\right)\beta,\ in\ \left(\frac{cm}{W}\right) \quad (9)$$

Moreover, the real part of the third order susceptibility can be obtained from the nonlinear refractive index through the relationship:

$$Re\chi^{(3)}(esu) = \left(\frac{10^{-4}\varepsilon_0 c^2 n_0^2}{\pi}\right) n_2,\ in\ \left(\frac{cm^2}{W}\right) \quad (10)$$

In the above equations, β is the nonlinear absorption coefficient, n_2 is the nonlinear refractive index, n_0 is the linear refractive index, c is the speed of light in the vacuum and ε_0 is the permeability coefficient in the vacuum.

However, the absolute value of nonlinear third-order susceptibility can be obtained by the following equation.

Table 1. Calculated third order nonlinear optical parameters of the title compound

$n_2 \times 10^{-6}$ cm²/W	$\beta \times 10^{-1}$ cm/W	Re $(\chi^{(3)}) \times 10^{-3}$ esu	Im $(\chi^{(3)}) \times 10^{-5}$ esu	$\chi^{(3)} \times 10^{-6}$ esu
–2.89	4.044	–1.5016	8.89	2.2627

$$\left|\chi^{(3)}\right| = \left\{\left[Re(\chi^{(3)})\right]^2 + \left[Im(\chi^{(3)})\right]^2\right\}^{1/2} \quad (11)$$

The values of the third-order nonlinear susceptibilitiies obtained for 4-(4,5-Diphenyl-1H-imidazole-2-yl) phenol are listed in table 1.

The high values of negative nonlinear refractive index and the third-order susceptibility of the sample, which are associated with a 2PA resonance enhancement, indicate that it can be potentially used as an optical limiter to protect tools and human eyes.

3. 5. Electronic Structure and One-Photon Absorption

Electronic properties such as ionization potential (IP), hardness (η), softness (S), and electron affinity (EA), can be evaluated from HOMO and LUMO energies. HOMO and LUMO energies, Band gap energy, hardness, softness ionization potential (IP), and electron affinity (EA) are summarized in Table 2.

Quantum mechanical calculations play an important role in the understanding of the relationship between the molecular structure and the nonlinear optical properties of the compounds. There are many factors contribute to enhancing the properties of NLO compounds such as: low bandgap energy, high dipole moment, reversing of ground-state charge distribution and the π-electronic cloud redistribution via the π-conjugated system.[47] In conjugated organic materials, electrons in π bond are delocalized and have more motions rather than other electrons. In this case the π-bond electrons can easily move in the whole molecule space. Increasing the electron charge distribution will result in a larger hyperpolarizability, which is linked to the nonlinearity.

The orbitals involved in the main transitions are shown in figure 6. As can be seen, the HOMO orbital is delocalized over the whole molecule. By contrast, the LUMO is mostly located over two phenyl rings 1 and 2.

Table 2. Theoretically computed HOMO and LUMO energies, Bond gap energy (E_{gap}), Hardness (η), softness (S), Ionization potential (IP), Electron affinity (EA)

E_{HOMO} eV	E_{LUMO} eV	η eV	S eV	IP KJ/mol	EA KJ/mol	E_{gap} eV
–4.9980	–1.8098	1.594	0.314	482.225	174.622	3.18

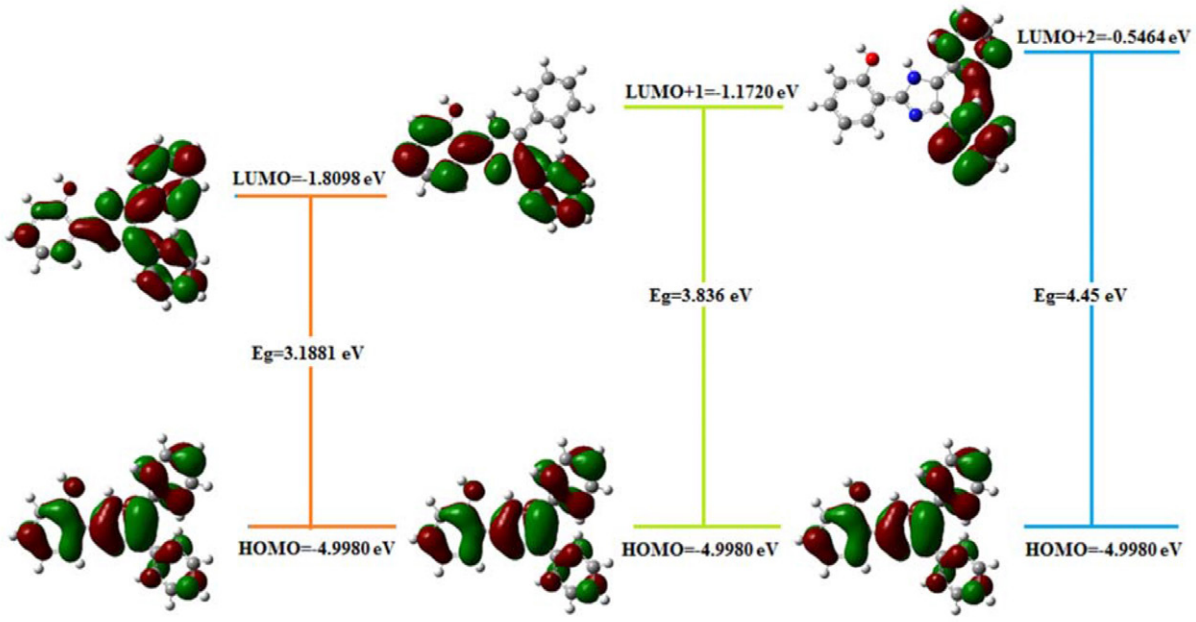


Figure 6. Frontier orbitals of 4-(4,5-Diphenyl-1H-imidazole-2-yl) phenol

Moreover, LUMO+1 is based more on the phenyl ring 2 and phenolic ring while, LUMO+2 is mostly delocalized on the two phenyl rings. Consequently, electron transition from ground to excited states facilitate an electron density transfer.

The short-circuit current density is an important component of the photoelectric conversion efficiency (PCE) is determined by the light-harvesting efficiency (LHE).

The light-harvesting efficiency (LHE) was approximately calculated from oscillator strength (f) using the following equation:[48]

$$LHE = 1-10^{-f} \quad (12)$$

As can be seen from table 3, both H→L and H→L+1 transitions dominantly dictate the electronic absorption profile of the studied molecule with sufficiently high f-values. However, the value of excitation energy related to H→L transition is comparable to the band gap value obtained from the Tauc equation. By contrast, the oscillator strength value of H→L+2 transition is too low to contribute to the absorption spectra. As expected, the low energy electronic excitations have substantial ICT character.

Both H→L and H→L+1 transitions with the high LHE will have a high short-circuit current density and so the high photoelectric conversion efficiency.

The partially density of states (PDOS) spectra of the title compound was also obtained using quantum mechanical calculations. According to PDOS spectra diagram (Figure 7), band gap was low which is in good agreement with other results.

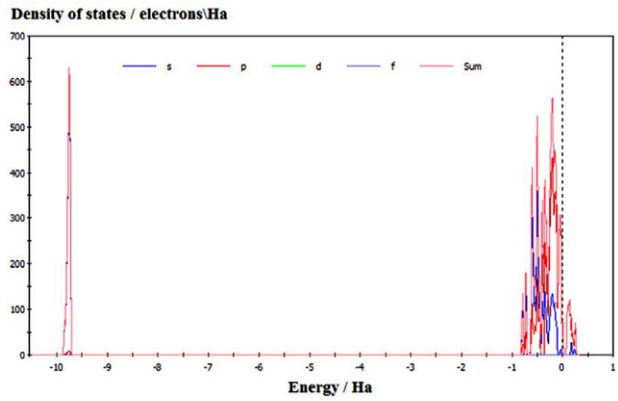


Figure 7. Calculated DOS spectra of 4-(4,5-Diphenyl-1H-imidazole-2-yl) phenol

Table 3. Excitation energies (E_{ex}), oscillator strengths (f), light harvesting efficiencies (LHE), and electronic transitions configurations of the title compound at TD-DFT-B3LYP/6-31+G(d,p) level in DMSO

Excited State	E_{ex}	f	LHE	Transition assignment
82 –> 83 (S)	2.9654 eV 418.10 nm	0.5678	0.7295	H→L (99.18%)
82 –> 84 (S)	3.3587 eV 369.14 nm	0.2601	0.4506	H→L+1 (96.24%)
82 –> 85 (S)	3.5015 eV 354.09 nm	0.0031	0.0071	H→L+2 (96.52%)

3. 6. Second-Order Nonlinear Optical (NLO) Response

The linear isotropic polarizability indicates the capacity of changing the charge density in the system under the influence of an external field. However, the magnitude of the isotropic polarizability α and anisotropy of polarizability (Δα) are calculated using the polarization components as follows.[49,50]

$$\alpha_{ve} = \frac{1}{3}(\alpha_{xx} + \alpha_{yy} + \alpha\alpha_{zz}) \quad (13)$$

$$\Delta\alpha = \frac{1}{2}\left[(\alpha_{xx} - \alpha_{yy})^2 + (\alpha_{xx} - \alpha_{zz})^2 + (\alpha_{yy} - \alpha_{zz})^2\right]^{1/2} \quad (14)$$

The first hyperpolarizability (β) , which is studied using second harmonic generation (SHG) is:

$$\beta_{tot} = \left[\begin{matrix}(\beta_{xxx} + \beta_{xyy} + \beta_{xzz})^2 + (\beta_{yyy} + \beta_{yzz} + \beta_{yxx})^2 \\ +(\beta_{zzz} + \beta_{zxx} + \beta_{zyy})^2\end{matrix}\right]^{1/2} \quad (15)$$

Also, the direction of charge transfer in the title compound was determined by the ratio of β_{vec} and β_{total} using the following equations:

$$\cos\theta = \frac{\beta_{vec}}{\beta_{tot}} \quad (16)$$

where β_{vec} is the vector component of first hyperpolarizability.[51]

$$\beta_{vec} = \frac{(\beta_x\mu_x + \beta_y\mu_y + \beta_z\mu_z)}{\mu} \quad (17)$$

The second hyperpolarizability (γ), which is studied using third-harmonic generation (THG) is:

$$\gamma \equiv \gamma_{zzzz} = \frac{1}{5}\left[\gamma_{xxxx} + \gamma_{yyyy} + \gamma_{zzzz} + \right. \\ \left. + \gamma_{zzzz} + 2(\gamma_{xxyy} + \gamma_{xxzz} + \gamma_{yyzz})\right] \quad (18)$$

The isotropic polarizability (α), the anisotropy of the polarizability (Δα), the vector component of the first hyperpolarizability and hyperpolarizabilities (β, γ) of the title compound are listed in the table 4.

Table 4 dipole polarizability (α), first and second hyperpolarizability (β, γ), the vector component of first hyperpolarizability (β_{vec}) and the anisotropy of the polarizability (Δα) of the title compound

α (a.u)	Δα (a.u)	β_{total} (a.u)	β_{vec}	<γ> (a.u)
–128.7264	255.5163	144.1682	133.6176	–4045.6719

As can be seen, 4-(4,5-Diphenyl-1H-imidazole-2-yl) phenol show the high total static dipole moment and hyperpolarizabilities (β, γ) which can be attributed to the positive contribution of their conjugation. The ratio of $\beta_{vec}/\beta_{total}$ in table 4 is equal to 0.93, which indicated the unidirectional charge transfer in the title compound. Therefore it is a good candidate for future studies of nonlinear optical properties.

4. Conclusion

I have synthesized 4-(4,5-Diphenyl-1H-imidazole-2-yl)phenol as an attractive material for potential application in nonlinear optics. The nonlinear optical properties of the title compound are investigated using the z-scan technique and quantum mechanical calculations. Both theoretical and experimental results reveal that the title compound exhibits large optical nonlinearity. The calculation of the HOMO-LUMO energy gap showed that the eventual charge transfer interactions occure within the molecule. Furthermore, the high value of total static dipole moment and hyperpolarizabilities (β, γ) were found for the title compound, which was attributed to the positive contribution of their conjugation. The calculated transition dipole moments for ground and excited states indicated an electron density transfer. Besides, the ratio of $\beta_{vec}/\beta_{total}$ indicated the unidirectional charge transfer in the title compound. In summary, from all theoretical studies, it was concluded that the title compound can use as potential NLO molecule.

The theoretical results are confirmed by the nonlinear refractive index, and the nonlinear absorption coefficient were determined by z-scan techniques. The magnitude and sign of the nonlinear refractive index (n_2) determined using close aperture z-scan. n_2 was in the range of 10^{-6} cm^2/W. The negative sign of n_2 indicated the occurrence of self-defocusing phenomena due to the local variation of the refractive index with temperature. The measured nonlinear absorption coefficient (β) by open aperture z-scan was in the range of 10^{-1} cm/W associated with the two-photon absorption (TPA) effect. Finally, the physicochemical studies on the title compound revealed the essential property of the title compound for application in the field of nonlinear optic.

Acknowledgments

The author are grateful to the Payame Noor University for encouragements.

5. References

1. M. H. Sadr, V. M. Mohammadi, B. Soltani, K. Jamshidi-Ghaleh, S. Z. Mousavi, *Optik*. **2016**, *127*, 6050–6055. **DOI:**10.1016/j.ijleo.2016.04.051
2. C. Mallet, G. Savitha, M. Allain, V. Kozmík, J. Svoboda, P. Frère, J. Roncali, *J. Org. Chem*. **2012**, *77*, 2041–2046. **DOI:**10.1021/jo202412t
3. A. N. Castro, L. R. Almeida, M. M. Anjos, G. R. Oliveira, H.

B. Napolitano, C. Valverde, B. Baseia, *Chem. Phys. Lett*. **2016**, *653*, 122–130. **DOI:**10.1016/j.cplett.2016.04.070
4. H. S. Nalwa, Handbook of Advanced Electronic and Photonic Materials and Devices, Academic Press, New York, **2001**.
5. M. I. Yongsheng, L. Pengxia, Y. Zhou, W. Dong, C. Hui, H. E. Wanli, Y. Huai, *Chem. Res. Chin. Univ*. **2015**, *31*, 992–996. **DOI:**10.1007/s40242-015-5241-9
6. X. H. Zhu, J. Peng, Y. Cao, J. Roncali, *Chem. Soc. Rev*. **2011**, *40*, 3509–3524. **DOI:**10.1039/c1cs15016b
7. S. Yao, H. Y. Ahn, X. Wang, J. Fu, E. W. Van Stryland, D. J. Hagan, K. D. Belfield, *J. Org. Chem*. **2010**, *75*, 3965–3974. **DOI:**10.1021/jo100554j
8. C. Herbivo, A. Comel, G. Kirsch, A. M. Fonseca, M. Belsley, M. M. Raposo, *Dyes Pigments*. **2010**, *86*, 217–226. **DOI:**10.1016/j.dyepig.2010.01.006
9. N. Wazzan, Z. Safi, *J. Mol. Struct*. **2017**, *1143*, 397–404.
10. A. Pron, P. Gawrys, M. Zagorska, D. Djurado, R. Demadrille, *Chem. Soc. Rev*. **2010**, *39*, 2577–632. **DOI:**10.1039/b907999h
11. A. Wojciechowski, M. M. Raposo, M. C. Castro, W. Kuznik, I. Fuks-Janczarek, M. Pokladko-Kowar, F. Bureš, *J. Mater. Sci. Mater. Electron*. **2014**, *25*, 1745–50. **DOI:**10.1007/s10854-014-1793-6
12. A. Mishra, P. Bäuerle, *Angew. Chem. Int. Ed.* **2012**, *51*, 2020–67. **DOI:**10.1002/anie.201102326
13. S. Ko, E. Verploegen, S. Hong, R. Mondal, E. T. Hoke, M. F. Toney, M. D. McGehee, Z. Bao, *J. Am. Chem. Soc*. **2011**, *133*, 16722–5. **DOI:**10.1021/ja207429s
14. M. Drobizhev, N. S. Makarov, S. E. Tillo, T. E. Hughes, A. Rebane, *J. Phys. Chem. B*. **2012**, *5*, 1736–1744. **DOI:**10.1021/jp211020k
15. M. L. Capobianco, G. Barbarella, A. Manetto, *Molecules*. **2012**, *17*, 910–933. **DOI:**10.3390/molecules17010910
16. V. Parthasarathy, S. Fery-Forgues, E. Campioli, G. Recher, F. Terenziani, M. Blanchard-Desce, *Small*. **2011**, *7*, 3219–3229. **DOI:**10.1002/smll.201100726
17. T. Wang, X. Wang, J. Zhang, C. Wang, J. Shao, Z. Jiang, Y. Zhang, *Dyes Pigments*. **2018**, *154*, 75–81. **DOI:**10.1016/j.dyepig.2018.02.031
18. D. Pegu, J. Deb, S. K. Saha, M. K. Paul, U. Sarkar, *J. Mol. Struct*. **2018**, *1160*, 167–176. **DOI:**10.1016/j.molstruc.2018.01.090
19. J. Liu, M. Zhang, W. Gao, A. A. Fedorchuk, I. V. Kityk, *J. Mol. Struct*. **2018**, *1165*, 223–227. **DOI:**10.1016/j.molstruc.2018.03.133
20. D. Q. Hu, W. J. Wang, R. R. Wang, B. Yang, B.Yu, *Chin. J. Chem. Phys*. **2015**, *28*, 645–649. **DOI:**10.1063/1674-0068/28/cjcp1502073
21. M. Akram, M. Adeel, M. Khalid, M. N. Tahir, M. U. Khan, M. A. Asghar, M. A. Ullah, M. Iqbal, *J. Mol. Struct*. **2018**, *1160*, 129–141. **DOI:**10.1016/j.molstruc.2018.01.100
22. P. Bragiel, I. Radkowska, R. Belka, B. Marciniak, Z. Bak, *J. Mol. Struct*. **2018**, *1154*, 27–38. **DOI:**10.1016/j.molstruc.2017.10.017
23. A Kundu, S Karthikeyan, Y Sagara, D Moon, SP.Anthony, *ACS Omega*. **2019**, *4*, 5147–5154. **DOI:**10.1021/acsomega.8b03099
24. A. A. Kocherzhenko, S. V. Shedge, X. Sosa Vazquez, J. Maat, J. Wilmer, A. F. Tillack, L. E. Johnson, C. M. Isborn, *J. Phys. Chem. C*, **2019**, *123*, 13818–13836. **DOI:**10.1021/acs.jpcc.8b12445
25. K. Sangeetha, L. G. Prasad, R. Mathammal, *J. Mol. Struct*. **2018**, *1155*, 598–609. **DOI:**10.1016/j.molstruc.2017.11.048
26. A. Szukalski, B. Sahraoui, B. Kulyk, C. A. Lazar, A. M. Manea, J. Mysliwiec, *RSC Advances*. **2017**, *7*, 9941–9947. **DOI:**10.1039/C6RA26781E
27. P. Han, D. Wang, H. Gao, J. Zhang, Y. Xing, Z. Yang, H. Cao, W. He, *Dyes Pigments*. **2018**, *149*, 8–15. **DOI:**10.1016/j.dyepig.2017.09.052
28. R. Medishetty, J. K. Zaręba, D. Mayer, M. Samoć, R. A. Fischer, *Chem. Soc. Rev*. **2017**, *46*, 4976–5004. **DOI:**10.1039/C7CS00162B
29. M. U. Khan, M. Khalid, M. Ibrahim, A. A. C. Braga, M. Safdar, A. A. Al-Saadi, M. R. S. A. Janjua, *J. Phys. Chem. C*, **2018**, *122*, 4009–4018. **DOI:**10.1021/acs.jpcc.7b12293
30. H. Patil, J. Chang, A. Gupta, A. Bilic, J. Wu, P. Sonar, S. V. *Molecules*. **2015**, *20*, 17362–17377. **DOI:**10.3390/molecules200917362
31. S. S. Fernandes, C. Herbivo, J. Aires-de-Sousa, A. Comel, M. Belsley, M. M. Raposo, *Dyes Pigments*. **2018**, *149*, 566–573. **DOI:**10.1016/j.dyepig.2017.10.001
32. S. B. Katariya, D. Patil, L. Rhyman, I. A. Alswaidan, P. Ramasami, N. Sekar, *J. Mol. Struct*. **2018**, *1150*, 493–506. **DOI:**10.1016/j.molstruc.2017.08.084
33. E. F. Oliveira, F. C. Lavarda, *Mater. Res*. **2014**, *17*, 1369–1374. **DOI:**10.1590/1516-1439.278814
34. H. Chen, L. Wang, W. Y. Wang, Y. Q. Qiu, H. M. Xie, *RSC Advances*. **2016**, *6*, 97063–97069. **DOI:**10.1039/C6RA22020G
35. S. M. Afzal, M. A. Razvi, S. A. Khan, O. I. Osman, A. H. Bakry, A. M. Asiri, Plos One. **2016**, *11*, 1–25. **DOI:**10.1371/journal.pone.0161613
36. K. Skonieczny, A. I. Ciuciu, E. M. Nichols, V. Hugues, M. Blanchard-Desce, *J. Mater. Chem*. **2012**, *22*, 20649– 20664. **DOI:**10.1039/c2jm33891b
37. M. R. S. A. Janjua, Inorg. Chem. **2012**, *51*, 11306−11314. **DOI:**10.1021/ic3002652
38. J. Kulhánek, F. Bureš, *Beilstein J. Org. Chem*. **2012**, *8*, 25–49. **DOI:**10.3762/bjoc.8.4
39. M. R. S. A. Janjua, A. Mahmood, M. F. Nazar, Z. Yang, S. Pan, *Acta Chim. Slov*. **2014**, *61*, 382–390.
40. M. Amir, I. Ahsan, W. Akhter, S. A. Khan, I. Ali, *Indian J. Chem*. **2011**, *50B*, 207–213.
41. M. J. Frisch, G. W. Trucks, H. B. Schlegel, G. E. Scuseria, M. A. Robb, J. R. Cheeseman, G. Scalmani, V. Barone, G. A. Petersson, H. Nakatsuji, X. Li, Gaussian 09, Revision A. 02, Gaussian, Inc., Wallingford, CT, **2016**.
42. E. H. Anouar, J. Gierschner, J. L. Duroux, P. Trouillas, *Food Chem*. **2012**, *131*, 79–89. **DOI:**10.1016/j.foodchem.2011.08.034
43. S. Markovic, J. Tosovic, *J. Phys. Chem. A*, **2015**, *119*, 9352–9362. **DOI:**10.1021/acs.jpca.5b05129
44. R. Bhatt, I. Bhaumik, S. Ganesamoorthy, A. K. Karnal, M. K.

Swami, H. S. Patel, P. K. Gupta, *Phys. Stat. Sol. (a).* **2012**, *209*, 176–180. **DOI:**10.1002/pssa.201127361
45. E. W. Van Stryland, M. Sheik-Bahae, *Characterization techniques and tabulations for organic nonlinear optical materials*, Routledge; **2018**. pp. 671–708.
46. J. Jayabharathi, V. Thanikachalam, K. B. Devi, M. V. Perumal, *Spect. Chim. Acta Part A,* **2012**, *86*, 69–75. **DOI:**10.1016/j.saa.2011.09.067
47. J. Preat, D. Jacquemin, E. A. Perpete, *Energy Environ. Sci.* **2010**, *3*, 891–904. **DOI:**10.1039/c000474j
48. P. Günter, editor. *Nonlinear optical effects and materials*. 4rd ed. Berlin: Springer; **2012**.
49. C. Valverde, S. A. L. Castro, G. R. Vaz, J. L. A. Ferreira, B. Baseia, F. A. P. Osório, *Acta Chim. Slov*. **2018**, *65*, 739–749. **DOI:**10.17344/acsi.2018.4462
50. Muhammad Ramzan Saeed Ashraf Janjua, Chun-Guan Liu, Wei Guan, Jia Zhuang,
51. S. Muhammad, L. K. Yan, Z. M. Su, *J. Phys. Chem. A*, **2009**, *113*, 3576–3587. **DOI:**10.1021/jp808707q

Povzetek

V prispevku opisujemo sintezo spojine 4-(4,5-difenil-1H-imidazol-2-il)fenol in eksperimentalne ter teoretične raziskave njenih nelinearnih optičnih lastnosti. Teoretične raziskave so bile izvedene z uporabo funkcij TD-DFT in B3LYP z običajno nastavitvijo 6-31 ++G(d,p). Rezultati analiz HOMO-LUMO in NBO kažejo nizko vrednost prepovedanega pasu, visok dipolni moment in hiperpolarizabilnost (β, γ) kot tudi prisotnost dipolarnih vzbujenih stanj z razmeroma visokimi spremembami dipolnega momenta, povezanimi z nelinearnostjo. Metoda z-skeniranja je potrdila NLO lastnosti spojine. Nelinearni absorpcijski koeficient, refrakcijski indeks in susceptibilnost tretjega reda znašajo 4.044×10^{-1} cmW^{-1}, 2.89×10^{-6} cm^{2}W^{-1} in 2.2627×10^{-6} esu. Negativna vrednost n_2 kaže na samo-defokusiranje in nelinearnost. Rezultati kažejo, da bi spojino lahko uporabljali kot potencialni NLO material.

Except when otherwise noted, articles in this journal are published under the terms and conditions of the Creative Commons Attribution 4.0 International License

DOI: 10.17344/acsi.2020.6305 *Acta Chim. Slov.* **2021,** *68,* 178–184
creative commons

Scientific paper

On the Validity of Minimum Magnetizability Principle in Chemical Reactions

Hiteshi Tandon,[1,*] Tanmoy Chakraborty[2,*] and Vandana Suhag[3]

[1] *Department of Chemistry, Manipal University Jaipur, Jaipur 303007, India*

[2] *Department of Chemistry and Biochemistry, School of Basic Sciences and Research, Sharda University, Greater Noida 201310, India*

[3] *Department of Applied Sciences, BML Munjal University, Gurugram 122413, India*

** Corresponding author: E-mail: tanmoychem@gmail.com, tanmoy.chakraborty@sharda.ac.in (T. Chakraborty) hiteshitandon@yahoo.co.in (H. Tandon)*

Received: 10-23-2020

Abstract

A new principle known as Minimum Magnetizability Principle has recently been introduced in the context of Density Functional Theory. In order to validate this principle, changes in the magnetizability ($\Delta\xi$) and its cube-root ($\Delta\xi^{1/3}$) are computed at B3LYP/LanL2DZ level of theory for some elementary chemical reactions. The principle is found to be valid for 77% of reactions under study. It is observed that the molecules with the lowest sum of ξ or $\xi^{1/3}$ are generally the most stable. The principle fails to work in the presence of hard species. A comparative study is also made with change in hardness ($\Delta\eta$), electrophilicity index ($\Delta\omega$), polarizability ($\Delta\alpha$) and their cube-roots ($\Delta\eta^{1/3}$, $\Delta\omega^{1/3}$, $\Delta\alpha^{1/3}$). It is observed that the Minimum Magnetizability Principle is nearly as reliable as Minimum Electrophilicity Principle. It appears that this principle could be helpful in predicting the direction of diverse reactions as well as stable geometrical arrangements.

Keywords: Density Functional Calculations; Magnetic Properties; Maximum Hardness Principle (MHP); Minimum Electrophilicity Principle (MEP); Minimum Polarizability Principle (MPP)

1. Introduction

Theoretical Chemistry aims at unearthing novel concepts and principles to explain a broad range of chemical reactions. The most common questions that arise for any kind of reaction are about the pace and extent of the reaction. It is logical that thermodynamic data is required for providing an answer to the latter. Constructively, numerous reactivity descriptors have been established within the context of Conceptual Density Functional Theory (CDFT).[1] These descriptors play a significant role in studying the changes taking place in a reacting system. This ultimately helps in understanding the reactivity and stability patterns of the reactants and products in a chemical reaction. Some of these descriptors are hardness (η),[2] electrophilicity index (ω),[3–6] and polarizability (α)[7] whose definitions are given as follows:

$$\eta = \left(\frac{\partial^2 E}{\partial N^2}\right)_{v(r)} = \frac{(E_L - E_H)}{2} \tag{1}$$

$$\omega = \frac{\mu^2}{2\eta} = \left\{\frac{[(E_L + E_H)/2]^2}{2[(E_L - E_H)/2]}\right\} \tag{2}$$

$$\alpha = -\left(\frac{\partial^2 E(\epsilon)}{\partial \epsilon^2}\right)_{(\epsilon=0)} \tag{3}$$

Here E refers to the system's energy with respect to the number of electrons N at fixed external potential $v(r)$. E_L and E_H stand for the frontier orbital energies while μ is the chemical potential. $\in$ represents the external electric field. Another reactivity descriptor is magnetizability (ξ) which is defined as the linear response of an atom, molecule or ion's electron cloud towards an external magnetic field.[8] It is expressed as:

$$\xi = -\left(\frac{\partial^2 E(B)}{\partial B^2}\right)_{(B=0)} \tag{4}$$

where B signifies the external magnetic field. It is an important descriptor to study chemical reactivity, stability and aromaticity of different atoms and molecules.[9–14] Dynamics of reactions have also been studied for molecules in

confinement using magnetizability.[15] This property is of multidisciplinary interest and has extensive applications in the realm of physical, biological, engineering and materials science such as organic electronics,[16] magnetically labelled cells, drugs and therapeutic agents,[17] magnetic flux concentrators,[18] magnetizable elastomers,[19] bionanocomposites,[20] magnetic immunoadsorbents,[21] magnetic nanoparticles/ nanofibres[17] and so on besides its use in general chemical science. Looking at the widespread relevance of this property, it is believed that further exploration on its behaviour and characteristics will assist in strengthening the fundamentals of the concept, thereby supporting its efficient and appropriate use in various applications.

Based on above mentioned concepts and descriptors, some principles have been formulated in the framework of Density Functional Theory (DFT). The Maximum Hardness Principle (MHP) states that "there seems to be a rule of nature that molecules arrange themselves so as to be as hard as possible".[22] Another principle known as Minimum Polarizability Principle (MPP) proposes that "the natural direction of evolution of any system is toward a state of mimimum polarizability".[23] A Minimum Electrophilicity Principle (MEP) was also suggested according to which "the natural direction of a chemical reaction is toward a state of minimum electrophilicity".[24] Numerous efforts have been made to verify the reliability of these principles in diverse reactions/species.[25,26] However, a breakdown of these principles was also observed in many cases.[27–30]

Recently, one more principle, known as the Minimum Magnetizability Principle (MMP), has been introduced in the context of DFT based on the descriptor magnetizability. According to this principle, "a stable configuration/conformation of a molecule or a favourable chemical process is associated with a minimum value of the magnetizability".[31] In case of MMP, unlike other principles, no study has been performed yet to test the validity of this principle for chemical reactions. As understandable, operational efficiency of a principle can only be determined through performing a validation procedure. Accordingly, in order to employ MMP for practical purposes, it is necessary to carry out its verification based on some criteria. Thus, in the present study we have tried to assess the potential and accuracy of this principle for the first time with respect to some chemical reactions.

2. Method of Computation

In order to verify the validity of Minimum Magnetizability Principle along with comparing it to the other principles, *viz.* MHP, MPP and MEP, 30 elementary reactions are selected. Geometry optimizations for each of the reactant and product molecules have been performed at B3LYP/LanL2DZ level of theory. This is a very common and powerful method employed in computations and incorporates the correlation effects. Hence, the energy values of the HOMO (Highest Occupied Molecular Orbital) (E_H) and the LUMO (Lowest Unoccupied Molecular Orbital) (E_L) as well as molecular polarizability are obtained for the molecules. The canonical molecular orbitals differ from Kohn-Sham orbitals, nevertheless their values for orbital energy are found to be comparable.[32] As a result, the operational forms of hardness and electrophilicity presented in Eq. (1) and Eq. (2) are used to calculate the value for hardness and electrophilicity. Further, magnetizabilities are computed using the Keith and Bader's method[33] at the same level of theory. All computations have been performed on the computational software Gaussian 03.[34]

Next, in view of the MMP, the reaction is favoured only when the products to be formed are of lower magnetizability than the reactants. Thus, for a chemical reaction (A_j), represented as $\Sigma a_j A_j = 0$ in a condensed form, where a_j corresponds to the stoichiometry of the j^{th} atom/molecule, the corresponding deviation in a parameter X through the reaction can be clearly expressed as:

$$\Delta X = \sum_j a_j X_j \tag{5}$$

In Eq. (5), X_j refers to the value of X for the j^{th} atom/molecule in the given chemical reaction. It follows that the direction in which the chemical reaction will progress may be indicated by the sign of ΔX. Thus in accordance with MMP, it appears that the sign of $\Delta\xi$ provides an evidence of the direction in which any reaction proceeds. Hence, we have calculated the change in parameter X, *viz.* hardness ($\Delta\eta$), electrophilicity ($\Delta\omega$), polarizability ($\Delta\alpha$), and magnetizability ($\Delta\xi$), for the selected reactions using Eq. (5). Change in the cube-roots of hardness ($\Delta\eta^{1/3}$), electrophilicity ($\Delta\omega^{1/3}$), polarizability ($\Delta\alpha^{1/3}$) and magnetizability ($\Delta\xi^{1/3}$) have also been calculated. Enthalpy change ($\Delta_f H^0$) for each molecule is also calculated using the atomization energy data from reference [35].

3. Results and Discussion

The study presents validity of Minimum Magnetizability Principle using chosen 30 elementary reactions. A comparison of the results is also presented with respect to the other principles, *viz.* MHP, MPP and MEP. It must be noted that several of the chosen reactions are hypothetical. All the reactions are exothermic signifying that the products are thermodynamically stable. Also, the variation of chosen parameters is not considered along the reaction path, but merely the overall change in these parameters in the chemical reaction is evaluated, which can be simply computed as long the geometry can be. Further, it should be noted that the reactants in reaction 14 are the same as in reaction 19, however the type of products formed in both are different.

The computed values for hardness (η), electrophilicity index (ω), polarizability (α), magnetizability (ξ) and

HOMO (E_H) and LUMO (E_L) energy, along with magnetizability (ξ_T) data from the literature,[36] for all the reactants and products of the selected reactions are presented in Table 1. A comparison of computed magnetizabilities (ξ) with tabulated magnetizabilities[36] (ξ_T) reveals a good similarity between the two datasets ($R^2 = 0.997$) indicating the efficacy of our computed data. The changes in enthalpy ($\Delta_f H^0$) and in parameter values with their reaction are provided in Table 2. As mentioned above, the formation of products is only favoured when the magnetizability of reactant is more than that of the products to be formed according to the MMP. Moreover the sign of $\Delta\xi$ gives an idea of the direction in which any reaction proceeds. A close look at Table 2 reveals that Minimum Magnetizability Principle is valid for chemical reactions since $\Delta\xi < 0$ for various reactions. Further, $\Delta\xi$ is negative in numerous cases which undoubtedly demonstrates that $\Delta\xi$ provides a sign for the most stable species. Thus, the favoured direction of a chemical reaction is towards less magnetizability. When the stability of products is more than the reactants, change in enthalpy is less than zero ($\Delta_f H^0 < 0$). This condition is also clearly met by the reactions in the study. However, MMP is not valid always. It is reliable for approximately 77% of the selected reactions and fails in case of the remaining reactions. It is observed that the majority of the reactions where the principle fails contain a hard base such as OH, F, Cl, N, etc. It is further noted that MEP is as convincing as MMP and proves to be valid for 77% of the reactions tested. MPP performs slightly better than MHP; however it is less suitable than MEP and MMP. MPP works for 50% of the reactions while MHP is applicable for 47% of the considered reactions. It is observed that the minimum magnetizability

Table 1. Computed frontier orbital energies (E_H and E_L), hardness (η), electrophilicity index (ω), polarizability (α) and magnetizability (ξ) values of the reactant and product molecules of the selected reactions using B3LYP/LanL2DZ method and their tabulated magnetizabilities (ξ_T) (in au)

S. No.	Molecules	E_H	E_L	η	ω	α	ξ	ξ_T [a]
1	H_2	–0.429	0.116	0.272	0.045	2.013	–0.588	–1.145
2	O_2	–0.281	–0.212	0.034	0.887	5.834	719.683	718.631
3	H_2O_2	–0.266	–0.030	0.118	0.093	9.738	–2.523	–3.641
4	CO	–0.382	–0.059	0.161	0.151	9.890	–1.030	–2.062
5	CO_2	–0.298	–0.071	0.113	0.149	17.215	–0.120	–4.419
6	H_2O	–0.300	0.061	0.179	0.040	4.698	–1.911	–2.755
7	CH_4	–0.177	–0.037	0.070	0.081	14.634	–3.408	–3.662
8	Cl_2	–0.331	–0.199	0.066	0.529	13.712	–6.890	–8.502
9	HCl	–0.331	0.003	0.167	0.080	4.751	–3.794	–4.756
10	H_2S	–0.264	0.026	0.145	0.049	11.533	–4.135	–5.366
11	N_2	–0.420	–0.053	0.183	0.153	8.363	–2.448	–2.525
12	NH_3	–0.227	0.098	0.162	0.013	7.050	–2.206	–
13	NO	–0.246	–0.139	0.054	0.344	7.342	299.490	307.443
14	HCN	–0.373	–0.007	0.183	0.098	11.917	–1.602	–
15	NO_2	–0.312	–0.136	0.088	0.285	13.776	22.419	31.565
16	N_2O_4	–0.351	–0.139	0.106	0.283	32.779	–4.207	–4.839
17	OH	–0.339	0.058	0.198	0.050	3.329	10.493	–
18	C_2H_6	–0.339	0.126	0.232	0.025	22.136	–5.338	–5.639
19	C_3H_8	–0.323	–0.125	0.099	0.254	32.538	–4.428	–8.122
20	C_2H_6O	–0.249	0.081	0.165	0.021	25.055	–3.821	–7.070
21	$(CH_3)_2S$	–0.219	0.038	0.129	0.032	36.373	–5.720	–9.448
22	C_2H_4	–0.273	–0.001	0.136	0.069	19.380	–1.850	–3.956
23	C_2H_2	–0.212	0.111	0.161	0.008	18.424	–2.029	–4.377
24	C_2H_5Cl	–0.291	0.007	0.149	0.067	28.433	–5.145	–
25	Cl_2CCH_2	–0.279	–0.032	0.123	0.098	34.821	–8.833	–10.353
26	C_2H_5CN	–0.332	0.020	0.176	0.069	33.637	–5.485	–
27	$(CH_2OH)_2$	–0.218	0.069	0.143	0.019	19.665	–4.571	–8.164
28	CH_3F	–0.343	0.060	0.201	0.050	11.571	–1.695	–3.745
29	CHF_3	–0.423	0.066	0.244	0.065	12.669	–3.148	–
30	CF_4	–0.406	–0.195	0.106	0.427	17.824	–3.656	–
31	N_2H_4	–0.135	0.097	0.116	0.002	12.053	–3.145	–42.297
32	CH_3CHO	–0.262	–0.044	0.109	0.107	23.007	–1.859	–4.671
33	C_6H_6	–0.253	–0.009	0.122	0.070	54.838	–6.692	–11.531
34	CH_3OH	–0.269	0.065	0.167	0.031	14.780	–2.643	–4.503
35	C_6H_5OH	–0.189	–0.110	0.039	0.283	62.282	–5.527	–12.752
36	$C_6H_5NH_2$	–0.113	–0.006	0.053	0.033	79.933	–5.147	–13.131

[a] Data obtained from reference [36] and converted into atomic units (au). 1 au of $\xi = e^2a_0^2/m_e = 4.75209$ cgs–ppm.[37]

Table 2. Computed changes in the enthalpy ($\Delta_f H^0$) (at 298K in kJ mol^{-1}), hardness ($\Delta\eta$) (in au), electrophilicity index ($\Delta\omega$) (in au), polarizability ($\Delta\alpha$) (in au) and magnetizability ($\Delta\xi$) (in au) along with MHP, MEP, MPP and MMP validity (+) or invalidity (–) for selected reactions

S. No.	Reaction	$\Delta_f H^0$ [a]	$\Delta\eta$	+/–	$\Delta\omega$	+/–	$\Delta\alpha$	+/–	$\Delta\xi$	+/–
1	$CO_2 + 4H_2 \rightarrow 2H_2O + CH_4$	–148	–0.774	–	–0.168	+	1.237	–	–4.756	+
2	$Cl_2 + H_2 \rightarrow 2HCl$	–185	–0.004	–	–0.414	+	6.223	–	–0.111	+
3	$3H_2 + N_2 \rightarrow 2NH_3$	–71	–0.675	–	–0.262	+	0.303	–	–0.199	+
4	$2NO \rightarrow O_2 + N_2$	–180	0.110	+	0.352	–	–0.487	+	118.256	–
5	$2NO + 2H_2 \rightarrow N_2 + 2H_2O$	–647	–0.111	–	–0.545	+	–0.951	+	–604.072	+
6	$CH_4 + 2O_2 \rightarrow CO_2 + 2H_2O$	–786	0.333	+	–1.625	+	–0.308	+	–1439.901	+
7	$CO + 3H_2 \rightarrow CH_4 + H_2O$	–198	–0.729	–	–0.164	+	3.403	–	–2.523	+
8	$2NO_2 \rightarrow N_2O_4$	–47	–0.070	–	–0.287	+	–5.228	+	–49.046	+
9	$2C_2H_2 + 5O_2 \rightarrow 4CO_2 + 2H_2O$	–2503	0.318	+	–3.771	+	–12.235	+	–3598.660	+
10	$2OH \rightarrow H_2O_2$	–213	–0.279	–	–0.006	+	–3.080	+	–23.509	+
11	$H_2O_2 \rightarrow O_2 + H_2O$	–98.5	0.078	+	0.390	–	2.123	–	360.454	–
12	$H_2O_2 + Cl_2 \rightarrow O_2 + 2HCl$	–50	0.185	+	0.424	–	–8.114	+	721.507	–
13	$4NH_3 + 5O_2 \rightarrow 4NO + 6H_2O$	–899	0.469	+	–2.868	+	–0.187	+	–2403.099	+
14	$C_2H_6 + O_2 \rightarrow (CH_3)_2O$	–108.5	–0.084	–	–0.446	+	–0.001	+	–358.325	+
15	$C_2H_2 + 2H_2 \rightarrow C_2H_6$	–304	–0.473	–	–0.074	+	0.314	–	–2.132	+
16	$C_2H_4 + HCl \rightarrow C_2H_5Cl$	–72	–0.154	–	–0.082	+	4.302	–	0.499	–
17	$C_2H_2 + Cl_2 \rightarrow Cl_2CCH_2$	–230	–0.104	–	–0.440	+	–2.685	+	0.085	–
18	$HCN + C_2H_5Cl \rightarrow C_2H_5CN + HCl$	–64	0.011	+	–0.017	+	–1.963	+	–2.533	+
19	$C_2H_6 + O_2 \rightarrow (CH_2OH)_2$	–312	–0.123	–	–0.892	+	8.306	–	–718.916	+
20	$C_3H_8 + 5O_2 \rightarrow 3CO_2 + 4H_2O$	–2015	0.787	+	–4.078	+	8.727	–	–3601.992	+
21	$CH_3F + CHF_3 \rightarrow CH_4 + CF_4$	–88	–0.270	–	0.394	–	–8.218	+	–2.221	+
22	$N_2H_4 + O_2 \rightarrow N_2 + 2H_2O$	–652	0.391	+	–0.655	+	0.128	–	–722.808	+
23	$(CH_3)_2O + H_2S \rightarrow (CH_3)_2S + H_2O$	–73	–0.003	–	0.002	–	4.484	–	0.325	–
24	$2CH_3OH + 3O_2 \rightarrow 2CO_2 + 4H_2O$	–1321	0.507	+	–2.262	+	6.158	–	–2161.648	+
25	$C_2H_5OH + 3O_2 \rightarrow 2CO_2 + 3H_2O$	–1306	0.496	+	–2.262	+	–5.966	+	–2161.202	+
26	$C_2H_5OH + Cl_2 \rightarrow CH_3CHO + 2HCl$	–53	0.212	+	–0.283	+	–6.258	+	1.263	–
27	$CH_3CHO \rightarrow CH_4 + CO$	–135	0.122	+	0.125	–	1.517	–	–2.579	+
28	$C_6H_5OH + H_2 \rightarrow C_6H_6 + H_2O$	–234	–0.011	–	–0.218	+	4.760	–	–2.487	+
29	$2C_6H_6 + 15O_2 \rightarrow 12CO_2 + 6H_2O$	–6309	1.679	+	–11.406	+	–37.574	+	–10794.771	+
30	$C_6H_5NH_2 + H_2 \rightarrow C_6H_6 + NH_3$	–86	–0.041	–	0.005	–	20.058	–	–3.162	+

[a] Computed by taking energies of atomization from reference [35].

principle is almost as valuable as minimum electrophilicity principle in predicting the direction of a reaction. The sign of $\Delta\xi$ can be used to provide an indication for higher stability of products thermodynamically.

In order to understand the significance of the results, a brief statistical analysis is performed for each parameter with respect to $\Delta_f H^0$. Our study is based on the stability criterion, i.e. minimum energy condition, thus it is important to validate the correlation of $\Delta_f H^0$ with these descriptors. Regression analysis has been performed for this purpose. An attempt to explore the relationship of $\Delta\alpha$ with $\Delta_f H^0$ is futile ($R^2 = 0.4871$, $R = +0.70$, $p = 0.001$), although $\Delta\eta$ is found to follow a satisfactory linear relation with $\Delta_f H^0$ ($R^2 = 0.6266$, $R = -0.79$, $p = 0.001$). Lower values of R^2 denote inferior correlation of $\Delta\alpha$ and $\Delta\eta$ with $\Delta_f H^0$ whereas p-values indicate that the result is significant. It can be inferred that MPP and MHP may not always follow the minimum energy criterion and may become invalid in several cases. An analysis of $\Delta\xi$ and $\Delta\omega$ with $\Delta_f H^0$ presents an excellent relationship. For $\Delta\xi$ and $\Delta_f H^0$, $R^2 = 0.9792$, $R = +0.99$ and $p = 0.001$ while $R^2 = 0.9679$, $R = +0.98$ and $p = 0.001$ for $\Delta\omega$ and $\Delta_f H^0$. Such high values of R^2 clearly signify the outstanding correlation between the parameters. Further, a perfect positive correlation is presented for $\Delta\xi$ and $\Delta_f H^0$. Significance of the correlation is highlighted by the p-values. It is concluded that MMP as well as MEP are highly related to $\Delta_f H^0$ and thus follow the minimum energy and high stability condition. As the validity of minimum energy principle increases, MMP and MEP become valid as well.

The cube-roots of exact polarizability $\Delta\alpha^{1/3} = \sum_j a_j \alpha_j^{1/3}$ have been proved to be more useful in comparison to $\Delta\alpha$ to predict the direction of a chemical reaction.[35] Hence, following the above notion, we have determined the cube--roots for hardness, electrophilicity index, polarizability as well as magnetizability and these are presented in Table 3. It is apparent from the outcomes that the validity of MHP as well as MPP increases when their cube-roots are considered. In fact, the soundness of MHP increases drastically as compared to MPP. As expected, these results indicate efficiency of cube-roots of hardness and polarizability in predicting the path followed by a reaction. Although in

comparison to other principles, MHP and MPP still remain the least accurate for the reactions considered in the present study and have no predictive value. Conversely, the validity of MEP and MMP is found to be decreased in this case. As evident from Table 3, a decrease in the validity of MMP takes place when the cube-roots of magnetizability are considered. However MMP is still valid for several reactions ($\Delta\xi^{1/3} < 0$) and performs remarkably in contrast to MHP and MPP. As a result, it appears that $\Delta\xi^{1/3}$ is more or less as reliable as $\Delta\xi$. It is further observed that MEP is the most the convincing of all principles considering its high validity in both the cases. Next, $\Delta_f H^0$ demonstrates an excellent linear relationship with $\Delta\xi^{1/3}$ ($R^2 = 0.9818$) and $\Delta\omega^{1/3}$ ($R^2 = 0.8916$) but poor connections are found with $\Delta\eta^{1/3}$ ($R^2 = 0.5530$) or $\Delta\alpha^{1/3}$ ($R^2 = 0.5338$).

We have tried to accommodate reactions with different types of molecules, *viz.* inorganic, aliphatic and aromatic, in the present study to consider as many chemical effects as possible. Although for further studies it is suggested that the validity of this principle should be assessed in case of other reaction classes as well.

4. Conclusion

We have tried to validate Minimum Magnetizability Principle employing 30 elementary chemical reactions. Change in the magnetizability ($\Delta\xi$) and its cube-root ($\Delta\xi^{1/3}$) is computed in order to check the applicability of the principle in determining the direction of the reaction as well as stability of the products. We have also calculated change in hardness ($\Delta\eta$), electrophilicity index ($\Delta\omega$), polarizability ($\Delta\alpha$) and their cube-roots ($\Delta\eta^{1/3}$, $\Delta\omega^{1/3}$, $\Delta\alpha^{1/3}$) in order to make a comparative study. It is observed that the Minimum Magnetizability Principle is valid for chemical reactions however with some limitations. The principle fails to work in the presence of hard species. Minimum Electrophilicity Principle and Minimum Magnetizability Principle are found to have comparable reliability followed by Minimum Polarizability Principle, however Maximum Hardness Principle appears to be less valid for the chosen reactions. In conclusion, Minimum Magnetizability Principle is found to be fairly valid for reactions and can be successfully employed solely or in

Table 3. Computed changes in the enthalpy ($\Delta_f H^0$) (at 298K in kJ mol^{-1}), cube–root of hardness ($\Delta\eta^{1/3}$) (in au), cube–root of electrophilicity index ($\Delta\omega^{1/3}$) (in au), cube–root of polarizability ($\Delta\alpha^{1/3}$) (in au) and cube–root of magnetizability ($\Delta\xi^{1/3}$) (in au) along with MHP, MEP, MPP and MMP validity (+) or invalidity (–) for selected reactions

S. No.	Reaction	$\Delta_f H^0$ [a]	$\Delta\eta^{1/3}$	+/–	$\Delta\omega^{1/3}$	+/–	$\Delta\alpha^{1/3}$	+/–	$\Delta\xi^{1/3}$	+/–
1	$CO_2 + 4H_2 \rightarrow 2H_2O + CH_4$	–148	–1.537	–	–0.836	+	–1.837	+	–0.142	+
2	$Cl_2 + H_2 \rightarrow 2HCl$	–185	0.049	+	–0.302	+	–0.294	+	–0.379	+
3	$3H_2 + N_2 \rightarrow 2NH_3$	–71	–1.421	–	–1.133	+	–1.983	+	1.258	–
4	$2NO \rightarrow O_2 + N_2$	–180	0.137	+	0.094	–	–0.057	+	–5.767	+
5	$2NO + 2H_2 \rightarrow N_2 + 2H_2O$	–647	–0.356	–	–0.894	+	–1.033	+	–15.535	+
6	$CH_4 + 2O_2 \rightarrow CO_2 + 2H_2O$	–786	0.550	+	–1.139	+	–0.115	+	–19.393	+
7	$CO + 3H_2 \rightarrow CH_4 + H_2O$	–198	–1.513	–	–0.824	+	–1.814	+	0.778	–
8	$2NO_2 \rightarrow N_2O_4$	–47	–0.417	–	–0.659	+	–1.594	+	–7.254	+
9	$2C_2H_2 + 5O_2 \rightarrow 4CO_2 + 2H_2O$	–2503	0.352	+	–2.393	+	–0.606	+	–46.730	+
10	$2OH \rightarrow H_2O_2$	–213	–0.676	–	–0.282	+	–0.851	+	–5.740	+
11	$H_2O_2 \rightarrow O_2 + H_2O$	–98.5	0.236	+	0.369	–	0.439	–	4.601	–
12	$H_2O_2 + Cl_2 \rightarrow O_2 + 2HCl$	–50	0.532	+	0.561	–	0.633	–	9.106	–
13	$4NH_3 + 5O_2 \rightarrow 4NO + 6H_2O$	–899	1.087	+	–0.885	+	1.152	–	–20.284	+
14	$C_2H_6 + O_2 \rightarrow (CH_3)_2O$	–108.5	–0.229	–	–0.493	+	–0.782	+	–4.296	+
15	$C_2H_2 + 2H_2 \rightarrow C_2H_6$	–304	–1.226	–	–0.620	+	–2.359	+	1.194	–
16	$C_2H_4 + HCl \rightarrow C_2H_5Cl$	–72	–0.535	–	–0.434	+	–1.315	+	1.061	–
17	$C_2H_2 + Cl_2 \rightarrow Cl_2CCH_2$	–230	–0.451	–	–0.547	+	–1.769	+	1.102	–
18	$HCN + C_2H_5Cl \rightarrow C_2H_5CN + HCl$	–64	0.013	+	–0.028	+	–0.427	+	–0.427	+
19	$C_2H_6 + O_2 \rightarrow (CH_2OH)_2$	–312	–0.416	–	–0.983	+	–2.583	+	–8.873	+
20	$C_3H_8 + 5O_2 \rightarrow 3CO_2 + 4H_2O$	–2015	1.622	+	–2.475	+	2.252	–	–49.609	–
21	$CH_3F + CHF_3 \rightarrow CH_4 + CF_4$	–88	–0.327	–	0.416	–	0.465	–	–0.387	+
22	$N_2H_4 + O_2 \rightarrow N_2 + 2H_2O$	–652	0.883	+	0.144	–	1.286	–	–11.326	+
23	$(CH_3)_2O + H_2S \rightarrow (CH_3)_2S + H_2O$	–73	–0.006	–	0.016	–	–0.197	+	0.139	–
24	$2CH_3OH + 3O_2 \rightarrow 2CO_2 + 4H_2O$	–1321	1.148	+	–1.080	+	1.555	–	–30.069	+
25	$C_2H_5OH + 3O_2 \rightarrow 2CO_2 + 3H_2O$	–1306	1.137	+	–1.072	+	1.862	–	–30.030	–
26	$C_2H_5OH + Cl_2 \rightarrow CH_3CHO + 2HCl$	–53	0.627	+	0.251	–	0.887	–	–0.883	+
27	$CH_3CHO \rightarrow CH_4 + CO$	–135	0.478	+	0.490	–	1.748	–	–1.285	+
28	$C_6H_5OH + H_2 \rightarrow C_6H_6 + H_2O$	–234	0.071	+	–0.257	+	0.248	–	–0.519	+
29	$2C_6H_6 + 15O_2 \rightarrow 12CO_2 + 6H_2O$	–6309	3.330	+	–6.815	+	6.432	–	–144.017	+
30	$C_6H_5NH_2 + H_2 \rightarrow C_6H_6 + NH_3$	–86	0.018	+	–0.030	+	0.146	–	–0.622	+

[a] Computed by taking energies of atomization from reference [35].

conjunction with other principles for theoretical as well as practical applications.

Author Contributions

Hiteshi Tandon: Conceptualization, Methodology, Software, Resources, Formal analysis, Validation, Investigation, Writing – Original Draft, Visualization. **Tanmoy Chakraborty:** Conceptualization, Supervision, Writing – Review & Editing. **Vandana Suhag:** Supervision, Writing – Review & Editing.

Conflicts Of Interest

The authors declare no conflicts of interest.

Funding

This research did not receive any specific grant from funding agencies in the public, commercial, or not-for-profit sectors.

Acknowledgements

Dr. Tanmoy Chakraborty is thankful to Sharda University and Dr. Hiteshi Tandon is thankful to Manipal University Jaipur for providing computational resources and research facility.

5. References

1. P. Geerlings, F. De Proft, W. Langenaeker, *Chem. Rev.* **2003**, *103*, 1793–1874. **DOI:**10.1021/cr990029p
2. R. G. Parr, R. G. Pearson, *J. Am. Chem. Soc.* **1983**, *105*, 7512–7516. **DOI:**10.1021/ja00364a005
3. R. G. Parr, L. von Szentpaly, S. Liu, *J. Am. Chem. Soc.* **1999**, *121*, 1922–1924. **DOI:**10.1021/ja983494x
4. H. Tandon, T. Chakraborty, V. Suhag, *J. Struct. Chem.* **2019**, *60*, 1725–1734. **DOI:**10.1134/S0022476619110040
5. H. Tandon, T. Chakraborty, V. Suhag, *J. Math. Chem.* **2020**, *58*, 2188–2196. **DOI:**10.1007/s10910-020-01176-5
6. P. Yadav, H. Tandon, B. Malik, T. Chakraborty, *J. Chem. Res.* **2020. DOI:**10.1177/1747519820937272
7. H. Tandon, T. Chakraborty, V. Suhag, *J. Math. Chem.* **2019**, *57*, 2142–2153. **DOI:**10.1007/s10910-019-01055-8
8. P. Dahle, K. Ruud, T. Helgaker, P. R. Taylor, in: Z. B. Maksid, W. J. Orville-Thomas (Eds.): Theoretical and Computational Chemistry, Vol. 6, Elsevier, Amsterdam, **1999**, pp. 147–188. **DOI:**10.1016/S1380-7323(99)80008-9
9. P. K. Chattaraj, S. Giri, *J. Phys. Chem. A*, **2007**, *111*, 11116–11121. **DOI:**10.1021/jp0760758
10. P. F. Provasi, G. I. Pagola, M. B. Ferraro, S. Pelloni, P. Lazzeretti, *J. Phys. Chem. A* **2014**, *118*, 6333–6342. **DOI:**10.1021/jp408969k
11. C. Foroutan-Nejad, *Theor. Chem. Acc.* **2015**, *134*, 8. **DOI:**10.1007/s00214-015-1617-7
12. N. Zarycz, P. F. Provasi, G. I. Pagola, M. B. Ferraro, S. Pelloni, P. Lazzeretti, *J. Comput. Chem.* **2016**, *37*, 1552–1558. **DOI:**10.1002/jcc.24369
13. S. Pelloni, P. F. Provasi, G. I. Pagola, M. B. Ferraro, P. Lazzeretti, *J. Phys. Chem. A* **2017**, *121*, 9369–9376. **DOI:**10.1021/acs.jpca.7b09104
14. T. Janda, C. Foroutan-Nejad, *ChemPhysChem* **2018**, *19*, 2357–2363. **DOI:**10.1002/cphc.201800364
15. M. Khatua, U. Sarkar, P. K. Chattaraj, *Int. J. Quantum Chem.* **2015**, *115*, 144–157. **DOI:**10.1002/qua.24801
16. R. Das, A. Chakraborty, S. Pan, P. K. Chattaraj, *Curr. Org. Chem.* **2013**, *17*, 2831–2844. **DOI:**10.2174/13852728113179990129
17. B. J. Tefft, S. Uthamaraj, J. J. Harburn, O. Hlinomaz, A. Lerman, D. Dragomir-Daescu, G. S. Sandhu, *J. Magn. Magn. Mater.* **2017**, *427*, 100–104. **DOI:**10.1016/j.jmmm.2016.11.007
18. C. Carretero, I. Lope, J. Acero, *IEEE J. Emerg. Sel. Topics Power Electron.* **2019. DOI:**10.1109/JESTPE.2019.2935226
19. D. I. Merkulov, A. V. Muravlev, E. D. Martynova, D. A. Pelevina, V. A. Turkov, V. A. Naletova, *J. Magn. Magn. Mater.* **2019**, *470*, 81–84. **DOI:**10.1016/j.jmmm.2018.02.038
20. M. A. Alheety, A. Raoof, S. A. Al-Jibori, A. Karadağ, A. I. Khaleel, H. Akbaş, O. Uzun, *Mater. Chem. Phys.* **2019**, *231*, 292–300. **DOI:**10.1016/j.matchemphys.2019.04.040
21. C. Gholve, S. Banerjee, S. Kulkarni, *J. Radioanal. Nucl. Chem.* **2020**, *323*, 1041–1046. **DOI:**10.1007/s10967-020-07023-w
22. R. G. Pearson, *J. Chem. Educ.* **1987**, *64*, 561–567. **DOI:**10.1021/ed064p561
23. P. K. Chattaraj, S. Sengupta, *J. Phys. Chem.* **1996**, *100*, 16126–16130. **DOI:**10.1021/jp961096f
24. S. Noorizadeh, *Chin. J. Chem.*, **2007**, *25*, 1439–1444. **DOI:**10.1002/cjoc.200790266
25. P. K. Chattaraj, P. Fuentealba, B. Gomez, R. Contreras, *J. Am. Chem. Soc.* **2000**, *122*, 348–351. **DOI:**10.1021/ja992337a
26. F. A. Pasha, H. K. Srivastava, P. P. Singh, *Int. J. Quantum Chem.* **2005**, *104*, 87–100. **DOI:**10.1002/qua.20569
27. Y. L. Zhang, Z. Z. Yang, *Int. J. Quantum Chem.* **2006**, *106*, 1723–1735. **DOI:**10.1002/qua.20952
28. P. Selvarengan, P. Kolandaivel, *J. Mol. Struct.* (*Theochem*) **2004**, *671*, 77–86. **DOI:**10.1016/j.theochem.2003.10.021
29. K. Anandan, P. Kolandaivel, R. Kumaresan, *Int. J. Quantum Chem.* **2005**, *104*, 286–298. **DOI:**10.1002/qua.20559
30. S. Noorizadeh, *J. Mol. Struct.* (*Theochem*) **2005**, *713*, 27–32. **DOI:**10.1016/j.theochem.2004.09.029
31. A. Tanwar, S. Pal, D. R. Roy, P. K. Chattaraj, *J. Chem. Phys.* **2006**, *125*, 056101. **DOI:**10.1063/1.2227381
32. J. F. Janak, *Phys. Rev. B* **1978**, *18*, 7165–7168. **DOI:**10.1103/PhysRevB.18.7165
33. T. A. Keith, R. F. W. Bader, *Chem. Phys. Lett.* **1993**, *210*, 223–231. **DOI:**10.1016/0009-2614(93)89127-4
34. M. J. Frisch, G. W. Trucks, H. B. Schlegel, G. E. Scuseria, M. A. Robb, J. R. Cheeseman, J. A. Montgomery, Jr., T. Vreven, K. N. Kudin, J. C. Burant, J. M. Millam, S. S. Iyengar, J. Tomasi, V. Barone, B. Mennucci, M. Cossi, G. Scalmani, N. Rega, G. A. Petersson, H. Nakatsuji, M. Hada, M. Ehara, K. Toyota,

R. Fukuda, J. Hasegawa, M. Ishida, T. Nakajima, Y. Honda, O. Kitao, H. Nakai, M. Klene, X. Li, J. E. Knox, H. P. Hratchian, J. B. Cross, C. Adamo, J. Jaramillo, R. Gomperts, R. E. Stratmann, O. Yazyev, A. J. Austin, R. Cammi, C. Pomelli, J. W. Ochterski, P. Y. Ayala, K. Morokuma, G. A. Voth, P. Salvador, J. J. Dannenberg, V. G. Zakrzewski, S. Dapprich, A. D. Daniels, M. C. Strain, O. Farkas, D. K. Malick, A. D. Rabuck, K. Raghavachari, J. B. Foresman, J. V. Ortiz, Q. Cui, A. G. Baboul, S. Clifford, J. Cioslowski, B. B. Stefanov, G. Liu, A. Liashenko, P. Piskorz, I. Komaromi, R. L. Martin, D. J. Fox, T. Keith, M. A. Al-Laham, C. Y. Peng, A. Nanayakkara, M. Challacombe, P. M. W. Gill, B. Johnson, W. Chen, M. W. Wong, C. Gonzalez, J. A. Pople, *Gaussian 03, Revision C.01*. Gaussian, Inc., Wallingford CT, **2004**.

35. U. Hohm, *J. Phys. Chem. A* **2000**, *104*, 8418–8423. **DOI:**10.1021/jp0014061
36. W. M. Haynes (Ed.), CRC Handbook of Chemistry and Physics, Vol. 97, CRC Press, Boca Raton, FL, **2017**.
37. E. Steiner, P. W. Fowler, in: B. Grimm, R. J. Porra, W. Rüdiger, H. Scheer (Eds.): Chlorophylls and Bacteriochlorophylls: Biochemistry, Biophysics, Functions and Applications, Springer, Netherlands, **2006**, pp. 337–347.

Povzetek

Novo načelo, znano kot načelo minimalne magnetizabilnosti, je bilo nedavno predstavljeno v okviru teorije gostotnega funkcionala (DFT). Da bi potrdili to načelo, smo na ravni teorije B3LYP/LanL2DZ izračunali spremembe v magnetizabilnosti ($\Delta\xi$) in tretjem korenu iz $\Delta\xi$ ($\Delta\xi^{1/3}$) za nekatere osnovne kemijske reakcije. Ugotovili smo, da načelo velja za 77% preučevanih reakcij. Opazili smo, da so molekule z najnižjo vsoto ξ ali $\xi^{1/3}$ na splošno najbolj stabilne. Načelo ne deluje v prisotnosti trdih zvrsti. Izvedli smo tudi primerjalno študijo s spreminjanjem trdote ($\Delta\eta$), indeksa elektrofilnosti ($\Delta\omega$), polarizabilnosti ($\Delta\alpha$) in njihovih tretjih korenov ($\Delta\eta^{1/3}$, $\Delta\omega^{1/3}$, $\Delta\alpha^{1/3}$). Opazili smo, da je načelo minimalne magnetizabilnosti skoraj tako zanesljivo kot načelo minimalne elektrofilnosti. Zdi se, da bi to načelo lahko pomagalo pri napovedovanju smeri različnih reakcij in stabilnih geometrijskih ureditev.

Except when otherwise noted, articles in this journal are published under the terms and conditions of the Creative Commons Attribution 4.0 International License

Scientific paper

Electrodeposition and Growth of Iron from an Ethylene Glycol Solution

Vusala Asim Majidzade,[1,*] Akif Shikhan Aliyev,[1] Mahmoud Elrouby,[2] Dunya Mahammad Babanly[1,3] and Dilgam Babir Tagiyev[1]

[1] *Institute of Catalysis and Inorganic Chemistry named after M.Nagiyev, Azerbaijan National Academy of Sciences, AZ1143, H.Javid 113*

[2] *Chemistry Department, Faculty of Science, Sohag University, 82524 Sohag, Egypt*

[3] *French Azerbaijani University (UFAZ), AZ1010, Baku, Nizami 189*

* *Corresponding author: E-mail: vuska_80@mail.ru*

Received: 07-29-2020

Abstract

The electrochemical reduction of iron (III) ions into zero-valent iron from a solution of ethylene glycol was accomplished. The kinetics and mechanism of the electroreduction process were investigated by cyclic and linear polarization techniques. The influence of temperature, potential sweep rate, and concentration of iron (III) ions on the electroreduction process was also studied. The observed values of effective activation energy revealed that the investigated electroreduction process is accompanied by mixed kinetics control. Moreover, the results of SEM and X-ray diffraction analysis confirmed the deposition of thin Fe films under the optimized conditions.

Keywords: Polarization curves; chronoamperometry; iron ions; electroreduction; ethylene glycol.

1. Introduction

Currently, due to the decrease in natural energy sources, the use of environmentally friendly solar energy is very important.[1–4]

Iron disulfide (FeS_2) due to its non-toxicity and wide distribution on earth, it has the probability of becoming an inexpensive alternative material for fabricating highly efficient solar cells.[5–10] Depending on its optical properties, it can be used in solar cells as a photoactive absorbing layer or as a frontal transparent layer in heterostructured cells.[11] The preparation of these films has been carried out by various methods. The electrochemical deposition method has been used in this work, due to its simplicity to be optimized, and non-cost. For the co-electrodeposition of two or more components simultaneously, firstly the electrochemical reduction of each component should be studied individually. Therefore, this work aims to study the electrochemical reduction of iron ions, the kinetics, and the mechanism of the process in a non-aqueous solution of ethylene glycol.

The electroreduction and electrodeposition of iron ions have been reported.[12–18] The results presented in the previously published work[12] showed that the electrodeposition of iron in an acidic sulfate medium occurred, at least, through three adsorbed intermediates. It was observed that on the nonlinear part of the polarization curves, the electrodeposition of iron occurred, but with very low efficiency. In this area, the main cathodic reaction is the reduction of hydrogen, and low-efficient electrodeposition of iron was obtained through two intermediates. One of these adsorbed intermediates catalyzed the reduction of hydrogen, while the other blocked the process. The third intermediate appeared only at the potential region corresponding to the linear part of the polarization curves. It was also noted that the concentration of the adsorbed species at the surface strongly depends on the electrode potential.

The metallic Fe films onto a copper substrate from a mixture of ChCl, urea, and $FeCl_3$ has been previously electrodeposited.[13] It was found that the use of direct current coating technology gives uniform, dense, gray, dull, and pure iron coatings. The electrodeposition at the ambient temperature produced iron films of high corrosion resistance and stable for several weeks. The surface morphology of the obtained iron films was also studied as a function

of the applied current density. As a result, fine-grained and microcrystalline iron deposits without defects were obtained.

The influence of ammonium ion on the electrodeposition of iron from the iron sulfate bath was studied by other authors.[14] During the cathodic polarization process in a solution of 0.02 M $FeSO_4$ at pH = 3 by using the quartz crystals microbalance technique, the presence of ammonium sulfate increased the mass of the electrodeposited Fe metal. The obtained pH (at the surface of the working electrode) – potential curves showed that in the presence of ammonium sulfate, the pH simultaneously increased to the alkaline levels during the electrolysis process. These results suggest that ammonium ion facilitates the formation of ammoniated ferrous iron (e.g., $Fe(NH_3)_2^{2+}$ and $Fe(NH_3)_4^{2+}$). This prevents the deposition of $Fe(OH)_2$ on the electrode, which can lead to passivation of the surface and, therefore, to a limited deposition of Fe metal.

Nanocrystalline iron was electrodeposited from 1-butyl-1-methylpyrrolidinium bis (trifluoromethylsulfonyl) amide ([Py1,4] TFSA) ionic liquid at 100 °C.[15] The electrodeposition of iron from ([Py1,4] TFSA) was accomplished by using Fe $(TfO)_2$ and $FeCl_2$ as precursors. Cyclic voltammetry was used to investigate the electrochemical behavior of $FeCl_2$, $Fe(TfO)_2$, and ($FeCl_2$+$AlCl_3$) in the presence of ionic liquid as a supporting electrolyte. But, a thick iron film was obtained from $FeCl_2$ / [Py1,4] TfO at these conditions.

Iron metal films were also electrodeposited on copper substrates by the galvanostatic method at various pH, temperature, and current density from weak acidic (pH = 5.7) solutions containing iron sulfate and sodium gluconate.[16] It was found that the optimal conditions for obtaining stable Fe films are as follows; a solution consists of 0.038 mol · dm^3 $Fe_2(SO_4)_3.7H_2O$ and 0.14 mol·dm^3 sodium gluconate, at current density (j) = 0.33 A / cm^2, pH = 5.7, and temperature 25 °C. The obtained Fe films from this electrolyte have a single-phase crystal structure.

The polarization curves for the discharge of iron and hydrogen ions during the electrolysis of sulfate solutions with various concentrations of amino-acetic acid showed that the presence of glycine in the electrolyte inhibited both the discharge of iron and hydrogen ions.[17] The obtained results showed that the current efficiency of the iron electrodeposition depends linearly upon the concentration of glycine passes. The influence of pH and temperature on the quality of the coating was also investigated. From the previous work, the optimum conditions for obtaining a high-quality deposit were as follows; sulfate electrolyte containing 0.1–0.15 M glycine, pH = 1.9–0.1, temperature 20 °C, and current density (j) = 20 mA / cm^2 should be applied.

The electrodeposition of iron metal was also studied from the ether solution.[18] The electrodeposition bath consisted of iron (II) chloride ($FeCl_2$), diglyme (G2) as a complexing agent, and aluminum chloride ($AlCl_3$). The effect of hydrogen gas evolution on the morphology of iron deposits was investigated by using different aqueous electrolytes. A thin Fe film was obtained using $FeCl_2$ –G_2 – $AlCl_3$ in the absence of the hydrogen gas evolution, and the nucleation of iron was explained by the instant nucleation mechanism. As a result, the surface morphology of the thin Fe film was found to be compact and smooth compared to that obtained from aqueous and nonaqueous electrolytes.

M.A. Miller et. al.[19] used ethylene glycol as an electrolyte but in the presence of choline chloride (ChCl) and $FeCl_2$ that gave different behavior and results compared with the present work. They also used different ratios from ChCl:EG: $FeCl_2$ and obtained different results at each ratio. But in the present work, EG and $Fe(NO_3)_3$ were used, where nitrates salts have a considerable solubility compared with chloride and other salts. Furthermore, the electrodeposition process was accomplished at room temperature and not at 80 °C. S. Higashino et. al.[20] used $FeCl_3$ as a precursor in presence of acetamide as a complexing agent that gave different results compared with our work.

According to the published literature, the kinetics and mechanism of the electrochemical deposition of iron from different aqueous electrolytes were studied. Therefore, our work aims to study the kinetics and mechanism of the electroreduction of iron ions from non-aqueous electrolytes (using ethylene glycol). The current work is considered to be one from a series of our works on the electrochemical synthesis of chalcogenide compounds.[21–23]

2. Experimental Part

The electrolyte for the electrochemical reduction of iron (III) ions was prepared as follows: an appreciated amount of $Fe(NO_3)_3 \cdot 9H_2O$ was dissolved in ethylene glycol by stirring in the temperature range of 313–323 K to give 0.1 M. Polarization and chrono-amperometric curves were accomplished by a potentiostat IVIUMSTAT electrochemical interface. An electrochemical three-electrode cell with a capacity of 100 ml was used. A Pt sheet with an area of 3×10^{-3} dm^2 and a Ni sheet with an area of 2 cm^2 were used as working electrodes. The silver chloride electrode was used as a reference electrode and the platinum sheet with an area of 4 cm^2 as an auxiliary electrode. The UTU-4 universal ultra-thermostat was utilized to regulate the temperature in the bath of the electrolytic cell.

The phase composition of the obtained thin films was analyzed using a Bruker D2 Phaser X-ray diffractometer (CuK_α; Ni filter). The morphology and chemical elemental composition of the samples were determined by Carel Zeiss Sigma scanning electron microscopy (SEM).

At the beginning of the experiments, the surface of Pt electrodes was cleaned in concentrated nitric acid and then washed with bidistilled water. Furthermore, after each experiment, the Pt electrodes were kept in boiling ni-

tric acid for 30 minutes. This is necessary to get rid of the adsorbed small amounts of ferric chloride on the electrode surface. After that, they were washed thoroughly with ordinary water, then with distilled water, and finally rinsed with alcohol or acetone. Ni electrode was subjected to electrochemical polishing in a solution consists of H_2SO_4, H_3PO_4, and citric acid (T = 293–303K, i = 50 A/dm^2, τ = 180 seconds), and was washed with bidistilled water.

3. Results and Discussion

The study of the electroreduction of iron ions (III) from non-aqueous solutions was carried out by the potentiodynamic method. As can be seen from Figure 1, the electrochemical reduction of iron (III) ions at the cathode occurred in two stages within the potential range of 0.8 – (–1.2) V. The first stage (I) was observed at the potential range of 0.8 – (–0.36) V that shows the reduction of Fe (III) to Fe (II) as in the following reaction: $Fe^{3+} + e^- = Fe^{2+}$.

The second stage corresponds to the reduction of Fe (II) to the atomic iron in the potential range of –0.36–(–0.8) V, which agreed with previously published work. [24] After the potential value of –0.8 V, iron is deposited on the substrate.

To study the kinetics of the electroreduction of iron (III) ions, polarization curves of a linear nature were recorded depending on the temperature at a temperature range of 288–348 K. As can be seen from Fig. 2, the potential of the electroreduction of iron (III) ions moves towards a positive direction and the current increases due to the ion mobility which increases with increasing the temperature. With the aid of these polarizing curves, the dependence of lgi_k on 1/T in the potential interval of 0.0 – (–0.5) V was depicted as in Fig. 3(a), and the value of tgα was calculated from the obtained curves. The value of the effective activation energy was calculated using the equation of $A_{eff.} = 2.3Rtg\alpha$. The values of A_{eff} showed that the electroreduction of iron ions (III) from non-aqueous electrolytes is accompanied by mixed kinetics. In the potential range of

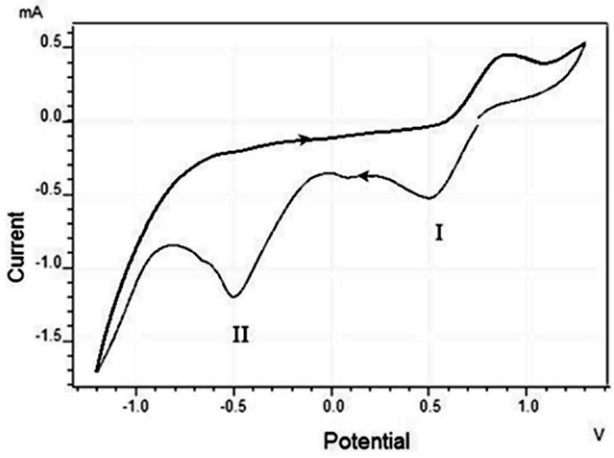


Fig. 1. Cyclic voltammetric curves of the electroreduction of iron (III) ions on a Pt electrode in a non-aqueous medium. The electrolyte composition in (M): 0.1 M $Fe(NO_3)_3 \cdot 9H_2O + CH_2OH\text{-}CH_2OH$; at T = 293 K, and E_V=0.02 V/s.

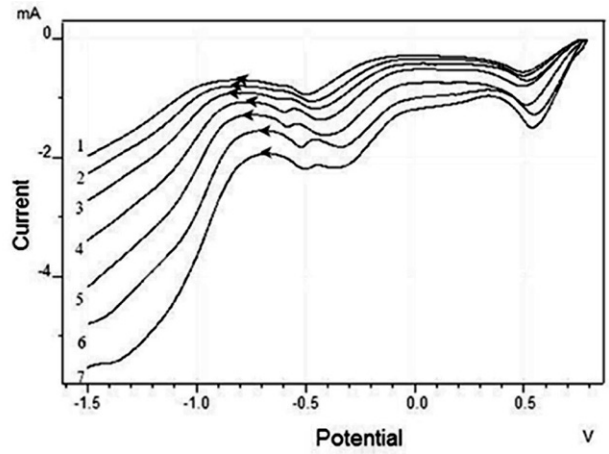


Fig. 2. The effect of temperature on the electroreduction of iron (III) ions. The electrolyte composition in (M): 0.1 $Fe(NO_3)_3 \cdot 9H_2O + CH_2OH\text{-}CH_2OH$; at different T (K): 1- 288; 2- 298; 3- 308; 4- 318; 5- 328; 6- 338; 7- 348, and scan rate E_V= 0.02 V/s

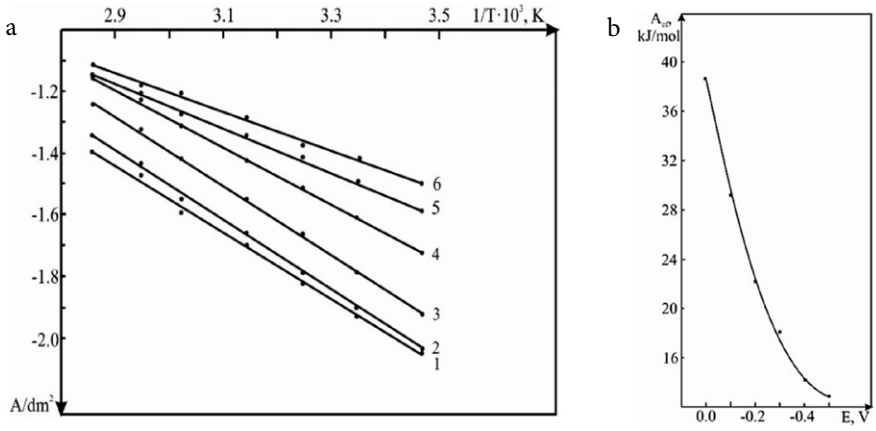


Fig. 3. (a) lgi_k – 1/T dependence, at different E(V) = 1- 0.0; 2- (–0.1); 3- (–0.2); 4- (–0.3); 5- (–0.4); 6- (–0.5). (b) Dependence of the activation energy upon the electrode potential.

0.0 – (–0.2) V the process proceeds under electrochemical polarization control, and after –0.2 V under concentration polarization control (Fig. 3 b).

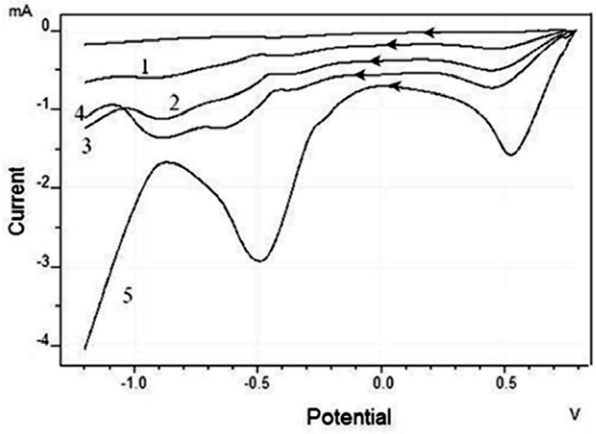


Fig. 4. The influence of the concentration of iron (III) ions on the electroreduction process on the Pt electrode. The electrolyte composition in (M): $Fe(NO_3)_3 \cdot 9H_2O + CH_2OH\text{-}CH_2OH$; 1-0.005; 2-0.05; 3- 0.1; 4- 0.15; 5- 0.2. At T = 293 K, and E_V=0.02 V/s

The effect of concentration on the electroreduction of iron (III) ions has been also studied. Polarization curves at different concentrations of iron (III) ions are presented as in Fig. 4. As can be seen from the curves, the cathodic current of iron electrodeposition increases from –0.2 to –4.1 mA with the increase of the Fe^{3+}concentration in the electrolyte. Moreover, the reduction potential is shifted to the positive direction up to 0.05 V. This can be explained on the basis that, with an increase in the concentration of iron (III) ions in the electrolyte, the migration rate of these ions to the electrode increases, and hence electroreduction occurs faster than that of the previous concentration.

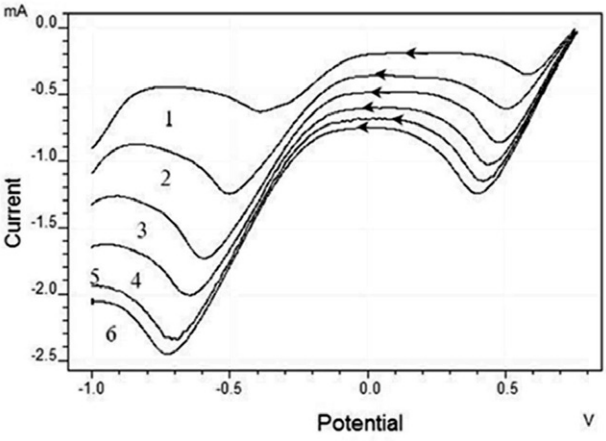


Fig. 5. The effect of the scan rate on the electroreduction of iron (III) ions. Electrolyte composition in (M): 0,1 $Fe(NO_3)_3 \cdot 9H_2O + CH_2OH\text{-}CH_2OH$. Scan rate (V/s): 1-0,005; 2- 0,02; 3- 0,04; 4- 0,06; 5- 0,08; 6- 0,1. At T = 293 K.

The influence of the scan rate on the electroreduction of iron (III) ions was also studied. Fig. 5 exhibits the cathodic potentiodynamic polarization curves of the process. As can be seen from Fig. 5, with an increase in the potential scan rate, the cathodic current of the electroreduction of iron (III) ions increase:, the cathodic current was -9.11×10^{-4} A at 0.005 V/s and -27.60×10^{-4} A at 0.1 V/s.

The chronoamperometric (CA) method was used for obtaining more precise information about the electrochemical deposition process, at which the potential can be fixed at the deposition potential. Mechanisms of the nucleation and growth of the electrodeposited particles can be investigated via CA method. Current-time curves were accomplished at different applied potentials; –0.40, –0.45, –0.50, –0.55, and –0.60 V at room temperature as shown in Fig. 6. It seems from the shown figure that the initial regime of the current-time curve is characterized by a sudden decrease in the current under application of the deposition potential. This can be attributed to the presence of the double-layer between the surface of the substrate and the ions of the solution, which lead to the formation of immediate nucleation of iron in all cases (Fig. 6).

This sudden decrease is followed by a little increase in the resultant current. This is due to an increase in the electroactive surface area which correlated with the crystal growth. It can be noted that during the electrodeposition, in all cases, the current density increases by increasing the deposition potential. The mechanism of crystal nucleation and growth can be determined by the analysis of the obtained current-time curves.

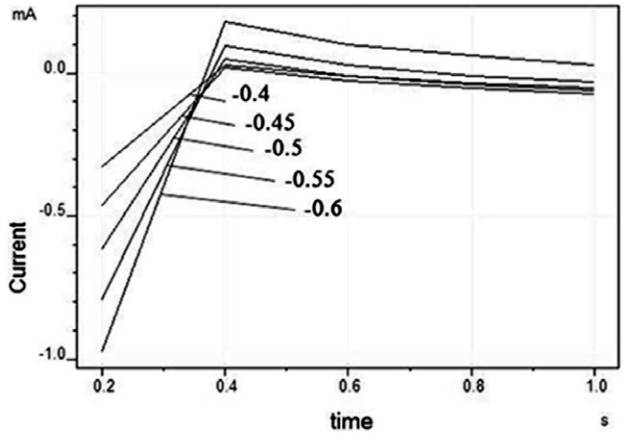


Fig. 6. Current-time curves of the electrodeposition of iron on Pt in the electrolyte of the 0.1 $Fe(NO_3)_3 \cdot 9H_2O + CH_2OH\text{-}CH_2OH$ composition at room temperature and different deposition potentials: -0.4; -0.45; –0.5; –0.55; and –0.6 V vs. Ag/AgCl.

The analysis of these curves can be achieved by applying the two equations of Scharifker-Hills [25] compared with the experimental calculated data as shown in Fig. 7 (a-e). The models of the theoretical transients for the in-

stantaneous and the progressive 3D nucleation are given by equations (1) and (2), respectively:

$$\frac{I(t)^2}{I_{max}} = \frac{1.9542}{t/t_{max}} \left\{1 - exp\left[-1.2564\left[\frac{t}{t_{max}}\right]\right]\right\}^2 \quad (1)$$

$$\frac{I(t)^2}{I_{max}} = \frac{1.2254}{t/t_{max}} \left\{1 - exp\left[-2.3367\left[\frac{t}{t_{max}}\right]^2\right]\right\}^2 \quad (2)$$

Fig. 7 (a-e) shows the nondimensional I^2/I^2_{max} vs. t/t_{max} plots derived from the CA data at different conditions as in Fig. 6. The solid lines of black and red color are the theoretical transients of the instantaneous and the progressive nucleation, and blue lines for the experimental data. The nucleation and growth processes of iron at these conditions can be derived from Fig. 7 (a–e). At the early stage, the experimental curve fits well with the curve of the progressive nucleation model by which the iron nucleation occurred on many active sites of Pt substrates. Subse-

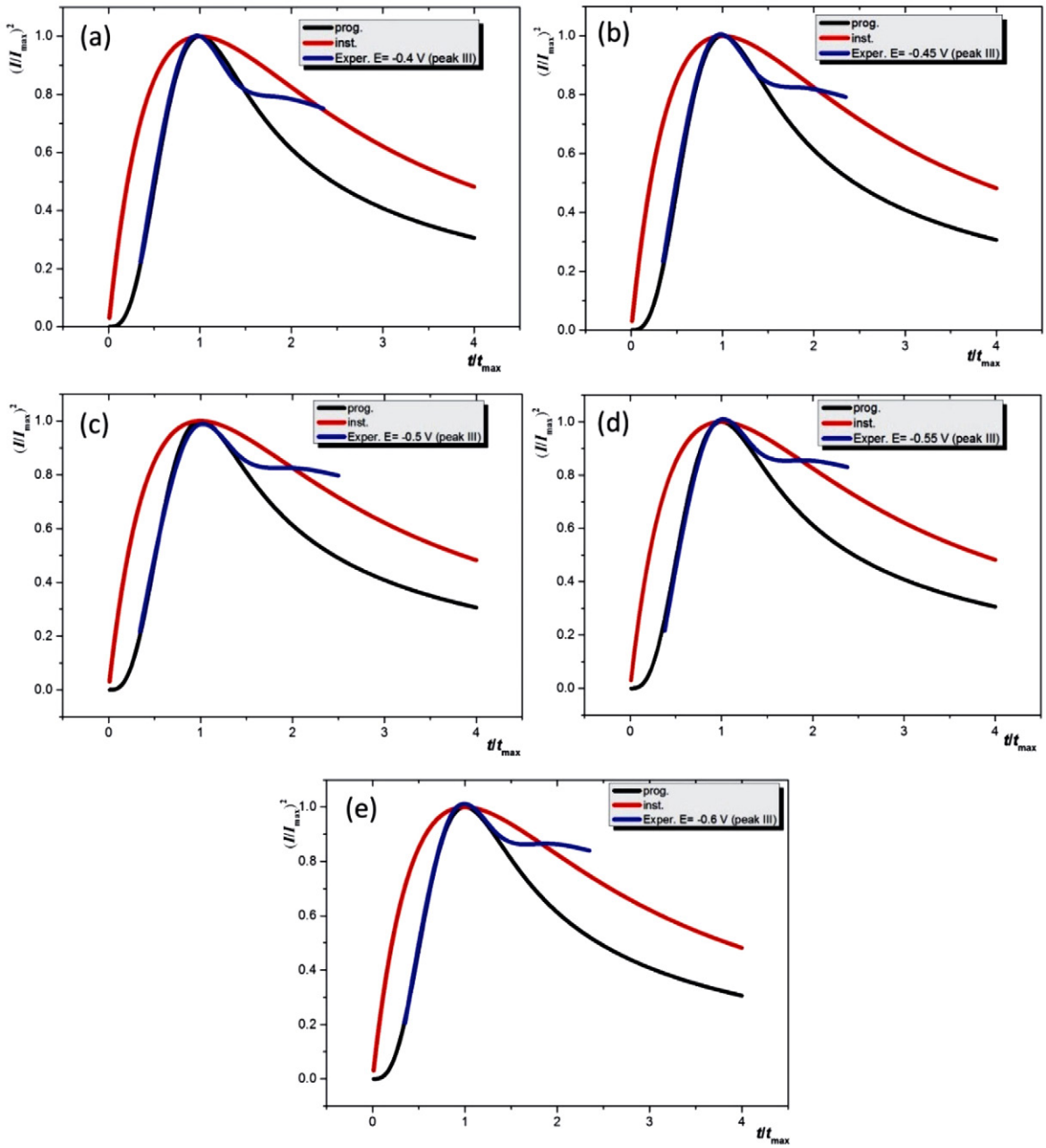


Fig. 7. Comparison of the theoretical non-dimensional $(I / I_{max})^2$ vs (t / t_{max}) plots for instantaneous (red) and progressive (black) nucleation with experimental data (blue) of potentiostatic transients in the solution of 0.1 $Fe(NO_3)_3 \cdot 9H_2O + CH_2OH\text{-}CH_2OH$ at different constant potentials: (a) -0.4, (b) -0.45, (c) -0.50, (d) -0.55 and (e)-0.6 V

quently, the deposition deviates from the progressive nucleation as shown in Fig. 7 (a, b, c, d, and e). The deviation from the ideal assumption of the Scharifker model may be attributed to that the nuclei grow under diffusion control at these conditions.

Bypassing time through the nuclei growth, the electrodeposition of iron will be under mixed control (diffusion and charge transfer). The deviation can be also interpreted as due to the hydrogen evolution reaction during the formation of nuclei which causes a morphology change of the nucleus. Further information for the growth mechanism can be obtained by calculating the density of actives sites for nucleation (N_0) by using the following equation;

$$N_0 = 0.065\left(\frac{8\pi CM}{\rho}\right)^{-1/2}\left(\frac{zfC}{t_{max}i_{max}}\right)^2 \quad (3)$$

where, C is the bulk concentration in mol cm^{-3}, zf the molar charge of electrodepositing species, M and ρ are the molar mass and the density of the deposited material in g cm^{-3}, respectively. The diffusion coefficient D of the active species in the electrolyte can be calculated via the chronoamperometric method. According to the theoretical nucleation model, the D is related to the i_{max} and the t_{max}[25, 26] by the following equation;

$$D = \frac{i_{max}{}^2 t_{max}}{0.1629(zfC)} \quad (4)$$

The values of i_{max}, t_{max}, D, and N_0 at different deposition potentials are shown in Table 1. The D values of the electroactive species are very small at these conditions, which is due to the high relative density of the electrolyte and the high relative diameter of iron ions. Therefore, the diffusion of iron ions from the bulk of the electrolyte towards the polarized electrode will be very small. Accordingly, the process is controlled by the diffusion step. Also, the value of D is a function of the polarization potential as listed in Table 1.

It is noted from the table that nuclei densities N_0 decrease significantly with the increase of the deposition potential. This decrease is due to the decrease of the activation of the nucleation sites at higher potentials, which deviates from the classical nucleation models as confirmed by Fig. 6. This deviation can also be explained as, by increasing the deposition potential the polarization of the working electrodes increases. But the diffusion of the active species is still slow because of the high density of surrounding media which hinders the diffusion of the active species.

The data of the XRD pattern (Fig. 8) and SEM images (Fig. 9) confirmed the obtained films of the electrodeposited iron on the Ni electrode.

Table 1. Experimental data on the electrodeposition of Fe on a Pt electrode

E, V	D, $cm^2\ s^{-1}$	N_o, cm^2
−0.40	1.429×10^{-17}	5.00×10^{15}
−0.45	6.556×10^{-18}	10.09×10^{15}
−0.50	3.619×10^{-17}	1.98×10^{15}
−0.55	1.468×10^{-16}	0.49×10^{15}
−0.60	5.240×10^{-16}	0.14×10^{15}

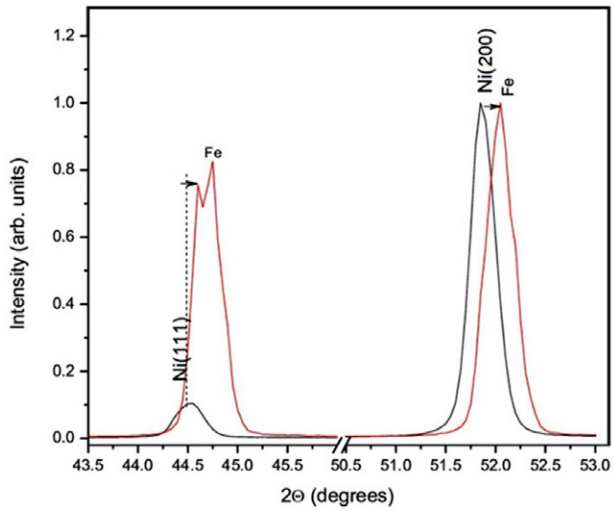
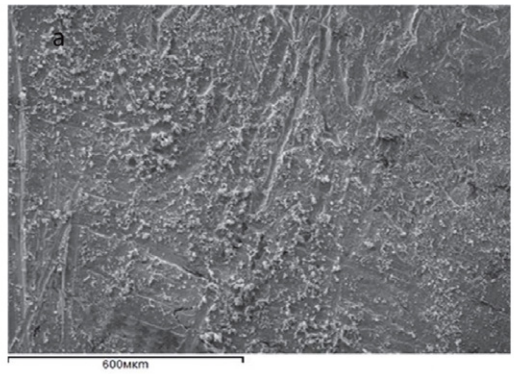


Fig. 8. The results of the XRD analysis of electrodeposited iron from 0.1 M Fe $(NO_3)_3 \times 9H_2O$ + CH_2OH-CH_2OH electrolyte on the Ni electrode. E_V = 0.02 V / s, T = 293 K.



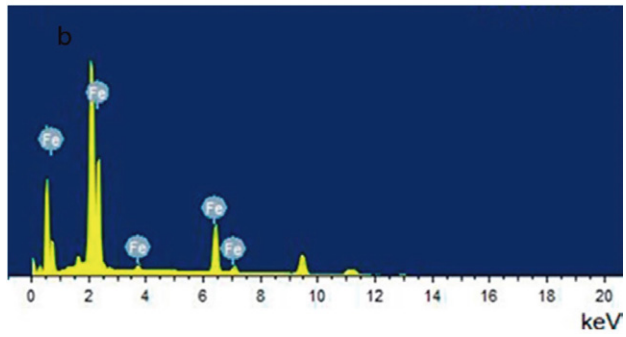


Fig. 9. The image of SEM (a) and EDAX analysis (b) of electrodeposited iron from the 0.1 M Fe $(NO_3)_3 \times 9H_2O$ + CH_2OH- CH_2OH electrolyte on the Ni electrode. At E_V = 0.02 V / s, and T = 293 K.

The SEM image showed that the nickel substrate is well coated. It seems to be relatively homogeneous and has a few cracks (Fig. 9). However, judging by the obtained X-ray pattern, these coatings are very thin (Fig. 8). It is noted that nickel peaks are also shifted towards large diffraction angles (2θ). This is because of a slight contraction of the modified crystal lattice, which is due to the incorporation of iron atoms into the nickel lattice. All experimental results exhibit that, in order to achieve the process and obtain compact, smooth deposits, an optimal electrolyte composition of 0.1 M Fe $(NO_3) \cdot 9H_2O + CH_2OH\text{-}CH_2OH$, at 293 K, and a potential range of 0.6 – (– 0.9) V should be applied.

4. Conclusion

Electrochemical reduction of iron (III) ions on Pt electrode from ethylene glycol solution was studied by the potentiodynamic method. During the study of kinetics and mechanism of the process by the cyclic and linear polarization curves, it was revealed that the nature of polarization is accompanied by mixed kinetics. It is worth mentioning that, in the potential range of 0.0 – (–0.2) V, the process proceeds under electrochemical polarization control, whereas after –0.2 V it is controlled by concentration polarization. The obtained results show that the electroreduction of iron (III) ions is affected by concentration, temperature, and the potential scan rate. From these results, the optimal mode and composition of the electrolyte for the preparation of the compact and smooth iron films have been detected. SEM and XRD data confirm the electrodeposition of thin Fe films.

5. References

1. MR Palacín, P Simon, JM Tarascon, *Acta Chim. Slov.* **2016**, *63*, 417–423. **DOI:**10.17344/acsi.2016.2314
2. VN Fateev, OK Alexeeva, SV Korobtsev, EA Seregina, TV Fateeva, AS Grigoriev, ASh Aliyev, *Chemical Problems*. **2018**, *4*, 453–483. **DOI:**10.32737/2221-8688-2018-4-453-483
3. TL Kulova, II Nikolaev, VN Fateev, ASh Aliyev, *Chemical Problems*. **2018**, *1*, 9–34. **DOI:**10.32737/2221-8688-2018-1-9-34
4. VN Fateev, TL Kulova, EA Seregina, NA Ivanova, DD Spasov, *Chemical Problems*. **2019,** *3*, 349–357. **DOI:**10.32737/2221-8688-2019-3-349-357
5. V Aluri, KTR Reddy, YM Reddy, *Nanotechnol. Rev.* **2015**, *4*, 469–472. **DOI:**10.1515/ntrev-2014-0043
6. X Wang, G Wang, J Chen, X Zhu, J Tian, C Jiang, Y Zhang, X Liu, R Wang, *Mater. Lett.* **2013**, *110*, 144–147. **DOI:**10.1016/j.matlet.2013.07.107
7. A Gomes, JR Ares, IJ Ferrer, MI da Silva Pereira, C Sanchez, *Mater. Res. Bull.* **2003**, *38*, 1123–1133. **DOI:**10.1016/S0025-5408(03)00116-8
8. YZ Dong, YF Zheng, H Duan, YF Sun, YH Chen, *Mater. Lett.* **2005**, *59*, 2398–2402. **DOI:**10.1016/j.matlet.2005.03.025
9. YZ Dong, YF Zheng, XG Zhang, H Duan, YF Sun, YH Chen, *Sci. China Technol. Sci.* **2005**, *48*, 601–611. **DOI:**10.1360/102004-32
10. S Nakamura, A Yamamoto, *Sol. Energy Mater. Sol. Cells.* **2001**, *65*, 79–85. **DOI:**10.1016/S0927-0248(00)00080-5
11. IG Orletskii, PD Mar'yanchuk, EV Maistruk, MN Solovan, VV Brus, *Phys. Solid State.* **2016**, *58*, 37–41. **DOI:**10.1134/S1063783416010224
12. SL D´ıaz, JA Caldero´n, OE Barcia, OR Mattos, *Electrochim. Acta*. **2008**, *53*, 7426–7435. **DOI:**10.1016/j.electacta.2008.01.015
13. R Böck, S-E Wulf, *Trans. Jnst. Met. Fin.* **2009**, *87*, 28–32. **DOI:**10.1179/174591908X379601
14. M Deelo, K Weil, KA Osseo-Asare, *In* Electrochem. in Miner. Metal Proc. VII. **2006**, 293–303. **DOI:**10.1179/174591908X379601
15. P Giridhar, B Weidenfeller, El Abedin S Zein, F Endres, *Phys. Chem. Chem. Phys.* **2014**, *16*, 9317–9326. **DOI:**10.1039/c4cp00613e
16. SS Abd El Rehin, EA Abd El Meguid, EM Moustafa, *Trans. Jns. Met. Fin.* **2003**, *81*, 79–82. **DOI:**10.1080/00202967.2003.11871503
17. NV Evreinova, IA Shoshina, VN Naraev, KI Tikhonov, *Russ. J. of Appl. Chem.* **2008**, *81*, 1180–1183. **DOI:**10.1134/S1070427208070100
18. Z Zhang, A Kitada, K Fukami, Z Yao, K Murase, *Electrochim. Acta*. **2020**, *348*, 136289. **DOI:**10.1016/j.electacta.2020.136289
19. MA Miller, JS Wainright, RF Savinell, *J. Electrochem. Soc.* **2017**, *164 (4)*, A796–A803. **DOI:**10.1149/2.1141704jes
20. S Higashino, AP Abbott, M Miyake, T Hirato, *Electrochim. Acta* **2020**, *351*, 136414. **DOI:**10.1016/j.electacta.2020.136414
21. VA Majidzade, SP Mammadova, ES Petkucheva, E P Slavcheva, ASh Aliyev, DB Tagiyev, *Bulg. Chem. Commun.* **2020,** *52 Special Issue E,* 73 – 78
22. VA Majidzade, PH Guliyev, ASh Aliyev, M Elrouby, DB Tagiyev, *J. Mol. Struc.* 2017, 1136, 7–13. **DOI:**10.1016/j.molstruc.2017.01.082
23. VA Majidzade, ASh Aliyev, DM Babanly, M Elrouby, DB Tagiyev, *Acta Chim. Slov.* **2019**, *66*, 155–162. **DOI:**10.17344/acsi.2018.4733
24. AA Sukhotin (Ed): Handbook of Electrochemistry, Chemistry, Leningrad, Russian, **1981**, p. 488.
25. B Scharifker, G Hills, Electrochim. Acta. **1983**, 28, *7*, 879–889. **DOI:**10.1016/0013-4686(83)85163-9
26. MR Khelladi, L Mentar, A Azizi, A Sahari, A Kahoul, *Mater. Chem. Phys.* **2009**, *115*, 385–390. **DOI:**10.1016/j.matchemphys.2008.12.017

Povzetek

Dosegli smo elektrokemijsko redukcijo železovih (III) ionov v elementarno železo iz raztopine etilen glikola. Kinetiko in mehanizem procesa elektroredukcije smo raziskovali s cikličnimi in linearnimi polarizacijskimi tehnikami. Preučevali smo tudi vpliv temperature, hitrosti spreminjanja potenciala in koncentracije ionov železa (III) na postopek elektroredukcije. Opazovane vrednosti efektivne aktivacijske energije so pokazale, da je preiskovani postopek elektroredukcije kontroliran s procesi mešane kinetike. Poleg tega so rezultati analize SEM in rentgenske difrakcije potrdili, da lahko pod optimalnimi pogoji dosežemo odlaganje tankih filmov Fe.

Except when otherwise noted, articles in this journal are published under the terms and conditions of the Creative Commons Attribution 4.0 International License

Scientific paper

Manganese(II) β-Diketonate Complexes with Pyridin-4-one, 3-Hydroxypyridin-2-one and 1-Fluoropyridine Ligands: Molecular Structures and Hydrogen-bonded Networks

Anže Čavić and Franc Perdih*

Faculty of Chemistry and Chemical Technology, University of Ljubljana, Večna pot 113, P. O. Box 537, SI-1000 Ljubljana, Slovenia

** Corresponding author: E-mail: franc.perdih@fkkt.uni-lj.si*

Received: 08-21-2020

Abstract

Manganese(II) bis(4,4,4-trifluoro-1-phenylbutane-1,3-dionate) complexes with pyridin-4-one (pyon), 3-hydroxypyridin-2-one (hpyon), 1-fluoropyridine (pyF) and methanol were prepared and the solid-state structures were determined by single-crystal X-ray analysis. The coordination of the metal center in all complexes was found to be octahedral. In compounds $[Mn(tfpb)_2(pyon)_2]$ (**1**) and $[Mn(tfpb)_2(hpyon)_2]$ (**2**) extended hydrogen bonding is present facilitating the formation of a three-dimensional supramolecular structure in **1** and a layered structure in **2** through N–H···O hydrogen bonding enhanced by C–H···O interactions as well as C–F···π interactions. In $[Mn(tfpb)_2(pyF)_2]$ (**3**) a layered structure is formed through C–H···O and C–H···F interactions as well as π···π and C–F···π interactions. In $[Mn(tfpb)_2(MeOH)_2]$ (**4**) a layered structure is formed through a combination of O–H···O and C–F···π interactions.

Keywords: β-Diketonates; manganese; pyridines; crystal structure; π···π interaction

1. Introduction

Inorganic–organic hybrids, metal–organic coordination polymers and especially metal–organic frameworks (MOFs) are currently an extremely important topic and an active area of research because of their intriguing architectures and topologies,[1,2] as well as due to their potential applications in catalysis, chemical separation processes, wastewater treatment, gas storage, magnetism and as sensors.[3] Control of the solid-state arrangement of molecules within a crystal is the central challenge of materials chemistry. In metal–organic frameworks and coordination polymers, covalent bonding using bridging organic ligands for creation of robust polymeric structures is of prime importance. Various kinds of these materials have been designed with special attention dedicated to the geometry of the metal ions as well as flexibility, bridging potential and coordination preferences of different organic linkers.[1] On the other hand, in inorganic–organic hybrids non-covalent bonds adjust the dimensionality and enable new topologies to arise. Non-covalent forces, such as hydrogen bonding, C–H···π/F interactions, π···π stacking, and halogen bonding are much weaker compared to the covalent bonds, however, their multitude makes them a powerful tool in the crystal engineering. Also, a great variety of non-covalent donors–acceptors and their numbers, their unique directionality and simple introduction into structures make them a particularly good choice for the construction of self-assemblies.

Here we report the influence of pyridin-4-one (4-pyridone; pyon), 3-hydroxypyridin-2-one (hpyon), and 1-fluoropyridine (pyF) ligands on the molecular and supramolecular structure in the cases of $[Mn(tfpb)_2(pyon)_2]$ (**1**), $[Mn(tfpb)_2(hpyon)_2]$ (**2**), $[Mn(tfpb)_2(pyF)_2]$ (**3**) complexes as well as the structure of $[Mn(tfpb)_2(MeOH)_2]$ (**4**), where tfpb is the 4,4,4-trifluoro-1-phenylbutane-1,3-dionate (or 4,4,4-trifluoro-3-oxo-1-phenylbutan-1-olate) ligand. The tfpb ligand was selected because it is not symmetric and possesses phenyl and trifluoromethyl groups enabling also the formation of C–H···F, F···F and C–F···π interactions besides the π···π and C–H···π interactions.[4] Pyridin-4-on and 3-hydroxypyridin-2-one were selected since the tautomeric equilibrium between the lactam and lactim forms enables various coordination modes and also

due to their different hydrogen bond formation abilities when coordinated in lactam/lactim form. On the other hand, 1-fluoropyridine was selected in order to be able to study the influence of an additional fluorine substituent on the formation of supramolecular aggregation in the absence of the competing strong hydrogen bond donors.

2. Experimental

2. 1. Materials and Characterization

Reagents and chemicals were obtained as reagent grade from commercial sources and were used as purchased without any further purification. $[Mn(tfpb)_2(H_2O)_2]$ was prepared according to the literature procedure.[5] Infrared (IR) spectra (4000–600 cm^{-1}) of the samples were recorded using a Perkin–Elmer Spectrum 100, equipped with a Specac Golden Gate Diamond ATR as a solid sample support. Elemental (C, H, N) analyses were obtained using a Perkin–Elmer 2400 Series II CHNS/O Elemental Analyzer.

2. 2. Synthesis

Synthesis of [Mn(tfpb)$_2$(pyon)$_2$] (1)

$[Mn(tfpb)_2(H_2O)_2]$ (0.065 g, 0.125 mmol) was dissolved in acetone (8 mL) and then pyon (0.024 g, 0.250 mmol) was added. The reaction mixture was stirred for 15 min at ~50 °C and then allowed to stand at room temperature. Orange crystals suitable for X-ray analysis were obtained after slow evaporation of the solvent over a few days. Yield: 0.036 g, 43%. Anal. Calcd. $[Mn(tfpb)_2(pyon)_2]$ ($C_{30}H_{22}F_6MnN_2O_6$) (MW = 675.44): C 53.35, H 3.28, N 4.15; Found C 52.92, H 2.90, N 4.06. IR (ATR, cm^{-1}): 3244w, 3080w, 2663w, 1606s, 1597m, 1573m, 1527m, 1501m, 1471s, 1374m, 1315m, 1283s, 1248m, 1179s, 1127s, 1072m, 1025m, 996m, 939m, 831m, 763m, 717m, 697s, 635m.

Synthesis of [Mn(tfpb)$_2$(hpyon)$_2$] (2)

$[Mn(tfpb)_2(H_2O)_2]$ (0.065 g, 0.125 mmol) was dissolved in warm ethanol (12 mL) and then hpyon (0.028 g, 0.250 mmol) was added. The reaction mixture was stirred for 15 min at ~60 °C and then allowed to stand at room temperature. Orange crystals suitable for X-ray analysis were obtained after slow evaporation of the solvent over a few days. Yield: 0.058 g, 66%. Anal. Calcd. $[Mn(tfpb)_2(hpyon)_2]$ ($C_{30}H_{22}F_6MnN_2O_8$) (MW = 707.44): C 50.91, H 3.14, N 3.96; Found C 50.72, H 3.14, N 3.90. IR (ATR, cm^{-1}): 3251w, 3120w, 2958w, 1605m, 1596m, 1570s, 1543m, 1529m, 1491m, 1471m, 1456m, 1419m, 1377m, 1284s, 1251m, 1187s, 1134s, 1058m, 937m, 885m, 761s, 717m, 699s, 635m.

Synthesis of [Mn(tfpb)$_2$(pyF)$_2$] (3)

$[Mn(tfpb)_2(H_2O)_2]$ (0.065 g, 0.125 mmol) was dissolved in pyF (2 mL). The reaction mixture was stirred for 15 min at ~60 °C and then allowed to stand at room temperature. Orange crystals suitable for X-ray analysis were obtained after slow evaporation of the solvent over a few days. Yield: 0.045 g, 53%. Anal. Calcd. $[Mn(tfpb)_2(pyF)_2]$ ($C_{30}H_{20}F_8MnN_2O_4$) (MW = 679.42): C 53.02, H 2.97, N 4.12; Found C 52.55, H 2.81, N 3.99. IR (ATR, cm^{-1}): 3381br, 1609s, 1597m, 1574s, 1532m, 1490m, 1458m, 1318m, 1281s, 1248m, 1182s, 1129s, 1096m, 1075m, 1025w, 941w, 798w, 768m, 718m, 699s, 635s.

Synthesis of [Mn(tfpb)$_2$(MeOH)$_2$] (4)

$[Mn(tfpb)_2(H_2O)_2]$ (0.065 g, 0.125 mmol) was dissolved in warm methanol (12 mL) and then pyon (0.024 g, 0.250 mmol) was added. The reaction mixture was stirred for 15 min at ~60 °C and then allowed to stand at room temperature. Orange crystals suitable for X-ray analysis were obtained after slow evaporation of the solvent over a few days. Yield: 0.040 g, 58%. Anal. Calcd. $[Mn(tfpb)_2(MeOH)_2]$ ($C_{22}H_{20}F_6MnO_6$) (MW = 549.32): C 48.10, H 3.67; Found C 47.94, H 3.38. IR (ATR, cm^{-1}): 2538br, 2421br, 1928w, 1876w, 1644m, 1602m, 1574m, 1350s, 1321m, 1259m, 1228m, 1191s, 1134m, 995s, 934s, 821s, 811s, 748w, 635s.

2. 3. X-ray Crystallography

Single-crystal X-ray diffraction data were collected at room temperature (**1**, **2**, **4**) or 150 K (**3**) on a Nonius Kappa CCD diffractometer or an Agilent Technologies SuperNova Dual diffractometer with an Atlas detector using monochromated Mo-K_α radiation (λ = 0.71073 Å). The data were processed using DENZO[6] or CrysAlis Pro.[7] The structures were solved by direct methods implemented in SHELXS[8] and SIR-97[9] and refined by a full-matrix least-squares procedure based on F^2 with SHELXL.[8] All non-hydrogen atoms were refined anisotropically. All H atoms were initially located in a difference Fourier maps. The hydrogen atoms on carbon atoms were treated as riding atoms in geometrically idealized positions. Hydrogen atoms attached to nitrogen and oxygen atoms were refined fixing the bond lengths and isotropic temperature factors as $U_{iso}(H) = kU_{eq}(N,O)$, where $k = 1.5$ for OH groups, and 1.2 for NH groups. In **1** and **4** the CF_3 groups are disordered over two positions in 0.76(2):0.24(2) and 0.71(3):0.29(3) (in **1**) and 0.66(3):0.34(3) (in **4**) ratio. In **1** a possible pseudo-translation was detected, however, no additional space group could be found using the Platon program. The crystallographic data are listed in Table 1.

3. Results and Discussion

Initial attempts to prepare **1** using methanol as a solvent gave **4** as the sole product. Thus, in the subsequent attempts of its synthesis other solvents were used instead. Compounds **1** and **2** were obtained by the reaction of

Table 1. Crystallographic and refinement data for **1**–**4**.

Parameter	$[Mn(tfpb)_2(pyon)_2]$ (**1**)	$[Mn(tfpb)_2(hpyon)_2]$ (**2**)	$[Mn(tfpb)_2(pyF)_2]$ (**3**)	$[Mn(tfpb)_2(MeOH)_2]$ (**4**)
Formula	$C_{30}H_{22}F_6MnN_2O_6$	$C_{30}H_{22}F_6MnN_2O_8$	$C_{30}H_{20}F_8MnN_2O_4$	$C_{22}H_{20}F_6MnO_6$
M_r	675.43	707.43	679.42	549.32
T (K)	293(2)	293(2)	150(2)	293(2)
Crystal system	Monoclinic	Triclinic	Monoclinic	Triclinic
Space group	$P2_1/n$	$P\bar{1}$	$P2_1/c$	$P\bar{1}$
a (Å)	16.1805(3)	7.3146(2)	11.8720(3)	10.4921(4)
b (Å)	10.5318(2)	9.9367(2)	8.8105(2)	10.5763(4)
c (Å)	17.8217(3)	10.7440(2)	14.5507(4)	12.4197(5)
α(°)	90	108.132(2)	90	70.893(2)
β (°)	91.558(2)	100.589(2)	108.628(3)	66.685(2)
γ (°)	90	91.833(2)	90	82.624(2)
Volume (Å^3)	3035.87(10)	726.16(3)	1442.24(7)	1195.92(8)
Z	4	1	2	2
D_{calc} (Mg/m^3)	1.478	1.618	1.565	1.525
μ (mm^{-1})	0.517	0.549	0.549	0.634
F(000)	1372.0	359.0	686.0	558.0
Crystal size (mm)	0.5 × 0.2 × 0.1	0.6 × 0.6 × 0.5	0.2 × 0.2 × 0.05	0.25 × 0.1 × 0.03
Reflections collected	28841	5959	13789	9395
Data/restraints/parameters	6949/2/471	3298/2/220	3311/0/205	5457/2/353
R_{int}	0.0322	0.0133	0.0333	0.0291
R, wR_2 [I>2σ(I)][a]	0.0416, 0.1040	0.0328, 0.0882	0.0399, 0.0961	0.0459, 0.1073
R, wR_2 (all data)[b]	0.0650, 0.1162	0.0352, 0.0904	0.0529, 0.1037	0.0812, 0.1264
GOF, S[c]	1.051	1.074	1.044	1.012
Max/min Δρ (e/Å^3)	0.21/–0.21	0.31/–0.34	0.83/–0.27	0.32/–0.27

[a] $R = \Sigma||F_o| - |F_c||/\Sigma|F_o|$. [b] $wR_2 = \{\Sigma[w(F_o^2 - F_c^2)^2]/\Sigma[w(F_o^2)^2]\}^{1/2}$. [c] $S = \{\Sigma[(F_o^2 - F_c^2)^2]/(n/p)\}^{1/2}$ where n is the number of reflections and p is the total number of parameters refined.

$[Mn(tfpb)_2(H_2O)_2]$ and the corresponding heteroaromatic ligands pyridine-4-on (pyon) and 3-hydroxypyridine-2-on (hpyon) in 1:2 molar ratio in warm ethanol or acetone, respectively. Compound **3** was prepared by the reaction of $[Mn(tfpb)_2(H_2O)_2]$ in warm 1-fluoropyridine (pyF) acting as a solvent and as a ligand. Crystals suitable for X-ray analyses were obtained by slow evaporation of the solvent at room temperature over a few days. The IR spectrum of **1** shows two bands at 3244 and 3080 cm^{-1} and the spectrum of **2** two bands at 3251 and 3120 cm^{-1} that suggest the involvement of the O–H and N–H groups of pyridone ligands in strong hydrogen bonding. The spectrum of **4** shows one broad band at 3381 cm^{-1} that suggests the involvement of the O–H groups of methanol ligands in strong hydrogen bonding. In all four compounds, there are bands in the frequency range 1609–1527 cm^{-1} characteristic for the ν(C=O) and ν(C=C) stretching of the tfpb ligand.

Compound **1** crystallizes in the monoclinic $P2_1/n$ space group. Selected bond distances and angles of **1** are summarized in Table 2. The asymmetric unit contains two crystallographically independent half-molecules (A and B), with both independent Mn^{II} atoms sitting on the inversion centers. Both manganese(II) atoms are octahedrally coordinated (Fig. 1). In the equatorial plane, both metal centers are surrounded by four oxygen atoms of two chelating tfpb ligands in a *trans* arrangement, with Mn–O distances 2.1365(14) and 2.1233(13) Å (for A) and 2.1245(13) and 2.1467(13) Å (for B). The $Mn(tfpb)_2$ fragments deviate from planarity, the angle between the mean plane formed by the equatorial MnO_4 core and that of the tfpb chelate C_3O_2 moiety being 14.48(6) and 16.47(6)°. In both complexes the axial positions are occupied by two pyon ligands bonded to the metal center through the O atom, with Mn1–O3 distance of 2.2358(12) Å and Mn1–O3–C23 angle of 131.10(11)° and Mn2–O6 distance of 2.2035(12) Å and Mn2–O6–C28 angle of 126.58(11)°. These distances are similar to those reported for the three known Mn complexes with tfpb.[10] The pyon ligands are inclined toward the tfpb moiety. The angle between the plane of the pyon ring and the plane of the equatorial MnO_4 core deviates from 90° being 78.60(5)° (for A) and only 44.51(5)° (for B). Superposition of both complexes shows that pyon ligands are oriented in the opposite direction (Fig. 2) with pyon ring in complex B inclined toward the phenyl ring of the tfpb ligand. Complex A is stabilized by an intramolecular C22–H22···O2^i interaction between pyon and tfpb ligand (Table 3) and C1–F3a/b···π interactions between $-CF_3$ group and pyon ring with F···*Cg*3 distances of 3.769(10) and 3.82(4) Å and C–F···*Cg*3 angles of 130.4(5) and 128(3)°, respectively, where *Cg*3 is N1/C21–C25 ring centroid (Fig. 3). Complex B is stabilized by an intramolecular

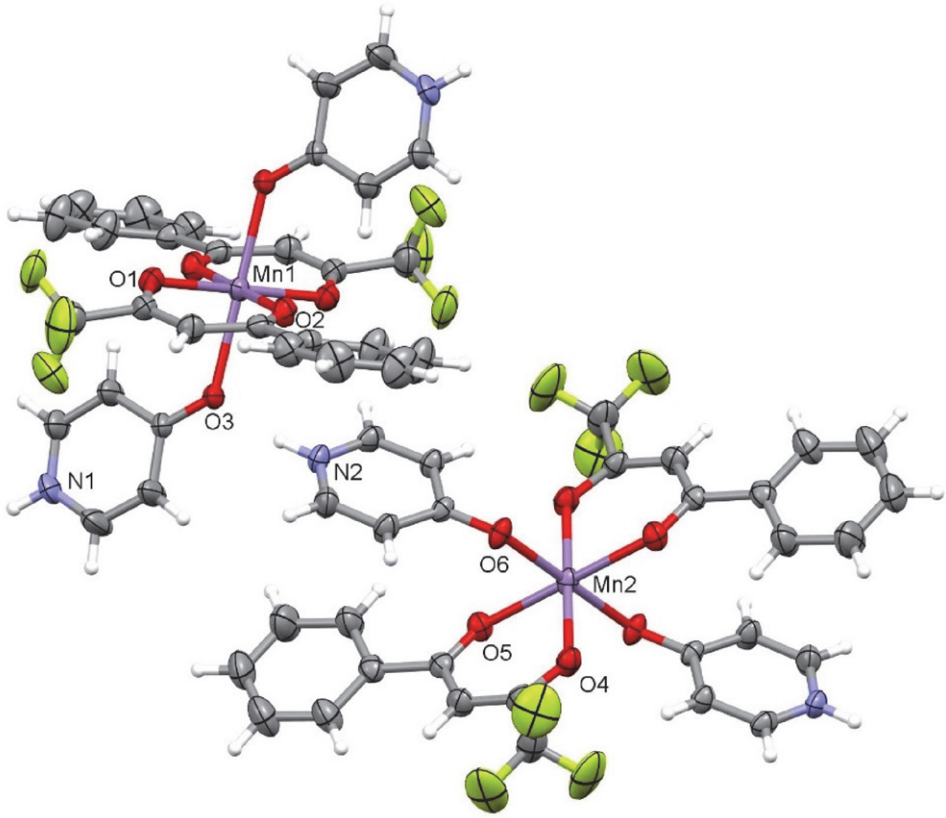


Figure 1. Crystallographically independent molecules in **1**. Disorder on CF_3 groups has been omitted for clarity. Displacement ellipsoids are drawn at 30% probability level.

C27–H27···O4^{ii} interaction between pyon and tfpb ligand. The NH groups of the pyon ligands of both independent complexes act as hydrogen-bond donors interacting with the tfpb carbonyl oxygens of the adjacent complexes, facilitating the formation of a hydrogen-bonded tree-dimensional supramolecular structure (Fig. 3). Complex A interacts with two complexes B through N1–H1···O6^{iii} bonding enabling the formation of an ABAB chain. Complex B interacts with two complexes A through N2–H2···O3 bonding enhanced by C26–H26···O1^{i} interaction with $R^2_2(7)$ ring motif[11] enabling the formation of an ABAB chain in the second dimension. Furthermore, complex B interacts with two adjacent complexes B through the centrosymmetric C29–H29···F6a^{iv} interactions with $R^2_2(18)$ ring motif forming a BBB chain in the third dimension (Table 3).

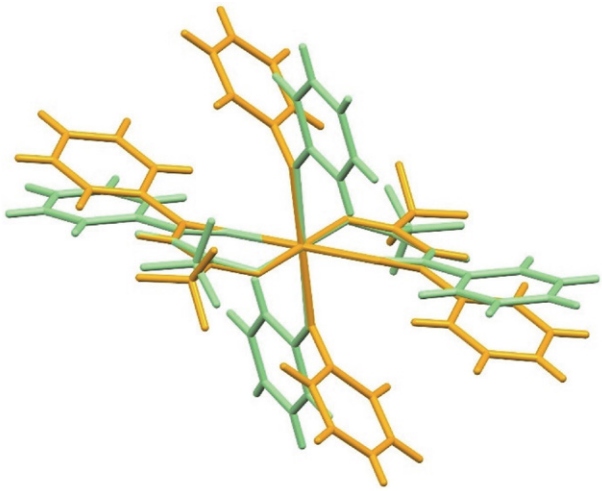


Figure 2. Superposition of crystallographically independent molecules A (green) and B (orange) in **1**. Disorder on CF_3 groups has been omitted for clarity.

Table 2. Selected bond distances and angles for **1**.

Distance	**(Å)**		
Mn1–O1	2.1365(14)	Mn2–O4	2.1245(13)
Mn1–O2	2.1233(13)	Mn2–O5	2.1467(13)
Mn1–O3	2.2358(12)	Mn2–O6	2.2035(12)
Angle	**(°)**		
O1–Mn1–O2	84.10(5)	O4–Mn2–O5	85.38(5)
O1–Mn1–O2^{i}	95.90(5)	O4–Mn2–O5^{ii}	94.62(5)
O1–Mn1–O3	85.43(5)	O4–Mn2–O6	85.82(5)
O1–Mn1–O3^{i}	94.57(5)	O4–Mn2–O6^{ii}	94.18(5)
O2–Mn1–O3	86.91(5)	O5–Mn2–O6	85.20(5)
O2–Mn1–O3^{i}	93.09(5)	O5–Mn2–O6^{ii}	94.80(5)

Symmetry codes: (i) 1 – *x*, –*y*, –*z*; (ii) 1 – *x*, –*y*, 1 – *z*.

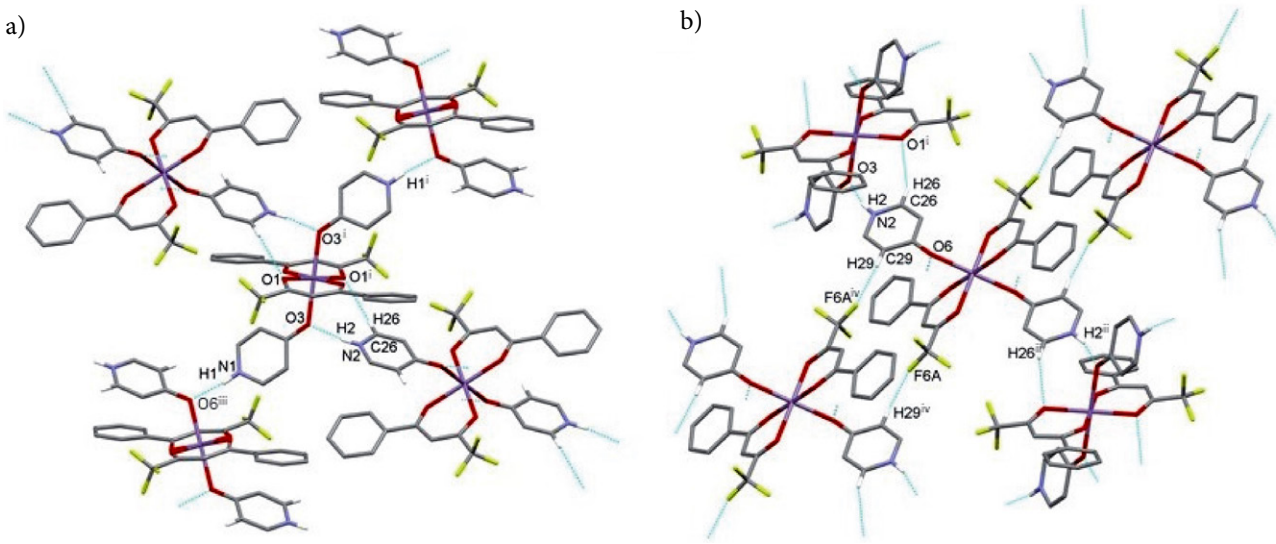


Figure 3. Three-dimensional supramolecular structure in **1** is achieved by hydrogen bonding around **a)** molecule A and **b)** molecule B through a series of N1–H1···O6^{iii}, N2–H2···O3, C26–H26···O1^{i} and C29–H29···F6a^{iv} interactions. Blue dashed lines indicate hydrogen bonds. For the sake of clarity, intramolecular interactions, disorder on CF_3 groups and H atoms not involved in the motif shown have been omitted. For symmetry codes see Table 3.

Table 3. Hydrogen bonds for **1–4** [Å and °]

D–H···A	d(D–H)	d(H···A)	d(D···A)	<(DHA)
1				
N1–H1···O6^{iii}	0.872(17)	1.854(17)	2.720(2)	172(3)
N2–H2···O3	0.888(16)	1.859(17)	2.723(2)	164(2)
C22–H22···O2^{i}	0.93	2.36	3.119(3)	139.1
C26–H26···O1^{i}	0.93	2.48	3.322(2)	151.1
C27–H27···O4^{ii}	0.93	2.47	3.206(2)	136.6
C29–H29···F6a^{iv}	0.93	2.47	3.394(7)	175.7
2				
O4–H4···O1^{i}	0.814(17)	1.952(18)	2.7495(16)	166(3)
N1–H1···O3^{ii}	0.882(14)	2.009(15)	2.8829(15)	170.2(18)
C13–H13···O4^{iii}	0.93	2.58	3.4770(19)	162.9
C15–H15···O2^{iv}	0.93	2.42	3.2428(19)	147.3
3				
C13–H13···F2^{ii}	0.95	2.42	3.287(3)	151.6
C14–H14···O1^{iii}	0.95	2.58	3.493(3)	161.3
4				
O5–H5···O1^{i}	0.822(10)	1.966(14)	2.772(2)	167(4)
O6–H6···O3^{ii}	0.813(10)	2.001(13)	2.801(2)	168(4)

Symmetry codes for **1**: (i) 1 – *x*, –*y*, –*z*; (ii) 1 – *x*, –*y*, 1 – *z*; (iii) –½ + *x*, ½ – *y*, –½ + *z*; (iv) 1 – *x*, 1 – *y*, 1 – *z*; for **2**: (i) 2 – *x*, 2 – *y*, –*z*; (ii) 1 – *x*, 2 – *y*, –*z*; (iii) 2 – *x*, 2 – *y*, 1 – *z*; (iv) –1 + *x*, *y*, *z*; for **3**: (ii) –*x*, 1 – *y*, –*z*; (iii) *x*, ½ – *y*, ½ + *z*; for **4**: (i) 2 – *x*, 1 – *y*, 1 – *z*; (ii) 2 – *x*, –*y*, 1 – *z*.

The supramolecular structure is further stabilized also by C11–F4a···π interaction between –CF_3 group of complex B and pyon ring of complex A with F···*Cg*3 distance of 3.806(11) Å and C–F···*Cg*3 angle of 139.1(5)°.

Compound **2** crystallizes in the triclinic *P*–1 space group. Selected bond distances and angles are summarized in Table 4. The asymmetric unit contains one half of the complex, with the Mn^{II} atom sitting on the inversion center. Octahedrally coordinated manganese(II) atom is surrounded by four oxygen atoms positioned in the equatorial plane, stemming from two chelating tfpb ligands in a *trans* arrangement, with Mn–O distances 2.1132(10) and 2.1218(9) Å (Fig. 4). The $Mn(tfpb)_2$ fragment deviates from planarity, the angle between the mean plane formed by the equatorial MnO_4 core and that of the tfpb chelate C_3O_2 moiety being 15.91(4)°. The axial positions are occupied by two hpyon ligands bonded to the metal center through the O3 atom, with Mn1–O3 distance of 2.2768(10) Å and Mn1–O3–C11 angle of 128.19(9)°. The hpyon ligand is inclined toward the tfpb moiety, with the angle between the plane of the hpyon ring and that of the equatorial MnO_4 core being 43.25(6)°. The hydroxy group of the hpyon ligand is involved in intramolecular hydrogen bonding with the tfpb ligand through O4–H4···O1^{i} interaction (Table 3). The NH group of the hpyon ligand acts as a hydrogen bond donor, facilitating the formation of a centrosymmetric hydrogen-bonded motif *via* N1–H1···O3^{ii} interactions with the ligated carbonyl O3 atom enhanced by C15–H15···O2^{iv} interactions with the graph-set motifs $R^2_2(8)$ and $R^2_2(7)$, respectively (Fig. 5 and Table 3). This interaction is further stabilized by C1–F3···π interaction between CF_3 group and the hpyon ring with *d*(F3···*Cg*3) = 3.2278(17) Å and <(C1–F3···*Cg*3) = 135.64(11)°, where *Cg*3 is N1/C11–C15 ring centroid. Consequently, a chain is formed along the *a* axis. The chains are further connected into layers along the *ac* plane *via* centrosymmetric C13–H13···O4^{iii} hydrogen bonding between hpyon CH moiety and the hydroxy group of the adjacent molecule (Fig. 5). There are no significant π···π interactions.

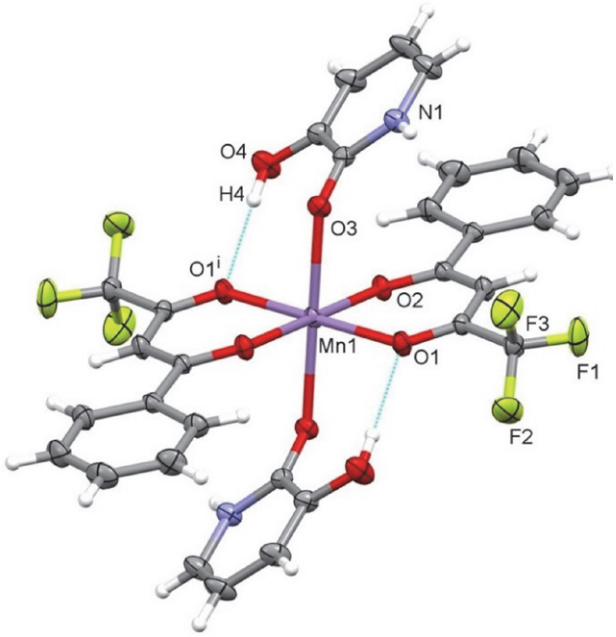


Figure 4. Structure of **2**. Displacement ellipsoids are drawn at the 30% probability level. Intramolecular hydrogen bonding is presented by dashed blue lines.

Table 4. Selected bond distances and angles for **2**.

Distance	**(Å)**		
Mn1–O1	2.1132(10)	Mn1–O2	2.1218(9)
Mn1–O3	2.2768(10)		
Angle	**(°)**		
O1–Mn1–O2	84.24(4)	O1–Mn1–O2^{i}	95.76(4)
O1–Mn1–O3	92.67(4)	O1–Mn1–O3^{i}	87.33(4)
O2–Mn1–O3	84.40(4)	O2–Mn1–O3^{i}	95.60(4)

Symmetry code: (i) 2 – *x*, 2 – *y*, –*z*.

In the solid state, pyridin-4-one and 3-hydroxypyridin-2-one are in the lactam form.[12,13] Also in metal complexes the lactam form of both predominates. A search of the Cambridge Structural Database (CSD, Version 5.41, plus updates)[14] has revealed 26 entries[15] of metal complexes where pyridin-4-one, in its lactam form, is bonded *via* O atom also observed in complex **1**. However, 9 entries with the lactim form (as 4-hydroxypyridine) bonded *via* N atom were found in the CSD with Re, Ir, Pt, and Ag[16] as well as Cu and Fe.[17] This observation can be explained by the Pearson HSAB (hard–soft acid–base) concept[18] since soft acids, such as Re, Ir, Pt, and Ag, show a preference for bonding *via* pyridine N atom (an intermediate base) as opposed to the –OH group (a hard base). Additionally, 3 entries with the lactim form bonded *via* OH group were also found with Nd, Tb, Dy.[19] In metal complexes with 3-hydroxypyridin-2-on lactam form with monodentate ligation *via* O atom[20,21] was found in 9 entries; the same type was also observed in complex **2**. Additionally, 3 entries were found with *O,O'*-chelating ligation.[21,22] However, no entries were found with lactim form (as 2,3-dihydroxypyridine) bonded to the metal center. For comparison, metal complexes with pyridine-2-one were more often investigated than complexes with pyridin-4-one and 3-hydroxypyridin-2-one and a variety of coordination modes has been observed.[21,23,24]

Compound **3** crystallizes in the monoclinic $P2_1/c$ space group. Selected bond distances and angles of **3** are summarized in Table 5. Initial attempts to collect XRD data at room temperature failed due to slow decomposition of the crystal when exposed to the air. Most probably 1-fluoropyridine molecule is eliminated from the complex and the crystal lattice is being thus destroyed. Similar loss of pyridine bonded in zinc picolinato complexes has been previously observed.[61,62] The asymmetric unit contains one half of the complex, with the Mn^{II} atom sitting on the inversion center. The manganese(II) atom in compound **3** is octahedrally coordinated (Fig. 6). In the equatorial plane, Mn^{II} atom is surrounded by four oxygen atoms stemming from the two chelating tfpb ligands, being in a *trans* arrangement, with Mn–O distances 2.1415(14) and 2.1337(14) Å. The $Mn(tfpb)_2$ fragment deviates from planarity, the angle between the mean plane formed by the MnO_4 core and that of the tfpb chelate C_3O_2 moiety being 18.00(7)°. The axial positions are occupied by two pyF ligands bonded to the metal center through the N1 atom, with Mn1–N1 distance of 2.3425(17) Å. PyF ligand plays the main role in the formation of a layered structure due to the absence of the competing strong hydrogen bond donors. As a hydrogen bond donor PyF is involved in C14–H14···O1^{iii} interaction with carbonyl oxygen atom and in centrosymmetric C13–H13···F2^{ii} interactions with fluorine atom of $–CF_3$ group of tfpb ligands of the adjacent complexes (Fig. 7 and Table 3). Thus, each complex is involved in eight hydrogen bonds with six adjacent complexes forming a layered structure. 2D structure is supported by centrosymmetric π···π interactions between adjacent pyF rings with centroid-to-centroid distance of 3.9403(14) Å, perpendicular distance between rings of 3.2624(10) Å and ring slippage of 2.210 Å. Layered structure is further supported also by C–F···π interactions between pyF fluorine atom and pyF aromatic ring with *d*(F4···*Cg*3) = 3.6714(19) Å and <(C11–F4···*Cg*3) = 75.63(13)° as well as by interactions between $–CF_3$ group and benzene ring of tfpb ligand with *d*(F2···*Cg*4) = 3.715(2) Å and <(C1–F2···*Cg*4) = 126.72(15)°, where *Cg*3 and *Cg*4 are N1/C11–C15 and C5–C10 ring centroids, respectively (Fig. 7).

The inclination of pyon and hpyon ligands toward the tfpb moiety in **1** and **2** is best compared with the compound **3** since the ligation of pyF *via* N atom cannot enable much deviation in comparison to the pyon and hpyon ligands bonded *via* O atom. Superposition of both crystallographically independent molecules in **1** as well as mole-

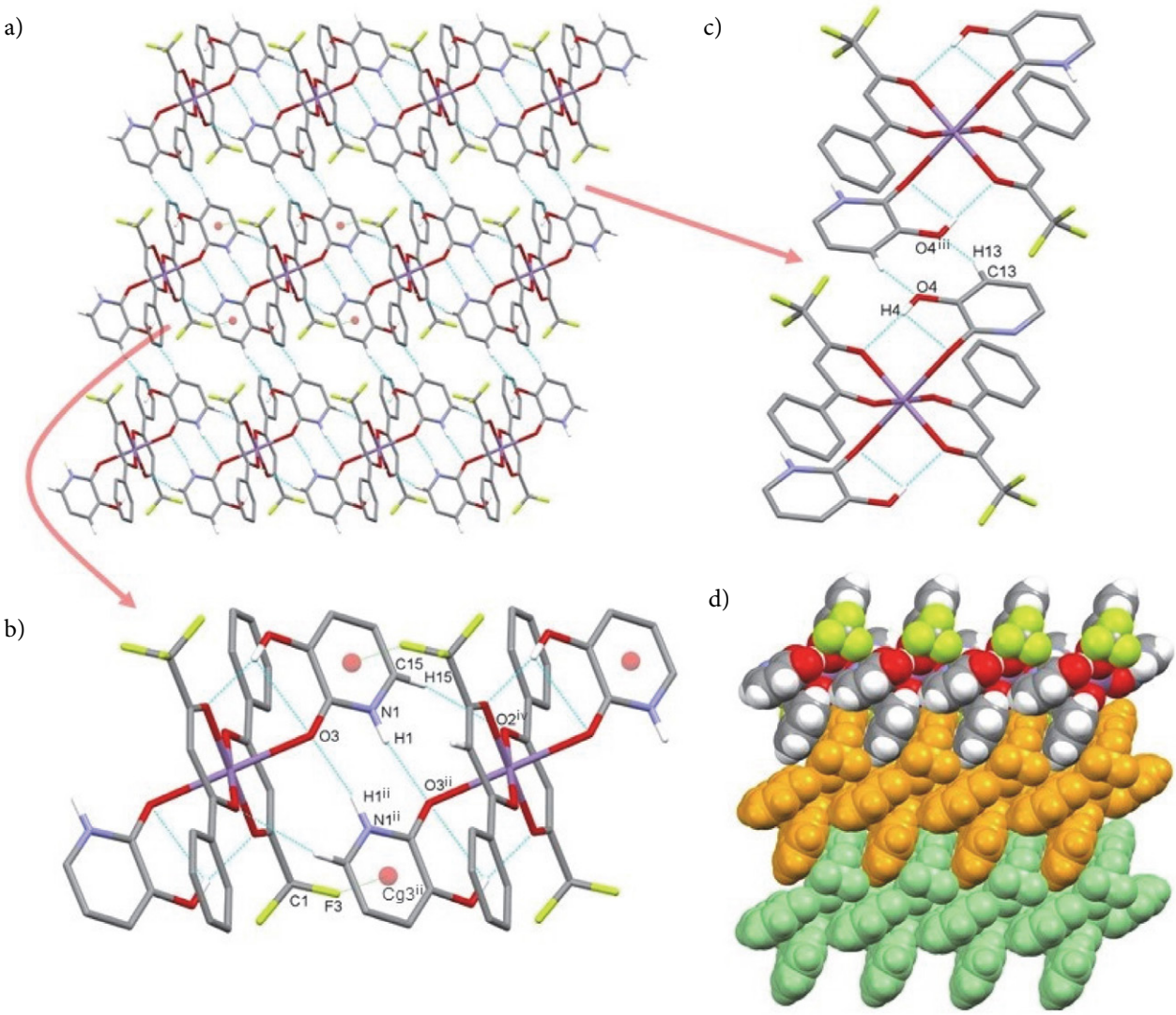


Figure 5. a) Hydrogen-bonded layer along the *ac* plane in **2** is formed by **b)** centrosymmetric N1–H1···O3^{ii}, C15–H15···O2^{iv} and C1–F3···Cg3^{ii} interactions and **c)** C13–H13···O4^{iii} interactions; **d)** packing of layers (arbitrary colors). Blue and green dashed lines indicate hydrogen bonds and C–F···π interactions, respectively. For the sake of clarity, H atoms not involved in the motif shown have been omitted. For symmetry codes see Table 3.

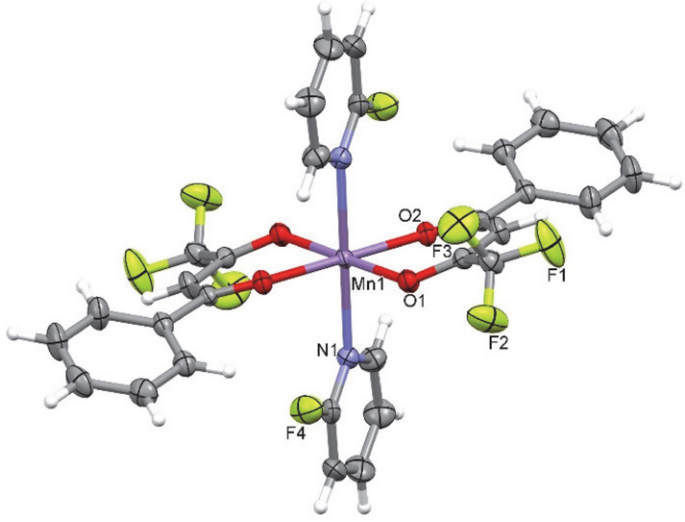


Figure 6. Structure of **3**. Displacement ellipsoids are drawn at 50% probability level.

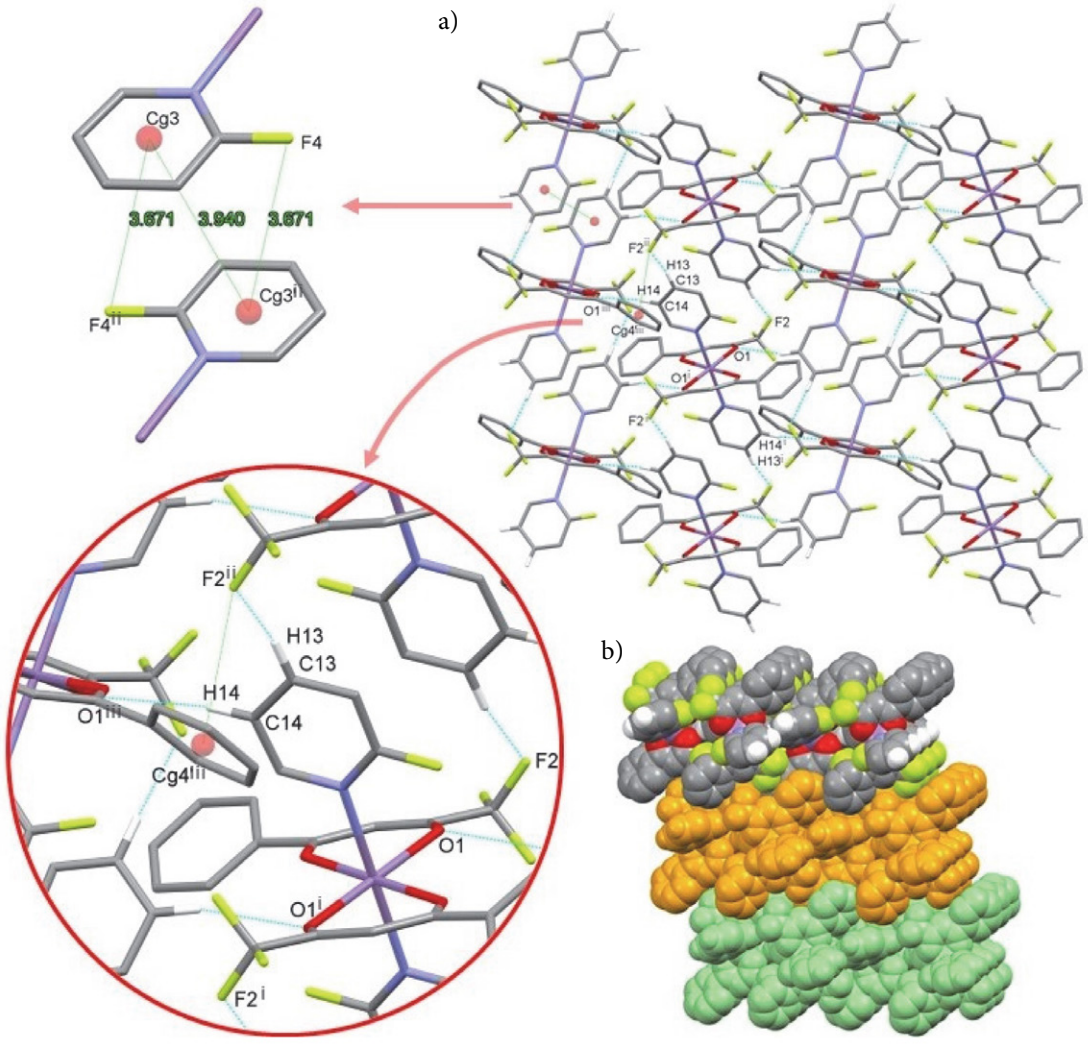


Figure 7. a) Hydrogen-bonded layer along the *ac* plane in **3** is formed by C13–H13···O1^{iii} and centrosymmetric C14–H14···F2^{ii} interactions as well as centrosymmetric π···π interactions and C–F···π interactions; **b)** packing of layers (arbitrary colors). Blue and green dashed lines indicate hydrogen bonds and π···π and C–F···π interactions, respectively. For the sake of clarity, H atoms not involved in the motif shown have been omitted. For symmetry codes see Table 3.

Table 5. Selected bond distances and angles for **3**.

Distance	**(Å)**		
Mn1–N1	2.3425(17)	Mn1–O1	2.1415(14)
Mn1–O2	2.1337(14)		
Angle	**(°)**		
N1–Mn1–O1	94.36(6)	N1–Mn1–O1^{i}	85.64(6)
N1–Mn1–O2	88.31(6)	N1–Mn1–O2^{i}	91.69(6)
O1–Mn1–O2	85.12(5)	O1–Mn1–O2^{i}	94.88(5)

Symmetry code: (i) –*x*, –*y*, –*z*.

cules **2** and **3** is presented in Fig. 8. Pyon and hpyon ligands are inclined toward the tfpb moiety by 78.60(5)° (molecule A in **1**), 44.51(5)° (molecule B in **1**) and 43.25(6)° (**2**) representing a substantial deviation from 90°. However, in the case of molecule B in **1** and molecule **2** also the phenyl rings of tfpb are evidently inclined toward pyridone moieties.

Compound **4** crystallizes in the triclinic *P*–1 space group. Selected bond distances and angles of **4** are summarized in Table 6. The asymmetric unit contains one complex molecule with *cis*-octahedral arrangement of methanol ligands on the manganese(II) central atom (Fig. 9). Two methanol ligands are bonded to the metal center with Mn1–O5 and Mn1–O6 distances of 2.1714(18) and 2.173(2) Å, respectively, and O5–Mn1–O6 angle of 88.54(8)°. The Mn1–O bond lengths with four oxygen atoms of the two chelating tfpb ligands are asymmetric with the longer ones of 2.1821(18) and 2.1751(17) Å at the trifluoromethyl substituent and the shorter ones of 2.1266(18) and 2.1315(18) Å at the phenyl substituent. The Mn(tfpb) fragments deviate from planarity, the tfpb ligands being in-

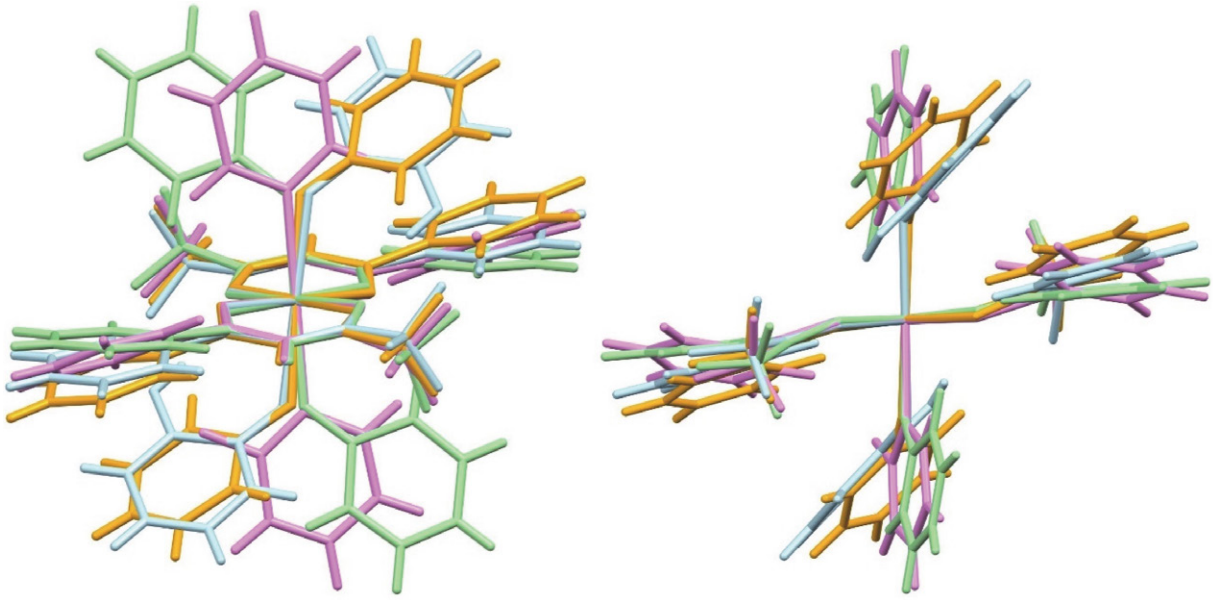


Figure 8. Two views on superposition of crystallographically independent molecules A (green) and B (orange) in **1**, **2** (blue) and **3** (violet). Disorder on CF_3 groups has been omitted for clarity.

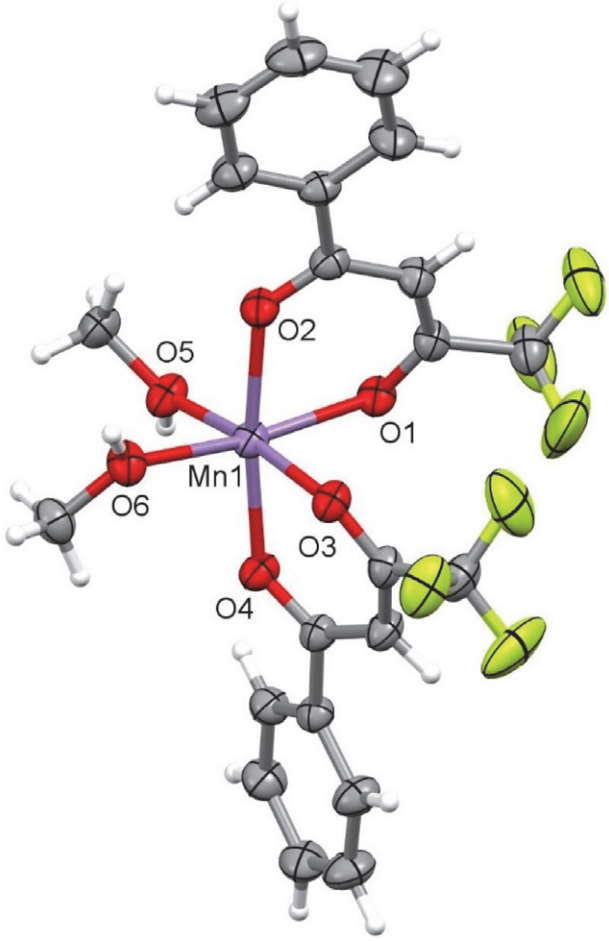


Figure 9. Structure of **4**. Disorder on both CF_3 groups has been omitted for clarity. Displacement ellipsoids are drawn at 30% probability level.

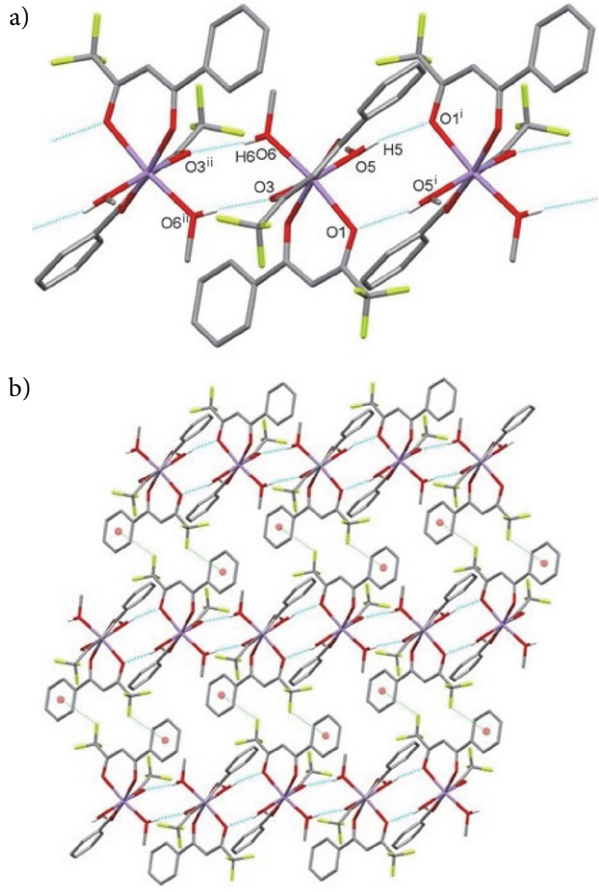


Figure 10. a) Hydrogen-bonded chain along *b* axis in **4** formed by centrosymmetric O5–H5···O1^{i} and O6–H6···O3^{ii} interactions; **b)** chains are linked into a layer through C–F···π interactions. Blue and green dashed lines indicate hydrogen bonds and C–F···π interactions, respectively. For the sake of clarity, H atoms not involved in the motif shown have been omitted. For symmetry codes see Table 3.

clined by 25.94(8) and 23.51(8)°. Each methanol ligand is involved in a centrosymmetric hydrogen-bonded motif *via* O5–H5···O1^{i} and O6–H6···O3^{ii} interactions with the carbonyl oxygen atom at the trifluoromethyl substituent of the adjacent complex. Both centrosymmetric hydrogen bonds have the graph-set motif $R^2_2(8)$ (Fig. 10 and Table 3) and enable the formation of a hydrogen-bonded chain along the *b* axis. A centrosymmetric C1–F3···π interaction between CF_3 group and the benzene ring of tfpb ligand of the adjacent molecule is present with *d*(F3···*Cg*3) = 3.661(4) Å and <(C1–F3···*Cg*3) = 121.9(3)°, where *Cg*3 is C5–C10 ring centroid, connecting chains into a layer along the *bc* plane (Fig. 10). There are no significant π···π interactions.

Table 6. Selected bond distances and angles for **4**.

Distance	**(Å)**		
Mn1–O1	2.1821(18)	Mn1–O2	2.1266(18)
Mn1–O3	2.1751(17)	Mn1–O4	2.1315(18)
Mn1–O5	2.1714(18)	Mn1–O6	2.173(2)
Angle	**(°)**		
O1–Mn1–O2	82.45(7)	O1–Mn1–O3	89.13(7)
O1–Mn1–O4	91.80(7)	O1–Mn1–O5	92.79(7)
O1–Mn1–O6	171.30(7)	O2–Mn1–O3	92.40(7)
O2–Mn1–O4	172.98(7)	O2–Mn1–O5	94.84(8)
O2–Mn1–O6	88.87(7)	O3–Mn1–O4	83.46(7)
O3–Mn1–O5	172.69(7)	O3–Mn1–O6	90.62(7)
O4–Mn1–O5	89.43(7)	O4–Mn1–O6	96.81(8)
O5–Mn1–O6	88.54(8)		

4. Conclusion

We have prepared and structurally characterized four manganese(II) bis(4,4,4-trifluoro-1-phenylbutane-1,3-dionate) complexes with pyon, hpyon, pyF and methanol ligands. In all prepared compounds the coordination of the metal center is octahedral. Complexes **1–3** possess *trans* arrangement of ligands while in complex **4** the arrangement is *cis*. In **1–3** the $Mn(tfpb)_2$ fragments deviate from planarity, the angles between the mean planes formed by the equatorial MnO_4 cores and that of the tfpb chelate C_3O_2 moieties being in the range 14.48(6)–18.00(7)°. In **1** and **2** the axial positions are occupied by two pyon and hpyon ligands, respectively, bonded to the metal center through the O atom. Pyon and hpyon ligands are inclined toward the tfpb moiety by 78.60(5)° (molecule A in **1**), 44.51(5)° (molecule B in **1**) and 43.25(6)° (**2**) representing a substantial deviation from 90°. Extended hydrogen bonding is present in **1** and **2** facilitating the formation of a three-dimensional supramolecular structure in **1** and a layered structure in **2** through N–H···O hydrogen bonding enhanced by C–H···O interactions as well as C–F···π interactions. In **3** pyF ligand plays the main role in the formation of crystal aggregation due to the absence of the competing strong hydrogen bond donors. A layered structure is formed through C–H···O and C–H···F interactions as well as π···π and C–F···π interactions. In **4** a layered structure is formed through a combination of O–H···O and C–F···π interactions.

Supplementary Material

CCDC 2024368–2024371 (**1**–**4**) contain the supplementary crystallographic data for this paper. These data can be obtained free of charge from The Cambridge Crystallographic Data Centre via www.ccdc.cam.ac.uk/data_request/cif.

Acknowledgment

Financial support from the Slovenian Research Agency through the grant P1–0230–0175 is gratefully acknowledged. We thank EN–FIST Centre of Excellence, Dunajska cesta 156, 1000 Ljubljana, Slovenia for using the Supernova diffractometer.

5. References

1. C. B. Aakeröy, N. R. Champness, C. Janiak, *CrystEngComm* **2010**, *12*, 22–43. **DOI:**10.1039/B919819A
2. M. G. Goesten, F. Kapteijn, J. Gascon, *CrystEngComm* **2013**, *15*, 9249–9257. **DOI:**10.1039/c3ce41241e
3. (a) J. Liu, L. Chen, H. Cui, J. Zhang, L. Zhang, C.-Y. Su, *Chem. Soc. Rev.* **2014**, *43*, 6011–6061; **DOI:**10.1039/C4CS00094C
(b) A. Dhakshinamoorthy, H. Garcia, *Chem. Soc. Rev.* **2014**, *43*, 5750–5765; **DOI:**10.1039/C3CS60442J
(c) A. Herbst, C. Janiak, *CrystEngComm* **2017**, *19*, 4092–4117; **DOI:**10.1039/C6CE01782G
(d) M. D. Allendorf, V. Stavila, *CrystEngComm* **2014**, *17*, 229–246; **DOI:**10.1039/C4CE01693A
(e) T. Stolar, K. Užarević, *CrystEngComm* **2020**, *22*, 4511–4525; **DOI:**10.1039/D0CE00091D
(f) A. Dhakshinamoorthy, A. M. Asiri, H. García, *Angew. Chem. Int. Ed.* **2016**, *55*, 5414–5445; **DOI:**10.1002/anie.201505581
(g) Z. Ajoyan, P. Marino, A. J. Howarth, *CrystEngComm* **2018**, *20*, 5899–5912; **DOI:**10.1039/C8CE01002A
(h) H. Li, K. Wang, Y. Sun, C. T. Lollar, J. Li, H.-C. Zhou, *Mater. Today* **2018**, *21*, 108–121; **DOI:**10.1016/j.mattod.2017.07.006
(i) A. J. Howarth, Y. Liu, J. T. Hupp, O. K. Farha, *CrystEngComm* **2015**, *17*, 7245–7253; **DOI:**10.1039/C5CE01428J
(j) P. A. Kobielska, A. J. Howarth, O. K. Farha, S. Nayak, *Coord. Chem. Rev.* **2018**, *358*, 92–107; **DOI:**10.1016/j.ccr.2017.12.010
(k) M. M. Sadiq, K. Suzuki, M. R. Hill, *Chem. Commun.*, **2018**, *54*, 2825–2837. **DOI:**10.1039/C8CC00331A
4. (a) T. Koleša-Dobravc, A. Meden, F. Perdih, *Acta Chim. Slov.* **2015**, **62**, 261–271; **DOI:**10.17344/acsi.2014.1041

(b) F. Perdih, *Acta Crystallogr.* **2012**, *C68*, m64–m68; **DOI:**10.1107/S0108270112004386
(c) F. Perdih, *J. Coord. Chem.* **2012**, **65**, 1580–1591; **DOI:**10.1080/00958972.2012.676168
(d) F. Perdih, *Struct. Chem.* **2014**, *25*, 809–819; **DOI:**10.1007/s11224-013-0344-8
(e) F. Perdih, *Monatshefte Chem.* **2012**, *143*, 1011–1017; **DOI:**10.1007/s00706-012-0760-2
(f) T. Koleša-Dobravc, A. Meden, F. Perdih, *New J. Chem.* **2015**, *39*, 4265–4277; **DOI:**10.1039/C5NJ00164A
(g) T. Koleša-Dobravc, A. Meden, F. Perdih, *Monatshefte Chem.* **2014**, *145*, 1263–1275; **DOI:**10.1007/s00706-014-1215-8
(h) L. Bejaoui, J. Rohlíček, V. Eigner, A. Ismail, M. E. Bour, R. B. Hassen, *Acta Chim. Slov.* **2019**, *66*, 603–613; **DOI:**10.17344/acsi.2019.5002
(i) R. Vafazadeh, Z. Mansouri, A. C. Willis, *Acta Chim. Slov.* **2020**, *67*, 516–521; **DOI:**10.17344/acsi.2019.5539
(j) R. Vafazadeh, A. Kazemi-nasab, A. C. Willis, *Acta Chim. Slov.* **2019**, *66*, 1010–1018. **DOI:**10.17344/acsi.2019.5333

5. (a) E. W. Berg, J. T. Truemper, *J. Phys. Chem.* **1960**, *64*, 487–490; **DOI:**10.1021/j100833a029
(b) G. S. Shephard, D. A. Thornton, *J. Mol. Struct.* **1976**, *34*, 83–91; **DOI:**10.1016/0022-2860(76)80082-8
(c) M. A. Al-Anber, H. Daoud, *Orient. J. Chem.* **2013**, *29*, 905–909. **DOI:**10.13005/ojc/290307
6. Z. Otwinowski, W. Minor, *Methods Enzymol.* **1997**, 276, 307–326. **DOI:**10.1016/S0076-6879(97)76066-X
7. Rigaku Oxford Diffraction, *CrysAlis PRO*, Rigaku Corporation, Tokyo, Japan, 2015.
8. G. M. Sheldrick, *Acta Crystallogr.* **2015**, *C71*, 3–8.
9. A. Altomare, M. C. Burla, M. Camalli, G. L. Cascarano, C. Giacovazzo, A. Guagliardi, A. G. G. Moliterni, G. Polidori, R. Spagna, *J. Appl. Crystallogr.* 1999, **32**, 115–119. **DOI:**10.1107/S0021889898007717
10. (a) M. H. Dickman, *Acta Crystallogr.* **1999**, *C55*, IUC9900146. **DOI:**10.1107/S0108270199098558
(b) D. A. Souza, A. S. Florencio, J. W. de M. Carneiro, S. S. Soriano, C. B. Pinheiro, M. A. Novak, M. G. F. Vaz, *Inorg. Chim. Acta* **2008**, *361*, 4024–4030; **DOI:**10.1016/j.ica.2008.03.043
(c) C. Benelli, A. Caneschi, D. Gatteschi, M. C. Melandri, P. Rey, *Inorg. Chim. Acta* **1990**, *172*, 137–139. **DOI:**10.1016/S0020-1693(00)80847-6
11. J. Bernstein, R. E. Davis, L. Shimoni, N.-L. Chang, *Angew. Chem. Int. Ed. Engl.* **1995**, *34*, 1555–1573. **DOI:**10.1002/anie.199515551
12. A. Tyl, M. Nowak, J. Kusz, *Acta Crystallogr.* **2008**, *C64*, o661–o664. **DOI:**10.1107/S0108270108033660
13. V. M. Deflon, K. E. Bessler, M. Kretschmar, U. Abram, *Z. Anorg. Allg. Chem.* **2000**, *626*, 1545–1549.
14. C. R. Groom, I. J. Bruno, M. P. Lightfoot, S. C. Ward, *Acta Crystallogr.* **2016**, *B72*, 171–179. **DOI:**10.1107/S2052520616003954
15. See, for example: (a) K. D. Hughey, N. C. Harms, K. R. O'Neal, A. J. Clune, J. C. Monroe, A. L. Blockmon, C. P. Landee, Z. Liu, M. Ozerov, J. L. Musfeldt, *Inorg. Chem.* 2020, *59*, 2127–2135; **DOI:**10.1021/acs.inorgchem.9b02394
(b) R. B. P. Pesci, E. J. de Souza, E. Niquet, O. R. Nascimento, R. B. Viana, V. M. Deflon, *J. Mol. Struct.* **2019**, *1194*, 104–111; **DOI:**10.1016/j.molstruc.2019.05.041
(c) F. A. Mautner, C. Berger, C. Gspan, B. Sudy, R. C. Fischer, S. S. Massoud, *Polyhedron* **2017**, *130*, 136–144; **DOI:**10.1016/j.poly.2017.04.012
(d) L.-F. Wang, J.-Z. Qiu, Y.-C. Chen, J.-L. Liu, Q.-W. Li, J.-H. Jia, M.-L. Tong, *Inorg. Chem. Front.* **2017**, *4*, 1311–1318; **DOI:**10.1039/C7QI00221A
(e) B. Zhou, D. Yan, *Angew. Chem. Int. Ed.* **2019**, *58*, 15128–15135. **DOI:**10.1002/anie.201909760
16. See, for example: (a) T. R. Hayes, P. A. Lyon, C. L. Barnes, S. Trabue, P. D. Benny, *Inorg. Chem.* **2015**, *54*, 1528–1534; **DOI:**10.1021/ic502520x
(b) D. Septiadi, A. Aliprandi, M. Mauro, L. D. Cola, *RSC Adv.* **2014**, *4*, 25709–25718. **DOI:**10.1039/C4RA02351J
17. (a) N. Uzun, A. T. Çolak, F. M. Emen, G. Kismali, O. Meral, M. Alpay, G. K. Çılgı, E. Şahin, *J. Coord. Chem.* **2015**, *68*, 949–967; **DOI:**10.1080/00958972.2014.1003371
(b) H. M. Kieler, M. J. Bierman, I. A. Guzei, P. J. Liska, R. W. McGaff, *Chem. Commun.* **2006**, 3326–3328. **DOI:**10.1039/B606537F
18. (a) R. G. Pearson, *J. Am. Chem. Soc.* **1963**, *85*, 3533–3539; **DOI:**10.1021/ja00905a001
(b) R. G. Parr, R. G. Pearson, *J. Am. Chem. Soc.* **1983**, *105*, 7512–7516. **DOI:**10.1021/ja00364a005
19. (a) K. Kumar, S. Chorazy, K. Nakabayashi, H. Sato, B. Sieklucka, S. Ohkoshi, *J. Mater. Chem. C* **2018**, *6*, 8372–8384; **DOI:**10.1039/C8TC01305E
(b) K. Kumar, D. Abe, K. Komori-Orisaku, O. Stefańczyk, K. Nakabayashi, J. R. Shakirova, S. P. Tunik, S. Ohkoshi, *RSC Adv.* **2019**, *9*, 23444–23449; **DOI:**10.1039/C9RA03276B
(c) S. Chorazy, J. Wang, S. Ohkoshi, *Chem. Commun.* **2016**, *52*, 10795–10798. **DOI:**10.1039/C6CC05337H
20. F. Perdih, *Acta Crystallogr.* **2017**, *C73*, 960–967.
21. S. Petriček, *Polyhedron* **2019**, *167*, 11–25. **DOI:**10.1016/j.poly.2019.03.050
22. A. A. Dar, S. Sen, S. K. Gupta, G. N. Patwari, R. Murugavel, *Inorg. Chem.* **2015**, *54*, 9458–9469. **DOI:**10.1021/acs.inorgchem.5b01308
23. J. M. Rawson, R. E. P. Winpenny, *Coord. Chem. Rev.* **1995**, *139*, 313–374. **DOI:**10.1016/0010-8545(94)01117-T
24. S. Petriček, *Molecules*, **2020**, *25*, 846. **DOI:**10.3390/molecules25040846
25. (a) T. Koleša-Dobravc, K. Maejima, Y. Yoshikawa, A. Meden, H. Yasui, F. Perdih, *New J Chem* **2017**, *41*, 735–746; **DOI:**10.1039/C6NJ02961B
(b) T. Koleša-Dobravc, K. Maejima, Y. Yoshikawa, A. Meden, H. Yasui, F. Perdih, *New J. Chem.* **2018**, *42*, 3619–3632. **DOI:**10.1039/C7NJ04189F

Povzetek

Sintetizirali smo manganove(II) bis(4,4,4-trifluoro-1-fenilbutan-1,3-dionato) komplekse s piridin-4-onom (pyon), 3-hidroksipiridin-2-onom (hpyon), 1-fluoropiridinom (pyF) in metanolom ter določili strukture z monokristalno rentgensko difrakcijo. V vseh kompleksih je koordinacija kovinskega centra oktaedrična. Pri spojinah $[Mn(tfpb)_2(pyon)_2]$ (**1**) in $[Mn(tfpb)_2(hpyon)_2]$ (**2**) so prisotne številne vodikove vezi, ki omogočajo tvorbo tridimenzionalne supramolekularne strukture v **1** in plastovite strukture v **2** z N–H···O vodikovimi vezmi ojačane z C–H···O interakcijami ter tudi C–F···π interakcije. Pri $[Mn(tfpb)_2(pyF)_2]$ (**3**) je prisotna plastovita struktura z C–H···O in C–H···F interakcijami ter tudi z π···π in C–F···π interakcijami. Pri $[Mn(tfpb)_2(MeOH)_2]$ (**4**) je prisotna plastovita struktura s kombinacijo O–H···O in C–F···π interakcij.

Except when otherwise noted, articles in this journal are published under the terms and conditions of the Creative Commons Attribution 4.0 International License

Scientific paper

CO_2 Improved Synthesis of Benzimidazole with the Catalysis of a New Calcium 4-Amino-3-hydroxybenzoate

Ruo-Xuan Gao, Yuan-Yuan Gao, Ning Zhu and Li-Min Han*

Chemical Engineering College, Inner Mongolia University of Technology, Hohhot, 010010, China

** Corresponding author: E-mail: hanlimin@imut.edu.cn*

Received: 09-02-2020

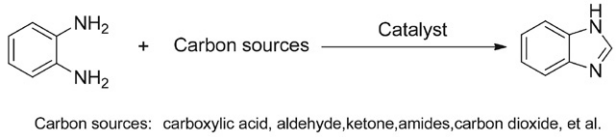
Abstract

In this paper, we explored the synthesis of benzimidazole by the reaction of DMF and *o*-phenylenediamine. In the process of catalyst screening, we found that 4-amino-3-hydroxybenzoic acid, benzoic acid, and benzene-1,3,5-tricarboxylic acid could catalyze the reaction. Moreover, the calcium 4-amino-3-hydroxybenzoate and CO_2 could more effectively catalyze the reaction, the synergistic effect of CO_2 and 4-amino-3-hydroxybenzoic acid calcium salt can increase the yield of benzimidazole from 28% to 94%.

Keywords: Calcium 4-amino-3-hydroxybenzoate, CO_2, benzimidazole, weak acid catalysis

1. Introduction

Benzimidazole and its derivatives are fundamental building blocks in many kinds of functional compounds, especially in drugs and bioactive molecules,[1–4] and widely used in anti-cancer,[5] anti-inflammatory,[6] anti-bacterial,[7] anti-oxidant,[8] anti-coagulant[9] and so on.[10] Therefore, it is of great significance to find a simple, economic and environmentally friendly method for the synthesis of benzimidazoles. Up to now, cycloaddition reaction of *o*-phenylenediamine and carbon source molecule seems to be an effective method for the synthesis of benzimidazoles. The carbon source generally involves a carboxylic acid,[9,11] aldehyde,[1,3,10] ketone,[12] amide,[11,13,14] and carbon dioxide[2,15,16] (Scheme 1). As a special amide, *N*,*N*-dimethylformamide (DMF) is not only a carbon source but also an effective polar solvent for the synthesis of benzimidazoles.[11,14,15,17,18]



Scheme 1. Carbon sources in the synthesis of benzimidazoles with *o*-phenylenediamine.

Catalysts, such as inorganic acids,[19] organic acids,[10] alkalis,[18] Lewis acids,[20] transition metals salts,[21] organometallic complexes,[22] play an important role in the synthesis of benzimidazoles. Hydrochloric acid is usually used in the synthesis of benzimidazoles, but it is corrosive and impossible to be reused.[19] Then many catalysts had been prepared for this reaction, for instance, azole-anion-based aprotic ionic liquids with tetrabutylphosphonium hydroxide,[23] ionic liquids of hydrochloric acid,[24] glyoxylic acid,[10] $B(C_6F_5)_3$[16] and zinc acetate dehydrate.[11] But they are usually used in combination with reducing substances such as hydrosilane, hydrogen, boron phosphorus and transition metal salts. In short, their application is undesirable under the green chemistry principles. It is of paramount importance to find an effective and pollution-free catalyst for the synthesis of benzimidazoles.

Recently, Ru,[25] Mn,[26] Co,[27,32] Cu,[28] Zr,[29] Fe[30] and Ir[31] organometallic complexes have been used to catalyze the synthesis of benzimidazoles, and the recycle times of catalysts were increased obviously. That provided a new idea for designing catalysts to catalyze the synthesis of benzimidazoles. When we investigated the catalytic mechanism of these organometallic salts, it was found that the main catalytic species was still hydrogen cation (*i.e.* proton).[15,24] Hence, we planned to consider catalytic effects of several acids or salts especially 4-amino-3-hydroxybenzoic acid

and its calcium salt on the synthesis of the benzimidazole and the results obtained are described in this paper.

2. Experimental

2. 1. Chemicals

All of the reagents were purchased from commercial sources and used without further purification. Benzene-1,3,5-tricarboxylic acid, 4-amino-3-hydroxybenzoic acid, *o*-aminophenol, calcium benzoate, *N*,*N*-dimethylformamide and *o*-phenylenediamine were purchased from Shanghai Aladdin Biological Technology Co., Ltd. (Shanghai, China). $Ca(NO_3)_2{\cdot}4H_2O$, phenol and benzoic acid were purchased from Sinopharm Chemical Regagent Co., Ltd. (Shanghai, China). Calcium benzene-1,3,5-tricarboxylate was synthesized according to the method in the literature.[32]

2. 2. Apparatus

FT-IR spectra were measured on a Perkin–Elmer FT-IR spectrum. Fluorescence spectra were obtained by an Agilent Technologies Cary Fluorescence Spectrophotometer analyzer. NMR spectra in DMSO-d_6 were recorded with an Agilent 500 MHz DD2 spectrometer. The molecular structure of calcium 4-amino-3-hydroxybenzoate was obtained on a Bruker D8 VENTURE diffractometer. X-ray powder diffraction (XRD) spectra were recorded on a Rigaku (SmartLab 9KW) diffractometer for a Cu-target tube.

2. 3. Preparation of Calcium 4-Amino-3-hydroxybenzoate

4-Amino-3-hydroxybenzoic acid (91.8 mg, 0.6 mmol) and $Ca(NO_3)_2$ $4H_2O$ (141.7 mg, 0.6 mmol) were dissolved in MeOH (15 mL) in a flask, then the reaction mixture was stirred and refluxed for 3 hours. The resulting solution was cooled to room temperature and filtered. The filtrate was allowed to stand at room temperature for slow evaporation. IR: 3377.96 (m, γ_{O-H}), 3307.00 (m, γ_{N-H}), 1609.45 (m, δ_{N-H}), 1532.81 (vs, γ_{as} COO), 1413.58 (vs, γ_{as} COO), 1223.39 (s, δ_{C-O}), 1024.68 (m, γ_{C-N}).

2. 4. Structure Determination

Single-crystal X-ray diffraction measurements were carried out on a Bruker D8 VENTURE diffractometer. The diffraction data were collected with MoKα radiation (λ = 0.71073 Å). The structures were solved by direct methods and refined against F^2 by full-matrix least-squares methods with SHELXTL-2014.[33] All non-hydrogen atoms were refined with anisotropic thermal parameters. The hydrogen atoms were set in calculated positions and refined as riding atoms with a common fixed isotropic thermal parameter. Crystal data and details of the data collection and the structure refinements are given in Table S1.

2. 5. The Synthesis of Benzimidazole

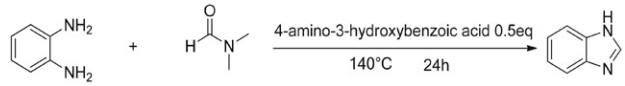
o-Phenylenediamine (108.1 mg, 1 mmol) was catalyzed by calcium 4-amino-3-hydroxybenzoate (0.25 eq) with CO_2 (3 bar) and DMF (2 mL) in a high-pressure reactor. Most of the *o*-phenylenediamine was consumed completely after the reaction mixture was stirred at 140 °C for 24 h. Then the reaction mixture was extracted with ethyl acetate, and the crude product (110.8 mg, 94%) was purified by column chromatography through a silica-gel column to afford the desired products eluted by CH_3OH and CH_2Cl_2. Anal. Calcd. (%) for $C_7H_4N_2$: C, 71.10; H, 5.12; N, 23.71. Found (%): C, 70.76; H, 5.51; N, 23.29. ^{1}H NMR (500 MHz, DMSO-d_6, 25 °C, TMS) δ 12.43 (s, 1H), 8.20 (s, 1H), 7.62–7.55 (m, 2H), 7.19 (dt, J_1 = 6.0 Hz, J_2 = 3.4 Hz, 2H). ^{13}C NMR (500 MHz, DMSO-d_6, 25 °C, TMS): δ 141.78, 121.56. IR: 3064.18 (m, γ_{C-H}), 1592.49 (s, γ_{C-N}), 1555.05 (w, γ_{C-N}), 1480.17 (s, γ_{C-N}), 1203.69 (m, γ_{C-H}), 742.89 (m, δ_{N-H}). ESI-MS (CH_3OH, *m/z*): 119.05 (M^+). UV-Vis (CH_3OH): 243, 278.

3. Results and Discussion

Initially, the 4-amino-3-hydroxybenzoic acid-catalyzed cycloaddition reaction of *o*-phenylenediamine and DMF was investigated. The equivalents of the catalyst used, reaction temperatures and yields are listed in Table 1.

As shown in Table 1, the reaction temperature (Table 1, entries 1–5) and the equivalent of 4-amino-3-hydroxybenzoic acid used (Table 1, entries 5–9) could significantly influnce the reaction yield. The benzimidazole could be obtained in 84% yield after 24 hours of reaction at 140 °C when the equivalent of 4-amino-3-hydroxybenzoic acid was 0.5 (Table 1, entry 5).

Table 1. The cyclization of *o*-phenylenediamine and DMF catalyzed by 4-amino-3-hydroxybenzoic acid

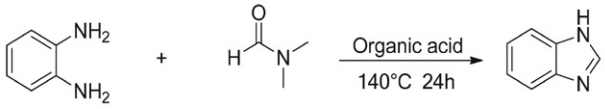


Entry	Cats [equiv.]	*T* [°C]	Yield [%]
1	0.5	100	26
2	0.5	110	40
3	0.5	120	57
4	0.5	130	71
5	0.5	140	84
6	0.25	140	67
7	0.125	140	37
8	0.05	140	15
9	0	140	–

reaction condition: *o*-phenylenediamine (1 mmol), DMF (2 mL), reaction time 24 h, isolated yield

With the optimized reaction conditions, the catalytic performance of different weak organic acids was investigated (Table 2).

Table 2. The cyclization of *o*-phenylenediamine and DMF catalyzed by an organic acid



Entry	Catalyst	Cats [equiv.]	Yield [%]
1	phenol	0.5	trace
2	*o*-aminophenol	0.5	trace
3	benzoic acid	0.5	85
4	4-amino-3-hydroxybenzoic acid	0.5	84
5	benzene-1,3,5-tricarboxylic acid	0.167	95

reaction condition: *o*-phenylenediamine (1 mmol), DMF (2 mL), 24 h at 140 °C, isolated yield

As shown in Table 2, the yield of benzimidazole increased with the increasing of acidity of the catalyst. The phenol (pK_a ≈ 9.99) and *o*-aminophenol (pK_a ≈ 9.28) could not effectively catalyze the synthesis of benzimidazole. The benzoic acid (pK_a ≈ 4.20), benzene-1,3,5-tricarboxylic acid (pK_a ≈ 2.12) and 4-amino-3-hydroxybenzoic acid (pK_a ≈ 4.74) could effectively catalyze the synthesis of benzimidazole.[34] It is further proved that the catalytic species is proton.[15,24] But when the reactions (presented in Tables 1 and 2) were performed, it was difficult to perform effective separation and recovery of the catalyst. Therefore, instead of the acids metal salts were used to catalyze this reaction.

First, calcium 4-amino-3-hydroxybenzoate was prepared, its single crystal structure was determined by X-ray crystallography at 0 °C, showing that it crystallized in the monoclinic space group *C*2/*c* and showed an irregular dodecahedron. The molecular structure and coordination polyhedron of calcium 4-amino-3-hydroxybenzoate are shown in Figure 1. The calcium is in the center of eight oxygen atoms, four of them are from two polycarboxylic

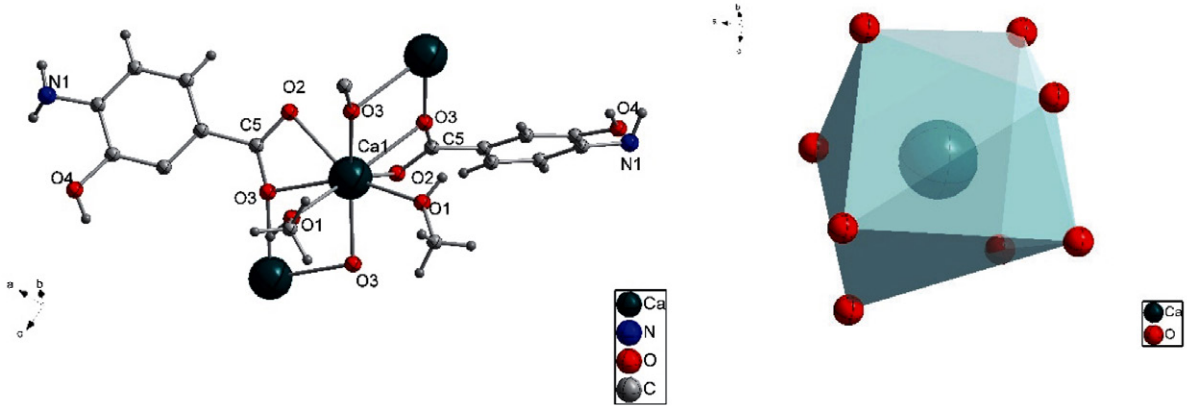


Figure 1. The molecular structure (left) and coordination polyhedron (right) of calcium 4-amino-3-hydroxybenzoate.

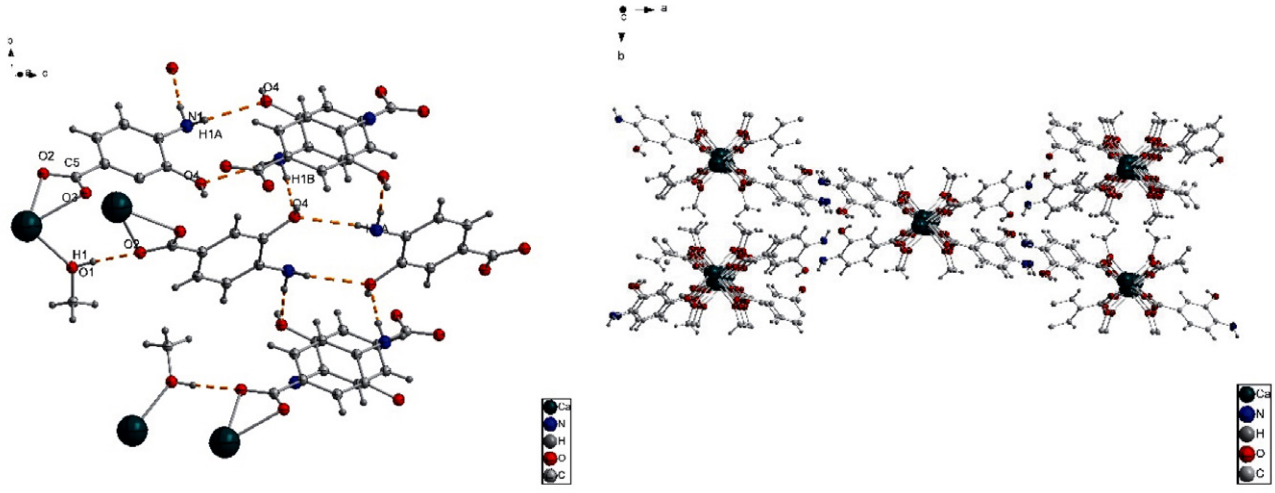


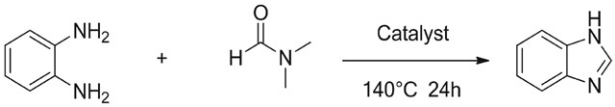
Figure 2. Structure of the calcium 4-amino-3-hydroxybenzoate showing the hydrogen bonding interactions (left) and packing diagram (right).

groups, two of them are from CH_3OH, and two of them are from two polycarboxylic groups coordinated with other calcium atoms. The bond length of Ca–O is in the range of 2.384–2.517 Å, and there is a little difference in the distance between calcium atoms and eight oxygen atoms. The result of crystal structure analysis is consistent with the FT-IR spectrum (Figure S3).

There are two kinds of hydrogen bonds in the structure of calcium 4-amino-3-hydroxybenzoate, shown in Figure 2 and Table S3. O(1)–H(1)···O(2) formed between the hydrogen atom on the methanol hydroxyl group coordinated with calcium ion and the oxygen atom on the carboxylic acid coordinated with the adjacent calcium ion. The distance between H(1) and acceptor O(2) was 1.92 Å, and the angle between donor and acceptor was 176°. The other more weak interaction N(1)–H(1B)···O(4) formed between the hydrogen atom on the ligand amino group and the oxygen atom on the hydroxyl group of the adjacent ligand. The distance between H(1B) and acceptor O(4) was 1.98 Å, and the angle between donor and acceptor was 167°. Moreover, the structure of the calcium 4-amino-3-hydroxybenzoate had some porous framework features, due to many uncoordinated amino and hydroxyl groups.

The catalytic performance of the calcium 4-amino-3-hydroxybenzoate was tested, and compared with that of calcium benzoate, calcium benzene-1,3,5-tricarboxylate and 4-amino-3-hydroxybenzoic acid (Table 3.).

Table 3. The cyclization of *o*-phenylenediamine and DMF catalyzed by various calcium salts and 4-amino-3-hydroxybenzoic acid



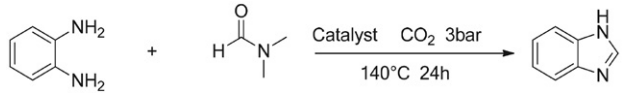
Entry	Catalyst	Cats [equiv.]	Yield [%]
1	calcium benzoate	0.5	10
2	calcium benzene-1,3,5-tricarboxylate	0.167	20
3	calcium 4-amino-3-hydroxybenzoate	0.25	28
4	4-amino-3-hydroxybenzoic acid	0.5	84

reaction condition: *o*-phenylenediamine (1 mmol), DMF (2 mL), 24 h, 140 °C, isolated yield

As shown in Table 3, although the catalyst separation became easier, the calcium salts (*i.e.* calcium benzoate, calcium benzene-1,3,5-tricarboxylate and calcium 4-amino-3-hydroxybenzoate) did not exhibit the desired catalytic activity. Especially, with comparing corresponding carboxylic acid, the three calcium salts of thecarboxylic acids lost their catalytic activity seriously. Through exploration of their molecular structures, it was found that the benzoic acid exists in the crystal cell structure of calcium benzoate (Figure S5). And one of carboxyl groups of benzene-1,3,5-tricarboxylic acid was monodentate and might provide an active hydrogen (Figure S6). In the structure of calcium 4-amino-3-hydroxybenzoate, the active hydrogen might originate from an un-coordinated hydroxyl group. This small amount of the hydrogen in the crystal cell might be the catalytic species.

In order to study the catalysis of weak acids further, CO_2 was introduced into the reaction system of the cyclization of *o*-phenylenediamine and DMF. When we introduced CO_2 at 3 bar into the reaction system (and no catalyst was added), nearly no benzimidazole was obtained (Table 4, entry 1). When the reaction was repeated with the addition of 0.5 equivalent of 4-amino-3-hydroxybenzoic acid, the yield of benzimidazole increased to 93% (Table 4, entry 2), which was higher than the previously obtained 84% (Table 3, entry 4). It was comfirmed that the presence of CO_2 improved the reaction yield. Hence we introduced CO_2 into other catalytic reaction systems of the cyclization of *o*-phenylenediamine and DMF (Table 4, entries 3–5). In calcium benzoate and calcium benzene-1,3,5-tricarboxylate catalytic reaction systems, no obvious improvement effect occurred (Table 4, entries 3 and 4). But in calcium 4-amino-3-hydroxybenzoate catalytic reaction system, the yield of benzimidazole (Table 4, entry 5) was almost the same as that of 4-amino-3-hydroxybenzoic acid catalytic reaction system. CO_2 significantly improved the catalytic activity of calcium 4-amino-3-hydroxybenzoate. However, when the reaction mixture with separated calcium 4-amino-3-hydroxybenzoate catalyst was repeated, it lost its activity (Table 4, entry 6). By comparing the XRD patterns before and after its use (Figure 3), it was found that the structure of calcium 4-amino-3-hydroxybenzoate was destroyed during the reaction and can thus not be used again.

Table 4. The cyclization of *o*-phenylenediamine and DMF catalyzed by the calcium salts in the presence of CO_2



Entry	Catalyst	Cats [equiv.]	Yield [%]
1	no	0	trace
2	4-amino-3-hydroxybenzoic acid	0.5	93
3	calcium benzoate	0.5	12
4	calcium benzene-1,3,5-tricarboxyate	0.167	23
5	calcium 4-amino-3-hydroxybenzoate	0.25	94
6	calcium 4-amino-3-hydroxybenzoate, reused	0.25	32

reaction condition: *o*-phenylenediamine (1 mmol), DMF (2 mL), 24 h, 140 °C, 3 bar CO_2, isolated yield

Although, the calcium 4-amino-3-hydroxybenzoate could not be reused, CO_2 also could significantly improved

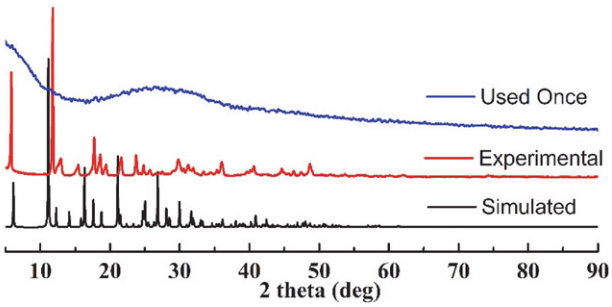
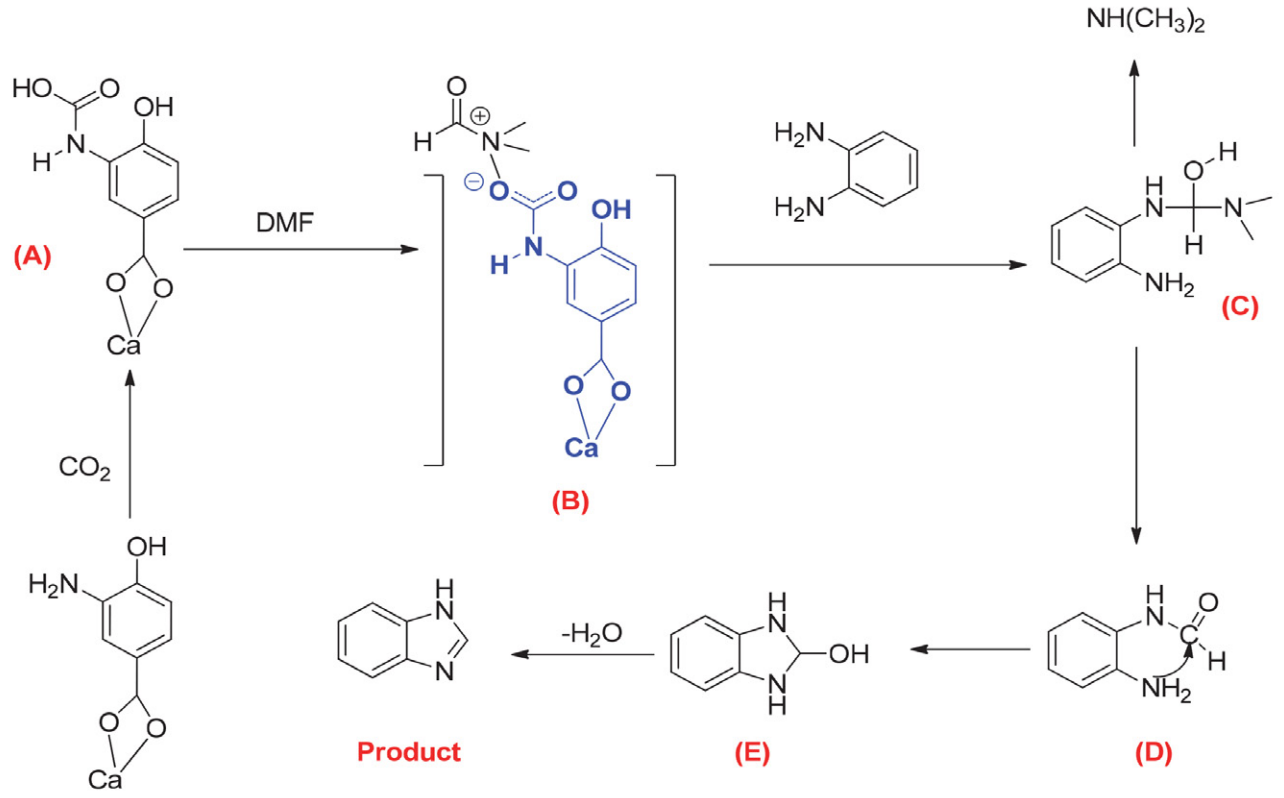


Figure 3. XRD pattern of the simulated and experimental calcium 4-amino-3-hydroxybenzoate and the catalyst used once.

catalytic activity of calcium 4-amino-3-hydroxybenzoate whithout improved catalytic activity of the calcium benzoate and calcium benzene-1,3,5-tricarboxylate. That was still an interesting problem.

4-amino-3-hydroxybenzoate has the above group characteristics. On the basis of the experimental results and previous reports,[14,20,24] a possible mechanism of carbon dioxide-assisted catalytic reaction was proposed (Scheme 2). First, the CO_2 reacted with the un-coordinated amine of calcium 4-amino-3-hydroxybenzoate to form an intermediate A. Then the intermediate A activated DMF to form an intermediate B. The activated DMF reacted with the *o*-phenylenediamine to form an intermediate C, and the rest of the intermediate B returned to the intermediate A and participated in the further activation of DMF. The intermediate C lost a dimethylamine to form an intermediate D. Finally, the intermediate D fromed the product through the intermediate E. Because the intermediate A could not return to the original calcium 4-amino-3-hydroxybenzoate. Hence, the XRD pattern of the used catalyst was no longer the original pattern of calcium 4-amino-3-hydroxybenzoate.



Scheme 2. Possible reaction mechanism.

Why CO_2 could significantly improve catalytic activity of calcium 4-amino-3-hydroxybenzoate? According to the literature, CO_2 easily interacts with amino groups forming carbamate,[35] and many porous MOF materials with amino groups can adsorb CO_2.[36–38] In addition, more studies showed that a mixture of an alcohol and an amine was a good material for CO_2 capture and enrichment.[39,40] The un-coordinated amino and hydroxyl of calcium

4. Conclusions

In this paper, the catalytic performance on the synthesis of the benzimidazole was compared. The catalysts investigated were phenol, *o*-aminophenol, benzoic acid, 4-amino-3-hydroxybenzoic acid and benzene-1,3,5-tricarboxylic acid. We further verified that the proton was the key factor in the catalysis of this reaction. In order to improve the reusability of the catalyst, the catalytic perfor-

mance of calcium benzoate, calcium benzene-1,3,5-tricarboxylate and calcium 4-amino-3-hydroxybenzoate were evaluated, but they did not provide the desired results. When CO_2 was added as weak acid to catalyze this reaction, the yield was very unsatisfactory. But an interesting result was obtained showing that CO_2 could significantly improve the catalytic activity in the presence of calcium 4-amino-3-hydroxybenzoate. The cooperation of carbon dioxide and this salt increased the yield of product from 28% to 94%, and a possible mechanism was proposed to explain why cooperation of carbon dioxide and the salt could improved the catalytic activity.

Acknowledgements

We are grateful to the Program for New Century Excellent Talents in University (NCET-08-858) and the Natural Science Foundation of China (NSFC-21462029).

Supplementary Material

Supplementary (synthesis of the benzimidazole, IR, ^1H and ^{13}C NMR, UV-Vis) data associated with this article can be found, in the online version. Crystallographic data for structures reported in this paper in the form of CIF files have been deposited with the Cambridge Crystallographic Data Centre as supplementary publication CCDC No.2011696. Copy of the data can be obtained free of charge from the Director, CCDC, 12 Union Road, Cambridge CB2 1EZ, UK (Fax: +44-1223-336033; E-mail: deposit@ccdc.cam,ac.uk).

5. References

1. F. P. Roudsari, M. Seddighi, F. Shirini, H. Tajik, *ChemistrySelect* **2019**, *4*, 6382–6389. **DOI:**10.1002/slct.201900806
2. I. H. Biswas, S. Biswas, M. S. Islam, S. Riyajuddin, P. Sarkar, K. Ghosh, S. M. Islam, *New J. Chem.* **2019**, *43*, 14643–14652. **DOI:**10.1039/C9NJ03015H
3. M. Schou, C. Halldin, *J. Labelled Compd. Rad.* **2012,** *55*, 460–462. **DOI:**10.1002/jlcr.2972
4. M. Asif, *Chem. Methodol.* **2019**, *3*, 620–631. **DOI:**10.33945/SAMI/ CHEMM.2019.6.1
5. S. Tahlan, S. Kumar, K. Ramasamy, S. M. Lim, S. A. A. Shah, V. Mani, B. Narasimhan, *BMC Chem.* **2019**, *13*, 1–22. **DOI:**10.1186/s13065-019-0608-5
6. S. N. A. Bukhari, G. Lauro, I. Jantan, C. F. Chee, M. W. Amjad, G. Bifulco, H. Sher, I. Abdullah, N. A. Rahman, *Futuer Med. Chem.* **2016**, *8*, 1953–1967. **DOI:**10.4155/fmc-2016-0062
7. D. Song, S. Ma, *ChemMedChem* **2016,** *11*, 646–659. **DOI:**10.1002/cmdc.201600041
8. H. Bektas, C. Albay, B. B. Sökmen, S. Aydın, E. Menteşe, G. Aydın, D. Şen, *J. Heterocycl. Chem.* **2018**, *55*, 2400–2407. **DOI:**10.1002/jhet.3304
9. P. Singla, V. Luxami, K. Paul, *RSC Adv.* **2014**, *4*, 12422–12440. **DOI:**10.1039/c3ra46304d
10. S. S. Pawar, D. V. Dekhane, M. S. Shingare, S. N. Thore, *Chinese Chem. Lett.* **2008**, *19*, 1055–1058. **DOI:**10.1016/j.cclet.2008.06.028
11. D. B. Nale, B. M. Bhanage, *Synlett* **2015**, *26*, 2835–2842. **DOI:**10.1055/s-0035-1560319
12. K. Aghapoor, F. Mohsenzadeh, H. Sayahi, S. Rastgar, H. R. Darabi, *Environ Chem. Lett.* **2018**, *16*, 1109–1116. **DOI:**10.1007/s10311-018-0733-8
13. P. P. Kattimani, R. R. Kamble, G. Y. Meti, *RSC Adv.* **2015**, *5*, 29447–29455. **DOI:**10.1039/C5RA00021A
14. H. Mostafavi, M. R. Islami, E. Ghonchepour, A. M. Tikdari, *Chem. Pap.* **2018**, *72*, 2973–2978. **DOI:**10.1007/s11696-018-0540-5
15. Z. Ke, B. Yu, H. Wang, J. Xiang, J. Han, Y. Wu, Z. Liu, P. Yang, Z. Liu, *Green Chem.* **2019**, *21*, 1695–1701. **DOI:**10.1039/C9GC00095J
16. Z. Zhang, Q. Sun, C. Xia, W. Sun, *Org. Lett.* **2016**, *18*, 6316–6319. **DOI:**10.1021/acs.orglett.6b03030
17. K. B. Rasal, G. D. Yadav, *Org. Process Res. Dev.* **2016**, *20*, 2067–2073. **DOI:**10.1021/acs.oprd.6b00244
18. B. Yu, H. Zhang, Y. Zhao, S. Chen, J. Xu, L. Hao, Z. Liu, *ACS Catal.* **2013**, *3*, 2076–2082. **DOI:**10.1021/cs400256j
19. A. J. Kadhim, *Orient. J. Chem.* **2018**, *34*, 473–481. **DOI:**10.13005/ojc/340152
20. X. Gao, B. Yu, Q. Mei, Z. Yang, Y. Zhao, H. Zhang, L. Hao, Z. Liu, *New J. Chem.* **2016**, *40*, 8282–8287. **DOI:**10.1039/C6NJ01721E
21. T. Kimura, K. Kamata, N. Mizuno, *Angew Chem. Int. Ed. Engl.* **2012**, *51*, 6700–6703. **DOI:**10.1002/anie.201203189
22. V. Ravi, E. Ramu, K. Vijay, A. S. Rao, *Chem. Pharm. Bull.* **2007**, *55*, 1254–1257. **DOI:**10.1248/cpb.55.1254
23. Y. Zhao, Y. Wu, G. Yuan, L. Hao, X. Gao, Z. Yang, B. Yu, H. Zhang, Z. Liu, *Chem-Asian J.* **2016**, *11*, 2735–2740. **DOI:**10.1002/asia.201600281
24. Z. Gan, Q. Tian, S. Shang, W. Luo, Z. Dai, H. Wang, D. Li, X. Wang, J. Yuan, *Tetrahedron* **2018**, *74*, 7450–7456. **DOI:**10.1016/j.tet.2018.11.014
25. B. Yu, H. Zhang, Y. Zhao, S. Chen, J. Xu, C. Huang, Z. Liu, *Green Chem.* **2013**, *15*, 95–99. **DOI:**10.1039/C2GC36517K
26. K. Das, A. Mondal, D. Srimani, *J. Org. Chem.* **2018**, *83*, 9553–9560. **DOI:**10.1021/acs.joc.8b01316
27. P. Daw, Y. Ben-David, D. Milstein, *ACS Catal.* **2017**, *7*, 7456–7460. **DOI:**10.1021/acscatal.7b02777
28. M. Li, Y. Tang, H. Gao, G. Rao, Z. Mao, *Asian J. Org. Chem.* **2020**, *in press*. **DOI:**10.1002/ajoc.202000236
29. S. Karhale, K. Patil, C. Bhenki, G. Rashinkar, V. Helavi, *Res. Chem. TIntermediat* **2016**, *42*, 7257–7268. **DOI:**10.1007/s11164-016-2534-7
30. K. R. Balinge, V. B. Khajone, A. G. Khiratkar, K. J. Bhansali, S. K. Datir, P. R. Bhagat, *Res. Chem. Intermediat* **2019**, *45*, 155–168. **DOI:**10.1007/s11164-018-3595-6
31. A. K. Sharma, H. Joshi, R. Bhaskar, A. K. Singh, *Dalton Trans.* **2017**, *46*, 2228–2237. **DOI:**10.1039/C6DT04271F
32. M. J. Platers, R. A. Howie, A. J. Roberts, *Chem. Commun.*

1997, 893–894. **DOI:**10.1039/a700675f
33. G. M. Sheldrick, *SHELXS-2014 and SHELXL-2014, Program for Crystal Structure Determination*. University of Göttingen, Göttingen: Germany, **2014**.
34. J. A. Dean, *Lange's Handbook of Chemistry*. McGraw-Hill, Inc.: New York, **1972**; pp 8.24–8.72.
35. R. L. Siegelman, T. M. McDonald, M. I. Gonzalez, J. D. Martell, P. J. Milner, J. A. Mason, A. H. Berger, A. S. Bhown, J. R. Long, *J. Am. Chem. Soc.* **2017**, *139*, 10526–10538. **DOI:**10.1021/jacs.7b05858
36. Y. H. Li, S. L. Wang, Y. C. Su, B. T. Ko, C. Y. Tsaib, C. H. Lin, *Dalton Trans.* **2018**, *47*, 9474–9481. **DOI:**10.1039/C8DT01405A
37. R. Vaidhyanathan, S. S. Iremonger, K. W. Dawson, G. K. H. Shimizu, *Chem. Commun* **2009**, 5230–5232. **DOI:**10.1039/b911481e
38. X. Wang, H. Li, X.-J. Hou, *J. Phys. Chem. C* **2012**, *116*, 19814–19821. **DOI:**10.1021/jp3052938
39. B. Zhao, L. Liu, X. Yang, C. Liu, F. Sha, J. Zhang, *Phys. Chem. Liq.* **2016**, 1–16. **DOI:**10.1080/00319104.2016.1269176
40. L. Zhao, Q. Li, L. Ma, C. Liu, F. Sha, J. Zhang, *J. Mol. Liq.* **2017**, *241*, 374–385. **DOI:**10.1016/j.molliq.2017.05.144

Povzetek

V tem prispevku predstavljamo raziskavo sinteze benzimidazola z reakcijo DMF in *orto*-fenilendiamina. Med preučevanjem učinkovitosti različnih možnosti smo ugotovili, da so 4-amino-3-hidroksibenzojska kislina, benzojska kislina in benzen-1,3,5-trikarboksilna kislina uspešni katalizatorji za to reakcijo. Kalcijev 4-amino-3-hidroksibenzoat se je v prisotnosti CO_2 izkazal kot še posebej učinkovita možnost, saj se je zaradi sinergističnega učinka med CO_2 in kalcijevo soljo 4-amino-3-hidroksibenzojske kisline izkoristek benzimidazola povečal z 28 % na 94 %.

Except when otherwise noted, articles in this journal are published under the terms and conditions of the Creative Commons Attribution 4.0 International License

DOI: 10.17344/acsi.2020.6379 *Acta Chim. Slov.* **2021,** *68,* 212–221
creative commons

Scientific paper

Catecholase-Like Activity and Theoretical Study in Solid State of a New Ru(III)-Schiff Base Complex

Niladri Biswas,[1] Sandeepta Saha,[1,2] Ennio Zangrando,[3] Antonio Frontera[4] and Chirantan Roy Choudhury[1,*]

[1] *Department of Chemistry, West Bengal State University, Barasat, Kolkata-700126, India*

[2] *Sripur High School, Madhyamgram Bazar, Madhyamgram, Kolkata – 700130, India*

[3] *Department of Chemical and Pharmaceutical Sciences, University of Trieste, Via L. Giorgieri 1, 34127 Trieste, Italy*

[4] *Departament de Química, Universitat de les Illes Balears, Crta. De Valldemossa km 7.5, 07122 Palma de Mallorca, Baleares, Spain*

** Corresponding author: E-mail: crchoudhury2000@yahoo.com*
Tel: + 91-9836306502; Fax: +91-33-2524-1577

Received: 09-13-2020

Abstract

A new ruthenium(III) complex of molecular formula $[Ru(PPh_3)Cl_2(L)]$ (1) has been synthesized using the Schiff base ligand obtained from 5-chlorosalicylaldehyde and *N*,*N*-dimethylethylenediamine and characterized by FT-IR, UV-Vis, cyclic voltammetry and single crystal X-ray structural analysis. The metal ion exhibits a slightly distorted octahedral environment where the chelating Schiff base ligand contributes with its NNO donor set. The coordination geometry around the Ru(III) ion is completed by a PPh_3 ligand and two chloride anions, and the charge balance is assured by the phenoxo oxygen of the Schiff base. With the aim to analyse the energy related to the halogen bonding interactions in solid state, a theoretical study has been performed on complex 1, by using the MEP and NCl plot computational tools. Furthermore, complex 1 shows catecholase-like activity in conversion of the model substrate 3,5-di-*tert*-butylcatechol (3,5-DTBC) to the corresponding 3,5-di-*tert*-butylquinone (3,5-DTBQ) under aerobic condition. The parameters regarding the enzymatic kinetics have been evaluated from the Lineweaver-Burk plot using the Michaelis-Menten approach of enzyme catalysis. A significant high T.O.N value (2.346×10^3 h^{-1}) indicates that complex 1 has a very good catalytic efficiency towards 3,5-DTBC.

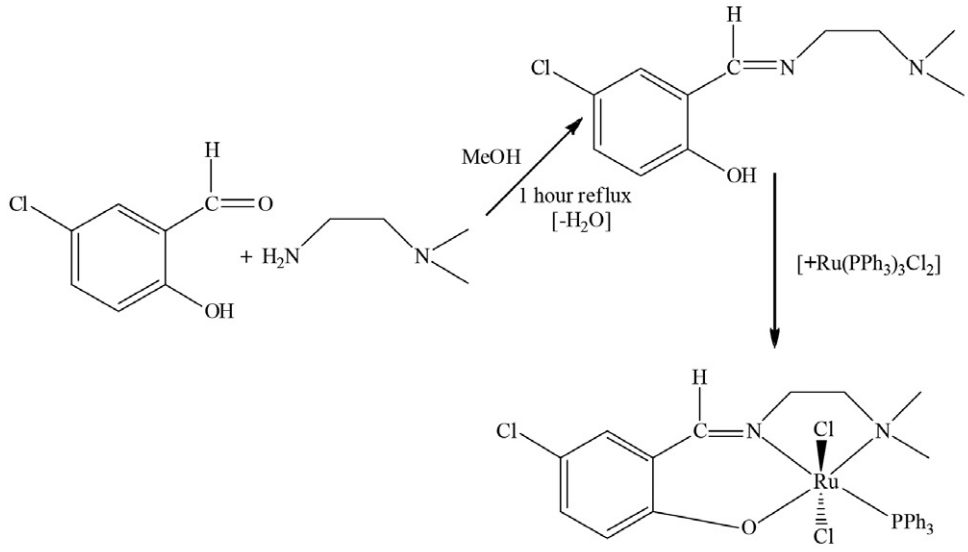
Keywords: Ru-(III) complex · Schiff base · crystal structure · halogen interaction · catecholase-like activity

1. Introduction

In last decade, coordination chemistry of transition metal ions with Schiff bases has evolved as an an area of active research.[1,2] Schiff bases affect electronic factors of the metal centres, stabilizing different oxidation states, address the performance of complexes, which can acquire a variety of suitable properties like that to act as homogeneous and/or heterogeneous catalysts.[3–6] Moreover, design of metal complexes having catalytic activity may be helpful to elucidate the mechanistic aspects of biochemically important metalloenzyme reactions. In fact, structurally simpler and more robust metal complexes can mimic catalytic oxidation of 3,5-di-tert-butylcatechol to quinone, as well as hydrolytic reactions (catecholase and phosphatise activity, respectively).[7] In the last decade a variety of ruthenium complexes, that provide great interest specially for their catalytic activity, has been developed.[8–10]

Ruthenium metal complexes may be also relevant as therapeutic agents and one of these has successfully entered advanced clinical trials.[11] In fact the energy barrier for the oxidation state change from Ru(III) to Ru(II) inside the cell is very low and due to the larger coordination number with respect to platinum-(II), ruthenium-(III/II) can form complexes with a number of elements having different electronegativity as well as chemical hardness.[11–14] Till date, there are plenty of reports on Ru(II/III) compounds with bidentate ligands but design of such complexes with somewhat more rigid, tridentate Schiff bases ligands are rarely found.[15]

Intermolecular interactions, in addition to their structural role, influence the physical and chemical properties of crystalline solids.[16,17] The advancement of these features has been one of the priorities of crystal engineering, a budding interdisciplinary field of research in modern



Scheme 1. Synthesis of the Schiff base ligand (HL) and complex **1**.

chemistry with interest in the rational design of functional molecular solids.[18] Even though hydrogen bonding and coordination bonds still remain at the forefront of crystal engineering strategies, Other interactions have received escalating interest over recent years, markedly, halogen bonds,[19] non-classical hydrogen bonds,[20] π–π interactions,[21] *lp-π* interactions[22] nitroso···nitroso interactions[23] along with halogen···halogen contacts.[20d–f] Intermolecular interactions involving halogen substituents, mostly chlorine, have been observed to favour crystal formation, providing a tool for crystal engineering study.[24]

Keeping this in mind, and taking into account that triphenylphosphine transition metal complexes are very good candidate for catalytic organic transformations, we report here the synthesis (Scheme 1) of a ruthenium(III) complex, $[Ru(PPh_3)Cl_2(L)]$ (**1**), which was characterized by different spectroscopic techniques, cyclic voltammetry. The single crystal X-ray structural analysis revealed interesting crystalline supra-molecular interactions. In addition, the complex has also been evaluated as model system for catecholase-like activity.

2. Experimental Section

2. 1. Materials

All starting chemicals and solvents used in this study were of reagent grade and was used as purchased without further purification. Tris(triphenylphosphine)ruthenium(II) dichloride $[Ru(PPh_3)_3Cl_2]$, 5-chlorosalicylaldehyde, 3,5-di-tert-butylcatechol (3,5-DTBC) and tetrabutylammonium perchlorate (TBAP) were purchased from Sigma-Aldrich, USA and N,N-dimethylethylenediamine from Spectrochem. Spectroscopic grade methanol and dimethyl sulfoxide (DMSO) were obtained from E-Merck, India.

2. 2. Physical Measurements

FT-IR spectrum of complex **1** was measured in the range 400–4000 cm^{-1} in solid KBr pellets by using a Perkin-Elmer SPECTRUM-2 FT-IR spectrophotometer. The UV-Vis spectra were recorded using a Perkin-Elmer Lambda-35 UV-Vis spectrophotometer in Tris-HCl buffer medium at 300K. Elemental analyses were performed with a Perkin-Elmer 2400 II elemental analyzer. Electrochemical experiment was carried out with three electrode configuration using a CH 660E cyclic voltammeter in Tris-HCl buffer medium. Saturated calomel electrode (SCE) as reference, Pt wire-electrode as counter electrode and glassy carbon electrode as working electrode were used as three electrode system with tetrabutylammonium perchlorate (TBAP) as supporting electrolyte at a scan rate of 50 mV sec^{-1}. Electrochemical data were recorded under a dry nitrogen environment. Nitrogen gas was passed into the sample solution at a constant rate for 1 minute.

2. 3. Synthetic Procedures

2. 3. 1. Synthesis of Schiff Base Ligand (HL)

The Schiff base ligand was prepared by the standard procedure mentioned in the literature.[25a–c] 5-chlorosalicylaldehyde (0.783 g, 5 mmol) in methanol medium was carefully added to a methanolic solution of N,N-dimethylethylenediamine (0.538 mL, 5 mmol). The colour of the solution turned light yellow and the reaction mixture was allowed to reflux for one hour and then cooled at room temperature (Scheme 1). The synthesized Schiff base ligand was used for complex preparation without further purification.

2. 3. 2. Synthesis of Complex $[Ru(PPh_3)Cl_2(L)]$(1)

Solid $[Ru(PPh_3)_3Cl_2]$ (1.92 g, 2 mmol) was added to 30 mL methanolic solution of the Schiff base ligand (2

mmol) followed by continuous stirring. After 6 hours of continuous reflux, shiny green coloured crystals were separated out (Scheme 1), collected by filtration, washed with diethyl ether and dried *in vacuo*. These crystals were used for the X-ray structural determination. Yield: 67% (0.256 g).

Anal. Calc. Ffor [$C_{29}H_{29}C_{l3}N_2OPRu$]: C, 52.73; H, 4.39; N, 4.24 %. Found: C, 52.65; H, 4.32; N, 4.18%.

IR (KBr cm^{-1}) 3436 (b), 1631, 696 and 744 (s), 496, 481 and 1530 (m). Electronic spectrum in Tris-HCl buffer medium, λ_{max} (nm): 260 ($\pi\rightarrow\pi^*$), 360 ($n\rightarrow\pi^*$) and 683 (d→d). ESI-MS: (m/z) [found (calcd)]: 661.0511 (659.93).

2. 4. Single Crystal X-ray Diffraction Study

Data collection of complex **1** was performed at the X-ray diffraction beamline (XRD1) of the Elettra Synchrotron of Trieste (Italy), with a Pilatus2M image plate detector. Complete dataset was collected at 100 K with a monochromatic wavelength of 0.700 Å with the rotating crystal method. The crystal was dipped in N-paratone and mounted on the goniometer head with a nylon loop. The diffraction data were indexed, integrated and scaled using XDS.[26] The structure was solved by direct methods[27] and successive Fourier analysis and the refinement was performed by the full-matrix least-squares methods based on F^2 implemented in SHELXL-2014.[27] Anisotropic thermal motion was allowed for all non-hydrogen atoms, and H atoms, at calculated positions, were included in the final cycles of refinement. All calculations were done with the Wingxpackage Version 2013.3,[28] and the molecular graphics were prepared by using Cameron[29] and DiamondVer 3.2k[30] programs. Relevant crystallographic data and structure refinement parameters are summarized in Table T1 (Supplementary information).

2. 5. Theoretical Methods

The geometry of the complex included in this study was computed at the M06-2X-D/def2-TZVP level of theory using the crystallographic coordinates. We have used the GAUSSIAN-09 program[31] was used for the calculations of the interaction energies and the molecular electrostatic potential (MEP) surfaces (at the same level of theory). We have also used the Grimme's dispersion[32] correction being this adequate for the evaluation of noncovalent interactions. The NCI plot[33] isosurfaces have been used to characterize noncovalent interactions. These correspond to both favorable and unfavorable interactions, as differentiated by the sign of the second density Hessian eigen value and illustrated by the isosurface color. The color scheme is a red-yellow-green-blue scale, where red indicates ρ^+_{cut} (repulsive) and blue for ρ^-_{cut} (attractive). The Gaussian-09 M06-2X-D/def2-TZVP wave function has been used to generate the NCI plot.

2. 6. Catecholase Activity Study

The catecholase-like activity of complex **1** has been investigated under aerobic condition at room temperature by using 3,5-di-*tert*-butylcatechol (3,5DTBC) as model substrate. Since complex **1** and the substrate are highly soluble in DMSO, the catalytic study was investigated in this particular solvent. The concentration of 3,5-DTBC was 100 times greater than that of the complex **1**. The process was followed spectrophotometrically at intervals of 10 mins. in the range of 200–600 nm, and a significant increase of the 3,5-DTBQ concentration was observed by measuring its absorbance near 393 nm. For each set of catalytic reaction, initial rates were calculated and the rate *versus* concentration of substrate was determined according to the Michaelis–Menten approach of enzymatic kinetics in order to get a Lineweaver–Burk plot.[34–36] This methodology allowed to determine the K_m, V_{max} and k_{cat} values.

3. Results and Discussion

3. 1. Infrared Spectral Study

IR spectrum of complex **1** (Fig. S**1**) showed a medium sharp band at 1631 cm^{-1}, ascribed to the ν(C=N) stretching, indicating the coordination of the azomethine nitrogen to the ruthenium(III) centre.[37–39] A broad band found at 3436 cm^{-1} is due to the N-H stretching frequency. Well resolved bands, which appeared at 696, 744 and 1530 cm^{-1}, are due to the stretching frequency of PPh_3,[40,41] while Ru-N and Ru-O stretching frequencies appeared at 496 and 581 cm^{-1}, respectively.

3. 2. Electronic Spectral Study

The electronic spectrum of complex **1**, recorded in Tris-HCl buffer medium, displayed three absorption bands in the UV-Vis region (Fig. S2). The high intensity band at 260 nm, is assigned to intra ligand $\pi\rightarrow\pi^*$transition of the imine in coordinated Schiff base, while the low intensity band at 360 nm can be attributed to $n\rightarrow\pi^*$ transition of the azomethine group. In addition, low energy band has been observed at 683 nm, which can be assigned to *d→d* transition. In order to confirm the stability of complex **1**, the UV-Vis spectral study was carried out for three successive days with same concentration of **1** in same medium, but no distinct change in the spectrum was observed.

3. 3. Cyclic Voltammetric Study

The redox behaviour of complex **1** was studied by cyclic voltammetry by using a saturated calomel electrode (SCE) as reference. The ruthenium complex was found to be redox-active in the potential range from +2.0 to −2.0 V (Fig. S**3**), and the redox potential was examined by well-defined waves at 0.37 and 0.72 V for the oxidation, and at −0.64 V for the reduction process. Of these, the peak at +0.37 V (*vs*. SCE) can be attributed to the Ru(III)/Ru(IV) oxidation, while that at +0.72 V can be assigned to the Schiff base oxidation. The irreversible reduction peak at −0.86 V (*vs*. SCE) is associated to the Ru(III)/Ru(II) redox couple.

3. 4. X-ray Crystal Structure Description

The complex crystallizes in the monoclinic system, space group $P2_1/c$. The molecular structure of the complex is displayed in Fig. 1, while a packing diagram is shown in Fig. S5. (Supplementary information). All the relevant crystallographic data and structure refinement parameters for the complex reported are summarized in Table T1 (Supplementary information). A selection of bond distances and angles is collected in Table T2 (Supplementary information). The asymmetric unit consists of one complete complex molecule which is built by the tridentate Schiff base ligand meridionally coordinated, the triphenylphosphine molecule and two chlorides mutually located in *trans* position. The coordination geometry of the complex can be better described as distorted octahedral where the equatorial plane is formed by the donor atoms O1, N1, and N2 donors of the chelating Schiff base (forming a six- and five-member ring) along with the P donor of the phosphine moiety. The coordination bond lengths Ru-O1, Ru-N1 and Ru-N2 of the chelating ligand are 1.9757(13), 2.0384(15) and 2.2141(16) Å, respectively, where the Ru-N bond values differ due to the different hybridization of the N atoms (sp^2 *vs.* sp^3). Finally the coordination geometry is completed by the phosphine with Ru-P distance is of 2.4058 (5) Å and two chlorides having comparable Ru-Cl bond length of 2.3485(5) and 2.3569(5) Å. Thus the +3 charge of the metal atom is satisfied by the chloride anions and the phenoxo oxygen (O1) of the Schiff base ligand. The distortion in the octahedron are well described by the bond angle values and the larger deviation from the ideal geometry is shown by the N2-Ru-P1 angle of 102.22(4)°, that appears induced by steric requirements. All the coordination distances (Table T2, Supplementary information) agree well with those reported for similar Ru(III) complexes.[41–44]

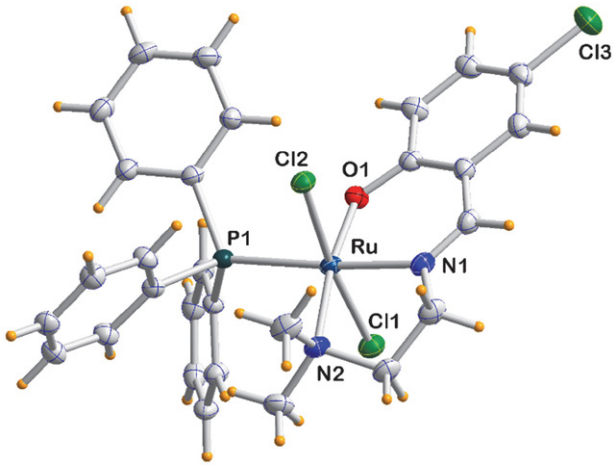


Fig. 1. ORTEP view of complex **1** with displacement ellipsoids drawn at 50% probability level (labels of C atoms not shown for clarity).

3. 5. Theoretical Study

The crystal packing of **1** shows the complexes associated in pair through a symmetry center where C–Cl bond of the aromatic ring points towards one chloride ligand of the symmetry related complex. This halogen-halogen like-interaction can be inferred taking into consideration the anisotropy of the charge density around the Cl atom. The theoretical study, using the MEP and NCI plot computational tools, is devoted to analyse the energy associated to this halogen interaction and to characterize it.

First the MEP surface of compound **1** was computed. It is worth mentioning that the more negative values of MEP are located at the chloro ligands (–45 kcal/mol). Since using the large scale given by the maximum and minimum MEP values the anisotropy around the chlorine cannot be appreciated, so the MEP around this atom using a reduced scale is represented in Fig. 2. As a result, the σ-hole, of moderate energy (+5 kcal/mol), appears at the extension of the C–Cl bond, while the typical negative

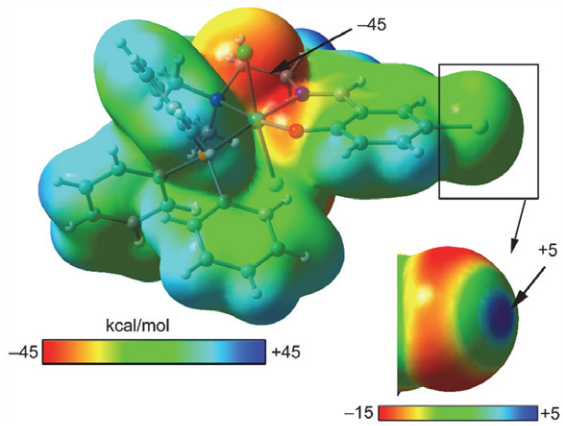


Fig. 2. MEP surface (isodensity = 0.002 a.u.) of compound **1**. The values are selected points of the surface are indicated. Negative values are in red and positive in blue colour.

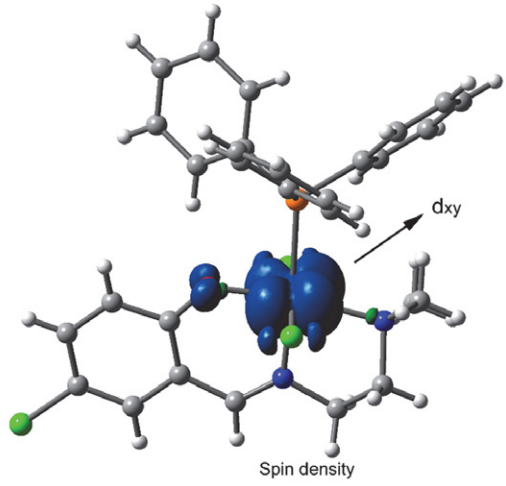


Fig. 3. Spin density plot of compound **1**. Isodensity = 0.004 a.u.

belt around the Cl atom is larger in absolute value than the σ-hole (–15 kcal/mol). So, the MEP analysis confirms that the Cl···Cl like-like interactions are electrostatically favoured. The spin density plot (Fig. 3) of compound **1** was also computed in order to analyse the location of the unpaired electron that is located, as expected, at the Ru metal centre with some little delocalization onto the atoms directly bonded to it.

Fig. 4a shows a detail of the crystal packing of **1** with formation of the self-assembled dimer, where two symmetrically equivalent Cl···Cl interactions are established in addition to an antiparallel π–π interaction. This arrangement also designates a double Cl···π interaction, being the Cl located over one C atom of the aromatic ring at a distance (3.63 Å)slightly longer than the sum of the Van der Waals radii (Σr_{vdW} = 3.45 Å). It should be mentioned that the Cl···Cl distance is also slightly longer (3.86 Å) that the sum of Van der Waals radii (Σr_{vdW} = 3.50 Å). Therefore, by using DFT calculations, the dimerization energy of the pair of complexes were computed in solid state, and it was found to be moderately strong (ΔE_1 = –12.0 kcal/mol) and accounts for the π–π, Cl···Cl halogen and other long range Van der Waals interactions (Fig. 4b). In an attempt to evaluate the contribution of the halogen bonding interactions, an additional model was used where the chloro ligands have been replaced by two hydrides (indicated by small arrows in Fig. 4c). As a consequence, the reduced interaction energy (ΔE_2 = –11.1 kcal/mol) determines the contribution of the π–π interaction and indicates that both the Cl···Cl interactions are very week (–0.9 kcal/mol), as expected taking into consideration the small MEP value observed at the σ-hole (Fig. 2). The "Non-Covalent Interaction (NCI) plot" was computed in order to characterize the interactions in the dimer of **1**. The NCI plot is considered as an intuitive visualization index which enables the identification of non-covalent interactions easily and efficiently. In addition it is convenient for host–guest interaction analysis since it clearly shows the interacting molecular regions. Fig. 4d shows the representation of the NCI plot, where the colour scheme is shown in red-yellow-green-blue scale: red means repulsive and blue stands for attractive interactions. Yellow and green surfaces correspond to weak repulsive or weak attractive interactions, respectively. As noted, the halogen bonds are characterized by the presence of a small green isosurface that is located between the Cl atoms, confirming the existence of the interaction. The NCI plot also shows the presence of a green and more extended isosurface between the π-systems of the ligands, indicating the existence of π-interactions that are also main contributor to the formation of the self-assembled dimer. Finally, the analysis reveals that the green isosurface extends in between the pair of the Cl atom and the aromatic-system, thus unequivocally confirms the existence of the Cl···π interactions.

3. 6. Oxidation of 3,5-di-tert-butylcatechol (Kinetics Studies)

The catalytic conversion of 3,5-DTBC to 3,5-DTBQ (Scheme 2) has already been investigated by a number of

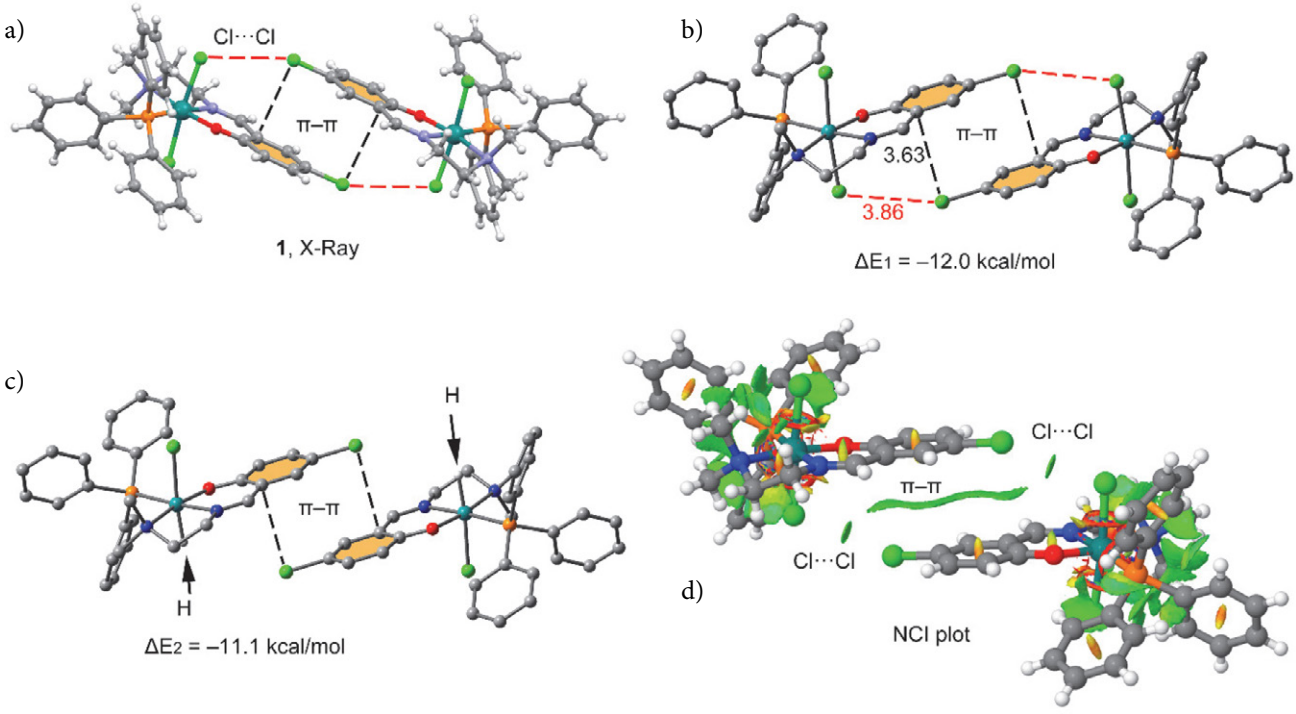
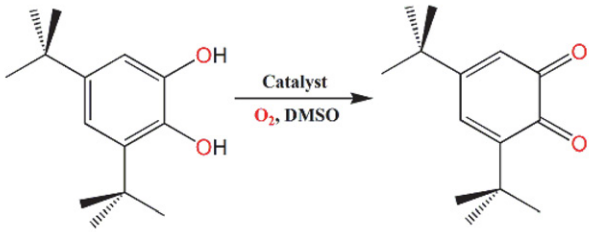


Fig. 4. (a) Detail of the crystal packing of **1**. (b,c) Theoretical models used to evaluate the interaction energies. Distances in Å. (d) NCI surface of the assembly present in compound **1**. The gradient cut-off is s = 0.35 a.u., and the color scale is –0.04 <ρ< 0.04 a.u.



Scheme 2. Oxidation process of 3,5-DTBC to 3,5-DTBQ.

scientist as a model catalytic reaction by using a variety of mono-,[45–60] di-,[31,51–63] tri/tetra-,[64–66] and poly-nuclear metal complexes.[67] 3,5-DTBC is the most widely used model substrate in catalytic oxidation process due to its low redox potential value that favours the oxidation to 3,5-DTBQ, which shows absorbance maximum at 400 nm in DMSO.

It is evident that due to bulky substituent groups, no further ring opening oxidation reaction can take place.[68] The exceptionally high stability of 3,5-DTBQ is indicative of a single reaction pathway and the formed benzoquinone does not undergo further oxidative cleavage.

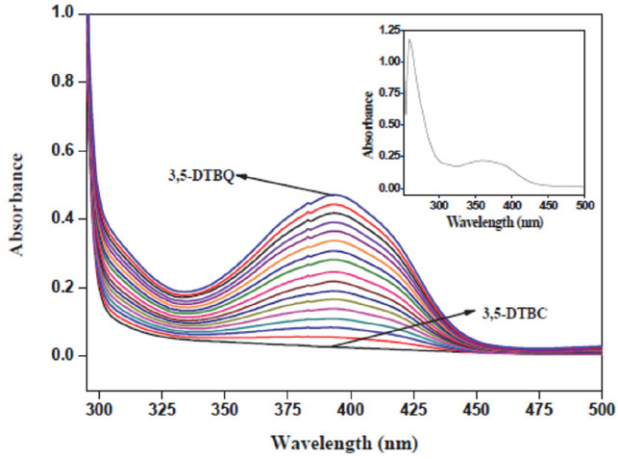


Fig. 5. Increase of the 3,5-DTBQ absorbance band at 393 nm after addition of 1×10^{-4} M DMSO solution of complex **1** to 100 equivalents of 3,5-DTBC at various intervals from 10 to 160 mins. Inset shows the UV-Vis spectrum of **1** in DMSO at room temperature.

However, before investigating a detailed catalytic study, it was important to verify the ability of complex **1** to oxidise 3,5-DTBC. For this reason, a DMSO solution 1×10^{-4} M of complex **1** was treated with 100 equivalents of 3,5-DTBC following the reaction by UV-Vis spectroscopy over the first 160 mins. After addition of 3,5-DTBC to the solution of **1**, the time dependent spectral scans display a smooth increase of the quinone band at 393 nm, indicating a significant catalytic activity of the complex as shown in Fig. 5. Thus the kinetics of the oxidation of 3,5-DTBC to 3,5-DTBQ was investigated by the method of initial rates by monitoring the growth of quinone band at 393 nm as a function of time. A graph of the absorbance difference (ΔA) of **1** at 393 nm in presence of 3,5-DTBC was plotted

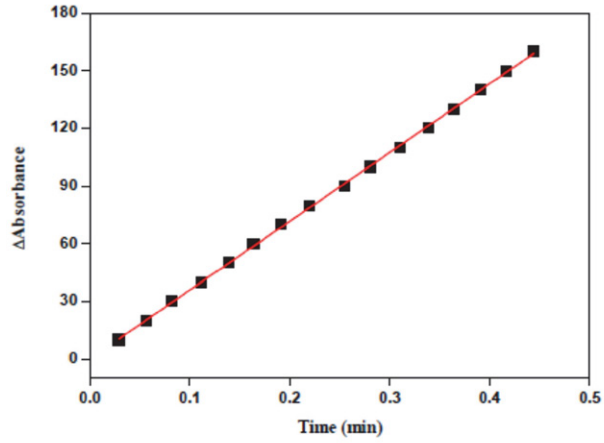


Fig. 6. Plot of absorbance difference (ΔA) *vs.* time to determine the initial rate of the catalytic oxidation of 3,5-DTBC by complex **1** in DMSO.

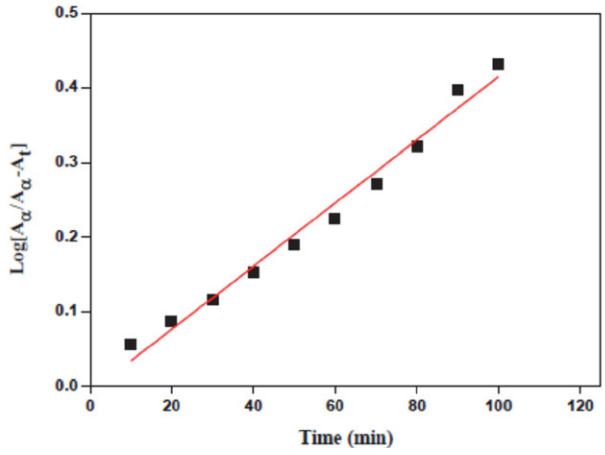


Fig. 7. Change in absorption maxima at 393 nm with time after incremental addition of DMSO solution 1×10^{-4} M of complex **1** to 100 equivalents of 3,5-DTBC.

against time to determine the rate/velocity for the catalyst to substrate concentration ratio (Fig. 6). The rate constant was determined from the slope of the plot $\log[A_\alpha/(A_\alpha-A_t)]$ *vs.* time (t) (where A_α and A_t are the absorbance at infinite and 't' time, respectively). The obtained straight line (Fig. 7) passes through the origin with a slope of 5.28×10^{-3}.

The rate constant *vs.* substrate concentration plot was well explained on the basis of Michaelis–Menten approach of enzymatic kinetics and its graphical representation was done in the form of the Lineweaver–Burk plot allowed to determine the kinetic parameters. The Michaelis binding constant (K_M), maximum velocity (V_{max}), rate constant for the dissociation of the substrate (*i.e.*, turnover number, k_{cat}) for complex **1** were calculated from the Lineweaver–Burk plot of 1/V *vs.* 1/[S] (Fig. 8) using the equation $1/V = \{K_m/V_{max}\}\{1/[S]\} + 1/V_{max}$. For the complex, a first-order catalytic reaction was detected at low concentration of the substrate 3,5-DTBC, while saturation kinetics was observed at higher concentration (shown in Fig. 8). At ex-

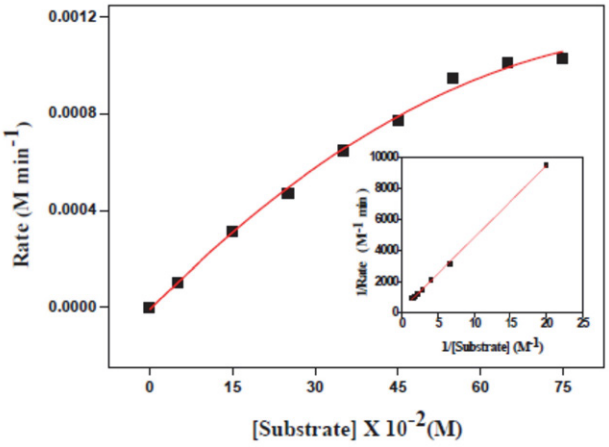


Fig. 8. Plot of initial rate versus substrate concentration [3,5-DTBC] for the catalytic oxidation reaction by complex **1**. The inset shows the Lineweaver -Burk plot.

cess substrate condition, the Michaelis–Menten approach of enzymatic kinetics is the best appropriate method.[46] The k_{cat} value was calculated by dividing V_{max} value by the concentration of complex **1**. The kinetic parameters for the catalytic oxidation of 3,5-DTBC mediated by complex **1** were determined as follows: V_{max} = 9.31 × 10^{-3} M min^{-1}, K_M = 1.805 M, T.O.N (K_{cat}) = 2.346 × 10^3 h^{-1}, efficiency (K_{cat}/K_M) = 21.66 $M^{-1}min^{-1}$. Manganese(II/III), nickel(II), copper(II), zinc(II) and cobalt(II/III) complexes have been used as prominent catalysts for catechol oxidation. Previous studied revealed that the oxidation occurs with catalyst only and not with impurities.[69] In Table 1 the k_{cat} value of complex **1** in DMSO, of 2.346 × 10^3 h^{-1}, is compared with that of related reported metal complexes. It is worth of note that complex **1** exhibits a moderate turnover number among the other Ru(III) metal complexes (Table T3, Supplementary information).

It can be concluded that the Ru(III) catalyst reported in this work appears an efficient synthetic complex for the catecholase reaction and can also be considered as a functional model for this process.

Table 1. Representative examples of metal catalysts for catechol oxidase activity having comparable TON value to **1** along with their turnover numbers.

Complexes having comparable T.O.N value to **1**.

Complexes	T.O.N × 10^3 (K_{cat}) (h^{-1})	References
1. $[Co(L)_2(ClO_4)_3]$	5.02	58
2. $[Cu_2(Sbal)_2(H_2O)_2]$	1.287	36
3. $[Cu_2(Sab_4)_2(H_2O)_2].0.5H_2O$	3.8	36
4. $[Co(L)_3]= C_{42}H_{39}N_6O_3S_3Co$	3.47	56
5. $[Ni(L)_2]= C_{28}H_{26}N_4O_2S_2Ni$	2.68	56
6. $[Cu_2(Ala_5OMe)_2]$	2.580	63
7. $[Cu_2(Ala_5Cl)_2]$	1.410	63
8. $[Cu_2(Ala_5Br)_2]$	1.80	63
9.$[Cu_2(Val_5Br)_2(H_2O)]\cdot0.5H_2O$	2.760	63
10. $[Cu_2(Leu_5Br)2]\cdot0.2H_2O$	3.960	63
11. $Ni(L^1)ClO_4$	8.0	55
12. $Ni(L^2)ClO_4$	2.7	55
13. $[Ru(PPh_3)Cl_2(L)]$	2.346	this paper

4. Conclusion

The following are the salient observations and findings of the present work:

(a) At our knowledge this is the first Ru(III) complex structurally characterized of Ru(III) with the Schiff base ligand derived from 5-chlorosalicylaldehyde and N,N-dimethylethylenediamine (HL).

(b) The complex $[Ru(PPh_3)Cl_2(L)]$ was characterized by elemental analysis and available spectroscopic IR, UV-Vis techniques, along with single crystal X-ray analysis.

(c) The crystal packing of the present compound exhibits halogen bonding interactions in solid state. The energies associated to these interactions have been evaluated using DFT calculations, and further corroborated with NCI plot index computational tool.

(d) The complex shows promising catalytic activity in the conversion of 3,5-DTBC to 3,5-DTBQ, and its T.O.N value is significantly higher in comparison with other Ru complexes.

Conflict of interest

There are no conflicts of interest to declare.

5. Acknowledgements

S. Saha, N. Biswas, C. Roy Choudhury are grateful to Late Prof. Samiran Mitra, Department of Chemistry, Jadavpur University, for his work about this manuscript. S. Saha gratefully acknowledges UGC for awarding Senior Research Fellowship (SRF). N. Biswas acknowledges CSIR, New Delhi, Govt. of India, for awarding junior research fellowship (Project No: 01/2537/11- EMR - II). C. Roy Choudhury acknowledges DST- FIST (Project No. SR/FST/CSI-246/2012) New Delhi, Govt. of India for instrumental support under capital heads.

Appendix A. Supplementary data

CCDC 1854395 contains the supplementary crystallographic data for complex **1**. These data can be obtained free of charge via http://www.ccdc.cam.ac.uk/conts/retrieving.html, or from the Cambridge Crystallographic Data Centre, 12 Union Road, Cambridge CB2 1EZ, UK;

fax: (+44) 1223-336-033; or e-mail: deposit@ccdc.cam.ac.uk. Supplementary data associated with this article can be found, in the online version, at http://

6. References

1. K. C. Gupta, A. K. Sutar, *Coord. Chem. Rev*. **2008**, *252*, 1420–1450. **DOI:**10.1016/j.ccr.2007.09.005
2. E. Ritter, P. Przybylski, B. Brzezinski, F. Bartl, *Curr. Org. Chem*. **2009**, *13*, 241–249. **DOI:**10.2174/138527209787314805
3. I. P. Ejidike, P. A. Ajibade, *Bioinorg. Chem. Appl*. **2016**, *2016*, 1–11. **DOI:**10.1155/2016/9672451
4. T. Opstal, F. Verpoort, *Angew. Chem. Int. Ed*., **2003**, *42*, 2876–2879. **DOI:**10.1002/anie.200250840
5. B. De Clercq, F. Lefebvre, F. Verpoort, *Appl. Catal. A Gen*. **2003**, *247*, 345–364. **DOI:**10.1016/S0926-860X(03)00126-1
6. A. Gölcü, M. Tümer, H. Demirelli, R. A. Wheatley, *Inorg. Chim. Acta* 2005, *358*, 1785–1797. **DOI:**10.1016/j.ica.2004.11.026
7. A. Neves, L. M. Rossi, A. J. Bortoluzzi, B. Szpoganicz, C. Wiezbicki, E. Schwingel, W. Haase, S. Ostrovsky, *Inorg. Chem*. **2002**, *41*, 1788–1794. **DOI:**10.1021/ic010708u
8. A. F. Shoair, A. R. El-Shobaky, E. A. Azab, *Spectrochim. Acta. Part A: Mol. Biomol. Spectrosc*. **2015**, *151*, 322–334. **DOI:**10.1016/j.saa.2015.06.011
9. Y. Yamamoto, K. Fukatsu, H. Nishiyama, *Chem. Commun*. **2012**, *48*, 7985–7987. **DOI:**10.1039/c2cc34044e
10. P. Barbaro, C. Bianchini, A. Meli, M. Moreno, F. Vizza, *Organometallics* **2002**, *21*, 1430–1437. **DOI:**10.1021/om011005n
11. I. Bratsos, S. Jedner, T. Gianferrara, E. Alessio, *CHIMIA Int J Chem*. **2007**, *61*, 692–697. **DOI:**10.2533/chimia.2007.692
12. A. A. A. Aziz, H. A. Elbadawy, *Spectrochim. Acta. Part A: Mol. Biomol. Spectrosc.* **2014**, *124*, 404–415. **DOI:**10.1016/j.saa.2014.01.050
13. P. Schluga, C. G. Hartinger, A. Egger, E. Reisner, M. Galanski, M. A. Jakupec, B. K. Keppler, *Dalton Trans*. **2006**, *2006*, 1796–1802. **DOI:**10.1039/b511792e
14. V. Brabec, *Nucleic Acid Res. Mol. Biol*. **2002**, *71*, 1–68. **DOI:**10.1016/S0079-6603(02)71040-4
15. A. Garza-Ortiz, P. U. Maheswari, M. Siegler, A. L. Spek, J. Reedijk, *New J. Chem*. **2013**, *37*, 3450–3460. **DOI:**10.1039/c3nj00415e
16. H. M. Yamamoto, J. Yamaura, R. Kato, J. *Am. Chem. Soc*. **1998**, *120*, 5905–5913. **DOI:**10.1021/ja980024u and references therein.
17. (a) L. Brammer, Chem. Soc. Rev. 2004, *33*, 476–489. **DOI:**10.1039/b313412c
    (b) A. Matsumoto, T. Tanaka, T. Tsubouchi, K. Tashiro, S. Saragai, S. Nakamoto, *J. Am. Chem. Soc*. 2002, *124*, 8891–8902. **DOI:**10.1021/ja0205333
    (c) L. R. MacGillivray, J. L. Reid, J. A. Ripmeester, *J. Am. Chem. Soc*. 2000, *122*, 7817–7818. **DOI:**10.1021/ja001239i
    (d) L. R. MacGillivray, *Cryst. Eng. Comm*. 2002, *4*, 37–41. **DOI:**10.1039/b200332e
    (e) M. Fourmigué, *Recent advances Curr. Opin. Solid State Mater Sci*. 2009, *13*, 36–45. **DOI:**10.1016/j.cossms.2009.05.001
18. G. R. Desiraju, Crystal Engineering. The Design of Organic Solids, Elsevier, Amsterdam, 1989.
19. (a) L. Brammer, G. Mínguez Espallargas, S. Libri, *Cryst. Eng. Comm*. **2008**, *10*, 1712–1727. **DOI:**10.1039/b812927d
    (b) P. Metrangolo, T. Pilati, G. Resnati, *Cryst. Eng. Comm*. **2006**, *8*, 946–947. **DOI:**10.1039/b610454a
    (c) K. Rissanen, *Cryst. Eng. Comm*. **2008**, *10*, 1107–1113. **DOI:**10.1039/b803329n
    (d) S. Samai, K. Biradha, *Cryst. Eng. Comm.* **2009**, *11*, 482–492. **DOI:**10.1039/B813263A
    e) P. Metrangolo, T. Pilati, G. Terraneo, S. Biella, G. Resnati, *Cryst. Eng. Comm*. **2009**, *11*, 1187–1196. **DOI:**10.1039/b821300c
    (f) G. R. Desiraju, P. S. Ho, L. Kloo, A. C. Legon, R. Marquardt, P. Metrangolo, P. Politzer, G. Resnati, K. Rissanen, *Pure Appl. Chem*. **2013**, *85*, 1711–1713. **DOI:**10.1351/PAC-REC-12-05-10
20. (a) D. Braga, F. Grepioni, New J. Chem. **1998**, *22*, 1159–1161. **DOI:**10.1039/a806554c
    (b) G. R. Desiraju, T. Steiner, The Weak Hydrogen Bond in Structural Chemistry and Biology, Oxford University Press, New York, **1990**
    (c) P. J. Langley, J. Hulliger, R. Thaimattamand, G. R. Desiraju, *New J. Chem*. **1998**, *22*, 1307–1309. **DOI:**10.1039/a807552b
    (d) G. R. Desiraju, R. Parthasarathy, *J. Am. Chem. Soc*. **1989**, *111*, 8725–8726. **DOI:**10.1021/ja00205a027
    (e) A. R. Jagarlapudi, P. Sarma, G. R. Desiraju, *Acc. Chem. Res*. **1986**, *19*, 222–228. **DOI:**10.1021/ar00127a005
    (f) C. M. Reddy, M. T. Kirchner, R. V. Gundakaram, K. A. Padmanabhan, G. R. Desiraju, *Chem. Eur. J*. **2006**, *12*, 2222–2234. **DOI:**10.1002/chem.200500983
21. (a) S. Saha, N. Biswas, A. Sasmal, C.J. Gómez-García, E. Garribba, A. Bauza, A. Frontera, G. Pilet, G. Rosair, S. Mitra, C. Roy Choudhury, *Dalton Trans*. 2018, *47*, 16102–16118. **DOI:**10.1039/C8DT02417K
    (b) S. Saha, A. Sasmal, C. Roy Choudhury, G. Pilet, S. Mitra, *Inorg. Chim. Acta* 2015, *425*, 211–220. **DOI:**10.1016/j.ica.2014.10.007
22. S. Saha, C. Roy Choudhury, C. J. Gómez-García, E.Garribba, A. Bauzá, A. Frontera, G. Pilet, S. Mitra, *Inorg. Chim. Acta* 2017, *461*, 183–191. **DOI:**10.1016/j.ica.2017.02.016
23. S. Saha, A. Sasmal, G. Pilet, A. Bauzá, A. Frontera, S. Mitra, *Cryst. Eng. Comm*. **2014**, *16*, 654–666. **DOI:**10.1039/C3CE41765D
24. P. Metrangolo, F. Meyer, T. Pilati, G. Resnati, G. Terraneo, *Angew. Chem. Int. Ed*. **2008**, *47*, 6114–6127. **DOI:**10.1002/anie.200800128 and references therein.
25. *(a)* S. Y. Liu, H. N. Hu, Y. P. Ma, *Synth. React. Inorg. Met-Org. Nano-Metal Chem*.**2013**, *43*, 734–738. **DOI:**1080/15533174.2012.754764
    (b) Z. L. You, Q. Z. Jiao, S. Y. Niu, J. Y. Chi, Z.*Anorg. Allgem. Chem. **2006**, 632, 2481–2485.* **DOI:***10.1002/zaac.200600198*
    (c) A. Bhattacharjee, S. Halder, K. Ghosh,, C. Rizzoli, P. Roy, *New J. Chem.* **2017**, *41*, 5696–5706. **DOI:**10.1039/C7NJ00846E
26. W. Kabsch, *Acta Cryst*. **2010,** *D66*, 125–132.

DOI:10.1107/S0907444909047337
27. G. M. Sheldrick, *Acta Cryst*. **2008**, *A64*, 112–122. **DOI:**10.1107/S0108767307043930
28. L .J. Farrugia, J. *Appl. Cryst*. **2012**, *45*, 849–854. **DOI:**10.1107/S0021889812029111
29. D. J. Watkin, C. K. Prout, L. J. Pearce, **1996,** CAMERON. Chemical Crystallography Laboratory, Oxford, England.
30. K. Brandenburg, **1999**, DIAMOND. Crystal Impact GbR, Bonn, Germany.
31. M. J. Frisch, G. W. Trucks, H. B. Schlegel, G. E. Scuseria, M. A. Robb, J. R. Cheeseman, G. Scalmani, V. Barone, B. Mennucci, G. A. Petersson, H. Nakatsuji, M. Caricato, X. Li, H. P. Hratchian, A. F. Izmaylov, J. Bloino, G. Zheng, J. L. Sonnenberg, M. Hada, M. Ehara, K. Toyota, R. Fukuda, J. Hasegawa, M. Ishida, T. Nakajima, Y. Honda, O. Kitao, H. Nakai, T. Vreven, J. A. Montgomery, Jr., J. E. Peralta, F. Ogliaro, M. Bearpark, J. J. Heyd, E. Brothers, K. N. Kudin, V. N. Staroverov, R. Kobayashi, J. Normand, K. Raghavachari, A. Rendell, J. C. Burant, S. S. Iyengar, J. Tomasi, M. Cossi, N. Rega, J. M. Millam, M. Klene, J. E. Knox, J. B. Cross, V. Bakken, C. Adamo, J. Jaramillo, R. Gomperts, R. E. Stratmann, O. Yazyev, A. J. Austin, R. Cammi, C. Pomelli, J. W. Ochterski, R. L. Martin, K. Morokuma, V. G. Zakrzewski, G. A. Voth, P. Salvador, J. J. Dannenberg, S. Dapprich, A. D. Daniels, Ö. Farkas, J. B. Foresman, J. V. Ortiz, J. Cioslowski, D. J. Fox, Gaussian 09 Gaussian, Inc., Wallingford CT, **2009**.
32. S. Grimme, J. Antony, S. Ehrlich, H. Krieg, *J. Chem. Phys*. **2010**, *132*, 154104–154119. **DOI:**10.1063/1.3382344
33. J. Contreras-García, E. R. Johnson, S. Keinan, R. Chaudret, J. P. Piquemal, D. N. Beratan, W. Yang, *J. Chem. Theory Comput*. **2011**, *7*, 625–632. **DOI:**10.1021/ct100641a
34. K. Ghosh, A. Banerjee, A. Bauza, A. Frontera, S. Chattopadhyay, *RSC Adv*. **2018**, *8*, 28216–28137. **DOI:**10.1039/C8RA03035A
35. C. Gerdemann, C.Eicken, B. Krebs, *Acc. Chem. Res*. 2002, *35*, 183–191. **DOI:**10.1021/ar990019a
36. C. T. Yang, M. Vetrichelvan, X. Yang, B. Moubaraki, K. S. Murray, J. J. Vittal. *Dalton Trans*. 2004, 113–121. **DOI:**10.1039/B310262A
37. P. Kalaivani, R. Prabhakaran, E. Vaishnavi, T. Rueffer, H. Lang, P. Poornima, R. Renganathan, V. VijayaPadma, K. Natarajan, *Inorg. Chem. Front*. **2014**, *1*, 311–324. **DOI:**10.1039/c3qi00070b
38. R. Prabhakaran, C. Jayabalakrishnan, V. Krishnan, K. Pasumpon, D. Sukanya, H. Bertagnolli, K. Natarajan, Appl.Organomet. Chem. 2006, *20*, 203–213. **DOI:**10.1002/aoc.1026
39. R. Prabhakaran, R. Karvembu, T. Hashimoto, K. Shimizu, K. Natarajan, *Inorg. Chim. Acta,* **2005**, *358*, 2093–2096. **DOI:**10.1016/j.ica.2004.12.051
40. N. Raja, R. Ramesh, *Spectrochim. Acta Part A. Mol. Biomol. Spectrosc*. 2010, *75*, 713– 718. **DOI:**10.1016/j.saa.2009.11.044
41. A. K. Das, S. M. Peng, S. Bhattacharya, *J. Chem. Soc., Dalton Trans*. 2000, 181–184. **DOI:**10.1039/a907021d
42. P. Bhattacharyya, M. L. Loza, J. Parr, A. M. Z. Slawin, *J. Chem. Soc. Dalton Trans*. 1999, 2917–2921. **DOI:**10.1039/a904905c
43. R. Raveendran, S. Pal, *Inorg. Chim. Acta* **2006**, *359*, 3212–3220. **DOI:**10.1016/j.ica.2006.04.004
44. J. G. Małecki, I. Gryca, *Polyhedron* **2013**, *51*, 102–110. **DOI:**10.1016/j.poly.2012.12.012
45. Z. F. Chen, Z. R. Liao, D. F. Li, W. K. Li, X. G. Meng, *J. Inorg. Biochem*. **2004**, *98*, 1315–1318. **DOI:**10.1016/j.jinorgbio.2004.04.006
46. S. Sreedaran, K. S. Bharathi, A. K. Rahinan, K. Rajesh, G. Nirmala, V. Narayanan, *J. Coord. Chem*. **2008**, *61*, 3594–3609. **DOI:**10.1080/00958970802087425
47. M. Gonzales-Alvares, G. Alzuet, J. Borras, S. Garcia-Granda, J. M. Montejo-Bernardo, *J. Inorg. Biochem*. **2003**, *96*, 443–451. **DOI:**10.1016/S0162-0134(03)00263-0
48. M. R. Malachowski, J. Carden, M. G. Davidson, W. L. Driessen, J. Reedijk, *Inorg. Chim. Acta* **1997**, *257*, 59–67. **DOI:**10.1016/S0020-1693(96)05448-5
49. A. L. Abuhijleh, *J. Inorg. Biochem*. **1994**, *55*, 255–262. **DOI:**10.1016/0162-0134(94)85010-0
50. P. S. Subramian, E. Suresh, P. Dastidar. *Polyhedron* **2004**, *23*, 2515–2522. **DOI:**10.1016/j.poly.2004.08.020
51. M. Thirumavalavan, P. Akilan, M. Kandasmary, K. Chinnakali, G. S. Kumar, H. K. Fun, *Inorg. Chem*. **2003**, *42*, 3308–3317. **DOI:**10.1021/ic020633
52. A. Jancso, Z. Paksi, N. Jakab, B. Gyurcsik, A. Rockenbauer, T. Gadja, *J. Chem. Soc., Dalton Trans*. **2005**, 3187–3194. **DOI:**10.1039/b507655b
53. A. Allam, I. Dechamps-Olivier, J.-B. Behr, R. Plantier-Royon, L. Bopont, *Inorg. Chim. Acta* 2011, *366*, 310–319. **DOI:**10.1016/j.ica.2010.11.011
54. S. Mistri, H. Puschmann, S. C. Manna, *Polyhedron* 2016, *115*, 155–163. **DOI:**10.1016/j.poly.2016.05.003
55. M. Das, R. Nasani, M. Saha, S. M. Mobin, S. Mukhopadhyay, *Dalton Trans*. **2015**, *44*, 2299–2310. **DOI:**10.1039/C4DT02675F
56. A. K. Ghosh, M. Mitra, A. Fathima, H. Yadav, A. R. Choudhury, B. U. Nair, R. Ghosh, *Polyhedron* 2016, *107*, 1–18. **DOI:**10.1016/j.poly.2016.01.015
57. N. Beyazit, B. Çatıkkas, S. Bayraktar, C. Demetgül, *J.Mol. Struct*. 2016, *1119*, 124–132. **DOI:**10.1016/j.molstruc.2016.04.047
58. A. K. Maji, A. Chatterjee, S. Khan, B. K. Ghosh, R. Ghosh. *J. Mol. Struct*. 2017, *1146*, 821–827. **DOI:**10.1016/j.molstruc.2017.06.077
59. S. Mondal, B. Pakhira, A. J. Blake, M. G. B. Drew, S. K. Chattopadhyay, *Polyhedron*, 2016, *117*, 327–337. **DOI:**10.1016/j.poly.2016.05.052
60. P. Selvakumar, N. Nanjundan, K. Velmurugan, R. Nandhakuma, R. Narayanasamy, J. Braz. Chem. Soc. 2017, 28, 1414–1429. **DOI:**10.21577/0103-5053.20160318
61. S. Anbu, E. C. B. A. Alegria, A. J. L. Pombeiro, *Inorg. Chim. Acta* **2015**, *431*, 139–144. **DOI:**10.1016/j.ica.2014.11.038
62. P. Adak, B. Ghosh, A. Bauzá, A. Frontera, A. J. Blake, M. Corbella, C. D. Mukhopadhyay, S. K. Chattopadhyay, *RSC Adv*. **2016**, *6*, 86851–86861. **DOI:**10.1039/C6RA14059A
63. Y. Thio, X. Yang, J. J. Vittal, *Dalton Trans*. **2014**, *43*, 3545–3556. **DOI:**10.1039/c3dt52829d
64. S. Majumder, S. Sarkar, S. Sasmal, E. C. Sanudo, S. Mohanta,

Inorg. Chem. 2011, *50*, 7540–7554. **DOI:**10.1021/ic200409d
65. V. K. Bhardwaj, N. Aliaga-Alcalde, M. Corbella, G. Hundal, *Inorg. Chim. Acta* 2010, *363*, 97–106. **DOI:**10.1016/j.ica.2009.09.041
66. (a) A. Szorcsik, F. Matyuska, A. Benyei, N. V. Nagy, R. K. Szilagyi, T. Gajda, *Dalton Trans*. 2016, *45*, 14998–15012. **DOI:**10.1039/C6DT01228K
(b) R. E. H. M. B. Osorio, A. Neves, T. P. Camargo, S. L. Mireski, A. J. Bortoluzzi, E. E. Castellano, W. Haase, Z. Tomkowicz, *Inorg. Chim. Acta* 2015, *435*, 153–158. **DOI:**10.1016/j.ica.2015.06.023
(c) S. Calancea, S. G. Reis, G. P. Guedes, R. A. A. Cassaro, F. Semaan, F. Lopez-Ortiz, M. G. F. Vaz, *Inorg. Chim. Acta* 2016, *453*, 104–114. **DOI:**10.1016/j.ica.2016.07.057
67. A. Majumder, S. Goswami, S. R. Batten, M. S. E. Fallah, J. Ribas, S. Mitra, *Inorg. Chim. Acta* **2006**, *359*, 2375–2382. **DOI:**10.1016/j.ica.2006.01.045
68. J. Mukherjee, R. Mukherjee, *Inorg. Chim. Acta* **2002**, *337*, 429–438. **DOI:**10.1016/S0020-1693(02)01106-4
69. (a) M. Das, Z. Afsan, D. Basak, F. Arjmand, D. Ray, *Dalton Trans*. **2019**, *48*, 1292–1313. **DOI:**10.1039/C8DT04183K
(b) K. Ghosh, K. Harms, S. Chattopadhyay, *Chemistry Select* **2017**, *2*, 8207–8220. **DOI:**10.1002/slct.201701536
(c) A. Hazari, L. K. Das, R. M. Kadam, A. Bauzá, A. Frontera, A. Ghosh, *Dalton Trans*. **2015**, *44*, 3862–3876. **DOI:**10.1039/C4DT03446E
(d) S. Das, A. Sahu, M. Joshi, S. Paul, M.Shit, A. R. Choudhury, B. Biswas, *Chemistry Select*. **2018**, *3*, 10774–10781. **DOI:**10.1002/slct.201801084

Povzetek

Z uporabo Schiffove baze, pripravljene iz 5-klorosalicilaldehida in *N*,*N*-dimetiletilendiamina kot liganda smo sintetizirali nov rutenijev(III) kompleks z molekulsko formulo $[Ru(PPh_3)Cl_2(L)]$ (**1**). Spojino smo karakterizirali z metodami FT-IR, UV-Vis, ciklično voltametrijo in monokristalno rentgensko analizo. Okolica kovinskega iona je nekoliko popačen oktaeder kjer kelatni ligand prispeva donorski niz NNO. Koordinacija okoli rutenija je zaključena s PPh_3 ligandom in dvema kloridnima anionoma, ki skupaj s fenokso kisikom Schiffove baze zagotovijo nevtralnost spojine. Z namenom preučevanja energije povezane z vezavo halogena smo opravili tudi teoretsko analizo kompleksa, pri čemer smo uporabili MEP in NCI metode. Kompleks **1** kaže aktivnost primerljivo s kateholazo v pretvorbi modelnega substrata 3,5-di-*tert*-butilkatehola (3,5-DTBC) v ustrezni 3,5-di-*tert*-butilkinon (3,5-DTBQ) pod aerobnimi pogoji. Parametre encimatske kinetike smo določili iz Lineweaver-Burkovega diagrama z uporabo Michaelis-Mentenovega modela encimske katalize. Visoka vrednost T.O.N (2.346×10^3 h^{-1}) kaže na zelo dobro katalitsko delovanje kompleksa **1** pri pretvorbi 3,5-DTBC.

Except when otherwise noted, articles in this journal are published under the terms and conditions of the Creative Commons Attribution 4.0 International License

DOI: 10.17344/acsi.2020.6390 *Acta Chim. Slov.* **2021,** *68,* 222–228
creative commons

Scientific paper

Protective Effects of 3-benzoyl-7-hydroxy Coumarin on Liver of Adult Rat Exposed to Aluminium Chloride

Ahmet Özkaya* and Kenan Türkan

Department of Chemistry, Faculty of Science and Art, Adiyaman University, Adiyaman, Turkey

** Corresponding author: E-mail: aozkaya@adiyaman.edu.tr*
Telephone: +90-416-2233800

Received: 09-17-2020

Abstract

In this study, the effects of 3-benzoyl-7-hydroxy coumarin molecule on mineral and antioxidant enzymes were investigated in rat liver exposed to oxidative stress with aluminium chloride ($AlCl_3$). Adult male Wistar albino rats were divided into four groups as Control, Coumarin, $AlCl_3$, and Coumarin + $AlCl_3$. Coumarin at the dose of 10 mg/kg and $AlCl_3$ at the dose of 8.3 mg/kg were administered for 30 days every other day. In $AlCl_3$ group, malondialdehyde (MDA), iron (Fe), aluminium (Al) and copper (Cu) levels increased compared to the control group, while glutathione (GSH) level, glutathione S-transferase (GST), and carboxylesterase (Ces) enzyme activity levels decreased. In Coumarin + $AlCl_3$ group, MDA, Fe, Al and Cu levels decreased with the effect of coumarin compared to $AlCl_3$ group, while GSH level, and GST enzyme activity levels increased. According to our results, $AlCl_3$ generates oxidative stress in rat livers, and we believe that 3-benzoyl-7-hydroxy coumarin has an ameliorative effect on antioxidant enzyme system, Al, Fe and Cu levels.

Keywords: Aluminium; coumarin; rat; liver; carboxylesterase; mineral

1. Introduction

Aluminium (Al) is a metal commonly found in soil. People are exposed to Al throughout life in many ways such as through cooking utensils, drinking water, antacids, deodorants, food additives, spices, teas and dialysis processes. Al accumulates in many organs such as liver, brain, heart and lung. As a result of its toxic effects, Al causes many disorders such as anaemia, brain diseases, muscle weakness and lung problems.[1,2] In particular, in Alzheimer's Disease, it has been suggested to play a role in the progression of the disease.[3] Liver is one of the most important organs of metabolism, regulating detoxification and secretory functions. Studies have reported that Al accumulates in liver and causes harmful effects.[4,5] Significant changes in haemato-biochemical parameters of rats and rabbits exposed to Al were detected. Al causes an increase in hepatic MDA levels and a decrease in antioxidant enzymes.[6,7]

Coumarins are defined as "2H-1-benzopyran-2-on". These chemicals are one of the important members of the natural class of polyphenolic compounds.[8] In addition to being isolated from plants, coumarins were also synthesized synthetically. Coumarins have many biochemical effects such as anticancer,[9] antiinflammatory,[10] and antihyperlipidemic.[11] In our study, 3-benzoyl-7-hydroxy coumarin was used. Hydroxycoumarins are a phenolic compound. The free radical scavenger and metal chelator properties of these substances are known.[12]

There are many esterase enzymes such as acetylcholine esterase, buthylcholin esterase, carboxylesterase, cholesterol esterase, which differ in biological functions in our body. Increases in metabolites produced by these enzymes can lead to pathological conditions, such as Alzheimer's Disease, hypercholesterolemia, brain cancer, and Coronary Artery Disease; and therefore, researchers have focused on various esterase inhibitors.[13] Among these enzymes, carboxylesterase is an important detoxification enzyme. Carboxylesterase (Ces, EC 3.1.1.1) is a member of the superfamily of esterase that catalyses the hydrolysis of esters, amides and thioesters.[14] These enzymes are expressed mainly in the liver of mammals.[15] Many drugs and xenobiotics have effects on the influence expression of Ces enzymes.[16] Another important detoxification enzyme is Glutathione S-transferase (GST). The most important task of this enzyme is to scavenge reactive oxygen species (ROS).[17] Reduced glutathione (GSH) is a non-enzymatic antioxidant molecule, and is essential for antioxidant functions.[18] Macro and trace elements have many functions in human metabolism, such as cofactors and antiox-

idants. Lack and excess of elements in metabolism cause serious damage. In some studies, it has been reported that the levels of other elements change as a result of Al exposure.[19]

There is information in the literature about the protective role of various coumarin derivatives (fraxin, esculetin, grandi vittin, agosyllin, aegolinol benzoate, osthol etc.) against oxidative stress[8], but there is no information about the effect of the 3-benzoyl-7-hydroxy coumarin we used in our study against oxidative stress. Therefore, in the present study, the effects of 3-benzoyl-7-hydroxy coumarin on Fe, Al, Cu, zinc (Zn), magnesium (Mg), manganese (Mn), CES, GST, GSH and MDA were investigated in the liver of rats exposed to $AlCl_3$.

2. Materials and Methods

2. 1. Animals and Experimental Procedure

All experimental protocols were approved by the Local Ethics Committee of Adiyaman University (Number of the permission: 2019/27). Rats used in the experiment were treated in accordance with national and international laws and policies regarding the care and use of experimental animals. Twenty-eight adult (aged 2.5 months) male *Wistar albino* rats (260 ± 10 g body weight) were obtained from the Department of Animal Experiments Local Ethics Committee of Adiyaman University (Adiyaman, Turkey). Rats were randomly divided into four groups as Control (C), 3-benzoyl-7-hydroxy coumarin (CM), $AlCl_3$ (A), and 3-benzoyl-7-hydroxy coumarin+$AlCl_3$ (CM+A) (n = 7 each group). The C group rats received vehicle solutions with only distilled water. $AlCl_3$ was dissolved in distilled water, and the animals were given 8.3 mg / kg intraperitoneally (IP).[20] 3-benzoyl-7-hydroxy coumarin was administered to the animals in distilled water at a dose of 10 mg / kg orogastrically.[21] During the application, in order to prevent possible complex formation between aluminium and coumarin, $AlCl_3$ and coumarin exposures were applied at different time intervals. The exposure of $AlCl_3$ was made between 09:00 am and 10:00 am every other day for 30 days. Coumarin administration was performed between 04:00 pm and 05:00 pm every other day for 30 days. The rats were housed under a standard light/dark schedule (12-h light/12-h dark cycle) at constant temperature (21 ± 1°C) and humidity (55 ± 5%) with free access to pelleted food and fresh tap water. The rats were sacrificed at the end of day 30. For biochemical analyses, liver samples were stored at –50ºC until the assays were performed.

2. 2. Homogenization and Centrifugation of Liver Tissue

Ice-cooled 0.1 M K-phosphate buffer containing 0.15 M KCl, 1 mM EDTA and 1 mM DTT in a 1 : 4 ratio of total tissue weight (w/v) was used to homogenize liver samples. Homogenization was performed with a Heidolph RZ 2021 brand homogenizer. The homogenates were centrifuged at 15000 g for 30 minutes at 4 degrees Celsius using the Hettich ROTINA 420 R centrifuge. The supernatant obtained after centrifugation was used for testing enzyme activity. The levels of MDA, reduced GSH, and activities of Ces and GST were determined spectrophotometrically at appropriate wavelengths using a microplate reader system (ThermoTM Varioskan Flash, Thermo Scientific).

2. 3. Measurement of Glutathione S-transferase Activities

The GST activity was measured using a modified version of the method developed by Habig et al. (1974), and adapted to the microplate reader system.[22] The mixture consisted of 100 mM K-phosphate buffer (pH 6.5), 1 mM GSH (used as cofactor), 10 mM CDNB (used as a substrate) and supernatant. During the measurement, 10 microliter supernatant, 100 microliters phosphate buffer + 100 µl GSH mixture and finally CDNB were pipetted into microplate wells, respectively. Absorbance changes expressing the decrease in CDNB amount depending on the reduced GSH consumed during the reaction were measured at 344 nm for 3 min at 25 °C, and the specific GST activity was calculated as nmol $min^{-1}g$ $protein^{-1}$.

2. 4. Measurement of Ces Activities

The Ces activity was determined using the modified version of the procedure described by Santhoshkumar and Shivanandappa (1999) for the microplate reader.[23] The reaction solution consisted of 5 µL of supernatant and 0.1 mM 250 µL pH 7.4 trizma buffer. The reaction mixture pipetted into microplate wells was incubated for 3 min at 25 °C. The reaction was initiated by the addition of 5 µL of the 0.5 mM p-nitrophenol acetate (PNPA), into the reaction solution in wells. The p-nitrophenol released during the reaction due to the use of p-nitrophenol acetate as a substrate by Ces was monitored at 405 nm for 2 min at 25 °C. The specific Ces activity was calculated as nmol $min^{-1}g$ $protein^{-1}$.

2. 5. Determination of Malondialdehyde and Reduced GSH Levels in Tissues

The analysis of MDA, a secondary product of lipid peroxidation was carried out as described by Placer et al. (1966).[24] The reaction mixture was freshly prepared by adding 500 µL homogenate to 1.5 mL reaction solution by mixing equal volume of 15% trichloroacetic acid, 0.375% thiobarbituric acid, 0.25 N HCl (1:1:1, w/v). The reaction mixture was heated for 30 min at 100 °C in a water bath. After the mixture was cooled to room temperature, the centrifugation was performed at 15000 g for 15 min. Subsequently, by transferring supernatant samples into mi-

croplate wells, absorbance changes depending on MDA formed during the reaction were recorded at 532 nm. MDA levels were expressed as (nmol/g wet weight tissue). The reduced GSH level was determined by measuring the absorbance value at 412 nm of a compound formed by the reaction of reduced GSH with 5.5-dithiobis 2-nitro-benzoic acid (DTNB).[25] The level of reduced GSH was expressed as nmol mg^{-1} protein.

2. 6. Determination of Total Protein in Samples

The total protein content in the supernatant samples was determined using the colourimetric method of Bradford 1976, and with Bovine Serum Albumin (BSA) as the standard.[26] Results were expressed as milligram protein. All analyses were performed in triplicates. Total protein level was used to determine for GSH level and CES, GST enzyme activities in the liver.

2. 7. Liver Mineral Analyses

Liver Al, Fe, Cu, Zn, Mg, and Mn concentrations were measured using a NexION 350 inductively-coupled plasma mass spectrometer (ICP-MS, Perkin Elmer, MA, USA) at the Central Research Laboratory of Adiyaman University. The livers (250 mg) were digested in an acid solution (5 ml of nitric acid (HNO_3, 65%) using a microwave digestion system.[27] The digestion solutions were diluted and analysed by using the ICP-MS. For quality control, duplicate samples were used to measure the precision of the analysis. Detection limits were calculated as three times the standard deviation for the reagent blanks.[28] The results of the liver mineral concentrations are presented as ppm for Al, Fe, Cu, Zn, Mg, and Mn.

2. 8. Synthesis of 3-benzoyl-7-hydroxy Coumarin Molecule

The synthesis of 3-benzoyl-7-hydroxy coumarin compound was carried out according to reference[29] briefly as follows: 2.4-dihydroxybenzaldehyde (2.762 g), ethyl benzoyl acetate (3.844 g), piperidine (three drops) and acetone (50 mL) were added into a three-necked reaction flask and then, it was refluxed for 2 hours on a magnetic stirrer. At the end of the process, the reaction mixture was transferred into excess methanol to precipitate the 3-benzoyl-7-hydroxy coumarin compound (Figure 1). Finally, it was recrystallized in ethanol and dried under vacuum.

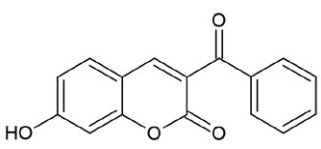


Figure 1: Schematic representation of 3-benzoyl-7-hydroxy coumarin

2. 9. Statistical Analyses

Data were expressed as mean ± SEM (standard error of mean). Statistical comparison of biochemical parameters was done using One-Way Analysis of Variance followed by the Tukey-HSD test. $P < 0.05$ was considered to be statistically significant.

3. Results

Liver mineral levels are presented in Table 1. Fe and Cu levels of group A increased compared to all other groups ($p < 0.05$). There was no statistical difference between the Zn levels of all groups ($p > 0.05$). While the Al level of group A increased compared to all other groups ($p < 0.001$, $p < 0.05$), Al level of CM+A group decreased compared to A group (p 0.05). Mn levels of A and CM+A groups decreased compared to C and CM groups.

Table 1: Liver mineral levels (ppm)

Minerals	C	CM	A	CM+A
Fe	103.20±3.49	100.55±3.00^{x}	116.84±2.38^{a}	102.25±2.2^{x}
Zn	25.79±1.66	25.95±0.66	24.43±1.26	29.16±1.22
Mg	238.06±6.09	230.34±5.11	232.74±9.28	240.56±1.93
Al	29.98±3.64	28.75±3.08^{z}	94.14±5.44^{c}	69.07±6.33^{cx}
Mn	2.90±0.07	2.94±0.06^{x}	2.55±0.04^{a}	2.65±0.09^{a}
Cu	5.37±0.76	4.69±0.23^{x}	7.32±0.53^{a}	5.29±0.40^{x}

Comparison with group C. a: $p < 0.05$, b: $p < 0.01$, c: $p < 0.001$
Comparison with group A. x: $p < 0.05$, y: $p < 0.01$, z: $p < 0.001$

Liver MDA, GSH and enzyme activity levels are shown in Table 2. Group A's MDA level was found to be increased compared to other groups ($p < 0.001$; $p < 0.05$). GSH level of group A decreased compared to other groups ($p < 0.05$; $p < 0.001$). Ces enzyme activity levels of A and CM + A groups decreased compared to C and CM groups ($p < 0.05$). GST enzyme activity level of A group decreased compared to other groups ($p < 0.05$).

Table 2: MDA, GSH and enzyme activity levels of the liver. GST and Ces activities are expressed as nmol/min/mg protein ± mean standard error. GSH and MDA levels are expressed as nmol GSH/mg protein ± mean standard error, and nmol MDA/g wet weight tissue ± mean standard error, respectively.

Parameters	C	CM	A	CM+A
MDA	45.02±2.54	48.05±3.41^{z}	78.75±5.85^{c}	58.56±3.65^{ax}
GSH	88.45±3.02	96.41±4.23^{z}	73.75±4.05^{a}	86.32±5.45^{x}
Ces	1.78±0.06	1.81±0.05^{x}	1.47±0.02^{a}	1.48±0.09^{a}
GST	31.41±0.76	33.80±1.67^{x}	24.34±1.04^{a}	32.20±1.90^{x}

Comparison with group C. a: $p < 0.05$, b: $p < 0.01$, c: $p < 0.001$
Comparison with group A. x: $p < 0.05$, y: $p < 0.01$, z: $p < 0.001$

4. Discussion

Al is a metal commonly found in air, soil and water. This metal is widely used in industry, agriculture, transportation and daily lives of people. Al, absorbed by the gastrointestinal tract, accumulates in the liver and other organs. In many studies, Al has been reported to cause hepatotoxicity, nephrotoxicity and cardiotoxicity.[30,31]

In the present study, we observed that Al, Fe and Cu concentrations increased significantly in the liver of rats that were given $AlCl_3$ intraperitoneally. In many experimental studies, it has been reported that the concentration of Al increases in rat liver exposed to Al.[32,33] Al is a non-redox metal, and many studies have reported that Al affects concentrations of other metal ions.[34,35] Yang et al. reported that the Al, Fe, Cu concentrations were increased in rat liver overloaded with Al.[19] In addition, it has been reported that Fe levels increase in rat liver exposed to Al.[36] Al is known to be linked to transfer protein carrying Fe^{3+}, thereby reducing the binding of Fe^{2+}. The increase in free intracellular Fe^{2+} causes peroxidation of membrane lipids, thereby causing membrane damage.[37] Chronic Cu^{2+} and Fe^{3+} overload causes accumulation of Cu^{2+} and Fe^{3+} in the liver and kidney, which causes Fe^{2+} overload. Al has been reported to increase Fe-induced oxidative stress injuries.[38–40]

In this study, liver Mn concentration of the A and combination groups decreased compared to the C group. In some studies, it has been reported that the Mn concentration decreases in rat liver exposed to Al.[41,42] In our study, we observed that the Zn and Mg concentration levels of group A decreased relatively compared to group C. Trace elements have important physiological functions in metabolism, and their abnormal usability causes serious negative effects. Trace elements, such as Cu, Zn, Fe, Mn, and Mg are essential co-factors for antioxidant enzymes. These enzymes are very important in preventing the oxidation of nucleic acids, lipids or proteins.[43]

In our study, the level of MDA increased in rat liver treated with $AlCl_3$. Also, GSH levels and GST and Ces enzyme activity levels decreased in antioxidant defence system. Based on these results, we believe that increased oxidative stress with $AlCl_3$ and reduction of enzymes involved in antioxidant defence could be caused by peroxidation damages. The glutamyl-cysteine-synthetase enzyme carries out the synthesis of the GSH molecule in the liver. In addition, it was found that enzymes, such as glucose-6-phosphate dehydrogenase and NADP-isocitrate dehydrogenase control the synthesis of the GSH molecule in the liver. In many studies, the inhibition effect of $AlCl_3$ on enzymes controlling GSH biosynthesis has been reported. $AlCl_3$ has pro-oxidant activity, and causes changes in the activity of antioxidant enzymes. In similar studies, while $AlCl_3$ increased the level of MDA in rat liver, it decreased GSH level and the activity of Glutathione peroxidase (GSH-Px), superoxide dismutase (SOD) and catalase.[44–46] In another study, it was reported that activities of catalase, GPx, SOD, and GST enzyme decreased in rat liver tissues with the toxic effects of Al.[47]

In the present study, it was observed that the Al, Fe and Cu levels increased in the liver of the rats exposed to oxidative stress with $AlCl_3$, and the 3-benzoyl-7-hydroxy coumarin substance decreased the levels of these metals. In addition, it was determined that the level of MDA, which is the high lipid peroxidation product of $AlCl_3$, was reduced by 3-benzoyl-7-hydroxy coumarin. It was observed that 3-benzoyl-7-hydroxy coumarin substance improved the GSH level and GST enzyme activity, which are effective in the antioxidant system. In this study, Ces enzyme activity decreased due to the toxic effect of $AlCl_3$. Also, in the combination group, the activity of Ces enzyme decreased with the effect of 3-benzoyl-7-hydroxy coumarin.

The results of the present study show that 3-benzoyl-7-hydroxy coumarin exerted antioxidant properties against the pro-oxidant effects of $AlCl_3$. We found that 3-benzoyl-7-hydroxy coumarin improves both Al, Fe and Cu concentrations in the liver, and positively affects the antioxidant system. The antioxidant activity of coumarin is due to its ability to scavenge free radicals and chelate metal ions. The antioxidant capacity of many coumarin substances has been reported to be due to its molecular structure.[48] The number and location of hydroxy, acetoxy and methoxy groups in the structure of coumarin affect the antioxidant capacity. These functional groups are very important for detoxification functions of coumarins.[48] In a similar study, the hepatoprotective effect of four different coumarins (coumarin (1,2- benzopyran), esculetin (6,7-dihydroxycoumarin), scoparone (6,7-dimethoxycoumarin), and 4-methylumbelliferone (7-hyroxy-4- methyl) were investigated against hepatic damage caused by CCl_4 in rat liver, and it was reported that two coumarins (esculetin and scoparone) had hepatoprotective effects. It has been explained that antioxidant properties of coumarins are attributed to their chemical structure.[49] In another study, the ameliorative effect of coumarin (1,2-benzopyron) was investigated in rats with ferric nitrilotriacetate (Fe-NTA)-induced renal oxidative stress. Fe-NTA increases the level of MDA with the effect of oxidative stress while decreasing the GSH level and GST enzyme activity. However, the ameliorative effect of the coumarin (1,2-benzopyrone) molecule has also been reported.[48] Many studies have shown that coumarin has an antioxidative effect against various oxidative stress agents.[50–52] Atmaca et al. (2011) suggested that coumarin and its derivatives showed antioxidative effects against rat liver damage induced by carbon tetrachloride by testing various antioxidant biomarkers.[49] Various studies have shown that coumarin derivatives, such as fraxin, esculetin, grandivittin, agacyllin, aegolinol benzoate and osthol have free radical scavenging effects.[8]

In our study, we revealed the relationship between the toxic effect of Al on the liver and the detoxification enzymes such as Ces and GST. Al reduced GST and Ces en-

zyme activities in rat liver. We could not find studies related to Ces enzyme activity to compare our results; however, there are reports indicating that Al decrease GST enzyme activity. In our previous study, we had found that Ces and GST enzyme activities decreased in liver of rats given lead acetate.[53] In this study, although we saw the ameliorative effect of 3-benzoyl-7-hydroxy coumarin in GST enzyme activity, we also found that this had no ameliorative effect on Ces enzyme activity in the combination group. It may be considered that the ineffectiveness of coumarin on Ces activity depends on the dose applied. Perhaps Ces activity would have been affected if different doses of coumarin were tried. We believe that more in vitro and in vivo studies are needed regarding the effect of coumarin on Ces activity. In the study conducted by Khan et al., it was reported that coumarin applied in increasing doses against the oxidative stress induced by Fe-NTA has an ameliorative effect on GST enzyme activity at high dose.[48]

In advanced pharmacological studies, we believe that this study is important for the effects of coumarin-derived substances on Ces enzyme activities.

5. Conclusion

In conclusion, we observed that $AlCl_3$ induces oxidative stress in rat liver. We have determined ameliorative effects of 3-benzoyl-7-hydroxy coumarin on deleterious effects of aluminium on the antioxidant enzymes, Fe, Cu and Al levels. However, we observed that the 3-benzoyl-7-hydroxy coumarin did not ameliorate the effect of Ces enzyme activity. In future studies, we believe that this study is important for investigating the effects of toxic substances and coumarin derivatives on Ces enzyme activity. As a result, we believe that 3-benzoyl-7-hydroxy coumarin may have an ameliorative effect against oxidative stress induced by Al.

Funding Information

This study was supported by Adiyaman University Scientific Research Projects Unit (ADYUBAP, Project no. FEFYL/2020-0001).

Conflict of Interest

The authors declare that they have no conflict of interest.

6. References

1. V. Kumar, K.D. Gill, *Arch Toxicol.* **2009**, *83(11)*, 965–978. **DOI:**10.1007/s00204-009-0455-6
2. L. A. Beyer, G. Greenberg, B. D. Beck, *Hum Ecol Risk Assess.***2014,** *20(1)*,111–136. **DOI:**10.1080/10807039.2013.770350
3. H. Luo, G. Liu, R. Zhang, Y. Bai, S. Fu, Y. Hou, *J Hazard Mater.***2014**, *270*,153–159. **DOI:**10.1016/j.jhazmat.2014.01.050
4. M. A. Gonzalez, M. L. Alvarez, G. B. Pisani, C. A. Bernal, M. G. Roma, M. C. Carrillo, *Biol Trace Elem Res.* **2007**, *116*, 329–348. **DOI:**10.1007/BF02698017
5. M. A. Gonzalez, C. A. Bernal, S. Mahieu, M. C. Carrillo, *Biol Trace Elem Res.* **2009**, *127 (2)*,164–176. **DOI:**10.1007/s12011-008-8234-4
6. M. I. Yousef, *Toxicology*. **2004**, *199 (1)*, 47–57. **DOI:**10.1016/j.tox.2004.02.014
7. A. S. Newairy, A. F. Salama, H. M. Hussien, M. I. Yousef, *Food Chem Toxicol.* **2009**, *47(6)*,1093–1098. **DOI:**10.1016/j.fct.2009.01.032
8. K. N. Venugopala, V. Rashmi, B. Odhav, *Biomed Res Int*. **2013**, 2013:963248. **DOI:**10.1155/2013/963248
9. K. V. Sashidhara, A. Kumar, M. Kumar, J. Sarkar, S. Sinha, *Bioorg Med Chem Lett*. **2010**, *20(24)*, 7205–11. **DOI:**10.1016/j.bmcl.2010.10.116
10. C. A. Kontogiorgis, D. J. Hadjipavlou-Litina, *J Med Chem.* **2005**, *48(20)*, 6400–6408. **DOI:**10.1021/jm0580149
11. K. V. Sashidhara, A. Kumar, M. Kumar, A. Srivastava, A. Puri, *Bioorg Med Chem Lett.* **2010**, *20*, 6504–6507. **DOI:**10.1016/j.bmcl.2010.09.055
12. E. J. Lien, S. Ren, H. H. Bui, R. Wang, *Free Radic Biol Med.* **1999**, *26(3–4)*, 285–94. **DOI:**10.1016/S0891-5849(98)00190-7
13. M. Alipour, M. Khoobi, A. Foroumadi, H. Nadri, A. Moradi, A. Sakhteman, M. Ghandi, A. Shafiee, *Bioorg Med Chem*, **2012**, *20*, 7214–7222. **DOI:**10.1016/j.bmc.2012.08.052
14. M. K Ross, A. Borazjani, C.C. Edwards, P. M. Potter, *Biochem Pharmacol.* **2006**, *71(5)*, 657–69. **DOI:**10.1016/j.bcp.2005.11.020
15. E. W Morgan, B. Yan, D. Greenway, A, Parkinson, *Arch Biochem and Biophy*. **1994**, *315(2)*, 513–526. **DOI:**10.1006/abbi.1994.1532
16. R. S. Holmes, M. W. Wright, S. J. F. Laulederkind, L. A. Cox, M. Hosokawa, T. Imai, S. Ishibashi, R. Lehner, M. Miyazaki, E. J. Perkins, P. M. Potter, M. R. Redinbo, J. Robert, T. Satoh, T. Yamashita, B. Yan, T. Yokoi, R. Zechner, L. J. Maltais, *Mamm Genome.* **2010**, *21(9–10)*, 427–441. **DOI:**10.1007/s00335-010-9284-4
17. S. Amjad, S. Umesalma, *J Mol Biomark Diagn.* **2015**, *6(1)*, 1–7.
18. L. DeLeve, N. Kaplowitz, *Pharmacol Ther.* **1991**, *52(3)*, 287–305. **DOI:**10.1016/0163-7258(91)90029-L
19. Y. Yang, H. Wang, Y. Guo, W. Lei, J. Wang, X. Hu, J. Yang, Q. He, *Biol Trace Elem Res.* **2016**, *173*, 126–131. **DOI:**10.1007/s12011-016-0627-1
20. A. Ozkaya, S. Celik, A. Yuce, Z. Sahin, O. Yilmaz, *Kafkas Univ Vet Fak Derg*. **2010**, *16 (2)*: 263–268.
21. N. Khan, S. Sharma, S. Sultana, *Redox Rep.* **2004**, *9(1)*, 19–28. **DOI:**10.1179/135100004225003860

22. W. H. Habig, M. J. Pabst, W. B. Jakoby, *J Biol Chem.* **1974**, *249(22)*, 7130–7139.
23. P. Santhoshkumar, T. Shivanandappa, *Chem Biol Interact.* **1999**, *119–120*, 277–282. **DOI:**10.1016/S0009-2797(99)00037-X
24. Z. A. Placer, L. L. Cushman, B. C. Johnson, *Anal Biochem*. **1966**, *16(2)*, 359–364. **DOI:**10.1016/0003-2697(66)90167-9
25. M. S. Moron, J. W. Depierre, B. Mannervik, *Biochim Biophys Acta.* **1979**, *582(1)*, 67–78. **DOI:**10.1016/0304-4165(79)90289-7
26. M. M. Bradford, *Anal Biochem.* **1976**, *72*, 248–254. **DOI:**10.1016/0003-2697(76)90527-3
27. S. Rattanachongkiat, G. E. Millward, M. E. Foulkes, *J Environ Monit.* **2004**, *6(4)*:254–261. **DOI:**10.1039/B312956J
28. I. De Blas Bravo, R. S. Castro, N. L. Riquelme, C. T. Diaz, D.A., *J Trace Elem Med Biol.* **2007**, *21(1)*:14–17. **DOI:**10.1016/j.jtemb.2007.09.017
29. A. Kurt, A. F. Ayhan, M. Koca, *Sakarya Univ J Sci.* **2018**, *22(3)*,880–887.
30. G. Crisponi, D. Fanni, C. Gerosa, S. Nemolato, V.M. Nurchi, M. Crespo-Alonso, J. I. Lachowicz, G. Faa, *Biomol Concepts.* **2013**, *4(1)*:77–87. **DOI:**10.1515/bmc-2012-0045
31. F. Geyikoglu, H. Türkez, T. O. Bakir, M. Cicek, *Toxicol Ind Health*. **2013**, *29(9)*, 780–791. **DOI:**10.1177/0748233712440140
32. N. Kaneko, H. Yasui, J. Takada, K. Suzuki, H. Sakurai, *J Inorg Biochem.* **2004**, *98(12)*, 2022–2031. **DOI:**10.1016/j.jinorgbio.2004.09.008
33. M. G. Abubakar, A. Taylor, G. A. Ferns, *Int J Exp Pathol.* **2003**, *84(1)*, 49–54. **DOI:**10.1046/j.1365-2613.2003.00244.x
34. A. Mohammadiras, M. Abdollahi, *Int J Pharmacol.* **2011**, *7(1)*, 12–21.
35. M. L. Turski, D. J. Thiele, *J Biol Chem.* **2009**, *284(2),* 717–721. **DOI:**10.1074/jbc.R800055200
36. R. J. Ward, Y. Zhang, R. R. Crichton, *J Inorg Biochem*. **2001**, 87(1–2), 9–14. **DOI:**10.1016/S0162-0134(01)00308-7
37. B. Nehru, P. Anand, *J Trace Elem Med Biol.* **2005**,*19(2–3),* 203–208. **DOI:**10.1016/j.jtemb.2005.09.004
38. H. Malhi, B. Joseph, M. L. Schilsky, S. Gupta, *Regen Med.* **2008***, 3(2)*, 165–173. **DOI:**10.2217/17460751.3.2.165
39. K. Bishu, R. Agarwal, *Clin J Am Soc Nephrol.* **2006**, *1*, 19–23.
40. A. Becaria, A. Campbell, S. C. Bondy, *Toxicol Ind Health.* **2002**, *18(7)*, 309–20. **DOI:**10.1191/0748233702th157oa
41. J. L. Esparza, M. Gomez, J. L. Domingo, *Biol Trace Elem Res.* **2019**,*188(1)*, 60–67. **DOI:**10.1007/s12011-018-1372-4
42. A. Ozkaya, H. Ciftci, A. Dayangac, B.S. Cevrimli, A. Olcucu, S. Celik, *Turk J Biochem.* **2013**, *38(3)*:345–349. **DOI:**10.5505/tjb.2013.29291
43. C. Meplan, *J Trace Elem Med Biol.* **2011**, *25(1),* 11–16. **DOI:**10.1016/j.jtemb.2010.10.002
44. S. Shrivastava*, J Trace Elem Med Biol*. **2012**, *26(2–3)*, 210–214. **DOI:**10.1016/j.jtemb.2012.04.014
45. M. E. Mahmoud, S. S. Elsoadaa, *J Nat Sci Res.* **2013**, *3(1)*,102–112.
46. I. Bouasla, A. Bouasla, A. Boumendjel, M. Messarah, C. Abdennour, M. S. Boulakoud, A. E. Feki, *Biol Trace Elem Res.* **2014**, *162(1–3)*,252–261. **DOI:**10.1007/s12011-014-0114-5
47. N. H. Nour-Eldein, E. A. Hassanin, W. M. El-Sayed, *Biol Trace Elem Res. 2018*, *183(1)*:128–137. **DOI:**10.1007/s12011-017-1126-8
48. N. Khan, S. Sharma, S. Sultana, *Cancer Lett.* **2004**, *210(1)*, 17–26. **DOI:**10.1016/j.canlet.2004.01.011
49. M. Atmaca, H. M. Bilgin, B. D. Obay, H. Diken, M. Kelle, E. Kale, *J Physiol Biochem.* 2011, *67(4)*,569–76. **DOI:**10.1007/s13105-011-0103-5
50. H. C. Lin, S. H. Tsai, C. S. Chen, Y. C. Chang, C. M. Lee, Z. Y. Lai, C. M. Lin, *Biochem Pharmacol*, **2008**, *75(6)*, 1416–1425. **DOI:**10.1016/j.bcp.2007.11.023
51. C. R. Wu, M. Y. Huang, Y. T. Lin, H. Y. J u, H. Ching, *Food Chem*, **2007**, *104(4)*, 1464–1471. **DOI:**10.1016/j.foodchem.2007.02.023
52. A. Tseng, *Proc A. Assoc Cancer Res* **1991**, *32*, 2257.
53. A. Ozkaya, Z. Sahin, M. Kuzu, Y.S. Saglam, M. Ozkaraca, M. Uckun, E. Yologlu, V. Comakli, R. Demirdag, S. Yologlu, *Arch Physiol Biochem.* **2018**, *124(1),* 80–87. **DOI:**10.1080/13813455.2017.1364772

Povzetek

V tej raziskavi so so bili proučeni učinki molekule 3-benzoil-7-hidroksi kumarina na minerale in antioksidativne encime v jetrih podgan, izpostavljenih oksidativnemu stresu z aluminijevim kloridom ($AlCl_3$). Odrasli samci podgan Wistar albino so bili razdeljeni v štiri skupine, poimenovane kontrola, kumarin, $AlCl_3$ in kumarin + $AlCl_3$. Kumarin v odmerku 10 mg/kg in $AlCl_3$ v odmerku 8,3 mg/kg sta bila aplicirana 30 dni vsak drugi dan. V skupini $AlCl_3$ so se v primerjavi s kontrolno skupino zvišale koncentracije malondialdehida (MDA), železa (Fe), aluminija (Al) in bakra (Cu), medtem ko so se ravni glutationa (GSH) in encimske aktivnosti glutation S-transferaze (GST) in karboksilesteraze (Ces) zmanjšala. V skupini kumarin + $AlCl_3$ so se ravni MDA, Fe, Al in Cu z delovanjem kumarina zmanjšale v primerjavi s skupino $AlCl_3$, medtem ko so se ravni GSH in aktivnost encima GST povečale. Glede na naše rezultate, $AlCl_3$ povzroča oksidativni stres v jetrih podgan in verjamemo, da ima 3-benzoil-7-hidroksi kumarin blažilni učinek na antioksidativni encimski sistem in ravni Al, Fe ter Cu.

Except when otherwise noted, articles in this journal are published under the terms and conditions of the Creative Commons Attribution 4.0 International License

Scientific paper

Physico-Chemical Properties of the Pyrolytic Residue Obtained by Different Treatment Conditions of Meat and Bone Meal

Marija Zupančič and Nataša Čelan Korošin*

Faculty of Chemistry and Chemical Technology, University of Ljubljana, Večna pot 113, 1000 Ljubljana, Slovenia

** Corresponding author: E-mail: Natasa.Celan@fkkt.uni-lj.si*
Phone: +386 1 4798 524

Received: 09-25-2020

Abstract

The depletion of phosphate rock reserves has led to the search for new, alternative and environmentally friendly products and processes. One of the safe and environmentally friendly sources of phosphate is animal bone char (ABC), the residue from the pyrolysis of meat and bone meal (MBM), a slaughterhouse waste material. The presented study investigated the physico-chemical properties of the residues (ABC) obtained from the pyrolysis of MBM under different treatment conditions. Two different end temperatures (600 °C and 1000 °C) and five different heating rates (5 °C min^{-1}, 10 °C min^{-1}, 20 °C min^{-1}, 50 °C min^{-1} and 100 °C min^{-1}) were used. The ABC samples obtained were characterised by X-ray powder diffraction, IR spectroscopy, elemental CHNS analysis and SEM/EDS analysis. The results showed the strong influence of both the pyrolysis end temperature and the heating rate on the morphology and chemical composition of the final products.

Keywords: Bone char, meat and bone meal, natural hydroxyapatite, phosphate sources, pyrolysis, thermogravimetry

1. Introduction

One of the main problems in many modern agricultural systems is the lack of sustainable development. The unauthorized use of chemicals, e.g. in phosphate fertilizers, has led to the eutrophication of waters, to the harming of many beneficial soil organisms and, as a result, to a negative impact on the level of biodiversity. The careful use of phosphate fertilizers leads to the better management of existing phosphorus sources and its continued circulation in nature. The existing fertilizer industry is based exclusively on non-renewable resources, i.e., a high grade phosphate ores that, according to one report, could be exhausted in as little as 60–80 years.[1]

Meat and bone meal (MBM) is a by-product of the rendering industry. Due to the medium-high heating value of MBM, the pyrolysis, gasification, combustion and co-combustion processes were studied as an environmentally friendly alternative to landfilling.[2-12] During the controlled pyrolysis process raw MBM decompose into number of useful products i.e. gas, tar, oil and char, that make it more attractive than other thermal processes. The speed and the extent of the decomposition depend on process parameters such as the temperature in the reactor, the heating rate of the biomass, the pressure and the composition of the raw material.[13]

The solid residue of pyrolysed meat and bone meal, animal bone char (ABC), is a granular material that, in contrast to the biochar from plant biomass, contains a much smaller percentage of organic carbon (about 10 %). For this reason, it cannot be categorized as biochar, but as pyrogenic carbonated material.[14,15] The carbon, which remains trapped in the structure after pyrolytic decomposition of MBM, increases the specific surface of ABC compared to crystalline hydroxyapatite (HA).[16] Due to its high phosphate content, ABC can be used as a source for P-fertilizer production or as a stabilizing agent in the remediation of potentially toxic elements (PTE) contaminated sites.[17-20]

A few studies investigated the influence of treatment conditions of pyrolysis of bone meal on the properties of the bone char obtained.[21-23] In contrast to the pyrolysis of bone meal, the pyrolysis of MBM poses a much greater challenge. Despite many studies that have investigated

the pyrolysis process of MBM, data on the influence of experimental conditions on the properties of MBM pyrolysis products are seldom available. In order to improve the knowledge in this field, the aim of this work was to evaluate the influence of the MBM pyrolysis end temperature and the different heating rates on physico-chemical properties and the composition of the solid residue, ABC, focusing on a detailed analysis of the morphology and composition of the ABC samples. The pyrolysis of the MBM sample was performed at five different heating rates (from 5 °C min^{-1} to 100 °C min^{-1}). Due to the large amount of organic matter in MBM the lowest pyrolysis end temperature examined was chosen at 600 °C. The characteristics of these residues were compared with residues obtained at MBM pyrolysis end temperature of 1000 °C, where the release of CO_2 from carbonates is expected to be completed.[24]

2. Experimental

MBM sample category 3 (low-risk material from the production of goods intended for human consumption using slaughtered animals not affected by any sign of diseases that are transmissible to humans or other animals) was obtained from a local slaughterhouse, where non-harmful animal remains are ground up, heated with steam for sterilization and with the animal fats squeezed out to obtain meat and bone meal. The sample was first dried for 24 hours at 100 °C, ground with a planetary mill (Retsch PM100, Germany) into fine powder and sieved through a 0.250 mm test sieve (ISO 3310-1, Retsch, Germany).

The MBM was pyrolysed in a Mettler Toledo (CH) TGA/SDTA 851e LF1100 system for Thermal Analysis. Subsamples of 20 mg were inserted into the alumina crucible (150 μL) and heat treated in an argon atmosphere (99.999 % high purity by Linde, 100 mL min^{-1}). After an initial 30 min of isothermal conditioning at 25 °C the samples were dynamically heated up to 600 °C or 1000 °C to obtain the samples group T1ABC or group T2ABC (see Table 1 for sample abbreviations), respectively. We used five different heating rates (5 °C min^{-1}, 10 °C min^{-1}, 20 °C min^{-1}, 50 °C min^{-1} and 100 °C min^{-1}) for the samples for both end temperatures. The baseline measured with an empty alumina crucible was subtracted for all the measurements. In order to achieve reproducibility of the results, a small particle size, which is limited by a high content of fat components and a sufficiently high initial mass of the sample, was required, as reported elsewhere.[6] To evaluate the repeatability, three replications of each thermal process, under the same conditions, were performed. The one-way analysis of variance (ANOVA) was used to determine the statistically significant differences between the samples.

To determine the ash content in the MBM and T1ABC samples the TGA method, analogous to DIN 51719, was used.[14] Approximately 5 mg of sample in a 150 μL alumina crucible was measured in the TGA/DSC1 Mettler Toledo (CH) thermoanalyser using the following multi-segment thermal program: (1) heating with a rate of 5 °C min^{-1} to 106 °C in a nitrogen atmosphere (99.999 % high purity by Linde, 100 mL min^{-1}), (2) hold in a nitrogen atmosphere at 106 °C for 30 min (100 mL min^{-1}), (3) temperature increase with a 5 °C min^{-1} heating rate to 550 °C in an oxygen atmosphere (99.999 % high purity by Linde, 100 mL min^{-1}), and (4) hold in an oxygen atmosphere at 550 °C for 60 min (100 mL min^{-1}). The hygroscopic moisture content and the ash content were calculated from the mass loss up to the end of the second step and from the mass loss up to the end of the fourth step of the program run, respectively. The baseline measured with an empty alumina crucible was subtracted for all the measurements. For the evolved gases determination, the thermoanalyser was coupled to a Balzers Thermostar Mass Spectrometer ($2.4 \cdot 10^{-6}$ mbar vacuum) *via* a 75 cm long capillary heated at 190 °C. The initial sample mass was 2.9 mg.

The semi-total concentrations of the elements in the MBM and T1H005 (bulk sample of replicates) were determined after aqua regia digestion. To an amount of 0.200 g ± 0.005 g of the sample in a PFA digestion vessel (561B, Savillex, Minnesota, USA) 3 mL of HNO_3 (≥69.0 %, TraceSelect, Fluka) and 9 mL of HCl (37 %, TraceSelect, Fluka, Sigma-Aldrich Chemie) were added, left in the loosely closed vessel in a fume hood overnight, then the vessel was tightly closed and the sample was digested at a temperature of reflux on a hot plate for 8 hours. The cold contents were filtered through a 0.45 μm membrane filter and diluted to 30 mL with Milli-Q water. The samples were digested in triplicate, including three blank samples. The concentration of metals in the digested diluted samples was analysed with ICP-MS Agilent 7500ce (Cr, Ni, Cu, Zn, As, Mo, Cd and Pb) and Varian 240 AA system (Fe, Na, K, Ca and Mg). The limit of detection (LOD) was calculated as the concentration corresponding to three times the standard deviation ($3s$, $N = 3$) of the blank determinations. Total P content in digested diluted samples were determined according to SIST EN ISO 6878:2004 (Water quality – Determination of phosphorus – Ammonium molybdate spectrometric method).

The content of C, H, N and S in the raw MBM sample and the ABC samples obtained after the pyrolysis of the MBM sample up to 600 °C (T1ABC samples) was determined with a Perkin Elmer Elemental Analyser Series II CHNS/O. The inorganic carbon content was determined according to DIN 51726.[14] The organic carbon content (C_{org}) in the samples was derived from the total carbon content minus the inorganic carbon content.

A Perkin Elmer Spectrum 100 spectrometer was used for the FTIR spectroscopy of the MBM and ABC samples. The analyses of the samples were performed with a single reflection monolithic diamond ATR (Specac's Golden Gate ATR) in the wavenumber range from 600 cm^{-1} to

4000 cm^{-1} (background correction, resolution 2 cm^{-1}, 10 scans for each spectrum).

The mineralogical properties of the ABC samples were examined with a PANalytical X'Pert PRO MPD powder diffractometer using Cu Kα X-rays (wavelength of 1.5406 Å). The measurements were made in the 2θ range 5–80° with a step interval of 0.033°. The results were evaluated with the Crystallographica Search-Match program.

SEM/EDS analyses of ground ABC samples on adhesive carbon tape were used to investigate the morphology and elemental composition of the samples. The Zeiss ULTRA Plus field emission scanning electron microscope was equipped with an energy dispersive spectrometer (EDS Oxford X-Max SDD 50 mm^2 106 detector) and INCA 4.14 X-ray microanalysis software. Before analysis, the samples were coated with Au/Pd (80:20). SEM images were taken at an acceleration voltage of 5 kV and a working distance of 5.5 mm with the SE detector, while the elemental analysis of the particles was performed by EDS at 20 kV.

3. Results and Discussion

3. 1. Pyrolysis of Meat and Bone Meal

The dynamic TGA measurements of the MBM pyrolysed up to 600 °C and 1000 °C show (Figure 1) a similar course for the samples heated at all the heating rates for the observed time period. The mass loss of the samples pyrolysed up to 600 °C varied between 57.6 % and 59.7 % (Figure 1a, Table 1) with relative standard deviations of the replicates being between 0.76 % and 1.75 %. Although there are statistically significant differences ($p < 0.05$) in the mass losses of the samples with different heating rates, a weak correlation between the heating rates and the mass losses was observed. An additional step can be observed in the curves heated up to 1000 °C (Figure 1b), resulting in a total mass loss of at most 71.4 % and 71.5 % for the heating rates of 5 °C min^{-1} and 10 °C min^{-1}, respectively. With the increased heating rate, the mass loss of the sample diminishes, so that at a heating rate of 100 °C min^{-1} it is only 66.6 % (Table 1). We can conclude that at higher heating rates there was not enough time for some of the thermal processes to be completed and therefore certain components were not released from the system.

The same curves on a common temperature scale (Figure 2) indicate that the first step, i.e., dehydration, occurs up to 150 °C and is relatively small and similar for all the heating rates (2–4 %). The main mass loss after that temperature, for the curve with the lowest heating rate, can be distinguished in a few related steps. The weight loss up to 210 °C (1.6 %) is attributed to the evaporation of low-molecular-weight compounds and the decomposition reactions. The major event occurs in the temperature interval 210–450 °C and is due to the degradation reactions of the organic intermediates.[25] A shoulder at 340–350 °C (Figure 1a, DTG curve-embedded graph) probably corresponds to the start of the degradation of the bones[2,4]. The latter processes overlap at higher heating rates. In the last part of the decomposition, which takes place from 600 °C to 1000 °C, additional mass losses can be attributed to the

Table 1. Sample abbreviations and comparison of the results of the dynamic pyrolysis measurements up to 600 °C and up to 1000 °C.

Sample	T interval /°C	Heating rate /°C min^{-1}	Group name	Total mass loss/%	Inflection point /°C
T1H005	25–600	5	T1ABC	59.5	309.4
T1H010		10		57.7	320.2
T1H020		20		57.6	335.1
T1H050		50		58.4	351.1
T1H100		100		59.7	361.2
T2H005	25–1000	5	T2ABC	71.4	308.4
T2H010		10		71.5	323.1
T2H020		20		68.6	338.0
T2H050		50		68.1	352.3
T2H100		100		66.6	365.2

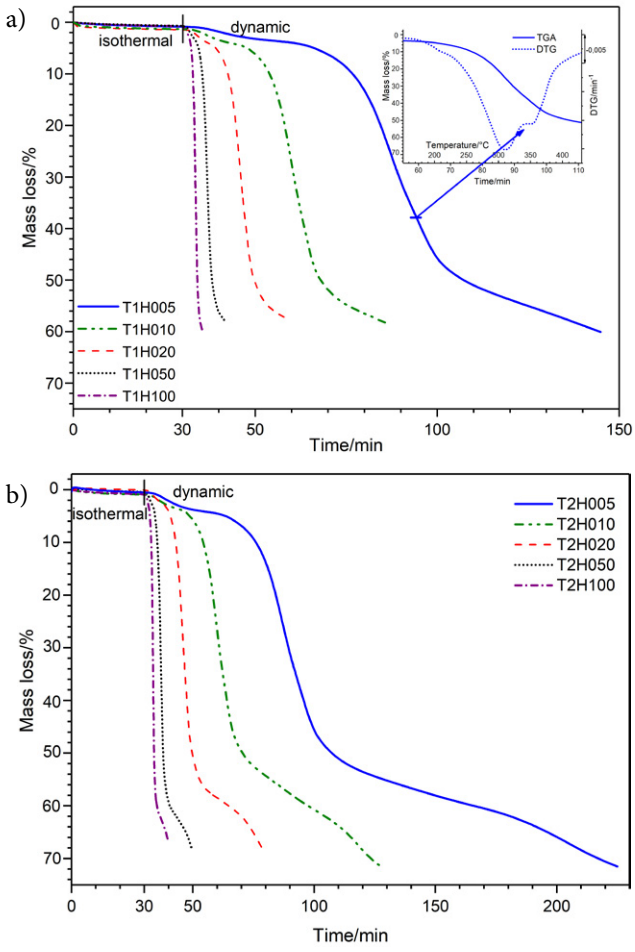


Figure 1. Dynamic TGA curves of the MBM pyrolysed up to 600 °C (a) and pyrolysed up to 1000 °C (b) measured with five different heating rates (5 °C min^{-1}, 10 °C min^{-1}, 20 °C min^{-1}, 50 °C min^{-1} and 100 °C min^{-1}).

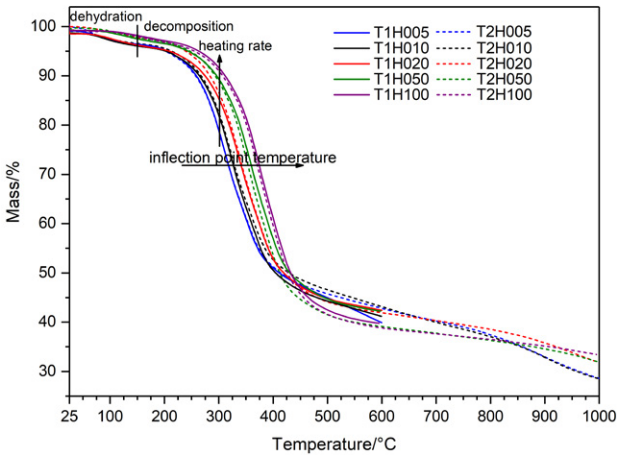


Figure 2. Inflection point determination for the dynamic pyrolysis curves up to 600 °C and up to 1000 °C at all heating rates (5 °C min^{-1}, 10 °C min^{-1}, 20 °C min^{-1}, 50 °C min^{-1} and 100 °C min^{-1}).

decomposition of the carbonates and other mineral components.

All the curves (in Figure 2), regardless of the final temperature, show a shift in the temperatures of the maximum rate of decomposition (inflection point) which expand between 309.4 °C and 361.2 °C for the samples heated up to 600 °C and between 308.4 °C and 365.2 °C for the samples heated up to 1000 °C to higher temperatures at even temperature intervals with the increasing heating rate (Table 1). These temperatures are in accordance with the data given by other authors for a heating rate of 10 °C min^{-1}, for example, 310 °C by Chaala and Roy[3], 335 °C by Conesa et al.[4], and 346 °C by Ayllón et al.[6] The inflection points occur in the range 72.3–74.6 % of the sample mass, as indicated by the position of the arrow on the graph. The appearance of an inflection point in the first part of the MBM decomposition indicates that a decomposition process above 600 °C seen on the curves measured up to 1000 °C, is slower and gradual.

3. 2. Determination of the Ash Content in MBM and T1ABC Samples

The results of TGA determination of the ash content in the MBM and T1ABC samples are presented in Figure 3. For all the curves a similar course with several distinctive step losses was observed. The first one, the release of hygroscopic moisture in the temperature range up to 106 °C in a nitrogen atmosphere, for all the ABC samples and the MBM is expected to be small and similar, between 2.9 % and 3.8 % (Table S1 in Supplementary Material). In the temperature range between 106 °C and 550 °C in an oxygen atmosphere the major contributions to the weight loss of the samples appear; these are associated with the two-step exothermic decomposition of the organic matter as can be seen for the DSC curve of sample T1H100 in Figure 4, associated with the formation and later decomposition of the intermediate fractions, which only occur in the presence of oxygen.[4] The remainder of the isothermal part at 550 °C is the amount of ash in the sample. The results show that the ash quantity in the T1ABC samples increases with the heating rate of the MBM pyrolysis: from 57.4 % at 5 °C min^{-1} to 66.6 % at the highest heating rate.

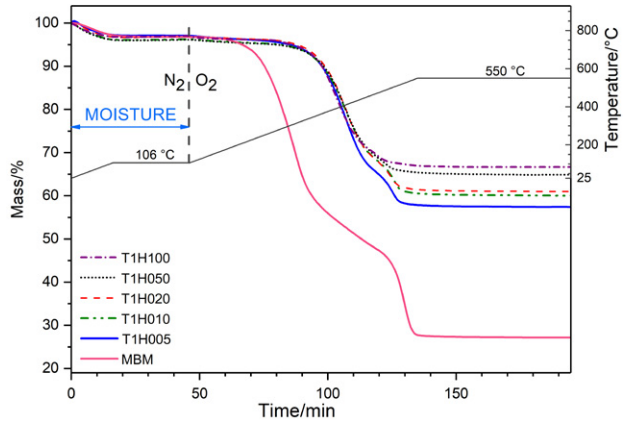


Figure 3. Ash-content determination for T1ABC curves at all five heating rates and MBM sample up to 550 °C.

Figure 4 shows the result curves for the simultaneous TGA–DSC–MS analysis as a sample case, which was performed on the pyrolytic residue of the T1H100 sample using the ash-content determination method. The monotonic decline in the signal *m*/*z* 18 and *m*/*z* 44 for the ambient moisture (beside the hygroscopic moisture on the sample) and the carbon dioxide captured in the oven when opening, appears in the nitrogen segments. Switching to the oxygen atmosphere at 106 °C, gives rise to the CO_2 gas with accompanying two consecutive exothermic peaks seen on DSC curve, which could be due to the combustion of light aliphatic hydrocarbons C_4H_4, C_2H_6 (*m*/*z* 52 and *m*/*z* 30)

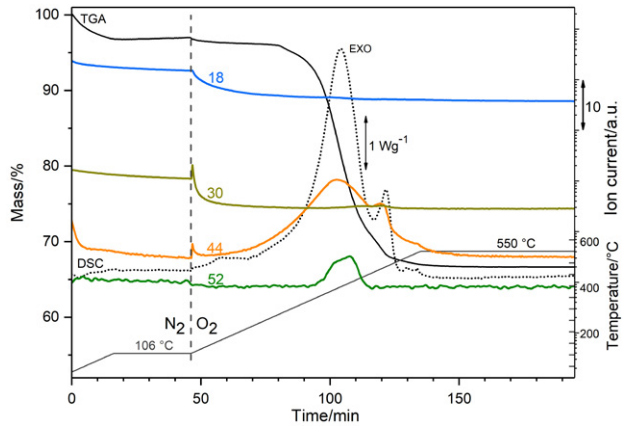


Figure 4. Simultaneous TGA–DSC–MS analysis of the residue of the T1H100 sample up to 550 °C.

and in particular to the burned organic residue after the pyrolysis (char), in accordance with database of National Institute of Standards and Technology (NIST).

3. 3. Elemental Analyses of MBM and ABC Samples

To evaluate the potential hazard posed by PTE in the MBM sample the semi-total concentrations of Cr, Ni, Cu, Zn, As, Mo, Cd and Pb were determined in the MBM and T1H005 sample and to evaluate the mineral-part composition of the samples also the concentrations of some macro elements. The elements contained in the original biomass, except elements that are volatile at the pyrolysis temperature, remain in the final products and are therefore more concentrated. The results (see Table S2 in Supplementary Material) showed that the concentrations of PTE in the MBM and T1H005 samples are very low, confirming the low potential environmental risk of both samples according to the PTE content. The concentrations of the PTE elements in both samples are far below the thresholds recommended by the EBC for biochar intended for agricultural use.[14]

The results of the CHNS analyses of the MBM and ABC samples, obtained after the pyrolysis of MBM up to 600 °C (T1ABC samples), are presented in Table 2. As a result of the heat treatment of the MBM, the mass content of the C, H, N and S in the residues decreased. The C, H, N and S contents in the MBM sample are comparable with the literature data, where broad concentration intervals are reported for these elements.[2] This important variation in MBM composition strongly influences the thermochemical treatment of MBM.

Pyrolysed organic matter with a carbon content lower than 50 % is classified as pyrogenic carbonaceous material.[14] The presence of C in the pyrolytic residues is the result of small organic remains, carbonized in argon, and the present of inorganic carbonate groups (CO_3^{2-}), while H, N and S are found predominantly incorporated within the aromatic rings as hetero-atoms and thought to be a major contribution to the highly heterogeneous surface chemistry and reactivity of biochar.[26] The content of sulphur in all the T1ABC samples (Table 2) is below the detection limit, while the concentrations of C, H and N decreased with increasing heating rate. The results are in accordance with the findings of previous studies, which showed that with increasing pyrolysis rate of biomass the yield of solid char decreases while the yields of gas and liquid phase increases.[7,27] A lower heating rate allows most of the decomposed organic part of the MBM to be carbonized and thus remain in the solid residue, resulting in a higher carbon content in the samples prepared at a lower heating rate. At higher heating rates, the organic part of the MBM meal decomposes to a lesser extent, but the greater part of the decomposed organic matter is converted to the gas and liquid phase as it is carbonized and remains in the solid residue.

The molar ratios H/C_{org} and N/C_{org} are carbonization degree parameters that characterize the degree of aromaticity of the biochar samples.[14] The H/C_{org} as well as the N/C_{org} molar ratios in the T1ABC samples are comparable (on average 0.53 ± 0.04 and 0.162 ± 0.004, respectively) and represent nearly 30 % and 78 % of the H/C_{org} and N/C_{org} molar ratios of the MBM samples (Table 2). The results indicate a greater loss of H-related than N-related functional groups during the heat treatment of MBM up to 600 °C.

Although there are few studies on the characteristics of ABC obtained by pyrolysis of bone meal, the literature on the composition and characteristics of MBM pyrolysis products is sparse. Ayllón et al.[7] investigated the influence of temperature (between 300 °C and 900 °C) and heating rate (from 2 °C to 14 °C) on the fixed bed pyrolysis of MBM. The MBM used in their study had a much higher organic matter content (higher content of CHNS) and consequently an almost 10 % lower ash content than MBM used in our study, making the composition and properties of char samples prepared under conditions similar to those used in our study difficult to compare.

Table 2. Results of CHNS analyses of MBM and T1ABC samples and calculated quantities and ratios.

Sample	*w*(C) /%	*w*(H) /%	*w*(N) /%	*w*(S) /%	*w*(C_{org}) /%	*n*(H) /*n*(C_{org})	*n*(N) /*n*(C_{org})
MBM	38.23	5.52	9.16	0.62	37.71	1.74	0.21
T1H005	29.95	1.27	5.55	<0.1	28.40	0.53	0.17
T1H010	29.28	1.16	5.30	<0.1	27.80	0.50	0.16
T1H020	28.34	1.12	5.12	<0.1	26.95	0.49	0.16
T1H050	22.38	1.06	3.83	<0.1	20.97	0.53	0.16
T1H100	21.08	0.86	3.66	<0.1	19.54	0.60	0.16

3. 4. FTIR Spectroscopy

FTIR spectroscopy was used to compare the presence of functional groups in the untreated MBM sample and the residues after pyrolysis of the MBM sample. The FTIR spectra of the original MBM sample and the commercially available hydroxyapatite (Merck, p.a.) are shown in Figure 5. The broad bands at 3671 cm^{-1} and 3281 cm^{-1} in the vibrations-rich FTIR spectrum of the MBM are attributed to the stretching vibrations of the O–H bond. The peak near 3700 cm^{-1} corresponded to vibrations of the OH groups in inorganic components of the MBM sample, while the O–H vibrations of the organic matter appeared at approximately 3000–3300 cm^{-1}.[28] The sharp bands at 2919 cm^{-1} and 2851 cm^{-1} belong to the asymmetric and symmetric stretching vibrations of the C–H bond. In the range from 1750 cm^{-1} to 1600 cm^{-1} the C=O stretching vibrations of amide (amide I vibra-

tions) could be assigned, while C–N stretching vibrations strongly coupled with N–H bending vibrations (amide II) and N–H in plane bending vibrations coupled with C–N stretching vibrations (amide III) including C–H and N–H deformation vibrations are found in the range from 1600 cm^{-1} to 1500 cm^{-1} and 1350 cm^{-1} to 1200 cm^{-1}, respectively.[29] All these bands represent the organic phase of the MBM.[23] The carbonate asymmetric stretching vibrations typically occur between 1410 cm^{-1} to 1530 cm^{-1}.[21,25,30] The presence of carbonate in our sample also indicates the observed weak band at 880 cm^{-1} which could be attributed to the carbonate out-of-plane bending vibrations. The bands in the range from 1100 cm^{-1} to 1000 cm^{-1} (asymmetric stretching vibrations) and from 600 cm^{-1} to 500 cm^{-1} belong to the relatively strong vibrations of the P–O bond of the phosphate group.[31] The most prominent band in the FTIR spectrum of synthetic HA (Figure 5) and the main evidence for the presence of the phosphate group in the compounds is observed at 1026 cm^{-1}. A small band at 892 cm^{-1} could belong to the vibrations of the HPO_4^{2-} group and indicates the presence of the calcium-deficient apatite $Ca_{10-x}(HPO_4)_x(PO_4)_{6-x}(OH)_{2-x}$.[5,31]

During the pyrolysis of MBM most of the organic substances decompose and remain in ABC as small carbonized residues or removed as gas products. The FTIR spectra of the residues of the pyrolysed MBM up to 600 °C (T1ABC) are present in Figure 6a. Weak vibrations of the O–H group in the mineral matter are observed near 3670 cm^{-1}. The intense broad band near 3300 cm^{-1}, observed in the FTIR spectra of the MBM, and which corresponded to the vibrations of the OH group in the organic matter, disappeared, suggesting that a large amount of free and associated hydroxyl groups and structural hydroxyl groups were decomposed during the MBM pyrolysis up to 600 °C.[28] The weak split bands of the asymmetric and symmetric stretching vibrations of the C–H bond (2987 cm^{-1} and 2901 cm^{-1}) were further observed. The group of bands with the maximum at 1407 cm^{-1} could be attributed to C–C stretching vibrations together with the asymmetric stretching vibrations of the C–O bond in the carbonate group.[21,30] The presence of carbonate also indicates the absorption band at about 871 cm^{-1}. The most intense band in the spectra of the T1ABC samples belongs to the stretching vibrations of the phosphate group where a slow shift of the band maxima from 1067 cm^{-1} at sample T1H100 to 1026 cm^{-1} at sample T1H005 was observed.

The main phosphate-group vibration bands in the FTIR spectra of MBM pyrolysis residues during the thermal treatment up to 1000 °C (Figure 6b) are found at 1026 cm^{-1} for all the T2ABC samples. Small band shoulders near 957 cm^{-1} and 1100 cm^{-1} were observed which can be assigned to the β-tricalcium phosphate phases.[30] The presence of the β-$NaCaPO_4$ phase was also confirmed in XRD spectra of T2ABC samples (see Figure 7), prepared at lower heating rates. At 3670 cm^{-1} the weak band of stretching vibrations of the inorganic O–H group was still visible. We also observed the weak bands of the C–H stretching vibrations (2987 cm^{-1} and 2901 cm^{-1}),

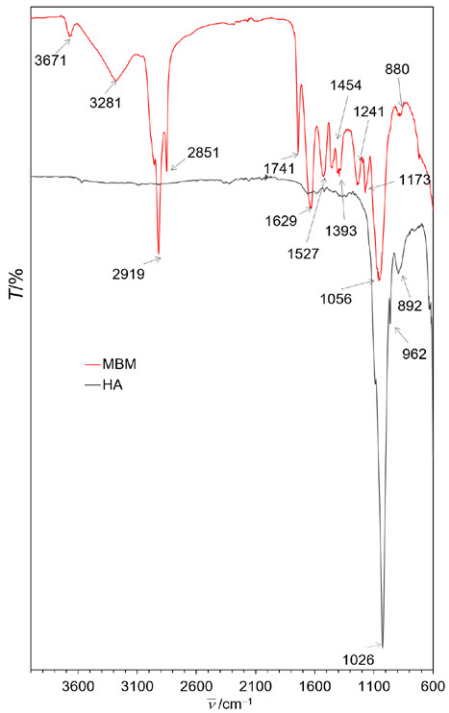


Figure 5. FTIR spectra of untreated MBM sample and commercially available hydroxyapatite.

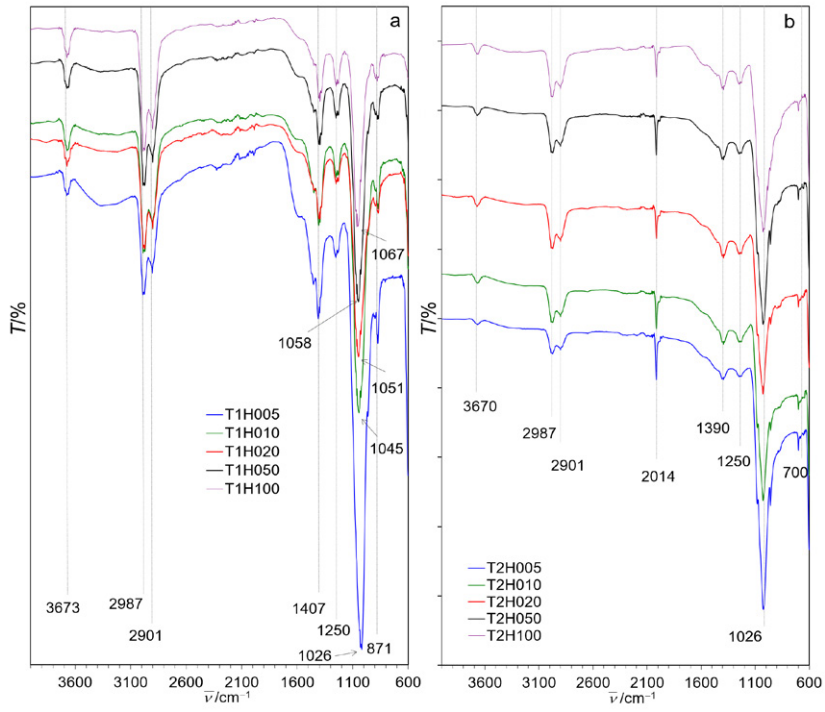


Figure 6. FTIR spectra of residues after MBM pyrolysis up to 600 °C (a) and up to 1000 °C (b) at five different heating rates.

while the carbonate group vibrations (1407 cm^{-1} and 871 cm^{-1}) disappeared. In all T2ABC samples, a new sharp band of unknown origin is observed at 2014 cm^{-1}, which is also observed in FTIR spectra of animal bones pyrolysed at 450 °C and higher[22] and in FTIR spectra of monolithic bone blocks pyrolysed at 800 °C.[21] Since the band is not observed in the FTIR spectrum of synthetic hydroxyapatite (see Figure 5), we conclude that it probably belongs to an inorganic form of C that was trapped in the structure.

3. 5. X-ray Powder Diffraction Analysis

The results of the X-ray powder-diffraction analyses showed that the peak intensities of all the T1ABC samples, regardless of the heating rate, indicate the presence of poorly crystalline phases (Figure 7). The weak broad peaks with no visible peak splitting observed can be attributed to Cl-bearing hydroxyapatite. A decrease in the peak width and a considerable increase in the peak intensity can be observed for the ABC prepared for the pyrolysis end temperature of 1000 °C (T2ABC samples) at lower heating rates. This indicates an increase in the size of the crystals, since crystallinity is a measure of the particle size.[26] The crystallinity of the samples decreases with the higher heating rates, suggesting that some of the phases present are still not well crystallized. The presence of crystalline Cl-bearing hydroxyapatite ($Ca_5(PO_4)_3$(-Cl,OH) and β-sodium calcium phosphate ($NaCaPO_4$) was confirmed.

3. 6. SEM/EDS Analysis

The results of the SEM/EDS analyses revealed the strong influence of both, the pyrolysis end temperature and the heating rate on the morphology and the chemical composition of the final products. Figure 8 presents SEM images of the MBM pyrolysis residues obtained at pyrolysis end temperature 600 °C (upper row) and 1000 °C (bottom row) and at heating rates of 5 °C min^{-1} (a and d), 20 °C min^{-1} (b and e) and 100 °C min^{-1} (c and f).

In the SEM images of the T1ABC samples (Figure 8, upper row) large amorphous agglomerates with varying rough to smooth surface texture were observed. In sample T1H005 the very beginning of small, poorly crystalline particles (up to few 100 nm), together with amorphous spilled formations (the EDS analysis shows us that these are amorphous KCl and NaCl – see Figure 9) are clearly visible.

The SEM images of the T2ABC samples (Figure 8, bottom row) give us a completely different picture. The difference in particle size is clearly visible. The size of the well-crystallized particles of T1H005 ranges from less than 0.5 μm to several tens of μm. Also in the sample T2H020 the particles are already well crystallized, but in contrast to the particles in the sample T2H005 they are much smaller (from less than 1 μm up to a few μm) and stacked together into larger aggregates. The particles in the sample T2H100 exhibit very poor crystallinity. They are located in small aggregates and reach a size of up to 1 μm.

The distribution of elements over a particular area of the sample can be viewed using EDS elemental mapping. Element maps of the samples T1H005, T2H005, T1H100

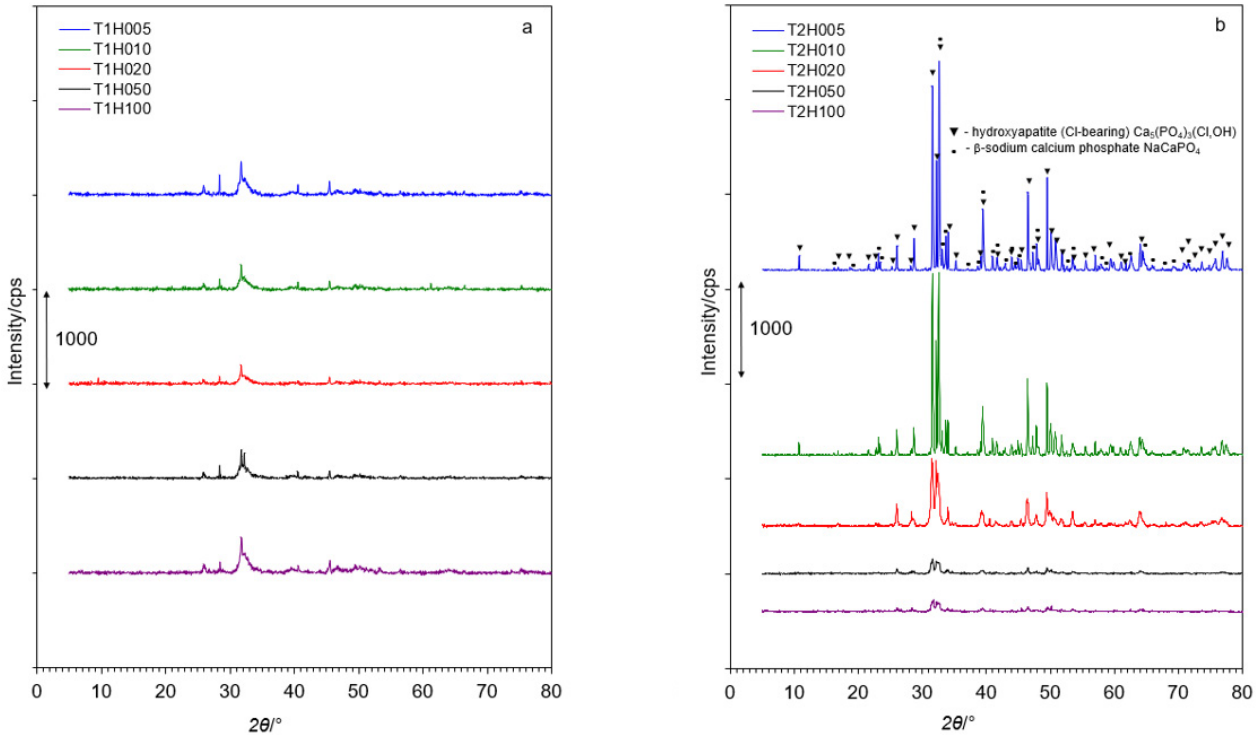


Figure 7. XRD pattern of residues after pyrolytic MBM decomposition up to 600 °C (left) and 1000 °C (right) for different heating rates.

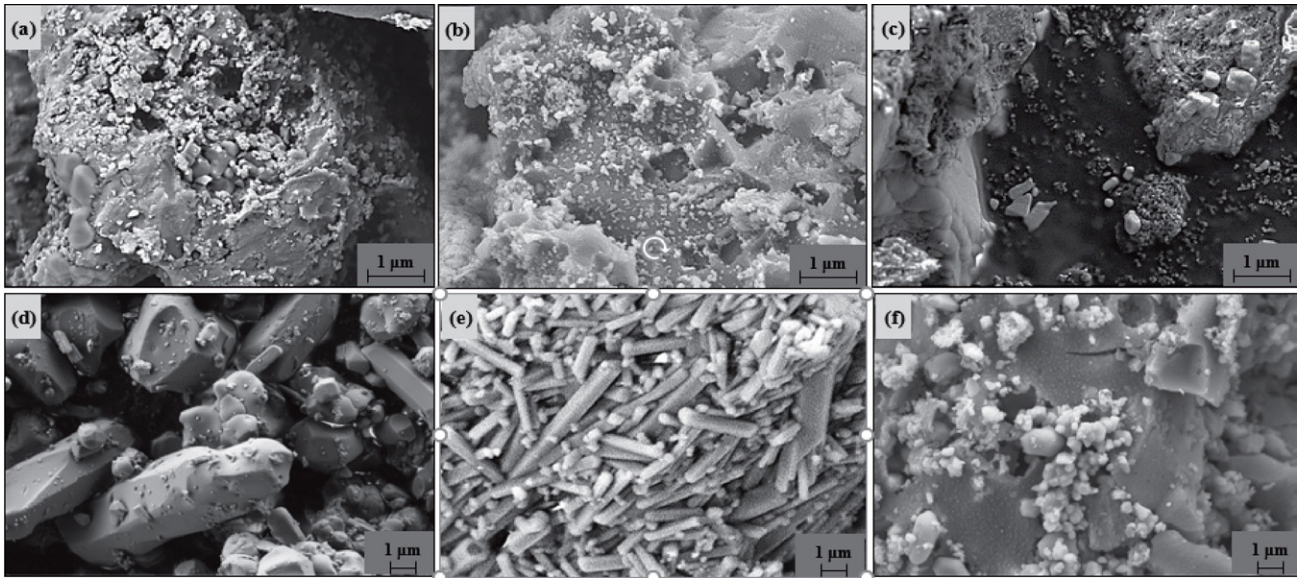


Figure 8. SEM images of T1ABC (upper row) and T2ABC (bottom row) samples at heating rates 5 °C min^{-1} (a and d), 20 °C min^{-1} (b and e) and 100 °C min^{-1} (c and f).

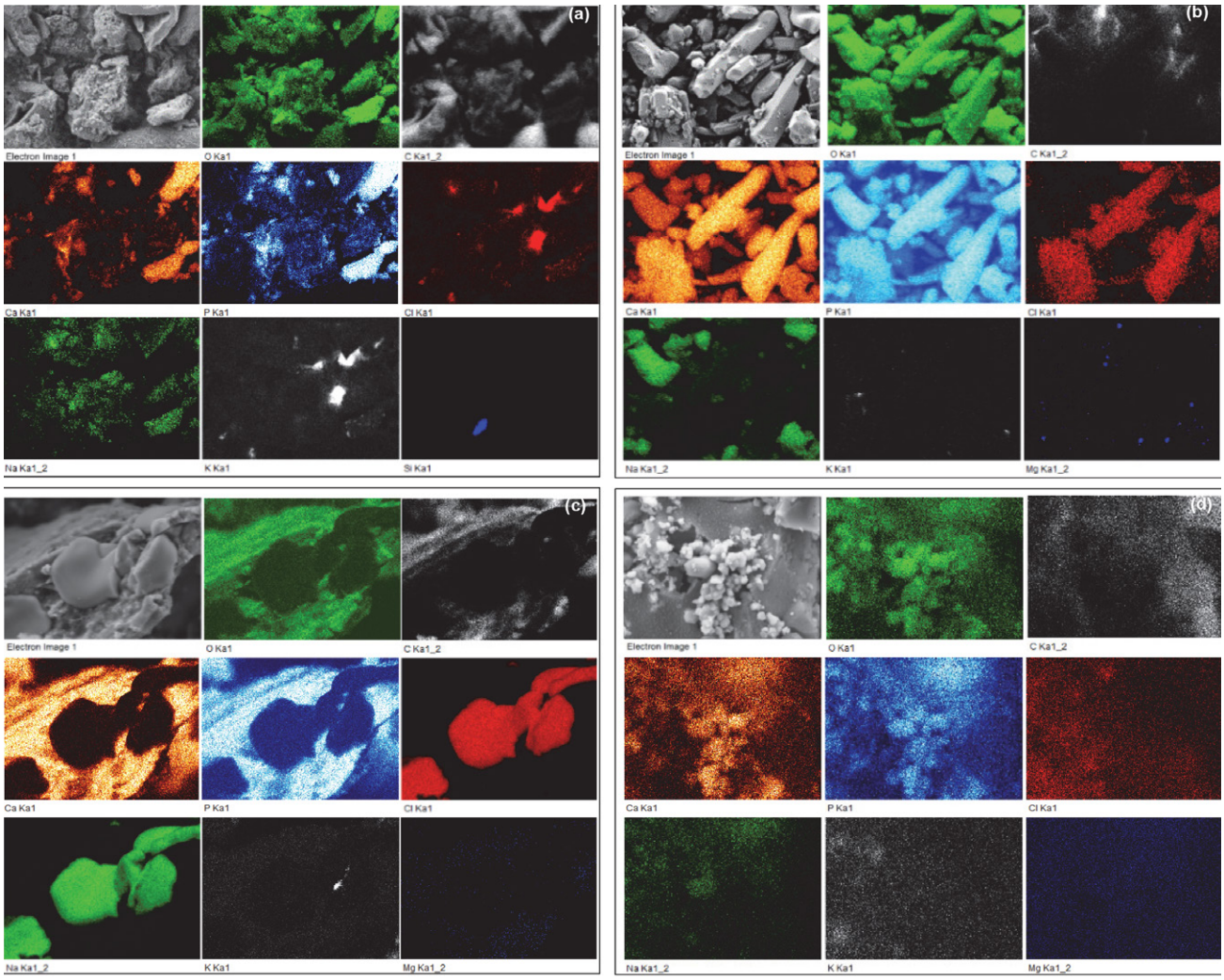


Figure 9. EDS maps of elemental distribution in the samples T1H005 (a), T2H005 (b), T1H100 (c) and T2H100 (d). Distribution of the elements from left to right for all samples: upper line – electron image, oxygen, carbon; in the middle – calcium, phosphorus, chlorine; bottom line – sodium, potassium, magnesium or silicon (sample T1H005).

and T2H100 are shown in Figure 9. The EDS analyses revealed that carbon (grey images in the top right of the maps (a) and (c)) is still present in samples T1H005 and T1H100. The co-appearance of oxygen (green images in the first line), calcium (orange images) and phosphorus (pale-blue images) is clearly evident for all four samples, indicating the presence of apatite. For sample T1H005 a dispersed distribution of sodium is observed, although it is generally consistent with the distribution of Ca and P. The presence of KCl and a small particle containing silicon are also observed. For sample T1H100, sodium is observed in the form of amorphous NaCl, deposited onto the porous surface of the apatite.

Compared to the sample T1H005, where the composition of the apatite particles is relatively uniform, a more diverse composition of apatite is observed in the T2H005 sample. The chlorine-bearing (red image) apatite particles, whose presence was confirmed by XRD analysis, contain the largest amount of calcium. In the apatite particles with a lower calcium content the higher sodium content was observed. The presence of β-sodium calcium phosphate was also confirmed by XRD analysis. In the sample T2H100 the disperse distribution of the elements is observed, although the co-association of O, Ca and P is clearly visible.

4. Conclusions

The results of the MBM pyrolysis study at various final temperatures of pyrolysis and various heating rates revealed the strong influence of both, not only the pyrolysis end temperature, but also the strong influence of the heating rate on the morphology and chemical composition of the final products.

The TGA measurements showed a similar course of pyrolysis for the MBM samples heated at all the heating rates with the major pyrolytic event occurring in the temperature interval 210–450 °C being due to the degradation reactions of organic intermediates. An additional mass loss up to 12 % above 600 °C at low heating rates can be attributed to the decomposition of carbonates and other mineral components. Diminishing of the mass loss with increasing heating rate suggest a shortage of time for some thermal processes to be completed. The ash content in the T1ABC samples was in general increased with the increasing heating rate.

The concentrations of PTE in the MBM are very low, which confirmed that the MBM pyrolytic residues are environmentally acceptable materials. The results of the CHNS analyses of the MBM and T1ABC samples showed that the concentrations of carbon, hydrogen and nitrogen decreased with increasing heating rate and indicated a greater loss of H-related than N-related functional groups. The results of the X-ray powder diffraction analyses showed that the peak intensity of all the residues of the pyrolysis end temperature at 600 °C, regardless of the rate of heating, indicates a low crystallinity, while the crystallinity of the samples obtained for the pyrolysis of the MBM to 1000 °C is reduced at higher heating rates. The presence of Cl-bearing hydroxyapatite and β-sodium calcium phosphate was determined. The results of the SEM/EDS analyses revealed the strong influence of the pyrolysis end temperature and the heating rate on the morphology and chemical composition of the final products of the meat and MBM pyrolysis and confirmed the results of the XRD analyses.

Although in practice raw MBM samples differ considerably in organic matter content, which can have a very strong influence on the pyrolysis process itself, our results have clearly shown that both, a pyrolysis end temperature of at least 600 °C or higher and lower heating rates are required to produce ABC samples with satisfactory properties.

The results of this study imply the utilization of the pyrolysis residue of industrial by-products such as MBM as one of the attractive approaches that could improve the sustainable use of phosphate-bearing sources.

Acknowledgements

The authors would like to thank the Slovenian Research Agency (ARRS) for the financial support of the Network of Research Infrastructure Centres of the University of Ljubljana (MRIC UL), on whose equipment the part of the research was carried out, and for the financial support from the research programme P1-0134b: Chemistry for Sustainable Development. Thanks also to the native speaker Dr. Paul John McGuiness for his contribution to the improvement of the English language.

Declaration of conflicting interest

The authors declare that they have no known competing financial interests or personal relationships that could have appeared to influence the work reported in this paper.

5. References

1. N. Vassilev, E. Martos, G. Mendes, V. Martos and M. Vassileva, *J. Sci. Food Agric.* **2013**, *93*, 1799–1804. **DOI:**10.1002/jsfa.6130
2. E. Cascarosa, G. Gea and J. Arauzo, *Renewable Sustainable Energy Rev.* **2012**, *16*, 942–957. **DOI:**10.1016/j.rser.2011.09.015
3. A. Chaala and C. Roy, *Environ. Sci. Technol.* **2003**, *37*, 4517–4522. **DOI:**10.1021/es026346m
4. J. A. Conesa, A. Fullana and R. Font, *J. Anal. Appl. Pyrolysis* **2003**, *70*, 619–630. **DOI:**10.1016/S0165-2370(03)00044-5
5. E. Deydier, R. Guilet, S. Sarda and P. Sharrock, *J. Hazard. Mater.* **2005**, *121*, 141–148. **DOI:**10.1016/j.jhazmat.2005.02.003
6. M. Ayllón, G. Gea, M. B. Murillo, J. L. Sánchez and J. Arauzo, *J. Anal. Appl. Pyrolysis* **2005**, *74*, 445–453. **DOI:**10.1016/j.jaap.2004.11.022

7. M. Ayllón, M. Aznar, J. L. Sánchez, G. Gea and J. Arauzo, *Chem. Eng. J.* **2006**, *121*, 85–96. **DOI:**10.1016/j.cej.2006.04.013
8. M. Coutand, M. Cyr, E. Deydier, R. Guilet and P. Clastres, *J. Hazard. Mater.* **2008**, *150*, 522–532. **DOI:**10.1016/j.jhazmat.2007.04.133
9. I. Gulyurtlu, D. Boavida, P. Abelha, M. H. Lopes and I. Cabrita, *Fuel* **2005**, *84*, 2137–2148. **DOI:**10.1016/j.fuel.2005.04.024
10. G. Skodras, P. Grammelis, P. Basinas, S. Kaldis, E. Kakaras and G. P. Sakellaropoulos, *Fuel Process. Technol.* **2007**, *88*, 787–794. **DOI:**10.1016/j.fuproc.2007.03.009
11. O. Senneca, *Fuel* **2008**, *87*, 3262–3270. **DOI:**10.1016/j.fuel.2008.04.012
12. E. Cascarosa, L. Gasco, G. García, G. Gea and J. Arauzo, *Resour. Conserv. Recycl.* **2012**, *59*, 32–37. **DOI:**10.1016/j.resconrec.2011.06.005
13. S. Bhardwaj, M. Sharon and M. Sharon, in: W. S. Donahue, J. C. Brandt (Ed): Pyrolysis: Types, Processes, and Industrial Sources and Products, Nova Science Publishers, UK, **2009**, pp. 117–130.
14. EBC, European Biochar Certificate - Guidelines for a sustainable production of biochar. European Biochar Foundation (EBC). Version 8.2E of 19th April 2019). **DOI:** 10.13140/RG.2.1.4658.7043
15. M. J. Zwetsloot, J. Lehmann, T. Bauerle, S. Vanek, R. Hestrin and A. Nigussie, *Plant Soil* **2016**, *408*, 95–105. **DOI:**10.1007/s11104-016-2905-2
16. N. A. Medellin-Castillo, R. Leyva-Ramos, E. Padilla-Ortega, R. O. Perez, J. V. Flores-Cano and M. S. Berber-Mendoza, *J. Ind. Eng. Chem.* **2014**, *20*, 4014–4021. **DOI:**10.1016/j.jiec.2013.12.105
17. S. B. Chen, Y. G. Zhu, Y. B. Ma and G. McKay, *Environ. Pollut.* **2006**, *139*, 433–439. **DOI:**10.1016/j.envpol.2005.06.007
18. J. C. Moreno-Piraján, R. Gómez-Cruz, V. S. García-Cuello and L. Giraldo, *J. Anal. Appl. Pyrolysis* **2010**, *89*, 122–128. **DOI:**10.1016/j.jaap.2010.06.007
19. M. Morshedizad, D. Zimmer and P. Leinweber, *J. Soil Sci. Plant Nutr.* **2016**, *179*, 388–398. **DOI:**10.1002/jpln.201500604
20. E. Gruden, P. Bukovec and M. Zupančič, *Acta Chim. Slov.* **2017**, *64*, 577–581. **DOI:**10.17344/acsi.2016.2889
21. M. Krzesińska and J. Majewska, *J. Anal. Appl. Pyrolysis* **2015**, *116*, 202–214. **DOI:**10.1016/j.jaap.2015.09.009
22. S. Patel, J. Han, W. Qiu and W. Gao, *J. Environ. Chem. Eng.* **2015**, *3*, 2368–2377. **DOI:**10.1016/j.jece.2015.07.031
23. C. K. Rojas-Mayorga, A. Bonilla-Petriciolet, I. A. Aguayo-Villarreal, V. Hernández-Montoya, M. R. Moreno-Virgen, R. Tovar-Gómez and M. A. Montes-Morán, *J. Anal. Appl. Pyrolysis* **2013**, *104*, 10–18. **DOI:**10.1016/j.jaap.2013.09.018
24. K. Tõnsuaadu, K. A. Gross, L. Plūduma and M. Veiderma, *J. Therm. Anal. Calorim.* **2012**, *110*, 647–659. **DOI:**10.1007/s10973-011-1877-y
25. B. Charmas, *Thermochim. Acta* **2013**, *573*, 73–81. **DOI:**10.1016/j.tca.2013.08.032
26. J. Bourke, M. Manley-Harris, C. Fushimi, K. Dowaki, T. Nunoura and M. J. Antal, *Ind. Eng. Chem. Res.* **2007**, *46*, 5954–5967. **DOI:**10.1021/ie070415u
27. P. T. Williams and S. Besler, *Renew. Energy* **1996**, *7*, 233–250. **DOI:**10.1016/0960-1481(96)00006-7
28. J. Jin, Y. Li, J. Zhang, S. Wu, Y. Cao, P. Liang, J. Zhang, M. H. Wong, M. Wang, S. Shan and P. Christie, *J. Hazard. Mater.* **2016**, *320*, 417–426. **DOI:**10.1016/j.jhazmat.2016.08.050
29. E. P. Paschalis, R. Mendelsohn and A. L. Boskey, *Clin. Orthop. Relat. Res.* **2011**, *469*, 2170–2178. **DOI:**10.1016/j.tca.2006.04.013
30. S. Meejoo, W. Maneeprakorn and P. Winotai, *Thermochim. Acta* **2006**, *447*, 115–120. **DOI:**10.1016/j.tca.2006.04.013
31. A. Destainville, E. Champion, D. Bernache-Assollant and E. Laborde, *Mater. Chem. Phys.* **2003**, *80*, 269–277. **DOI:**10.1016/S0254-0584(02)00466-2

Povzetek

Izčrpavanje zalog fosfatnih rud kot glavnega vira fosforja je privedlo do iskanja novih, alternativnih in okolju prijaznejših produktov in procesov pridobivanja. Eden izmed varnih in okolju prijaznih fosfatnih virov je oglje iz živalskih kosti (ABC), pridobljeno s pirolizo mesno-kostne moke (MBM). V predstavljeni študiji smo raziskovali vpliv pogojev pirolize MBM na fizikalno-kemijske lastnosti pripravljenih produktov (ABC). Pirolizo MBM smo izvedli pri dveh končnih temperaturah (600 °C in 1000 °C) in petih različnih hitrosti segrevanja (5 °C min^{-1}, 10 °C min^{-1}, 20 °C min^{-1}, 50 °C min^{-1} in 100 °C min^{-1}). Pridobljene vzorce ABC smo okarakterizirali z rentgensko praškovno difrakcijo, IR spektroskopijo, elementno CHNS analizo in SEM/EDS analizo. Rezultati so pokazali močan vpliv tako končne temperature pirolize kot tudi hitrosti segrevanja na morfologijo in kemijsko sestavo pridobljenih produktov.

Except when otherwise noted, articles in this journal are published under the terms and conditions of the Creative Commons Attribution 4.0 International License

Scientific paper

Hydrogen Bonds in Bis(1*H*-benzimidazole-κN^3)cadmium(II) Dibenzoate: Hirshfeld Surface Analysis and AIM Perspective

Jia-Jun Wang,[1,2] Li-Nan Dun,[1,2] Bao-Sheng Zhang,[1,2] Zhong-Hui Wang,[3] He Wang,[1,2] Chuan-Bi Li[1,2,*] and Wei Liang[1,2,*]

[1] *Key Laboratory of Preparation and Application of Environmental Friendly Materials, Ministry of Education, Jilin Normal University, Changchun 130103, China*

[2] *Chemistry Department of Jilin Normal University, Siping 136000, China*

[3] *Sulfuric Acid Plant, Jilin Petrochemical Company Acrylonitrile Factory, Jilin 132021, China*

** Corresponding author: E-mail: li_c_b@163.com (Chuan-Bi Li); 16433576@qq.com (Wei Liang)*

Received: 10-09-2020

Abstract

The coordination complex bis(1*H*-benzimidazole-κN^3)cadmium(II) dibenzoate has been synthesized and characterized by single crystal diffraction analysis. Cadmium center is six coordinated and formed a distorted octahedron coordinated geometry. The Hirshfeld analysis shows that in the d_{norm}-surface of the compound, there are dark red spots near the hydrogen-bonds acceptor and donor atoms, while intermolecular interactions result in faint-red spots. The AIM analysis was performed, there exist a BCP in each N(C)–H···O hydrogen bond, the bond paths also can be seen, the $|V(b)|/G(b) < 1$ and the $H(b) > 0$, the interaction is indicative of being a closed shell. The TG results are consistent with the X-ray diffraction structure.

Keywords: Cd Complex, Crystal Structure, TG, Hirshfeld Surface Analysis, AIM Analysis

1. Introduction

Crystal engineering based on coordination complexes[1] have been fast developing in the last few years owing to their potential applications such as absorption,[2] catalysis,[3] luminescence,[4] *etc.* Coordination complexes have already been applied in all aspects of life, and also used for removing the highly toxic heavy metal ions.[5]

The benzimidazoles (Bzim) possess a phenyl ring fused with imidazole ring.[6] Many substances with benzimidazole scaffold have been deeply participated in variety of life activities. For instance, mebendazole is used for treatment of parasitic diseases,[7] and omeprazole is used for gastric ulcers,[8] etc. Many other important properties of metal complexes containing benzimidazoles have also been investigated by researchers. The antibacterial activity of Bzim Zn(II) and Co(II) complexes have been investigated.[9,10] For Bzim's Ir(III) N-heterocyclic carbene complexes' anticancer and antitumor properties were evaluated.[11,12] Bzim derivate's Pt(II) and Cu(II) complexes have DNA binding and/or antioxidant activity.[13,14] Even the Bzim-functionalized ruthenium complexes can be used for dye-sensitized solar cells (DSSC) or energy-storage.[15–17] Thus, exploring the benzimidazole metal coordination complexes is extremely important.

The hydrogen bonds are critical in life science[18] and chemistry.[19] The Hirshfeld surface analysis[20] and the Atom in Molecule (AIM) theory[21] are two powerful tools to research hydrogen bonds from different perspectives. The Hirshfeld sufaces analysis is able to be utilized to identify a type and region of intermolecular interactions (including hydrogen bonds). Hirshfeld surface analyses comprises d_{norm}- and shape index surfaces, and 2D fingerprint plots (FP). While the AIM theory enables us to analyze the properties of hydrogen bonds. In AIM view, the main concept is based on the bond critical point (BCP), they are the evidence of hydrogen bond is the existence of a bond path and a BCP between the donor hydrogen and the acceptor. People also developed the criteria for the assessment of the existence of hydrogen bonds.[22]

In this article, we synthesized a new benzimidazole coordinated cadmium(II) dibenzoate ($Cd(Bzim)_2(BA)_2$

(where Bzim is benzimidazole and BA is benzoate) through the low temperature hydrothermal method, obtained the crystal structure, calculated the molecular orbitals, carried out the Hirshfeld analysis and the AIM analysis, and we mainly focused on the analysis of the hydrogen bonds.

2. Experiments

$Cd(Ac)_2 \cdot 2H_2O$ (0.235 g, 1.0 mmol), benzimidazole (Bzim, 0.236 g, 2.0 mmol), benzoic acid (BA, 0.244g, 2.0 mmol) and 15 mL water were mixed with stirring followed by adjusting the pH value to 6.5 with an aqueous solution of NaOH. Then the mixture was sealed in a 25 mL Teflon-lined stainless-steel reactor and heated at 100 °C for 96 h to give dark yellow crystals of the title compound after cooling. Yield: 32% (based on Cd). IR (cm^{-1}): 3315(w), 3236(w), 1680(s), 1653(s), 1477(s), 1430(s), 1346(w), 877(w), 787(m), 449(m). Anal. Calcd. (%) for $C_{28}H_{22}CdN_4O_4$: C, 56.86; H, 3.72; N, 9.48; Found (%): C, 56.79; H, 3.81; N, 9.53.

3. Structure Determination and Physical Measurements

A yellow block crystal for **1** was chosen for X-ray diffraction analysis. Crystal structure measurement was performed on a Bruker SMART APEX II CCD diffractometer equipped with a graphite-monochromatic Mo*K*α (λ = 0.71073 Å) radiation. Data integration and reduction were performed using SaintPlus 6.01.[23] Absorption corrections were applied with a multi-scan mode.[24] The structure was solved by direct methods with SHELXS[25] and refined by full-matrix least-squares techniques using SHELXL-2018[26] within WINGX.[27] All non-hydrogen atoms were refined anisotropically. All H atoms on C atoms were positioned geometrically and refined as riding, with C–H = 0.93 and $U_{iso}(H) = 1.2U_{eq}(C)$. The molecular graphics was prepared using program Diamond 3.2.[28]

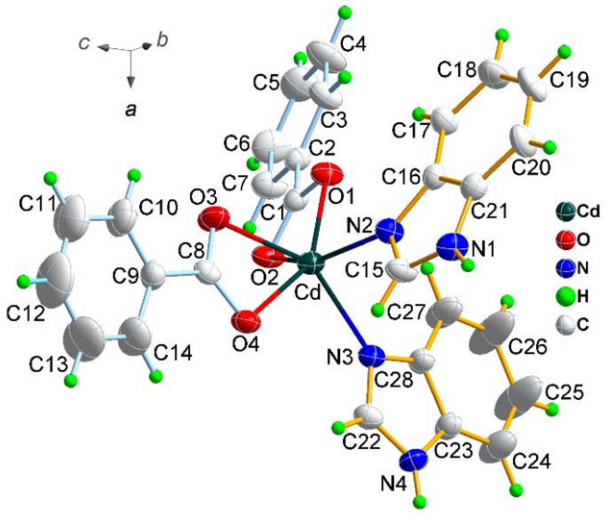


Fig. 1. Molecular structure of $[Cd(Bzim)_2(BA)_2]$, (ellipsoid probability at 30 %).

4. Results and Discussion

4. 1. Structure Description

Table 1. Summary of data collection and structure refinement for the compound.

CCDC	780823
Formula	$C_{28}H_{22}CdN_4O_4$
Formula weight	590.89
Crystal system	Orthorhombic
Space group	*Pbca*
a/Å	14.0359(6)
b/Å	17.7081(8)
c/Å	21.8928(12)
α, b, γ/°	90
V/Å^3	5441.4(5)
Z	8
ρ_{calc}/g cm^{-3}	1.443
Crystal size/mm	0.23×0.20×0.18
F(000)	2384
Reflections collected / unique	37904/6759
R_{int}	0.1203
Data/restraints/parameters	6759 / 0 / 334
Goodness of fit on F^2	0.971
*R*1, *wR*2 (I > 2σ (I))	0.0411, 0.0572
*R*1, *wR*2 (all data)	0.1336, 0.0672
Peak and hole/ e.A^{-3}	0.670, –0.400

A perspective view of the compound, with the atomic numbering scheme, is shown in Fig. **1**. The compound crystallizes in the space group *Pbca* (Table 1). Asymmetric unit consists of a cadmium, two benzimidazole molecules and two benzoic acid ions. The cadmium center is six coordinated and connected four oxygen from two benzoic acids and two nitrogen atoms from two Bzims. Bzim coordinates Cd center in κN coordinate mode and each benzoate ion is bonded to Cd center in a chelating mode. So, the compound can be described as bis(1*H*-benzimidazole-κN^3)cadmium(II) dibenzoate and possess an distorted octahedron geometry.

The Cd–N distances are 2.258(3) and 2.279(3) Å (Table 2), which are not only shorter than the average Cd–$N_{imidazole}$ distance (2.302(3) Å),[29] but also shorter than the Cd–$N_{N\text{-}alkylimidazoles}$ (2.357(2) Å).[30] The Cd–O distances are in the range 2.263(2)–2.490(2) Å, these distances are shorter than the Cd–O distances of the acetate (O_2CMe in chelating mode, 2.294(4)–2.615(3) Å).[31, 32]

The packing diagram is in Fig. 2. In crystal lattice, there are π···π and C-H···π interactions (Table SI). The distances between the center of gravity of the π rings (*Cg*···*Cg* distance) are from 3.68 to 3.97 Å, and the distances between

Table 2. Selected Bond Length and Angles for the Compound.

Bond Length/Angle	Å/º	Bond Angle	º	Bond Angle	º
Cd–N3	2.258(3)	N3–Cd–O1	112.92(10)	O1–Cd–O4	151.39(10)
Cd–O3	2.367(3)	N3–Cd–N2	92.37(10)	N2–Cd–O4	91.57(10)
Cd–O1	2.263(2)	O1–Cd–N2	96.80(10)	O3–Cd–O4	54.82(9)
Cd–O4	2.375(3)	N3–Cd–O3	147.27(10)	N3–Cd–O2	88.65(9)
Cd–N2	2.279(3)	O1–Cd–O3	96.86(9)	O1–Cd–O2	54.60(8)
Cd–O2	2.490(2)	N2–Cd–O3	97.48(10)	N2–Cd–O2	148.68(10)
O4–Cd–O2	119.61(8)	N3–Cd–O4	93.93(10)	O3–Cd–O2	98.43(9)

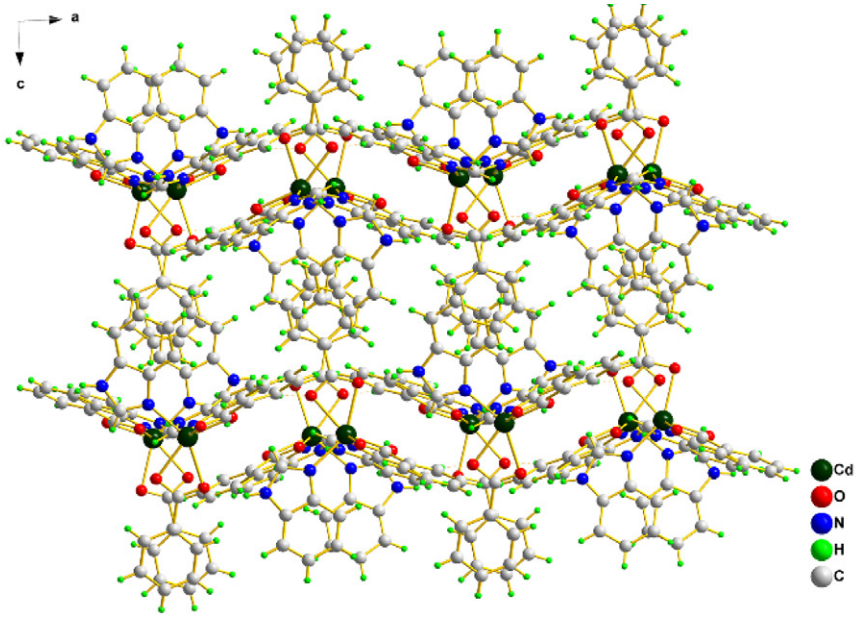


Fig. 2. The packing diagram of the compound.

C atom and *Cg* of the π rings (C···Cg distance) are 3.49 and 3.63 Å. There also exist the N–H···O and C–H···O[33] hydrogen bonds in crystal structure (Table 3), the N···O distances are 2.75 and 2.80 Å, while the C···O distances are 3.21and 3.35 Å. The D–H···A angle of N–H···O (161 and 176°) is larger than the angle of C–H···O (134 and 157°).

Table 3. Hydrogen bonds (Å and °).

Donor-H	Acceptor	D-H	H···A	D···A	D-H···A
N1–H1	O2^{i}	0.86	1.94	2.803(4)	176
N4–H4	O3^{ii}	0.86	1.92	2.748(4)	161
C3–H3	O4^{iii}	0.93	2.47	3.350(4)	157
C22–H22	O1^{ii}	0.93	2.49	3.211(5)	134

Symmetry codes: i = ½ – *x*, ½ + *y*, *z*; ii = ½ + *x*, *y*, ½ – *z*; iii = –½ +*x*, *y*, ½ – *z*.

4. 2. Hirshfeld Surface Analysis

In the last few years the analysis of molecular crystal structures using tools based on Hirshfeld surfaces has rapidly gained in popularity,[34–36] and they were carried out and plotted using CrystalExplorer software.[20,37–41] Hirshfeld surface analysis comprising d_{norm}- and shape index-surfaces, and 2D fingerprint plots (FP).

In d_{norm}-surface, hydrogen-bonds result in dark red spots near the hydrogen-bonds acceptor and donor atoms while intermolecular interactions result in faint-red spots. Further, the presence of patterns of red- and blue triangles on the same region of the shape-index surfaces is characteristic of π···π stacking. The d_{norm}- and shape index-surfaces of the compound are shown in Fig. 3 and Fig. 4.

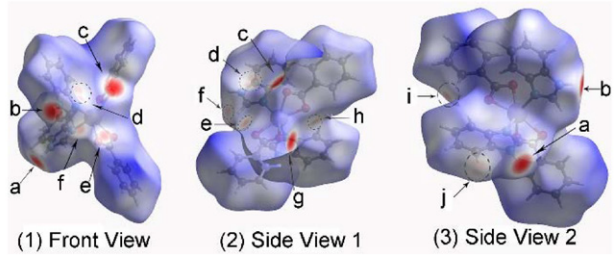


Fig. 3. The d_{norm} surfaces of the compound.

The N–H···O hydrogen-bonds in title compound can be seen in the d_{norm}-surfaces as bright-red spots marked as *a, b, c* and *g* (the spots located near the atom each correspondence are: *a* → N1, *b* → N4, *c* → O2, *g* → O3) in Fig. 3, so that the *a*, *b*, *c* and *g* spots are due to N1–H1···O2 and N4–H4···O3 hydrogen bonds.

The weak C–H···O hydrogen bond interactions (including intramolecular and intermolecular hydrogen bonds) in the compound are also demonstrated in the d_{norm}-surface as faint-red color spots (Fig. 3) and signed as *e, f, h, i*. (that is, each correspondence are: *e* → O4, *f* → C22, *h* → O1, *i* → C3). The faint-red spots above the center of the benzimidazole ring in the d_{norm}-surface of the compound (Fig. 3), all marked as *d*, arise from the C20–H20···π(Cg5) and C20–H20···π(Cg6) interaction, observed in crystal structure. The offset π···π interactions observed in the crystal structure are identified by distinctive patterns of red- and blue-triangles across the respective phenyl rings on the shape-index surface plots of the molecule (see the circle in Fig. 4).

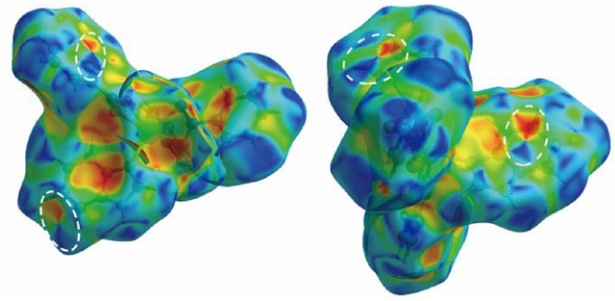


Fig. 4. The shape-index-surfaces.

The quantitative analysis of the intermolecular interactions apparent in crystal structure was attempted by observing the 2D FP's (Fig. 5). The H···O intermolecular interactions in the compound, appeared as two distinct long sharp spikes in the FP, at $d_i + d_e \approx 1.75$ Å which is roughly close to the observed N1–H1···O2 and N4–H4···O3 distance of 1.92, 1.94 Å (Table 3). In one molecule, these two spikes appear at (d_i, d_e) ≈ (0.70 Å, 1.05 Å) and (d_e, d_i) ≈ (0.70 Å, 1.05 Å, Fig. 5d), and the spikes appear in the same manner.

The C–H···π interactions appear as pair of blunt spikes at (d_e, d_i) ≈ (1.78 Å, 1.0 Å) and (d_e, d_i) ≈ (1.0 Å, 1.78 Å) in the FP, occurring at $d_i + d_e \approx 2.78$ Å, it appear as the spikes at $d_i + d_e$ distances are close to the H···π(Cg) distances in crystal (2.57, 2.80 Å, Table SI, Fig.5 (c)). The C–H···π interactions (Table SI) are also supported by the 'two wings' characters,[39–41] the wings are sites at the upper left and the bottom right. For the C···C close contacts (Fig. 5 (e)) with the shortest $d_i + d_e$ (distances ≈ 1.73 + 1.73 = 3.46 Å) is roughly accord with the C···C distances 3.68–3.97 Å in Table SI. It corresponds to the π···π stacking interactions.

The relative contributions of the intermolecular interactions to the Hirshfeld surface for the compound was calculated (see the upper bar diagram in Fig. 5(g)). The greatest contribution (47.2%) is from H···H contacts, followed by H···C/C···H contacts (which is stands for the C-H···π intermolecular interactions, 27.4%), then is the H···O/O···H contacts (the C-H···O or N-H···O hydrogen bond interactions 14.0%), the contribution from the H···N/N···H contacts is 4.2%, other contacts is 1.1%.

4. 3. Atom in Molecules Analysis

The topology analysis proposed by Bader was initially used for researching electron density in "atoms in

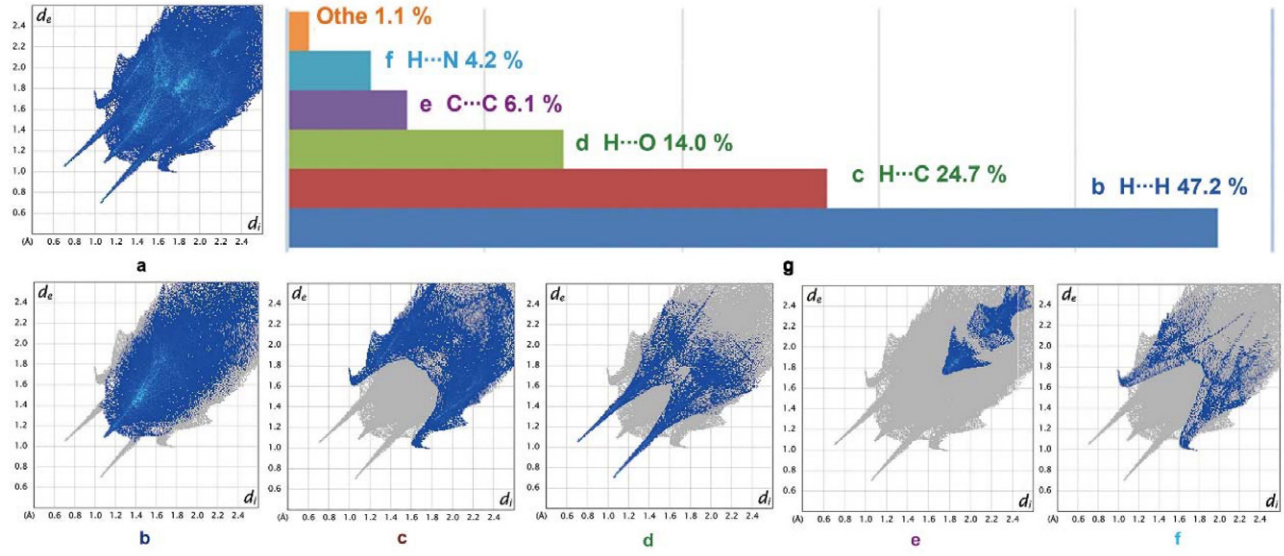


Fig. 5a The full image of Fingerprint Plot. **Fig. 5b** The H···H contacts show the contribution of 47.2%. **Fig. 5c** The H···C contacts have a contribution of 24.7%. **Fig. 5d** The H···O contacts have a contribution of 14.0% which is manifested by the interactions due to hydrogen bonds of N–H···O and C-H···O type. **Fig. 5e** The C···C contacts display the contribution of 6.1%. **Fig. 5f** The H···N contacts exhibit the contribution of 4.2%. **Fig. 5g** The bar graph shown the proportion of each contacts.

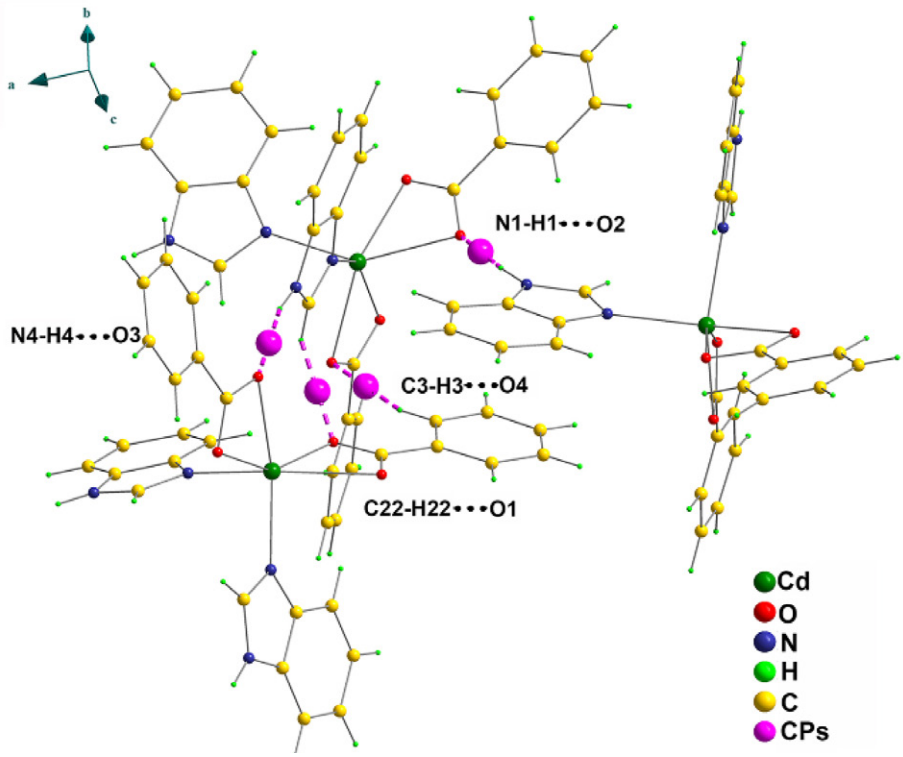


Fig. 6. The general view of hydrogen bonds BCP (pink ball) from the three coordinated unit model of the compound.

molecules" (AIM) theory.[21,42,43] In this theory, based on the bond critical point (BCP), Popelier[22] proposed the hydrogen bond's electron density at the BCP (ρ_{BCP}) should be in the scope of 0.002–0.035 a.u. and the electron density Laplacian value ($\nabla^2\rho_{BCP}$) should be confined in the region from 0.024 to 0.139 a.u.

For investigating the hydrogen bonds, we select three coordination units to form the model (it contain three molecules), in which it can exhibit the hydrogen bonds and the π···π interactions from the cif file (see supporting information) and calculate the single point to get the fchk file (see supporting information) from Gaussian 09 program[44] at ωB97XD[45]/GenECP (6-31+G** basis set for C, H, O, N and Lanl2dz[46] basis set for Cd), finally, we use the Multiwfn program[47] to study the topological properties of the hydrogen bonds in title compound (The Multiwfn produced CPs.pdb, Path.pdb and CPprop.txt are also in supporting information).

Fig. 6 shows the existence of a BCP in each N–H···O and each C–H···O hydrogen bond. The bond paths associated with the hydrogen bonds can be seen in Fig. 5 (and also be seen in Fig. S1). The BCP electron density of the hydrogen bonds is listed in Table 4. The ρ_{BCP} value (from 0.009 to 0.032 a.u.) for the N–H···O and C–H···O hydrogen bonds are all in the suggested interval of 0.002–0.035 a.u.[48] for the hydrogen bond. The two negative Hessian matrix eigenvalues of electron density, λ_1 and λ_2, can measure the scope of contraction of ρ_{BCP} which is perpendicular to the bond toward the critical point, while the positive λ_3 eigenvalue weighs the extent of contraction parallel to the bond and from the BCP toward each of the adjacent nuclei. The sum of eigenvalues λ_1, λ_2, and λ_3 is $\nabla^2\rho_{BCP}$. In addition, the numeric value of $\nabla^2\rho_{BCP}$ (0.0322–0.1091 a.u.) for N(C)–H···O interactions are in the recommend region of 0.024–0.139 a.u. for hydrogen bonds. Bader et al. deemed that for the closed-shell interactions (including

Table 4. The electron density (ρ_{BCP}), the Laplacian of electron density ($\nabla^2\rho_{BCP}$), and the eigenvalues of Hessian at BCP (λ_1, λ_2 and λ_3)[a]. Computed at ωB97XD/GenECP Level (6-31+G(d) for C, H, O, N and LanL2DZ for Cd).

Interactions	ρ_{BCP}	$\nabla^2\rho_{BCP}$	λ_1	λ_2	λ_3
N1–H1···O2	0.0324	0.1091	−0.0458	−0.0456	0.2006
N4–H4···O3	0.0254	0.0950	−0.0320	−0.0326	0.1596
C3–H3···O4	0.0093	0.0322	−0.0086	−0.0092	0.0500
C22–H22···O1	0.0091	0.0343	−0.0087	−0.0080	0.0510

a – The unit is atom unit.

the ionic bonds, hydrogen bonds, and van der Waals interactions) the $\nabla^2\rho_{BCP}$ value is positive.[21,43,49–54] On the basis of Table 4, the N–H···O and C–H···O hydrogen bonds are typical closed-shell interactions. Clearly, the topological properties of the hydrogen bonds studied are closed-shell interactions.

Table 5 The local properties at BCP: the potential energy density, V(b); the Lagrangian kinetic energy density, G(b); and the total energy density H(b)[a]. The calculations at ωB97XD/GenECP level (6-31+G(d) for C, H, O, N and LanL2DZ for Cd).

Interactions	V(b)	G(b)	H(b)	|V(b)|/G(b)
N1–H1···O2	–0.02476	0.02602	0.00126	0.92158
N4–H4···O3	–0.02100	0.02237	0.00137	0.93876
C3–H3···O4	–0.00655	0.00731	0.00075	0.89603
C22–H22···O1	–0.00622	0.00740	0.00116	0.84054

a – The unit is atom unit (a.u.).

Morrison,[55] and Espinosa[56] et al.[57] suggested that bond interactions are sorted according to the $|V(b)|/G(b)$ ratio, the ratio $|V(b)|/G(b) < 1$, the bonded interaction is taken for the closed shell, when $|V(b)|/G(b) > 2$, it is typically covalent interaction; and when $1 < |V(b)|/G(b) < 2$, it is the intermediate character. As it is depicted in Table 5, the Lagrangian kinetic energy density is only slightly larger than the potential energy density for all the (N)C–H···O interactions. It brings about the total energy density $H(b)$ is drawn near to 0 and the $|V(b)|/G(b)$ ratio is a little less than 1.0. Consequently, the N(C)–H···O interactions are mainly the closed shell for the model of the compound. This conclusion is agreement with the $\nabla^2\rho_{BCP} > 0$.

4. 4. Thermogravimetric Analysis

The TG of the title compound at the heating rate of 10 °C/min in nitrogen atmosphere is shown in Fig. 7.

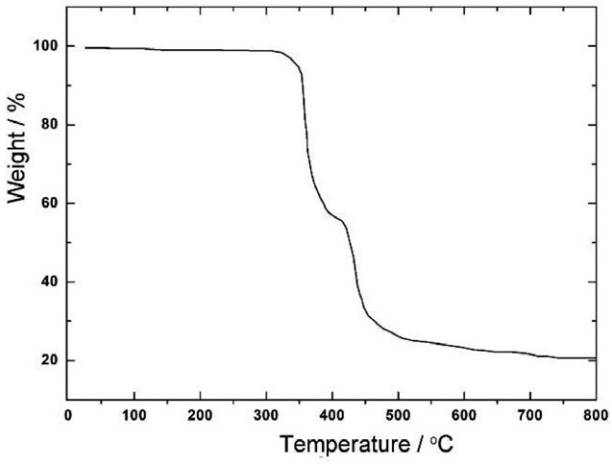


Fig. 7. The TG Analysis of the Compound.

There are two weight loss steps. The first weight loss stage mainly takes place from 301 to 393 °C, it may be related to the removal of the coordinated benzimidazole molecules (found: 41.14%; calcd: 39.99%). The second weight loss step mainly takes place from 405 to 636 °C, it corresponds to the release of the coordinated benzoate anion (found: 36.3%, calcd.: 40.99%). After 650 °C, nearly no weight loss is observed and the residue weight is 20.59%, which suggests it may be the cadmium oxide (CdO, calcd.: 21.73%).

5. Conclusion

The coordination complex bis(1*H*-benzimidazole-κN^3)cadmium(II) dibenzoate has been synthesized, the crystal structures were characterized by the single crystal diffraction analysis, Hirshfeld analysis and the AIM analysis. The structure analysis reveals that the cadmium center is six coordinated and forms an distorted octahedron coordinated geometry, and the compound's formula is $Cd(Bzim)_2(C_6H_5COO)_2$. The Hirshfeld analysis shows that in the d_{norm}-surface, there are dark red spots near the hydrogen-bond acceptor and donor atoms, while intermolecular interactions result in faint-red spots, the offset π···π interactions observed are identified by distinctive patterns of red- and blue-triangles across the respective phenyl rings on the shape-index surface plots, and the 2D fingerprint plots were also investigated. The AIM analysis shows there exists a BCP in each N–H···O and each C–H···O hydrogen bond, the bond paths associated with the hydrogen bonds can be seen, and the $|V(b)|/G(b) < 1.0$ and the $H(b) > 0$, these results manifested that the interaction is a closed shell system. The TG plot shows two weight loss steps (corresponding to BA and Bzim), the residue may be the cadmium oxide (CdO).

Acknowledgments

Supported by the Project of the Education Department of Jilin Province, China (No. JJKH20180777KJ) and the Science and Technology Development Projects of Siping City (No. 2017057).

6. References

1. S. R. Batten, N. R. Champness, X. M. Chen, J. Garcia-Martinez, S. Kitagawa, L. Öhrström, M. O'Keeffe, M. P. Suh, J. Reedijk, *Pure Appl. Chem.* **2013**, *85*, 1715–1724. **DOI:**10.1351/PAC-REC-12-11-20
2. P. García-Holley, B. Schweitzer, T. Islamoglu, Y. Y. Liu, L. Lin, S. Rodriguez, M. H. Weston, J. T. Hupp, D. A. Gómez-Gualdrón, T. Yildirim, O. K. Farha, *ACS Energy Lett.* **2018**, *3*, 748–754. **DOI:**10.1021/acsenergylett.8b00154
3. H. Kaur, M. Venkateswarulu, S. Kumar, V. Krishnana, R. R.

Koner, *Dalton Trans.* **2018**, *47*, 1488–1497. **DOI:**10.1039/C7DT04057A
4. Y. Rachuri, B. Parmar, E. Suresh, *Cryst. Growth Des.* **2018**, *18*, 3062–3072. **DOI:**10.1021/acs.cgd.8b00204
5. H. R. Wang, W. Meng, J. Wu, J. Ding, H. W. Hou, Y. T. Fan, *Coord. Chem. Rev.* **2016**, *307*, 130–146. **DOI:**10.1016/j.ccr.2015.05.009
6. M. Faheem, A. Rathaur, A. Pandey, V. K. Singh, A. K. Tiwari, *ChemistrySelect* **2020** *5*, 3981–3994. **DOI:**10.1002/slct.201904832
7. R. Cañete, A.A. Escobedo, P. Almirall, M.E. González, K. Brito, S. Cimerman, *Trans. R. Soc. Trop. Med. Hyg.* **2009**, *103*, 437–442. **DOI:**10.1016/j.trstmh.2008.11.029
8. L. Witzel, H. Gütz, W. Hüttemann, W. Schepp, *Aliment. Pharmacol. Ther.* **1995**, *9*, 19–24. **DOI:**10.1111/j.1365-2036.1995.tb00346.x
9. K. Chkirate, K. Karrouchi, N. Dege, N. K. Sebbar, A. Ejjoummany, S. Radi, N. N. Adarsh, A. Talbaoui, M. Ferbinteanu, E. M. Essassia, Y. Garcia, *New J. Chem.* **2020**, *44*, 2210–2221. **DOI:**10.1039/C9NJ05913J
10. S. O. Podunava-Kuzmanovi, D. M. Cvetkovi, *J. Serb. Chem. Soc.* **2007**, *72*, 459–466. **DOI:**10.2298/JSC0705459P
11. Y. Han, X. Liu, Z. Tian, X. Ge, J. Li, M. Gao, Y. Li, Y. Liu, Z. Liu. *Chem.-Asian J.* **2018**, *13*, 3697–3705. **DOI:**10.1002/asia.201801323
12. X. Liu, Y. Han, X. Ge, Z. Liu, *Front. Chem.* **2020**, *8*, 182. **DOI:**10.3389/fchem.2020.00182
13. Ö. Tarı, F. Gümüsß, L. Açık, B. Aydın, *Bioorg. Chem.* **2017**, *74*, 272–283. **DOI:**10.1016/j.bioorg.2017.08.015
14. H. Wu, F. Kou, F. Jia, B. Liu, J. Yuan, Y. Bai, *Bioinorg. Chem. Appl.* **2011**, 105431. **DOI:**10.1155/2011/105431
15. M. Tercan, O, Dayan, *J. Electron. Mater.* **2019**, *48*, 642–648. **DOI:**10.1007/s11664-018-6758-8
16. W. K. Huang, C. W. Cheng, S. M. Chang, Y. P. Lee, E. W. G. Diau, *Chem. Commun.* **2010**, *46*, 8992–8994. **DOI:**10.1039/c0cc03517c
17. D. Motoyama, K. Yoshikawa, H. Ozawa, M. Tadokoro, Masa-aki Haga, *Inorg. Chem.* **2017**, *56*, 6419–6428. **DOI:**10.1021/acs.inorgchem.7b00518
18. G. A. Jeffrey, W. Saenger, Hydrogen Bonding in Biological Structures. Springer, 1991.pp 169–464. **DOI:**10.1007/978-3-642-85135-3
19. K. Choi, A. D. Hamilton, *Coord. Chem. Rev.* **2003**, *240*, 101–110. **DOI:**10.1016/S0010-8545(02)00305-3
20. S. K. Seth, D. Sarkar, A. D. Jana, T. Kar, *Cryst. Growth Des.* **2011**, *11*, 4837–4849. **DOI:**10.1021/cg2006343
21. R. F. W. Bader, T. S. Slee, D. Cremer, E. Kraka, *J. Am. Chem. Soc.*, **1983**, *105*, 5061–5068. **DOI:**10.1021/ja00353a035
22. P. L. A. Popelier, *J. Phys. Chem. A* **1998**, *102*, 1873–1878. **DOI:**10.1021/jp9805048
23. Bruker, *SAINT-V6.28A Data Reduction Software*, Bruker AXS Inc., Madison, WI, USA, **2001**.
24. T. Higashi, *Program for Absorption Correction*. Rigaku Corporation, Tokyo, Japan, **1995**.
25. G. M. Sheldrick, *Acta Cryst.* **2008**, *A64*, 112–122. **DOI:**10.1107/S0108767307043930
26. G. M. Sheldrick, Acta Cryst. (2015). C71, 3–8. **DOI:**10.1107/S2053229614024218
27. L. J. Farrugia, *J. Appl. Cryst.* **2012**, *45*, 849–854. **DOI:**10.1107/S0021889812029111
28. H. Putz, K. Brandenburg, Diamond - Crystal and Molecular Structure Visualization Crystal Impact - Brandenburg GbR, Kreuzherrenstr. 102, 53227 Bonn, Germany, http://www.crystalimpact.com/diamond
29. G. C. Liu, J. X. Zhang, X. L. Wang, H. Y. Lin, A. X. Tian, Y. F. Wang, *Z. Naturforsch*. **2011**, *66b*, 125–132. **DOI:**10.1515/znb-2011-0204
30. E. A. H. Griffith, N. G. Charles, E. L. Amma, *Acta Cryst. Sect. B* **1982**, *38*, 942–944. **DOI:**10.1107/S0567740882004518
31. J. Ryu, G. M. Lee, S. W. Lee, *Bull. Korean Chem. Soc.* **2019**, 40, 958–962. **DOI:**10.1002/bkcs.11853
32. W. Harrison, J. Trotter, *J. Chem. Soc. Dalton Trans.* **1972**, 956–960. **DOI:**10.1039/dt9720000956
33. T. Steiner, *Cryst. Rev.* **1996,** *6*, 1–57. **DOI:**10.1080/08893110310001621772
34. L. Bejaoui, J. Rohlíček, V. Eigner, A. Ismail, M. E. Bour, R. B. Hassen, *Acta. Chim. Slov.* **2019**, 66, 603–613. **DOI:**10.17344/acsi.2019.5002
35. R. Vafazadeh, Z. Mansouri, A. C. Willis, *Acta. Chim. Slov.* **2020**, 67, 516–521. **DOI:**10.17344/acsi.2019.5539
36. L. Bejaoui, J. Rohlicek, R. B. Hassen, *J. Mol. Struct.* **2018**, 1173, 574e582. **DOI:**10.1016/j.molstruc.2018.07.017
37. M. A. Spackman, D. Jayatilaka. *Cryst. Eng. Comm.* **2009**, *11*, 19–32. **DOI:**10.1039/B818330A
38. M. J. Turner, J. J. McKinnon, S. K. Wolff, D. J. Grimwood, P. R. Spackman, D. Jayatilaka and M. A. Spackman, CrystalExplorer17, University of Western Australia. 2017. http://hirshfeldsurface.net
39. M. A. Spackman, P. G. Byrom, *Chem. Phys. Lett.* **1997**, *267*, 215–220. **DOI:**10.1016/S0009-2614(97)00100-0
40. J. J. McKinnon, A. S. Mitchell, M. A. Spackman, *Chem. Eur. J.* **1998**, *4*, 2136–2141. **DOI:**10.1002/(SICI)1521-3765(19981102)4:11<2136::AID-CHEM2136>3.0.CO;2-G
41. J. J. McKinnon, M. A. Spackman, A. S. Mitchell, *Acta Crystallogr., Sect. B* **2004**, *60*, 627–668. **DOI:**10.1107/S0108768104020300
42. R. F. W. Bader, *Acc. Chem. Res.* **1985**, *18*, 9–15. **DOI:**10.1021/ar00109a003
43. R. F. W. Bader, *Chem. Rev.* **1991**, *91*, 893–928. **DOI:**10.1021/cr00005a013
44. M. J. Frisch, G. W. Trucks, H. B. Schlegel, G. E. Scuseria, M. A. Robb, J. R. Cheeseman, G. Scalmani, V. Barone, B. Mennucci, and D. J. Fox, et.al. Gaussian 09, Revision D.01, Gaussian, Inc., Wallingford CT, 2009.
45. J. D. Chai, M. Head-Gordon, *Phys. Chem. Chem. Phys.* **2008**, *10*, 6615–6620. **DOI:**10.1039/b810189b
46. P. J. Hay, W. R. Wadt, *J. Chem. Phys.* **1985**, *82*, 270–283. **DOI:**10.1063/1.448799
47. T. Lu, F. W. Chen, *J. Comp. Chem.* **2012**, *33*, 580–592. **DOI:**10.1002/jcc.22885
48. U. Koch, P. Popelier, *J. Phys. Chem.* 1995, *99*, 9747–9754. **DOI:**10.1021/j100024a016

49. R. F. W. Bader, *J. Phys. Chem. A* **1998**, *102*, 7314–7323. **DOI:**10.1021/jp981794v
50. F. Biegler-König, R. F. W. Bader, T.H. Tang, *J. Comput. Chem.* **1982**, *3*, 317–328. **DOI:**10.1002/jcc.540030306
51. T. H. Tang, R. F.W. Bader, P. MacDougall, *Inorg. Chem.* **1985**, *24*, 2047–2053. **DOI:**10.1021/ic00207a018
52. F. Biegler-König, J. Schonbohm, D. Bayles, *J. Comput. Chem.* **2001**, *22*, 545–559. **DOI:**10.1002/1096-987X(20010415)22:5<545::AID-JCC1027>3.0.CO;2-Y
53. F. Biegler-König, J. Schonbohm, *J. Comput. Chem.* **2002**, *23*, 1489–1494. **DOI:**10.1002/jcc.10085
54. R. F. W. Bader, Atoms in Molecules–A Quantum Theory, Oxford University Press, New York, 1990, pp. 290–315.
55. S. Jenkins, I. Morrison, *Chem. Phys. Lett.* **2000**, *317*, 97–102. **DOI:**10.1016/S0009-2614(99)01306-8
56. E. Espinosa, I. Alkorta, J. Elguero, E. Molins, *J. Chem. Phys.* **2002**, *117*, 5529–5542. **DOI:**10.1063/1.1501133
57. S. Dinda, A. G. Samuelson, *Chem. Eur. J.* **2012**, *18*, 3032–3042. **DOI:**10.1002/chem.201101219

Povzetek

Sintetizirali smo koordinacijsko spojino bis(1*H*-benzimidazol-κN^3)kadmijev(II) dibenzoat in ga okarakterizirali z rentgensko monokristalno analizo. Kadmijev center je heksakoordiniran s popačeno oktaedrično geometrijo. Hirshfeldova analiza razkrije, da so na površini d_{norm} temno rdeče točke blizu akceptorjev in donorjev vodikovih vezi, medtem ko bledordeče točke predstavljajo intermolekularne interakcije. AIM analiza pokaže, da so BCP pri vsaki N(C)–H···O vodikovi vezi, |V(b)|/G(b) < 1 in H(b) > 0 pa nakazujeta na closed shell interakcijo. TG analiza potrjuje kristalno strukturo.

Except when otherwise noted, articles in this journal are published under the terms and conditions of the Creative Commons Attribution 4.0 International License

DRUŠTVENE VESTI IN DRUGE AKTIVNOSTI
SOCIETY NEWS, ANNOUNCEMENTS, ACTIVITIES

Vsebina

Doktorska in magistrska dela, diplome v letu 2020 ..... S3
Navodila za avtorje S32

Contents

Doctoral theses, master degree theses, and diplomas in 2020 ..... S3
Instructions for authors S32

UNIVERZA V LJUBLJANI
FAKULTETA ZA KEMIJO IN KEMIJSKO TEHNOLOGIJO
1. januar – 31. december 2020

DOKTORATI

DOKTORSKI ŠTUDIJSKI PROGRAM KEMIJSKE ZNANOSTI

KEMIJA

Luka ŽNIDERŠIČ
RAZVOJ ANALIZNE METODE ZA DOLOČEVANJE IZBRANIH ONESNAŽEVAL IZ MATERIALOV ZA STIK Z ŽIVILI V PIJAČAH
Mentorica: prof. dr. Helena Prosen
Datum zagovora: 10. 1. 2020

Miha DREV
KATALITSKO HETEROARILIRANJE KOT SINTEZNI PRISTOP V PRIPRAVI POLIDENTATNIH LIGANDOV
Mentor: izr. prof. dr. Franc Požgan
Somento: izr. prof. dr. Franc Perdih
Datum zagovora: 31. 1. 2020

Tina SNOJ EKMEČIČ
UPORABA SOLVATNEGA MODELA ZA NAPOVEDOVANJE RETENCIJSKIH ČASOV PRI REVERZNOFAZNI TEKOČINSKI KROMATOGRAFIJI
Mentorica: izr. prof. dr. Irena Kralj Cigić
Datum zagovora: 28. 2. 2020

Kristijan VIDOVIĆ
REAKCIJE NASTAJANJA IN STARANJA NITROAROMATSKIH SPOJIN, KI PREDSTAVLJAJO POMEMBEN DELEŽ RJAVEGA OGLJIKA V OZRAČJU
Mentorica: znan. svet. dr. Irena Grgić
Datum zagovora: 5. 3. 2020

Gašper POKLUKAR
NOVI KIRALNI FOSFINSKI LIGANDI IN NJIHOVA UPORABA V HOMOGENEM ASIMETRIČNEM HIDROGENIRANJU
Mentorica: dr. Barbara Mohar
Datum zagovora: 22. 4. 2020

Kristina LAMPIČ
RAZVOJ ANALIZNE METODE ZA DOLOČANJE METABOLITOV AZATIOPRINA V POSUŠENIH KRVNIH MADEŽIH
Mentor: izr. prof. Tomaž Vovk
Somentorica: prof. dr. Helena Prosen
Datum zagovora: 30. 6. 2020

Jana AUPIČ
NAČRTOVANJE DE NOVO PROTEINSKEGA KONFORMACIJSKEGA STIKALA NA OSNOVI MOTIVA OVITE VIJAČNICE
Mentor: prof. dr. Roman Jerala
Datum zagovora: 9. 7. 2020

Ana ROBBA
ANORGANSKI KATODNI MATERIALI ZA MAGNEZIJEVE AKUMULATORJE
Mentor: izr. prof. dr. Robert Dominko
Datum zagovora: 25. 9. 2020

Aleksander Bruno MARTEK
DVOJNA VLOGA PALADIJEVEGA KATALIZATORJA V ALKINILIRANJU ARIL HALIDOV
Mentor: prof. dr. Janez Košmrlj
Datum zagovora: 28. 9. 2020

Sandi BRUDAR
MEDDELČNE INTERAKCIJE V VODNIH RAZTOPINAH GLOBULARNIH PROTEINOV
Mentorica: prof. dr. Barbara Hribar Lee
Datum zagovora: 28. 9. 2020

Patricija HRIBERŠEK
ASOCIACIJSKI PROCESI V VODNIH RAZTOPINAH POLI(α-ALKIL KARBOKSILNIH KISLIN)
Mentorica: prof. dr. Ksenija Kogej
Datum zagovora: 28. 10. 2020

Ana TESTEN
PROFIL NEČISTOT KLJUČNEGA PREKURZORJA ZA SINTEZO ZAVIRALCA ANGIOTENZINSKIH KONVERTAZ
Mentorica:izr. prof. dr. Irena Kralj Cigić
Somentor: izr. prof. dr. Bogdan Štefane
Datum zagovora: 27. 11. 2020

Jerneja KLADNIK
SINTEZA IN BIOLOŠKA AKTIVNOST KOORDINACIJSKIH SPOJIN ANALOGOV PIRITIONA
Mentor: prof. dr. Iztok Turel
Datum zagovora: 2. 12. 2020

KEMIJSKO INŽENIRSTVO

Damjan LAŠIČ JURKOVIĆ
PLAZEMSKI IN KATALITSKI PROCESI AKTIVACIJE METANA IN OGLJIKOVEGA DIOKSIDA
Mentor: doc. Andrej Pohar
Datum zagovora: 22. 1. 2020

Nejc PAVLIN
MODIFICIRANI CELULOZNI SEPARATORJI V LITIJ-ŽVEPLOVIH AKUMULATORJIH
Mentor: izr. prof. dr. Robert Dominko
Datum zagovora: 4. 3. 2020

Brigita HOČEVAR
KINETIKA IN TRANSPORTNI POJAVI PRI KATALITSKI HIDROGENACIJI GLUKARNE KISLINE DO ADIPINSKE KISLINE
Mentor: izr. prof. dr. Blaž Likozar
Datum zagovora: 6. 3. 2020

Helena TRNOVEC
ODSTRANJEVANJE NEČISTOČ Z IONSKO-IZMENJEVALNIMI MEMBRANSKIMI ADSORBERJI
Mentor: prof. dr. Aleš Podgornik
Datum zagovora: 14. 9. 2020

Marko HERGA
VPLIV PROCESNIH POGOJEV NA KRISTALIZACIJO ESOMEPRAZOLA
Mentor: izr. prof. dr. Blaž Likozar
Somentor: izr. prof. dr. Bogdan Štefane
Datum zagovora: 14. 10. 2020

Lucija MAJAL BELCA
OPTIMIZACIJA KRISTALIZACIJE AKTIVNIH FARMACEVTSKIH UČINKOVIN S POMOČJO UPORABE IN-SITU ANALITSKIH TEHNIK
Mentor: prof. dr. Matjaž Krajnc
Datum zagovora: 16. 12. 2020

MAGISTRSKI ŠTUDIJ

MAGISTRSKI ŠTUDIJSKI PROGRAM 2. STOPNJE – KEMIJA

Anja PIRC
UPORABA KROMATOGRAFIJE Z MEŠANIMI REŽIMI ZA DOLOČEVANJE IONIZIRANIH FARMACEVTSKIH UČINKOVIN
Mentor: prof. dr. Matevž Pompe
Datum zagovora: 13. 2. 2020

Danijela KONČAN
TERMODINAMSKE ZNAČILNOSTI ZVITJA S CITOZINI BOGATE VERIGE DNA IZ PROMOTORSKE REGIJE PROTOONKOGENA C-MYC
Mentor: prof. dr. Jurij Lah
Datum zagovora: 27. 2. 2020

Miha RAVBAR
UPORABA PolyHIPE POLIMERA Z VEZANIM PALADIJEM ZA KATALIZO SUZUKI REAKCIJE
Mentor: izr. prof. dr. Jernej Iskra
Datum zagovora: 27. 2. 2020

Maja TIHOMIROVIĆ
KOORDINACIJSKE SPOJINE BAKRA, CINKA IN KOBALTA Z ANIONOM VINSKE KISLINE
Mentor: doc. dr. Bojan Kozlevčar
Datum zagovora: 9. 3. 2020

Anja AJDOVEC
FUNKCIONALIZIRANI MEZOPOROZNI SiO2 DELCI Z VGRAJENIM BARVILOM ZA INDIKACIJO RELATIVNE VLAŽNOSTI
Mentorica: doc. dr. Andrijana Sever Škapin
Somentorica: izr. prof. dr. Romana Cerc Korošec
Datum zagovora: 7. 4. 2020

Domen KASTELIC
PRIMERJAVA HPLC TEHNIK Z UPORABO REAGENTOV IONSKIH PAROV TER MEŠANIH SEPARACIJSKIH REŽIMOV ZA DOLOČEVANJE FARMACEVTSKIH UČINKOVIN
Mentor: prof. dr. Matevž Pompe
Datum zagovora: 30. 4. 2020

Simon MADŽARAC
RAZVOJ METODE ZA DOLOČEVANJE β-BLOKERJEV Z GC-MS
Mentorica: prof. dr. Helena Prosen
Datum zagovora: 7. 5. 2020

Vita HUDI
NAPOVEDNI MODELI ZA IDENTIFIKACIJO POTENCIALNIH INHIBITORJEV RAZLIČNIH PROTEINOV VIRUSA EBOLE
Mentor: doc. dr. Črtomir Podlipnik
Datum zagovora: 29. 5. 2020

Teja PODRŽAJ
RAZVOJ KROMATOGRAFSKE METODE ZA DOLOČANJE FENOLNIH SPOJIN V MEDU
Mentor: izr. prof. dr. Drago Kočar
Datum zagovora: 9. 6. 2020

Ives HUDOBIVNIK
DOLOČEVANJE SPOJIN SPECIFIČNIH ZA IZGOREVANJE LESNE BIOMASE
Mentor: prof. dr. Matevž Pompe
Datum zagovora: 18. 6. 2020

Maša KASTNER
RUTENIJ/PALADIJ DVOJNO ARILIRANJE HETEROARIL KINAZOLINSKIH DERIVATOV
Mentor: izr. prof. dr. Bogdan Štefane
Datum zagovora: 23. 6. 2020

Blaž KOZJAN
IZGRADNJA SPEKTRALNE KNJIŽNICE ZA NAMENE IDENTIFIKACIJE DELCEV V PARENTERALNIH IZDELKIH
Mentorica: doc. dr. Nina Lah
Somentorica: izr. prof. dr. Irena Kralj Cigić
Datum zagovora: 23. 6. 2020

Anja Marija PILAR
ANALIZA AKTINIDOV V NETOPNIH OSTANKIH PO RAZKROJU TAL IN SEDIMENTOV Z RAZLIČNIMI RAZKROJNIMI TEHNIKAMI
Mentorica: znan. svet. dr. Ljudmila Benedik
Somentorica: prof. dr. Helena Prosen
Datum zagovora: 23. 6. 2020

Tina PEČARIČ STRNAD
RUTENIJ/PALADIJ DVOJNO ARILIRANJE 3-HETEROARILIZOKINOLINOV
Mentor: izr. prof. dr. Bogdan Štefane
Datum zagovora: 23. 6. 2020

Urša ROZMAN
PALADIJ/RUTENIJ DVOJNO ARILIRANJE HETEROARIL KINOLINSKIH DERIVATOV
Mentor: izr. prof. dr. Bogdan Štefane
Datum zagovora: 24. 6. 2020

Grega KOS
SINTEZA BICIKLO[2.2.2]OKTENOV IZ RAZLIČNIH 2H-PIRAN-2-ONOV TER MALEIMIDA OZIROMA NJEGOVIH DERIVATOV KOT OSNOVA ZA RAZISKOVANJE HALOGENSKIH VEZI
Mentor: doc. dr. Krištof Kranjc
Datum zagovora: 7. 7. 2020

Tjaša PAVLOVČIČ
INHIBICIJA KOROZIJE ALUMINIJEVE ZLITINE Z DODATKOM VANADATA IN MOLIBDATA V KLORIDNO RAZTOPINO
Mentor: prof. dr. Matija Tomšič
Somentorica: znan. svet. dr. Ingrid Milošev
Datum zagovora: 8. 7. 2020

Maja MAJCEN
OKSIDATIVNE PRETVORBE 1,3-ENINOV
Mentor: prof. dr. Marjan Jereb
Datum zagovora: 8. 7. 2020

Kaja PANCAR
VPLIV MODIFIKACIJ NA LASTNOSTI MEZOPOROZNEGA SILICIJEVEGA DIOKSIDA
Mentorica: izr. prof. dr. Romana Cerc Korošec
Somentorica: doc. dr. Andrijana Sever Škapin
Datum zagovora: 8. 7. 2020

Nejc POVIRK
STRUKTURNE, FOTOKATALITSKE IN OPTIČNE LASTNOSTI TANKIH PLASTI TiO_2-SiO_2, DOPIRANIH Z VANADIJEM
Mentorica: viš. znan. sod. dr. Angelja Kjara Surca
Somentorica: prof. dr. Urška Lavrenčič Štangar
Datum zagovora: 8. 7. 2020

Natalija KLANČNIK
POLIMORFIZEM DIHIDRATA ACETILEN DIKARBOKSILNE KISLINE
Mentorica: izr. prof. dr. Amalija Golobič
Datum zagovora: 19. 8. 2020

Jana ČIMŽAR
7-SUBSTITUIRANI DERIVATI NITROKSOLINA KOT POTENCIALNI INHIBITORJI KATEPSINA B
Mentor: izr. prof. dr. Bogdan Štefane
Datum zagovora: 26. 8. 2020

Lia ŠIBAV
SINTEZA IN KARAKTERIZACIJA PRODUKTOV MEHANOKEMIJSKE SINTEZE IMIDAZOLATOV IN TETRAHIDRIDOBORATOV LAHKIH KOVIN
Mentor: prof. dr. Anton Meden
Datum zagovora: 27. 8. 2020

Tjaša LISAC
KATIONSKA IZMENJAVA V STRUKTURAH KOVINSKO-ORGANSKIH MATERIALOV ZA ZAJEMANJE PLINOV
Mentor: viš. znan. sod. dr. Matjaž Mazaj
Somentorica: izr. prof. dr. Amalija Golobič
Datum zagovora: 27. 8. 2020

Aljaž ŠKRJANC
POSKUS ESTRENJA POD POGOJI FOTOKATALITSKE MITSUNOBU REAKCIJE
Mentor: prof. dr. Janez Košmrlj
Datum zagovora: 28. 8. 2020

Dominik JANKOVIČ
SINTEZA MONOSUBSTITUIRANIH 'KLIK' TRIAZOLOV
Mentor: doc. dr. Martin Gazvoda
Datum zagovora: 31. 8. 2020

Ana SILJANOVSKA
UČINKOVITA SINTEZA SUBSTITUIRANIH CINOLINOV PREKO VMESNIH DIAZONIJEVIH SOLI
Mentor: prof. dr. Janez Košmrlj
Datum zagovora: 31. 8. 2020

Jure GREGORC
ORGANOKATALIZIRANA ASIMETRIČNA SINTEZA DERIVATOV DIHIDROPIRANOPIROLA
Mentor: izr. prof. dr. Uroš Grošelj
Datum zagovora: 31. 8. 2020

Tilen BERGLEZ
MODELIRANJE ATAKTIČNE IN IZOTAKTIČNE POLIMETAKRILNE KISLINE S POUDARKOM NA ODVISNOSTI STRUKTURE OD TAKTIČNOSTI IN DIELEKTRIČNE KONSTANTE TOPILA
Mentorica: prof. dr. Ksenija Kogej
Datum zagovora: 1. 9. 2020

Žiga PONIKVAR
UPORABA ELEKTROKEMIJSKIH METOD V ORGANSKI SINTEZI ZA TVORBO PINAKOLNE VEZI IZ SUBSTITUIRANIH ALDEHIDOV ALI KETONOV
Mentor: doc. dr. Krištof Kranjc
Datum zagovora: 3. 9. 2020

Brigita KRAJNC
SPEKTROFOTOMETRIČNO DOLOČEVANJE VEZAVE MIKROELEMENTOV NA KOSTANJEV EKSTRAKT
Mentor: izr. prof. dr. Bogdan Štefane
Datum zagovora: 3. 9. 2020

Petra STARE
SINTEZE KOORDINACIJSKIH SPOJIN CINKA(II) S KINALDINATOM IN IZBRANIMI ALKOHOLAMINI.
Mentorica: doc. dr. Barbara Modec
Datum zagovora: 7. 9. 2020

Katarina ŽIBERNA
FEROELEKTRIČNA DOMENSKA STRUKTURA PIEZOELEKTRIČNE TRDNE RAZTOPINE BiFeO3-SrTiO3
Mentor: viš. znan. sod. dr. Tadej Rojac
Somentor: prof. dr. Anton Meden
Datum zagovora: 7. 9. 2020

Taja ŽIBERT
TERMODINAMSKE LASTNOSTI MEŠANIC VODE IN AMONIJAKA TER VODE IN METANOLA
Mentor: prof. dr. Tomaž Urbič
Datum zagovora: 9. 9. 2020

Katja PIKŠ
TERMODINAMSKE ZNAČILNOSTI PRETVORBE DVOVERIŽNE DNA IZ PROMOTORSKE REGIJE PROTOONKOGENA C-MYC V G-KVADRUPLEKS IN I-MOTIV
Mentor: prof. dr. Jurij Lah
Datum zagovora: 10. 9. 2020

Svit MENART
ELEKTROAKTIVNI MATERIALI NA OSNOVI PIRAZINSKIH IN KINONSKIH ENOT
Mentor: znan. sod. dr. Klemen Pirnat
Somentor: izr. prof. dr. Jernej Iskra
Datum zagovora: 10. 9. 2020

Andraž OŠTREK
MODULARNA SINTEZA PIRITIDOV
Mentor: prof. dr. Jurij Svete
Somentor: doc. dr. David Šarlah
Datum zagovora: 11. 9. 2020

Dejan SLAPŠAK
SINTEZA DERIVATOV PIRAZOLO[1,2-A]PIRAZOLA IN NJIHOVA INHIBICIJA DIHIDROOROTAT DEHIDROGENAZE
Mentor: prof. dr. Jurij Svete
Datum zagovora: 14. 9. 2020

Neli SEDEJ
KONFORMACIJSKA DINAMIKA K-Ras4B V INTERAKCIJI Z MEMBRANO
Mentor: prof. dr. Jurij Reščič
Somentor: izr. prof. Franci Merzel
Datum zagovora: 14. 9. 2020

Teja GABRŠČEK
AMIDNI DERIVATI DIPIKOLINSKE KISLINE KOT POTENCIALNI LIGANDI ZA VEZAVO NA CINKOVE IONE
Mentor: izr. prof. dr. Franc Perdih
Datum zagovora: 16. 9. 2020

Matej JAKLIN
VPLIVI PUFROV IN SOLI NA LASTNOSTI PROTEINOV BSA IN HEWL
Mentorica: prof. dr. Barbara Hribar Lee
Datum zagovora: 17. 9. 2020

Jure KUHAR
VPLIV DOLŽINE ALKILNE VERIGE 1-METIL-3-ALKILIMIDAZOLIJEVEGA KLORIDA NA VISKOZNOSTNI B-KOEFICIENT V VODNIH RAZTOPINAH
Mentorica: prof. dr. Marija Bešter Rogač
Datum zagovora: 21. 9. 2020

Matic BELAK VIVOD
VPLIV SOLI NA FAZNO STABILNOST MEŠANICE BSA S POLIETILEN GLIKOLOM
Mentor: izr. prof. dr. Miha Lukšič
Datum zagovora: 24. 9. 2020

Lea GAŠPARIČ
OBRAVNAVA VODIKOVIH VEZI MED KOVINSKIMI HIDROKSIDI IN ORGANSKIMI MOLEKULAMI Z MOLEKULSKIM MODELIRANJEM
Mentor: prof. dr. Andrej Jamnik
Somentor: viš. znan. sod. dr. Anton Kokalj
Datum zagovora: 25. 9. 2020

Andrej GRUDEN
SINTEZA RUTENIJEVIH KOMPLEKSOV S TIOSEMIKARBAZONI
Mentor: prof. dr. Iztok Turel
Datum zagovora: 30. 9. 2020

Jure DRAGAN
DOLOČANJE KONCENTRACIJE ANTIKOAGULANTA V EPRUVETAH ZA VAKUUMSKI ODVZEM KRVI
Mentorica: izr. prof. dr. Nataša Gros
Datum zagovora: 30. 9. 2020

Anja LONČAR
AKTIVNOST IN STABILNOST IRIDIJEVIH KATALIZATORJEV ZA OKSIDACIJO VODE
Mentor: znan. sod. dr. Nejc Hodnik
Somentor: prof. dr. Miran Gaberšček
Datum zagovora: 30. 9. 2020

Luka REPAR
PRIPRAVA KIRALNIH SELENIJEVIH-π-KISLIN NA OSNOVI SPIRO-INDANSKEGA JEDRA
Mentor: doc. dr. Krištof Kranjc
Somentor: prof. dr. Alexander Breder
Datum zagovora: 1. 10. 2020

Mateja ŽNIDARIČ
SINTEZA IZBRANIH PIRIDIL-TRIAZOLOV
Mentor: doc. dr. Martin Gazvoda
Datum zagovora: 14. 10. 2020

Maruša JELŠEVAR
PRIPRAVA IN KARAKTERIZACIJA LIPOSOMSKEGA MATIČNEGA MLEČKA
Mentor: izr. prof. dr. Mitja Kolar
Datum zagovora: 26. 10. 2020

Domen KRANJC
KARAKTERIZACIJA VEZIV Z INFRARDEČO SPEKTROSKOPIJO IN PLINSKO KROMATOGRAFIJO SKLOPLJENO Z MASNO SPEKTROMETRIJO
Mentorica: izr. prof. dr. Irena Kralj Cigić
Datum zagovora: 29. 10. 2020

Robert KOMAN
PRIPRAVA SILIKATNIH PROSOJNIH SUPERHIDROFOBNIH POVRŠIN NA STEKLU
Mentor: doc. dr. Bojan Šarac
Datum zagovora: 12. 11. 2020

Filip CERNATIČ
ŠTUDIJA STRUKTURNE DINAMIKE JEDRNEGA RECEPTORJA PPARγ S SIMULACIJAMI MOLEKULSKE DINAMIKE
Mentor: dr. Roland Stote
Somentor: doc. dr. Črtomir Podlipnik
Datum zagovora: 19. 11. 2020

Martina MOŽE
DETEKCIJA IN KVANTIFIKACIJA RAZTOPLJENE ORGANSKE SNOVI Z DETEKTORJEM NABITIH AEROSOLOV
Mentor: izr. prof. dr. Drago Kočar
Datum zagovora: 4. 12. 2020

Urška PETRAČ
HIDROTERMALNA SINTEZA NANOSTRUKTURIRANEGA TiO2 FOTOKATALIZATORJA
Mentorica: prof. dr. Urška Lavrenčič Štangar
Datum zagovora: 30. 12. 2020

MAGISTRSKI ŠTUDIJSKI PROGRAM 2. STOPNJE – KEMIJSKO INŽENIRSTVO

Barbara JERAS
RAZVOJ PROCESA KONTINUIRNE KROMATOGRAFIJE ZA MONOKLONSKA PROTITELESA
Mentor: prof. dr. Aleš Podgornik
Datum zagovora: 9. 1. 2020

Barbara VREČER
KONSTRUKCIJA POLŠARŽNEGA HIDROTERMALNEGA REAKTORJA Z DODAJANJEM SUBSTRATA ZA SINTEZO KRISTALNIH DVOJČKOV RUTILA
Mentor: prof. dr. Aleš Podgornik
Datum zagovora: 16. 1. 2020

Klemen ZLATNAR
IZBOLJŠAVA HOMOGENOSTI NANOSOV FILMA NA STEKLENE POVRŠINE
Mentor: doc. dr. Aleš Ručigaj
Datum zagovora: 17. 2. 2020

Matjaž VELKOVRH
VPLIV MIKRO IN NANOCELULOZE NA LASTNOSTI KOMPOZITOV IZ NENASIČENE POLIESTRSKE SMOLE
Mentorica: prof. dr. Urška Šebenik
Datum zagovora: 17. 2. 2020

Tilen TURK
VPLIV MIKROPLASTIKE NA MALO VODNO LEČO *(LEMNA MINOR)*
Mentorica: doc. dr. Gabriela Kalčikova
Datum zagovora: 18. 2. 2020

Nastja SMOLNIKAR
UPORABA FENTONOVE OKSIDACIJE ZA ODSTRANJEVANJE ANTIBIOTIKOV IZ FARMACEVTSKIH ODPADNIH VOD
Mentorica: prof. dr. Andreja Žgajnar Gotvajn
Datum zagovora: 5. 3. 2020

Ana LISAC
VPLIV FIZIOLOŠKEGA STANJA BAKTERIJE ESCHERICHIA COLI NA POJAV HIBERNACIJE PRI TVORBI BAKTERIOFAGOV
Mentor: prof. dr. Aleš Podgornik
Datum zagovora: 12. 3. 2020

Domen OŠTIR
SINTEZA Z DUŠIKOM DOPIRANEGA GRAFENA ZA UPORABO V NAPRAVAH ZA SHRANJEVANJE IN PRETVORBO ENERGIJE
Mentor: doc. dr. Boštjan Genorio
Datum zagovora: 15. 4. 2020

Dejan MIŠIĆ
SINTEZA IN KARAKTERIZACIJA HETEROGENIH KATALIZATORJEV IN VREDNOTENJE NJIHOVIH LASTNOSTI V PROCESU SUHEGA REFORMINGA METANA
Mentor: prof. dr. Igor Plazl
Datum zagovora: 22. 5. 2020

Sandra ZAPLOTNIK
VPLIV INTENZITETE ULTRAZVOČNE KAVITACIJE NA FUNKCIONALIZACIJO GRAFENA
Mentor: doc. dr. Aleš Ručigaj
Datum zagovora: 22. 5. 2020

Vivian ERKLAVEC ZAJEC
IMOBILIZACIJA ENCIMOV V NANOSTRUKTURAH INTEGRIRANIH V MIKROREAKTORJE
Mentorica: prof. dr. Polona Žnidaršič Plazl
Datum zagovora: 1. 6. 2020

Matej SAŠEK
UPORABA ODPADNEGA MATERIALA KOT KATALIZATORJA ZA HETEROGENO FENTONOVO OKSIDACIJO
Mentorica: doc. dr. Gabriela Kalčikova
Datum zagovora: 22. 6. 2020

Luka GOLOB
IMOBILIZACIJA IZBRANE AMIN TRANSAMINAZE V MIKROPRETOČNI REAKTOR
Mentorica: prof. dr. Polona Žnidaršič Plazl
Datum zagovora: 24. 6. 2020

Nejc BUTALA
KATALITSKE SPOSOBNOSTI RAZVEJANIH STRUKTUR TITANOVEGA DIOKSIDA
Mentor: prof. dr. Aleš Podgornik
Somentor: izr. prof. dr. Blaž Likozar
Datum zagovora: 24. 6. 2020

Eva KORUNIČ
OVREDNOTENJE STRUPENOSTI FARMACEVTSKE UČINKOVINE PO FENTONOVI OKSIDACIJI IN OZONACIJI
Mentorica: doc. dr. Gabriela Kalčikova
Datum zagovora: 29. 6. 2020

Miha HORVAT
VPLIV TOPILA NA UČINKOVITOST SAMOCELJENJA EPOKSI MATERIALA Z DIELS-ALDER KOMPONENTAMI
Mentor: doc. dr. Aleš Ručigaj
Datum zagovora: 10. 7. 2020

Matej BENEDIK
ELEKTROKEMIJA ANTRAKINONA V ORGANSKIH TOPILIH
Mentor: doc. dr. Boštjan Genorio
Datum zagovora: 16. 7. 2020

Kevin STOJANOVSKI
ROTIRAJOČA DISK ELEKTRODA KOT METODA ZA MERJENJE AKTIVNOSTI IN STABILNOSTI ELEKTROKATALIZATORJEV REAKCIJE EVOLUCIJE KISIKA NA OSNOVI IRIDIJA
Mentor: prof. dr. Miran Gaberšček
Datum zagovora: 17. 7. 2020

Lorena KUNC
FUNKCIONALIZACIJA POROZNEGA POLIMERNEGA NOSILCA Z DEKSTRANSKIM SLOJEM ZA VEZAVO CELIC
Mentor: prof. dr. Aleš Podgornik
Datum zagovora: 25. 8. 2020

Iris MALNARIČ
DVOKOMPONENTNI BENZOKSAZINSKI MATERIALI IZ BIO-OBNOVLJIVIH VIROV Z ZMOŽNOSTJO OBLIKOVNEGA UČINKA
Mentor: doc. dr. Aleš Ručigaj
Datum zagovora: 28. 8. 2020

Klemen ERHATIČ
PLAZMONSKI Au/TiO2 FOTOKATALIZATORJI ZA OKSIDATIVNO RAZGRADNJO BISFENOLA A V VODNI RAZTOPINI
Mentor: prof. dr. Igor Plazl
Datum zagovora: 8. 9. 2020

Julija SIMAKOVIĆ
FUNKCIONALIZACIJA GRAFENA S POLIVINIL ALKOHOLOM S POMOČJO ULTRAZVOČNE KAVITACIJE
Mentor: doc. dr. Aleš Ručigaj
Datum zagovora: 11. 9. 2020

Alen RUPNIK
IZDELAVA ELEKTROKEMIJSKIH PRETOČNIH REAKTORSKIH SISTEMOV S POMOČJO TEHNOLOGIJE 3D TISKANJA ZA IZVAJANJE REDOKS REAKCIJ KINONOV
Mentor: doc. dr. Aleš Ručigaj
Datum zagovora: 11. 9. 2020

Barbara KLUN
SINTEZA MAGNETO-OPTIČNIH KOMPOZITNIH NANOSTRUKTUR S SPAJANJEM ZLATIH MIKROPLOŠČIC Z MAGNETNIMI HEKSAFERITNIMI NANOPLOŠČICAMI
Mentor: prof. dr. Darko Makovec
Somentor: izr. prof. dr. Marjan Marinšek
Datum zagovora: 21. 9. 2020

Tina ROČNIK
TESTIRANJE BIORAZGRADLJIVOSTI FILMOV NA OSNOVI HITOZANA Z DODANIM KOSTANJEVIM EKSTRAKTOM V VODNEM OKOLJU
Mentorica: doc. dr. Gabriela Kalčikova
Somentor: izr. prof. dr. Blaž Likozar
Datum zagovora: 22. 9. 2020

Matej ŽULA
MATEMATIČNO MODELIRANJE ACIDOLIZE BENZIL FENIL ETRA KOT MODELNE KOMPONENTE LIGNINA IN VALIDACIJA MODELA
Mentorica: prof. dr. Polona Žnidaršič Plazl
Somentorica: znan. sod. dr. Edita Jasiukaityte Grojzdek
Datum zagovora: 23. 9. 2020

Tina ĐUKIĆ
FUNKCIONALIZACIJA REDUCIRANEGA GRAFEN OKSIDA Z REDOKS AKTIVNIMI MOLEKULAMI S POMOČJO KAVITACIJE
Mentor: doc. dr. Boštjan Genorio
Datum zagovora: 24. 9. 2020

Nina ŠVIGELJ
NAPREDNI POLIMERNI MATERIALI NA OSNOVI BIO-OSNOVANEGA BENZOKSAZINA IN EPOKSIDA
Mentor: doc. dr. Aleš Ručigaj
Datum zagovora: 27. 10. 2020

Rene OBLAK
UPORABA LASERSKE NAPRAVE SPEEDMARKER CL 30 W ZA VŽIGANJE ODPRTIN V TABLETE NA OSNOVI OSMOTSKE ČRPALKE
Mentorica: doc. dr. Gabriela Kalčikova
Datum zagovora: 4. 11. 2020

Mark SELAN
NAČRTOVANJE IN UPORABA MIKROSEPARATORJA PRI EKSTRAKCIJI IN SEPARACIJI DVOFAZNEGA TOKA
Mentor: prof. dr. Igor Plazl
Datum zagovora: 18. 11. 2020

Petra MARKOVIČ
TERMIČNO AKTIVIRANO SAMOCELJENJE BIO-OSNOVANIH POLIBENZOKSAZINOV
Mentor: doc. dr. Aleš Ručigaj
Datum zagovora: 8. 12. 2020

Jan KOTNIK
VPLIV RAZLIČNIH MEŠANIC BIOPOLIMEROV NA KONTROLIRANO SPROŠČANJE UČINKOVIN IZ ZAMREŽENIH HIDROGELOV
Mentor: doc. dr. Aleš Ručigaj
Datum zagovora: 8. 12. 2020

Dana MARINIČ
TERMIČNE IN MEHANSKE LASTNOSTI KOPOLIMEROV BIO-OSNOVANIH BENZOKSAZINOV IN HITOZANA
Mentor: doc. dr. Aleš Ručigaj
Datum zagovora: 8. 12. 2020

Žiga TOMAN
SINTEZA, KARAKTERIZACIJA IN UPORABA ABRAZIVNEGA POLIURETANSKEGA NANOSA
Mentor: izr. prof. dr. Marjan Marinšek
Datum zagovora: 15. 12. 2020

Peter POLES
SINTEZA CENOVNO UGODNE NENASIČENE POLIESTRSKE SMOLE ZA ABRAZIJSKO ODPORNE POLIESTRSKE KOMPOZITE
Mentorica: prof. dr. Urška Šebenik
Datum zagovora: 15. 12. 2020

MAGISTRSKI ŠTUDIJSKI PROGRAM 2. STOPNJE – BIOKEMIJA

Petra VIVOD
TARČNA INTEGRACIJA HETEROLOGNIH GENOV MONOKLONSKEGA PROTITELESA V GENOM CELIC CHO
Mentor: doc. dr. Gregor Gunčar
Datum zagovora: 29. 1. 2020

Marija ATANASOVA
DOLOČANJE STOPNJE METILACIJE DNA KANDIDATNIH GENOV IN KOLIČINE cfDNA PRI BOLNIKIH Z DEPRESIJO
Mentorica: doc. dr. Alja Videtič Paska
Datum zagovora: 6. 2. 2020

Bine TRŠAVEC
IDENTIFIKACIJA MEMBRANSKIH SUBSTRATOV CISTEINSKIH KATEPSINOV NA CELIČNI LINIJI RAKA DOJKE SK-BR-3
Mentor: prof. ddr. Boris Turk
Datum zagovora: 26. 5. 2020

Ernest ŠPRAGER
PRODUKCIJA IN KARAKTERIZACIJA MODIFICIRANIH OBLIK PROTEINSKIH PLINSKIH VEZIKLOV V E. COLI
Mentorica: doc. dr. Mojca Benčina
Somentor: izr. prof. dr. Marko Novinec
Datum zagovora: 10. 6. 2020

Rok MIKLAVČIČ
OVREDNOTENJE VPLIVA AKTIVACIJE Z AMP AKTIVIRANE PROTEIN KINAZE NA INFLAMASOM NLRP3
Mentorica: viš. znan. sod. dr. Iva Hafner Bratkovič
Somentor: doc. dr. Gregor Gunčar
Datum zagovora: 9. 7. 2020

Neža KORITNIK
PRIPRAVA IN KARAKTERIZACIJA NOVEGA AKTINOPORINOM PODOBNEGA PROTEINA IZ MEDITERANSKE KLAPAVICE *(MYTILUS GALLOPROVINCIALIS)*
Mentorica: izr. prof. dr. Marjetka Podobnik
Somentor: doc. dr. Miha Pavšič
Datum zagovora: 20. 8. 2020

Karmen ŽBOGAR
BIOFIZIKALNE IN BIOKEMIJSKE LASTNOSTI G4C2 PONOVITEV DNA
Mentor: prof. dr. Boris Rogelj
Datum zagovora: 5. 8. 2020

Katarina Petra VAN MIDDEN
OPTIMIZACIJA PRIPRAVE ZUNAJCELIČNEGA DELA DISINTEGRINSKE METALOPROTEAZE TACE IN ANALIZA CEPITVE PROTEINA EpCAM IN VITRO
Mentorica: prof. dr. Brigita Lenarčič
Datum zagovora: 25. 8. 2020

Zala ŽIVIČ
VZPOSTAVITEV SISTEMA ZA SPREMLJANJE REGULACIJE IZRAŽANJA TOKSIN-ANTITOKSIN MODULOV IN VIVO.
Mentor: doc. dr. San Hadži
Somentorica: doc. dr. Marina Klemenčič
Datum zagovora: 27. 8. 2020

Jerneja KOCUTAR
CITOTOKSIČNOST LIPOSOMSKE OBLIKE BUPIVAKAINA
Mentor: prof. dr. Tomaž Marš
Datum zagovora: 1. 9. 2020

Anamarija HABIČ
ODKRIVANJE INTERAKCIJSKIH PARTNERJEV PROTEINA ORF1p IZ ČLOVEŠKEGA RETROTRANSPOZONA LINE1
Mentorica: doc. dr. Vera Župunski
Datum zagovora: 7. 9. 2020

Tina POŽUN
VPLIV INZULINA IN ADRENALINA NA URAVNAVANJE Z AMP AKTIVIRANE PROTEIN KINAZE (AMPK) V KULTURI SKELETNOMIŠIČNIH CELIC
Mentor: doc. dr. Sergej Pirkmajer
Datum zagovora: 7. 9. 2020

Blaž LEBAR
KARAKTERIZACIJA INTERAKCIJE KATEPSINA B S HEPARINOM Z MESTNO-SPECIFIČNO MUTAGENEZO
Mentor: izr. prof. dr. Marko Novinec
Datum zagovora: 10. 9. 2020

Valentina LEVAK
STRATEGIJA RAZVOJA BIOSENZORJEV IMUNSKEGA ODZIVA V KROMPIRJU
Mentorica: prof. dr. Kristina Gruden
Somentor: izr. prof. dr. Marko Dolinar
Datum zagovora: 10. 9. 2020

Matej KOLARIČ
Proteolitično procesiranje receptorja za urokinazni aktivator plazminogena s cisteinskimi katepsini
Mentor: prof. ddr. Boris Turk
Datum zagovora: 10. 9. 2020

Barbara LIPOVŠEK
VPLIV METABOLIČNEGA STRESA NA PROTEOM LIPIDNIH KAPLJIC V RAKAVIH CELICAH
Mentor: znan. sod. dr. Toni Petan
Somentor: doc. dr. Miha Pavšič
Datum zagovora: 10. 9. 2020

Gašper ŽUN
O PRENOSU VZROČNIH VARIANT ZA POLIGENSKE LASTNOSTI KVASOVKE
Mentor: prof. dr. Uroš Petrovič
Datum zagovora: 11. 9. 2020

Simon ALEKSIČ
STRUKTURNA ŠTUDIJA Z GVANINI BOGATEGA OBMOČJA V PROMOTORJU ČLOVEŠKE HELIKAZE FANCJ
Mentor: prof. dr. Janez Plavec
Datum zagovora: 11. 9. 2020

Katja KUNČIČ
PREOBLIKOVANJE MEDCELIČNIH STIKOV V NEVRETENČARSKIH EPITELIH MED MORFOGENEZO INTEGUMENTA IN PREBAVNEGA SISTEMA
Mentorica: doc. dr. Nada Žnidaršič
Datum zagovora: 14. 9. 2020

Miha KOPRIVNIKAR KRAJNC
VLOGA KEMOKINA CCL5 IN NJEGOVEGA RECEPTORJA CCR5 TER NOVE MOŽNOSTI ZDRAVLJENJA GLIOBLASTOMA
Mentorica: prof. dr. Tamara Lah Turnšek
Datum zagovora: 18. 9. 2020

Primož TIČ
VPLIV SOLI NA STRUKTURNO STABILNOST ANTITOKSINA Phd IZ MODULA Phd/Doc BAKTERIOFAGA P1
Mentor: prof. dr. Jurij Lah
Datum zagovora: 29. 9. 2020

Elizabeta JEVNIKAR
VPLIV ZUNAJTELESNEGA KRVNEGA OBTOKA SAMEGA IN V KOMBINACIJI Z ZUNAJTELESNO IMUNOADSORPCIJO OZIROMA METILPREDNIZOLONOM NA ZUNAJCELIČNE VEZIKLE PRI SRČNIH OPERACIJAH
Mentorica: doc. dr. Katarina Černe
Somentor: prof. dr. Matej Podbregar
Datum zagovora: 29. 9. 2020

Gašper VIRANT
ENCIMSKA PRETVORBA 5-HIDROKSIMETILFURFURALA (HMF) DO 2,5-FURANDIKARBOKSILNE KISLINE (FDCA) IN KARAKTERIZACIJA FIZIKALNIH LASTNOSTI KISLINSKIH DERIVATOV HMF
Mentorica: prof. dr. Ksenija Kogej
Somentor: izr. prof. dr. Blaž Likozar
Datum zagovora: 12. 10. 2020

Nina MAVEC
RAZVOJ ENCIMSKOIMUNSKEGA TESTA NA OSNOVI NANOTELESA SdAb19 ZA DOLOČITEV KONCENTRACIJE VIRUSNEGA PROTEINA Nef V PLAZMI
Mentorica: doc. dr. Metka Lenassi
Somentor: znan. svet. dr. Dušan Turk
Datum zagovora: 15. 10. 2020

Tomislav KOSTEVC
IZBOLJŠAVA CAR-T CELIČNE IMUNOTERAPIJE Z IMPLEMENTACIJO VERIGE CD3ε
Mentor: prof. dr. Roman Jerala
Somentor: doc. dr. Gregor Gunčar
Datum zagovora: 4. 12. 2020

MAGISTRSKI ŠTUDIJSKI PROGRAM 2. STOPNJE – TEHNIŠKA VARNOST

Polona ČUJEC
VPLIV GOSPODARSKE KRIZE NA POŠKODBE PRI DELU
Mentor: doc. dr. Jože Šrekl
Datum zagovora: 20. 1. 2020

Maša LEGAN
UPORABA MOBILNIH ELEKTRONSKIH NAPRAV IN NEMOBILNOST UPORABNIKOV
Mentorica: doc. dr. Klementina Zupan
Datum zagovora: 7. 5. 2020

Andraž NADLER
VPLIV TEMPERATURE IN UPORABE GASILSKIH OBLEK NA IZGLED NJIHOVIH TKANINSKIH VLAKEN
Mentor: prof. dr. Matija Tomšič
Somentorica: doc. dr. Klementina Zupan
Datum zagovora: 13. 5. 2020

Gregor HORVAT
POŽARNA VARNOST V VAROVANIH STANOVANJIH IN DOMOVIH ZA STAREJŠE
Mentor: doc. dr. Domen Kušar
Datum zagovora: 28. 8. 2020

Sabina TURK
ERGONOMSKO STANJE V PREDAVALNICAH IN SEMINARSKIH SOBAH NA FAKULTETI ZA KEMIJO IN KEMIJSKO TEHNOLOGIJO UNIVERZE V LJUBLJANI
Mentorica: doc. dr. Klementina Zupan
Datum zagovora: 7. 9. 2020

Sebastjan TUHTAR
STATISTIKA POŽAROV V SLOVENIJI IN ZDRUŽENIH DRŽAVAH AMERIKE
Mentor: prof. dr. Tomaž Urbič
Datum zagovora: 23. 9. 2020

Barbara JESENKO
POVEZAVA VARNOSTI PRI DELU IN GOSPODARSKE RAZVITOSTI
Mentor: prof. dr. Tomaž Urbič
Datum zagovora: 29. 9. 2020

Mateja KOČEVAR
KONTROLA OPREME POD TLAKOM
Mentor: izr. prof. dr. Boris Jerman
Datum zagovora: 30. 9. 2020

Klemen BORIN
ANALIZA BOLNIŠKEGA STALEŽA V PODJETJU
Mentor: izr. prof. dr. Simon Schnabl
Somentor: prof. dr. Tomaž Urbič
Datum zagovora: 9. 10. 2020

Ana ŽABJEK
EMISIJE OGLJIKOVEGA OKSIDA PRI GORENJU TEKSTILNIH MATERIALOV
Mentor: izr. prof. dr. Simon Schnabl
Datum zagovora: 11. 11. 2020

DIPLOME - UNIVERZITETNI ŠTUDIJ

KEMIJA – 1. STOPNJA

Marko VUZEM
DOLOČANJE SO2 IN H2S S PASIVNIMI VZORČEVALNIKI
Mentorica: izr. prof. dr. Irena Kralj Cigić
Datum zagovora: 16. 9. 2020

Martin TOMAŽIČ
STRUKTURNA KARAKTERIZACIJA IZBRANIH DERIVATOV INDAZOLA V PREPOVEDANIH SUBSTANCAH Z JEDRSKO MAGNETNO RESONANCO
Mentor: prof. dr. Janez Košmrlj
Datum zagovora: 13. 2. 2020

Matej CORN
ŠTUDIJA AEROBNE OKSIDACIJE DIBENZOTIOFENA IN TIANTRENA Z DUŠIKOVO KISLINO KOT KATALIZATORJEM V FLUORIRANIH ALKOHOLIH
Mentor: izr. prof. dr. Jernej Iskra
Datum zagovora: 3. 3. 2020

Ariana ŠUŠTARIČ
OPTIMIZACIJA METODE HFME ZA DOLOČANJE BENZOTRIAZOLOV V NARAVNIH VODAH
Mentorica: prof. dr. Helena Prosen
Datum zagovora: 23. 4. 2020

Tjaša DROŽINA
MOLEKULSKI MODELI ZAVIRALCEV TIROZIN KINAZ
Mentor: doc. dr. Črtomir Podlipnik
Datum zagovora: 7. 5. 2020

Pavlina LOKAR
REOLOŠKO OBNAŠANJE POVRŠINSKO AKTIVNIH SNOVI
Mentor: doc. dr. Bojan Šarac
Datum zagovora: 15. 5. 2020

Grega PAVLIN
PRIPRAVA PREMOSTENIH BICIKLIČNIH [2.2.2] SISTEMOV Z DIELS-ALDERJEVIMI REAKCIJAMI ZAŠČITENIH 3-AMINO-2H-PIRAN-2-ONOV
Mentor: doc. dr. Krištof Kranjc
Datum zagovora: 18. 5. 2020

Mateja KNAP
SURFAKTANTI V ČISTILNIH SREDSTVIH ZA TELO IN NJIHOVA INTERAKCIJA S KOŽO
Mentor: doc. dr. Bojan Šarac
Datum zagovora: 25. 5. 2020

Ines KULAŠIĆ
SINTEZA DERIVATOV BIFENILA Z RAZLIČNIMI ELEKTRON-PRIVLAČNIMI SKUPINAMI
Mentor: prof. dr. Janez Košmrlj
Datum zagovora: 24. 6. 2020

Ana ŠIŠKO
PRIMERJAVA RAZLIČNIH TESTNIH PAPIRJEV ZA DOLOČITEV VSEBNOSTI ALKALNE ZALOGE
Mentorica: izr. prof. dr. Irena Kralj Cigić
Datum zagovora: 24. 6. 2020

Maja ŠUBIC
PREGLED METOD ZA DOLOČEVANJE ORGANSKIH KISLIN V VINU
Mentor: izr. prof. dr. Drago Kočar
Datum zagovora: 24. 6. 2020

Jasmin RAČIĆ
RAZVOJ METODE ZA DOLOČANJE BTEX V TLEH
Mentorica: prof. dr. Helena Prosen
Datum zagovora: 29. 6. 2020

Ervin REMS
ELEKTROKEMIJSKA KARAKTERIZACIJA KINONSKIH DERIVATOV ZA UPORABO V ORGANSKIH BATERIJAH
Mentor: doc. dr. Boštjan Genorio
Datum zagovora: 7. 7. 2020

Jan ŠEGINA
SINTEZA IZOTIOCIANATOV NA OSNOVI OKSINDOLA IN NJIHOVA UPORABA V ORGANOKATALIZIRANIH PRETVORBAH
Mentor: izr. prof. dr. Uroš Grošelj
Datum zagovora: 7. 7. 2020

Anja DEŽELAK
POLPREVODNIKI IN POLPREVODNIŠKI ELEKTRONSKI ELEMENTI NA OSNOVI GRAFENA
Mentor: prof. dr. Matija Tomšič
Datum zagovora: 8. 7. 2020

Andraž ŠKOFLEK
KVANTNO-KEMIJSKA ŠTUDIJA STABILNOSTI KOORDINACIJSKIH KOMPLEKSOV KOVINSKIH IONOV Z EDTA
Mentor: izr. prof. dr. Miha Lukšič
Datum zagovora: 8. 7. 2020

Maja BENSA
DOLOČANJE FENOLNIH SPOJIN V INVAZIVNIH TUJERODNIH DRESNIKIH *(FALLOPIA SPP.)*
Mentor: izr. prof. dr. Mitja Kolar
Datum zagovora: 9. 7. 2020

Melita NOVAK
DOLOČANJE MAŠČOBNIH KISLIN V PEKOVSKIH IZDELKIH S PLINSKO KROMATOGRAFIJO
Mentorica: prof. dr. Helena Prosen
Datum zagovora: 10. 7. 2020

Tajda BLAZNIK
SINTEZA IN LASTNOSTI CINK-ALUMINIJEVIH IN CINK-KROMOVIH PLASTOVITIH DVOJNIH HIDROKSIDOV IN NJIHOVIH MEŠANIH OKSIDOV
Mentorica: izr. prof. dr. Romana Cerc Korošec
Datum zagovora: 18. 8. 2020

Manca ŠPENDAL
DOLOČANJE FENOLNIH SPOJIN V VINU IN V VINSKEM KAMNU
Mentor: izr. prof. dr. Drago Kočar
Datum zagovora: 19. 8. 2020

Kris ANTOLINC
SINTEZA IN IZOLACIJA (1S,2S,4R)-7,7-DIMETIL-1-(PIROLIDIN-1-METIL)BICIKLO[2.2.1]HEPTAN-2-AMINA
Mentor: prof. dr. Jurij Svete
Datum zagovora: 21. 8. 2020

Matija POVH
VPLIV pH NA STABILNOST IZBRANIH BARVIL IN PIGMENTOV
Mentorica: izr. prof. dr. Irena Kralj Cigić
Datum zagovora: 26. 8. 2020

Verica ZLATEVSKA
DOLOČANJE TOPNOSTI KALIJEVEGA HIDROGENTARTRATA
Mentor: izr. prof. dr. Drago Kočar
Datum zagovora: 27. 8. 2020

Katarina Barbara REBERC
PREGLED 2H-PIRAN-2-ONOV IN SINTEZA DVEH SUBSTITUIRANIH 3-BENZOILAMINO-2H-PIRAN-2-ONOV
Mentor: doc. dr. Krištof Kranjc
Datum zagovora: 27. 8. 2020

Patrik ZAVRŠNIK
UPORABNOST MODIFICIRANIH ELEKTROD IZ OGLJIKOVE PASTE V POTENCIOMETRIJI
Mentor: izr. prof. dr. Mitja Kolar
Datum zagovora: 27. 8. 2020

Sara LAZNIK
ZNAČILNOSTI VEZANJA PROTITELES NA NEKANONIČNE STRUKTURE DNA
Mentor: prof. dr. Jurij Lah
Datum zagovora: 31. 8. 2020

Tomaž MRŽLJAK
PASIVNO VZORČENJE METANOJSKE IN ETANOJSKE KISLINE IZ ZRAKA
Mentorica: izr. prof. dr. Irena Kralj Cigić
Datum zagovora: 2. 9. 2020

Aleksandra ZAMLJEN
SINTEZA IN KARAKTERIZACIJA CINKOVIH IMIDAZOLATNIH OGRODIJ
Mentor: prof. dr. Anton Meden
Datum zagovora: 2. 9. 2020

Neža ŠULC
REAKCIJE LAKTONOV S SILANSKIMI DERIVATI
Mentor: izr. prof. dr. Jernej Iskra
Datum zagovora: 2. 9. 2020

Katja GABROVEC
POLIJODIRANJE AROMATOV Z OKSIDATIVNIM PRISTOPOM
Mentor: izr. prof. dr. Jernej Iskra
Datum zagovora: 2. 9. 2020

Mina NIKOLIĆ
PREGLED METOD ZA DOLOČEVANJE VITAMINOV V PREHRANSKIH DOPOLNILIH
Mentor: izr. prof. dr. Drago Kočar
Datum zagovora: 2. 9. 2020

Martin Rafael GULIN
OPTIMIZACIJA ODDYJEVEGA TESTA
Mentor: prof. dr. Matija Strlič
Datum zagovora: 2. 9. 2020

Daša TEROBŠIČ
EMISIJA OCETNE KISLINE IZ CELULOZE ACETATA
Mentor: prof. dr. Matija Strlič
Datum zagovora: 2. 9. 2020

Pia KRŽAN
DOLOČEVANJE FENOLNIH KISLIN V AEROSOLNIH DELCIH S KAPILARNO ELEKTROFOREZO
Mentor: prof. dr. Matevž Pompe
Datum zagovora: 3. 9. 2020

Tadeja PINTAR
SINTEZA LIGANDOV ZA PRIPRAVO KLEŠČASTIH KOMPLEKSOV
Mentor: izr. prof. dr. Janez Cerkovnik
Datum zagovora: 3. 9. 2020

Grega VENTURINI
ELEKTROKEMIJSKE LASTNOSTI CELULOZNIH KOMPOZITOV V LITIJEVIH AKUMULATORJIH
Mentor: izr. prof. dr. Robert Dominko
Datum zagovora: 3. 9. 2020

Zala IVANČIČ
DOLOČANJE NEONIKOTINOIDNIH PESTICIDOV V CVETNEM PRAHU
Mentorica: prof. dr. Helena Prosen
Datum zagovora: 3. 9. 2020

Andreja KRUŠIČ
SINTEZA ZAVIRALCEV BUTIRILHOLINESTERAZE NA OSNOVI INDOLA IN NAFTALENA
Mentor: izr. prof. dr. Uroš Grošelj
Datum zagovora: 7. 9. 2020

David BEZLAJ
PRIPRAVA NCN KLEŠČASTIH LIGANDOV
Mentor: izr. prof. dr. Janez Cerkovnik
Datum zagovora: 7. 9. 2020

Lara BARTOL
PRETVORBA KARBONILNIH SPOJIN V BIOLOŠKO ZANIMIVE PRODUKTE
Mentor: prof. dr. Marjan Jereb
Datum zagovora: 7. 9. 2020

Leja TOMINEC
SODOBNI OKOLJU PRIJAZNI PRISTOP V ORGANSKI KEMIJI 2H-PIRAN-2-ONSKIH DERIVATOV: SINTEZE, REAKTIVNOST, UPORABNOST
Mentor: doc. dr. Krištof Kranjc
Datum zagovora: 8. 9. 2020

Kaja PROSENAK
NEKOVALENTNA ORGANOKATALIZA
Mentor: izr. prof. dr. Uroš Grošelj
Datum zagovora: 8. 9. 2020

Veronika KORADIN
GROBOZRNATI MODELI LIPIDNIH MEMBRAN IN NJIHOVA UPORABA
Mentor: prof. dr. Jurij Reščič
Datum zagovora: 8. 9. 2020

Miha HOTKO
KARAKTERIZACIJA VZORCEV NASTALIH PRI REAKCIJI (NH4)2[MOCL5(H2O)] IN KOCN V PIRIDINU
Mentorica: doc. dr. Nives Kitanovski
Datum zagovora: 8. 9. 2020

Anamarija KASTELIC
DOLOČANJE ELEKROFORETSKE MOBILNOSTI FULERENHEKSAMALONATNEGA IONA S KAPILARNO ELEKTROFOREZO
Mentor: izr. prof. dr. Janez Cerar
Datum zagovora: 8. 9. 2020

Monika VIDMAR
UPORABA IONSKE KROMATOGRAFIJE ZA SEPARACIJO N-GLIKANOV
Mentor: prof. dr. Matevž Pompe
Datum zagovora: 8. 9. 2020

Zala ŠTEFANIČ
VPLIV DISKRETNE RAZPOREDITVE NABOJA NA SILO MED NABITIMI NANODELCI
Mentor: prof. dr. Jurij Reščič
Datum zagovora: 9. 9. 2020

Jona ŽOHAR
SEPARACIJA GLIKANOV S KROMATOGRAFIJO Z MEŠANIMI REŽIMI
Mentor: prof. dr. Matevž Pompe
Datum zagovora: 9. 9. 2020

Maksimiljan DEKLEVA
DOLOČANJE NEPOLARNIH BENZOTRIAZOLOV V OKOLJU
Mentorica: prof. dr. Helena Prosen
Datum zagovora: 9. 9. 2020

Matic Anton PIPP
AKTIVACIJA C-H VEZI IMIDAZOLILBENZENSKIH DERIVATOV POD POGOJI KATALIZE S KOVINAMI PREHODA
Mentor: izr. prof. dr. Franc Požgan
Datum zagovora: 9. 9. 2020

Klara ŠIFRER
FOTOKATALITSKA RAZGRADNJA ANTIBIOTIKA TETRACIKLINA S TANKIMI PLASTMI TITANOVEGA DIOKSIDA
Mentorica: prof. dr. Urška Lavrenčič Štangar
Datum zagovora: 9. 9. 2020

Katja VODLAN
SINTEZA IN STRUKTURNA KARAKTERIZACIJA GALIJ-STRONCIJEVEGA TITANATA(IV)
Mentorica: izr. prof. dr. Amalija Golobič
Datum zagovora: 9. 9. 2020

Blagoj MUKAETOV
SINTEZA IZBRANIH PROPARGIL TRIAZOLIJEVIH SOLI
Mentor: prof. dr. Janez Košmrlj
Datum zagovora: 9. 9. 2020

Luka JEDLOVČNIK
SINTEZA NOVE PIRIDINIJEVE SOLI S TRIAZOLILIDENSKIM FRAGMENTOM
Mentor: prof. dr. Janez Košmrlj
Datum zagovora: 9. 9. 2020

Anže BRUS
SINTEZA IN KARAKTERIZACIJA RUTENIJEVIH KOMPLEKSOV Z BIGVANIDNIMI LIGANDI
Mentor: prof. dr. Iztok Turel
Datum zagovora: 9. 9. 2020

Petra KREMŽAR
SINTEZA IN OPTIČNE LASTNOSTI NEKATERIH N,N-DIMETIL-4-(FENILETINIL)ANILINOV
Mentor: prof. dr. Janez Košmrlj
Datum zagovora: 9. 9. 2020

Ana BRODNIK
SINTEZA MOŽNIH METABOLNIH PRODUKTOV ANALOGA FDDNP
Mentor: prof. dr. Janez Košmrlj
Datum zagovora: 9. 9. 2020

Peter KOVAČEVIĆ
SEPARACIJA N-GLIKANOV Z UPORABO HIDROFILNIH INTERAKCIJ
Mentor: prof. dr. Matevž Pompe
Datum zagovora: 9. 9. 2020

Blaž KISOVEC
SINTEZA BIFUNKCIONALNIH ROČIC ZA VEZAVO TIOLOV
Mentor: prof. dr. Janez Košmrlj
Datum zagovora: 9. 9. 2020

Jan DEŽAN
PRIPRAVA IN KARAKTERIZACIJA ALUMINIJ-KALCIJEVEGA TITANATA(IV)
Mentorica: izr. prof. dr. Amalija Golobič
Datum zagovora: 10. 9. 2020

Leon ŽAGAR
DEPOLIMERIZACIJA POLIAMIDA 1010 S HIDROLIZO V KISLEM IN VPLIVOM MIKROVALOV
Mentorica: izr. prof. dr. Irena Kralj Cigić
Datum zagovora: 10. 9. 2020

Petra LUZAR
STRUKTURNE LASTNOSTI Z GVANINI BOGATEGA ZAPOREDJA V INDUCIBILNEM PROMOTORJU MDM2
Mentor: prof. dr. Janez Plavec
Datum zagovora: 10. 9. 2020

Tjaša GAŠPERIČ
PROGRAM EXCEL KOT ORODJE ZA STATISTIČNO VREDNOTENJE REZULTATOV KEMIJSKIH ANALIZ
Mentorica: izr. prof. dr. Nataša Gros
Datum zagovora: 10. 9. 2020

Tadej KLOBUČAR
DOLOČANJE KATIONOV V CITRATNEM MATRIKSU Z IONSKO KROMATOGRAFIJO
Mentorica: izr. prof. dr. Nataša Gros
Datum zagovora: 10. 9. 2020

Urša VONČINA
FOTOKATALITSKE PRETVORBE NEKATERIH 3-(DIMETILAMINO)PROPANOATOV
Mentor: izr. prof. dr. Bogdan Štefane
Datum zagovora: 10. 9. 2020

Matic DOKL
DOLOČANJE TRITIJA V OKOLJSKIH VODAH
Mentorica: izr. prof. dr. Irena Kralj Cigić
Datum zagovora: 10. 9. 2020

Natalija SITNIKOVA
NANOS TiO2-FOTOKATALIZATORJA NA MILIMETRSKE GRANULE
Mentorica: prof. dr. Urška Lavrenčič Štangar
Datum zagovora: 10. 9. 2020

Hana ZUPAN
RAZTAPLJANJE Y{3+} IONA V FLUOROVODIKOVI KISLINI: KVANTNO-KEMIJSKA RAZISKAVA
Mentor: prof. dr. Tomaž Urbič
Datum zagovora: 17. 9. 2020

Eva KERČMAR
KVANTNO MEHANSKE LASTNOSTI MOLEKUL INHIBITORJEV GLIKOGEN FOSFORILAZE
Mentorica: prof. dr. Barbara Hribar Lee
Datum zagovora: 21. 9. 2020

Andrej PODKORITNIK
PRETVORBE KARBONILNIH SPOJIN PRI KLASIČNIH POGOJIH
Mentor: prof. dr. Marjan Jereb
Datum zagovora: 25. 9. 2020

Jaka KRUŠIČ
DOLOČEVANJE OGLJIKOVIH HIDRATOV S FLUORESCENČNO DETEKCIJO
Mentor: prof. dr. Matevž Pompe
Datum zagovora: 30. 9. 2020

Elvir MAJDANČIĆ
EKSTRAKCIJSKE METODE ZA NEPOLARNE BENZOTRIAZOLE V TRDNIH OKOLJSKIH VZORCIH
Mentorica: prof. dr. Helena Prosen
Datum zagovora: 2. 10. 2020

KEMIJSKO INŽENIRSTVO – 1. STOPNJA

Jernej SLAK
OBLIKOVNI UČINEK KOPOLIMEROV BENZOKSAZINA IN EPOKSIDNIH SMOL
Mentor: doc. dr. Aleš Ručigaj
Datum zagovora: 5. 2. 2020

Neža VESEL
BOROFEN KOT ADITIV ZA PREMAZE VISOKOTEMPERATURNIH SOLARNIH ABSORBERJEV
Mentor: doc. dr. Boštjan Genorio
Datum zagovora: 13. 2. 2020

Tadej ŽURIČ
VPLIV pH VREDNOSTI IN TEMPERATURE NA KONTROLIRANO SPROŠČANJE UČINKOVIN IZ HIDROGELOV
Mentor: doc. dr. Aleš Ručigaj
Datum zagovora: 17. 2. 2020

Miha OKORN
PRIPRAVA BELEGA PIGMENTA IZ HIDRATIZIRANEGA TITANOVEGA OKSIDA
Mentor: izr. prof. dr. Marjan Marinšek
Datum zagovora: 16. 4. 2020

Živa NOVAK
PREVERJANJE ELEKTROKEMIJSKIH LASTNOSTI JEKEL PRIDOBLJENIH S POSTOPKOM PODHLAJEVANJA
Mentor: prof. dr. Miran Gaberšček
Datum zagovora: 23. 4. 2020

Filip BERGELJ
VPLIV PROCESNIH PARAMETROV NA KVALITETO GALVANSKE OBDELAVE
Mentor: doc. dr. Aleš Ručigaj
Datum zagovora: 8. 5. 2020

Tia HAFNER
TEHNIKE PEGILACIJE PROTEINOV
Mentor: prof. dr. Aleš Podgornik
Datum zagovora: 8. 6. 2020

Tine VRAVNIK
MODELIRANJE KEMIJSKIH REAKCIJ Z UPORABO MOLEKULSKE DINAMIKE
Mentor: prof. dr. Igor Plazl
Datum zagovora: 1. 7. 2020

Eva TERBOVŠEK
ČIŠČENJE R-FIKOERITRINA V MIKROFLUIDNEM SISTEMU Z INTEGRIRANO ULTRAFILTRACIJO
Mentorica: prof. dr. Polona Žnidaršič Plazl
Datum zagovora: 2. 7. 2020

Gašper KRAJEC
DEVULKANIZACIJA GUME
Mentorica: prof. dr. Urška Šebenik
Datum zagovora: 6. 7. 2020

Ana MARKOVIĆ
KOMPOZITNI MATERIALI ZA LATENTNO SHRANJEVANJE ENERGIJE
Mentorica: prof. dr. Urška Šebenik
Datum zagovora: 6. 7. 2020

Mitja KOSTELEC
PAMETNI BIOPOLIMERNI MATERIALI NA OSNOVI HITOZANA
Mentor: doc. dr. Aleš Ručigaj
Datum zagovora: 6. 7. 2020

Pia FACKOVIČ VOLČANJK
VULKANIZACIJA Z UPORABO AKTIVATORJA IZ SLADKORNEGA TRSA
Mentorica: prof. dr. Urška Šebenik
Datum zagovora: 6. 7. 2020

Katarina VUKOSAV
REVERZIBILNOST PROCESOV NA MAGNEZIJEVI ANODI
Mentor: izr. prof. dr. Robert Dominko
Datum zagovora: 7. 7. 2020

Marcel LEVSTEK
UMETNA INTELIGENCA V BIOINŽENIRSTVU
Mentorica: prof. dr. Polona Žnidaršič Plazl
Datum zagovora: 8. 7. 2020

Marko TRAVICA
SUPERKRITIČNA EKSTRAKCIJA
Mentor: prof. dr. Aleš Podgornik
Datum zagovora: 25. 8. 2020

Jošt OBLAK
SINTEZA BOROFENOV NA KOVINSKIH SUBSTRATIH
Mentor: doc. dr. Boštjan Genorio
Datum zagovora: 27. 8. 2020

Rok PEZDIRC
SINTEZA IN APLIKACIJA MXENOV
Mentor: doc. dr. Boštjan Genorio
Datum zagovora: 27. 8. 2020

Špela BRATUŠ
TRETJA GENERACIJA SOLARNIH CELIC
Mentor: izr. prof. dr. Marjan Marinšek
Datum zagovora: 28. 8. 2020

Nejc LAPAJNE
PEROVSKITI IN PIEZOELEKTRIČNI EFEKT
Mentor: izr. prof. dr. Marjan Marinšek
Datum zagovora: 28. 8. 2020

Žan SPOLENAK
EMAJLIRANA PLOČEVINA
Mentor: izr. prof. dr. Marjan Marinšek
Datum zagovora: 28. 8. 2020

Peter GARTNAR
REOLOŠKE LASTNOSTI GELOV ZA LASE
Mentorica: doc. dr. Lidija Slemenik Perše
Datum zagovora: 31. 8. 2020

Luka TACER
ADSORPCIJA KOVIN NA MIKROPLASTIKO
Mentorica: doc. dr. Gabriela Kalčikova
Datum zagovora: 2. 9. 2020

Primož ŠPRINGER
VPLIV OKOLJSKO RELEVANTNE MIKROPLASTIKE NA MALO VODNO LEČO LEMNA MINOR
Mentorica: doc. dr. Gabriela Kalčikova
Datum zagovora: 3. 9. 2020

Anja VOLK
PRIMERJAVA UČINKOVITOSTI ČIŠČENJA ODPADNE VODE Z RASTLINSKO ČISTILNO NAPRAVO V ZIMSKEM IN POLETNEM OBDOBJU
Mentorica: prof. dr. Andreja Žgajnar Gotvajn
Datum zagovora: 3. 9. 2020

Tadej ZADRAVEC
BREZTOKOVNO IN TOKOVNO NANAŠANJE NIKLJA NA MAGNETNE Nd-Fe-B MIKRO DELCE
Mentor: izr. prof. dr. Marjan Marinšek
Datum zagovora: 4. 9. 2020

Taja ČERNIC
EFEKT SAMOPOPRAVLJIVOSTI V BETONIH
Mentor: izr. prof. dr. Marjan Marinšek
Datum zagovora: 4. 9. 2020

Sebastijan RAJŠTER
MATEMATIČNO MODELIRANJE SOČASNE EKSTRAKCIJE IN REAKCIJE V MIKROFLUIDNEM SISTEMU
Mentor: prof. dr. Igor Plazl
Datum zagovora: 4. 9. 2020

Miha MIHOVEC
REVERZIBILNO ZAMREŽEN POLIURETAN S PINAKOLNO VEZJO
Mentorica: prof. dr. Urška Šebenik
Datum zagovora: 4. 9. 2020

Jaka NOVAK
TRIBOLOŠKE LASTNOSTI GRAFENA
Mentor: doc. dr. Boštjan Genorio
Datum zagovora: 4. 9. 2020

Rok POLJANC
SPREMLJANJE ACR REAKCIJE SKOZI MIKROSTRUKTURNO ANALIZO BETONOV Z DOLOMITNIM AGREGATOM
Mentor: izr. prof. dr. Marjan Marinšek
Datum zagovora: 4. 9. 2020

Nik SMRKOLJ
NOVI OGLJIKOVI ALOTROPI
Mentor: doc. dr. Boštjan Genorio
Datum zagovora: 4. 9. 2020

Alexander Marjan MULEC
VPLIV VELIKOSTI IN LASTNOSTI MOLEKUL NA HITROST SPROŠČANJA IZ HIDROGELOV
Mentor: doc. dr. Aleš Ručigaj
Datum zagovora: 4. 9. 2020

Žan BOČEK
VPLIV DODATKA MODIFIKATORJA NA LASTNOSTI HIDROGELOV IZ HITOZANA
Mentor: doc. dr. Aleš Ručigaj
Datum zagovora: 4. 9. 2020

Ožbej VODEB
MODELIRANJE TRANSPORTA OB ELEKTRODAH ZA MERJENJE AKTIVNOSTI ELEKTROKATALIZATORJEV
Mentor: prof. dr. Miran Gaberšček
Datum zagovora: 7. 9. 2020

Katja DROBEŽ
PRIPRAVA IN TESTIRANJE SODOBNIH KATALIZATORJEV ZA SINTEZO METANOLA
Mentor: izr. prof. dr. Marjan Marinšek
Datum zagovora: 7. 9. 2020

Jošt OBLAK
SINTEZA GRAFEN OKSIDA IZ OSTANKOV ELEKTROLITSKIH GRAFITNIH ELEKTROD
Mentor: doc. dr. Boštjan Genorio
Datum zagovora: 7. 9. 2020

Nika OŠLAJ
PRIPRAVA ELEKTRIČNO PREVODNIH GRAFENSKIH KOMPOZITOV
Mentor: doc. dr. Boštjan Genorio
Datum zagovora: 7. 9. 2020

Nina KUKOVIČIČ
SPREMLJANJE UČINKOVITOSTI PILOTNE INFILTRACIJSKE MALE KOMUNALNE ČISTILNE NAPRAVE
Mentorica: prof. dr. Andreja Žgajnar Gotvajn
Datum zagovora: 7. 9. 2020

Leja PLEŠKO
OKOLJSKO RELEVANTNO TESTIRANJE STRUPENOSTI NETOPNIH PREMAZOV
Mentorica: doc. dr. Gabriela Kalčikova
Datum zagovora: 7. 9. 2020

Sara OMERZEL
DOLOČANJE VPLIVA SPREMENLJIVEGA TLAKA NA ŠOBI NA DELOVANJE VINOGRADNIŠKEGA PRŠILNIKA
Mentor: izr. prof. dr. Marko Hočevar
Datum zagovora: 7. 9. 2020

Ana SIMČIČ ZULJAN
BIOLOŠKA PRIPRAVA RAZLIČNIH ALDARNIH KISLIN
Mentor: izr. prof. dr. Blaž Likozar
Datum zagovora: 7. 9. 2020

Timi BABIČ
SINTEZA IN DEKORACIJA NANOŽIC MOLIBDENOVIH OKSIDOV
Mentor: doc. dr. Boštjan Genorio
Datum zagovora: 7. 9. 2020

Maja CAF
ULTRA VISOKOTLAČNA KROMATOGRAFIJA MAKROMOLEKUL
Mentor: prof. dr. Aleš Podgornik
Datum zagovora: 8. 9. 2020

Neja KAVČIČ
KROMATOGRAFIJA VIRUSOV IN VIRUSOM PODOBNIH DELCEV
Mentor: prof. dr. Aleš Podgornik
Datum zagovora: 8. 9. 2020

Urban OBLAK
PREGLED POSTOPKOV IZOLACIJE IN ČIŠČENJA KORDICEPINA IZ GLIVE *CORDYCEPS MILITARIS*
Mentorica: prof. dr. Polona Žnidaršič Plazl
Datum zagovora: 9. 9. 2020

Zarja MEDVED
RAZGRADNJA LIGNOCELULOZNE BIOMASE IN VALORIZACIJA LIGNINA
Mentorica: prof. dr. Polona Žnidaršič Plazl
Datum zagovora: 9. 9. 2020

Andrej ŽERJAL
NEPOSREDNO ZAJEMANJE OGLJIKOVEGA DIOKSIDA IZ OZRAČJA
Mentor: prof. dr. Igor Plazl
Datum zagovora: 9. 9. 2020

Špela HREN
VPLIV IZLUŽKOV MIKROPLASTIKE NA RAST MALE VODNE LEČE
Mentorica: doc. dr. Gabriela Kalčikova
Datum zagovora: 10. 9. 2020

Mark STARIN
ELEKTROKEMIJSKI POSTOPKI ZA ODSTRANJEVANJE ANTIBIOTIKOV IZ ODPADNIH VOD
Mentorica: prof. dr. Andreja Žgajnar Gotvajn
Datum zagovora: 10. 9. 2020

Klemen OMAN
NAČINI ZAMREŽEVANJA TEMPO MODIFICIRANE NANOCELULOZE ZA UPORABO V DOSTAVNIH SISTEMIH ZDRAVIL
Mentor: doc. dr. Aleš Ručigaj
Datum zagovora: 10. 9. 2020

Gašper TEGELJ
OPTIMIZACIJA AKTIVACIJE REOLOŠKEGA ADITIVA V POSTOPKU PROIZVODNJE 2K PUR HS PREMAZA
Mentor: prof. dr. Matevž Dular
Datum zagovora: 10. 9. 2020

Vid URBANČIČ
VPLIV ANTIBIOTIKOV V ODPADNEM BLATU NA PROIZVODNJO BIOPLINA
Mentorica: prof. dr. Andreja Žgajnar Gotvajn
Datum zagovora: 10. 9. 2020

Anže KOVAČIČ
VPLIV REOLOŠKIH LASTNOSTI TEKOČEGA PREMAZA NA LASTNOSTI SUHEGA FILMA NA SUBSTRATU
Mentorica: doc. dr. Lidija Slemenik Perše
Datum zagovora: 10. 9. 2020

Nanja BRELIH
PROIZVODNJA BIOGORIV IZ LIGNOCELULOZNE BIOMASE
Mentor: prof. dr. Igor Plazl
Datum zagovora: 17. 9. 2020

Gaja MASTNAK SUBAN
UPORABA AKRILNIH HIDROGELOV V BIOMEDICINI
Mentorica: prof. dr. Urška Šebenik
Datum zagovora: 29. 9. 2020

Jure VELKAVRH
UČINKOVITOST KROMATOGRAFSKIH KOLON
Mentor: prof. dr. Aleš Podgornik
Datum zagovora: 2. 10. 2020

Samo STANKOVIČ
PRIPRAVA IN UPORABA KOVINSKIH PEN
Mentor: prof. dr. Aleš Podgornik
Datum zagovora: 12. 10. 2020

Maja GEORGIEVSKI
UPORABA IONSKIH KAPLJEVIN IN EVTEKTIČNIH TOPIL ZA IZVEDBO BIOTRANSFORMACIJ
Mentorica: prof. dr. Polona Žnidaršič Plazl
Datum zagovora: 28. 12. 2020

BIOKEMIJA – 1. STOPNJA

Nika GORŠEK
PRIPRAVA IN OSNOVNA BIOKEMIJSKA KARATERIZACIJA TREH TIPOV METAKASPAZ IZ ALG
Mentorica: doc. dr. Marina Klemenčič
Datum zagovora: 24. 2. 2020

Barbara SLAPNIK
ANALIZA HUMANEGA MITOHONDRIJSKEGA GENOMA S TEHNOLOGIJO SEKVENCIRANJA NASLEDNJE GENERACIJE (NGS)
Mentor: prof. dr. Simon Horvat
Datum zagovora: 22. 6. 2020

Anja KOBAL
MOLEKULSKO KLONIRANJE IN PRIPRAVA REKOMBINANTNIH VARIANT PROTEINOV Cas9 IN EXOIII V BAKTERIJI *ESCHERICHIA COLI*
Mentor: izr. prof. dr. Marko Dolinar
Datum zagovora: 10. 7. 2020

Tina KOLENC MILAVEC
VPLIV KANABIDIOLA IN KANABIGEROLA NA INVAZIVNOST DIFERENCIRANIH GLIOBLASTOMSKIH CELIC IN MATIČNIH RAKAVIH CELIC GLIOBLASTOMA
Mentorica: prof. dr. Tamara Lah Turnšek
Datum zagovora: 31. 8. 2020

Anja MAVER
STANDARDIZACIJA PROTOKOLA MERITEV L-LAKTATA V POSAMEZNI CELICI 3T3-L1
Mentor: prof. dr. Robert Zorec
Datum zagovora: 31. 8. 2020

Ajda KRČ
SPREMLJANJE KOTRANSLACIJSKEGA VSTAVLJANJA IN SESTAVLJANJA MEMBRANSKEGA PROTEINA Z VEČ TRANSMEMBRANSKIMI VIJAČNICAMI IN VIVO V *ESCHERICHII COLI*
Mentor: izr. prof. dr. Marko Novinec
Datum zagovora: 31. 8. 2020

Liza ULČAKAR
RAZMERJE MED STRUKTURO IN AKTIVNOSTJO IZBRANIH RASTLINSKIH FENOLOV IN NJIHOV MEHANIZEM INHIBICIJE KATEPSINOV B IN L
Mentor: izr. prof. dr. Marko Novinec
Datum zagovora: 31. 8. 2020

Nika MIKULIČ VERNIK
IDENTIFIKACIJA PROTEINSKIH TARČ DERIVATA PIRAZOLA V BAKTERIJI *ESCHERICHIA COLI*
Mentor: izr. prof. dr. Marko Novinec
Datum zagovora: 31. 8. 2020

Špela SUPEJ
IZOLACIJA IN KARAKTERIZACIJA MUTANTOV ANEKSINA A11 D40G IN ΔN1-118
Mentorica: doc. dr. Vera Župunski
Datum zagovora: 3. 9. 2020

Doroteja ARMIČ
BIOINFORMATSKA ANALIZA IN MOLEKULSKO KLONIRANJE LEGUMAINA IZ ZELENE ALGE *CHLAMYDOMONAS REINHARDTII*
Mentorica: doc. dr. Marina Klemenčič
Datum zagovora: 3. 9. 2020

Urša ŠTRANCAR
Določanje Izražanja mRNA Alfa-7 Nikotinskih Receptorjev V Krvi Pri Človeku
Mentor: doc. dr. Uroš Kovačič
Datum zagovora: 4. 9. 2020

Matija RUPARČIČ
RAZLIKOVANJE MED GOSENICAMI VEŠČ SOVK NA OSNOVI ČRTNE KODE DNA
Mentor: izr. prof. dr. Marko Dolinar
Datum zagovora: 7. 9. 2020

Jernej IMPERL
VZPOSTAVITEV EKSPERIMENTALNEGA SISTEMA NA OSNOVI FOTOSINTEZNIH BARVIL ZA SPREMLJANJE RASTI VODNIH MIKROORGANIZMOV V KOKULTURI
Mentor: izr. prof. dr. Marko Dolinar
Datum zagovora: 7. 9. 2020

Tadej MEDVED
KLONIRANJE SKRAJŠANE RAZLIČICE ZAPISA ZA DIHIDROOROTAT DEHIDROGENAZO IZ ORGANIZMA *PLASMODIUM FALCIPARUM* IN IN SILICO ŠTUDIJA INHIBICIJE PROTEINA Z IZBRANIMI INHIBITORJI
Mentorica: doc. dr. Marina Klemenčič
Datum zagovora: 7. 9. 2020

Martina LOKAR
OZNAČEVANJE AKTIVNE OBLIKE MLKL
Mentor: doc. dr. Gregor Gunčar
Datum zagovora: 7. 9. 2020

Urška ZAGORC
DOLOČANJE VELIKOSTI IN KARAKTERIZACIJA LIPIDNIH VEZIKLOV
Mentorica: prof. dr. Ksenija Kogej
Datum zagovora: 7. 9. 2020

Martin ŠPENDL
OPTIMIZACIJA RABE KODONOV SINTETIČNIH GENOV ZA IZRAŽANJE V E. COLI S STROJNIM UČENJEM
Mentor: doc. dr. Gregor Gunčar
Datum zagovora: 7. 9. 2020

Aljaž BRATINA
BIOINFORMACIJSKA ANALIZA ZUNAJCELIČNE DOMENE ADAM17 IN PRIPRAVA ZAPISOV ZA NJENE SKRAJŠANE OBLIKE
Mentorica: prof. dr. Brigita Lenarčič
Datum zagovora: 8. 9. 2020

Anamarija AGNIČ
PRIPRAVA MUTANTNIH OBLIK EpCAM ZA ŠTUDIJ CEPITVE S PROTEAZO TACE
Mentor: doc. dr. Miha Pavšič
Datum zagovora: 8. 9. 2020

Špela Katarina DEUČMAN
SODOBNI ANALIZNI PRISTOPI PRI KARAKTERIZACIJI PROPOLISA
Mentor: izr. prof. dr. Mitja Kolar
Datum zagovora: 9. 9. 2020

Klementina POLANEC
FILOGENETSKA ANALIZA PROTEINOV DRUŽINE FET PRI SESALCIH
Mentorica: doc. dr. Vera Župunski
Datum zagovora: 9. 9. 2020

Patrik LEVAČIĆ
IZBOR PROTITELES ZA KVANTITATIVNO DOLOČITEV KANABINOIDNIH RECEPTORJEV V CELIČNIH LINIJAH RAKA DOJKE
Mentorica: izr. prof. dr. Nataša Debeljak
Datum zagovora: 10. 9. 2020

Luka FRATINA
UPORABA HALOALKAN DEHALOGENAZNE DOMENE ZA OZNAČEVANJE PROTEINA MLKL
Mentor: doc. dr. Gregor Gunčar
Datum zagovora: 10. 9. 2020

Ajda GODEC
HETERODIMERIZACIJA ČLOVEŠKIH ALFA-AKTININOV-1 IN -4
Mentor: doc. dr. Miha Pavšič
Datum zagovora: 10. 9. 2020

Luka GNIDOVEC
EVOLUCIJA TDP-43 IN NJEGOVIH PSEVDOGENOV PRI SESALCIH
Mentorica: doc. dr. Vera Župunski
Datum zagovora: 10. 9. 2020

Lea KNEZ
IZBITJE GENSKE GRUČE SNORD116 IZ PRADER-WILLI LOKUSA V SESALSKIH CELIČNIH LINIJAH
Mentor: prof. dr. Boris Rogelj
Datum zagovora: 10. 9. 2020

TEHNIŠKA VARNOST – 1- STOPNJA

Aneja NOVAK
ERGONOMSKA ANALIZA DELOVNEGA MESTA Z RAČUNALNIKOM
Mentorica: doc. dr. Klementina Zupan
Datum zagovora: 27. 1. 2020

Anja MASTNAK
ERGONOMIJA PRI DELU VOZNIKA CISTERNE
Mentorica: doc. dr. Klementina Zupan
Datum zagovora: 4. 5. 2020

Mevla SAGRKOVIĆ
ERGONOMSKA UREDITEV LINIJE V PROIZVODNJI SVETIL
Mentorica: doc. dr. Klementina Zupan
Datum zagovora: 13. 5. 2020

Duška BAJUK
PREHRANA IN UČINKOVITOST PRI DELU
Mentorica: doc. dr. Klementina Zupan
Datum zagovora: 1. 7. 2020

Gašper POGAČAR
ANALIZA VPLIVOV AKTIVNE POŽARNE ZAŠČITE NA RAZVOJ POŽARA V SKLADIŠČU OKOLJU NEVARNIH ODPADKOV
Mentor: izr. prof. dr. Simon Schnabl
Datum zagovora: 6. 7. 2020

Petra ERZETIČ
PRIMERJAVA IWAY ZAHTEV S SLOVENSKO ZAKONODAJO
Mentor: izr. prof. dr. Simon Schnabl
Datum zagovora: 17. 8. 2020

Matej PLESTENJAK
EVAKUACIJA GLEDALIŠKE DVORANE
Mentorica: doc. dr. Klementina Zupan
Datum zagovora: 28. 8. 2020

Miha BIZJAK
TAKTIČNI POSTOPKI PRI GAŠENJU POŽAROV V NARAVNEM OKOLJU
Mentor: izr. prof. dr. Simon Schnabl
Datum zagovora: 4. 9. 2020

Urša KNE
ANALIZA DELOVNEGA MESTA PO PRINCIPU METODE OWAS
Mentorica: doc. dr. Klementina Zupan
Datum zagovora: 4. 9. 2020

Kristina POKRIVAČ
ERGONOMIJA PRIHODNJIH GENERACIJ
Mentorica: doc. dr. Klementina Zupan
Datum zagovora: 7. 9. 2020

Nika ŠTER
STATISTIČNA ANALIZA NEZGOD V FARMACEVTSKEM PODJETJU
Mentor: prof. dr. Tomaž Urbič
Datum zagovora: 9. 9. 2020

Haris HAJRLAHOVIĆ
DOLOČITEV IZBRANIH KOVIN V POVRŠINSKI VODI Z ICP-OES IN OCENA NJIHOVIH VPLIVOV NA ZDRAVJE LJUDI
Mentorica: doc. dr. Barbara Novosel
Datum zagovora: 9. 9. 2020

Nadja BEKELJA
TOPLOTNE OBREMENITVE PRI DELU NA PROSTEM
Mentorica: prof. dr. Marija Bešter Rogač
Datum zagovora: 10. 9. 2020

Matjaž ŠIREC
NEGORLJIVI MATERIALI KOT ZAŠČITA PRI POŽARIH
Mentorica: prof. dr. Marija Bešter Rogač
Datum zagovora: 10. 9. 2020

Jan KROMAR
ANALIZA UPORABNOSTI OVČJE VOLNE ZA IZOLACIJO ZGRADB IN VARNOSTNIH OBLAČIL S STALIŠČA POŽARNE VARNOSTI
Mentor: izr. prof. dr. Simon Schnabl
Datum zagovora: 10. 9. 2020

Blaž ZUPANČIČ
PRESOJA VARNE UPORABE FITOFARMACEVTSKIH SREDSTEV IN ALTERNATIVNIH METOD ZA ZATIRANJE AMBROZIJE
Mentorica: doc. dr. Barbara Novosel
Datum zagovora: 10. 9. 2020

Kristjan REŠETIČ
VPLIVI ADITIVOV NA EMISIJE MOTORJEV Z NOTRANJIM IZGOREVANJEM
Mentorica: doc. dr. Barbara Novosel
Datum zagovora: 22. 9. 2020

Janja KERIČ
ODGOVORNA RABA KEMIKALIJ V SREDNJIH IN OSNOVNIH ŠOLAH
Mentorica: doc. dr. Barbara Novosel
Datum zagovora: 26. 10. 2020

Nejc ZAVIRŠEK
POŽARI V NARAVI OD LETA 2005 DO 2019 V SLOVENIJI
Mentor: izr. prof. dr. Simon Schnabl
Datum zagovora: 3. 12. 2020

DIPLOME – VISOKOŠOLSKI STROKOVNI ŠTUDIJ

KEMIJSKA TEHNOLOGIJA – 1. STOPNJA

Luka DOLAR
PREGLED, ZGODOVINA IN UPORABA METAMATERIALOV
Mentor: prof. dr. Aleš Podgornik
Datum zagovora: 6. 1. 2020

Boštjan ZARNIK
NIKLJEVE IN KOBALTOVE SPOJINE S CITRONSKO KISLINO
Mentor: doc. dr. Bojan Kozlevčar
Datum zagovora: 31. 1. 2020

David DRAGAN
VPLIV SINTEZNIH PARAMETROV NA VELIKOST KRISTALOV ZEOLITA P: SINTEZA IN STRUKTURNA KARAKTERIZACIJA
Mentor: prof. dr. Anton Meden
Datum zagovora: 6. 2. 2020

Renata SKUŠEK
KEMIJSKO RAVNOTEŽJE V VSAKDANJEM ŽIVLJENJU
Mentor: prof. dr. Andrej Jamnik
Datum zagovora: 7. 2. 2020

Domen IPAVEC
PRIPRAVA 3-METOKSI-1H-INDOL-2-KARBOKSILNE KISLINE KOT KLJUČNEGA INTERMEDIATA ZA SINTEZO CEPHALANDOLA C
Mentor: doc. dr. Martin Gazvoda
Datum zagovora: 13. 2. 2020

Viljem VOLF
MATERIALI ZA VARČEVANJE Z ENERGIJO V NOVEJŠIH GRADNJAH
Mentorica: doc. dr. Klementina Zupan
Datum zagovora: 9. 4. 2020

Uroš MEZEK
SINTEZA ORGANOKATALIZATORJEV NA OSNOVI KINUKLIDINA
Mentor: izr. prof. dr. Uroš Grošelj
Datum zagovora: 10. 4. 2020

Blaž TOPLAK
DOLOČANJE VITAMINA E V RASTLINSKIH OLJIH Z DIFERENČNO PULZNO VOLTAMETRIJO
Mentor: izr. prof. dr. Mitja Kolar
Datum zagovora: 5. 5. 2020

Nika MUZGA
REOLOŠKE LASTNOSTI JOGURTA MASOVNE IN DOMAČE PROIZVODNJE
Mentorica: doc. dr. Lidija Slemenik Perše
Datum zagovora: 6. 5. 2020

Lara Eva RUDOLF
RAZVOJ EKSTRAKCIJSKE METODE ZA DOLOČANJE BENZOTRIAZOLOV V TLEH
Mentorica: prof. dr. Helena Prosen
Datum zagovora: 6. 5. 2020

Luka SETNIKAR
LUMINISCENČNE LASTNOSTI CINKOVIH KOORDINACIJSKIH SPOJIN Z INDOL-3-KARBOKSILATNIM LIGANDOM
Mentor: izr. prof. dr. Franc Perdih
Datum zagovora: 15. 5. 2020

Jan KOLER
OPTIMIZACIJA SINTEZE BAKROVIH(I) KOORDINACIJSKIH SPOJIN S FOSFINSKIMI LIGANDI IN NEOKUPROINOM
Mentor: doc. dr. Jakob Kljun
Datum zagovora: 21. 5. 2020

Nika MARINČ
KOBALTOVE SPOJINE Z BENZOJSKO KISLINO
Mentor: doc. dr. Bojan Kozlevčar
Datum zagovora: 22. 5. 2020

Uroš PAVLIN
PRIPRAVA KLEŠČASTIH KOMPLEKSOV
Mentor: izr. prof. dr. Janez Cerkovnik
Datum zagovora: 8. 6. 2020

Matevž ŠTEFANČIČ
VALIDACIJA HPLC METODE ZA SELEKTIVNO DOLOČEVANJE KANABINOIDOV
Mentor: prof. dr. Matevž Pompe
Datum zagovora: 9. 6. 2020

Jure JAKOŠ
RAZVOJ PROGRAMSKE OPREME ZA DOLOČEVANJE STRUKTUR ORGANSKIH MOLEKUL NA PODLAGI IR IN 1H NMR SPEKTROSKOPIJE
Mentor: doc. dr. Martin Gazvoda
Datum zagovora: 24. 6. 2020

Hanno BRADEŠKO
LUMINISCENČNE LASTNOSTI CINKOVIH KOORDINACIJSKIH SPOJIN Z DIKETONATNIMI IN KARBOKSILATNIMI LIGANDI
Mentor: izr. prof. dr. Franc Perdih
Datum zagovora: 10. 7. 2020

Ajda URANIČ
ČIŠČENJE EKSTRAKTOV TRDNIH VZORCEV S HFME
Mentorica: prof. dr. Helena Prosen
Datum zagovora: 10. 7. 2020

Diana MARINKOVIĆ
KARAKTERIZACIJA VZORCA NASTALEGA PRI REAKCIJI BAKROVEGA SULFATA IN KALIJEVEGA OKSALATA
Mentorica: doc. dr. Nives Kitanovski
Datum zagovora: 10. 7. 2020

Žiga VESEL
DERIVATI OKSINDOLA IN ISATINA TER NJIHOVA UPORABA V ORGANOKATALIZIRANIH PRETVORBAH – SINTEZA IZOTIOCIANATOV NA OSNOVI 5-FLUOROINDOLIN-2,3-DIONA
Mentor: izr. prof. dr. Uroš Grošelj
Datum zagovora: 20. 8. 2020

Lucijan KOLENC
IMOBILIZACIJA CuO FOTOKATALIZATORJA
Mentorica: prof. dr. Urška Lavrenčič Štangar
Datum zagovora: 27. 8. 2020

Mateja KLEMENIĆ
IMOBILIZACIJA TiO2 NANOSTRUKTURIRANIH MIKRODELCEV
Mentorica: prof. dr. Urška Lavrenčič Štangar
Datum zagovora: 27. 8. 2020

Eva TERKAJ
IDENTIFIKACIJA KRISTALINIČNIH SNOVI V KREMAH ZA SONČENJE Z RENTGENSKO PRAŠKOVNO DIFRAKCIJO
Mentor: prof. dr. Anton Meden
Datum zagovora: 27. 8. 2020

Jerneja MAČEK
DOLOČANJE NAPAK PRI NEVTRALIZACIJSKIH TITRACIJAH
Mentor: izr. prof. dr. Drago Kočar
Datum zagovora: 27. 8. 2020

Martin NAGODE
SINTEZA IN REAKTIVNOST PIRENMETILAMINSKEGA FLUORESCENČNEGA DERIVATIZACIJSKEGA REAGENTA
Mentor: izr. prof. dr. Franc Požgan
Datum zagovora: 27. 8. 2020

Klavdija GRANDLJIČ
TEHNIKE TERMIČNE ANALIZE ZA PREUČEVANJE MATERIALOV KULTURNE DEDIŠČINE
Mentorica: izr. prof. dr. Romana Cerc Korošec
Datum zagovora: 27. 8. 2020

Uroš KASTELIC
MERJENJE VLAŽNOSTI V FARMACIJI
Mentor: viš. pred. dr. Andrej Godec
Datum zagovora: 31. 8. 2020

Teja BELE
RENTGENSKA PRAŠKOVNA DIFRAKCIJA PREHRANSKIH DOPOLNIL
Mentor: prof. dr. Anton Meden
Datum zagovora: 2. 9. 2020

Rene URH
TEORIJSKA OBRAVNAVA FAZNEGA RAVNOTEŽJA TEKOČINA-PARA
Mentor: prof. dr. Andrej Jamnik
Datum zagovora: 2. 9. 2020

Klara METLIČAR
KARAKTERIZACIJA KOORDINACIJSKE SPOJINE KROMA S PIRIDINSKIMI IN HALOGENIDNIMI LIGANDI
Mentorica: doc. dr. Nives Kitanovski
Datum zagovora: 2. 9. 2020

Matic KRIVEC
DIDAKTIČNI MODUL ZA UČENJE UMERJANJA MERILNIKOV
Mentor: izr. prof. dr. Janez Cerar
Datum zagovora: 4. 9. 2020

Lara ŽIBERNA
KATIONSKA MODIFIKACIJA A-CELULOZE IN KRISTALINIČNE NANOCELULOZE Z GIRARD REAGENTOM T
Mentor: viš. pred. dr. Branko Alič
Datum zagovora: 4. 9. 2020

Lucija PETRIČ
VPLIV DODATKOV NA LASTNOSTI SULFONIRANIH MELAMINSKO FORMALDEHIDIH PEN
Mentor: viš. pred. dr. Branko Alič
Datum zagovora: 4. 9. 2020

Tina ZUPANČIČ
PRETVORBE HALOGENIRANIH ORGANSKIH SPOJIN
Mentor: prof. dr. Marjan Jereb
Datum zagovora: 7. 9. 2020

Nataša ŠUKLJE
SINTEZA NEKATERIH HALKOGENIRANIH DERIVATOV
Mentor: prof. dr. Marjan Jereb
Datum zagovora: 7. 9. 2020

Rok BRULC
ADENIN KOT KATION V HEKSAFLUORIDOSILIKATNIH SOLEH
Mentor: doc. dr. Andrej Pevec
Datum zagovora: 7. 9. 2020

Urša JAMNIK
FIZIKALNO KEMIJSKE LASTNOSTI MEDU
Mentorica: prof. dr. Barbara Hribar Lee
Datum zagovora: 8. 9. 2020

Patrik HORŽEN
KOORDINACIJSKA KEMIJA CINKA(II) S PIPERAZINOM IN DERIVATI
Mentorica: doc. dr. Barbara Modec
Datum zagovora: 9. 9. 2020

Katja RUPARČIČ
PREGLED ANALIZNIH METOD ZA DOLOČANJE KALCIJA V PREHRANSKIH DOPOLNILIH
Mentor: izr. prof. dr. Drago Kočar
Datum zagovora: 9. 9. 2020

Marko BUNARKIĆ
ANALIZA SINTEZNIH POSTOPKOV IN STRUKTUR SREBROVIH KOORDINACIJSKIH SPOJIN Z IMIDAZOLIDIN-2-TIONI IN NAČRTOVANJE SINTEZ ANALOGNIH SREBROVIH KOORDINACIJSKIH SPOJIN S 1,2,4-TRIAZOLIDIN-3-TIONI.
Mentor: doc. dr. Jakob Kljun
Datum zagovora: 9. 9. 2020

Amela AVDIČEVIĆ
UPORABA METOD TERMIČNE ANALIZE ZA PREUČEVANJE TERMIČNE STABILNOSTI OLJ
Mentorica: izr. prof. dr. Romana Cerc Korošec
Datum zagovora: 9. 9. 2020

David HOČEVAR
MERJENJE TEMPERATURE V INDUSTRIJI
Mentor: doc. dr. Bojan Šarac
Datum zagovora: 9. 9. 2020

Andrej KUČIČ
PRETOČNI SISTEMI Z DINAMIKO PRVEGA IN DRUGEGA REDA
Mentor: izr. prof. dr. Janez Cerar
Datum zagovora: 10. 9. 2020

Špela NOVAK
MIKROINKAPSULACIJA TRDNEGA JEDRNEGA MATERIALA Z MELAMINSKO FORMALDEHIDNO SMOLO
Mentor: viš. pred. dr. Branko Alič
Datum zagovora: 14. 9. 2020

Sara MARINKOVIĆ
PIPERAZIN IN DERIVATI KOT LIGANDI V KOORDINACIJSKIH SPOJINAH BAKRA(II)
Mentorica: doc. dr. Barbara Modec
Datum zagovora: 18. 9. 2020

Vesna DAVIDOVIĆ
OKOLJU PRIJAZNA SINTEZA PROPILEN KARBONATA Z UPORABO KATALIZATORJEV NA OSNOVI CERIJEVEGA DIOKSIDA
Mentorica: prof. dr. Urška Lavrenčič Štangar
Datum zagovora: 18. 9. 2020

Monika LIŠTER
SINTEZA IN HIDROGENIRANJE SUBSTITUIRANEGA METIL AKRILATA
Mentor: izr. prof. dr. Bogdan Štefane
Datum zagovora: 24. 9. 2020

Tanja JANKO
ELEKTROKEMIJSKA PRETVORBA CO2 V GORIVA
Mentor: doc. dr. Črtomir Podlipnik
Datum zagovora: 24. 9. 2020

Gaja GERBEC
PRIPRAVA N-ZAŠČITENIH 5-ARIL-, 5-HETEROARIL- IN SORODNIH DERIVATOV 2H-PIRAN-2-ONOV TER NADALJNJE PRETVORBE Z DIELS–ALDERJEVIMI REAKCIJAMI DO BICIKLO[2.2.2]OKTENOV
Mentor: doc. dr. Krištof Kranjc
Datum zagovora: 25. 9. 2020

Sanja ZRNIĆ
IZRAČUN PORAZDELITVE ELEKTROLITA MED IZOTROPNO RAZTOPINO IN NABITO REŽO
Mentor: prof. dr. Jurij Reščič
Datum zagovora: 29. 9. 2020

Lavra KOS
ADENIN KOT KATION V HEKSAFLUORIDOTITANATNIH SOLEH
Mentor: doc. dr. Andrej Pevec
Datum zagovora: 5. 10. 2020

Klemen MOVRIN
ATOMI IN MOLEKULE V ELEKTRIČNEM IN MAGNETNEM POLJU
Mentor: prof. dr. Tomaž Urbič
Datum zagovora: 23. 10. 2020

Anja HREN
BAKROVE(II) SPOJINE Z ANIONOM 2-METILBENZOJSKE KISLINE
Mentor: doc. dr. Bojan Kozlevčar
Datum zagovora: 26. 10. 2020

Brina SANDA
SEMIEMPIRIČNA DOLOČITEV PARNEGA TLAKA ČISTIH TEKOČIN
Mentor: prof. dr. Andrej Jamnik
Datum zagovora: 10. 11. 2020

Jakub ODLAZEK HAJDARPAŠIĆ
VPLIV ADITIVOV V ŽVEPLOVO ELEKTRODO NA DELOVANJE MAGNEZIJEVEGA AKUMULATORJA
Mentor: izr. prof. dr. Robert Dominko
Datum zagovora: 25. 11. 2020

Eva GABRIJEL
MINERALNA SESTAVA KAMNIN IN PRSTI NA PODROČJU OTOČCA
Mentorica: izr. prof. dr. Amalija Golobič
Datum zagovora: 1. 12. 2020

Urban VOZEL
BIORAZGRADLJIVI TERMOGELI
Mentor: viš. pred. dr. Branko Alič
Datum zagovora: 8. 12. 2020

Nastja SKALA
TERMOPLASTIČNI IN TERMOSETNI POLIMERI
Mentorica: prof. dr. Ksenija Kogej
Datum zagovora: 9. 12. 2020

Metka KRIŽAN
ANALIZA PUDROV V PRAHU Z RENTGENSKO PRAŠKOVNO DIFRAKCIJO
Mentor: prof. dr. Anton Meden
Datum zagovora: 22. 12. 2020

Špela ŠUBELJ
BAKROVI KOMPLEKSI Z IZBRANIMI DIKETONATI
Mentor: prof. dr. Iztok Turel
Datum zagovora: 28. 12. 2020

UNIVERZA V MARIBORU
FAKULTETA ZA KEMIJO IN KEMIJSKO TEHNOLOGIJO

1. januar – 31. december 2020

DOKTORATI

DOKTORSKI ŠTUDIJ – 3. STOPNJA

Bojana BRADIĆ
IZOLACIJA HITINA IZ MORSKE BIOMASE Z UPORABO EVTEKTIČNIH TOPIL IN ŠTUDIJA KINETIKE N-DEACETILACIJE DO HITOZANA
Datum zagovora: 27. 10. 2020

Amadeja KOLER
MIKRO STRUKTURA poliHIPE POLIMEROV, DOSEŽENA S SINEREZO, HIPERZAMREŽENJEM IN GRAFTIRANJEM
Datum zagovora: 16. 11. 2020

Marijana LAKIĆ
SINTEZA VOTLIH SFERIČNIH MAGNETNIH STRUKTUR
Datum zagovora: 10. 1. 2020

Tanja MILOVANOVIĆ
HIDROTERMIČNI PROCESI ZA KONVERZIJO LIGNOCELULOZNE BIOMASE V PRODUKTE Z VIŠJO DODANO VREDNOSTJO
Datum zagovora: 12. 10. 2020

Martin ROZMAN
UPORABA INVERZNE GEOMETRIJSKE KONFIGURACIJE ZA RAZVOJ SENZORSKIH IN ELEKTROKROMNIH TRAKOV
Datum zagovora: 11. 11. 2020

Katja VASIĆ
VEZAVA ENCIMOV NA POVRŠINSKO MODIFICIRANE MAGNETNE NOSILCE
Datum zagovora: 4. 3. 2020

Doroteja VNUČEC PAUŠNER
UPORABA TERMIČNO MODIFICIRANIH PROTEINOV ZA BIO-LEPILA
Datum zagovora: 23. 6. 2020

MAGISTERIJI

MAGISTRSKI ŠTUDIJ – 2. STOPNJA

Daša BREZNIK
ANALIZA ZASTOJEV NA PROIZVODNI LINIJI PRETISNIH OMOTOV IN PREDLOGI ZA IZBOLJŠAVE
Datum zagovora: 16. 12. 2020

Viktorija FLUCHER
FUNKCIONALIZACIJA VOLNE S POLIETILEN IMINOM ZA POVEČANJE ADSORPCIJE KOVIN
Datum zagovora: 16. 12. 2020

Eva GIDER
IZKORIŠČANJE ODVEČNIH NIZKOTEMPERATURNIH TOPLOTNIH TOKOV ZA PROIZVODNJO ENERGIJE
Datum zagovora: 20. 5. 2020

Tjaša GOLTNIK
ODSTRANJEVANJE SLEDOV ORGANSKIH ONESNAŽEVAL IZ MODELNIH ODPADNIH VOD Z UPORABO OSMOZNEGA PROCESA
Datum zagovora: 9. 9. 2020

Domen HORVAT
IZOLACIJA KANABINOIDOV IZ INDUSTRIJSKE KONOPLJE
Datum zagovora: 28. 9. 2020

Natalija JANČIČ
ŠTUDIJA BIOLOŠKE OBDELAVE KONDENZACIJSKIH VOD PODJETJA CINKARNA CELJE
Datum zagovora: 16. 12. 2020

Laura KOVAČEC
RAZVOJ IN VALIDACIJA METODE Z MODIFICIRANO Bi-Cu ELEKTRODO IZ STEKLASTEGA OGLJIKA
Datum zagovora: 18. 3. 2020

Katja Andrina KRAVANJA
SINTEZA, OPTIMIZACIJA IN APLIKACIJA HITOZANSKIH IN ALGINATNIH AEROGELOV TER NJUNIH KOMPOZITOV
Datum zagovora: 18. 11. 2020

Mateja KREMPL
SOČASNO DOLOČANJE FERULNE, KAVNE IN p-KUMARNE KISLINE V RASTLINSKIH VZORCIH S TEKOČINSKO KROMATOGRAFIJO
Datum zagovora: 20. 5. 2020

Nika KUČUK
UPORABA UČINKOVIN IZ IZBRANIH VRST SADJA V BIOMEDICINSKE NAMENE
Datum zagovora: 9. 9. 2020

Špela LESIČAR
ANTIOKSIDATIVNE LASTNOSTI BIOLOŠKO AKTIVNIH KOMPONENT V EKSTRAKTIH ČRNE KUMINE IN NJIHOV VPLIV NA VIABILNOST HUMANIH CELIC
Datum zagovora: 8. 7. 2020

David MAJER
RAZVOJ IN VALIDACIJA ELEKTROANALIZNIH METOD ZA DOLOČANJE EPINEFRINA, ASKORBINSKE KISLINE IN SEČNE KISLINE
Datum zagovora: 9. 9. 2020

Manca MERSLAVIČ
UPORABA GLOBOKO EVTEKTIČNIH TOPIL KOT ZELENE ALTERNATIVE ZA EKSTRAKCIJO AKTIVNIH UČINKOVIN IZ PEGASTEGA BADLJA (SILYBUM MARIANUM)
Datum zagovora: 3. 9. 2020

Mihela MIHELIČ
ANALIZA PREVLEK, PRIPRAVLJENIH NA OSNOVI ELEKTROPREDENJA IN 3D-TISKANJA
Datum zagovora: 14. 5. 2020

Monika MULEC
DOLOČANJE TEŽKIH KOVIN V MORSKI HRANI Z ICP-OES
Datum zagovora: 16. 10. 2020

Alen PLAJNŠEK
ŠTUDIJA RAZTAPLJANJA ELEMENTARNEGA BAKRA Z ŽVEPLOVO (VI) KISLINO V AEROBNIH RAZMERAH
Datum zagovora: 21. 10. 2020

Anja RANER
RAZVOJ POROZNIH BIORAZGRADLJIVIH STRUKTUR ZA BIOMEDICINSKE APLIKACIJE
Datum zagovora: 23. 9. 2020

Matevž ROŠKARIČ
KATALITSKA HIDROGENACIJA OGLJIKOVEGA DIOKSIDA V METANOL V PRISOTNOSTI KATALIZATORJEV NA OSNOVI ŽLAHTNIH KOVIN
Datum zagovora: 9. 9. 2020

Ajda SUŠNIK
ADHEZIJA MODELNIH CELIC NA KOVINSKE ELEKTRODE ZA UPORABO V BIOSENZORIKI
Datum zagovora: 23. 12. 2020

Marko ŠKET
SPREMLJANJE REOLOŠKIH LASTNOSTI ANORGANSKIH PRAHOV
Datum zagovora: 19. 2. 2020

Zala ŠTUKOVNIK
IZDELAVA IN OPTIMIZACIJA ELEKTROKEMIJSKE CELICE ZA UPORABO V BIOSENZORIKI
Datum zagovora: 23. 10. 2020

Ines ŠVEGELJ
MODELIRANJE ŠARŽNEGA BIOPROCESA REKOMBINANTNEGA MONOKLONSKEGA PROTITELESA
Datum zagovora: 21. 10. 2020

Aleksandra VERDNIK
IZOLACIJA KERATINA IZ ODPADNE VOLNE S HIDROTERMIČNIMI POSTOPKI
Datum zagovora: 23. 9. 2020

Tina ZOREC
DOLOČANJE ANTIMIKROBNE UČINKOVITOSTI GRANATNEGA JABOLKA
Datum zagovora: 23. 9. 2020

Tomaž ZUPANC
RAZKROJ BLATA IZ RAZTOPINE PO RAZKLOPU ILMENITA/ŽLINDRE V LABORATORIJSKI MIKROVALOVNI PEČICI
Datum zagovora: 8. 7. 2020

DIPLOME – UNIVERZITETNI ŠTUDIJ

UNIVERZITETNI ŠTUDIJ – 1. STOPNJA

Nejc ARH
REGULACIJA TLAKA S POVRATNO-ZANČNO PID REGULACIJO IN VIRTUALIZACIJA PROCESA
Datum zagovora: 7. 9. 2020

Davor BABIČ
IZRAŽANJE DOLGE NEKODIRAJOČE RNA CCAT1 PRI BOLNIKIH Z RAKOM GLAVE IN VRATU
Datum zagovora: 9. 9. 2020

Martin BELCER
OPTIMALNA PROSTORSKA RAZPOREDITEV PROCESNIH NAPRAV ZA IZBOLJŠANJE INHERENTNE VARNOSTI
Datum zagovora: 18. 11. 2020

Nicole BLAŽEVIĆ
VPLIV ZAMREŽENJA POROZNE POLI(AKRILNE KISLINE) NA ABSORPTIVNE LASTNOSTI
Datum zagovora: 9. 9. 2020

Urška BRENCE
MODELIRANJE POSLEDIC IZLITJA RAZTOPIN VODIKOVEGA FLUORIDA IN NATRIJEVEGA HIDROKSIDA
Datum zagovora: 3. 9. 2020

Žan BRINOVŠEK
PROUČEVANJE METOD IN POSTOPKOV ČIŠČENJA KERAMIČNE MEMBRANE PO MIKROFILTRACIJI SUROVE SIROTKE
Datum zagovora: 9. 9. 2020

Adam BRUMEN
PREUČEVANJE ADSORPCIJSKIH LASTNOSTI ŠUNGITA
Datum zagovora: 9. 9. 2020

Nejc BRUNČEK
POLIMERIZACIJA BENZIL KLORIDNIH DERIVATOV V EMULZIJSKIH MEDIJIH
Datum zagovora: 9. 9. 2020

Nikolina CETIN
OPTIMIZACIJA ELEKTROKROMNEGA TRAKU Z RAZLIČNIMI VRSTAMI KOVINSKIH OKSIDOV
Datum zagovora: 9. 9. 2020

Anja COPOT
PAMETNE PREVLEKE ZA ZAŠČITO KONSTRUKCIJSKIH MATERIALOV
Datum zagovora: 9. 9. 2020

Ana Marija ČREŠNAR
Razgradnja pvc ODPADKOV s hidrotermičnimi procesi
Datum zagovora: 9. 9. 2020

Klemen DOPLIHAR
FORMULIRANJE NAPROKSENA V POLIMERE S SUPERKRITIČNIMI FLUIDI
Datum zagovora: 9. 9. 2020

Franjo FREŠER
TVORBA KOORDINACIJSKIH SPOJIN MED OSNOVNIMI GRADNIKI TANINOV IN Fe(II)
Datum zagovora: 9. 9. 2020

Maja GABRIČ
SPECIACIJSKA ANALIZA KROMA V VINU IN PIVU Z UPORABO TEKOČINSKE KROMATOGRAFIJE Z VISOKO LOČLJIVOSTJO, MASNE SPEKTROMETRIJE Z INDUKTIVNO SKLOPLJENO PLAZMO IN OBOGATENIH STABILNIH IZOTOPOV 53Cr(III) TER 50Cr(VI)
Datum zagovora: 3. 9. 2020

Tamara GALUN
FUNKCIONALIZACIJA GLICIDILMETAKRILATNIH HIERARHIČNO POROZNIH POLIMEROV
Datum zagovora: 9. 9. 2020

Maja GRAČNER
ENKAPSULACIJA ANTIBIOTIKOV V POROZNE POLIMERNE STRUKTURE
Datum zagovora: 3. 9. 2020

Laura GRUŠKOVNJAK
PRIPRAVA POROZNIH BIOMATERIALOV
Datum zagovora: 23. 9. 2020

Urban GSELMAN
VZDRŽLJIVOSTNI TESTI VOTLO-VLAKNASTIH OSMOZNIH MEMBRANSKIH MODULOV
Datum zagovora: 3. 9. 2020

Špela HABJANIČ
FERMENTACIJA ČAJA S KOMBUČO: TEHNOLOŠKI VIDIK PROCESA
Datum zagovora: 9. 9. 2020

Lucija HAJDINJAK
KROMATOGRAFSKO DOLOČANJE VSEBNOSTI BISFENOLA A V EMBALIRANIH VODAH
Datum zagovora: 9. 9. 2020

Tjaša HEDŽET
FENOLNE IN LIPIDNE KOMPONENTE V EKSTRAKTU KAVE Z RAZLIČNIM GEOGRAFSKIM POREKLOM
Datum zagovora: 7. 9. 2020

Mojca HRAŠ
OPTIMIZACIJA EKSTRAKCIJE IN VALIDACIJA ANALIZNE METODE AESCINA IZ EKSTRAKTA DIVJEGA KOSTANJA
Datum zagovora: 9. 9. 2020

Sara KARLOVŠEK
STABILNOST CINKOVEGA OKSIDA V GELSKIH STRUKTURAH IN NJEGOVO ANTIBAKTERIJSKO DELOVANJE
Datum zagovora: 9. 9. 2020

Klara Laura KONDA
KOFEIN KOT INHIBITOR KOROZIJSKIH PROCESOV V AGRESIVNEM MEDIJU
Datum zagovora: 9. 9. 2020

Sandra KOPŠE
VEČSTOPENJSKO ODSTRANJEVANJE TEŽKIH KOVIN IZ REČNIH SEDIMENTOV
Datum zagovora: 3. 9. 2020

Matic KOŠIR
PRIMERJAVA BIOPROCESOV S CELIČNO LINIJO CHO V RAZLIČNIH BIOREAKTORJIH
Datum zagovora: 9. 9. 2020

Marjetka KOUTER
KONTROLIRANO SPROŠČANJE FEBUKSOSTATA IN DOLOČITEV KONCENTRACIJE V SERUMU IN URINU
Datum zagovora: 7. 9. 2020

Adriana KRALJ
CITOTOKSIČNOST IN UČINKOVITOST C87-INHIBITORJA TUMORJE - NEKROTIZIRAJOČEGA FAKTORJA ALFA NA HUMANIH CELIČNIH LINIJAH
Datum zagovora: 9. 9. 2020

Analina KRALJ
PRIMERJAVA ENERGETSKE UČINKOVITOSTI VEČSTANOVANJSKIH OBJEKTOV V RAZLIČNIH OBDOBJIH
Datum zagovora: 9. 9. 2020

Špela Vivijana KRISTAN
DOLOČEVANJE TEŽKIH KOVIN IN TOKSIČNIH ORGANSKIH SPOJIN V EKSTRAKTIH LISTOV LAWSONIA INERMIS L
Datum zagovora: 28. 5. 2020

Eva KROPUŠEK
POVRŠINSKA FUNKCIONALIZACIJA MAGNETNIH NANODELCEV (MND) ZA UPORABO V OSMOTSKIH PROCESIH ČIŠČENJA ODPADNIH VOD
Datum zagovora: 3. 9. 2020

Mitja MACUR
STABILNOST INKAPSULIRANE HRENOVE PEROKSIDAZE
Datum zagovora: 21. 10. 2020

Kaja MAKOTER
DOLOČEVANJE LAHKOHLAPNIH IN TEŽJEHLAPNIH SPOJIN V EKSTRAKTIH RASTLIN IZ DRUŽINE ZINGIBERACEAE Z UPORABO RAZLIČNIH KROMATOGRAFSKIH TEHNIK
Datum zagovora: 3. 9. 2020

Ines MASTEN
DETEKCIJA OHRANJENIH VOD NA MEDPROTEINSKIH POVRŠINAH
Datum zagovora: 9. 9. 2020

Lara METLIKA
BIOOZNAČEVALCI ZA NAPOVED ODZIVA NA VEDOLIZUMAB PRI BOLNIKIH S KRONIČNO VNETNO ČREVESNO BOLEZNIJO
Datum zagovora: 17. 9. 2020

Erik MIHELIČ
RAZVOJ METODE ZA DOLOČEVANJE EKVIVALENTNE TOČKE PRI OBARJANJU FLUORIDOV IZ EKSTRAKTA PO OBDELAVI IZRABLJENIH KATODNIH OSTANKOV ELEKTROLIZE ALUMINIJA
Datum zagovora: 9. 9. 2020

Anže NOVAK
VALIDACIJA METODE ZA DOLOČANJE Zn(II), Cd(II) IN Pb(II) Z UPORABO INTERNEGA STANDARDA
Datum zagovora: 9. 9. 2020

Monika OSTROŠKO
POVEZAVA EPIGENETSKIH IN EKSPRESIJSKIH MARKERJEV PRI RAKU GLAVE IN VRATU
Datum zagovora: 9. 9. 2020

Nika OZIS
VPLIV STRUKTURE TIOLA NA POLIMERIZACIJE V KOLOIDNIH MEDIJIH
Datum zagovora: 9. 9. 2020

Janez PALČNIK
VPLIV CINHONIDINA NA TIOL-EN POLIMERIZACIJO MULTIFUNKCIONALNIH TIOLOV Z ALKENI
Datum zagovora: 9. 9. 2020

Nika PETELINŠEK
PRIDOBIVANJE NANODELCEV Mg1+xFe2-2xTixO4 S TERMIČNIM RAZKROJEM
Datum zagovora: 8. 7. 2020

Domen PETRIČ
OPTIMIRANJE INAKTIVACIJE ENCIMOV V GRAHAM MOKI
Datum zagovora: 23. 9. 2020

Vito PRŠA
BIOLOŠKA AKTIVNOST NARAVNIH EKSTRAKTOV IZ ZAČIMB
Datum zagovora: 9. 9. 2020

Matjaž RANTAŠA
SINTEZA IN KARAKTERIZACIJA HIDROFILNIH MAGHEMITNIH NANODELCEV PREVLEČENIH S CITRATOM
Datum zagovora: 3. 9. 2020

Simona SEDONJA
INHIBICIJSKA UČINKOVITOST PROPOLISA V NAMEN ZAŠČITE KONSTRUKCIJSKIH MATERIALOV
Datum zagovora: 9. 9. 2020

Tjaša SKARLOVNIK
ANALIZA REZULTATOV ZA POVRŠINSKO ZAŠČITO
Datum zagovora: 3. 9. 2020

Gal SLAČEK
VPLIV EKSTRAKCIJSKE METODE NA VSEBNOST BIOAKTIVNIH KOMPONENT BRUSNICE (VACCINIUM VITIS-IDAEA) IN ANTIMIKROBNI POTENCIAL
Datum zagovora: 9. 9. 2020

Saša STANKOVIĆ
SINTEZA IN KARAKTERIZACIJA MEZOPOROZNIH KISLINSKIH KATALIZATORJEV
Datum zagovora: 9. 9. 2020

Julija STRUNČNIK
ODPRTOKODNI PROCESNI SIMULATOR DWSIM KOT ALTERNATIVA PROCESNEMU SIMULATORJU ASPEN PLUS
Datum zagovora: 17. 8. 2020

Lucija ŠPES
VSEBNOST ŠČITNIČNIH HORMONOV IN VITAMINA D3 V KRVNEM SERUMU
Datum zagovora: 28. 9. 2020

Mihaela ŠVEC
STABILNOST LAKAZE V SC CO2
Datum zagovora: 9. 9. 2020

Eva TRATNIK
VPLIV POSTOPKA EKSTRAKCIJE NA KVALITETO EKSTRAKTA IZ YERBA MATE (ILEX PARAGUARIENSIS)
Datum zagovora: 3. 9. 2020

Katarina TURK
PROIZVODNJA AMONIJAKA IZ ODPADNIH PLINOV
Datum zagovora: 3. 9. 2020

Staša VELCL
ANALIZA KEMIJSKEGA PROSTORA, KI GA ZAVZEMAJO PROTIBAKTERIJSKE UČINKOVINE
Datum zagovora: 9. 9. 2020

Andrej ZIDARIČ
VPLIV TEMPERATURE NA IZOLACIJO KOMPONENT INDUSTRIJSKE KONOPLJE
Datum zagovora: 9. 9. 2020

Matija ZIMŠEK
PREVERJANJE LASTNOSTI SIROTKINEGA KONCENTRATA PO NANOFILTRACIJI
Datum zagovora: 7. 9. 2020

Nika ŽURGA
ANALIZA SLEDOV TEŽKIH KOVIN V KAPLJICI VZORCA S SISTEMOM LABORATORIJA NA ČIPU
Datum zagovora: 28. 8. 2020

DIPLOME – VISOKOŠOLSKI STROKOVNI ŠTUDIJ

VISOKOŠOLSKI STROKOVNI ŠTUDIJ – 1. STOPNJA

Tina FILE
RACIONALIZACIJA PRALNEGA POSTOPKA PUFRNIH REZERVOARJEV
Datum zagovora: 9. 9. 2020

Ana GARMUT
PREUČEVANJE VPLIVNIH DEJAVNIKOV ZA IZBOLJŠANJE KOAGULACIJE INDUSTRIJSKE ODPADNE VODE
Datum zagovora: 9. 9. 2020

Monika GOBEC
GOJENJE PLEUROTUS OSTREATUS NA RAZLIČNIH SUBSTRATIH IZ ODPADNEGA MATERIALA
Datum zagovora: 3. 9. 2020

Kaja Mateja HAFNER
KREIRANJE ZBIRKE VPRAŠANJ IN ELEKTRONSKEGA TESTA PRI PREDMETU MATERIALI
Datum zagovora: 17. 8. 2020

Maja HRLEC
DOLOČITEV KONSTANTE STABILNOSTI VKLJUČITVENIH KOMPLEKSOV METILORANŽ/Â-CIKLODEKSTRIN IN KVERCETIN/Â-CIKLODEKSTRIN
Datum zagovora: 9. 9. 2020

Amadeja JERAJ
SKUPNE GENSKE ZNAČILNOSTI BOLNIKOV Z ASTMO IN ATOPIJSKIM DERMATITISOM
Datum zagovora: 10. 7. 2020

Petra KORBER
PRIMERJAVA NEKATERIH EKSTRAKCIJSKIH METOD ZA DOLOČANJE VSEBNOSTI KALIJA V TRDNIH MATERIALIH
Datum zagovora: 9. 9. 2020

Živa NEKREP
VSEBNOST FTALATOV V BIOLOŠKEM MEDIJU
Datum zagovora: 7. 9. 2020

Denisa PERŠON VARGA
UČINKOVITOST FILTRIRNE STISKALNICE KOT METODE PREDČIŠČENJA KOMPOSTNE ODPADNE VODE
Datum zagovora: 22. 1. 2020

Nina PODLESNIK
FRAGMENTACIJA VLAKEN IZ MELAMINSKIH ETERIFICIRANIH SMOL V NARAVNEM OKOLJU
Datum zagovora: 9. 9. 2020

Maja POLJŠAK
ODSTRANJEVANJE TEŽKIH KOVIN IZ KONTAMINIRANIH ZEMLJIN S ŠIBKIMI KISLINAMI
Datum zagovora: 21. 10. 2020

Nejc POPRIJAN
OPTIMIZACIJA PROCESA DEKARBONATIZACIJE SUROVE VODE V TEŠ
Datum zagovora: 9. 9. 2020

Noemi SEP
ODSTRANJEVANJE TEŽKIH KOVIN IZ TRDNE FRAKCIJE DIGESTATA AKTIVNEGA BLATA S POMOČJO MAGNETNIH NANODELCEV
Datum zagovora: 9. 9. 2020

Kaja SMODIŠ
UPORABA TEKOČE FRAKCIJE DIGESTATA BLATA IZ ČISTILNIH NAPRAV KOT VIRA NUTRIENTOV ZA IMOBILIZIRANE ALGE
Datum zagovora: 3. 9. 2020

UNIVERZA V NOVI GORICI
FAKULTETA ZA PODIPLOMSKI ŠTUDIJ
1. januar – 31. december 2020

DOKTORATI

PODIPLOMSKI ŠTUDIJSKI PROGRAM ZNANOSTI O OKOLJU – 3. STOPNJA

Klemen TERAN
HOUSEHOLD AND ROAD DUST AS INDICATORS OF AIRBORNE PARTICULATE MATTER ELEMENTAL COMPOSITION
Mentorja: dr. Gorazd Žibret in prof. dr. Mattia Fanetti
Datum zagovora: 1. 12. 2020

FAKULTETA ZA ZNANOSTI O OKOLJU
1. januar – 31. december 2020

MAGISTERIJI

ŠTUDIJSKI PROGRAM OKOLJE – 2. STOPNJA

Mateja PEČNIK
OSNUTEK STRATEGIJE ZA PREHOD MESTNE OBČINE NOVA GORICA DO OBČINE BREZ ODPADKOV
Mentor: prof. dr. Andrej Kržan
Datum zagovora: 2. 3. 2020

Ajda DELIĆ
STARANJE NITROGVAJAKOLA POD VPLIVOM SONČNE SVETLOBE
Mentorja: dr. Martin Šala in dr. Ana Kroflič
Datum zagovora: 3. 6. 2020

DIPLOME

ŠTUDIJSKI PROGRAM OKOLJE – 1. STOPNJA

Ana PETRIČ
ANALIZA VPLIVA IZKUŠENJ IN ZNANJA NA ODNOS RAZLIČNIH INTERESNIH SKUPIN PREBIVALCEV SLOVENIJE DO RJAVEGA MEDVEDA TER NAČIN POROČANJA MEDIJEV O TEJ VRSTI
Mentorica: dr. Jana Laganis
Datum zagovora: 15. 7. 2020

Franci NOVAK
REDUCTION OF CARBON FOOTPRINT AT PORSCHE INTER AUTO
Mentorica: Renata Zupančič
Datum zagovora: 25. 8. 2020

Kaja KARNER
ŽIVLJENJE SLOVENSKEGA GOZDA
Mentorica: Nataša Gliha
Datum zagovora: 31. 8. 2020

Manuel PERSOGLIA
PONOVNA IZPOSTAVITEV IDEALNIH POGOJEV ZA VZDRŽEVANJE SPONTANIH KRAŠKIH RASTLIN Z RAZLIČNIMI EKOLOŠKIMI POTREBAMI V BOTANIČNEM VRTU CARSIANA
Mentor: dr. Manuel Tedesco
Datum zagovora: 8. 9. 2020

Klemen LEVIČNIK
MERILNE NAPRAVE ZA KARAKTERIZACIJO OGLJIČNIH AEROSOLOV IN NJIHOVA APLIKATIVNA UPORABA
Mentorica: doc. dr. Asta Gregorič
Datum zagovora: 14. 9. 2020

Matjaž KODRUN
TEHNOLOŠKA ZASNOVA ČISTILNE NAPRAVE ZA ČIŠČENJE ODPADNIH VODA NASTALIH PRI ČIŠČENJU BIOLOŠKE OBRASTI TRUPA LADIJ – PROJEKT GREENHULL
Mentor: dr. Matej Sedlar
Datum zagovora: 14. 9. 2020

Nataša CVETKOVIĆ
EKOLOŠKI MONITORING V PROIZVODNJI CEMENTA
Mentorica: Mirjam Košuta
Datum zagovora: 14. 9. 2020

Acta Chimica Slovenica

Author Guidelines

Submissions

Submission to ACSi is made with the implicit understanding that neither the manuscript nor the essence of its content has been published in whole or in part and that it is not being considered for publication elsewhere. All the listed authors should have agreed on the content and the corresponding (submitting) author is responsible for having ensured that this agreement has been reached. The acceptance of an article is based entirely on its scientific merit, as judged by peer review. There are no page charges for publishing articles in ACSi. The authors are asked to read the Author Guidelines carefully to gain an overview and assess if their manuscript is suitable for ACSi.

Additional information

- Citing spectral and analytical data
- Depositing X-ray data

Submission material

Typical submission consists of:

- full manuscript (PDF file, with title, authors, abstract, keywords, figures and tables embedded, and references)
- supplementary files
  - ***Full manuscript*** (original Word file)
  - ***Statement of novelty*** (Word file)
  - ***List of suggested reviewers*** (Word file)
  - ***ZIP file containing graphics*** (figures, illustrations, images, photographs)
  - ***Graphical abstract*** (single graphics file)
  - ***Proposed cover picture*** (optional, single graphics file)
  - ***Appendices*** (optional, Word files, graphics files)

Incomplete or not properly prepared submissions will be rejected.

Submission process

Before submission, authors should go through the checklist at the bottom of the page and prepare for submission.

Submission process consists of 5 steps.

Step 1: Starting the submission

- Choose one of the journal sections.
- Confirm all the requirements of the ***checklist.***
- Additional plain text comments for the editor can be provided in the relevant text field.

Step 2: Upload submission

- Upload full manuscript in the form of a Word file (with title, authors, abstract, keywords, figures and tables embedded, and references).

Step 3: Enter metadata

- First name, last name, contact email and affiliation for all authors, in relevant order, must be provided. Corresponding author has to be selected. Full postal address and phone number of the corresponding author has to be provided.
- ***Title and abstract*** must be provided in plain text.
- Keywords must be provided (max. 6, separated by semicolons).
- Data about contributors and supporting agencies may be entered.
- ***References*** in plain text must be provided in the relevant text filed.

Step 4: Upload supplementary files

- Original Word file (original of the PDF uploaded in the step 2)
- ***List of suggested reviewers*** with at least five reviewers with two recent references from the field of submitted manuscript must be uploaded as a Word file. At the same time, authors should declare (i) that they have no conflict of interest with suggested reviewers and (ii) that suggested reviewers are experts in the field of the submitted manuscript.
- All ***graphics*** have to be uploaded in a single ZIP file. Graphics should be named Figure 1.jpg, Figure 2.eps, etc.
- ***Graphical abstract image*** must be uploaded separately
- ***Proposed cover picture*** (optional) should be uploaded separately.
- Any additional ***appendices*** (optional) to the paper may be uploaded. Appendices may be published as a supplementary material to the paper, if accepted.
- For each uploaded file the author is asked for additional metadata which may be provided. Depending of the type of the file please provide the relevant title (Statement of novelty, List of suggested reviewers, Figures, Graphical abstract, Proposed cover picture, Appendix).

Step 5: Confirmation

- Final confirmation is required.

Article Types

Feature Articles are contributions that are written on editor's invitation. They should be clear and concise summaries of the most recent activity of the author and his/her research group written with the broad scope of ACSi in mind. They are intended to be general overviews of the authors' subfield of research but should be written in a way that engages and informs scientists in other areas. They should contain the following (see also general directions for article structure in ACSi below): (1) an introduction that acquaints readers with the authors' research field and outlines the important questions to which answers are being sought; (2) interesting, new, and recent contributions of the author(s) to the field; and (3) a summary that presents possible future directions. Manuscripts normally should not exceed 40 pages of one column format (letter size 12, 33 lines per page). Generally, experts in a field who have made important contribution to a specific topic in recent years will be invited by an editor to contribute such an **Invited Feature Article**. Individuals may, however, send a proposal (one-page

maximum) for an Invited Feature Article to the Editor-in-Chief for consideration.

Scientific articles should report significant and innovative achievements in chemistry and related sciences and should exhibit a high level of originality. They should have the following structure:

1. Title (max. 150 characters),
2. Authors and affiliations,
3. Abstract (max. 1000 characters),
4. Keywords (max. 6),
5. Introduction,
6. Experimental,
7. Results and Discussion,
8. Conclusions,
9. Acknowledgements,
10. References.

The sections should be arranged in the sequence generally accepted for publications in the respective fields and should be successively numbered.

Short communications generally follow the same order of sections as Scientific articles, but should be short (max. 2500 words) and report a significant aspect of research work meriting separate publication. Editors may decide that a Scientific paper is categorized as a Short Communication if its length is short.

Technical articles report applications of an already described innovation. Typically, technical articles are not based on new experiments.

Preparation of Submissions

Text of the submitted articles must be prepared with Microsoft Word. Normal style set to single column, 1.5 line spacing, and 12 pt Times New Roman font is recommended. Line numbering (continuous, for the whole document) must be enabled to simplify the reviewing process. For any other format, please consult the editor. Articles should be written in English. Correct spelling and grammar are the sole responsibility of the author(s). Papers should be written in a concise and succinct manner. The authors shall respect the ISO 80000 standard [1], and IUPAC Green Book [2] rules on the names and symbols of quantities and units. The Système International d'Unités (SI) must be used for all dimensional quantities.

Graphics (figures, graphs, illustrations, digital images, photographs) should be inserted in the text where appropriate. The captions should be self-explanatory. Lettering should be readable (suggested 8 point Arial font) with equal size in all figures. Use common programs such as MS Excel or similar to prepare figures (graphs) and ChemDraw to prepare structures in their final size. Width of graphs in the manuscript should be 8 cm. Only in special cases (in case of numerous data, visibility issues) graphs can be 17 cm wide. All graphs in the manuscript should be inserted in relevant places and **aligned left**. The same graphs should be provided separately as images of appropriate resolution (see below) and submitted together in a ZIP file (Graphics ZIP). Please do not submit figures as a Word file. In **graphs**, only the graph area determined by both axes should be in the frame, while a frame around the whole graph should be omitted. The graph area should be white. The legend should be inside the graph area. The style of all graphs should be the same. **Figures and illustrations** should be of sufficient quality for the printed version, i.e. 300 dpi minimum. **Digital images and photographs** should be of high quality (minimum 250 dpi resolution). On submission, figures should be of good enough resolution to be assessed by the referees, ideally as JPEGs. High-resolution figures (in JPEG, TIFF, or EPS format) might be required if the paper is accepted for publication.

Tables should be prepared in the Word file of the paper as usual Word tables. The captions should appear above the table and should be self-explanatory.

References should be numbered and ordered sequentially as they appear in the text, likewise methods, tables, figure captions. When cited in the text, reference numbers should be superscripted, following punctuation marks. It is the sole responsibility of authors to cite articles that have been submitted to a journal or were in print at the time of submission to ACSi. Formatting of references to published work should follow the journal style; please also consult a recent issue:

1. J. W. Smith, A. G. White, *Acta Chim. Slov.* **2008**, *55*, 1055–1059.
2. M. F. Kemmere, T. F. Keurentjes, in: S. P. Nunes, K. V. Peinemann (Ed.): Membrane Technology in the Chemical Industry, Wiley-VCH, Weinheim, Germany, **2008**, pp. 229–255.
3. J. Levec, Arrangement and process for oxidizing an aqueous medium, US Patent Number 5,928,521, date of patent July 27, **1999**.
4. L. A. Bursill, J. M. Thomas, in: R. Sersale, C. Collela, R. Aiello (Eds.), Recent Progress Report and Discussions: 5th International Zeolite Conference, Naples, Italy, 1980, Gianini, Naples, **1981**, pp. 25–30.
5. J. Szegezdi, F. Csizmadia, Prediction of dissociation constant using microconstants, http://www. chemaxon.com/conf/Prediction_of_dissociation _constant_using_microco nstants.pdf, (assessed: March 31, 2008)

Titles of journals should be abbreviated according to Chemical Abstracts Service Source Index (CASSI).

Special Notes

- Complete characterization, **including crystal structure**, should be given when the synthesis of new compounds in crystal form is reported.
- Numerical **data should be reported with the number of significant digits corresponding to the magnitude** of experimental uncertainty.
- **The SI system of units and IUPAC recommendations** for nomenclature, symbols and abbreviations should be followed closely. Additionally, the authors should follow the general guidelines when citing spectral and analytical data, and depositing crystallographic data.
- **Characters** should be correctly represented throughout the manuscript: for example, 1 (one) and l (ell), 0 (zero) and O (oh), x (ex), D7 (times sign), B0 (degree sign). Use Symbol font for all Greek letters and mathematical symbols.
- The rules and recommendations of the **IUBMB** and the **International Union of Pure and Applied Chemistry (IUPAC)** should be used for abbreviation of chemical names, nomenclature of chemical compounds, enzyme nomenclature, isotopic compounds, optically active isomers, and spectroscopic data.

- **A conflict of interest** occurs when an individual (author, reviewer, editor) or its organization is involved in multiple interests, one of which could possibly corrupt the motivation for an act in the other. Financial relationships are the most easily identifiable conflicts of interest, while conflicts can occur also as personal relationships, academic competition, etc. **The Editors** will make effort to ensure that conflicts of interest will not compromise the evaluation process; potential editors and reviewers will be asked to exempt themselves from review process when such conflict of interest exists. When the manuscript is submitted for publication, **the authors** are expected to disclose any relationships that might pose potential conflict of interest with respect to results reported in that manuscript. In the Acknowledgement section the source of funding support should be mentioned. The statement of disclosure must be provided as Comments to Editor during the submission process.
- **Published statement of Informed Consent.** Research described in papers submitted to ACSi must adhere to the principles of the Declaration of Helsinki (***http://www.wma.net/e/policy/b3.htm***). These studies must be approved by an appropriate institutional review board or committee, and informed consent must be obtained from subjects. The Methods section of the paper must include: 1) a statement of protocol approval from an institutional review board or committee and 2), a statement that informed consent was obtained from the human subjects or their representatives.
- **Published Statement of Human and Animal Rights.**When reporting experiments on human subjects, authors should indicate whether the procedures followed were in accordance with the ethical standards of the responsible committee on human experimentation (institutional and national) and with the Helsinki Declaration of 1975, as revised in 2008. If doubt exists whether the research was conducted in accordance with the Helsinki Declaration, the authors must explain the rationale for their approach and demonstrate that the institutional review body explicitly approved the doubtful aspects of the study. When reporting experiments on animals, authors should indicate whether the institutional and national guide for the care and use of laboratory animals was followed.
- To avoid conflict of interest between authors and referees we expect that not more than one referee is from the same country as the corresponding author(s), however, not from the same institution.
- Contributions authored by **Slovenian scientists** are evaluated by non-Slovenian referees.
- Papers describing **microwave-assisted reactions** performed in domestic microwave ovens are not considered for publication in *Acta Chimica Slovenica.*
- *Manuscripts that are **not prepared and submitted** in accord with the instructions for authors are not considered for publication.*

Appendices

Authors are encouraged to make use of supporting information for publication, which is supplementary material (appendices) that is submitted at the same time as the manuscript. It is made available on the Journal's web site and is linked to the article in the Journal's Web edition. The use of supporting information is particularly appropriate for presenting additional graphs, spectra, tables and discussion and is more likely to be of interest to specialists than to general readers. When preparing supporting information, authors should keep in mind that the supporting information files will not be edited by the editorial staff. In addition, the files should be not too large (upper limit 10 MB) and should be provided in common widely known file formats to be accessible to readers without difficulty. All files of supplementary materials are loaded separately during the submission process as supplementary files.

Proposed Cover Picture and Graphical Abstract Image

Graphical content: an ideally full-colour illustration of resolution 300 dpi from the manuscript must be proposed with the submission. Graphical abstract pictures are printed in size 6.5 x 4 cm (hence minimal resolution of 770 x 470 pixels). Cover picture is printed in size 11 x 9.5 cm (hence minimal resolution of 1300 x 1130 pixels)

Authors are encouraged to submit illustrations as candidates for the journal Cover Picture*. The illustration must be related to the subject matter of the paper. Usually both proposed cover picture and graphical abstract are the same, but authors may provide different pictures as well.

* The authors will be asked to contribute to the costs of the cover picture production.

Statement of novelty

Statement of novelty is provided in a Word file and submitted as a supplementary file in step 4 of submission process. Authors should in no more than 100 words emphasize the scientific novelty of the presented research. Do not repeat for this purpose the content of your abstract.

List of suggested reviewers

List of suggested reviewers is a Word file submitted as a supplementary file in step 4 of submission process. Authors should propose the names, full affiliation (department, institution, city and country) and e-mail addresses of five potential referees. Field of expertise and at least two references relevant to the scientific field of the submitted manuscript must be provided for each of the suggested reviewers. The referees should be knowledgeable about the subject but have no close connection with any of the authors. In addition, referees should be from institutions other than (and countries other than) those of any of the authors. Authors declare no conflict of interest with suggested reviewers. Authors declare that suggested reviewers are experts in the field of submitted manuscript.

How to Submit

Users registered in the role of author can start submission by choosing USER HOME link on the top of the page, then choosing the role of the Author and follow the relevant link for starting the submission process.

Prior to submission we strongly recommend that you familiarize yourself with the ACSi style by browsing the journal, particularly if you have not submitted to the ACSi before or recently.

Correspondence

All correspondence with the ACSi editor regarding the paper goes through this web site and emails. Emails are sent and recorded in the web site database. In the correspondence with the editorial office please provide ID number of your manuscript. All emails you receive from the system contain relevant links. **Please do not answer the emails directly but use the embedded links in the emails for carrying out relevant actions.** Alternatively, you can carry out all the actions and correspondence through the online system by logging in and selecting relevant options.

Proofs

Proofs will be dispatched via e-mail and corrections should be returned to the editor by e-mail as quickly as possible, normally within 48 hours of receipt. Typing errors should be corrected; other changes of contents will be treated as new submissions.

Submission Preparation Checklist

As part of the submission process, authors are required to check off their submission's compliance with all of the following items, and submissions may be returned to authors that do not adhere to these guidelines.

1. The submission has not been previously published, nor is it under consideration for publication in any other journal (or an explanation has been provided in Comments to the Editor).
2. All the listed authors have agreed on the content and the corresponding (submitting) author is responsible for having ensured that this agreement has been reached.
3. The submission files are in the correct format: manuscript is created in MS Word but will be **submitted in PDF** (for reviewers) as well as in original MS Word format (as a supplementary file for technical editing); diagrams and graphs are created in Excel and saved in one of the file formats: TIFF, EPS or JPG; illustrations are also saved in one of these formats. The preferred position of graphic files in a document is to embed them close to the place where they are mentioned in the text (See ***Author guidelines*** for details).
4. The manuscript has been examined for spelling and grammar (spell checked).
5. The ***title*** (maximum 150 characters) briefly explains the contents of the manuscript.
6. Full names (first and last) of all authors together with the affiliation address are provided. Name of author(s) denoted as the corresponding author(s), together with their e-mail address, full postal address and telephone/fax numbers are given.
7. The ***abstract*** states the objective and conclusions of the research concisely in no more than 150 words.
8. Keywords (minimum three, maximum six) are provided.
9. ***Statement of novelty*** (maximum 100 words) clearly explaining new findings reported in the manuscript should be prepared as a separate Word file.
10. The text adheres to the stylistic and bibliographic requirements outlined in the ***Author guidelines***.
11. Text in normal style is set to single column, 1.5 line spacing, and 12 pt. Times New Roman font is recommended. All tables, figures and illustrations have appropriate captions and are placed within the text at the appropriate points.
12. Mathematical and chemical equations are provided in separate lines and numbered (Arabic numbers) consecutively in parenthesis at the end of the line. All equation numbers are (if necessary) appropriately included in the text. Corresponding numbers are checked.
13. Tables, Figures, illustrations, are prepared in correct format and resolution (see ***Author guidelines***).
14. The lettering used in the figures and graphs do not vary greatly in size. The recommended lettering size is 8 point Arial.
15. Separate files for each figure and illustration are prepared. The names (numbers) of the separate files are the same as they appear in the text. All the figure files are packed for uploading in a single ZIP file.
16. Authors have read ***special notes*** and have accordingly prepared their manuscript (if necessary).
17. References in the text and in the References are correctly cited. (see ***Author guidelines***). All references mentioned in the Reference list are cited in the text, and vice versa.
18. Permission has been obtained for use of copyrighted material from other sources (including the Web).
19. The names, full affiliation (department, institution, city and country), e-mail addresses and references of five potential referees from institutions other than (and countries other than) those of any of the authors are prepared in the word file. At least two relevant references (important recent papers with high impact factor, head positions of departments, labs, research groups, etc.) for each suggested reviewer must be provided. Authors declare no conflict of interest with suggested reviewers. Authors declare that suggested reviewers are experts in the field of submitted manuscript.
20. Full-colour illustration or graph from the manuscript is proposed for graphical abstract.
21. ***Appendices*** (if appropriate) as supplementary material are prepared and will be submitted at the same time as the manuscript.

Privacy Statement

The names and email addresses entered in this journal site will be used exclusively for the stated purposes of this journal and will not be made available for any other purpose or to any other party.

ISSN: 1580-3155

Koristni naslovi

Slovensko kemijsko društvo
www.chem-soc.si
e-mail: chem.soc@ki.si

Wessex Institute of Technology
www.wessex.ac.uk

SETAC
www.setac.org

European Water Association
http://www.ewa-online.eu/

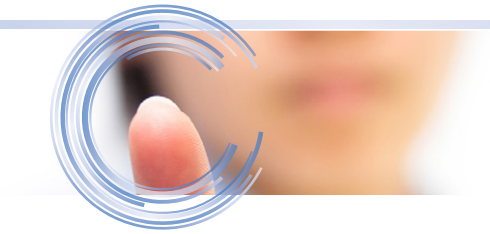
European Science Foundation
www.esf.org

European Federation of Chemical Engineering
https://efce.info/

International Union of Pure and Applied Chemistry
https://iupac.org/

Novice europske zveze kemijskih društev EuChemS najdete na:

Brussels News Updates
http://www.euchems.eu/newsletters/

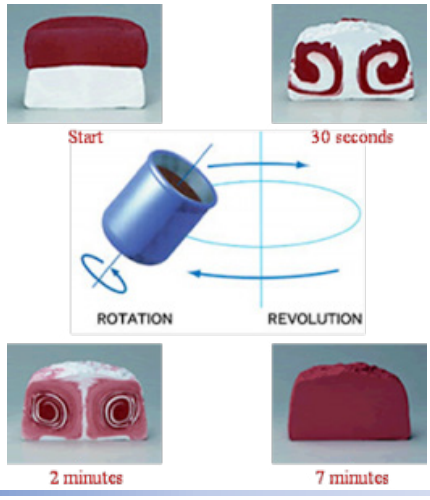


DONAU LAB Ljubljana
Member of LPPgroup

Donau Lab d.o.o., Ljubljana
Tbilisijska 85
SI-1000 Ljubljana
www.donaulab.si
office-si@donaulab.com

Planetarni centrifugalni mikser

ARM-310CE



Brezkontaktno mešanje in disperzija

Tudi za zelo viskozne materiale

Širok spekter uporabe

Atraktivna cena

THINKY



VITAMIN D3 Krka

ZAGOTOVITE SI SONCE

- **Edini kot zdravilo brez recepta**
- **Brez konzervansov in barvil**



NOVO

www.vitamind3krka.si

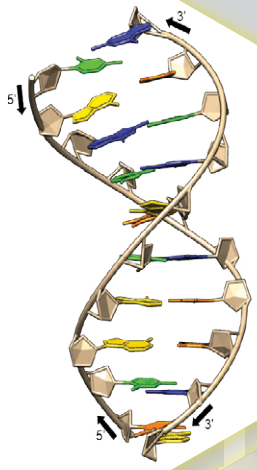
KRKA

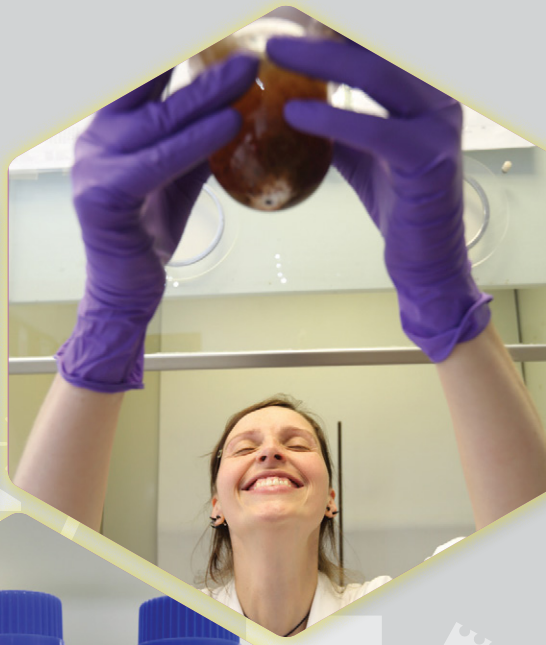
PRED UPORABO NATANČNO PREBERITE NAVODILO!
O TVEGANJU IN NEŽELENIH UČINKIH SE POSVETUJTE Z ZDRAVNIKOM ALI S FARMACEVTOM.

research EXCELLENCE

NATIONAL INSTITUTE OF CHEMISTRY

Hajdrihova 19
1000 Ljubljana
Slovenia
www.ki.si









Basic and applied research on materials, life sciences, biotechnology, chemical engineering, structural and theoretical chemistry, analytical chemistry and environmental protection.

In line with the priority areas of the EU Research and Innovation: nanotechnology, genomics and biotechnology for health, sustainable development, climate change, energy efficiency and quality and safety of food.

We expand knowledge and technology transfer to the domestic and foreign pharmaceutical, chemical, automotive and nanobiotechnologycal industries.

We are aware of the power of youth, so we transfer our knowledge on younger generations with providing many means of collaboration.

contact: mladi@ki.si

Acta Chimica Slovenica

Acta Chimica Slovenica

The use of continuous micro- and mesoscale systems offers several advantages for biotransformations with free biocatalysts, both in process development and in the realization of efficient sustainable productions (see page 1).



Year 2021, Vol. 68, No. 1

